Lecture Notes in Mechanical Engineering

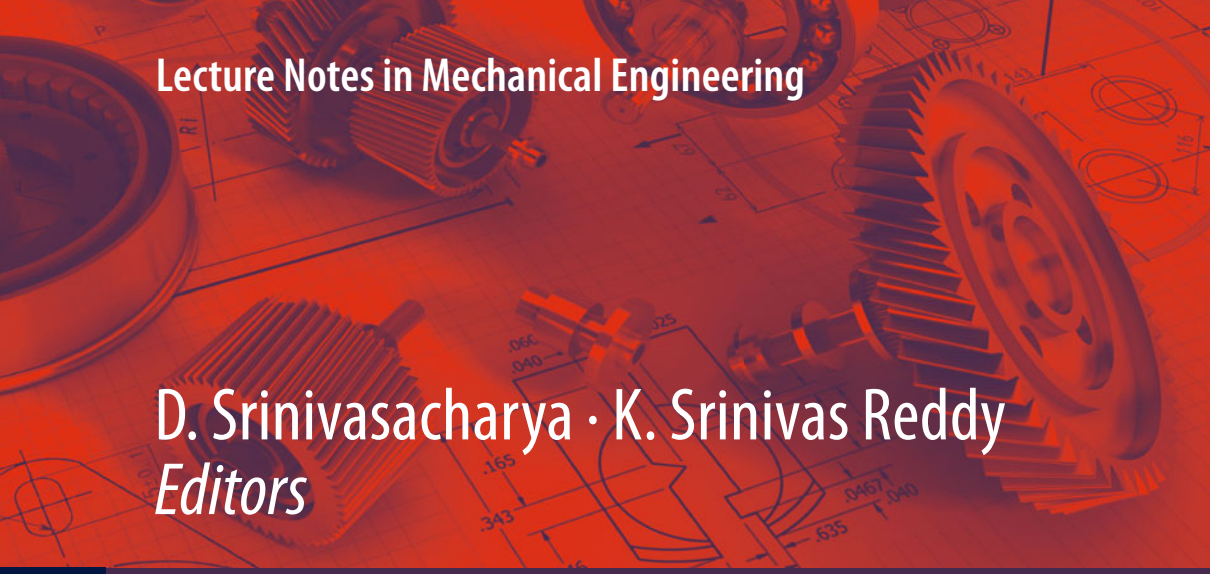

D. Srinivasacharya · K. Srinivas Reddy
Editors

Numerical Heat Transfer and Fluid Flow

Select Proceedings of NHTFF 2018

Springer

Lecture Notes in Mechanical Engineering

Lecture Notes in Mechanical Engineering (LNME) publishes the latest developments in Mechanical Engineering—quickly, informally and with high quality. Original research reported in proceedings and post-proceedings represents the core of LNME. Volumes published in LNME embrace all aspects, subfields and new challenges of mechanical engineering. Topics in the series include:

- Engineering Design
- Machinery and Machine Elements
- Mechanical Structures and Stress Analysis
- Automotive Engineering
- Engine Technology
- Aerospace Technology and Astronautics
- Nanotechnology and Microengineering
- Control, Robotics, Mechatronics
- MEMS
- Theoretical and Applied Mechanics
- Dynamical Systems, Control
- Fluid Mechanics
- Engineering Thermodynamics, Heat and Mass Transfer
- Manufacturing
- Precision Engineering, Instrumentation, Measurement
- Materials Engineering
- Tribology and Surface Technology

To submit a proposal or request further information, please contact: Dr. Leontina Di Cecco Leontina.dicecco@springer.com or Li Shen Li.shen@springer.com.

Please check the Springer Tracts in Mechanical Engineering at http://www.springer.com/series/11693 if you are interested in monographs, textbooks or edited books. To submit a proposal, please contact Leontina.dicecco@springer.com and Li.shen@springer.com.

More information about this series at http://www.springer.com/series/11236

D. Srinivasacharya · K. Srinivas Reddy
Editors

Numerical Heat Transfer and Fluid Flow

Select Proceedings of NHTFF 2018

Springer

Editors
D. Srinivasacharya
National Institute of Technology Warangal
Warangal, Telangana, India

K. Srinivas Reddy
Indian Institute of Technology Madras
Chennai, Tamil Nadu, India

ISSN 2195-4356 ISSN 2195-4364 (electronic)
Lecture Notes in Mechanical Engineering
ISBN 978-981-13-1902-0 ISBN 978-981-13-1903-7 (eBook)
https://doi.org/10.1007/978-981-13-1903-7

Library of Congress Control Number: 2018950200

This Springer imprint is published by the registered company Springer Nature Singapore Pte Ltd.
The registered company address is: 152 Beach Road, #21-01/04 Gateway East, Singapore 189721, Singapore

Contents

About the Editors

Dr. D. Srinivasacharya is Professor of mathematics at NIT Warangal. His major areas of research include computational fluid dynamics, convective heat and mass transfer, micropolar and couple stress fluid flows, non-Newtonian fluids, biomechanics, magnetohydrodynamics, and nanofluids flow modelling. He has authored more than 185 research papers in reputed and peer-reviewed international journals. He has been actively involved in teaching undergraduate and postgraduate students, guiding Ph.D. students, and conducting major research projects at NIT Warangal. He has successfully guided fifteen Ph.D. students, completed four major research projects, and is currently involved in three sponsored research projects funded by various national agencies. He has also organized several national and international workshops/conferences at NIT Warangal.

Dr. K. Srinivas Reddy is Professor of mechanical engineering at IIT Madras. His areas of specialization are renewable energy technologies, concentrating solar thermal and PV systems, energy efficiency, and the environment. Currently, he is also Honorary Professor at the University of Exeter, and Adjunct Professor at CEERI—CSIR, Chennai. He has published more than 200 research articles in leading international journals and conferences. He has co-authored a book entitled *Sustainable Energy and the Environment: A Clean Technology Approach* published by Springer. He is actively involved in the development of concentrating solar power technologies in India and has strong associations with various industry partners. He has received several awards, such as the WSSET Innovation Award and Shri J. C. Bose Patent Award. He has also organized several national and international workshops at IIT Madras. He is an expert member of various selection committees.

An Approximate Solution of Fingering Phenomenon Arising in Porous Media by Successive Linearisation Method

Bhumika G. Choksi, Twinkle R. Singh and Rajiv K. Singh

Abstract In this article, the phenomenon of fingering in a particular displacement method concerning two immiscible fluids through a dipping homogeneous porous medium with mean capillary pressure has been discussed analytically under certain conditions. This phenomenon gives a nonlinear partial differential equation as a governing equation, which we have solved by Successive Linearisation Method (SLM).

Keywords Fluid flow through porous media · Fingering phenomenon
Similarity transformation · Successive linearisation method (SLM)

1 Introduction

The fingering (instability) phenomenon [11] of the oil–water movement in a porous medium [9] is an important phenomenon of petroleum technology [8], where water drives are employed for the recovery of oil. In fact, the fingers are the discontinuities arising on the smooth common displacement front. Buckley and Levrett [1] discussed this problem without considering capillary pressure. While the other authors like Scheidegger-Johnson [6], McEwen [3] and Verma [10] discussed this problem from different viewpoints. Verma [11] and Mehta et al. [5] gave the numerical solution of this problem with capillary pressure effect.

Here, we assume that the individual pressure of the two flowing phases can be replaced by their mean capillary pressure [10, 11] and we have obtained an expression for phase saturation distribution. The mathematical formulation gives a nonlinear par-

B. G. Choksi (✉) · T. R. Singh
Department of Applied Mathematics & Humanities, S. V. National Institute of Technology, Surat 395007, Gujarat, India
e-mail: bhumikachoksi.30@gmail.com

R. K. Singh
Department of Applied Mathematics & Humanities, GIDC Degree Engineering College, Abrama, Navsari 396406, Gujarat, India

D. Srinivasacharya and K. S. Reddy (eds.), *Numerical Heat Transfer and Fluid Flow*, Lecture Notes in Mechanical Engineering,
https://doi.org/10.1007/978-981-13-1903-7_1

Fig. 1 Fingering phenomenon during the oil recovery process

tial differential equation. Also, the injection of water into an oil formation in porous media is furnishing a two-phase liquid–liquid flow problem. Generally, such problem is encountered in the secondary oil recovery process of petroleum technology [8], replenishment problem of groundwater hydrology, geophysics, reservoir engineering [8], etc. So it is very important to discuss this phenomenon.

2 Statement of the Problem

Here, we are injecting the fluid water (w) uniformly with constant velocity, into a finite cylindrical piece of a homogeneous porous medium of length L, which is completely saturated with a native fluid oil (o). This gives a well-developed finger flow, which is called the fingering (instability) phenomenon. Also, $x=0$ (x is measured in the direction of displacement) is called the initial boundary, and because of the effect of injecting water the entire oil on the initial boundary is displaced through a small distance. The cylinder is totally surrounded by an impermeable surface except its initial boundary as shown in Fig. 1. Our main goal of the present article is to obtain a solution of this phenomenon using Successive Linearization Method (SLM) [4], which is a newly developed method.

3 Statics of Fingers

Scheidegger-Johnson [6] considered average cross-sectional area engaged by the fingers only. It shows saturation of the displacing fluid water $S_w(x, t)$ at injected water level x with time t in the porous medium. Figure 2 shows the schematic demonstration of the fingering phenomenon [11].

Scheidegger-Johnson [1] gave the following relationship:

$$k_w = S_w \quad \text{and} \quad k_o = S_o = 1 - S_w \tag{1}$$

Fig. 2 Schematic diagram of the fingering phenomenon

4 Fundamental Equations

By Darcy's law, the filtration velocity (i.e. seepage velocity) of water (V_w) and oil (V_o) can be written as [7]

$$V_w = -\frac{k_w}{\mu_w} k \frac{\partial P_w}{\partial x} \tag{2}$$

$$\text{and} \quad V_o = -\frac{k_o}{\mu_o} k \frac{\partial P_o}{\partial x} \tag{3}$$

The equations of continuity [6, 7] are given by

$$\emptyset \frac{\partial S_w}{\partial t} + \frac{\partial V_w}{\partial x} = 0 \tag{4}$$

$$\text{and} \quad \emptyset \frac{\partial S_o}{\partial t} + \frac{\partial V_o}{\partial x} = 0 \tag{5}$$

Here, we consider the phase densities as constant and the porous medium is completely saturated, so we can write

$$S_w + S_o = 1 \tag{6}$$

In a two-phase fluid flow, the capillary pressure (P_c) is the pressure discontinuity between the phases across their common interface. Also, it is a function of phase saturation [2]. So consider a continuous linear function defined as

$$P_c = -\beta S_w \quad \text{and} \quad P_c = P_o - P_w \tag{7}$$

The value of the pressure of the oil (P_o) is given as [10, 11]

$$P_o = \bar{P} + \frac{P_c}{2} \text{ with } \bar{P} = \frac{P_o + P_w}{2} \tag{8}$$

Simplifying Eqs. (2–8), we get

$$\emptyset \frac{\partial S_w}{\partial t} + \frac{1}{2} \frac{\partial}{\partial x} \left[k \frac{k_w}{\mu_w} \frac{\partial P_c}{\partial S_w} \frac{\partial S_w}{\partial x} \right] = 0 \tag{9}$$

Now, the fictitious relative permeability is a function of water saturation. So for definiteness, consider [11]

$$k_{\mathrm{w}} = S_{\mathrm{w}} \tag{10}$$

By Eqs. (7), (9) and (10), we get

$$\frac{\partial S_{\mathrm{w}}}{\partial t} - \frac{k}{2}\frac{\beta}{\mu_{\mathrm{w}}\emptyset}\frac{\partial}{\partial x}\left[S_{\mathrm{w}}\frac{\partial S_{\mathrm{w}}}{\partial x}\right] = 0 \tag{11}$$

Changing Eq. (11) into a dimensionless form by substituting

$$X = \frac{x}{L}, T = \left(\frac{k\beta}{2\mu_{\mathrm{w}}\emptyset L^2}\right)t$$

$$\text{We get } \frac{\partial S_{\mathrm{w}}}{\partial T} - \frac{\partial}{\partial X}\left[S_{\mathrm{w}}\left(\frac{\partial S_{\mathrm{w}}}{\partial X}\right)\right] = 0 \tag{12}$$

$$\text{where } S_{\mathrm{w}}(0, T) = 0; T > 0 \quad \text{and} \quad S_{\mathrm{w}}(X, 0) = 1; X > 0 \tag{13}$$

Equation (12) is a nonlinear partial differential equation describing the fingering phenomenon with capillary pressure.

Using standard similarity transformation,

$$S_{\mathrm{w}}(X, T) = g(\eta); \eta = \frac{X}{2\sqrt{T}} \tag{14}$$

By Eq. (12), we get

$$g(\eta)g''(\eta) + 2\eta g'(\eta) + \left(g'(\eta)\right)^2 = 0 \tag{15}$$

$$\text{where } g(0) = 0 \quad \text{and} \quad g(\infty) = 1 \tag{16}$$

To use SLM [4], consider a solution of Eq. (15) as

$$g = g_i + \sum_{m=0}^{i-1} g_m; \quad i = 1, 2, 3, \ldots \tag{17}$$

By Eqs. (15) and (17), and neglecting nonlinear terms in g_i, we get

$$a_{i-1}g_i'' + b_{i-1}g_i' + c_{i-1}g_i = \varphi_{i-1} \tag{18}$$

with boundary conditions

$$g_i(0) = 0 = g_i(1) \tag{19}$$

where $a_{i-1} = \sum_{m=0}^{i-1} g_m$, $b_{i-1} = 2\left(\eta + \sum_{m=0}^{i-1} g'_m\right)$, $c_{i-1} = \left(\sum_{m=0}^{i-1} g''_m\right)$ and

$$\varphi_{i-1} = -\left[2\eta \sum_{m=0}^{i-1} g'_m + \left(\sum_{m=0}^{i-1} g_m\right)\left(\sum_{m=0}^{i-1} g''_m\right) + \left(\sum_{m=0}^{i-1} g'_m\right)^2\right] \tag{20}$$

Choose

$$g_0(\eta) = 1 - \mathrm{e}^{-\eta} \tag{21}$$

which satisfies the boundary conditions (16).

By solving Eq. (18) iteratively, we get each solution for $g_i (i \geq 1)$, and thus the approximate solution for $g(\eta)$ is obtained by assuming

$$\lim_{i \to \infty} g_i = 0 \tag{22}$$

$$\text{as } g(\eta) \approx \sum_{m=0}^{K} g_m(\eta) \tag{23}$$

Now $a_{i-1}, b_{i-1}, c_{i-1}$ and r_{i-1} of Eq. (18) are known from the previous iterations for $i = 1, 2, 3, \ldots$, so it can be solved by any numerical methods easily. Here, we solved Eq. (18) using the Chebyshev spectral collocation method [4]. To apply it, transform the physical region [0, 1] into the region $[-1, 1]$ using

$$\eta = \frac{\xi + 1}{2}; \quad -1 \leq \xi \leq 1 \tag{24}$$

Consider the Gauss–Lobatto collocation points [4] to define the Chebyshev nodes in $[-1, 1]$, viz.

$$\xi_j = \cos\frac{\pi j}{N}; j = 0, 1, 2, \ldots, N \tag{25}$$

The variable g_i can be written in the truncated Chebyshev series form as

$$g_i(\xi) = \sum_{k=0}^{N} g_i(\xi_k) T_k\left(\xi_j\right) \tag{26}$$

where $T_k(\xi) = \cos\left[k \cos^{-1}(\xi)\right]$ is the kth Chebyshev polynomial. The derivatives of g_i at points ξ_k can be given as

$$\frac{\mathrm{d}^r g_i}{\mathrm{d}\eta^r} = \sum_{k=0}^{N} D_{kj}^r g_i(\xi_k) \tag{27}$$

where $D = 2\mathcal{D}$ with $\mathcal{D}$ is the Chebyshev spectral differentiation matrix, whose entries are represented as

$$\mathcal{D}_{jk} = \frac{c_j}{c_k}\frac{(-1)^{j+k}}{\xi_j - \xi_k}; j \neq k; j, k = 0, 1, 2, \ldots, N;$$

$$\mathcal{D}_{kk} = \frac{\xi_k}{2\left(1-\xi_k^2\right)}; k = 1, 2, \ldots, N-1; \mathcal{D}_{00} = \frac{2N^2+1}{6} = -\mathcal{D}_{NN} \tag{28}$$

Substituting the values of Eqs. (26–28) in Eq. (18), we get

$$A_{i-1}G_i = \Phi_{i-1} \tag{29}$$

$$\text{subject to } g_i(\xi_N) = 0, \sum_{k=0}^{N} D_{Nk}g_i(\xi_k) = 0, g_i(\xi_0) = 0 \tag{30}$$

$$\text{where } A_{i-1} = a_{i-1}D^2 + b_{i-1}D + c_{i-1} \tag{31}$$

$$G_i = [g_i(\xi_0), g_i(\xi_1), \ldots, g_i(\xi_N)]^{\mathrm{T}} \tag{32}$$

$$\Phi_{i-1} = \left[\phi_{i-1}(\xi_0), \phi_{i-1}(\xi_1), \ldots, \phi_{i-1}(\xi_N)\right]^{\mathrm{T}} \tag{33}$$

Now applying the boundary conditions $g_i(\xi_0) = 0$ and $g_i(\xi_N) = 0$, we obtained solutions for $g_i(\xi_1), g_i(\xi_2), \ldots, g_i(\xi_{N-1})$ iteratively from solving

$$G_i = A_{i-1}^{-1}\Phi_{i-1} \tag{34}$$

5 Numerical and Graphical Representation

The numerical, as well as the graphical representation of (34) for the saturation of injected water, has been discussed using MATLAB. Figure 3 represents the graph of saturation of water (S_{w}) versus distance (X) for fixed time $T = 0.01$, 0.02, 0.03, 0.04, 0.05, 0.06, 0.07, 0.08, 0.09 and 0.10, and Table 1 indicates the numerical values.

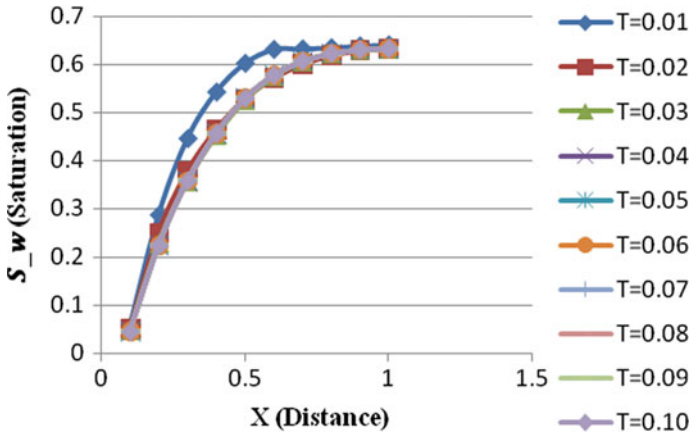

Fig. 3 Saturation of injected water $S_w(X, T)$ versus distance X for fixed time $T = 0.01, 0.02, 0.03, 0.04, 0.05, 0.06, 0.07, 0.08, 0.09$ and 0.10

Table 1 Saturation of water $S_w(X, T)$ for X and for time T

X	$T=0.01$	$T=0.02$	$T=0.03$	$T=0.04$	$T=0.05$
0.1	0.0546	0.0498	0.0462	0.0452	0.0453
0.2	0.2863	0.2488	0.2276	0.2233	0.2241
0.3	0.4454	0.3771	0.3553	0.3557	0.3574
0.4	0.5423	0.4637	0.4512	0.4552	0.4562
0.5	0.6021	0.5277	0.5246	0.529	0.5292
0.6	0.6311	0.5708	0.5745	0.5776	0.5772
0.7	0.6321	0.5996	0.6053	0.6067	0.6063
0.8	0.6345	0.6179	0.6221	0.6224	0.6221
0.9	0.6384	0.6289	0.6302	0.6302	0.6301
1.0	0.6404	0.6321	0.6321	0.6321	0.6321

(continued)

Table 1 (continued)

X	$T=0.06$	$T=0.07$	$T=0.08$	$T=0.09$	$T=0.10$
0.1	0.0454	0.0454	0.0454	0.0454	0.0454
0.2	0.2244	0.2244	0.2244	0.2244	0.2244
0.3	0.3574	0.3573	0.3573	0.3573	0.3573
0.4	0.4559	0.4558	0.4559	0.4559	0.4559
0.5	0.5289	0.5288	0.5289	0.5289	0.5289
0.6	0.5769	0.5770	0.5770	0.5770	0.5770
0.7	0.6062	0.6062	0.6062	0.6062	0.6062
0.8	0.6221	0.6221	0.6221	0.6221	0.6221
0.9	0.6301	0.6301	0.6301	0.6301	0.6301
1.0	0.6321	0.6321	0.6321	0.6321	0.6321

6 Conclusion

By SLM, we can find the saturation of injected water during the secondary oil recovery process for any distance X and any time $T > 0$. Looking at the graph, the saturation of injected water is increasing exponentially for small change in distance X and for any time T but the effect of time is very less for a small time $T \geq 0$, which is feasible with the physical phenomenon, i.e. as saturation of injected water increases, more oil can be produced during the oil recovery process.

References

1. Buckley, S.E., Leverett, M.C.: Mechanism of fluid displacement in sand. Trans. AIME. **146**, 107 (1942)
2. Chavent, G., Jaffr, J.: Mathematical models and finite elements for reservoir simulation: single phase, multiphase and multicomponent flows through porous media. Elsevier. 17 (1986)
3. McEwen, C.R.: A numerical solution of the linear displacement equation with capillary pressure. J. Petrol. Technol. **11**(08), 45–48 (1959)
4. Motsa, S.S., Marewo, G.T., Sibanda, P., Shateyi, S.: An improved spectral homotopy analysis method for solving boundary layer problems. Boundary Value Problems. **2011**(1), 3 (2011)
5. Parikh, A.K., Mehta, M.N., Pradhan, V.H.: Mathematical modeling and analysis of Fingero-Imbibition phenomenon in vertical downward cylindrical homogeneous porous matrix, In: Engineering (NUiCONE), 2013. Nirma University International Conferen on, IEEE. 1–6 (2013)
6. Scheidegger, A.E., Edward, F.J.: The statistical behavior of instabilities in displacement processes in porous media. Can. J. Phys. **39**(2), 326–334 (1961)
7. Scheidegger, A.E.: Physics of flow through porous media: In: Physics of flow throughporous media. University of Toronto pp. 201–229 (1963)
8. Skjveland, S.M., Kleppe, J.: Recent Advances in Improved Oil Recovery Methods for North Sea Sandstone Reservoirs. Norwegian Petroleum Directorate, Stavanger (1992)
9. Vafai K.: Handbook of Porous Media. Crc Press (2015)
10. Verma, A.P.: Flow of immiscible liquids in a displacement process in heterogeneous medium with capillary pressure. Vikram Univ. Math. J. 1(1), 31–46 (1966)
11. Verma, A.P.: Statistical behavior of fingering in a displacement process in heterogneous porous medium with capillary pressure. Can. J. Phys. **47**(3), 319–324 (1969)

Entropy Generation Analysis for a Micropolar Fluid Flow in an Annulus

D. Srinivasacharya and K. Himabindu

Abstract The present article investigates the entropy generation of micropolar fluid flow between two circular cylinders. The fluid flow in an annulus is due to the rotation of the outer cylinder with constant velocity. The two cylinders are maintained at different constant wall temperatures. A numerical solution using spectral quasi-linearisation method is obtained. The effect of coupling number, Brinkman number and Reynolds number on the fluid velocity, microrotation, temperature profile, entropy generation rate and Bejan number are represented graphically and analysed quantitatively.

keywords Entropy generation · Micropolar fluids · Annulus · Bejan number · Brinkman number

1 Introduction

The key concept of designing and developing the thermal machines in power plants, pipe networks and heat engines involves entropy generation. It gives the details of local and global losses of energy due to occurring of irreversibilities. The efficient utilisation of energy can be achieved by entropy generation minimisation. The entropy generation number concept is initially introduced by Bejan [1], and he examined the entropy generation profiles distribution. The performance of commercial viscometers, swirl nozzles, journal bearings, rotating electrical machines and chemical and mechanical mixing devices purely depends on the flow between two cylinders, where one or both may rotate. Mirzaparikhany et al. [2] studied the influence of Cou-

D. Srinivasacharya (✉)
Department of Mathematics, National Institute of Technology, Warangal 506004, Telangana, India
e-mail: dsc@nitw.ac.in; dsrinivasacharya@yahoo.com

K. Himabindu
Department of Mathematics, Kakatiya Institute of Technology and Science, Warangal 506004, Telangana, India

D. Srinivasacharya and K. S. Reddy (eds.), *Numerical Heat Transfer and Fluid Flow*, Lecture Notes in Mechanical Engineering,
https://doi.org/10.1007/978-981-13-1903-7_2

ette–Poiseuille slip flow on entropy generation in axially moving micro-concentric cylinders.

The fluids used in engineering and industrial processes exhibit flow properties that cannot be explained by Newtonian fluid flow model. Several models have been proposed to explain the behaviour of such fluids. One of these fluids is micropolar fluid developed by Eringen [3]. These fluids sustain body couples and couple stresses, and stress tensor is not symmetric. The objective of this paper is to analyse the entropy generation in an annulus due to micropolar fluid flow.

2 Mathematical Formulation

Consider the laminar, steady, incompressible micropolar fluid flow between vertical concentric cylinders. The radii of inner and outer cylinders are 'a' and 'b' ($a < b$), respectively. The inner cylinder is at rest, and outer cylinder is rotating with constant angular velocity ω. Cylindrical coordinate system (r, φ, z), and the flow depends only on 'r'. The inner and outer cylinders are maintained at a uniform temperatures T_a and T_b, respectively. The equations governing the steady flow of an incompressible micropolar fluid using the Boussinesq approximations are given by

$$\frac{\partial u}{\partial \varphi} = 0 \tag{1}$$

$$\frac{\partial p}{\partial r} = \frac{\rho u^2}{r} \tag{2}$$

$$-\kappa \frac{\partial \Gamma}{\partial r} + (\mu + \kappa)\left(\frac{1}{r}\frac{\partial u}{\partial r} - \frac{u}{r^2} + \frac{\partial^2 u}{\partial r^2}\right) + \rho g^* \beta_T (T - T_a) = 0 \tag{3}$$

$$-2\kappa\Gamma + \kappa\left(\frac{\partial u}{\partial r} + \frac{u}{r}\right) + \gamma\left(\frac{1}{r}\frac{\partial \Gamma}{\partial r} + \frac{\partial^2 \Gamma}{\partial r^2}\right) = 0 \tag{4}$$

$$K_f\left(\frac{1}{r}\frac{\partial T}{\partial r} + \frac{\partial^2 T}{\partial r^2}\right) + 2\kappa\left(\frac{1}{2r}\frac{\partial (ru)}{\partial r} - \Gamma\right)^2 + (\mu + \kappa)\left(\frac{\partial u}{\partial r} - \frac{u}{r}\right)^2 + \gamma\left(\frac{\partial \Gamma}{\partial r}\right)^2 = 0 \tag{5}$$

Introducing the following transformations

$$r = b\sqrt{\lambda}, \quad u = \frac{\Omega}{\sqrt{\lambda}} f(\lambda), \quad \Gamma = \frac{\Omega}{b} g(\lambda), \quad T - T_a = (T_b - T_a)\theta(\lambda) \tag{6}$$

in Eqs. (1)–(5), we get

$$-\frac{2N}{1-N}\lambda g' + \frac{4\lambda}{1-N} f'' + \sqrt{\lambda}\frac{\mathrm{Gr}}{\mathrm{Re}}\theta = 0 \tag{7}$$

$$-g + f' + \frac{2(2-N)}{m^2}(g' + \lambda g'') = 0 \tag{8}$$

$$(\lambda^3\theta'' + \lambda^2\theta') + \frac{\mathrm{Br}}{1-N}\left[(N/2)\lambda^2(f'-g)^2 + (f-\lambda f')^2 + \frac{N(2-N)}{m^2}\lambda^3 g'^2\right] = 0 \tag{9}$$

The dimensionless boundary conditions are

$$f(\lambda_0) = 0,\ g(\lambda_0) = 0,\ \theta(\lambda_0) = 0,\ f(1) = b,\ g(1) = \left[\frac{\mathrm{d}f}{\mathrm{d}\lambda}\right]_{\lambda=1},\ \theta(1) = 1$$
$$\text{where } \lambda_0 = \left(\frac{a}{b}\right)^2 \tag{10}$$

The entropy generation number [4–6] is given by

$$N_s = 4\lambda\left(\frac{\mathrm{d}\theta}{\mathrm{d}\lambda}\right)^2 + \frac{4\mathrm{Br}}{T_p}\left[\frac{1}{1-N}\left(f' - \frac{f}{\lambda}\right)^2 + \frac{N}{2(1-N)}\left(\frac{\mathrm{d}f}{\mathrm{d}\lambda} - g\right)^2 + \frac{N\lambda}{1-N}\left(\frac{2-N}{m^2}\right)\left(\frac{\mathrm{d}g}{\mathrm{d}\lambda}\right)^2\right] \tag{11}$$

which can be expressed as the sum of the entropy generation due to heat transfer irreversibility (N_h) and due to viscous dissipation (N_v).

Bejan number is the ratio of entropy generation due to heat transfer irreversibility to the overall entropy generation which is given by $\mathrm{Be} = \frac{N_\mathrm{h}}{N_\mathrm{h}+N_\mathrm{v}}$.

3 Results and Discussion

The numerical solutions for (1)–(7) are obtained using the spectral quasi-linearisation method (for details, refer [5, 6]) by fixing the parameters as $m = 2$, $T_p = 1$ and $\mathrm{Gr} = 1$.

Figure 1 depicts the effect of coupling number N on the dimensionless velocity, microrotation, temperature, entropy generation and Bejan number. The velocity decreases as N increases as observed in Fig. 1a. Moreover, it is observed that the velocity in case of micropolar fluid is less than the viscous fluid case. Figure 1b depicts that increase in coupling number increases the microrotation. It is noticed that an increase in coupling number increases the temperature shown in Fig. 1c. Figure 1d shows an increase in the entropy generation with increase in N. It is observed from Fig. 1e that the Bejan number decreases as N increases.

Figure 2a shows the velocity profile with increase in Re. As Re increases, the flow velocity decreases. Figure 2b depicts that increase in Re increases the microrotation. From Fig. 2c, the increase in the value of Reynolds number slightly increases the temperature near the outer cylinder. The effect of Reynolds number on entropy generation is presented in Fig. 2d. As the value of Re increases, the entropy generation decreases at the inner cylinder and increases at the outer cylinder. As the

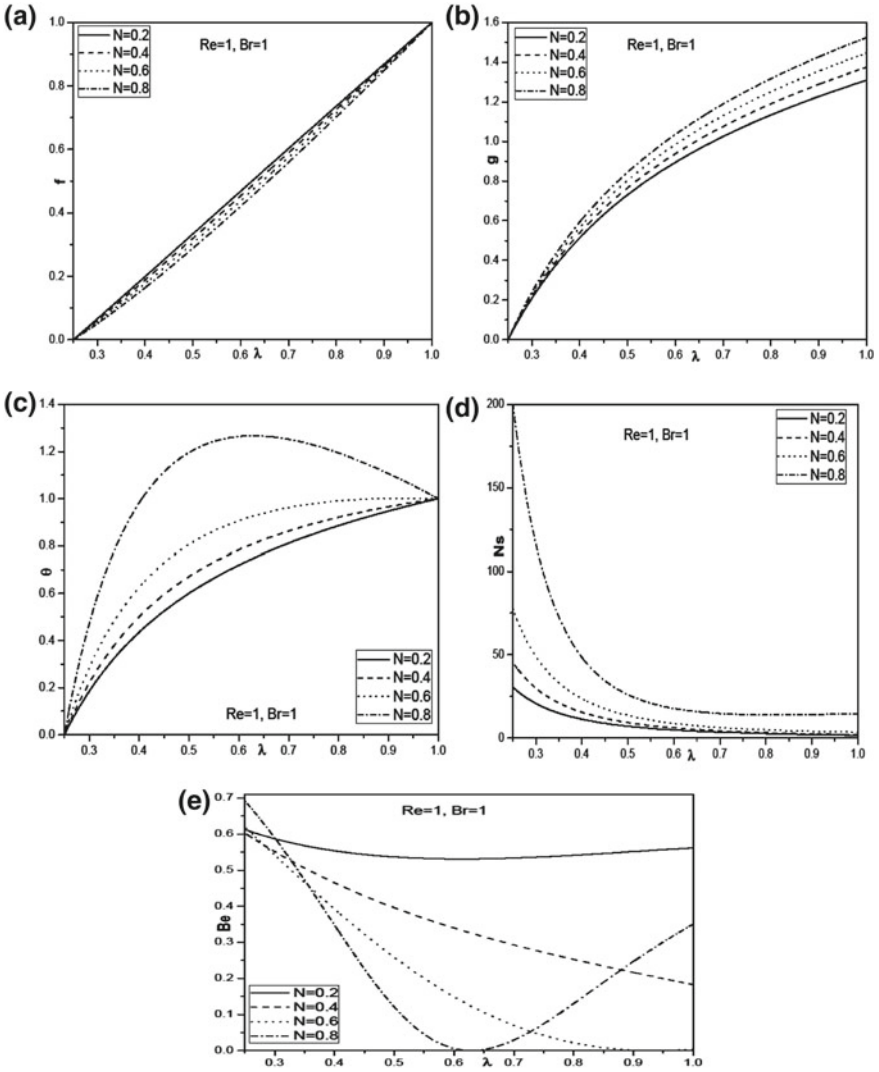

Fig. 1 Effect of coupling number on **a** velocity, **b** microrotation, **c** temperature, **d** entropy generation and **e** Bejan number

Reynolds number increases, the Bejan number increases at the inner cylinder with dominant effect of heat transfer irreversibility and decreases at the outer cylinder with increasing effect of fluid friction irreversibility as demonstrated in Fig. 2e.

It is observed from Fig. 3a that velocity does not change as the Br increases. From Fig. 3b, it is seen that as the Br increases the microrotation decreases at the outer cylinder and there is no effect of Br near the inner cylinder. Figure 3c illustrates the

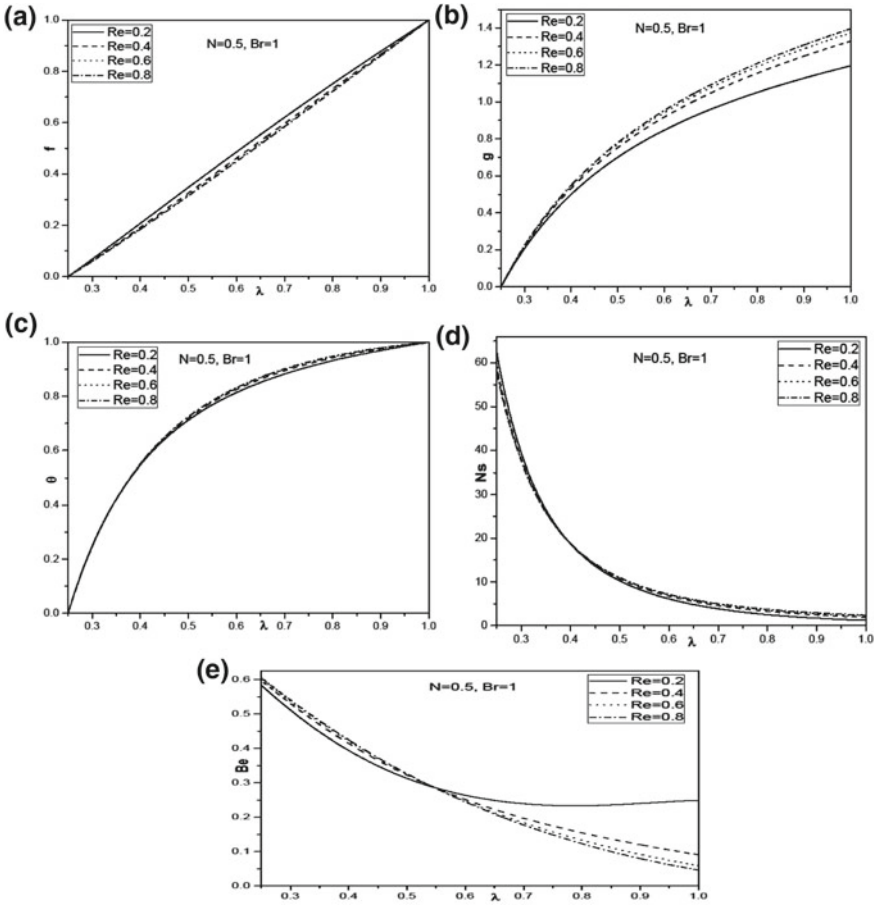

Fig. 2 Effect of Reynolds number on **a** velocity, **b** microrotation, **c** temperature, **d** entropy generation and **e** Bejan number

effect of Br on the temperature profile. It is also noticed that as Br increases, the temperature profile increases. According to definition, Br is the ratio of viscous heat generation to external heating. Thus, the higher the values of Br, the lesser will be the conduction of heat produced by viscous dissipation, and hence the larger is the temperature. The entropy generation profile for different values of Br is described in Fig. 3d. It is observed that as Br increases, the entropy generation at both cylinders increases. It has been observed that the inner cylinder behaves as a strong concentrator of irreversibility for all the parameters. As the temperature and velocity gradients are high near the inner cylinder, thus, the entropy generation number is observed as maximum in magnitude near the inner cylinder. It is observed from Fig. 3e that the Br increases near the inner and outer cylinders, while it decreases in the centre of the annulus.

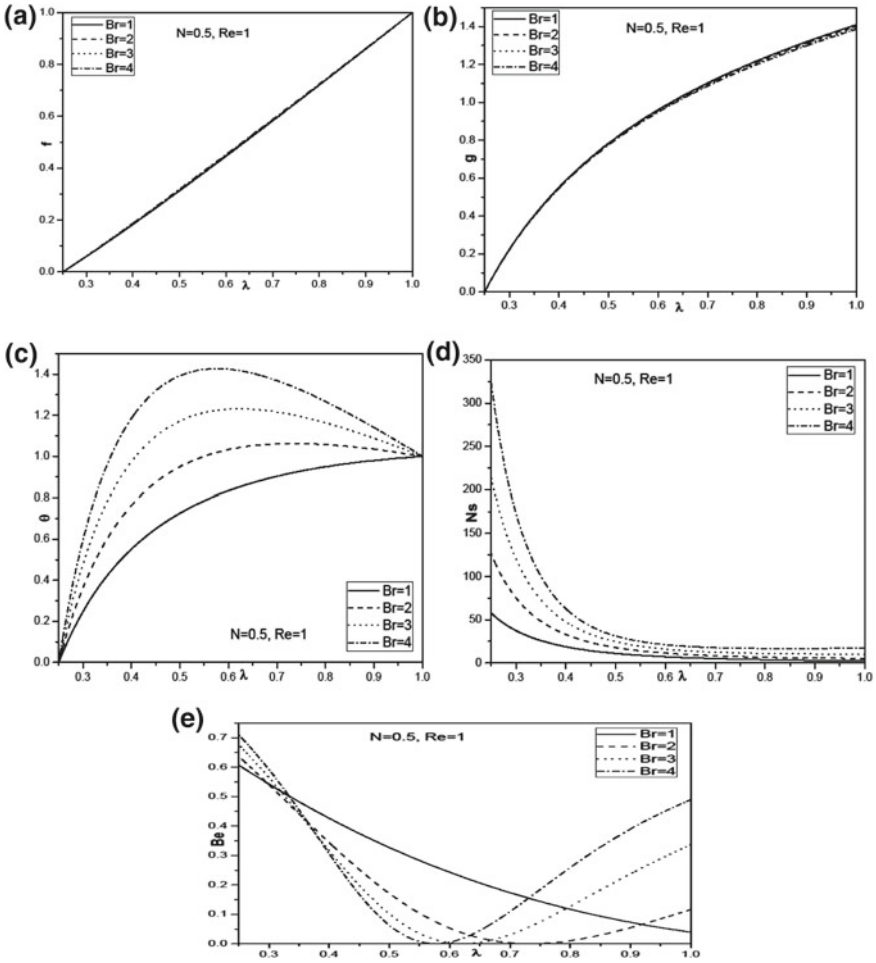

Fig. 3 Effect of Brinkman number on **a** velocity, **b** microrotation, **c** temperature, **d** entropy generation and **e** Bejan number

4 Conclusions

Entropy generation in a micropolar fluid flow between concentric circular cylinder is analysed. The velocity decreases with increasing the coupling number, whereas the microrotation and temperature increase. Bejan number decreases with the increase in the coupling number. As Brinkman number increases, Bejan number increases near the cylinders and decreases around the centre of the annulus. This is due to the differences in temperature gradients.

References

1. Bejan, A.: A study of entropy generation in fundamental convective heat transfer. J. Heat Transfer **101**, 718 (1979)
2. Mirzaparikhany, S., Abdoulalipouradl, M., Yari, M.: Entropy generation analysis for Couette-Poiseuille slip flow in a micro-annulus. J. Mach. Manuf. Autom. **3**(1) (2014)
3. Eringen, A.C.: Theory of micropolar fluids. J. Math. Mech. **16**, 1 (1966)
4. Bejan, A.: Entropy Generation Minimization. CRC Press, New York (1996)
5. Srinivasacharya, D., Himabindu, K.: Entropy generation in a porous annulus due to micropolar fluid flow with slip and convective boundary conditions. Energy **111**, 165–177 (2016)
6. Srinivasacharya, D., Himabindu, K.: Entropy generation of micropolar fluid flow in an inclined porous pipe with convective boundary conditions. Sadhana **42**(5), 729–740 (2017)

Solution of Eighth-Order Boundary Value Problems by Petrov–Galerkin Method with Quintic and Sextic B-Splines

K. N. S. Kasi Viswanadham and S. V. Kiranmayi Ch

Abstract In this paper, quintic B-splines (QBS) as basis (test) functions and sextic B-splines (SBS) as weight functions have been used in Petrov–Galerkin method to solve an eighth-order boundary value problem. The approximate solution has been modified into a form which takes care of most of the given boundary conditions. The weight functions are modified into a new set which suits for the Petrov–Galerkin method. Some examples are tested for the illustration purpose of the present method.

Keywords Boundary value problem · B-splines · Petrov–Galerkin method

1 Introduction

Consider a general eighth-order linear boundary value problem

$$p_0(t)u^{(8)}(t) + p_1(t)u^{(7)}(t) + p_2(t)u^{(6)}(t) + p_3(t)u^{(5)}(t) + p_4(t)u^{(4)}(t) + p_5(t)u'''(t) + p_6(t)u''(t) + p_7(t)u'(t) + p_8(t)u(t) = b(t),\ c < t < d \quad (1)$$

subject to boundary conditions

$$u(c) = A_0, u'(c) = A_1, u''(c) = A_2, u'''(c) = A_3,$$
$$u(d) = C_0, u'(d) = C_1, u''(d) = C_2, u'''(d) = C_3 \quad (2)$$

where $A_0, A_1, A_2, A_3, C_0, C_1, C_2$ and C_3 are finite real constants and $p_0(t), p_1(t), p_2(t), p_3(t), p_4(t), p_5(t), p_6(t), p_7(t), p_8(t)$ and $b(t)$ are all continuous functions defined on the interval $[c, d]$.

K. N. S. Kasi Viswanadham (✉) · S. V. Kiranmayi Ch
Department of Mathematics, National Institute of Technology,
Warangal 506004, Telangana, India
e-mail: kasi@nitw.ac.in

D. Srinivasacharya and K. S. Reddy (eds.), *Numerical Heat Transfer and Fluid Flow*, Lecture Notes in Mechanical Engineering,
https://doi.org/10.1007/978-981-13-1903-7_3

There are various physical processes in which an eighth-order boundary value problem arises in many applied areas [1, 2]. For the existence and uniqueness of the solutions for the problems of the type (1) and (2), one can refer [2]. Analytical solutions of these problems are available in rare cases. To solve these problems numerically, one can refer [3–10].

The present paper aims to present Petrov–Galerkin method with QBS as test functions and SBS as weight functions to solve the boundary value problems of the type (1)–(2). The quasilinearization technique has been applied to convert the nonlinear problem into a sequence of linear problems [11]. The present method has been applied to solve each one of the generated linear problems. The limit of solutions of these linear problems is the solution of the nonlinear problem. The justification of using the Petrov–Galerkin method is given in [12–14].

2 Description of the Method

The QBS, SBS and their properties are defined in [15–17]. Now suppose the approximate solution of Eqs. (1) and (2) is given by approximation for $u(t)$ as

$$u(t) = \sum_{k=-2}^{n+2} \alpha_k B_k(t) \tag{3}$$

where α_k's are the unknown parameters and $B_k(t)$'s are QBS functions. If the approximation satisfies many of the given boundary conditions, then it gives more accurate results. Accordingly, new set of test functions are defined from the test functions.

The redefinition of the test functions is given below.

Applying the boundary conditions of (2) except the third-order derivative boundary conditions to the approximation (3), we get

$$A_0 = u(c) = u(t_0) = \sum_{k=-2}^{2} \alpha_k B_k(t_0) \quad C_0 = u(d) = u(t_n) = \sum_{k=n-2}^{n+2} \alpha_k B_k(t_n) \tag{4}$$

$$A_1 = u'(c) = u'(t_0) = \sum_{k=-2}^{2} \alpha_k B'_k(t_0) \quad C_1 = u'(d) = u'(t_n) = \sum_{k=n-2}^{n+2} \alpha_k B'_k(t_n) \tag{5}$$

$$A_2 = u''(c) = u''(t_0) = \sum_{k=-2}^{2} \alpha_k B''_k(t_0) \quad C_2 = u''(d) = u''(t_n) = \sum_{k=n-2}^{n+2} \alpha_k B''_k(t_n) \tag{6}$$

Eliminating $\alpha_{-2}, \alpha_{n+2}, \alpha_{-1}, \alpha_{n+1}, \alpha_0$ and α_n from Eqs. (3) to (6), the approximation for $u(t)$ can be obtained as

$$u(t) = w(t) + \sum_{k=1}^{n-1} \alpha_k R_k(t) \tag{7}$$

where

$$w(t) = w_2(t) + \frac{A_2 - w_2''(t_0)}{Q_0'(t_0)} Q_0(t) + \frac{C_2 - w_2''(t_n)}{Q_n''(t_n)} Q_n(t)$$

$$w_2(t) = w_1(t) + \frac{A_1 - w_1'(t_0)}{P_{-1}'(t_0)} P_{-1}(t) + \frac{C_1 - w_1'(t_n)}{P_{n+1}'(t_n)} P_{n+1}(t)$$

$$w_1(t) = \frac{A_0}{B_{-2}(t_0)} B_{-2}(t) + \frac{C_0}{B_{n+2}(t_n)} B_{n+2}(t)$$

$$R_k(t) = \begin{cases} Q_k(t) - \frac{Q_k''(t_0)}{Q_0''(t_0)} Q_0(t), & k = 1, 2 \\ Q_k(t), & k = 3, 4, \ldots, n-3 \\ Q_k(t) - \frac{Q_k''(t_n)}{Q_n''(t_n)} Q_n(t), & k = n-2, n-1 \end{cases}$$

$$Q_k(t) = \begin{cases} P_k(t) - \frac{P_k'(t_0)}{P_{-1}'(t_0)} P_{-1}(t), & k = 0, 1, 2 \\ P_k(t), & k = 3, 4, \ldots, n-3 \\ P_k(t) - \frac{P_k'(t_n)}{P_{n+1}'(t_n)} P_{n+1}(t), & k = n-2, n-1, n \end{cases}$$

$$P_k(t) = \begin{cases} B_k(t) - \frac{B_k(t_0)}{B_{-2}(t_0)} B_{-2}(t), & k = -1, 0, 1, 2 \\ B_k(t), & k = 3, 4, \ldots, n-3 \\ B_k(t) - \frac{B_k(t_n)}{B_{n+2}(t_n)} B_{n+2}(t), & k = n-2, n-1, n, n+1 \end{cases}$$

The new test functions for the approximation $u(t)$ are $\{R_j(t), j = 1, 2, \ldots, n-1\}$. Here, $w(t)$ satisfies the given boundary conditions except the third-order derivative boundary conditions and $R_j(t)$'s and its first two derivatives are zero on the boundary. In Petrov–Galerkin method, the test functions for the approximation and weight functions should be equal in number. Here, the test functions used to approximate $u(t)$ described in (7) are $n-1$ and there are $n+6$ weight functions. We modify the weight functions to a set which contains $n-1$ weight functions. The modification of weight functions procedure is given below.

Let the approximation $v(t)$ is defined as

$$v(t) = \sum_{k=-3}^{n+2} \gamma_k S_k(t) \tag{8}$$

where $S_k(t)$'s are SBS and we assume that $v(t)$ and its first two derivatives are zero at c, d and third-order derivatives vanish at c. Applying this to (8), we get the approximate solution $v(t)$ as

$$v(c) = v(t_0) = \sum_{k=-3}^{2} \gamma_k S_k(t_0) = 0 \quad v(d) = v(t_n) = \sum_{k=n-3}^{n+2} \gamma_k S_k(t_n) = 0$$

$$v'(c) = v'(t_0) = \sum_{k=-3}^{2} \gamma_k S_k'(t_0) = 0 \quad v'(d) = v'(t_n) = \sum_{k=n-3}^{n+2} \gamma_k S_k'(t_n) = 0$$

$$v''(c) = v''(t_0) = \sum_{k=-3}^{2} \gamma_k S_k''(t_0) = 0 \quad v''(d) = v''(t_n) = \sum_{k=n-3}^{n+2} \gamma_k S_k''(t_n) = 0$$

$$v'''(c) = v'''(t_0) = \sum_{k=-3}^{2} \gamma_k S_k'''(t_0) = 0$$

Eliminating $\gamma_{-3}, \gamma_{-2}, \gamma_{-1}, \gamma_0, \gamma_n, \gamma_{n+1}$ and γ_{n+2} from the above set of equations and (8), we get the approximation for $v(t)$ as

$$v(t) = \sum_{k=1}^{n-1} \gamma_k \widehat{V}_k(t) \tag{9}$$

where

$$\widehat{V}_k(t) = \begin{cases} V_k(t) - \frac{V_k'''(t_0)}{V_0'''(t_0)} V_0(t), & k = 1, 2 \\ V_k(t), & k = 3, 4, \ldots., n-1 \end{cases}$$

$$V_k(t) = \begin{cases} U_k(t) - \frac{U_k''(t_0)}{U_{-1}''(t_0)} U_{-1}(t), & k = 0, 1, 2 \\ U_k(t), & k = 3, 4, 5, \ldots, n-4 \\ U_k(t) - \frac{U_k''(t_n)}{U_n'''(t_n)} U_n(t), & k = n-3, n-2, n-1 \end{cases}$$

$$U_k(t) = \begin{cases} T_k(t) - \frac{T_k'(t_0)}{T_{-2}'(t_0)} T_{-2}(t), & k = -1, 0, 1, 2 \\ T_k(t), & k = 3, 4, 5, \ldots, n-4 \\ T_k(t) - \frac{T_k'(t_n)}{T_{n+1}'(t_n)} T_{n+1}(t), & k = n-3, n-2, n-1, n \end{cases}$$

$$T_k(t) = \begin{cases} S_k(t) - \frac{S_k(t_0)}{S_{-3}(t_0)} S_{-3}(t), & k = -2, -1, 0, 1, 2 \\ S_k(t), & k = 3, 4, 5 \ldots, n-4 \\ S_k(t) - \frac{S_k(t_n)}{S_{n+2}(t_n)} S_{n+2}(t), & k = n-3, n-2, n-1, n, n+1. \end{cases}$$

Now the modified set of weight functions for $v(t)$ is $\left\{\widehat{V}_k(t)\ k = 1, 2, \ldots, n-1\right\}$. Here, $\widehat{V}_k(t)$'s, its first two derivatives are zero on the boundary. Also, its third-order derivative at left boundary vanishes. Using the Petrov–Galerkin method to (1) with the set of test functions $\{R_k(t), k=1, 2, \ldots, n-1\}$ and with the set of weight functions $\left\{\widehat{V}_k(t),\ k = 1, 2, \ldots, n-1\right\}$, we get

$$\int_{t_0}^{t_n} \left[p_0(t)u^{(8)}(t) + p_1(t)u^{(7)}(t) + p_2(t)u^{(6)}(t) + p_3(t)u^{(5)}(t) + p_4(t)u^{(4)}(t)\right.$$
$$\left. + p_5(t)u'''(t) + p_6(t)u''(t) + p_7(t)u'(t) + p_8(t)u(t)\right]\widehat{V}_i(t)\,\mathrm{d}t$$
$$= \int_{p_0}^{p_n} b(t)\hat{V}_i(t)\mathrm{d}t \quad \text{for} \quad i = 1, 2, \ldots, n-1. \tag{10}$$

The first four terms in Eq. (10) have been integrated by parts. The resulting terms are substituted in (10). After applying the approximation (7), we get a system of equations as

$$A\alpha = B,\ A = [a_{ij}];\ B = [b_i];\ \alpha = [\alpha_1\ \alpha_2 \ldots \alpha_{n-1}]^{\mathrm{T}}. \tag{11}$$

$$a_{ij} = \int_{t_0}^{t_n} \left\{p_4(t)\hat{V}_i(t)R_j^{(4)}(t) + \left[-\frac{d^5}{\mathrm{d}t^5}\left[p_0(t)\widehat{V}_i(t)\right] + \frac{d^4}{\mathrm{d}t^4}\left[p_1(t)\widehat{V}_i(t)\right]\right.\right.$$
$$\left. + p_5(t)\widehat{V}_i(t)\right]R_j''(t) + \left[\frac{d^4}{\mathrm{d}t^4}\left[p_2(t)\widehat{V}_i(t)\right] - \frac{d^3}{\mathrm{d}t^3}\left[p_3(t)\widehat{V}_i(t)\right]\right.$$
$$\left.\left. + p_6(t)\widehat{V}_i(t)\right]R_j''(t) + p_7(t)\widehat{V}_i(t)R_j'(t) + p_8(t)\hat{V}_i(t)\right]R_j(t)\Big\}\mathrm{d}t$$
$$- \frac{d^3}{\mathrm{d}t^3}\left[p_0(t)\widehat{V}_i(t)\right]_{t_n} R_J^{(4)}(t_n),$$

$$b_i = \int_{t_0}^{t_n} \left\{b(t)\hat{V}_i(t) - p_4(t)\widehat{V}_i(t)w^{(4)}(t) - \left[-\frac{d^5}{\mathrm{d}t^5}\left[a_0(t)\widehat{V}_i(t)\right]\right.\right.$$
$$+ \frac{d^4}{\mathrm{d}t^4}\left[a_1(t)\widehat{V}_i(t)\right] + p_5(t)\widehat{V}_i(t)\Big]w'''(t) - \left[\frac{d^4}{\mathrm{d}t^4}\left[p_2(t)\widehat{V}_i(t)\right]\right.$$
$$- \frac{d^3}{\mathrm{d}t^3}\left[p_3(t)\widehat{V}_i(t)\right] + p_6(t)\widehat{V}_i(t)\Big]w''(t) - p_7(t)\widehat{V}_i(t)w'(t)$$
$$\left. - p_8(t)\widehat{V}_i(t)\right]w(t)\Big\}\mathrm{d}t + \frac{d^3}{\mathrm{d}t^3}\left[p_0(t)\widehat{V}_i(t)\right]_{t_n} w^{(4)}(t_n) - \frac{d^4}{\mathrm{d}t^4}\left[p_0(t)\widehat{V}_i(t)\right]_{t_n} C_3$$
$$+ \frac{d^4}{\mathrm{d}t^4}\left[p_0(t)\widehat{V}_i(t)\right]_{t_0} A_3 + \frac{d^3}{\mathrm{d}t^3}\left[p_1(t)\widehat{V}_i(t)\right]_{t_n} C_3 + \frac{d^3}{\mathrm{d}t^3}\left[p_2(t)\widehat{V}_i(t)\right]_{t_n} C_2$$

3 Procedure of Finding the Parameters

A general element in the matrix A is evaluated by $\sum_{m=0}^{n-1} I_m$, where $I_m = \int_{t_m}^{t_{m+1}} v_i(t) r_j(t) Z(t)\,\mathrm{d}t$ and $r_j(t)$ are the QBS functions or their derivatives, and $v_i(t)$ are the SBS functions or their derivatives. To evaluate I_m, we used seven-point Gauss–Legendre quadrature formula. Here, $I_m = 0$ if $(t_{i-3}, t_{i+4}) \cap (t_{j-3}, t_{j+3}) \cap (t_m, t_{m+1}) = \varnothing$. With this, we can easily observe that the coefficient matrix A is a twelve-band diagonal matrix. Using the band matrix method, the system $A\alpha = B$ has been solved to get the parameter vector α.

4 Numerical Results

To illustrate the proposed method, we have solved one linear and one nonlinear boundary value problems. The absolute errors of approximations got by the proposed method are presented in Table 1.

Example 1 Consider the linear problem

$$u^{(8)} + \sin t\, u^{(5)} + (1 - t^2)u^{(4)} + u = (3 + \sin t - t^2)e^t, \quad 0 < t < 1 \tag{12}$$

subject to

$$u(0) = 1, u'(0) = 1,\ u''(0) = 1,\ u'''(0) = 1,$$
$$u(1) = e,\ u'(1) = e,\ u''(1) = e,\ u'''(1) = e.$$

The exact solution for (12) is $u(t) = e^t$. We have divided the interval [0, 1] into ten equal parts. The maximum absolute error obtained is 9.906925×10^{-6}.

Example 2 Consider the nonlinear problem

Table 1 Numerical results of examples 1 and 2

t	Absolute errors for example 1	Absolute errors for example 2
0.1	9.906925E−06	3.085434E−07
0.2	9.091438E−06	2.723425E−06
0.3	7.221976E−06	7.243222E−06
0.4	4.820858E−06	1.098052E−05
0.5	2.629579E−06	1.149645E−05
0.6	1.105119E−06	8.762168E−06
0.7	3.141213E−07	4.655873E−06
0.8	4.153490E−08	1.447534E−06
0.9	3.933907E−10	1.364112E−07

$$u^{(8)} + \sin u \; u''' = (1 + \sin(e^t))e^t, \quad 0 < t < 1 \tag{13}$$

subject to

$$u(0) = 1, \; u'(0) = e, \; u''(0) = 1, \; u'''(0) = 1, u(1) = 1,$$
$$u'(1) = e, \; u''(1) = e, \; u'''(1) = e.$$

The exact solution for the above problem is $u(t) = e^t$. Using quasilinearization technique [11] to (13), we get the sequence of linear boundary value problems as

$$u^{(8)}_{(m+1)} + \sin(u_{(m)})u'''_{(m+1)} + \cos(u_{(m)})u'''_{(m)}u_{(m+1)} = (1 + \sin(e^t))e^t$$
$$+ \cos(u_{(m)})u'''_{(m)}u_{(m)}, \quad m = 0, 1, 2, \ldots \tag{14}$$

subject to

$$u_{(m+1)}(0) = 1, u'_{(m+1)}(0) = 1, u''_{(m+1)}(0) = 1, u'''_{(m+1)}(0) = 1,$$
$$u_{(m+1)}(1) = e, u'_{(m+1)}(1) = e, u''_{(m+1)}(1) = e, u'''_{(m+1)}(1) = e.$$

Here, $u_{(m+1)}$ is the $(m+1)$th approximation for $u(t)$. We have divided the interval [0, 1] into ten equal parts. The maximum absolute error obtained is 1.931190×10^{-5}.

5 Conclusions

The numerical solutions of a linear and a nonlinear two-point eighth-order boundary value problems by Petrov–Galerkin method with QBS as test functions and SBS as weight functions are presented. To get the more accurate approximate solution, the QBS are defined as a set which suits to satisfy the most of the boundary conditions. The weight functions are modified according to the Petrov–Galerkin method. It is found that the obtained results are giving a little error. The strength of the method developed is the easiness of its application, accuracy, and efficiency.

References

1. Chandrasekhar, S.: Hydrodynamic and Hydromagnetic Stability. Dover, New York (1981)
2. Agarwal, R.P.: BVP for Higher Order Differential Equations. World Scientific, Singapore (1986)
3. Siddiqi, S.S., Twizell, E.H.: Int. J. Comput. Math. **60**, 295 (1996)
4. Rashidinia, J., Jalilian, R., Farajeyan, K.: Int. J. Comp. Math. **86**(8), 1319–1333 (2009)
5. Liu, G.R., Wu, T.Y.: J. Comput. Appl. Math. **145**, 223–235 (2002)
6. Akram, G., Siddiqi, S.S.: App. Math. Comput. **182**, 829–845 (2006)
7. Viswanadham, K.N.S.Kasi, Showri Raju, Y.: J. Appl. Math. **1**(1), 47–52 (2012)

8. Costabile, F., Napoli, A.: J. Appl. Math. Article id 276585, 1–9 (2014)
9. Akram, G., Rehman, H.U.: Numer. Algor. **62**, 527–540 (2013)
10. Viswanadham, K.N.S.K., Sreenivasulu, B.: Int. J. Comput. Appl. **89**(15), 7–13 (2014)
11. Bellman, R.E., Kalaba, R.E.: Quasilinearzation and Nonlinear Boundary Value Problems. American Elsevier, New York (1965)
12. Bers, L., John, F., Schecheter, M.: Partial Differential Equations. Wiley, New York (1964)
13. Lions, J.L., Magenes, E.: Non-homogeneous Boundary Value Problem and Applications. Springer, Berlin (1972)
14. Mitchel, A.R., wait, R.: The Finite Element Method in Partial Differential Equations. Wiley, London (1997)
15. Prenter, P.M.: Splines and Variational Methods. Wiley, New York (1989)
16. de-Boor, C.: A Practical Guide to Splines. Springer, Berlin (2001)
17. Schoenberg, I.J.: On Spline Functions, MRC Report 625, University of Wisconsin (1966)

A Mathematical Study on Optimum Wall-to-Wall Thickness in Solar Chimney-Shaped Channel Using CFD

Alokjyoti Dash and Aurovinda Mohanty

Abstract A number construct amendment in light of the laminar streams caused by regular convection in entries, utilizing a sun-oriented stack setup, for Rayleigh number $= 10^5$, a few estimations of the relative one end to the other space with various temperatures on the dividers has been performed. Numerical results for the average Nusselt number have been obtained for value of Rayleigh number $= 10^5$ for asymmetrical heating. The optimum thickness ratio for this condition has been presented. Air development in a normally ventilated room can be caused using a sun-based fireplace or Trombe divider. In this work, Trombe dividers are examined for summer cooling of structures. Simulation was done using ANSYS FLUENT, with adequate geometry design, meshing, and boundary condition. The present work is focused on the laminar natural convection $\left(\mathrm{Ra} = 10^5\right)$ with varying the wall spacing (0.005–0.5). The heating condition is asymmetrical (keeping outer wall as adiabatic and inner wall a constant temperature). Finding the optimum wall spacing for maximum heat transfer which will facilitate the room air in summer cooling is the main objective.

Keywords Asymmetrical heating · Trombe wall · Solar chimney

1 Introduction

Inactive solar heating has increasingly been applied internationally in last two tens. Thermosiphons, heat siphon, or solar chimneys are the most commonly used passive systems. They offer regular motions of air, by making temperature differences by solar warming. All around, the temperature distinction is realized by a coated sun-based smokestack that even can be called as Trombe wall. A Trombe divider is a southerner-confronting cement or workmanship divider which is darkened and secured on the outside by covering. The warm divider (stockpiling divider) serves

A. Dash (✉) · A. Mohanty
Veer Surendra Sai University of Technology, Burla 768018, Odisha, India
e-mail: aalokjyoti.dash@gmail.com

D. Srinivasacharya and K. S. Reddy (eds.), *Numerical Heat Transfer and Fluid Flow*, Lecture Notes in Mechanical Engineering,
https://doi.org/10.1007/978-981-13-1903-7_4

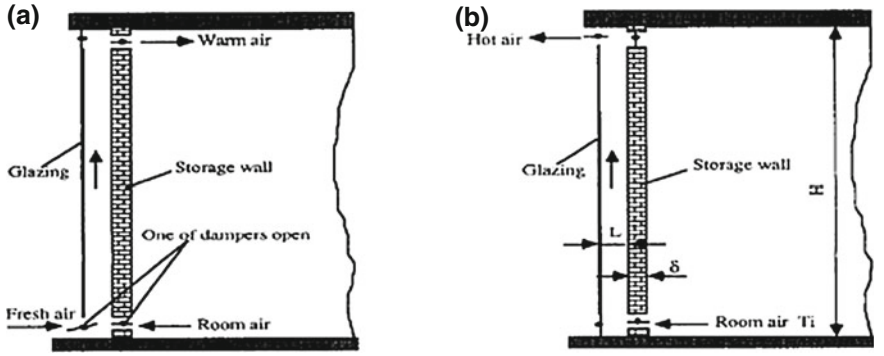

Fig. 1 Configuration for winter heating and summer cooling

to assemble sun-powered vitality. The vitality is kept between the ramparts. The putaway vitality is transported to within working for winter warming or causes room air development for summer cooling. In winter warming, air enters the space between the room divider and coated divider from the back vent. It is plain to the front room when the outside air temperature is lower or to the encompassing when the outside temperature is direct, for instance, >10 °C. The air is warmed up by the putaway sunlight-based vitality and streams upward because of the lightness impact. That hot air comes back to the living space through the best vent to keep the room temperature. For summer cooling, the form is set to such an extent that the lightness powers produced by the sunlight-based warmed air between the warm divider and coated divider draw room air through the back vent and outside air into the room through open windows or vents in other outside dividers. The warmed wind streams out to the encompassing through the summit vent. In hot districts, the outside air amid the daytime is regularly fiery. So ventilation for sensible cooling is not successful; however, the capacity divider gives a decent warm insulation to warm stream into the room. During the dark, due to the warm Trombe wall, the cool ambient air is drained into the gap between the walls and takes away heat from the inside of the edifice. Depending on the ambient temperature, the work of Trombe wall is distinguished as daytime ventilation or night cooling (Fig. 1).

1.1 Problem Description

A level section ought to be added to the vertical channel (measurements A^*E) for better recreation of sunlight-based smokestack channel and appropriate examination of the smooth movement and the warmth exchange marvels. The gap between the dividers is b. The trademark proportion of the focal upright channel is b/L, where L is the tallness of divider 1. The high-temperature air is gathered between the external divider 1 and the internal divider 2, and ascends because of thickness contrasts

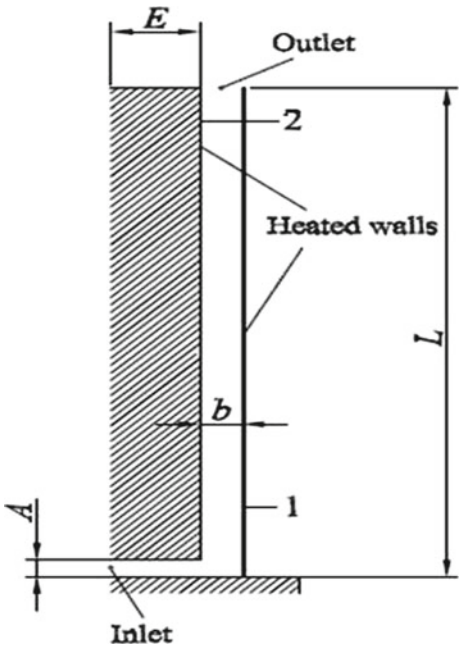

Fig. 2 Physical model and geometry

(buoyancy impact). In every one of the cases, level dividers are viewed as adiabatic. Uniform wall temperature, UWT (vertical walls at constant temperature), and heating conditions have been studied. In most cases, both the walls have the same temperature. Some results for asymmetrical heating (i.e., one wall is taken as adiabatic) have been additionally gotten. The geometry is given by thickness (b)/length (L) = 0.1 and horizontal section height (E)/length (L) = vertical height of inlet (A)/length (L) = 0.1. In parliamentary law to look at the impact of the one end to the other thickness over the issue delineated, the accompanying occasions have been investigated: b/L = 0.005–0.5, in the interim, the proportion of horizontal channel A/L and E/L stays equivalent to 0.1. Numerical answers for the normal Nusselt number have been acquired for estimations of Rayleigh number = 10^5, for deviated warming. The operational liquid is air (Pr = 0.74) (Fig. 2).

2 Mathematical Models

The Rayleigh number in view of L has been characterized as = () (Pr), being the Grashof number, for the UWT warming conditions.

$$\mathrm{Gr}_L = \frac{g\beta(T_w - T_\infty)L^3}{\nu^2} - \text{For uniform wall temperature} \tag{1}$$

Equations

The Boussinesq approximation is cast-off, accepting perpetual physical properties of the fluid, except for variation in density in the y-momentum equation. The simplified tensor formed averaged *N–S* equations of turbulent flow for steady, and 2-D incompressible flow is as follows:

Continuity Equation:

$$\frac{\partial U_j}{\partial x_j} = 0 \tag{2}$$

Averaged *N–S* Equation:

$$\frac{\partial U_i U_j}{\partial x_j} = -\frac{1}{\rho}\frac{\partial P}{\partial x_i} - g_i \beta (T - T_\infty) + \frac{\partial}{\partial x_j}\left(v\frac{\partial U_i}{\partial x_j} - \overline{u_\iota u_J}\right) \tag{3}$$

Energy Equation:

$$\frac{\partial \left(T U_j\right)}{\partial x_j} = \frac{\partial}{\partial x_j}\left(\frac{v}{\mathrm{Pr}}\frac{\partial T}{\partial x_j} - \overline{T' u_J}\right) \tag{4}$$

where U_i, T, and P are the velocity, temperature, and pressure, and β is the thermal expansion coefficient.

For laminar flow conditions, the equations can be obtained by taking $-\overline{U_\iota U_J} = -\overline{T' U_J} = 0$.

2.1 Numerical Analysis

The computational area will be constrained to the space between dividers. In UWT cases, the temperature of the vertical dividers is settled $T = \mathrm{Tw}$. In every one of the cases, the even dividers (entrance pipe) are taken as adiabatic. Some laminar calculations have been done with lopsided warming and after that divider 1 is accepted as adiabatic. The simulation is done by ANSYS FLUENT using SIMPLE (semi-implicit method for pressure-linked equation) algorithm. Special discretization methods used are as follows:

Gradient—Least square cell based,
Pressure—Second-order upwind,
Momentum—Second-order upwind, and
Energy—Second-order upwind.

The residual values are set to 0.001 for continuity, x and y velocities and 1E−06 for energy. The above schemes are used to have lower error values in discretization methods.

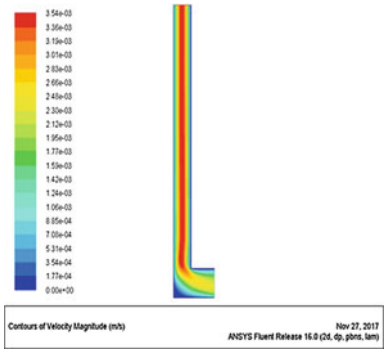

Fig. 3 Asymmetrical heating b/L=0.1 (Ra=10^5)

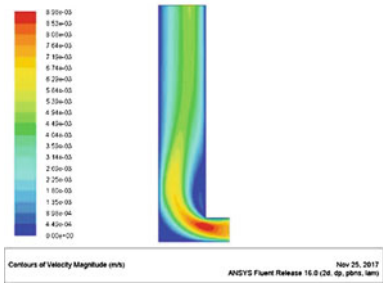

Fig. 4 Asymmetrical heating b/L=0.2 (Ra=10^5)

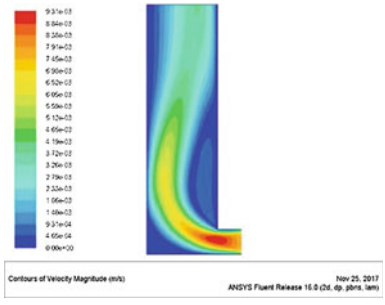

Fig. 5 Asymmetrical heating b/L=0.3 (Ra=10^5)

3 Conclusion and Future Work

The velocity contours for different thickness ratios obtained are shown in Figs. 3, 4, 5, 6.

The *b*/*L* ratios are 0.15, 0.2, 0.25, 0.3, 0.4, and 0.5, respectively (Table 1).

To get the ideal design of *L*-formed networks for greatest warmth exchange rate and for asymmetrical warming (divider 1 as adiabatic and divider 2 warmed at uniform temperature), the estimation of Nusselt number is plotted with various *b*/*L* ratios at Ra $= 10^5$. Here, we are getting optimum ratio of 0.125. The following works have to be done in future to find the optimum results,

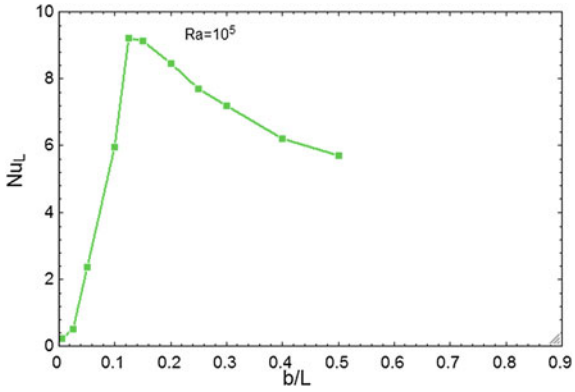

Fig. 6 Average nusselt number Nu_L versus aspect ratio b/L for Rayleigh number10^5

Table 1 Average Nusselt Number of the wall at different aspect ratios

Sl. No.	b/L	Nu_L
1	0.15	9.14
2	0.2	8.44
3	0.25	7.69
4	0.3	7.18
5	0.4	6.2
6	0.5	5.69

(1) Studies on average Nusselt number with different b/L ratios have to be done for both laminar and turbulent conditions, with symmetrical heating (constant wall temperature) and constant heat flux.
(2) Find the optimum wall-to-wall spacing for each condition.
(3) Study the relation of Nusselt number to b/L ratio in case of turbulent flow ($k-\in$ *model*).
(4) Studies have to be done on convergent channels, finding the optimum wall-to-wall spacing for maximum heat transfer.
(5) Also, study the flow rates and find the optimum thickness for it.

Estimation of Heat Transfer Coefficient and Reference Temperature in Jet Impingement Using Solution to Inverse Heat Conduction Problem

Anil R. Kadam, Vijaykumar Hindasageri and G. N. Kumar

Abstract The heat transfer estimation in case of impinging jets has been considered by mainly steady-state techniques. The present study reveals the transient technique to characterize the impinging jets. A solution to three-dimensional inverse heat conduction problem (IHCP) is used to estimate the unknown transient surface temperature distribution at the jet impinging side (front side) from known non-impingement side (backside) transient temperature distribution. Further to estimate front side heat flux distribution, the temperature gradient close to the front surface is computed by finite difference method, and then linearity between surface heat flux and corresponding surface temperature is utilized to find out heat transfer coefficient (HTC) and the reference temperature simultaneously. To validate and establish the present technique, numerical simulations are carried out in fluent. The numerically estimated back surface temperature data is used as input to the solution to IHCP. Hot as well as cold impinging jets are characterized with the help of this solution. Along with laminar jets, turbulent jets with varying Reynolds number are considered. The inversely estimated results are compared with numerically simulated data and match is within 1%.

Keywords IHCP · Heat transfer coefficient · Reference temperature
Impinging jet

A. R. Kadam · G. N. Kumar
Department of Mechanical Engineering, National Institute of Technology, Surathkal 575025, Karnataka, India

V. Hindasageri (✉)
Department of Mechanical Engineering, KLS Vishwanathrao Deshpande Rural Institute of Technology, Haliyal 581329, Karnataka, India
e-mail: vkhnitk@gmail.com

D. Srinivasacharya and K. S. Reddy (eds.), *Numerical Heat Transfer and Fluid Flow*, Lecture Notes in Mechanical Engineering,
https://doi.org/10.1007/978-981-13-1903-7_5

1 Introduction

Impinging jets are widely used since decades for cooling and heating applications in industrial and domestic application due to their high heat transfer ability. Researchers over the decade have contributed to this research by their experimental and numerical work on jet impingement. The reviews [1, 2] on experimental studies have reported effect of parameters such as Reynolds number (Re), the nozzle-to-plate spacing (Z/d), nozzle geometry, and turbulence intensity on the heat transfer characteristic of an impinging jet. The work [3] has critically reviewed several numerical studies on impinging jets and concluded that no RANS model is perfect in predicting the heat transfer of impinging jets. The heat transfer estimation to and from impinging jets has been studied by mostly steady-state techniques ranging from the naphthalene sublimation technique, thin foil technique, liquid crystal method to heat flux sensors. Further, heat transfer coefficient (HTC) is estimated as per Eq. (1).

$$q'' = h(T_{\text{ref}} - T_w) \tag{1}$$

The information of the reference temperature (RT) is important to obtain the appropriate value of HTC. The reference temperature for isothermal jet is nearly same as that of ambient temperature [4, 5]. Nonetheless, the evaluation of the RT is not direct for the hot jet temperature as hot jet temperature is different than its surrounding temperature, and in addition it changes along the plate in radially outward direction. In most studied thin foil technique, linearity between surface heat flux and corresponding surface temperature is utilized to find out HTC and RT simultaneously. The only other technique which can estimate HTC and RT simultaneously is the application of inverse heat conduction problem (IHCP) to impinging jet studies. Recently, study [6] has employed transient three-dimensional approach in analytical IHCP study to estimate front surface temperature and corresponding heat flux from back surface temperature data.

In the present study, a solution [6] to three-dimensional inverse heat conduction problem (IHCP) is used to estimate the unknown transient surface temperature distribution at the jet impinging side. Further temperature gradient is computed near the front wall to estimate front side heat flux distribution and then procedure similar to thin metal foil technique is used to estimate HTC and RT simultaneously for impinging jets. Laminar and turbulent jets with varying nozzle-to-plate spacing (Z/d) and Reynolds numbers are considered.

2 Construction of the Problem and Solution Procedure

The transient IHCP can be formulated by the assumption of transient flux condition at the impinging boundary [6] as shown in Fig. 1. The solution [6] assumes temperature-

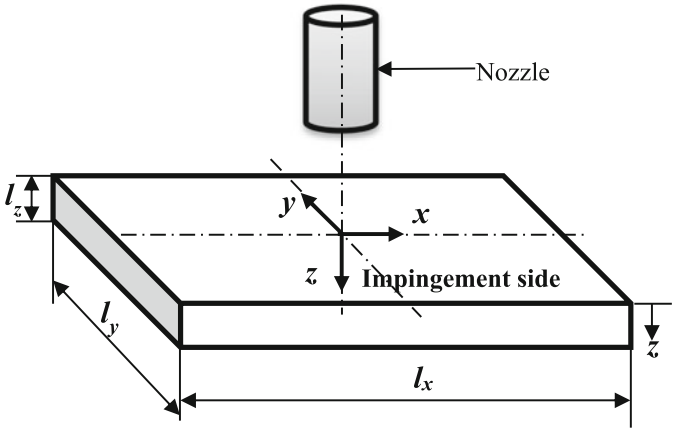

Fig. 1 Schematic of jet impingement setup

Table 1 Boundary conditions for IHCP solution [6]

Location	Boundary condition	Description
At $t = 0$	$T(x, y, z, t) = T_\infty$	Initial
At $x = 0, y = 0, z$	$\frac{\partial T}{\partial n^*} = 0$	Symmetry
At $x = l_x, y = l_y, z$	$\frac{\partial T}{\partial n^*} = 0$	Insulated
At $x, y, z = 0$	$-k\frac{\partial T}{\partial z} = q(x, y, t)$	Heat flux
At $x, y, z = l_z$	$\frac{\partial T}{\partial z} = 0$	Insulated

*n is the direction vector alongside x- and y-axes

independent material properties (k, ρ, and C) to solve transient three-dimensional IHCP. The boundary conditions assumed are as mentioned in Table 1.

This transient 3-D heat conduction problem is further brought to 1-D problem thru modal representation [6] as specified in Eqs. (2)–(3).

$$\theta(X, Y, Z, \tau) = \sum_{m,n=0,1....} \theta_{mn}(\tau, Z) \cos\frac{m\pi X}{L_x} \cos\frac{n\pi Y}{L_y} \tag{2}$$

$$f(X, Y, Z, \tau) = \sum_{m,n=0,1....} f_{mn}(\tau) \cos\frac{m\pi X}{L_x} \cos\frac{n\pi Y}{L_y} \tag{3}$$

The functions $\theta_{mn}(\tau, Z)$ and $f_{mn}(\tau)$ represent modal temperature and modal flux, respectively. Through thermal quadrupole, the relationship between temperature and heat flux on the front and back surface is established in Laplace domain. These related functions are further obtained in time domain through inverse Laplace transform of these simple polynomials. To estimate flux and temperature at modal points of

impinging face from the non-impinging face temperature, an iterative procedure is utilized. The successive iteration (K) is accomplished by Eqs. (4)–(5).

$$\theta_{mn}^{(K+1)}(\tau, 0) = \left[\theta_{mn}^{(K)}(\tau, 0) + \frac{1}{[(2K+1)\pi/2]^2 + C_{mn}^2} \frac{\mathrm{d}\theta_{mn}^{(K)}(\tau, 0)}{\mathrm{d}t}\right] \tag{4}$$

$$f_{mn}^{(K+1)}(\tau) = f_{mn}^{(K)}(\tau) + \frac{1}{C_{mn}^2 + (K\pi)^2} \frac{\mathrm{d}f_{mn}^{(K)}(\tau)}{\mathrm{d}\tau} \tag{5}$$

To employ this iterative scheme, the modal temperature $\theta_{mn}(\tau, Z)$ on the non-impingement side is needed and it can be obtained as given in Eq. (6).

$$\theta_{mn}(\tau, 1) = \frac{2^{2-(\delta_{0m}+\delta_{0n})}}{L_x L_y} \sum_i \sum_j \theta\left(X_i, Y_j, 1, \tau\right) \cos\frac{m\pi X_i}{L_x} \cos\frac{n\pi Y_j}{L_y} \delta X_i \delta Y_j \tag{6}$$

where $\left(X_i, Y_j\right)$ is the center of the (i, j)th grid and δX_i and δY_j are the sides of the grid. δ_{0m} and δ_{0n} are Kronecker delta functions, $m = 0, 1, 2, \ldots M$ and $n = 0, 1, 2, \ldots N$.

Equation (6) works for all mode numbers aside from $(m, n) = (0, 0)$. At $(m, n) = (0, 0)$, Eq. (7) which assumes constant uniform heat flux at the impingement side has been used.

$$\theta_{00}(\tau, Z) = f_{00}^0 \left[\tau + \frac{Z^2}{2} - Z + \frac{1}{3} - \frac{2}{\pi^2} \sum_{k=1}^{\infty} \frac{\cos(k\pi Z)}{k^2} \mathrm{e}^{-(k\pi)^2\tau}\right] \tag{7}$$

3 Simultaneous Estimation of HTC and RT

The linear correlation (of the form, $mx + c = y$, where m is the slope and c is the y-intercept of the graph of x vs. y) between surface flux and corresponding surface temperature has been used to estimate HTC and reference temperature simultaneously. Rearranging Eq. (1), as Eq. (8).

$$-\frac{q''}{h} + T_{\mathrm{ref}} = T_w \tag{8}$$

Accordingly, inverse of slope and intercept of the linear fit gives heat transfer coefficient and reference temperature, respectively.

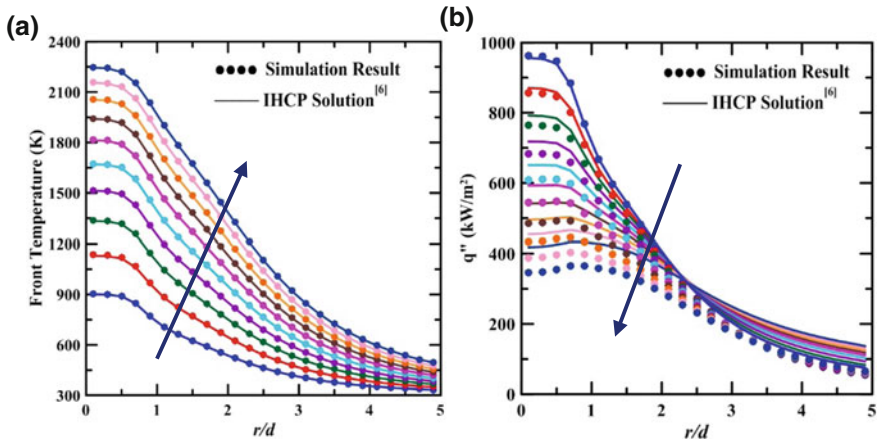

Fig. 2 **a** Front temperature, **b** heat flux computed by method [6] is compared with simulation results. The direction of arrow indicates the increasing value of t from 0.5 to 5 s in steps of 0.5

4 Results and Discussion

The solution to IHCP is validated, and then its application to obtain HTC and RT for different configurations of impinging jets is discussed.

The 3-D IHCP code is confirmed with numerical simulations carried out using CFD software Ansys (Fluent). The numerical procedure adopted is similar with the procedure mentioned [7].

The numerically simulated back face temperature is used as input to the analytical IHCP solution, and the front face temperature and surface heat flux are estimated. Figure 2a, b shows the comparison between front face temperature and surface heat flux data with numerically gained data, respectively. The estimated temperature data is in agreement within 1% with simulated data; on the other hand, the surface flux data estimated is overvalued at higher time. This overrated by the 3-D IHCP solution is because of the assumption of constant surface heat flux at $(m, n) = (0, 0)$.

Thus, to estimate accurate front side transient heat flux, the temperature gradient (first-order approximation) is taken very close (0.1 mm inside) to the wall. The surface heat flux estimated is in outstanding agreement with numerically simulated surface heat flux data as presented in Fig. 3.

To check linearity, transient surface heat flux is plotted against corresponding surface temperature for various *r/d* as shown in Fig. 4. At stagnation point, fit is exactly linear and values of HTC and RT are very much accurate. However, away from the stagnation point, reference temperature is continuously increasing which is not true. Similar observation is made in case of cold turbulent jet impingement.

A forward numerical simulation is carried out with HTC and RT as a boundary condition thru user-defined function (UDF). The demonstrative trend of HTC and RT for cold impinging jet (Plate at 500 K and jet at 300 K) and hot impinging jet

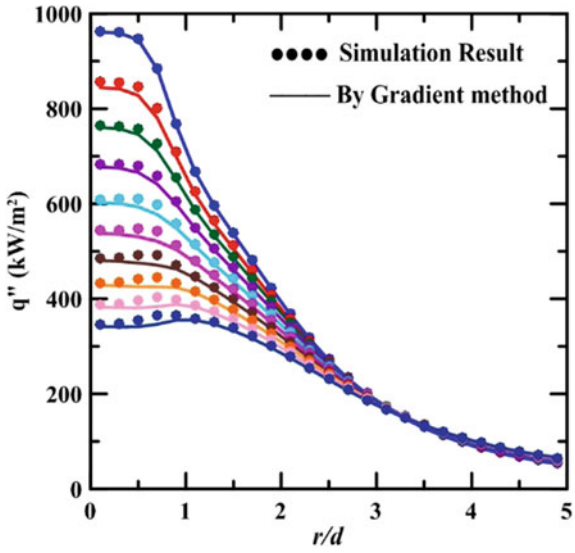

Fig. 3 Comparison of flux computed by temperature gradient method with simulation results

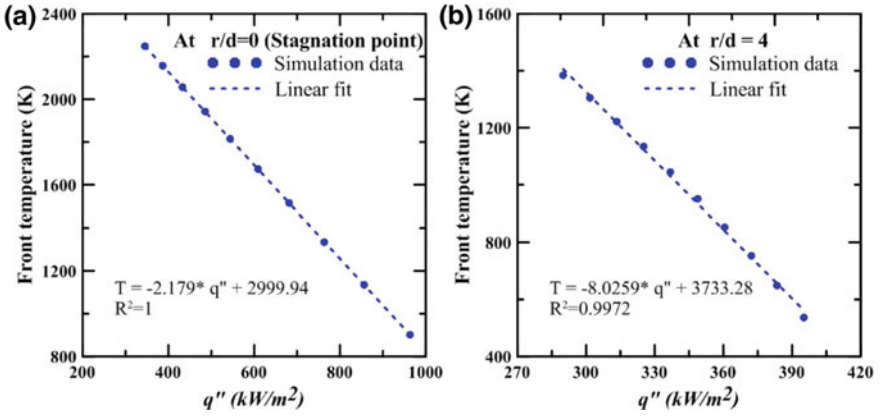

Fig. 4 Linear fit at **a** $r/d = 0$ and **b** $r/d = 4$

(Plate at 300 K) applied thru UDF were taken from the published experimental work [4, 8], respectively. The comparison plots are shown in Fig. 5.

5 Conclusions

The solution to IHCP is used to estimate front side temperatures with great accuracy. Further, front wall heat flux is obtained with first-order accurate temperature gradient method having match within 1% with simulated flux data. After validation, present

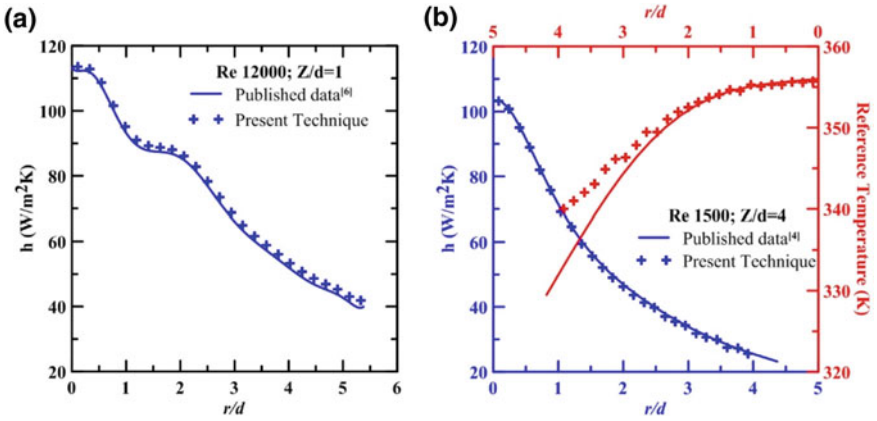

Fig. 5 Comparative plot for **a** turbulent cold jet **b** laminar hot jet

technique is applied to cold jet and hot jet to obtain HTC and RT simultaneously. For cold as well as hot jet, estimated heat transfer coefficient is in exceptional match with input heat transfer coefficient data, whereas estimated reference temperature exactly matches in stagnation region and overestimates around 2% at larger r/d.

References

1. Jambunathan, K., Lai, E., Moss, M.A., Button, B.L.: A review of heat transfer data for single circular jet impingement. Int. J. Heat Fluid Flow **13**, 106–115 (1992)
2. Viskanta, R.: Heat transfer to impinging isothermal gas and flame jet. Exp. Therm. Fluid Sci. **6**, 111–134 (1993)
3. Zuckerman, N., Lior, N.: Jet impingement heat transfer: physics, correlations, and numerical modeling. Adv. Heat Transfer **39**, 565–631 (2006)
4. Kuntikana, P., Prabhu, S.V.: Isothermal air jet and premixed flame jet impingement: heat transfer characterization and comparison. Int. J. Therm. Sci. **100**, 401–415 (2016)
5. Fénot, M., Vullierme, J.-J., Dorignac, E.: Local heat transfer due to several configurations of circular air jets impinging on a flat plate with and without semi-confinement. C R Mécanique **333**, 778–782 (2005)
6. Feng, Z.C., Chen, J.K., Zhang, Y., Griggs Jr., J.L.: Estimation of front surface temperature and heat flux of a locally heated plate from distributed sensor data on the back surface. Int. J. Heat Mass Transfer **54**, 3431–3439 (2011)
7. Remie, M.J., Särnerb, G., Cremers, M.F.G., Omrane, A., Schreel, K.R.A.M., Aldén, L.E.M., de Goey, L.P.H.: Heat-transfer distribution for an impinging laminar flame jet to a flat plate. Int. J. Heat Mass Transfer **51**, 3144–3152 (2008)
8. Katti, V.V., Nagesh Yasaswy, S., Prabhu, S.V.: Local heat transfer distribution between smooth flat surface and impinging air jet from a circular nozzle at low Reynolds numbers. Heat Mass Transfer **47**, 237–244 (2011)

Investigation of Thermal Effects in a Ferrofluid-Based Porous Inclined Slider Bearing with Slip Conditions

Paras Ram and Anil Kumar

Abstract A theoretical model has been considered for the analysis of a ferrofluid lubricated porous pad slider bearing under slip conditions. The lubricant is assumed to be incompressible, and its viscosity varies exponentially with the temperature. The expressions corresponding to the mean temperature, pressure, and the lifting force (capacity of carrying the load) have been obtained as a function of various parameters such as slip, material, thermal, magnetic field, and permeability. The behavior of mean temperature with other bearing characteristics across the fluid film thickness has also been investigated. The dependency of the lifting force and mean temperature on various bearing parameters has been seen graphically.

Keywords Jenkins model · Magnetic fluid · Slider bearing · Slip velocity Mean temperature

1 Introduction

Ferrofluid plays a vital role to enhance the lifting force and transfer of heat in lubrication of bearings. Due to long-term stability and high thermal conductivity, magnetic fluids have attracted the scholars working on problems of various geometries like helical pipes, cylinders, rotating disks, etc. [1–4].

In the present paper, the work done by Ram et al. [5] has been extended by introducing the concept of heat transfer in the slider. Using ferrofluid as a lubricant, thermal effects in the slider have been examined together with the slip boundary conditions. The term co-rotational derivative for magnetization [6] has also been taken into account because of its significant impact on the bearing characteristics. The present work is also an improvement in the work done by Singh and Ahmad [7], who have ignored the aforesaid term of the co-rotational derivative for magnetization. The expressions corresponding to the mean temperature, pressure, and the lifting

P. Ram · A. Kumar (✉)
Department of Mathematics, NIT-Kurukshetra, Thanesar, Haryana, India
e-mail: anilkumar6150013@gmail.com

D. Srinivasacharya and K. S. Reddy (eds.), *Numerical Heat Transfer and Fluid Flow*, Lecture Notes in Mechanical Engineering,
https://doi.org/10.1007/978-981-13-1903-7_6

force have been obtained as a function of various parameters such as slip, material, thermal, magnetic field, and permeability. For randomly chosen values of various nondimensional parameters, the values corresponding to the mean temperature and the lifting force have been computed by Simpson's 1/3rd method. The variations in mean temperature/thermal boundary layer thickness have been investigated across the fluid film thickness to examine the rate of heat transfer.

2 Formulation of the Problem

The governing equations of the flow in vector notation due to Ram et al. [5] are as follows:

$$\rho\left[\frac{\partial q}{\partial t} + (q \cdot \nabla)q\right] = -\nabla p + \mu\nabla^2 q + \mu_0(M \cdot \nabla)F_H + \rho\alpha^2\nabla \times \left(\frac{\tilde{M}}{M} \times M^*\right) \quad (1)$$

$$\nabla \cdot q = 0; \quad \nabla \times F_H = 0; \quad F_H = -\nabla\varphi; \quad \nabla \cdot (F_H + 4\pi M) = 0 \quad (2)$$

$$\beta\frac{D^2\tilde{M}}{Dt^2} = -4\pi p\frac{M_s}{\chi_0}\frac{\tilde{M}}{M_s - M} - \frac{2\alpha^2}{M}M^* + F_H; \quad (3)$$

where $M^* = \frac{D\tilde{M}}{Dt} + \frac{1}{2}(\nabla \times q) \times \tilde{M}$.

In (1)–(3), $\rho, q, p, \beta, \alpha^2, \mu, \tilde{M}, M^*, M, M_s, F_H, \mu_0$, and χ_0 are the fluid density, the fluid velocity, the pressure, the material constants, the coefficient of fluid's viscosity, the magnetization vector, co-rotational derivative of $\tilde{M}$, the magnitude of magnetization vector, the saturation magnetization, external applied field intensity, free space permeability, and initial susceptibility of the fluid (Fig. 1).

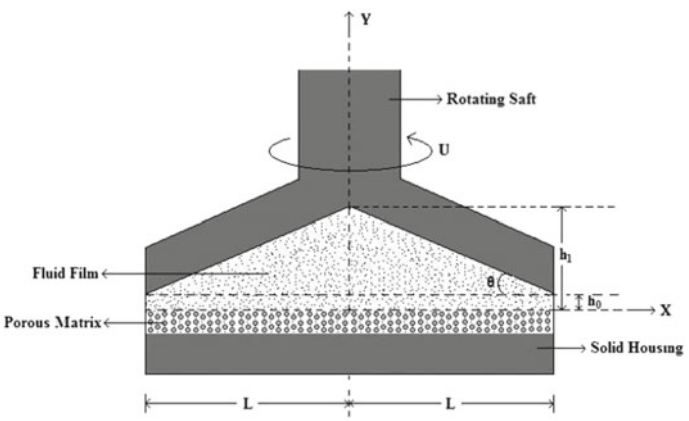

Fig. 1 A porous pad slider bearing filled with ferrofluid as lubricant

Now using all the appropriate boundary conditions, the expression for velocity and pressure obtained by Ram et al. [5] is given as follows:

$$u = \frac{\frac{\partial}{\partial x}\left(p - \frac{\mu_0\bar{\mu}}{2}F_H^2\right)}{\left(\mu - \frac{\rho\alpha^2\bar{\mu}}{2}F_H\right)}\frac{y^2}{2} + \left(U - \frac{\frac{\partial}{\partial x}\left(p - \frac{\mu_0\bar{\mu}}{2}F_H^2\right)}{\left(\mu - \frac{\rho\alpha^2\bar{\mu}}{2}F_H\right)}\frac{h^2}{2}\right)\left(\frac{1+sy}{1+sh}\right) \tag{4}$$

$$\begin{aligned}\frac{\partial}{\partial x}\left(p - \frac{\mu_0\bar{\mu}}{2}F_H^2\right) &= \frac{\mu^2[6Uh(2+sh)+12A(1+sh)]}{\left[6kl\left(2\mu(1+sh)-\rho\alpha^2\bar{\mu}F_H\right)+\mu h^3(4+sh)^2\right]} \\ &+ \frac{\mu F_H\rho\alpha^2\bar{\mu}[6Uh(2+sh)+12A(1+sh)]}{\left[6kl\left(2\mu(1+sh)-\rho\alpha^2\bar{\mu}F_H\right)+\mu h^3(4+sh)^2\right]^2} \\ &\times\left[3kh\left(\mu(1+sh)-\frac{\rho\alpha^2\bar{\mu}}{2}F_H\right)-\frac{\mu h^3}{2}(4+sh)\right]\end{aligned} \tag{5}$$

where U, s and A denote the component of uniform velocity of the slider along x-axis, the slip parameter, and the integral constant, respectively.

3 Solution of the Problem

The solution of the system is obtained by introducing the following nondimensional quantities:

$$\begin{aligned}&\bar{x} = \frac{x}{L}, \bar{y} = \frac{y}{h_0}, \bar{h} = \frac{h}{h_0}, \bar{M} = \frac{\mu}{\mu_0}, \bar{A} = \frac{12A}{Uh_0}, u_0 = \frac{u}{U}, \\ &p = \frac{ph_0^2}{\mu UL}, T = \frac{t}{t_0}, \bar{\alpha}^2 = \frac{\rho\alpha^2\bar{\mu}L}{2\mu}, \\ &\bar{\gamma}^2 = \frac{6k}{h_0^2}, \bar{\beta}^3 = \frac{12kl}{h_0^3}, T_m = \frac{t_m}{t_0}, P_r = \frac{\mu_0 C_p}{\bar{k}}, \\ &E = \frac{U^2}{C_p t_0}, B_0 = \beta t_0, \bar{\mu}^* = \frac{\bar{\mu}_0\bar{\mu}h_0^2L}{\mu U}, \bar{s} = sh_0\end{aligned}$$

where P_r, E, B_0, C_p, h_0, $\bar{h}$, h_1, T_m, t_m, t_0, L, l, k, and $\bar{k}$ are the Prandtl number, the Eckert number, the nondimensional coefficient of temperature, the specific value of heat, the minimum film thickness, the nondimensional film height, the maximum film thickness, the nondimensional mean temperature, mean temperature across the fluid film thickness, the temperature at ambient pressure, the bearing width, the bearing wall thickness, the matrix porosity, and the thermal's conductivity, respectively.

Assuming that the surfaces are inactive and flow of lubricant is active thermally [7] and using the condition, $T = 1$ at the boundary, i.e., at $\bar{y} = 0$ and $\bar{y} = \bar{h}$, the expression for mean temperature has been obtained as

$$T_m = 1 + \frac{\bar{M} P_r E}{240}\left[6\bar{h}^4\varphi^2 + \frac{5\bar{h}^2\bar{s}^2\left(4+\bar{h}^4\varphi^2-4\bar{h}^2\varphi\right)}{\left(1+\bar{s}\bar{h}\right)^2} + \frac{10\bar{h}^3\bar{s}\varphi\left(2-\bar{h}^2\varphi\right)}{\left(1+\bar{s}\bar{h}\right)}\right] \quad (6)$$

where $\varphi = \frac{\frac{\partial}{\partial\bar{x}}\left(\bar{p}-\frac{\bar{\mu}^*}{2}(1-\bar{x})\bar{x}\right)}{(1-\bar{\alpha}^2\sqrt{(1-\bar{x})\bar{x}})}$.

Equation (5) in dimensionless form is

$$\frac{\partial}{\partial\bar{x}}\left(\bar{p}-\frac{\bar{\mu}^*(1-\bar{x})}{2}\bar{x}\right) = \frac{\frac{1}{\bar{s}}\left(12\bar{h}+\bar{A}\right)+\bar{h}\left(6\bar{h}+\bar{A}\right)}{\frac{1}{\bar{s}}\left(\bar{\beta}^3\left(1-\bar{\alpha}^2\sqrt{(1-\bar{x})}\sqrt{\bar{x}}\right)+4\bar{h}^3\right)+\bar{h}\left(\bar{\beta}^3+\bar{h}^3\right)}$$
$$+\frac{\bar{\alpha}^2\bar{h}\left[\frac{1}{\bar{s}}\left(12\bar{h}+\bar{A}\right)+\bar{h}\left(6\bar{h}+\bar{A}\right)\right]}{\left[\frac{1}{\bar{s}}\left(\bar{\beta}^3\left(1-\bar{\alpha}^2\sqrt{(1-\bar{x})}\sqrt{\bar{x}}\right)+4\bar{h}^3\right)+\bar{h}\left(\bar{\beta}^3+\bar{h}^3\right)\right]^2}$$
$$\times\left[\frac{1}{\bar{s}}\left(\bar{\gamma}^2-4\bar{h}^2-\bar{\alpha}^2\sqrt{(1-\bar{x})}\sqrt{\bar{x}}\right)+\bar{h}\left(\bar{\gamma}^2-\bar{h}^2\right)\right]((1-\bar{x})\bar{x})^{1/2} \quad (7)$$

where the film thickness $\bar{h}(\bar{x}) = a(1-\bar{x})+\bar{x}$, and $a = h_1/h_0$, $0 \le \bar{x} \le 1$. Particularly, we take $a = 2 \Rightarrow \bar{h}(\bar{x}) = 2$. Now, the lifting force is given by

$$\bar{W} = \int_0^1 (\bar{p})\mathrm{d}\bar{x} = -\int_0^1 (\bar{x})\left(\frac{\mathrm{d}\bar{p}}{\mathrm{d}\bar{x}}\right)\mathrm{d}\bar{x} \quad (8)$$

Using (6) and (8), we obtain the final expression for the lifting force as

$$\bar{W} = \frac{\bar{\mu}^*}{12} - \int_0^1 \left(\bar{\alpha}^2\sqrt{(1-\bar{x})\bar{x}}-1\right)\bar{x}\sqrt{\frac{1}{6\bar{h}^2+\bar{h}^4\bar{s}^2+2\bar{h}^3\bar{s}}\left[\begin{array}{c}\frac{240(T_m-1)(1+\bar{s}\bar{h})^2}{\bar{h}^2\bar{M}P_rE} \\ -20\bar{s}^2-20\varphi\bar{h}\bar{s}\end{array}\right]}\,\mathrm{d}\bar{x} \quad (9)$$

4 Results and Discussion

On the behalf of the computation and investigations carried out for the present work, the following findings are recommended.

The variations of mean temperature (T_m) across the fluid film thickness ($\bar{h}$) have been analyzed for different values of the thermal parameter ($P_r \cdot E$) and the material parameter ($\bar{\alpha}^2$) in Figs. 2 and 3, respectively. As we move from outlet ($\bar{h} = 1$) to inlet ($\bar{h} = 2$) of the slider, it is noted that the behavior of the mean temperature is quite irregular. The area under the mean temperature curve is negligible for $1 \le \bar{h} \le 1.5$ and large for $1.5 \le \bar{h} \le 2$. It implies that width of the thermal boundary layer is quite large in the inner half of the bearing as compared to the outer half of the bearing. Therefore, the heat dissipation is very slow in the inner part as compared to the outer part of the slider, and hence the cooling is fast in the outer part as compared to the

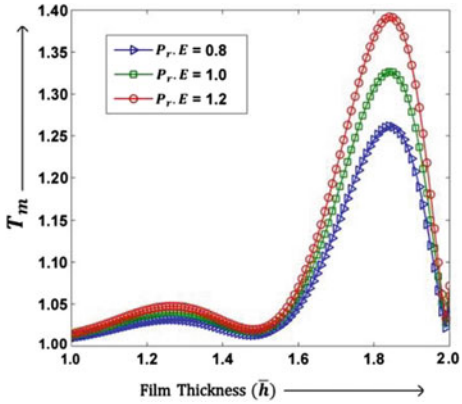

Fig. 2 Mean temperature versus fluid film thickness for different values of $P_r \cdot E$ at $1/\bar{s} = 1$, $\bar{\alpha}^2 = 0.8$, $\bar{\beta} = 1.3$, $\bar{\gamma}^2 = 1.2$

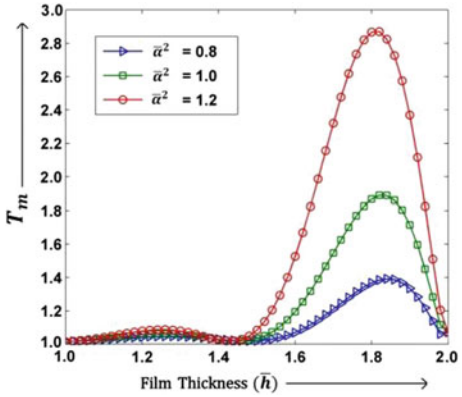

Fig. 3 Mean temperature versus fluid film thickness for different values of $\bar{\alpha}^2$ at $1/\bar{s} = 1$, $\bar{\beta} = 1.3$, $\bar{\gamma}^2 = 1.2$, $P_r \cdot E = 1.2$

inner part of the slider. Also from Fig. 7, we observe that the material parameter has a large effect on the mean temperature. So, for desirable heat transfer, the material parameter should be adjusted accordingly.

Figure 4 reveals the variation of mean temperature (T_m) with slip parameter ($1/\bar{s}$) for different values of the material parameter ($\bar{\alpha}^2$). It is seen that the effect of the material parameter on mean temperature depends on the value of slip parameter. For slip, $1/\bar{s} \leq 0.4$, the material parameter does not have any effect on mean temperature but for $1/\bar{s} > 0.4$, it has a notable effect on mean temperature. Therefore, for $1/\bar{s} > 0.4$, the material parameter should be adjusted according to the slip parameter.

In Figs. 5 and 6, the variations of the lifting force ($\bar{W}$) versus permeability parameter ($\bar{\beta}$) and slip parameter ($1/\bar{s}$) under the effect of magnetic field parameter ($\bar{\mu}^*$) have been observed. In these figures, it is noted that the lifting force enhances with an increase in the magnetic parameter. Increase in the magnetic field intensity causes an increase in the lubricant's viscosity, which causes an enhancement in the pressure and consequently, the lifting force. It is also seen that for $\bar{\beta} < 0.5$ and $1/\bar{s} > 0.6$,

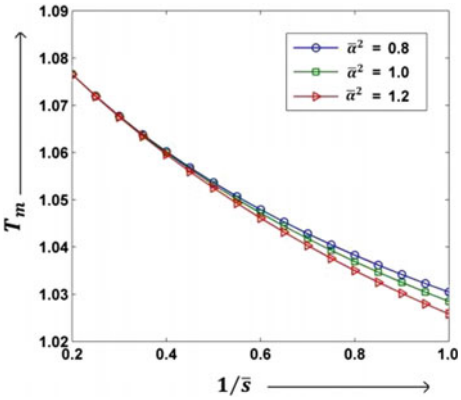

Fig. 4 Mean temperature versus parameter of slip for different values of $\bar{\alpha}^2$ at $\bar{\beta} = 1.3$, $\bar{\gamma}^2 = 1.2$, $\bar{x} = 0.6$, $P_r \cdot E = 1.2$

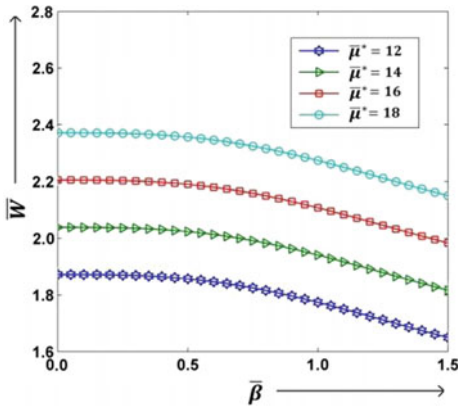

Fig. 5 Lifting force versus parameter of permeability for different values of $\bar{\mu}^*$ a $1/\bar{s} = 1$, $\bar{\alpha}^2 = 0.8$, $\bar{\gamma}^2 = 1.2$, $P_r \cdot E = 1.2$

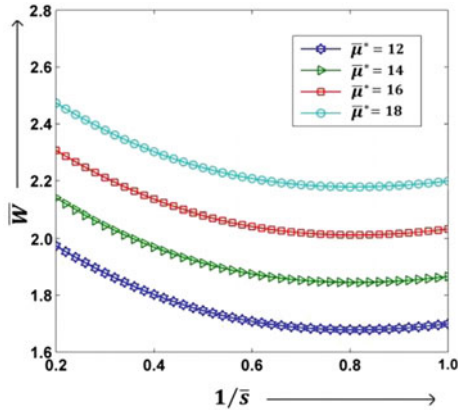

Fig. 6 Lifting force versus parameter of slip for different values of $\bar{\mu}^*$ at $\bar{\alpha}^2 = 0.8$, $\bar{\beta} = 1.3$, $\bar{\gamma}^2 = 1.2$, $P_r \cdot E = 1.2$

the lifting force is almost constant while for $\bar{\beta} \geq 0.5$ and $1/\bar{s} \leq 0.6$, it has a notable decrease with slip.

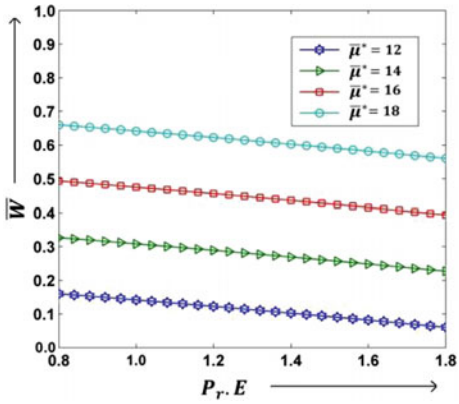

Fig. 7 Lifting force versus thermal parameter, i.e., $P_r \cdot E$ for different values of $\bar{\mu}^*$ at $1/\bar{s} = 1$, $\bar{\alpha}^2 = 1$, $\bar{\beta} = 1.3$, $\bar{\gamma}^2 = 1.2$

The lifting force ($\bar{W}$) with the thermal parameter ($P_r \cdot E$) for various values of the magnetic field parameter ($\bar{\mu}^*$) has been plotted in Fig. 7. It is observed that an increment in the thermal parameter causes an enhancement in the thickness of the thermal boundary layer which results in a low heat transfer rate in the slider. These developments cause decay in the lifting force and sometimes breaking of the bearing due to the higher temperature.

5 Conclusions

In the inner part of the slider, the heat transfer is slow due to the high thickness of the thermal boundary layer; therefore, the cooling is slow while in the outer part of the slider, the heat transfer rate is quite high due to thin boundary layer and hence the cooling is fast. The material parameter has also a notable effect on the thermal boundary layer so for acquiring a desirable heat transfer rate; its value should be adjusted accordingly.

Further, it is also concluded that the lifting force decelerates with an increase in the permeability, slip, and thermal parameter. This decrease is negligible for $\bar{\beta} < 0.5$, $1/\bar{s} > 0.6$ and notable for $\bar{\beta} \geq 0.5$, $1/\bar{s} \leq 0.6$. Due to the higher value of the thermal parameter, the thermal boundary layer thickness increases resulting in a low heat transfer rate and it may cause breaking up of the bearing. Therefore, the value of thermal parameter, i.e., Prandtl number and Eckert number, should be adjusted in such a way that the loss due to heating can be minimized.

References

1. Ram, P., Joshi, V.K., Makinde, O.D.: Unsteady convective flow of hydrocarbon magnetite nano-suspension in the presence of stretching effects. Defect Diffus. Forum **377**, 155–165 (2017)
2. Ram, P., Joshi, V.K., Sharma, K., Walia, M., Yadav, N.: Variable viscosity effects on time dependent magnetic nanofluid flow past a stretchable rotating plate. Open Phys. **14**(1), 651–658 (2016)
3. Verma, P.D.S., Ram, P.: On the low-Reynolds number magnetic fluid flow in a helical pipe. Int. J. Eng. Sci. **31**(2), 229–239 (1993)
4. Ellahi, R., Tariq, M.H., Hassan, M., Vafai, K.: On boundary layer nano-ferroliquid flow under the influence of low oscillating stretchable rotating disk. J. Mol. Liq. **229**, 339–345 (2017)
5. Ram, P., Kumar, A., Makinde, O.D., Kumar, P., Joshi, V.K.: Performance analysis of magnetite nano-suspension based porous slider bearing with varying inclination and slip parameter. Diffus. Found. **11**, 11–21 (2017)
6. Ram, P., Verma, P.D.S.: Ferrofluid lubrication in porous inclined slider bearing. Indian J. Pure Appl. Math. **30**(12), 1273–1282 (1999)
7. Singh, J.P., Ahmad, N.: Analysis of a porous-inclined slider bearing lubricated with magnetic fluid considering thermal effects with slip velocity. J. Braz. Soc. Mech. Sci. Eng. **33**(3), 351–356 (2011)

Thermal Convection in an Inclined Porous Layer with Effect of Heat Source

Anjanna Matta

Abstract The present study analyzes the effect of heat source on thermal convection in an inclined porous layer and also examines the Hadley flow in an inclined porous layer by applying the linear stability analysis. The stability of small-amplitude distributions is studied with corresponding longitudinal rolls using three-dimensional normal modes. The corresponding eigenvalue problem is analyzed numerically by applying the Chebyshev-Tau method for evaluating the critical thermal Rayleigh number (Rz) corresponding to various flow parameters.

Keywords Linear stability analysis · Inclined porous layer · Heat source

1 Introduction

Many authors have analyzed the thermal convection in a horizontal fluid-saturated porous medium, but very few have dealt with the thermal convection in an inclined porous layer in the last decade. The current investigation on thermal convection caused by an internal heat generation with an inclined porous medium is vital due to many real-life problems such as geophysical, the hydrology of aquifers, underground energy, transport and environmental problems, etc. The interest in the inclined porous layer with the thermal convective instability situation arises most relative to the transport in groundwater and in the exploitation of geothermal reservoirs. Other important areas are like the transport of pollutants, oil extracting, and food processing [1, 2]. The mechanism of thermal transport has a major application in environmental problems [3]. The convection in porous layer has been surveyed in the literature [4, 5].

In the literature first time, the inclined porous medium is analyzed by Bories and Combarnous [6], and later, it is extended by Weber [7]. Improving these studies, an inclined porous medium was continued by Caltagirone and Bories [8]. Rees and

A. Matta (✉)
Department of Mathematics, Faculty of Science and Technology,
ICFAI Foundation for Higher Education, Hyderabad 501203, Telangana, India
e-mail: anjireddyiith@ifheindia.org

D. Srinivasacharya and K. S. Reddy (eds.), *Numerical Heat Transfer and Fluid Flow*, Lecture Notes in Mechanical Engineering,
https://doi.org/10.1007/978-981-13-1903-7_7

Bassom [9] studied the thermal convection properties in an inclined layer, and they mentioned some of the outstanding results using linear stability analysis. Thermal convection in a saturated porous layer with internal heat source and mass flow is studied by Matta et al. [10]. The fluid flow in an inclined porous layer is carried out by Barletta and Storesletten [11], and further a fixed heat flux along the walls of the inclined porous medium is studied by Rees and Barletta[12]; also, the thermal convection of Darcy flow in an inclined layer is extended by Barletta and Rees [13]. A note is also given by Nield [14] on the inclined porous layer to give the answers for well-preferred patterns of the natural thermal convection, and then after, Nield et al. [15] find out the importance of the viscous dissipation effect of thermal instability in an inclined porous layer. A little set of articles on the inclined porous medium is available in the surveyed book of Nield and Bejan [16].

The importance of this analysis is to study the thermal convection on the inclined porous medium with the influence of an internal heat source. The applied thermal gradient and heat source lead to a possibly thermal instability in the inclined porous medium. The problem stated that equations have been modified as an eigenvalue problem, which is evaluated numerically by applying the Chebyshev-Tau method.

2 Mathematical Formulation

Let us choose an infinite length-inclined fluid-saturated porous layer with vertical height H considered as shown in Fig. 1. The inclination angle of porous layer is ϕ, which is along the x^*-axis. z^*-axis is taken vertically upward. The vertical thermal difference along the walls is $\triangle T$. The fluid flow inside the porous medium is ap-

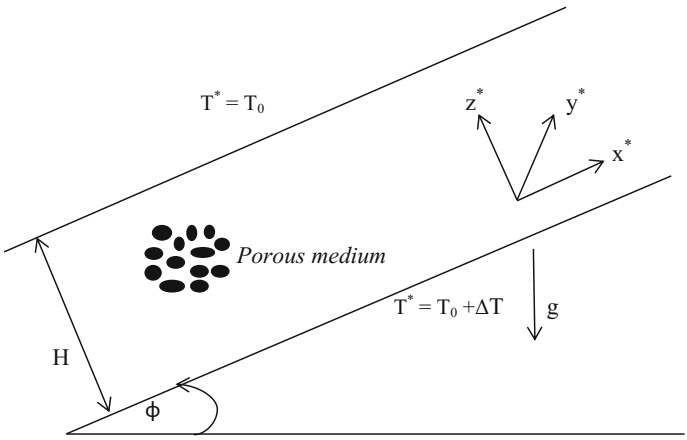

Fig. 1 The physical system

plicable the Darcy law and Boussinesq approximation. The governing equations in nondimensional form are

$$\nabla \cdot \mathbf{q} = 0 \,, \tag{1}$$

$$\mathbf{q} + \nabla P = R_z \theta \left[\sin(\phi) e_1 + \cos(\phi) e_3\right] \,, \tag{2}$$

$$\frac{\partial \theta}{\partial t} + \mathbf{q} \cdot \nabla \theta = \nabla^2 \theta + Q \,, \tag{3}$$

and the corresponding boundary conditions are

$$\left.\begin{array}{lll} z = 0 \,: & w = 0, & \theta = 1 \\ z = 1 \,: & w = 0, & \theta = 0 \end{array}\right\} \tag{4}$$

The corresponding dimensionless variables were used for dimensionless governing equations,

$$(x, y, z) = \frac{1}{H}\left(x^*, y^*, z^*\right), \qquad t = \frac{\alpha_m t^*}{a H^2} \,, \qquad \mathbf{q} = \frac{H \mathbf{q}^*}{\alpha_m} \,, \qquad P = \frac{K P^*}{\mu \alpha_m},$$

$$T^* = T_0 + \theta \triangle T \,, \qquad Q = \frac{H^2 Q^*}{k_m \triangle T}, \tag{5}$$

where

$$\alpha_m = \frac{k_m}{\left(\rho c_p\right)_f}, \quad a = \frac{(\rho c)_m}{\left(\rho c_p\right)_f}, \quad R_z = \frac{\rho_0 g \gamma_T K H \triangle T}{\mu \alpha_m}. \tag{6}$$

Here, the velocity is notated as $\mathbf{q}^*$, T^* is the temperature, P^* is the pressure, Q^* is a heat source, and g is the gravitational acceleration, where the subscripts m and f are referred to porous medium and fluid, respectively. Here, K is the permeability of the porous layer. Also, ρ, c, k_m, and μ denote the density, specific heat, thermal conductivity, and viscosity, respectively. Also, γ_T is the thermal expansion coefficient and the vertical thermal Rayleigh number is R_z.

3 Basic State Solution

The nondimensional governing Eqs. (1)–(3), corresponding to (4), has a steady-state solution as follows:

$$u_s = u\,(z) \,, \quad v_s = 0, \quad w_s = 0, \quad P_s = P\,(x, y, z)\,, \quad \theta_s = \theta\,(z) \,. \tag{7}$$

There is no net flow along the x-axis, and then $\int_0^1 u(z)dz = 0$. Hence, the steady-state solution is in the form of flow velocity and temperature in the given porous layer.

$$u_s = R_z \sin(\phi)\left[\frac{Q}{2}\left(z - z^2 - \frac{1}{6}\right) - z + \frac{1}{2}\right],$$

$$v_s = 0\,, \quad w_s = 0, \quad T_s = \frac{Q}{2}\left(z - z^2\right) + 1 - z\,. \tag{8}$$

4 Linear Stability Analysis

An arbitrarily disturbance quantities of the basic flow are defined as $\mathbf{q} = \mathbf{q}_s + \epsilon\,\overline{\mathbf{q}}$, $\theta = \theta_s + \epsilon\,\overline{\theta}$ and $P = P_s + \epsilon\,\overline{P}$, where ϵ is the perturbation parameter and submitted these disturbances in dimensionless governing Eqs. (1)–(3), and thereafter, by neglecting the nonlinear terms, got the linear system in the following form:

$$\nabla \cdot \overline{\mathbf{q}} = 0\,, \tag{9}$$

$$\overline{\mathbf{q}} + \nabla\overline{P} = \left[R_z\overline{\theta}\right](\sin(\phi)e_1 + \cos(\phi)e_3)\,, \tag{10}$$

$$\frac{\partial\overline{\theta}}{\partial t} + \mathbf{q}_s \cdot \nabla\overline{\theta} + \overline{\mathbf{q}} \cdot \nabla\theta_s = \nabla^2\overline{\theta}\,, \tag{11}$$

where

$$\nabla\theta_s = \left(0, 0, \frac{Q}{2}(1 - 2z) - 1\right).$$

The boundary conditions at the walls are

$$\left.\begin{array}{lll} z = 0 & : & \overline{w} = 0, \quad \overline{\theta} = 1 \\ z = 1 & : & \overline{w} = 0, \quad \overline{\theta} = 0 \end{array}\right\} \tag{12}$$

These conditions in Eq. (12) are clear that there is a zero perturbation in the velocity and temperature along the plates. The solution of Eqs. (9)–(11) funded in the form of normal modes

$$\left[\overline{P}, \overline{\theta}, \overline{\mathbf{q}}\right] = \left[P\,(z)\,, \theta\,(z)\,, \mathbf{q}\,(z)\right]\exp\left\{i\,[kx + ly] + \sigma t\right\}\,, \tag{13}$$

thereafter eliminates P from Eq. (10), and we get

$$\left(D^2 - \alpha^2\right)w + \left(\alpha^2\cos(\phi)\theta + ik\sin(\phi)D\theta\right)R_z = 0, \tag{14}$$

$$\left(D^2 - \alpha^2 - iku_s\right)\theta - \left(\frac{Q}{2}(1 - 2z) - 1\right)w = \sigma\theta. \tag{15}$$

Here, $D = \frac{d}{dz}$, and Eqs. (14)–(15) subject to boundary conditions (4) give an eigenvalue problem for thermal Rayleigh number R_z with k and l wave numbers along x and y directions. In the above, $\alpha = \sqrt{k^2 + l^2}$ is the overall wave number.

5 Results Analysis

The thermal instability analysis in an inclined fluid-saturated porous layer with effect of heat source is studied. The inclination angle ϕ is tested from 0° to 80°. The critical thermal Rayleigh number (R_z) is defined as the minimum of all R_z values as the wave number (α) is varied. The results are shown in Figs. 2, 3, and 4.

Variation of R_z is shown as a function of ϕ for different values of Q as given in Fig. 2. In the absence of heat source ($Q = 0$), the critical value of R_z is increasing slowly upto $\phi < 50^0$, and thereafter the value of R_z is increasing very fast, which indicate that as inclination angle increases, the system is stabilizing.

The response of critical values of R_z as a function of heat source (Q) is given in Fig. 3, for the absence and presence of an inclined angle (ϕ). When the internal heat source increases, then the critical R_z values are decreased, which means flow is destabilized due to enhancement of the heat source. The inclination angle (ϕ) is increased from 0° to 40°, and then the critical values of R_z also enhance, and it indicates that the flow is stable.

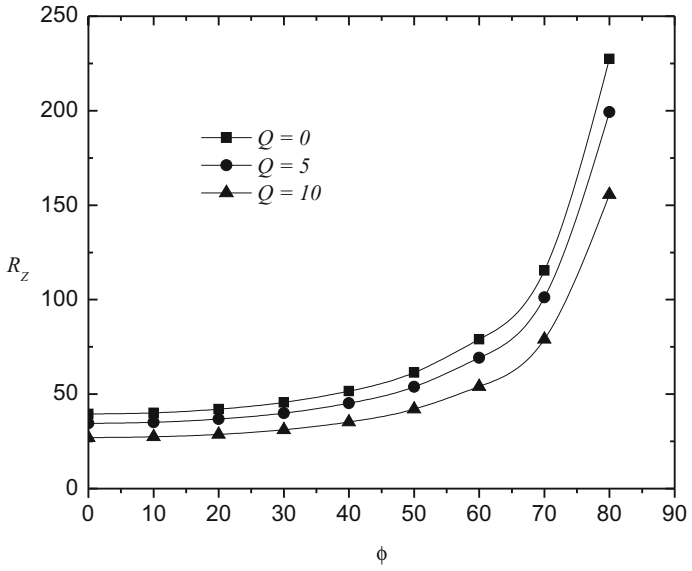

Fig. 2 Variation of R_z with ϕ

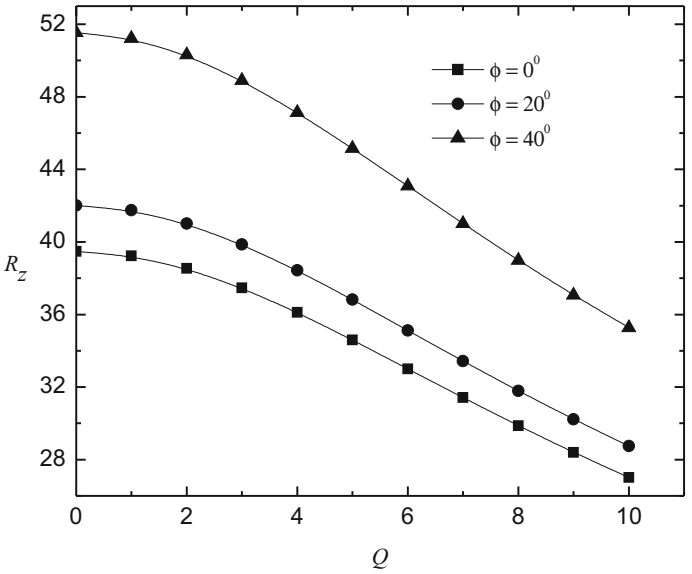

Fig. 3 Variation of R_z with Q

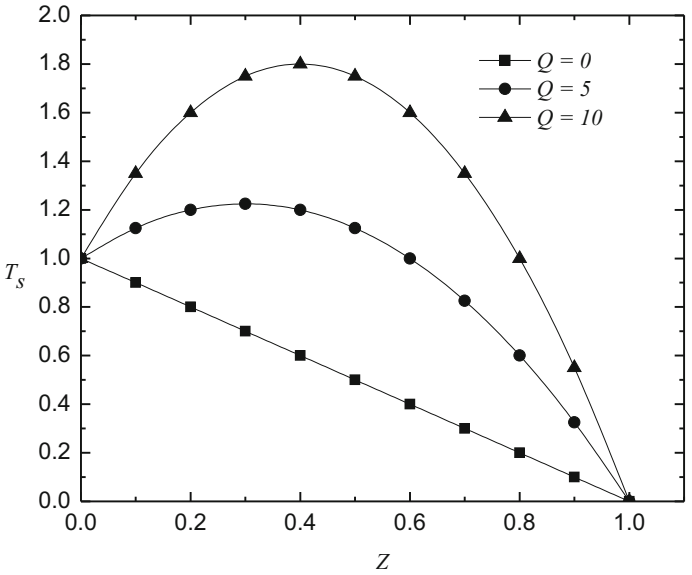

Fig. 4 Variation of T_s with z

The thermal contours are shown in Fig. 4 in the absence and presence of heat source Q. It is interesting to observe that the thermal profiles are parabolic in the presence of heat source. It is clearly appeared that as an internal heat source increases, the global temperature is also increased.

6 Conclusion

In this work, investigate the Hadley flow analysis of an inclined porous medium with effect of heat source studied by linear stability analysis. The critical value of R_z is studied in the longitudinal rolls, and those are investigated for various combinations of the flow field parameters. It is concluded from the figures that

- As inclination angle increases, it causes the strong stabilization irrespective of heat source.
- As heat source increases, it causes the strong destabilization irrespective of inclination angle.
- It is clear that overall the considerable changes appeared in the R_z subject to inclination angle and heat source.

References

1. Bendrichi, G., Shemilt, L.W.: Mass transfer in horizontal flow channels with thermal gradients. Can. J. Chem. Eng. **75**, 1067–1074 (1997)
2. Chen, X., Angui, L.: An experimental study on particle deposition above near-wall heat source. Build. Environ. **81**, 139–149 (2014)
3. Gill, A.E.: A proof that convection in a porous vertical slab is stable. J. Fluid Mech. **35**, 545–547 (1969)
4. Ingham, D.B., Pop, I.: Transport Phenomena in Porous Media. Pergamon, Oxford (1998)
5. Vafai, K.: Handbook of Porous Media, 2nd edn. CRC Press, Boca Raton, FL (2005)
6. Bories, S.A., Combarnous, M.A.: Natural convection in a sloping porous layer. J. Fluid Mech. **57**, 63–79 (1973)
7. Weber, J.E.: Thermal convection in a tilted porous layer. Int. J. Heat Mass Transf. **18**, 474–475 (1975)
8. Caltagirone, J.P., Bories, S.: Solutions and stability criteria of natural convective flow in an inclined porous layer. J. Fluid Mech. **155**, 267–287 (1985)
9. Rees, D.A.S., Bassom, A.P.: Onset of Darcy-Bénard convection in an inclined layer heated from below. Acta Mech. **144**, 103–118 (2000)
10. Matta, A., Narayana, P.A.L., Hill, A.A.: Nonlinear thermal instability in a horizontal porous layer with an internal heat source and mass flow. Acta Mechanica (2016)
11. Barletta, A., Storesletten, L.: Thermoconvective instabilities in an inclined porous channel heated from below. Int. J. Heat Mass Transf. **54**, 2724–2733 (2011)
12. Rees, D.A.S., Barletta, A.: Linear instability of the isoflux Darcy-Bénard problem in an inclined porous layer. Transp. Porous Media **87**, 665–678 (2011)
13. Barletta, A., Rees, D.A.S.: Linear instability of the Darcy-Hadley flow in an inclined porous layer. Phys. Fluids **24**, 074104 (2012)

14. Nield, D.A.: A note on convection patterns in an inclined porous layer. Transp. Porous Media **86**, 23–25 (2011)
15. Nield, D.A., Barletta, A., Celli, M.: The effect of viscous dissipation on the onset of convection in an inclined porous layer. J. Fluid Mech. **679**, 544–558 (2011)
16. Nield, D.A., Bejan, A.: Convection in Porous Media, forth edn. Springer, New York (2013)

MHD Flow and Heat Transfer of Immiscible Micropolar and Newtonian Fluids Through a Pipe: A Numerical Approach

Ankush Raje and M. Devakar

Abstract This study deals with the MHD steady flow and heat transfer of micropolar and Newtonian fluids, flowing immiscibly through a circular pipe. The pipe is assumed to be filled with uniform porous media. The micropolar and Newtonian fluids occupy core and peripheral regions, respectively. The equations governing the flow are coupled and non-linear. The solutions for velocity, microrotation and temperature are acquired numerically employing finite difference method. At fluid–fluid interface, continuity of velocities, shear stresses, temperatures and heat fluxes are considered. The results for velocity, microrotation and temperature are displayed graphically.

Keywords Micropolar fluid · MHD flow · Heat transfer · Finite difference method

1 Introduction

The theory of classical Newtonian fluid model was inadequate to describe the exact behaviour of complex fluids such as animal blood, liquid crystal, slurries, etc. This inadequacy was overpowered to some extent by the theory introduced by Eringen [1] in 1966. This theory is popularly known as the theory of micropolar fluids. Micropolar fluid consists of rigid randomly oriented bar-like elements or dumbbell-shaped molecules. A striking feature of micropolar fluid model is that the fluids whose molecules can rotate independently of the fluid stream velocity and local vorticity can be modelled by micropolar fluids. Unlike Newtonian fluids, the stress tensor in this theory is non-symmetric. An independent kinematic vector called microrotation vector is present in this model to take care of the rotation of the fluid particle. In view

A. Raje (✉) · M. Devakar
Department of Mathematics, Visvesvaraya National Institute of Technology, Nagpur 440010, Maharashtra, India
e-mail: ankush.mth@gmail.com

M. Devakar
e-mail: drmdevakar@gmail.com

D. Srinivasacharya and K. S. Reddy (eds.), *Numerical Heat Transfer and Fluid Flow*, Lecture Notes in Mechanical Engineering,
https://doi.org/10.1007/978-981-13-1903-7_8

of the aforementioned speciality of the theory, many researchers [2–5] showed their interest in studying micropolar fluids.

The study of immiscible fluid flows is having great importance due to its applications in the field of bio-fluid mechanics and chemical engineering. Several researchers [6–8] have contributed to the studies of this kind of flows in different geometries. In recent times, the MHD flows through horizontal channel gained considerable attention due to its practical relevance in diverse fields of engineering and science. For literature on MHD flows, [9, 10] and the references therein can be referred. The flow through porous medium is also of huge interest in bio-fluid dynamics and engineering fields. The seepage of water in river bed, flow of blood through small blood vessels, filtration of fluids, etc. can be modelled using flow through porous medium. In view of these applications of flow through porous media, a good amount of research has been reported in literature [11, 12]. The phenomena of heat transfer are used on a large scale in functioning of numerous devices and systems in engineering like thermal insulators, thermoelectric cooler and heat exchanger. Due to the abundant applications in engineering, many investigators have shown interest in the study of heat transfer [3, 13, 14].

The objective of the present paper is to investigate MHD flow and heat transfer of two immiscible incompressible micropolar and Newtonian fluids through a circular pipe filled with porous medium. A finite difference scheme is employed to obtain numerical solutions for fluid velocities, microrotation and fluid temperatures. Results are displayed through graphs, for variation of flow variables with flow parameters of interest, and the conclusions are presented.

2 Mathematical Modelling of the Problem

Consider the fully developed, laminar and axisymmetric flow of two immiscible fluids through a horizontal circular pipe of radius R_0. Immiscibility of the fluids leads to two distinct regions; region-I, i.e. core region and region-II, i.e. peripheral region. Region-I ($0 \leq r \leq R$) is filled with micropolar fluid having density ρ_1, viscosity μ_1, thermal conductivity K_1 and vortex viscosity κ, whereas region-II ($R \leq r \leq R_0$) is occupied by Newtonian fluid of density ρ_2, viscosity μ_2 and thermal conductivity K_2. Fluids in both regions are assumed to be incompressible and are free from body forces and body couples. A magnetic field of intensity H_0 is applied in transverse direction to the pipe. Both fluid regions are assumed to be filled with the uniform porous media of permeability k^*. Cylindrical polar coordinate system (r, θ, z) is used, with z-axis taken along the axis of the pipe (as shown in Fig. 1). A constant pressure gradient is applied in positive z direction to generate the flow. Due to the unidirectional nature of the flow, the fluid velocity in both regions is assumed to be in the form $\overline{q_I} = (0, 0, w_I(r))$ where the subscript $I = 1, 2$. These choices of velocities automatically satisfy the incompressibility conditions in respective flow regions. The fluids in both regions are assumed to be electrically conductive having σ as the coefficient of electrical conductivity. The temperature of the solid boundary

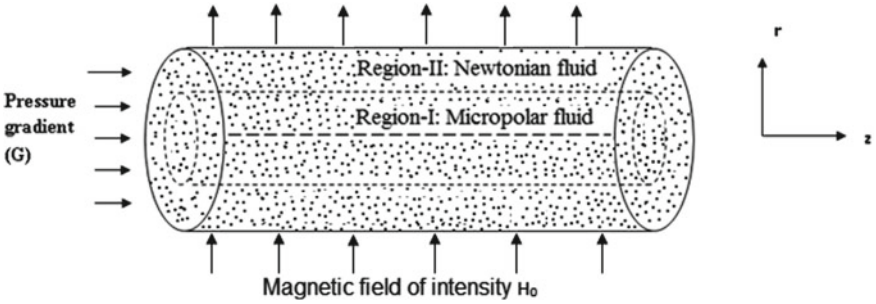

Fig. 1 Geometrical configuration

of pipe is assumed to be at fixed temperature T_w. In view of the unidirectional nature of the fluid velocity, the microrotation vector of the micropolar fluid region is taken as $\overline{\upsilon} = (0, b(r), 0)$. Further, the temperature in both regions is assumed in the form $T_I = T_I(r)$, where $I = 1, 2$ denotes distinct fluid regions. Under the above consideration, the governing equations of the current flow problem are given by [1, 2]. The non-dimensional governing differential equations take the form,

Region-I: $0 \leq r \leq 1$ [Micropolar fluid region]

$$(1+n_1)\frac{1}{r}\frac{d}{dr}\left(r\frac{dw_1}{dr}\right) + n_1\frac{1}{r}\frac{d}{dr}(rb) + Re\ G - \left[M^2 + \frac{1}{Da}\right]w_1 = 0, \tag{1}$$

$$\frac{d}{dr}\left(\frac{1}{r}\frac{d}{dr}(rb)\right) - n_2\frac{dw_1}{dr} - 2n_2 b = 0, \tag{2}$$

$$\frac{1}{r}\frac{d}{dr}\left(r\frac{dT_1}{dr}\right) + B_R\left[\left(\frac{dw_1}{dr}\right)^2 + n_1\left(\frac{dw_1}{dr} + 2b\right)^2 - 2\delta_1\frac{b}{r}\frac{db}{dr} + \delta_2\left(\left(\frac{db}{dr}\right)^2 + \frac{b^2}{r^2}\right)\right] = 0. \tag{3}$$

Region-II: $1 < r \leq s$ [Newtonian fluid region]

$$\frac{1}{r}\frac{d}{dr}\left(r\frac{dw_2}{dr}\right) + \frac{Re\,G}{m_1} - \left[\frac{M^2}{m_1} + \frac{1}{Da}\right]w_2 = 0, \tag{4}$$

$$\frac{1}{r}\frac{d}{dr}\left(r\frac{dT_2}{dr}\right) + \frac{B_R\, m_1}{K}\left(\frac{dw_2}{dr}\right)^2 = 0. \tag{5}$$

Correspondingly, the regularity, boundary and interface conditions, in non-dimensional form are,

$$\frac{dw_1}{dr} = 0, \quad \frac{db}{dr} = 0 \text{ and } \frac{dT_1}{dr} = 0 \text{ at } r = 0, \tag{6}$$

$$w_2(r) = 0 \text{ and } T_2(r) = 0 \text{ at } r = s, \tag{7}$$

$$w_1(r) = w_2(r) \text{ and } T_1(r) = T_2(r) \text{ at } r = 1, \tag{8}$$

$$b(r) = -\frac{1}{2}\frac{dw_1}{dr}, \quad \left(1 + \frac{n_1}{2}\right)\frac{dw_1}{dr} = m_1\frac{dw_2}{dr} \text{ and } \frac{dT_1}{dr} = K\frac{dT_2}{dr} \text{ at } r = 1, \tag{9}$$

where $s = \frac{R_0}{R} \geq 1$, $n_1 = \frac{\kappa}{\mu_1}$ is micropolarity parameter, $Re = \frac{\rho_1 W R}{\mu_1}$ is the Reynolds number, $G = -\frac{dp}{dz}$ is constant pressure gradient, $M = \sqrt{\frac{\sigma R^2 {H_0}^2}{\mu_1}}$ is the Hartmann number, $Da = \frac{k^*}{R^2}$ is the Darcy number, $B_R = \frac{\mu_1 W^2}{K_1 \triangle T}$ is the Brinkman number, $\delta_1 = \frac{\gamma}{R^2\mu_1}$ and $\delta_2 = \frac{\beta}{R^2\mu_1}$, $m_1 = \frac{\mu_2}{\mu_1}$ is the ratio of viscosities, and $K = \frac{K_2}{K_1}$ is the ratio of thermal conductivities.

3 Numerical Procedure for Solutions

The finite difference numerical technique is used to find approximate solution to the problem. It can be recognized that the differential equations (1), (2) and (4) are decoupled from the temperature; therefore, once the fluid velocities in both regions and microrotation in micropolar fluid region are known from Eqs. (1), (2) and (4), the temperature fields can be obtained subsequently from Eqs. (3) and (5).

3.1 Velocity and Microrotation Distributions

For obtaining fluid velocities and microrotation, the system of differential equations (1), (2) and (4) subjected to conditions (6)–(9) concerning w_1, w_2 and b is solved using finite difference method. For the numerical solution, let us fix $s = 2$ and discretize the domain [0, 2] uniformly with step size h in radial direction. Let (r_i) be a point in the computational domain, where i denotes the space discretization parameter. In discretized form, the flow region can be represented by $i = 0, 1, 2, 3, \ldots l-1, l$, where $l = \frac{2}{h}$. Discretized points in micropolar fluid region (region-I) are represented as $i = 0, 1, 2, 3, \ldots m-1$, and spatial points in Newtonian fluid region (region-II) are represented by $i = m+1, m+2, \ldots l-1$, where $m = \frac{l}{2}$ is the liquid–liquid interface.

Using the appropriate finite difference approximations of derivatives in equations (1), (2) and (4), and, invoking the conditions (6)–(9) in the system, we get the following linear system of $(3m + 1)$ equations in same number of unknowns,

$$Z\ X = \Phi, \tag{10}$$

where Z is the banded sparse matrix of order $(3m + 1)$ and Φ is the column vector of $(3m + 1)$ known entries. X is the column vector of unknown quantities, i.e. fluid velocities and microrotation.

Solving linear system (10) gives velocities and microrotation values at each grid point of the fluid regions.

3.2 Temperature Distribution

Having found the numerical values of velocities and microrotation, the aim now is to obtain numerical solution for temperature in both regions from Eqs. (3) and (5) invoking regularity, boundary and interface conditions (6)–(9) concerning the temperature.

Discretizing the domain [0, 2] in similar fashion as before, governing equations for temperature (3) and (5) after applying the finite difference schemes in both fluid regions, invoking the temperature conditions of (6)–(9) in discretized form gives again a linear system of $2m$ equations in $2m$ unknown temperature values as

$$\Theta\ Y = \Upsilon, \tag{11}$$

where Θ is a tri-diagonal matrix of order $2m$, and Υ is a column of $2m$ known values consisting of the values of velocities and microrotation obtained earlier. Y is the column vector of unknown quantities, i.e. fluid temperatures.

The linear system (11) is solved to obtain the temperature distribution in both fluid regions.

4 Results

The flow and heat transfer of two immiscible micropolar and Newtonian fluids through a horizontal circular pipe is considered in present study. A finite difference approach is used to compute numerical solution for fluid velocities, microrotation and temperatures. The solutions are obtained considering the spatial mesh size to be 0.01, i.e. taking 201×201 grid. Figures 2, 3, 4, 5, 6, 7, 8 and 9 display the velocity, microrotation and temperature profiles for several sets of parameters appearing in the problem. The set of fixed values of all parameters, when a particular parameter is varied to see the variation, is considered as $n_1 = 0.5$, $Re = 1$, $m_1 = 0.5$, $Br = 0.4$, $K = 2$, $G = 10$, $M = 0.5$, $Da = 0.5$, $\delta_1 = 2$, $\delta_2 = 2$.

It can be seen from Fig. 2 that, as the micropolarity effects are present only for micropolar fluid region, the fluid velocities in micropolar fluid region are decreasing with increase in values of n_1, but no significant change can be seen in Newtonian

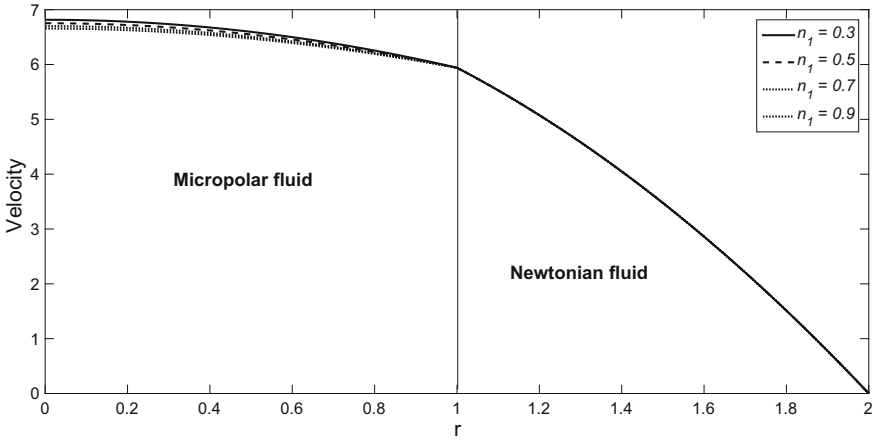

Fig. 2 Fluid velocities with varying micropolarity parameter

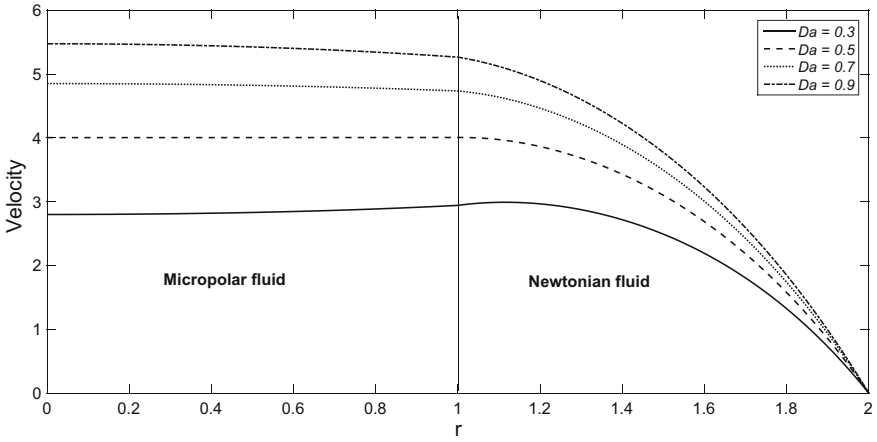

Fig. 3 Fluid velocities with varying Darcy number

fluid region. From Figs. 3 and 4, a remarkable variation is observed in fluid velocity values when they are plotted for various values of Darcy number Da and Hartmann number M. Fluid velocities are decreasing with the increasing M, and a reverse trend is seen with respect to Da. Microrotations are reducing with an increment of n_1 and are increasing with increasing Da (see Figs. 5 and 6).

Figure 7 displays that the fluid temperatures are decreasing with increasing values of micropolarity parameter. Brinkman number is the ratio between heat produced by viscous dissipation and heat transported by molecular conduction. Hence, the more

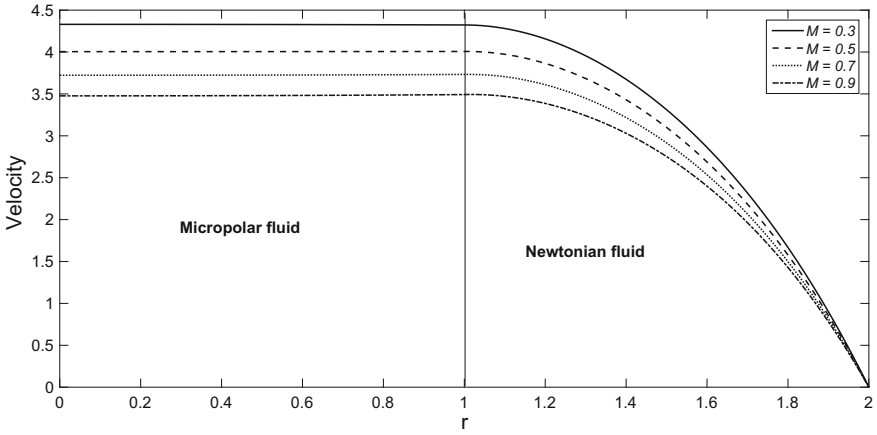

Fig. 4 Fluid velocities with varying Hartmann

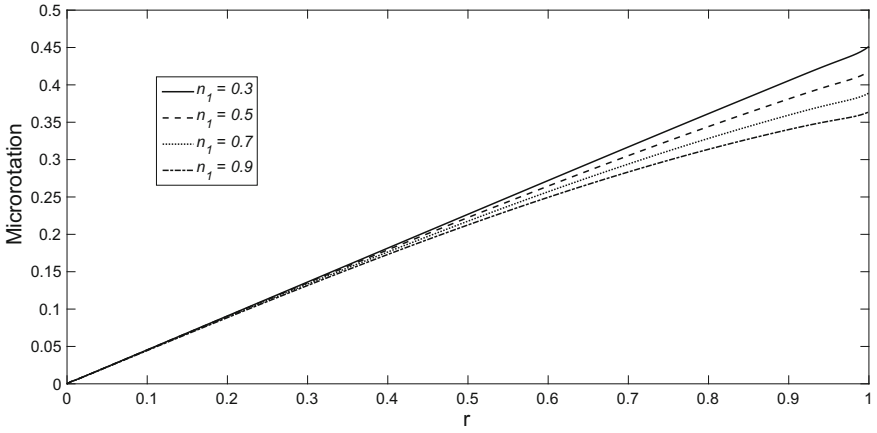

Fig. 5 Microrotation with varying micropolarity parameter

the Brinkman number, the more the viscous dissipation and the less the molecular conduction. As the viscous dissipation converts the work done into heat, naturally, a significant increase in the temperature is observed. In view of this, fluid temperatures in both regions tend to increase with increase in the values of Brinkman number (see Fig. 8). Also, it is evident from Fig. 9 that the fluid temperatures in both regions increase with Darcy number.

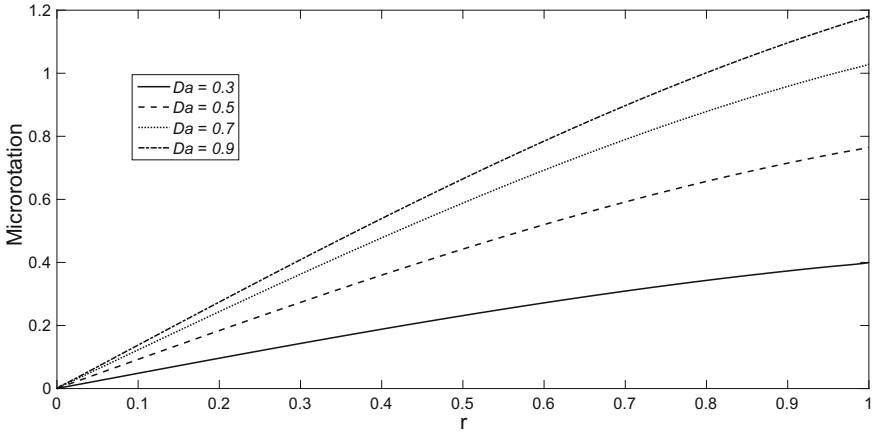

Fig. 6 Microrotation with varying Darcy number

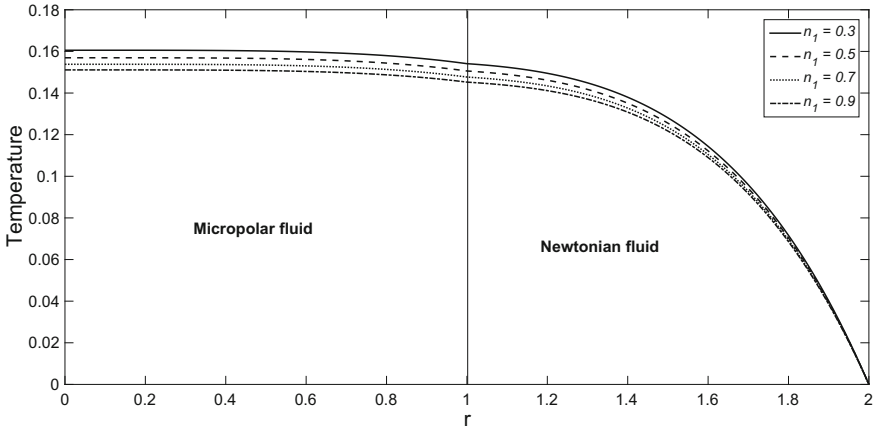

Fig. 7 Fluid temperature with varying micropolarity parameter

5 Conclusions

The main findings of the current study are listed as follows:

- Fluid velocities are increased by Darcy number and are decreased by the increase of magnetic effects and micropolarity effects.
- Microrotation is reduced by micropolarity parameter and is hiked by the hiking of Darcy number.
- The micropolarity parameter n_1 and Hartmann number M are reducing the fluid temperatures in both fluid regions, whereas temperature fields are increased by the increasing values of Brinkman number and Darcy number.

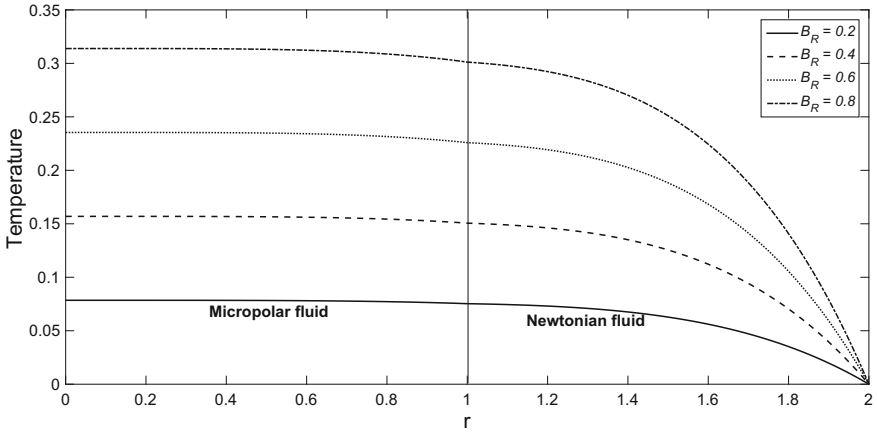

Fig. 8 Fluid temperature with varying Brinkman number

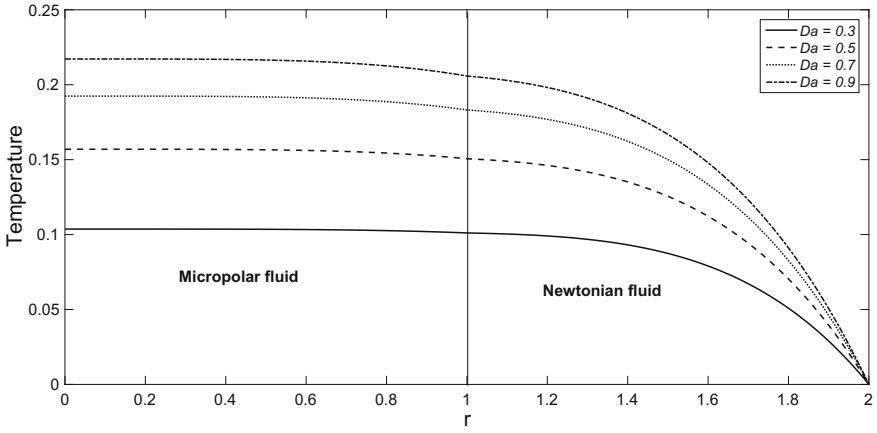

Fig. 9 Fluid temperature with varying Darcy number

Acknowledgements The authors are grateful to National Board for Higher Mathematics (NBHM), Department of Atomic Energy, Government of India, for the financial support through the research project Ref. No. 2/48(23)/2014/NBHM-R&D II/1083 dated 28–01–2015.

References

1. Eringen, A.C.: Theory of micropolar fluids. J. Math. Mech. **16**, 1 (1966)
2. Lukaszewicz, G.: Micropolar Fluids: Theory and Applications. Birkhauser, Boston (1999)

3. Mehmood, R., Nadeem, S., Masood, S.: Effects of transverse magnetic field on a rotating micropolar fluid between parallel plates with heat transfer. J. Magn. Magn. Mater. **401**, 1006–1014 (2016)
4. Srinivasacharya, D., Hima Bindu, K.: Entropy generation of micropolar fluid flow in an inclined porous pipe with convective boundary conditions. Sadhana Indian Acad. Sci. **42**(5), 729–740 (2016)
5. Miroshnichenko, I.V., Sheremet, M.A., Pop, I.: Natural convection in a trapezoidal cavity filled with a micropolar fluid under the effect of a local heat source. Int. J. Mech. Sci. **120**, 182–189 (2017)
6. Prathap Kumar, J., Umavathi, J.C., Chamkha, A.J., Pop, I.: Fully-developed free-convective flow of micropolar and viscous fluids in a vertical channel. Appl. Math. Model. **34**, 1175–1186 (2010)
7. Kumar, N., Gupta, S.: MHD free-convective flow of micropolar and Newtonian fluids through porous medium in a vertical channel. Meccanica **47**, 277–291 (2012)
8. Ramana Murthy, J.V., Srinivas, J.: Second law analysis for poiseuille flow of immiscible micropolar fluids in a channel. Int. J. Heat Mass Transf. **65**, 254–264 (2013)
9. Ramesh, K., Devakar, M.: Magnetohydrodynamic peristaltic transport of couple stress fluid through porous medium in an inclined asymmetric channel with heat transfer. J. Magn. Magn. Mater. **394**, 335–348 (2015)
10. Bhargava, R., Kumar, L., Takhar, H.S.: Numerical solution of free convection MHD micropolar fluid flow between two parallel porous vertical plates. Int. J. Eng. Sci. **41**, 123–136 (2003)
11. Santhosh, N., Radhakrishnamacharya, G., Chamkha, A.J.: Flow of a Jeffrey fluid through a porous medium in narrow tubes. J. Porous Media **18**, 71–78 (2015)
12. Devakar, M., Ramgopal, N.Ch.: Fully developed flows of two immiscible couple stress and Newtonian fluids through nonporous and porous medium in a horizontal cylinder. J. Porous Media. **18**, 549–558 (2015)
13. Tashtoush, B., Magableh, A.: Magnetic field effect on heat transfer and fluid flow characteristics of blood flow in multi-stenosis arteries. Heat Mass Transf. **44**, 297–304 (2008)
14. Priyadarsan, K.P., Panda, S.: Flow and heat transfer analysis of magnetohydrodynamic (MHD) second-grade fluid in a channel with a porous wall. J Braz. Soc. Mech. Sci. Eng. **39**(6), 2145–2157 (2017)

Modeling and Simulation of High Redundancy Linear Electromechanical Actuator for Fault Tolerance

G. Arun Manohar, V. Vasu and K. Srikanth

Abstract High redundancy actuator (HRA) is a linear actuator, having the capability of inherent fault tolerance. It provides the fault tolerance by using a large number of small actuation elements that are attached in series and parallel arrangement within. These actuation elements will work collectively to form as a single HRA. During the usual operation, some of these actuation elements may get faulty. In this circumstances, the HRA will still work, but with a graceful degradation in its performance. This paper discusses the mathematical modeling of the single actuator based on electromechanical actuation elements and based on that, an HRA with nine actuation elements has been modeled. The results are simulated with the help of MATLAB/Simulink module under both faulty and healthy conditions. The obtained results show that there is no sudden failure of the HRA even though there are faulty elements present within the actuator.

Keywords Electromechanical actuator · HRA · Fault tolerance

1 Introduction

Faulty elements in the system lead to system failure, which may cause disasters. The consequences of faults might be damage to the system, people within its vicinity, or its environment. So, there is a very much need to improve the safety of the system, especially for safety-critical systems. A powerful tool for improving the safety in any automated system was fault tolerance (FT), and it is the capability of a system to continue functioning properly in the event of the failure of some of its components or one or more faults within. Fault tolerance is generally achieved through redundancy. Redundancy is the addition of information, resources, or time beyond what is needed

G. Arun Manohar (✉) · V. Vasu · K. Srikanth
Department of Mechanical Engineering, NIT Warangal, Warangal 506004, Telangana, India
e-mail: arunmanohar.nitw@gmail.com

D. Srinivasacharya and K. S. Reddy (eds.), *Numerical Heat Transfer and Fluid Flow*, Lecture Notes in Mechanical Engineering,
https://doi.org/10.1007/978-981-13-1903-7_9

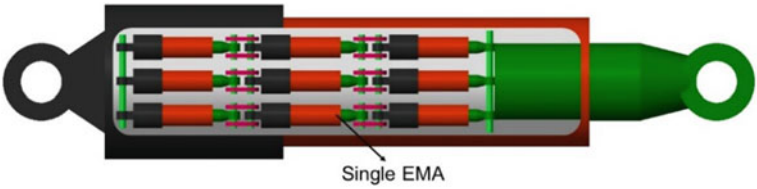

Fig. 1 Example of a 3 × 3 high redundancy actuator

for a system to operate normally. FT system applications are found in aerospace like Airbus fly-by-wire system and Boeing 737 trailing edge flap drive system [1].

In general, FT actuators are adopted with over-actuation, where two are more actuation elements are connected in parallel, and each actuation element is having the capability to do the task individually when the other actuation elements get defective. But, by the adoption of over-actuation, the cost and size of the system increase; thus, the effectiveness of the system reduces [2]. Parallel arrangement exclusively will also of no use, in the existence of jamming of an actuator [2]. Thus to overcome this, the concept of high redundancy actuator (HRA) has been introduced.

HRA is a fault-tolerant linear electromechanical actuator (EMA) which consists of a large number of small actuation elements as shown in Fig. 1. All the actuation elements work collectively to form as a single actuator. To improve the availability and reliability, and also to reduce the need for oversizing, the arrangement of elements in the HRA is in parallel and series [3].

2 Background and Motivation

The current research has focused on HRA based on electromechanical actuator with a relatively low number of actuation elements. An initial work with four actuation elements was controlled through passive fault-tolerant method [1]. The four actuation elements were attached in a 2 × 2 series-in-parallel arrangement [4]. Another work with 16 elements HRA was modeled based on electromagnetic actuation elements. Another work with 12 elements HRA was modeled based on electromechanical actuation elements [2] to explore various fault detection and identification (FDI) and condition monitoring methods [2].

The present work aims to expand the work of Du (2008) by considering nine elements HRA based on electromechanical actuators in (3 × 3) series-in-parallel arrangement as shown in Fig. 1. Using the nine elements HRA, mathematical modeling equations were derived and a MATLAB/Simulink model was developed based on the equations to examine the performance of the HRA under healthy as well as faulty conditions.

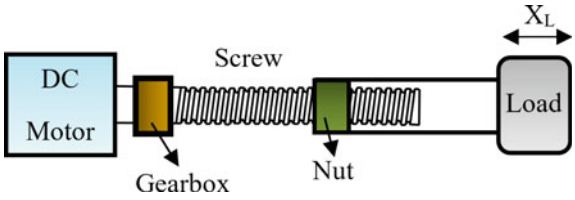

Fig. 2 Linear EMA physical model

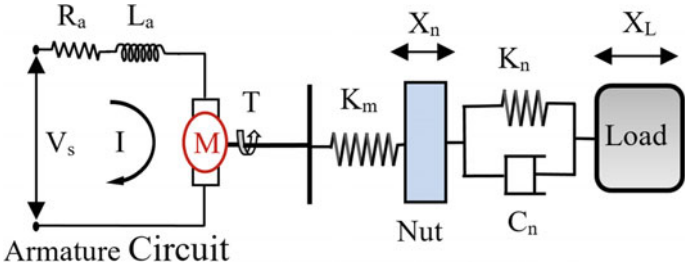

Fig. 3 Equivalent schematic diagram of EMA

3 Mathematical Modeling of Single EMA

Single EMA system modeling is very much necessary for constructing a multielement actuator like HRA. The mathematical modeling of single EMA is addressed in this section. EMAs can be divided into two parts: an electrical part and a mechanical part. A DC motor is considered under the electrical part (Eqs. 1 and 2) whereas a lead/ball screw and gearbox are considered under mechanical part (Eqs. 3 and 4).

All the components of the EMA are shown in Fig. 2. The DC motor converts the electrical energy into mechanical torque whereas the lead/ball screw converts the torque into linear motion. The coupling between the motor shaft and the lead/ball screw was provided by the gearbox. By changing the energy (voltage) supplied to the motor the desired position and force of the actuator can be achieved.

The schematic diagram of the linear EMA with all the parameter notations is shown in Fig. 3. Current I is passing through the armature, and T indicates the motor torque. X_L and X_n indicate the linear displacement of the load and nut, respectively. The term h in Eqs. (2) and (3) is to convert angular motion to linear motion, and it is equal to $l/2\pi N$, where N is the gear ratio and l is the screw lead.

$$\dot{I} = \frac{1}{L_a}\left[V_s - R_a I - K_e \dot{\theta}_m\right] \tag{1}$$

$$\ddot{\theta}_m = \frac{1}{J}\left[K_t I - K_m\left(h^2\theta_m - hX_n\right) - D\dot{\theta}_m\right] \tag{2}$$

$$\ddot{X}_n = \frac{1}{M_n}[K_m(h\theta_m - X_n) + K_n(X_L - X_n) + C_n\left(\dot{X}_L - \dot{X}_n\right) \tag{3}$$

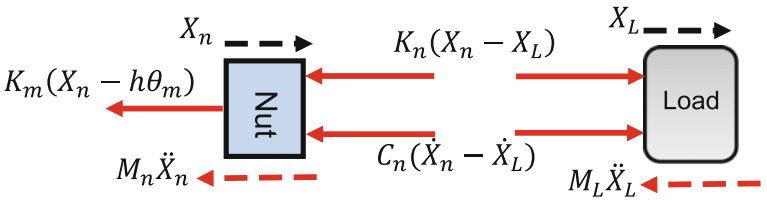

Fig. 4 Free body diagram of a single EMA mechanical part

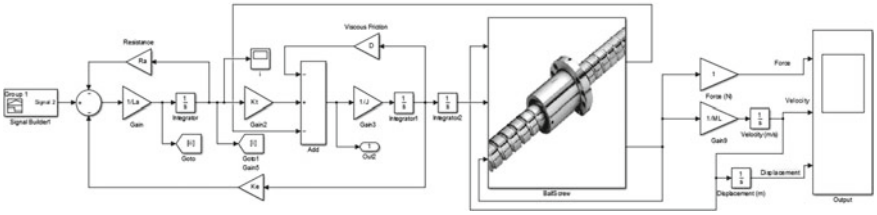

Fig. 5 Simulink model of single EMA

$$\ddot{X}_L = \frac{1}{M_L}[K_n(X_n - X_L) + C_n\left(\dot{X}_n - \dot{X}_L\right) \tag{4}$$

The equations are solved using MATLAB/Simulink and the Simulink model was shown in Fig. 5. All the parameter values used for solving the mathematical equations are mentioned in Table 1. Equation (1) refers to motor armature current, Eq. (2) refers to mechanical loading of the motor, and motor armature current is same for all the individual actuators in an HRA. Equations (3) and (4) refer to linear acceleration of nut and the load derived from the free body diagram shown in Fig. 4. Similarly, the equations of 3×3 HRA in series and parallel can be derived from their free body diagrams, and the simulation results are discussed in Sect. 3.

4 Simulation Results

By developing and simulating the model of single EMA and nine elements HRA using MATLAB/Simulink module, the performance of the actuator with faults and without faults are monitored. The faults introduced in the simulation model are open circuit failure and short circuit failure in the motor windings. In open circuit failure, no current nor torque will be produced by the DC motor, and in the model, this fault can be introduced by replacing the current value with zero.

In the short circuit failure, no voltage was supplied to the DC motor to generate the torque, and in the model, this fault can be introduced by supplying a zero voltage to the actuator.

Table 1 Parameter values used in Simulink model

Parameter	Notation	Value
Supply voltage	V_s	12 V
Armature resistance	R_a	0.4 Ω
Armature inductance	L_a	0.8 mH
Equivalent inertia at armature	J	4.4574e−5 kg m^2
Equivalent viscous friction	D	8.2986e−4 Nm/rad^{-1}
Motor back emf constant	K_e	0.036868 V/$rads^{-1}$
Motor torque constant	K_t	0.030891 Nm/A
Screw lead	l	2e−3 m/rev
Load mass	M_L	4 kg
Motor mass	M_m	1 kg
Motor stiffness	K_m	201,060,000 N/m
Nut damping	C_n	1200 N/ms^{-1}
Nut stiffness	K_n	1.8e5 N/m
Nut mass	M_n	0.5 kg

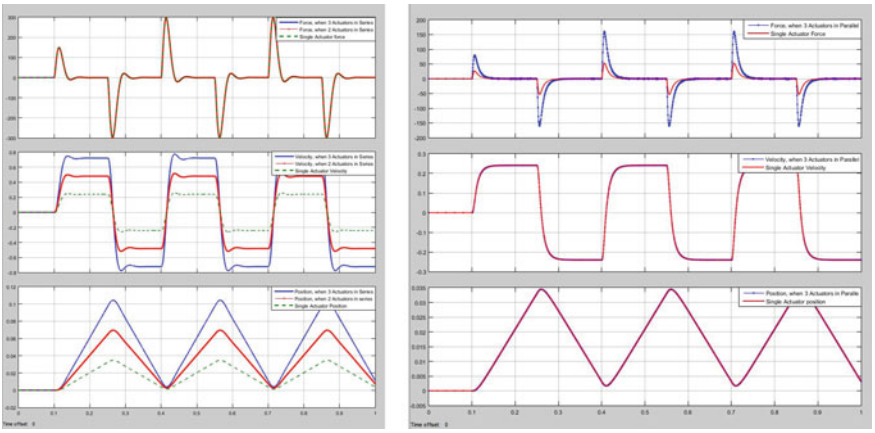

Fig. 6 Three actuation elements in series (left) and three actuation elements in parallel (right)

The performance of the actuator like force (in Newton), linear velocity (in m/s) and linear displacement (in meters) with respect to time are plotted under faulty and healthy conditions. Figure 6 shows the performance of the actuation elements when only three elements are connected in series and when only three elements are connected in parallel, respectively.

From the results, it was clear that in series arrangement, the linear velocity and displacements are increased but the force remains constant. And in the parallel arrangement, the linear velocity and displacements remain constant but the force increased.

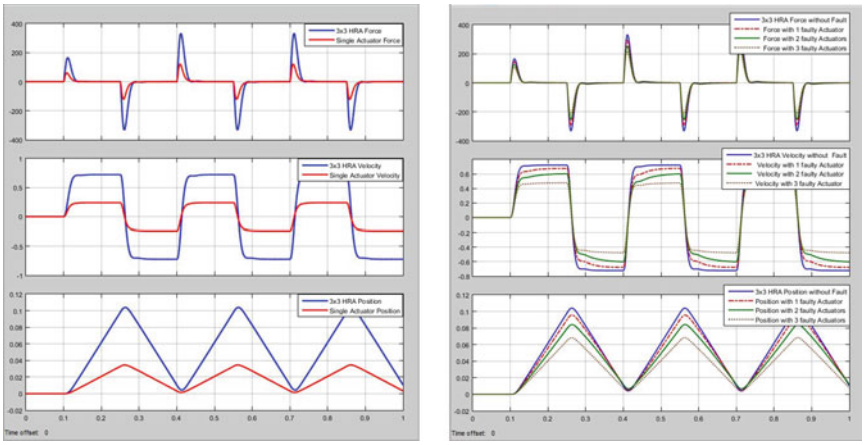

Fig. 7 Performance of single EMA and HRA (left), and performance of HRA under faults (right)

Table 2 The outputs of single EMA and HRA with and without faulty elements

Output	Single EMA	HRA			
		Without faults	With one faulty actuator	With two faulty actuators	With three faulty actuators
Force (N)	120	360	318	277	225
Velocity (m/s)	0.24	0.72	0.67	0.6	0.48
Position (m)	0.037	0.11	0.0958	0.0845	0.0687

Thus, the faults affecting the displacement can be tolerated by series arrangement and the faults affecting the force can be tolerated by parallel arrangement. Therefore by using the advantage of both the series and parallel arrangements, the nine elements in the HRA are arranged as 3×3 series-in-parallel configuration.

Figure 7 (left) shows the performance of single actuation element and HRA without faults and the observations show that the force, linear velocity, and displacement of HRA are approximately thrice that of the individual actuation element. Figure 7 (right) shows the performance of HRA without fault and with one, two, and three faults, respectively. The output performance values of single EMA and HRA are shown in Table 2.

5 Conclusion

In this paper, a mathematical model of single EMA and an HRA with nine actuation elements are discussed. The behavior of the HRA model under open circuit, short circuit failure, and also without failure conditions is observed. The effects of these failures on the displacement, velocity, and force of the actuator are studied, and there

is no sudden failure of the actuator but depending upon the number of faults the performance of the actuator will decrease. The values indicate that there is a certain level of FT was achieved but in the future by implementing a suitable control system, complete FT can be achieved even after three faulty elements present in the HRA.

References

1. Du, X., Dixon, R., Goodall, R.M., Zolotas, A.C.: Modelling and control of a high redundancy actuator. Mechatronics **20**, 102–112 (2010)
2. Antong, H., Dixon, R., Ward, C: High redundancy actuator with 12 elements: open and closed-loop model validation. Int. Fed. Autom. Control **49–21**, 254–259 (2016)
3. Antong, H., Dixon, R., Ward, C.: Modelling and building of experimental rig for high redundancy actuator. In: UKACC International Conference on Control, pp. 385–388, 9–11 July 2014
4. Du, X., Dixon, R., Goodall, R.M., Zolotas, A.C.: LQG Control of a High Redundancy Actuator. In: Mechatronics, IEEE, vol. 44, pp. 1–6 (2007)

Thermal Radiation and Thermodiffusion Effect on Convective Heat and Mass Transfer Flow of a Rotating Nanofluid in a Vertical Channel

V. Arundhati, K. V. Chandra Sekhar, D. R. V. Prasada Rao and G. Sreedevi

Abstract This paper presents a numerical study of thermal radiation and thermodiffusion effect of moving wall (oscillatory) velocity on unsteady convective heat transfer flow of two types of water-based nanofluids (Cu, Al_2O_3) in a vertical channel under the influence of heat sources. Employing regular perturbation method, the momentum and the energy equations are solved analytically. The results of the fluid velocity, temperature, and concentration profiles are presented graphically and discussed for the pertinent flow parameters.

Keywords Thermal radiation · Thermodiffusion · Nanofluids · Vertical channel

1 Introduction

The inherent heat transfer limitation of conventional fluid over metallic and non-metallic materials has led to the innovation in heat transfer by adding a homogeneous mixture of nanoscale particles to base fluid. The term nanofluids was first coined by Choi [1]. Several authors [2–6] have examined the influence of nanoparticles in heat and mass transfer problems with different models. The present work has considered the nanofluid model proposed by Tiwari and Das [7].

Fluid flows, driven by heat convection in open channels involving inclined or vertical plane surfaces, have assumed importance in electronic industry and specifically in solar photovoltaic (PV) systems. Barletta et al. [8], Hang and Pop [9], Xu et al. [10], Fakour et al. [11], Nield and Kuznetsov [12], Sheikholeslami and Ganji [13] have investigated the nanofluid flow with various conditions in a vertical channel. Sreedevi et al. [14] studied Soret effect in convective heat and mass transfer flow

V. Arundhati (✉) · K. V. Chandra Sekhar · G. Sreedevi
Department of Mathematics, K L University, Green Fields,
Vaddeswaram, Guntur 522 502, India
e-mail: venuarundhati@gmail.com

D. R. V. Prasada Rao
Department of Mathematics, S.K. University, Anantapur 515003, India

D. Srinivasacharya and K. S. Reddy (eds.), *Numerical Heat Transfer and Fluid Flow*, Lecture Notes in Mechanical Engineering,
https://doi.org/10.1007/978-981-13-1903-7_10

in vertical channel. Noreen et al. [15] studied Cu particles on peristaltically moving fluid in vertical channel.

This paper investigates the thermal radiation and thermodiffusion effect of moving wall (oscillatory) velocity on unsteady convective heat transfer flow of Al_2O_3–water and Cu–water nanofluids in a vertical channel.

2 Formulation of the Problem

Consider a steady, fully developed tridimensional flow of Al_2O_3 and Cu–water-based nanofluids in a vertical channel. Ho, the magnetic field strength, is induced normally to the channel. Following assumptions are made: (a) no applied voltage signifying absence of an electric field, (b) flow moves upwardly chosen in x-direction, (c) z-direction indicates normal to the channel, (d) Ω is the constant angular velocity which is a rotating fluid at z-direction, (e) Radiation heat flux is negligible at x over z-direction, (f) flow variables are functions of z and t only, and (g) $\nabla.\bar{J} = 0$ for equation of conversation, results Jz as constant. Invoking Seth et al. [16], the below governing equations are reduced to nondimensional coupled equations. Figure 1 shows the coordinate system of the problem.

Assuming the above and introducing the dimensionless variables, the momentum and thermal energy equations are in the form of nondimensional as

$$-S\frac{\partial u}{\partial z} - 2Rv = \frac{1}{A_1 A_3}\frac{\partial^2 u}{\partial z^2} + \frac{A_4}{A_3}G\theta - \frac{A_6 M^2}{A_3}u \tag{1}$$

$$-S\frac{\partial v}{\partial z} + 2Ru + \frac{1}{A_1 A_3}\frac{\partial^2 v}{\partial z^2} - \frac{A_6 M^2}{A_3}v \tag{2}$$

$$-S\ \mathrm{Pr}\frac{\partial \theta}{\partial z} = \frac{\partial^2 \theta}{\partial z^2} - \alpha\theta + \frac{4}{3F}\frac{\partial^2 \theta}{\partial z^2} \tag{3}$$

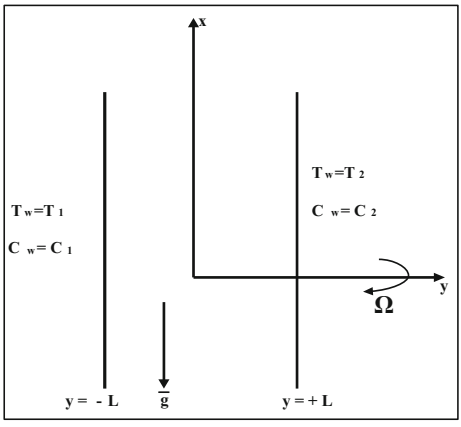

Fig. 1 Schematic diagram of the problem

$$-SSc\frac{\partial C}{\partial z} = \frac{\partial^2 C}{\partial z^2} - \gamma C + ScSr\frac{\partial^2 \theta}{\partial z^2} \tag{4}$$

where

$$A_1 = (1-\varphi)^{2.5},\ A_2 = \frac{k_{nf}}{k_f},\ A_3 = 1-\varphi+\varphi(\frac{\rho_s}{\rho_f}),\ A_4 = 1-\varphi+\varphi\left(\left(\frac{(\rho\beta)_s}{(\rho\beta)_f}\right),\right.$$
$$A_5 = 1-\varphi+\varphi\frac{(\rho C_P)_s}{(\rho C_P)_f},\ A_6 = \left(1+\frac{3(1-\sigma)\phi}{(\sigma+2)}\right), \sigma = \frac{\sigma_s}{\sigma_f}$$

The boundary conditions are

$$u(\pm 1) = 0, v(\pm 1) = 0, \theta(-1) = 0, \theta(+1) = 1, C(-1) = 0, C(+1) = 1 \tag{5}$$

Using Eq. (1), U_o (velocity characteristic) is defined as fluid velocity in the component form as $v(z,t) = u(z,t) + iv(z,t)$
Equations (1) and (2) reduce to

$$-S\frac{\partial V}{\partial z} - 2iRV = \frac{1}{A_1 A_3}\frac{\partial^2 V}{\partial z^2} + \frac{A_4}{A_3}G\theta - (A_6 M^2/A_3)V \tag{6}$$

The boundary conditions in (5) reduce to

$$V(\pm 1) = 0,\ \theta(-1) = 0,\ \theta(+1) = 1,\ \phi(-1) = 0,\ \phi(+1) = 1 \tag{7}$$

3 Method of the Problem

Solving Eqs. (4) and (6) by regular perturbation method (following Ganapathy [17]), the resultant equations are

$$V(z) = \exp\left(-\frac{b_9 z}{2}\right)(B_5\text{Cosh}(m_3 z) + B_6\text{Sinh}(m_3 z)$$
$$+ b_{14}\exp((m_1 - b_1)z) + b_{15}\exp(-(m_1 + b_1)z)$$
$$\theta(z) = \exp(-b_1 z)\left(\frac{\text{Cosh}(m_1 z)}{\text{Cosh}(m_1)}\text{Sinh}(b_1) + \frac{\text{Sinh}(m_1 z)}{\text{Sinh}(m_1)}\text{Cosh}(b_1)\right);$$
$$C(z) = \exp(-b_1 z)\left(\frac{\text{Cosh}(m_1 z)}{\text{Cosh}(m_1)}\text{Sinh}(b_1) + \frac{\text{Sinh}(m_1 z)}{\text{Sinh}(m_1)}(m_1)\text{Cosh}(b_1)\right)$$

The skin friction, Nusselt number, and Sherwood number are defined as
$C_f = \frac{\tau_w}{\rho_f U_o^2}$, Nu $= \frac{xq_w}{k_f(T_1-T_2)}$, and Sh $= \frac{xm_w}{D_B(C_1-C_2)}$, where τ_w is the wall shear, q_w is the wall heat, and m_w is the mass flux of the channel. They are represented as $\tau_w = \mu_{nf}\left(\frac{\partial u}{\partial z}\right)_{z=\pm L}$, $q_w = -k_{nf}\left(\frac{\partial T}{\partial z}\right)_{z=\pm L}$ *and* $m_w = -D_B\left(\frac{\partial C}{\partial z}\right)_{z=\pm L}$.

4 Important Results and Conclusions

Figures 2, 3, 4, 5, 6, 7, 8, 9, 10, 11 and 12 explain the attributes of rotational parameter R, radiation parameter F, thermodiffusion (Soret) Sr, chemical reaction parameter γ, nanoparticle volume fraction parameter ϕ on the nanofluid velocities (primary f' and secondary g), temperature θ, concentration C, skin friction τ, Nusselt number Nu, and Sherwood number Sh, which are discussed for Al_2O_3 and Cu–water-based nanofluids in a rotating system. Figures 2 and 3 display that f' reduces with an increase in R, whereas g reduces with increase in R. Further, it can be found that the Al_2O_3–water nanofluid exhibits higher velocity than the flow as compared to the Cu–water nanofluid. Over the boundary layer, f' and g accelerate due to value increase in F resulting in heat transfer enhancement, owing to increase in thermal boundary layer thickness, as displayed in Figs. 4 and 5. It is noticed that values of velocity component in the case of Al_2O_3–water nanofluid is comparatively less than that of Cu–water nanofluid. Figure 6 depicts that rise in F results in a growth in θ, consequently increasing the thermal boundary layer thickness. It should be noted that to have a faster cooling process, the radiation should be minimized. From Fig. 7, an increase in γ enhances C in both types of nanofluids.

From Fig. 8, it is found that higher the thermodiffusion effect, smaller the concentration in the flow region. Also, it can be noticed that the concentration reduces

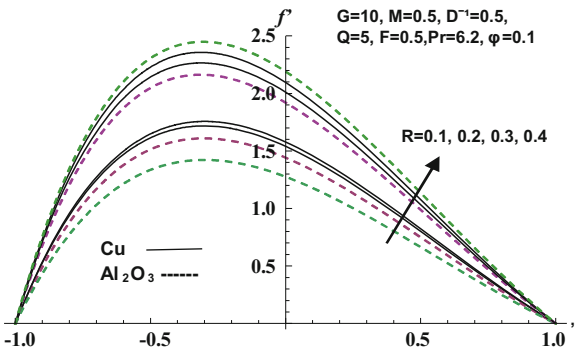

Fig. 2 The effect of R on $f'(\eta)$

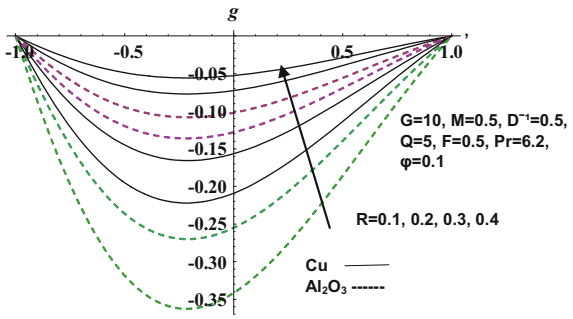

Fig. 3 The effect of R on $g(\eta)$

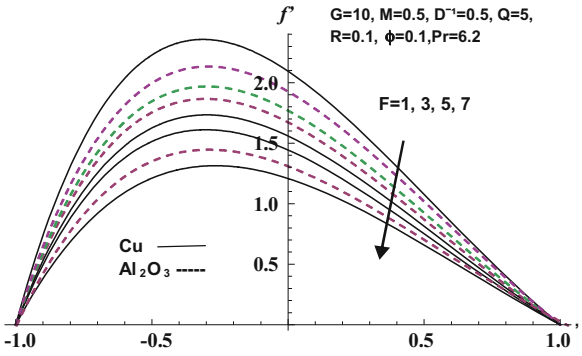

Fig. 4 The effect of F on $f'(\eta)$

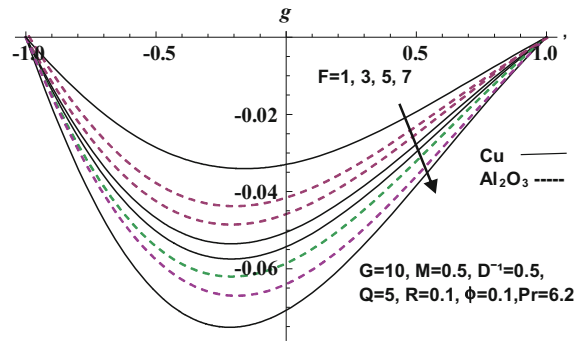

Fig. 5 The effect of F on g(η)

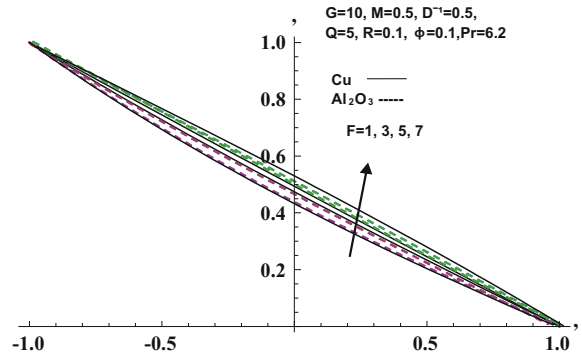

Fig. 6 The effect of F on θ

with increase in Sr in the vicinity of the left boundary, and in the remaining region, the concentration reduces with increase in Sr $\leq$ 1.0 and for higher values of Sr, concentration depreciates in the flow region. From Figs. 9 and 10, it can be seen that decrease in φ results in decrease of f' and g in the boundary layer. It can be noted that thickness of the boundary layer and thermal conductivity can be decreased by increasing the presence of nanoparticles.

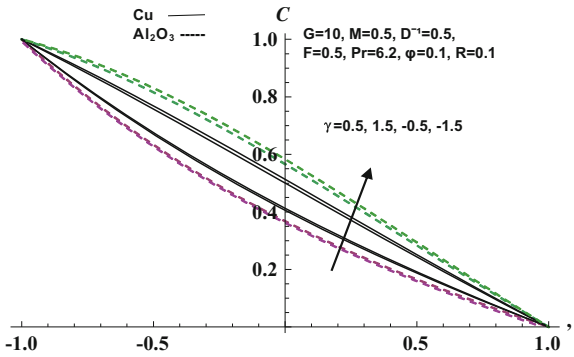

Fig. 7 The effect of γ on C

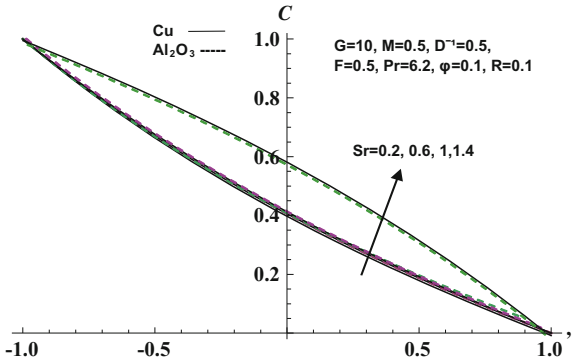

Fig. 8 The effect of Sr on C

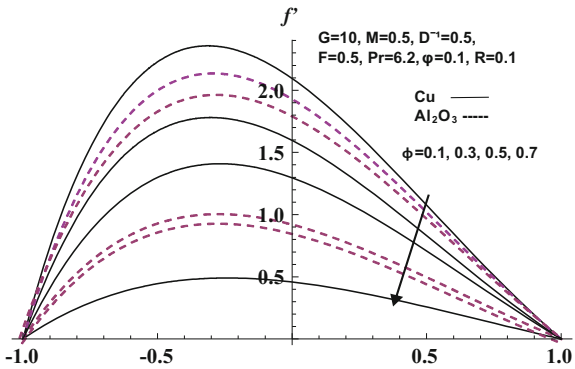

Fig. 9 The effect of φ on $f'(\eta)$

In the case of f', the values in Al_2O_3–water nanofluid are lesser than Cu–water nanofluid; however, in case of g, it is the opposite. Figure 11 illustrates that rise in ϕ, results in reduction of θ and growth in C in the flow region, which is due to diminishing thickness of thermal boundary layer. Further, comparatively, the values in Al_2O_3–water nanofluid are higher than Cu–water nanofluid. Figure 12 represents

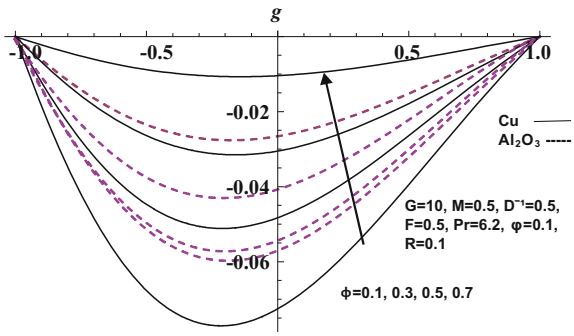

Fig. 10 The effect of φ on $g(\eta)$

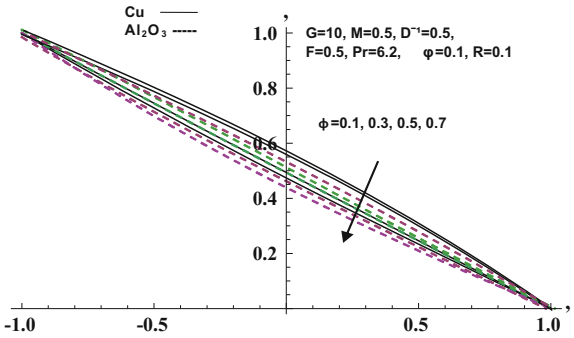

Fig. 11 The effect of φ on θ

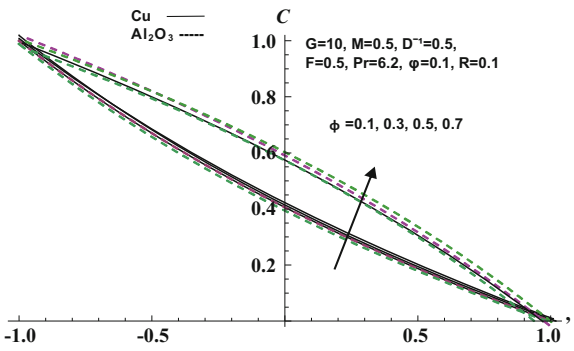

Fig. 12 The effect of φ on C

φ on C. An increase in the values of φ, C enhances the flow region owing to growth in the solutal boundary layer thickness.

Table 1 exhibits the local skin friction component $|\tau|$ behavior at the channel $\eta = \pm 1$. An increase in R enhances τ_x at $\eta = \pm 1$ in Cu–water nanofluid while in Al_2O_3–water nanofluids, $|\tau|$ reduces at $\eta = \pm 1$. An increase in ϕ, $|\tau|$ reduces at $\eta = \pm 1$ in Cu–water nanofluid, and in Al_2O_3–water fluid, it reduces at $\phi \leq 0.3$ and enhances with higher $\phi \geq 0.5$ at the leftward wall, while at the rightward wall, it uniformly enhances. $|\tau|$ enhances with increase in F at $\eta = \pm 1$ in Cu–water nanofluid

Table 1 Variation of skin friction τ_x, τ_y

Parameters			Cu–water		Al_2O_3–water		Cu–water		Al_2O_3–water	
R	F	φ	τ_x (−1)	τ_x (+1)	τ_x (−1)	τ_x (+1)	τ_y (−1)	τ_y (+1)	τ_y (−1)	τ_y (+1)
0.2	0.5	0.1	4.5141	−0.9100	7.1389	−0.4570	−6.480	0.01537	−0.1286	0.0086
0.4	0.5	0.1	5.90001	−1.3827	0.01757	−1.0718	−0.2717	0.151059	−0.0892	0.03077
0.6	0.5	0.1	6.02916	−1.4369	0.51415	−0.9100	−0.4179	0.19911	−0.064	0.02153
0.1	1.5	0.1	5.87753	−1.3813	3.26748	−0.8981	−0.1391	0.05006	−0.0644	0.02788
0.1	5	0.1	6.05566	−1.4470	1.49755	−0.4854	−0.1447	0.05234	−0.0231	0.01198
0.1	0.5	0.3	3.26779	−0.8982	5.89692	−1.3810	−0.0644	−0.2717	−0.1390	0.05005
0.1	0.5	0.5	1.49751	−0.4854	6.05555	−1.4470	−0.0231	−0.4179	−0.1447	0.05234

Table 2 Variation of Nusselt number Nu and Sherwood number Sh

Parameter		Cu–water		Al_2O_3–water		Parameter		Cu–water		Al_2O_3–water	
F	φ	Nu (−1)	Nu (+1)	Nu (−1)	Nu (+1)	Sr	γ	Sh (−1)	Sh (+1)	Sh (−1)	Sh (+1)
1.5	0.1	0.5754	0.4609	0.57003	0.4634	1	0.5	0.7254	0.3583	0.7253	0.3508
5	0.1	0.5184	0.48848	0.51596	0.4894	1.5	0.5	0.7457	0.3508	0.7457	0.3527
0.5	0.3	0.5698	0.4635	0.5756	0.4608	0.2	1.5	0.7457	0.3508	0.7457	0.3527
0.5	0.5	0.5159	0.4894	0.51846	0.4884	0.2	−0.5	0.8658	0.3077	0.7406	0.3518
–	–	–	–	–	–	0.2	−0.5	0.4591	0.4649	0.7558	0.3458
–	–	–	–	–	–	0.2	−1.5	0.2815	0.546	0.756995	0.3453

while in Al_2O_3–water fluid, $|\tau|$ reduces with F at $\eta = \pm 1$ fixing the other parametric values.

Table 2 illustrates the variation of Nu and Sh with various parametric values. An increase in $F \leq 1.5$ reduces Nu and enhances with higher $F \geq 3.5$ at both the walls in Cu–water fluid and in Al_2O_3–water nanofluids, Nu reduces at the leftward wall and enhances at the rightward wall. An increase in $\phi \leq 0.3$ enhances Nu at $\eta = -1$ and reduces at $\eta = +1$ in Cu–water fluid while in Al_2O_3–water fluid, it reduces at $\eta = +1$. Higher Sr ≤ 1, smaller Sh at $\eta = -1$ and larger Sh at $\eta = +1$. Further, a reversal effect is noticed with higher values of Sr ≥ 1.5 in both the fluids. With reference to γ, Sh enhances at $\eta = -1$ and reduces at $\eta = +1$ in $\gamma < 0$ case while in $\gamma > 0$, Sh exhibits a reversed behavior in Cu–water fluid. In Al_2O_3–water, Sh enhances at $\eta = -1$ and reduces at $\eta = +1$ in both γ cases.

References

1. Choi, S.U.S.: Enhancing thermal conductivity of fluids with nanoparticles. ASME Fluids Eng. Div. **231**, 99–105 (1995)
2. Watanabe, T., Pop, I.: Hall effects on magnetohydrodynamic boundary layer flow over a continuous moving flat plate. Acta Mech. **108**, 35–47 (1995)

3. Yu, W., France, D.M., Choi, S.U.S., Routbout, J.L.: Review and Assessment of Nanofluid Technology for Transportation and Other Applications. Argonne National Laboratory (ANL) No. ANL/ESD, 07-09 (2007)
4. Wang, X.Q., Mujumdar, A.S.: A review on nanofluids—part I: theoretical and numerical investigations. Braz. J. Chem. Eng. J. **25**(4), 613–630 (2008)
5. Makinde, O.D., Iskander, T., Mabood, F., Khan, W.A., Tshehla, M.S.: MHD Couette-Poiseuille flow of variable viscosity nanofluids in a rotating permeable channel with Hall effects. J. Mol. Liq. **221**, 778–787 (2016)
6. Kasaeian, A., Daneshazarian, R., Mahian, O., Kolsi, L., Chamkha, A.J., Wongwises, S., Pop, I.: Nanofluid flow and heat transfer in porous media: A review of the latest developments. Int. J. Heat Mass Transf. **107**, 778–791 (2017)
7. Tiwari, R.K., Das, M.K.: Heat transfer augmentation in a two-sided lid-driven differentially heated square cavity utilizing nanofluids. J. Heat Mass Transf. **50**, 2002–2018 (2007)
8. Barletta, A., Celli, M., Magyari, E., Zanchini, E.: Buoyant MHD flows in a vertical channel: the levitation regime. Heat Mass Transf. **44**, 1005–1013 (2007)
9. Hang, X., Pop, I.: Fully developed mixed convection flow in a vertical channel filled with nanofluids. Int. Commun. Heat Mass Transf. **39**, 1086–1092 (2012)
10. Xu, H., Fan, T., Pop, I.: Analysis of mixed convection flow of a nanofluid in a vertical channel with the Buongiorno mathematical model. Int. Commun. Heat Mass Transf. **44**, 15–22 (2013)
11. Fakour, M., Vahabzadeh, A., Ganji, D.D.: Scrutiny of mixed convection flow of a nanofluid in a vertical channel. Therm. Eng. **4**, 15–23 (2014)
12. Nield, D.A., Kuznetsov, A.V.: Forced convection in a parallel-plate channel occupied by a nanofluid or a porous medium saturated by a nanofluid. Int. J. Heat Mass Transf. **70**, 430–433 (2014)
13. Sheikholeslami, M., Ganji, D.D.: Magnetohydrodynamic flow in a permeable channel filled with nanofluid. Sci. Iran. B **21**(1), 203–212 (2014)
14. Sreedevi, G., Prasada Rao, D.R.V., Rao, R.R.: Numerical study of convective heat and mass transfer flow in channels. In: Ansari, A.R. (ed.) Advances in Applied Mathematics, Springer Proceedings in Mathematics and Statistics, vol. 87, pp. 115–125, Springer, Kuwait (2014)
15. Noreen, S., Rashidi, M.M., Qasim, M.: Blood flow analysis with considering nanofluid effects in vertical channel. Appl. Nanosci. **7**, 193–199 (2017)
16. Seth, G.S., Hussain, S.M., Sarkar, S.: Hydromagnetic oscillatory Couette flow in rotating system with induced magnetic field. Appl. Math. Mech. **35**(10), 1331–1344 (2014)
17. Ganapathy, R.: A note on Oscillatory Couette flow in a rotating system. ASME J. Appl. Mech. **61**, 208–209 (1994)

Transient Analysis of Third-Grade Fluid Flow Past a Vertical Cylinder Embedded in a Porous Medium

Ashwini Hiremath and G. Janardhana Reddy

Abstract The concept of heatlines formulates the present problem for cylindrical flow geometry through a porous medium. The current work demonstrates the coupled, highly nonlinear, complex equations of third-grade fluid with unsteady characteristics. The Crank–Nicolson type of implicit numerical scheme is applied to the solution domain subject to suitable initial and boundary conditions. In the considered flow-domain for understanding the visualization technique of heat transfer, the heatlines are the best alternate tools than usual isotherms and streamlines since it is connected to the heat transfer rate all over the geometry. The flow visualization of thermal energy transfer demonstrates that the heatline contours are thicker in the precinct of base edge of the heated vertical surface. It is witnessed that as the Darcy number increases, the heatlines show less deviation from the hot wall. Also, as third-grade fluid parameter increases, the deviation of heatlines varies slightly for the fixed Darcy number.

Keywords Finite difference method · Third-grade fluid parameter
Darcy number

1 Introduction

In recent years, non-Newtonian fluid theories are playing a dominant role because of its emerging applications in biomedicine technology, mining engineering, heat storage, and chemical industry. Out of those non-Newtonian fluids, viscoelastic fluids have received unique attention in the research field. The classification of viscoelastic fluids has been done by Rivlin and Ericksen [1]. Truesdell and Noll [2] have given the constitutive relationship for stress tensor. The grouping of fluids with viscoelastic characteristics is possible keeping their rheological phenomenon in mind. This

A. Hiremath · G. J. Reddy (✉)
Department of Mathematics, Central University of Karnataka,
Kalaburagi 585367, Karnataka, India
e-mail: gjr@cuk.ac.in

D. Srinivasacharya and K. S. Reddy (eds.), *Numerical Heat Transfer and Fluid Flow*, Lecture Notes in Mechanical Engineering,
https://doi.org/10.1007/978-981-13-1903-7_11

categorization introduced the differential type model whose primary class is second-grade fluid. The prediction of the normal-stress differences (which defines the non-Newtonian characteristic) is the peculiar property of this kind. However, it fails to account for the shear thickening (or thinning) phenomena. But the third-grade fluid overcomes this disadvantage and also interprets the non-Newtonian characteristics. The examples of third-grade fluid are slurries, dilute polymers (e.g., polyethylene oxide in water, methyl-methacrylate in n butyl acetate, polyisobutylene, etc.), silicone oils (with greater viscosity), all manufacturing oils, molten plastics, etc. Hayat et al. [3] considered the temperature-dependent thermal conductivity for third-grade fluid flowing past a surface which is stretching exponentially. Further, Hayat et al. [4] deliberate the influence of third-grade and second-grade fluid parameters on the flow region.

Also, the fluid flow in a porous medium is a crucial study due to its pervasive applications in geophysics, biophysics, hydrology, computational biology, engineering (construction, petroleum, and bioremediation), drug delivery, transport in biological tissue, advanced medical imaging and tissue replacement production, etc. To be acquainted with this phenomenon, it is necessary to understand the flow characteristics through a porous medium. A comprehensive study of convective flow on porous media has been done by Nield and Bejan [5], Ingham and Pop [6]. Chamkha et al. [7] investigated the thermophoresis effects through a porous medium for cylindrical geometry. A numerical investigation has been given and showed that velocity and thermal boundary layer increases as permeability parameter increases [8]. The facts relating to temperature distribution will be furnished with the assistance of isotherms in the considered domain. But, the visualization of heat transfer intensity is not feasible using isotherms. Hence, the present study is focused on analyzing the heat visualization effects applying the notion of heatlines in addition to streamlines and isotherms. The heatline concept for the flow visualization was initially introduced by Kimura and Bejan [9] and others [10, 11]. Also, recent studies on heatlines are given in [12–18].

2 Problem Description

The unsteady 2D free convective flow of a third-grade viscoelastic fluid from a cylinder of radius r_0 directed vertically up to semi-infinite height embedded in a porous medium is taken. Figure 1 elucidated problem geometry and symbolized the flow with all variables. The axial coordinate ("x-axis") is precisely chosen along the cylinder's axis in vertically ascending direction. The coordinate in a radial direction ("r-axis") is orientated normal to the axial coordinate. The ambient temperature of fluid T'_∞, which is stationary and same as the free stream temperature, T'_∞. At the initial time,

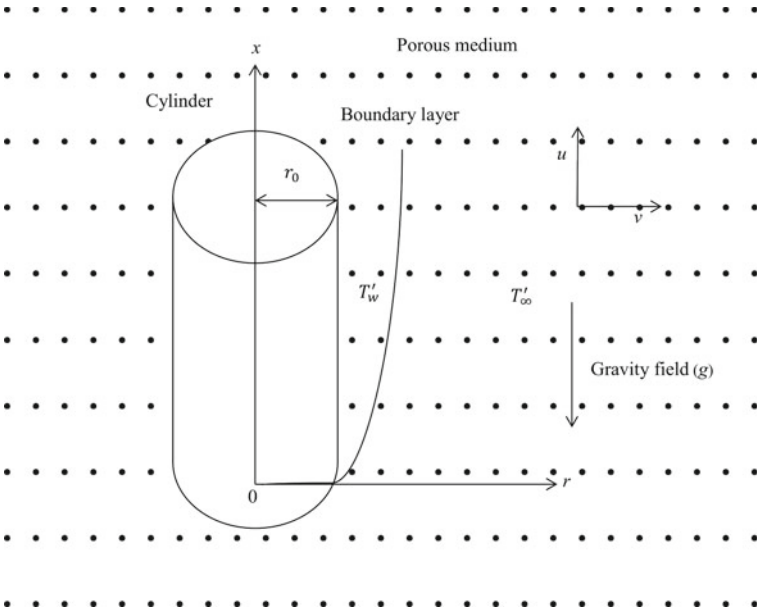

Fig. 1 Geometrical explanation of the problem

i.e., $t' = 0$, both fluid and the geometry are maintained at same temperature T'_∞. Later time ($t' > 0$), $T'_w\left(> T'_\infty\right)$ is the amplified cylinder's temperature and which is preserved uniformly there afterward. The influence of dissipation of viscosity is inconsequential in the thermal equation. Under these suppositions and Boussinesq's approximation, the non-dimensional conservative equations of third-grade fluid in a porous medium are given by

$$\frac{\partial U}{\partial X} + \frac{\partial V}{\partial R} + \frac{V}{R} = 0 \tag{1}$$

$$\frac{\partial U}{\partial t}+U\frac{\partial U}{\partial X}+V\frac{\partial U}{\partial R}=\theta+\frac{1}{R}\frac{\partial}{\partial R}\left(R\frac{\partial U}{\partial R}\right)$$
$$+\alpha_1\Bigg[\frac{1}{R}\frac{\partial^2 U}{\partial R\partial t}+\frac{\partial^3 U}{\partial R^2\partial t}+V\frac{\partial^3 U}{\partial R^3}+\frac{V}{R}\frac{\partial^2 U}{\partial R^2}$$
$$+2\frac{\partial V}{\partial R}\frac{\partial^2 U}{\partial R^2}+U\frac{\partial^3 U}{\partial X\partial R^2}+\frac{U}{R}\frac{\partial^2 U}{\partial X\partial R}+4\frac{\partial U}{\partial R}\frac{\partial^2 U}{\partial X\partial R}+\frac{\partial U}{\partial R}\frac{\partial^2 V}{\partial R^2}$$
$$+3\frac{\partial^2 U}{\partial R^2}\frac{\partial U}{\partial X}+\frac{3}{R}\frac{\partial U}{\partial X}\frac{\partial U}{\partial R}+\frac{1}{R}\frac{\partial U}{\partial R}\frac{\partial V}{\partial R}\Bigg]+\alpha_2\Bigg[\frac{2}{R}\frac{\partial U}{\partial X}\frac{\partial U}{\partial R}+\frac{2}{R}\frac{\partial U}{\partial R}\frac{\partial V}{\partial R}$$
$$+2\frac{\partial^2 V}{\partial R^2}\frac{\partial U}{\partial R}+2\frac{\partial^2 U}{\partial R^2}\frac{\partial U}{\partial X}+4\frac{\partial U}{\partial R}\frac{\partial^2 U}{\partial X\partial R}+2\frac{\partial V}{\partial R}\frac{\partial^2 U}{\partial R^2}\Bigg]$$
$$+\beta\Bigg[4\left(\frac{\partial U}{\partial R}\right)^2\frac{\partial^2 U}{\partial X^2}+(Gr)^2\frac{2}{R}\left(\frac{\partial U}{\partial R}\right)^3$$
$$+2\frac{\partial U}{\partial X}\frac{\partial U}{\partial R}\frac{\partial^2 U}{\partial X\partial R}+6(Gr)^2\left(\frac{\partial U}{\partial R}\right)^2\frac{\partial^2 U}{\partial R^2}\Bigg]-\frac{1}{\mathrm{Da}}U \tag{2}$$

$$\frac{\partial\theta}{\partial t}+U\frac{\partial\theta}{\partial X}+V\frac{\partial\theta}{\partial R}=\frac{1}{Pr}\left(\frac{\partial^2\theta}{\partial R^2}+\frac{1}{R}\frac{\partial\theta}{\partial R}\right) \tag{3}$$

where the non-dimensionalized quantities are defined as $\mathrm{U}=Gr^{-1}ur_0/\upsilon$, $\mathrm{V}=\upsilon r_0/\upsilon$, $X=Gr^{-1}x/r_o$, $R=r/r_o$, $\theta=\left(T'-T'_\infty\right)/(T'_w-T'_\infty)$, $\mathrm{t}=\upsilon t'/r_0^2$. In the above equations where $Gr=\left\{\mathrm{g}\beta_T r_o^3\left(T'_w-T'_\infty\right)\right\}/\upsilon^2$ indicates the thermal Grashof number, β—third-grade fluid parameter, $Pr(=\upsilon/\alpha)$—Prandtl number, υ—kinematic viscosity, β_T—volumetric coefficient of thermal expansion, U, V—dimensionless velocity components of in X and R direction, respectively, t—dimensionless time, T'—fluid temperature, θ—dimensionless temperature, T'_w—wall temperature, and T'_∞—free stream temperature.

The conditions at the initial time and at the boundary in their non-dimensionalized forms are taken as

$$t\le 0:\theta=0,\quad V=0,U=0\quad\text{for all X and R}$$

$$t>0:\theta=1,V=0,U=0\quad\text{at } R=1;$$

$$\theta=0,V=0,U=0\quad\text{at } X=0;$$

$$U\to 0,\frac{\partial U}{\partial R}\to 0,\ V\to 0,\theta\to 0\text{ as }R\to\infty \tag{4}$$

The non-dimensional form of stream function and heat function is given by

$$\frac{\partial^2 \psi}{\partial X^2} + \frac{\partial^2 \psi}{\partial R^2} = U + R\frac{\partial U}{\partial R} - R\frac{\partial V}{\partial X}. \tag{5}$$

$$\frac{\partial^2 \Omega}{\partial X^2} + \frac{\partial^2 \Omega}{\partial R^2} = Pr\left[R\frac{\partial (V\theta)}{\partial X} - R\frac{\partial (U\theta)}{\partial R} - U\theta\right] - R\frac{\partial^2 \theta}{\partial X \partial R} \tag{6}$$

3 Numerical Procedure

The time-dependent flow field Eqs. (1)–(3) along with (4) are elucidated using implicit iterative numerical ("Crank–Nicolson type") method [17]. The discretized equations are resolved by using algorithms called Thomas and pentadiagonal. The results of these finite difference equations obtained in the rectangular grid with $X_{\max} = 1, X_{\min} = 0$, $R_{\max} = 20$ and $R_{min} = 0$, where R_{max} corresponds to $R = \infty$.

4 Results and Discussion

Figures 2, 3, and 4 explain the "streamlines", "isotherms", and "heatlines" under steady-state conditions for different values of β and Da, respectively. The values of ψ, θ, and Ω are calculated by the central differences of order 2. The variation of β and Da is shown in each figure. Few important remarks are made here from all these figures. It is observed that the isotherms and heatlines occur very immediate to the heated surface when matched with that of streamlines. Figure 2 depicts the result that as β (third-grade parameter) intensifies, the variation is minimum in the streamlines. Also, it is observed that from Fig. 2 the streamlines are moving to a distance away from the wall as Da (Darcy number) upsurges. It is also noticed that for augmenting Da, there are variations in the streamlines pattern. These lines are thicker in the locality the leading edge of the cylinder, and it is noticed in Fig. 2. Also, as X value amplifies the intensity of heat transfer is maximum from the cylinder surface to the third-grade fluid and it is minimum for decreasing values of X.

From Fig. 3, the slight displacement of isotherms toward the hot wall is observed as Da increases or β decreases. Also, the smallest variation in isotherms is noticeable, as β or Da augments. Also, the temperature intensities in the flow-domain are key factors to identify the isotherms, but heatlines are alternate tools to isotherms for effective heat transfer visualization and analysis.

Henceforth, the visualization of heat transmission and fluid flow are the topics of analysis which is possible with the assistance of heatlines which is revealed in Fig. 4. A similar tendency is proposed for both isotherms and heatlines. The heatlines demonstrates the process as heat drawing out from a hot surface. The heatlines are the resourceful tools for the visualization of heat transmission as an alternative to the isotherms. Heatlines show a little shift toward the hot wall as Da escalates and for

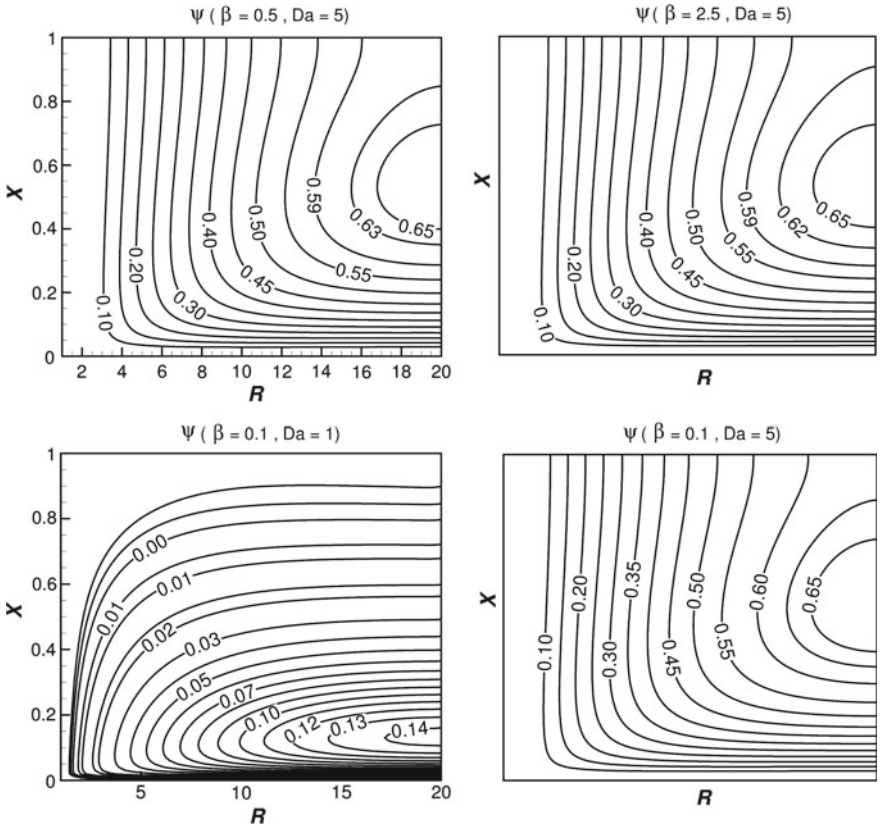

Fig. 2 Time-independent state streamlines (ψ) in (X, R) for several values of β and Da with $Pr = 0.63$

β, it is totally reverse. Likewise, as β falls or Da upsurges, there will be an increase in Ω to gain maximum value. Lastly, it is determined that the changes in heatlines occur in the proximity of the hot wall compared to that of isotherms and streamlines.

5 Concluding Remarks

The present study is focused on the flow visualization of time-dependent free convective flow of third-grade fluid from a cylinder surrounded in a porous medium using Bejan's heatline concept. The technique called so Crank–Nicolson type is executed

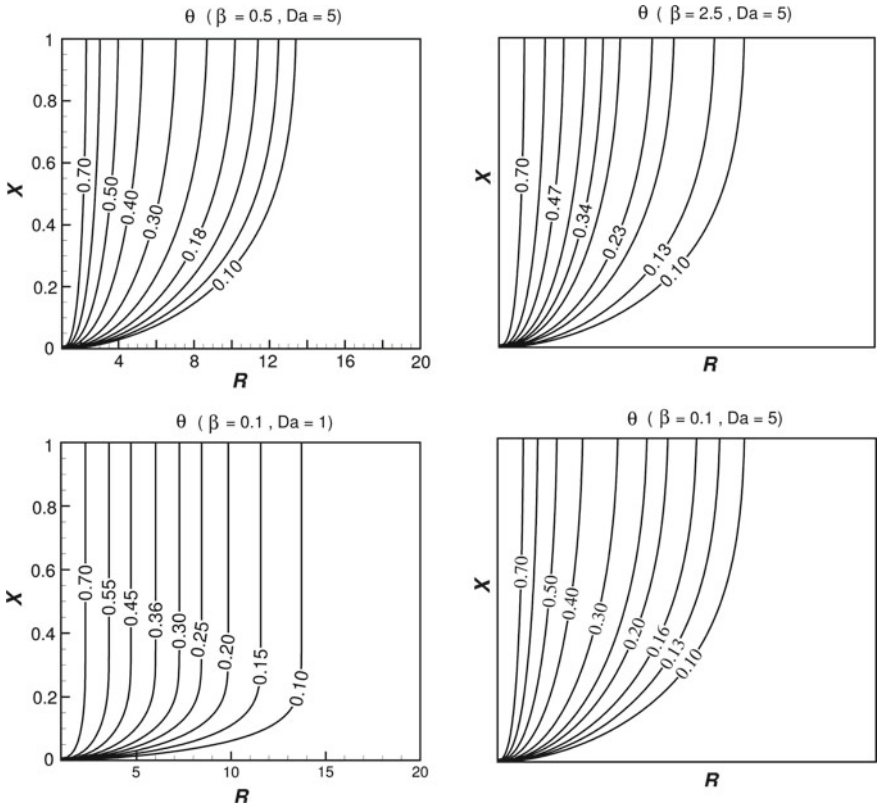

Fig. 3 Time-independent state isotherms (θ) in (X, R) for several values of β and Da with $Pr = 0.63$

to simplify the governing equations. Bejan's heat flow model embraces the heatline plots very clearly. To understand the visualization of heat transmission in the flow-domain, the physical characteristics of heatlines play a significant role. Also, at all levels, the rate of heat transmission in a specified region is evaluated by heatlines. The heat function analogy is used to analyze the flow region. On the hot cylindrical wall, this function has the value which is closely related to the overall heat transfer rate (Nusselt number). The influences of third-grade fluid parameter (β) and Darcy parameter (Da) on flow profiles are discussed. The important observation is, flow visualization indicates that the occurrence of streamlines spread all over the flow-domain, whereas the heatlines and isotherms spread over restricted area immediate to the heated wall .

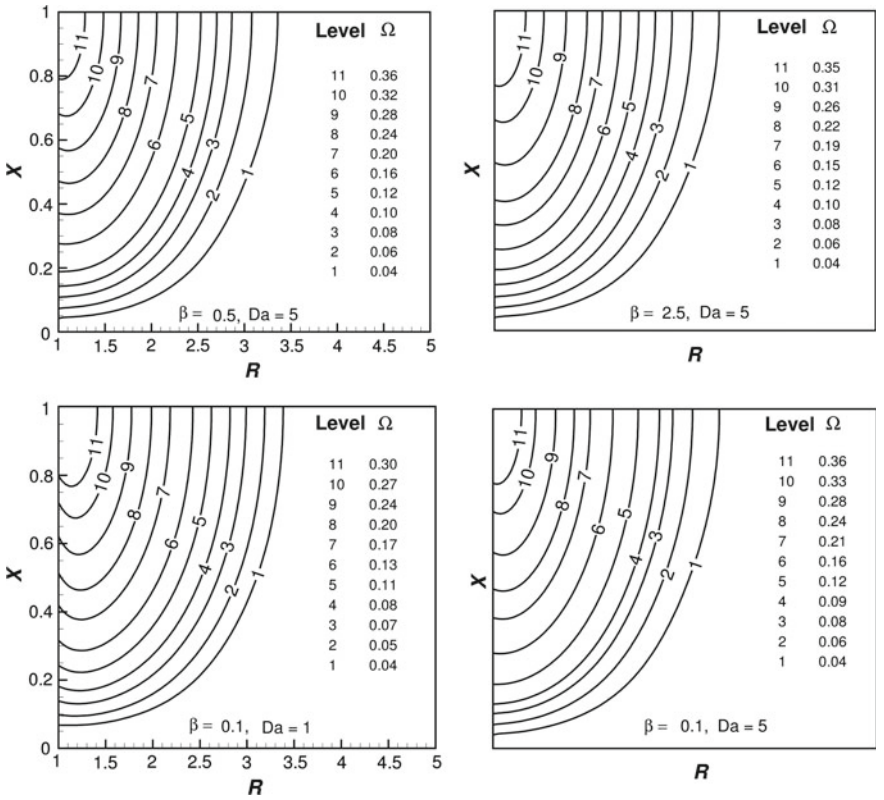

Fig. 4 Time-independent state heatlines (Ω) in (X, R) for several values of β and Da with $Pr = 0.63$

Acknowledgements The first author Ashwini Hiremath wishes to thank DSTINSPIRE (Code No. IF160409) for he grant of research fellowship and Central University of Karnataka for providing the research facilities. Also, the corresponding author G. Janardhana Reddy acknowledges the financial support of UGC-BSR Start-Up Research Grant.

References

1. Rivlin, R.S., Ericksen, J.L.: Stress deformation relations for isotropic materials. J. Rational Mech. Anal. **4**, 323 (1955)
2. Truesdell, C., Noll, W.: The non-linear field theories of mechanics, 2nd edn. Springer, New York (1965)
3. Hayat, T., Shafiq, A., Alsaedi, A., Asghar, S.: Effect of inclined magnetic field in flow of third grade fluid with variable thermal conductivity. AIP Adv. **5**, 087108–087115 (2015)
4. Hayat, T., Shafiq, A., Alsaedi, A.: MHD axisymmetric flow of third-grade fluid by a stretching cylinder. Alexandria Eng. J. **54**, 205–212 (2015)
5. Nield, D.A., Bejan, A.: Convection in Porous Media, 4th edn. Springer, New York (2013)

6. Ingham, D.B., Pop, I.: Transport Phenomena in Porous Media, 1st edn. Elsevier Science, Oxford (1998)
7. Chamkha, A.J., Jaradat, M., Pop, I.: Thermophoresis free convection from a vertical cylinder embedded in a porous medium. Int. J. Appl. Mech. Eng. **9**, 471–481 (2004)
8. Loganathan, P., Eswari, B.: Natural convective flow over moving vertical cylinder with temperature oscillations in the presence of porous medium. Global J. Pure App. Math. **13**, 839–855 (2017)
9. Kimura, S., Bejan, A.: The heatline visualization of convective heat transfer. ASME J. Heat Trans. **105**, 916–919 (1983)
10. Aggarwal, S.K., Manhapra, A.: Use of heatlines for unsteady buoyancy-driven flow in a cylindrical enclosure. ASME J. Heat Trans. **111**, 576–578 (1989)
11. Bejan, A.: Convection Heat Transfer, 1st edn. Wiley and Sons, New York (1984)
12. Rani, H.P., Reddy, G.J.: Heatline visualization for conjugate heat transfer of a couple stress fluid from a vertical slender hollow cylinder. Int. Comm. Heat Mass Transf. **48**, 46–52 (2013)
13. Reddy, G.J., Kethireddy, B., Umavathi, J.C., Sheremet, M.A.: Heat flow visualization for unsteady Casson fluid past a vertical slender hollow cylinder. Therm. Sci. Eng. Prog. **5**, 172–181 (2018)
14. Rani, H.P., Reddy, G.J., Kim, C.N., Rameshwar, Y.: Transient couple stress fluid past a vertical cylinder with Bejan's heat and mass flow visualization for steady-state. ASME J. Heat Transfer **137**, 032501-12 (2015)
15. Reddy, G.J., Kethireddy, B., Rani, H.P.: Bejan's heat flow visualization for unsteady micropolar fluid past a vertical slender hollow cylinder with large Grashof number. Int. J. Appl. Comput. Math. **4**, 39 (2018)
16. Das, D., Basak, T.: Analysis of average Nusselt numbers at various zones for heat flow visualizations during natural convection within enclosures (square vs triangular) involving discrete heaters. Int. Comm. Heat Mass Transfer. **75**, 303– 310 (2016)
17. Rani, H.P., Kim, C.N.: A numerical study on unsteady natural convection of air with variable viscosity over an isothermal vertical cylinder. Korean J. Chem. Eng. **27**, 759–765 (2010)
18. Reddy, G.J., Hiremath, A., Kumar, M.: Computational modeling of unsteady third-grade fluid flow over a vertical cylinder: a study of heat transfer visualization. Results Phys. **8**, 671–682 (2018)

Natural Convective Flow of a Radiative Nanofluid Past an Inclined Plate in a Non-Darcy Porous Medium with Lateral Mass Flux

Ch. Venkata Rao and Ch. RamReddy

Abstract This computational work aims to investigate the effects of lateral mass flux and thermal radiation on the natural convective flow of a nanofluid along a semi-infinite inclined plate in a non-Darcy porous medium. The effects of thermophoresis and Brownian motion are incorporated to initiate the Buongiorno's nanofluid model. The governing system of nonlinear boundary layer equations is cast into a dimensionless form by introducing a set of similarity transformations. The resulting ordinary differential equations are then solved by employing a spectral local linearization method (SLLM). In some special cases, the present outcomes are compared with the published results in the literature, and they are in good agreement. The combined effects of thermal radiation, inclination angle, non-Darcy parameter, and suction/injection parameter on the velocity, temperature, and solid volume fraction profiles along with Nusselt and nanoparticle Sherwood numbers are discussed.

Keywords Nanofluid · Inclined plate · Thermal radiation · Non-Darcy porous medium

1 Introduction

The study of convective heat and mass transfer in porous media has been one of the major research areas owing to its wide range of applications in geosciences and engineering such as energy storage systems, thermal insulations, geothermal energy systems, filtration processes, petroleum recovery, packed bed reactors, oil recovery technology, disposal of nuclear and chemical wastage, etc. The study of heat transfer in geothermal systems has been reviewed by Cheng [1]. The effects of fluid injection

Ch. Venkata Rao (✉) · Ch. RamReddy
Department of Mathematics, National Institute of Technology,
Warangal 506004, Telangana, India
e-mail: venki003@gmail.com

Ch. RamReddy
e-mail: chittetiram@gmail.com

D. Srinivasacharya and K. S. Reddy (eds.), *Numerical Heat Transfer and Fluid Flow*, Lecture Notes in Mechanical Engineering,
https://doi.org/10.1007/978-981-13-1903-7_12

and suction on the free convective flow with heat transfer in a Darcy porous medium have been investigated by Cheng [2] and Merkin [3]. Later, Plumb and Huenefeld [4], Bejan and Poulikakos [5], Nakayama et al. [6] used the Forchheimer's extension law to investigate the natural convective heat transfer over the non-isothermal vertical surface in a non-Darcy porous medium. The effects of lateral mass flux and thermal dispersion on free convective flow over the vertical and horizontal plate in a non-Darcy porous media have been studied by Murthy and Singh [7, 8]. A detailed survey of convective heat and mass transfer in a non-Darcy and Darcy porous medium has been reported by Nield and Bejan [9].

In the recent days, many researchers have focused their attention on nanofluids due to its significant applications in science and engineering. The term "nanofluid" is coined by Choi [10] and described as a suspension of nanoparticles or fibers with 1–100 nm diameters in conventional fluids like oil, water, ethylene glycol, etc. The main feature of nanofluids is the quality of improving thermal conductivity. Buongiorno [11] experimentally investigated seven slip mechanisms, namely, inertia, Brownian diffusion, Magnus effect, diffusiophoresis, gravity settling, fluid drainage, and thermophoresis. As an outcome of this experimentation, he noted that the thermophoresis and Brownian diffusion effects are more important to investigate the convective flows of a nanofluid. For more details on the nanofluids, one can follow the works of Das et al. [12], Das and Stephen [13], and Kakac and Pramuanjaroenkij [14]. Motivated by the above literature, the natural convective flow of a nanofluid past an inclined plate in a non-Darcy porous medium with thermal radiation and lateral mass flux is considered in this paper.

2 Boundary Layer Analysis

The 2-D steady, laminar natural convective flow of a nanofluid along a vertically inclined plate, with an angle A ($0° \leq A \leq 90°$), in a non-Darcy porous medium is considered. An inclination angle is characterized by 0° (for the vertical plate case), $0° < A < 90°$ (for an inclined plate case) and 90° (for the horizontal plate case). The temperature of an inclined plate is assumed to be uniform $\tilde{T}_w$ and is greater than to the ambient temperature $\tilde{T}_\infty$. The isothermal surface is considered to be permeable with a lateral mass flux of the form $\tilde{v}_w(\tilde{x}) = A\ \tilde{x}^l$. It is noted that $\tilde{v}_w(\tilde{x}) = 0$ corresponds to the case of impermeable surface. Following the above assumptions and Oberbeck–Boussinesq approximations, the boundary layer equations for the continuity, momentum, energy, and nanoparticle volume fraction (see Murthy et al. [15]) are given by

$$\frac{\partial \tilde{u}}{\partial \tilde{x}} + \frac{\partial \tilde{v}}{\partial \tilde{y}} = 0 \tag{1}$$

$$\frac{\partial \tilde{u}}{\partial \tilde{y}} + \frac{c\sqrt{K}}{(\mu/\rho f_\infty)} \frac{\partial \tilde{u}^2}{\partial \tilde{y}} = \frac{Kg(1-\tilde{\phi}_\infty)\rho f_\infty \beta_1}{\mu} \left[\frac{\partial \tilde{T}}{\partial \tilde{y}} - \frac{(\rho_p - \rho f_\infty)}{(1-\tilde{\phi}_\infty)\rho f_\infty \beta_1} \frac{\partial \tilde{\phi}}{\partial \tilde{y}} \right] \cos A \tag{2}$$

$$\tilde{u}\frac{\partial \tilde{T}}{\partial \tilde{x}} + \tilde{v}\frac{\partial \tilde{T}}{\partial \tilde{y}} = \alpha_m \frac{\partial^2 \tilde{T}}{\partial \tilde{y}^2} + \frac{\varepsilon(\rho c)_p}{(\rho c)_f} \frac{\partial \tilde{T}}{\partial \tilde{y}} \left[D_B \frac{\partial \tilde{\phi}}{\partial \tilde{y}} + \frac{D_T}{\tilde{T}_\infty} \frac{\partial \tilde{T}}{\partial \tilde{y}} \right] + \frac{1}{(\rho c)_p} \frac{16\sigma \tilde{T}_\infty^3}{3k^*} \frac{\partial^2 \tilde{T}}{\partial \tilde{y}^2} \tag{3}$$

$$\frac{1}{\varepsilon}\left(\tilde{u}\frac{\partial \tilde{\phi}}{\partial \tilde{x}} + \tilde{v}\frac{\partial \tilde{\phi}}{\partial \tilde{y}} \right) = D_B \frac{\partial^2 \tilde{\phi}}{\partial \tilde{y}^2} + \frac{D_T}{\tilde{T}_\infty} \frac{\partial^2 \tilde{T}}{\partial \tilde{y}^2} \tag{4}$$

where $(\tilde{u}, \tilde{v})$ are the components of Darcy velocities in $(\tilde{x}, \tilde{y})$-directions, respectively. Next, $\tilde{T}$ and $\tilde{\phi}$ are the temperature and nanoparticle volume fraction, respectively, K is the permeability, g is the acceleration due to gravity, c is the empirical constant related with the Forchheimer porous inertia, $\alpha_m = k_m/(\rho c)_f$ is the thermal diffusivity, ε is the porosity, σ is the Stefan Boltzmann constant and k^* is the Rosseland mean absorption coefficient. Further, β_1, k_m, and μ are the volumetric thermal expansion coefficient, thermal conductivity, and viscosity, while ρ_p is the nanoparticle density, $(\rho c)_f$ and $(\rho c)_p$ are the heat capacity of the fluid and the nanoparticles, and D_B and D_T are the thermophoretic and Brownian diffusion coefficients, respectively.

The associated boundary conditions are

$$\left.\begin{aligned} &\tilde{v} = \tilde{v}_w(\tilde{x}) = A\tilde{x}^l,\ \tilde{T} = \tilde{T}_w,\ D_B \frac{\partial \tilde{\phi}}{\partial \tilde{y}} + \frac{D_T}{\tilde{T}_\infty} \frac{\partial \tilde{T}}{\partial \tilde{y}} = 0 \text{ at } \tilde{y} = 0 \\ &u = 0,\ \tilde{T} = \tilde{T}_\infty,\ \tilde{\phi} = \tilde{\phi}_\infty \text{ as } \tilde{y} \to \infty \end{aligned}\right\} \tag{5}$$

In view of the continuity Eq. (1), now we introduce the stream function ψ such that $\tilde{u} = \partial\psi/\partial\tilde{y}$, $\tilde{v} = -\partial\psi/\partial\tilde{x}$ and we recommend the following nondimensional transformations:

$$\left.\begin{aligned} &\eta = \frac{\tilde{y}\, Ra_{\tilde{x}}^{1/2}}{\tilde{x}},\ F(\eta) = \frac{\psi}{\alpha_m\, Ra_{\tilde{x}}^{1/2}},\ T(\eta) = \frac{\tilde{T}-\tilde{T}_\infty}{\tilde{T}_w-\tilde{T}_\infty},\ G(\eta) = \frac{\tilde{\phi}-\tilde{\phi}_\infty}{\tilde{\phi}_\infty} \end{aligned}\right\} \tag{6}$$

where $Ra_{\tilde{x}} = [(1-\tilde{\phi})\rho f_\infty g K \beta_1\ (T_w - T_\infty)\ \tilde{x}]/[\mu\alpha_m]$ is the local Rayleigh number.

Using the stream function and Eq. (6), we obtain the following coupled and nonlinear system of similarity equations:

$$F'' + 2G^* F' F'' - (T' - Nr\, G')\cos A = 0 \tag{7}$$

$$\left(1 + \frac{4}{3}Rd\right) T'' + \frac{1}{2} FT' + Nb\, T'G' + Nt\left(T'\right)^2 = 0 \tag{8}$$

$$\frac{1}{Ln} G'' + \frac{1}{2} FG' + \frac{Nt}{Nb} T'' = 0 \tag{9}$$

where the prime shows differentiation with respect to η, $G^* = [c\sqrt{K}\,\alpha_m\, Ra_{\tilde{x}}]/[\nu\tilde{x}]$ is the non-Darcy parameter, $Nb = [\varepsilon(\rho c)_p D_B \tilde{\phi}_\infty]/[\alpha_m(\rho c)_f]$ is the Brownian motion parameter, $Nt = [\varepsilon(\rho c)_p D_T(\tilde{T}_w - \tilde{T}_\infty)]/[\alpha_m \tilde{T}_\infty(\rho c)_f]$ is the thermophoresis parameter, $Ln = \alpha_m/[\varepsilon D_B]$ is the nanoparticle Lewis number, $Rd = [4\sigma\tilde{T}_\infty^3]/[k\,k^*]$ is the thermal radiation parameter and $Nr = [(\rho_p - \rho f_\infty)\tilde{\phi}_\infty]/[\rho f_\infty \beta_1 (1 - \tilde{\phi}_\infty)(\tilde{T}_w - \tilde{T}_\infty)]$ is the nanofluid buoyancy parameter.

The associated boundary conditions (5) in terms of F, T, and G are

$$\left.\begin{aligned} &F(0) = f_w,\ \ T(0) = 1,\ \ Nb\ G'(0) + Nt\ T'(0) = 0 \\ &F'(\infty) \to 0,\ \ T(\infty) \to 0,\ \ G(\infty) \to 0 \end{aligned}\right\} \tag{10}$$

where the suction/injection parameter is given by $fw = -(2\tilde{x}/\alpha_m)\,\tilde{v}_w(\tilde{x})Ra_{\tilde{x}}^{l}$ and it will be independent of $\tilde{x}$ when $l = -1/2$, because it is necessary for the similarity solution to exist. The negative power distribution for injection/suction will lead to infinite injection/suction at the leading edge, which is unrealistic, but the method of similarity solution will still give accurate results sufficiently far from the leading edge.

The nondimensional local Nusselt and nanoparticle Sherwood numbers are given by

$$Nu_{\tilde{x}}/Ra_{\tilde{x}}^{1/2} = -T'(0) \ \text{ and } \ NSh_{\tilde{x}}/Ra_{\tilde{x}}^{1/2} = -G'(0) \tag{11}$$

3 Results and Discussion

Following the work of Motsa [16, 17], the governing system of nonlinear ordinary differential equations (7)–(9) together with the boundary conditions (10) is solved by using spectral local linearization method (SLLM). The major steps in SLLM are as follows: (i) First, we locally linearize all the equations in the sequential order of F, T and G. (ii) Next, we convert the resulting linearized system of equations into a matrix form of algebraic equations by using a pseudo-spectral collocation method. (iii) Finally, we solve the system of algebraic equations by taking suitable initial approximations.

The effects of thermal radiation, angle of inclination, suction/injection, and non-Darcy parameters on the dimensionless nanofluid velocity, temperature, volume fraction with heat and nanoparticle mass transfer rates along an inclined flat plate are discussed. The computational work is carried out by taking the fixed values $Ln = 10$, $Nr = 0.2$, $Nt = 0.1$ and $Nb = 0.3$. To validate the code generated in MATLAB, the present numerical results have been compared with the results published by Nield and Kuznetsov [18] in a special case and they are in good agreement as shown in Table 1.

Figures 1, 2 and 3 depict the influence of thermal radiation (Rd) and angle of inclination (A) on the nondimensional velocity (F), temperature (T) and volume fraction (G). It is seen from Figs. 1 and 2 that the velocity and temperature profiles

Table 1 Comparison values of $T'(0)$ for natural convective flow of a nanofluid along a vertical plate in a porous medium for $G^* = 0,\ A = 0,\ Rd = 0,\ Ln = 10,$ and $fw = 0$

Parameters	Nield and Kuznetsov [18]	Present
$Nr = Nb = Nt = 0$ (mono-diffusive regular fluid)	−0.4439	−0.44375103
$Nr = Nb = Nt = 0.2$ (mono-diffusive nanofluid)	−0.3343	−0.33415956

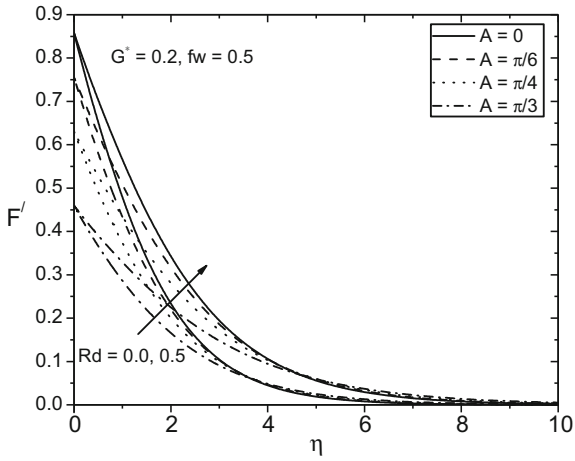

Fig. 1 Effects of A and Rd on the velocity profiles

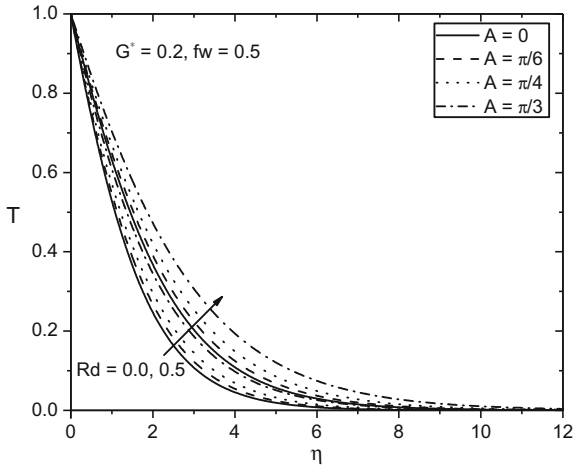

Fig. 2 Effects of A and Rd on the temperature profiles

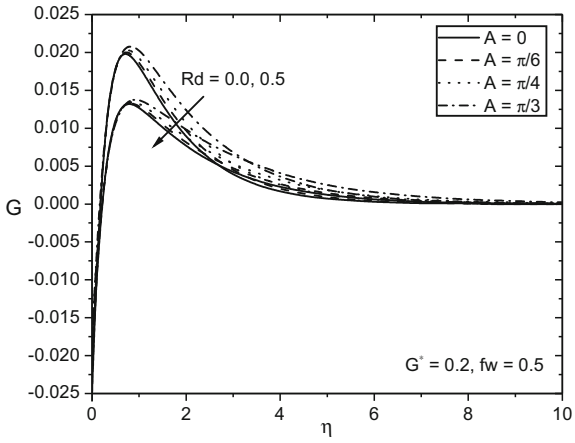

Fig. 3 Effects of A and Rd on the nanoparticle volume fraction profiles

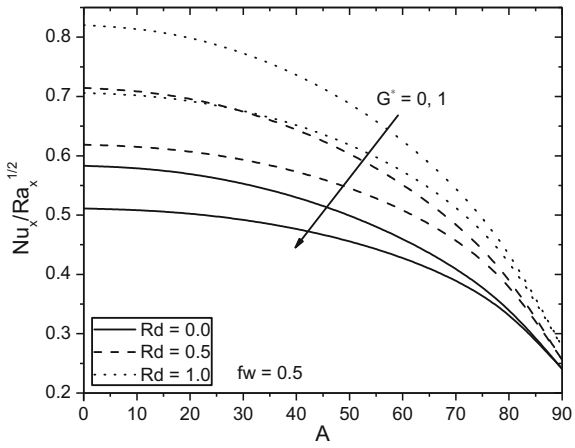

Fig. 4 Effects of Rd and G^* on the Nusselt number with varying A

increase with an increase in the thermal radiation parameter whereas the volume fraction profile decreases. It can also be noticed that the nanofluid velocity diminishes as the flat plate changes its position from the vertical direction to inclined, and inclined to horizontal direction. But the temperature and volume fraction profiles enhance for the same. The combined effects of thermal radiation (Rd) and non-Darcy parameter (G^*) on the variations of Nusselt number $Nu_{\tilde{x}}/Ra_{\tilde{x}}{}^{1/2}$ and nanoparticle Sherwood number $NSh_{\tilde{x}}/Ra_{\tilde{x}}{}^{1/2}$ against the angle of inclination are shown in Figs. 4 and 5. The Nusselt and nanoparticle Sherwood numbers decrease with an increase in G^*. That is, the heat and nanoparticle mass transfer rates get decrease in a non-Darcy porous medium in comparison with a Darcy porous medium as given in Figs. 4 and 5. Further, we notice that the Nusselt number decreases and nanoparticle Sherwood number increases as the vertical flat plate moves from vertical direction to horizontal direction.

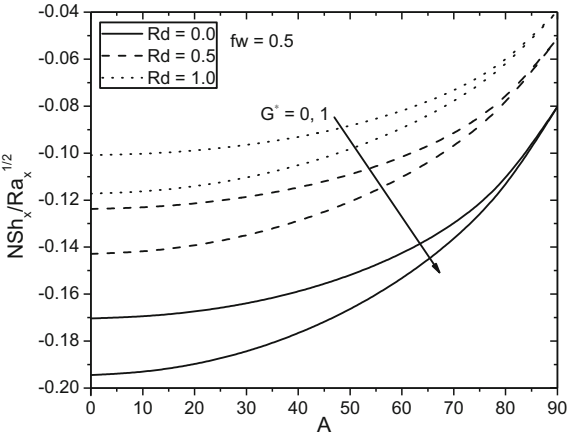

Fig. 5 Effects of Rd and G^* on the nanoparticle Sherwood number with varying A

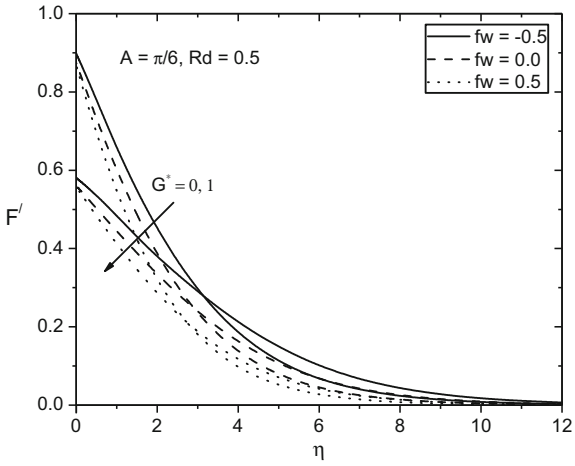

Fig. 6 Effects of fw and G^* on the velocity profiles

The combined effects of non-Darcy parameter (G^*) and suction/injection parameter (f_w) on the dimensionless velocity (F), temperature (T), and volume fraction (G) are plotted in Figs. 6, 7 and 8. The nanofluid velocity and temperature profiles decrease but volume fraction increases with the suction/injection parameter. That is, the velocity and temperature are more in the fluid injection case in comparison with the fluid suction and impermeability cases. But the reverse behavior is noticed for the volume fraction profiles. Moreover, the presence of non-Darcy parameter diminishes the velocity and volume fraction of the nanofluid but the temperature enhances. Figures 9 and 10 explore the combined effects of thermal radiation (Rd) and non-Darcy parameter (G^*) on the Nusselt number $Nu_{\tilde{x}}/Ra_{\tilde{x}}{}^{1/2}$ and nanoparticle

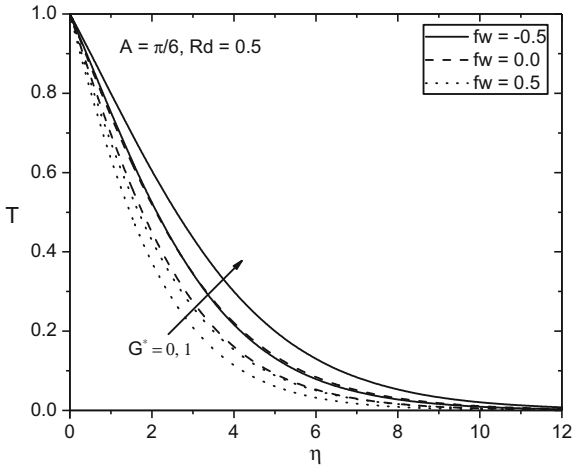

Fig. 7 Effects of fw and G^* on the temperature profiles

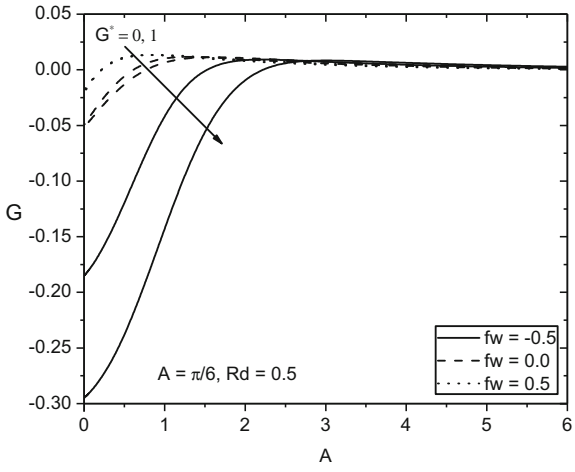

Fig. 8 Effects of fw and G^* on the nanoparticle volume fraction profiles

Sherwood number $NSh_{\tilde{x}}/Ra_{\tilde{x}}^{1/2}$ against the suction/injection parameter. With the rise of a thermal radiation parameter, there is a rapid enhancement in the Nusselt and nanoparticle Sherwood numbers in both the injection and suction cases. But the Nusselt number decreases and the nanoparticle Sherwood numbers increase with rising values of a non-Darcy parameter. Moreover, it is seen that the Nusselt number is more in the fluid suction case in comparison with the fluid injection case and nanoparticle Sherwood number shows an opposite behavior.

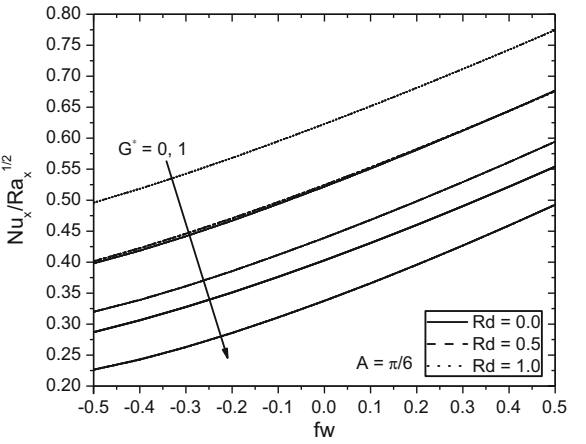

Fig. 9 Effects of Rd and G^* on the Nusselt number with varying fw

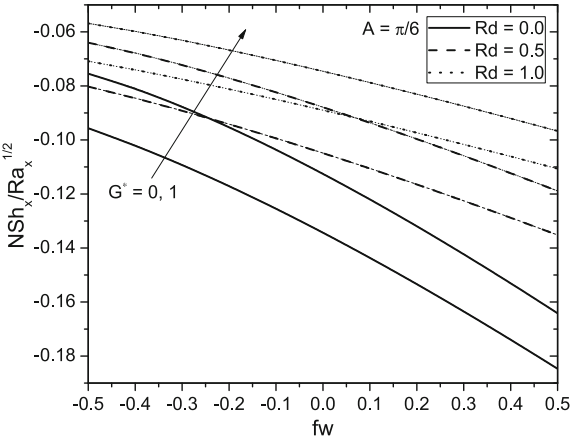

Fig. 10 Effects of Rd and G^* on the nanoparticle Sherwood number with varying fw

4 Conclusions

The main observations from the present study are noticed as follows:

– When the plate changes its direction from vertical to horizontal, the velocity and Nusselt number decrease whereas the temperature, volume fraction, and nanoparticle Sherwood number increase.
– The nanofluid velocity, temperature, Nusselt, and nanoparticle Sherwood numbers enhance but the volume fraction profile diminishes with rising of a thermal radiation parameter.
– The presence of non-Darcy parameter reduces the fluid velocity, volume fraction, and Nusselt number, but enhances the fluid temperature and nanoparticle Sherwood number for fixed values $A = \pi/6$ and $Rd = 0.5$.

– It is seen that the fluid velocity, temperature, and nanoparticle Sherwood number are more, and the volume fraction and Nusselt number are less in the fluid injection case in comparison with the fluid suction and impermeability surface cases.

References

1. Cheng, P.: Heat transfer in geothermal systems. Adv. Heat Transf. **14**, 1–105 (1978)
2. Cheng, P.: The influence of lateral mass flux on free convection boundary layers in a saturated porous medium. Int. J. Heat Mass Transf. **20**, 201–206 (1977)
3. Merkin, J.H.: Free convection boundary layers in a saturated porous medium with lateral mass flux. Int. J. Heat Mass Transf. **21**, 1499–1504 (1978)
4. Plumb, O., Huenefeld, J.C.: Non-Darcy natural convection from heated surfaces in saturated porous medium. Int. J. Heat Mass Transf. **24**, 765–768 (1981)
5. Bejan, A., Poulikakos, D.: The non-Darcy regime for vertical boundary layer natural convection in a porous medium. Int. J. Heat Mass Transf. **27**, 717–722 (1984)
6. Nakayama, A., Kokudai, T., Koyama, H.: Forchheimer free convection over a non-isothermal body of arbitrary shape in a saturated porous medium. J. Heat Transf. **112**, 511–515 (1990)
7. Murthy, P.V.S.N., Singh, P.: Thermal dispersion effects on non-Darcy natural convection over horizontal plate with surface mass flux. Arch. Appli. Mech. **67**, 487–495 (1997)
8. Murthy, P.V.S.N., Singh, P.: Thermal dispersion effects on non-Darcy natural convection with lateral mass flux. Heat Mass Transf. **33**, 1–5 (1997)
9. Nield, D.A., Bejan, A.: Convection in Porous Media, 4th edn. Springer, New York (2013)
10. Choi, S.: Enhancing thermal conductivity of fluids with nanoparticle: developments and applications of non-Newtonian flows. ASME-Publications-Fed. **231**, 99–106 (1995)
11. Buongiorno, J.: Convective transport in nanofluids. J. Heat Transf. **128**, 240–250 (2006)
12. Das, S.K., Choi, S.U.S., Yu, W., Pradeep, T.: Nanofluids: Science and Technology. Wiley Interscience, Hoboken, NJ (2007)
13. Das, S.K., Stephen, U.S.: A review of heat transfer in nanofluids. Adv. Heat Transf. **41**, 81–197 (2009)
14. Kakac, S., Pramuanjaroenkij, A.: Review of convective heat transfer enhancement with nanofluids. Int. J. Heat Mass Transf. **52**, 3187–3196 (2009)
15. Murthy, P.V.S.N., Sutradhar, A., RamReddy, C.H.: Double-diffusive free convection flow past an inclined plate embedded in a non-Darcy porous medium saturated with a nanofluid. Transp. Porous Med. **98**, 553–564 (2013)
16. Motsa, S.S.: A new spectral local linearization method for nonlinear boundary layer flow problems. J. Appl. Math. **2013**(423628), 15 (2013)
17. Motsa, S.S., Makukula, Z.G., Shateyi, S.: Spectral local linearization approach for natural convection boundary layer flow. Math. Probl. Eng. **2013**(765013), 7 (2013)
18. Nield, D.A., Kuznetsov, A.V.: The Cheng-Minkowycz problem for the double-diffusive natural convective boundary layer flow in a porous medium saturated by a nanofluid. Int. J. Heat Mass Transf. **54**, 374–378 (2011)

Joule Heating and Thermophoresis Effects on Unsteady Natural Convection Flow of Doubly Stratified Fluid in a Porous Medium with Variable Fluxes: A Darcy–Brinkman Model

Ch. Madhava Reddy, Ch. RamReddy and D. Srinivasacharya

Abstract In the present article, the effect of Joule heating and thermophoresis on unsteady natural convection flow of electrically conducting fluid along a vertical plate is analyzed. In addition, double stratification and a Darcy–Brinkman porous medium are considered. Initially, the governing nonlinear time-dependent equations are transformed into a set of dimensionless equations by using nondimensional transformations and then solved numerically by an accurate, efficient, and unconditionally stable implicit finite difference scheme. The behavior of flow characteristics (specifically, Nusselt number, Sherwood number, and local and average skin friction) with pertinent flow parameters is discussed through graphs. The outcome of the exploration may be beneficial for applications of engineering, biotechnology, and chemical industries.

Keywords Thermophoresis · Joule heating · Brinkman porous medium
Crank–Nicolson method · Double stratification · Electrically conducting fluid

1 Introduction

Several researchers conducted theoretical as well as a limited number of experimental studies on convective transport through porous media due to its wide range of applications in science and technology, for example, geophysics, chemical reactors, geothermal systems, heat exchangers, and thermal engineering, etc. The investigation of porous media at first began with the basic Darcy model and after that gradually it is extended to few non-Darcy models to defeat the constraints of the Darcy model, namely, Darcy–Forchheimer, Darcy–Brinkman and Darcy–Brinkman–Forchheimer model porous mediums. In view of above said applications, Poulikakos and Renken

Ch. Madhava Reddy (✉)
Department of Mathematics, NBKR IST, Vidyanagar, India
e-mail: madhavac@gmail.com

Ch. RamReddy · D. Srinivasacharya
Department of Mathematics, National Institute of Technology, Warangal, India

D. Srinivasacharya and K. S. Reddy (eds.), *Numerical Heat Transfer and Fluid Flow*, Lecture Notes in Mechanical Engineering,
https://doi.org/10.1007/978-981-13-1903-7_13

[1] scrutinized the Brinkman friction and variable porosity in the forced convection flow in a channel saturated with a porous medium. Nield et al. [2] examined the forced convection flow in a vertical channel with the consideration of Darcy–Brinkman—Forchheimer porous medium. Likewise, Murthy et al. [3], and Srinivasacharya and RamReddy [4] studied the collective influence of thermal and solutal stratifications on steady free convective flow embedded in both Darcian and non-Darcian porous medium. Due to the important applications of thermophoresis effect in the aerosol and optical fiber industries, many theoretical and experimental studies utilized the effect of thermophoresis in the analysis of thermal and solutal transport phenomena of fluid flow problems (for more details, see Talbot et al. [5], Batchelor and Shen [6], Alam et al. [7], Loganathan and Arasu [8]).

Joule heating is one of the ways to producing heat by passing an electric current through a metal and it occurs frequently in the electric heating devices, for example, electric iron, hair dryer, electric heater, etc. Because of these developing utilization of Joule effects on the steady and unsteady flows over various surface geometries, some of the researchers (Ganesan and Palani [9], Alam et al. [10], Chen [11], Kawala and Odda [12], and Zaib and Shafie [13]) revealed their findings utilizing various numerical techniques. Hence, the objective of this work is to examine the joule heating and thermophoresis effects on the MHD fully developed flow over a vertical plate with the consideration of double stratification. Crank–Nicolson method is used to obtain the numerical solution for the flow fields. This numerical study explores the impact of pertinent parameters on the fluid flow characteristics through graphs and the salient features are discussed in detail.

2 Mathematical Formulation

Consider an unsteady, laminar, incompressible, free convection two-dimensional flow of doubly stratified fluid flow along a vertical plate embedded in Brinkman porous medium. In addition, the effects of thermophoresis, MHD, and Joule heating are incorporated in the flow equations. Initially at $\tilde{t} = 0$, the fluid and the plate are assumed to be at the constant temperature and concentration, whereas the surface heat and mass fluxes are supplied to the fluid from the plate at a rate of $q_w(\tilde{x}) = \tilde{x}^m$ and $q_w^*(\tilde{x}) = \tilde{x}^n$, respectively, and both are maintained at the same level for all time $\tilde{t} > 0$. In the ambient medium, both temperature and concentration assumed to be vertically linearly stratified in the form $\tilde{T}_\infty(\tilde{x}) = \tilde{T}_{\infty,0} + A\tilde{x}$ and $\tilde{C}_\infty(\tilde{x}) = \tilde{C}_{\infty,0} + B\tilde{x}$, respectively. Under the above said assumptions and with linear Boussinesq approximations, the governing boundary layer equations of fluid flow are given by

$$\frac{\partial \tilde{u}}{\partial \tilde{x}} + \frac{\partial \tilde{v}}{\partial \tilde{y}} = 0 \tag{1}$$

$$\frac{1}{\varepsilon}\frac{\partial \tilde{u}}{\partial \tilde{t}} + \frac{\tilde{u}}{\varepsilon^2}\frac{\partial \tilde{u}}{\partial \tilde{x}} + \frac{\tilde{v}}{\varepsilon^2}\frac{\partial \tilde{u}}{\partial \tilde{y}} = \frac{\upsilon}{\varepsilon}\frac{\partial^2 \tilde{u}}{\partial \tilde{y}^2} - \frac{\mu}{k}\tilde{u} - \frac{\sigma B_0^2}{\rho}\frac{\tilde{u}}{\varepsilon} + g\left[\beta_{\tilde{T}}\left(\tilde{T} - \tilde{T}_\infty(\tilde{x})\right) + \beta_{\tilde{C}}\left(\tilde{C} - \tilde{C}_\infty(\tilde{x})\right)\right] \tag{2}$$

$$\frac{\partial \tilde{T}}{\partial \tilde{t}} + \tilde{u}\frac{\partial \tilde{T}}{\partial \tilde{x}} + \upsilon\frac{\partial \tilde{T}}{\partial \tilde{y}} = \alpha\frac{\partial^2 \tilde{T}}{\partial \tilde{y}^2} + \frac{\beta_0^2 \sigma}{\rho C p}\tilde{u}^2 \tag{3}$$

$$\frac{\partial \tilde{C}}{\partial \tilde{t}} + \tilde{u}\frac{\partial \tilde{C}}{\partial \tilde{x}} + \tilde{v}\frac{\partial C'}{\partial \tilde{y}} = D\frac{\partial^2 \tilde{C}}{\partial \tilde{y}^2} + \frac{\partial}{\partial \tilde{y}}\left(\frac{K_T \upsilon}{T_r}\tilde{C}\frac{\partial \tilde{T}}{\partial \tilde{y}}\right) \tag{4}$$

Here, $\beta_{\tilde{C}}, C_p, \tilde{T}, \sigma, \mu, D, \tilde{C}, \rho, \alpha, \varepsilon, \nu, k, (\tilde{u}, \tilde{v}), g, \beta_{\tilde{T}}, K_{\tilde{T}}$ denote the solutal expansion coefficient, specific heat, temperature, electrical conductivity, the coefficient of viscosity, mass diffusivity, concentration, density, thermal diffusivity, porosity, the kinematic viscosity, permeability, Darcy velocity components, acceleration due to gravity, thermal expansion coefficient, and the thermophoretic coefficient (see Batchelor and Shen [6]), respectively.

The boundary conditions are

$$\begin{aligned}
&\tilde{u}(\tilde{x}, \tilde{y}, \tilde{t}) = 0, \ \tilde{v}(\tilde{x}, \tilde{y}, \tilde{t}) = 0, \\
&\tilde{T}(\tilde{x}, \tilde{y}, \tilde{t}) = \tilde{T}_\infty(\tilde{x}), \ \tilde{C}(\tilde{x}, \tilde{y}, \tilde{t}) = \tilde{C}_\infty(\tilde{x}) \text{ for } \tilde{t} \le 0 \\
&\tilde{u}(\tilde{x}, \tilde{0}, \tilde{t}) = 0, \ \tilde{v}(\tilde{x}, \tilde{0}, \tilde{t}) = 0, \\
&\left.\frac{\partial \tilde{T}(\tilde{x}, \tilde{y}, \tilde{t})}{\partial \tilde{y}}\right|_{\tilde{y}=0} = -\frac{q_w(\tilde{x})}{k}, \ \left.\frac{\partial \tilde{C}(\tilde{x}, \tilde{y}, \tilde{t})}{\partial \tilde{y}}\right|_{\tilde{y}=0} = \frac{q_w^*(\tilde{x})}{D} \text{for } \tilde{t} > 0 \\
&\tilde{u}(0, \tilde{y}, \tilde{t}) = 0, \quad \tilde{v}(0, \tilde{y}, \tilde{t}) = 0, \\
&\tilde{T}(0, \tilde{y}, \tilde{t}) = \tilde{T}_{\infty,0}, \quad \tilde{C}(0, \tilde{y}, \tilde{t}) = \tilde{C}_{\infty,0} \text{ for } \tilde{t} > 0 \\
&\tilde{u}(\tilde{x}, \infty, \tilde{t}) \to 0, \quad \tilde{T}(\tilde{x}, \infty, \tilde{t}) \to \tilde{T}_\infty(\tilde{x}), \\
&\tilde{C}(\tilde{x}, \infty, \tilde{t}) \to \tilde{C}_\infty(\tilde{x}) \text{ for } \tilde{t} > 0
\end{aligned} \tag{5}$$

Using the following nondimensional variables

$$X = \frac{\tilde{x}}{\tilde{L}}, \quad Y = \frac{\tilde{y}}{\tilde{L}}Gr^{1/4}, \quad F = \frac{\tilde{u}\tilde{L}}{\upsilon}Gr^{-1/2}, \quad G = \frac{\tilde{v}\tilde{L}}{\upsilon}Gr^{-1/4}, \quad t = \frac{\tilde{t}\upsilon}{\tilde{L}^2}Gr^{1/2},$$
$$T = \frac{\left(\tilde{T} - \tilde{T}_\infty(\tilde{x})\right)Gr^{1/4}}{q_w\left(\tilde{L}\right)\tilde{L}/k}, C = \frac{\left(\tilde{C} - \tilde{C}_\infty(\tilde{x})\right)Gr^{1/4}}{q_w^*\left(\tilde{L}\right)\tilde{L}/D}$$

into Eqs. (1) to (4), we obtain the following system of nondimensional partial differential equations:

$$\frac{\partial F}{\partial X} + \frac{\partial G}{\partial Y} = 0 \tag{6}$$

$$\frac{1}{\varepsilon}\frac{\partial F}{\partial t}+\frac{F}{\varepsilon^2}\frac{\partial F}{\partial X}+\frac{G}{\varepsilon^2}\frac{\partial F}{\partial Y}=\frac{1}{\varepsilon}\frac{\partial^2 F}{\partial Y^2}-\frac{1}{DaGr^{1/2}}F-\frac{1}{\varepsilon}\frac{M}{Gr^{1/2}}F + Gr^{-1/4}T+Gr^{-1/4}NC \tag{7}$$

$$\frac{\partial T}{\partial t}+F\frac{\partial T}{\partial X}+G\frac{\partial T}{\partial Y}=\frac{1}{Pr}\frac{\partial^2 T}{\partial Y^2}-Gr^{1/4}\varepsilon_1 F+Gr^{-1/4}b_* F^2 \tag{8}$$

$$\frac{\partial C}{\partial t}+F\frac{\partial C}{\partial X}+G\frac{\partial C}{\partial Y}=\frac{1}{Sc}\frac{\partial^2 C}{\partial Y^2}-Gr^{1/4}\varepsilon_2 F + \frac{\tau}{Gr^{1/4}}\left[C\frac{\partial^2 T}{\partial Y^2}+\frac{\partial T}{\partial Y}\left(\frac{\partial C}{\partial Y}+\varepsilon_2\right)\right] \tag{9}$$

along with the corresponding initial and boundary conditions in a nondimensional form

$$\begin{aligned}
&F(X,Y,t)=0,\quad G(X,Y,t)=0,\quad T(X,Y,t)=0,\quad C(X,Y,t)=0 \text{ for } t\le 0\\
&F(X,0,t)=0,\quad G(X,0,t)=0,\\
&\frac{\partial T(X,Y,t)}{\partial Y}_{at\ Y=0}=-X^m,\quad \frac{\partial C(X,Y,t)}{\partial Y}_{at\ Y=0}=-X^n \text{ for } t>0\\
&F(0,Y,t)=0,\quad G(0,Y,t)=0,\ T(0,Y,t)=0,\quad C(0,Y,t)=0 \text{ for } t>0\\
&F(X,\infty,t)\to 0,\ T(X,\infty,t)\to 0,\quad C(X,\infty,t)\to 0 \text{ for } t>0
\end{aligned} \tag{10}$$

Here N, Da, M, EC, Pr, Sc, τ, ε_1, ε_2, $b*$, Gr, Gc denote the buoyancy ratio, Darcy number, magnetic parameter, Eckert number, Prandtl number, Schmidt number, thermophoretic parameter, thermal stratification parameter, solutal stratification parameters, Joule heating parameter, and thermal and solutal Grashof numbers, respectively. Mathematically, these parameters are given by

$$\begin{aligned}
&Gr=g\beta_T\tilde{L}^4 q_w\left(\tilde{L}\right)/k\upsilon^2,\ Gc=g\beta_C\tilde{L}^4 q_w^*\left(\tilde{L}\right)/D\upsilon^2,\\
&N=Gc/Gr,\ Da=k\upsilon/\left(\mu\tilde{L}^2\right),\ M=\sigma B_0^2\tilde{L}^2/(\rho\upsilon),\\
&EC=n_0^2/\left(Cpq_w\left(\tilde{L}\right)\right),\ n_0=\left(k\mu\upsilon/\left(\rho\tilde{L}^3\right)\right)^{1/2}Gr^{1/2},\\
&Pr=\upsilon/\alpha,\ Sc=\upsilon/D,\ \tau=K_T q_w\left(\tilde{L}\right)\tilde{L}/T_W k,\\
&\varepsilon_1=Ak/q_w\left(\tilde{L}\right),\ \varepsilon_2=BD/q_w^*\left(\tilde{L}\right),\ b*=(M/Ec)
\end{aligned}$$

Nondimensional average forms of local Nusselt number $Nu_X=-\left[Gr^{1/4}X\left(\frac{\partial T}{\partial Y}\right)_{Y=0}\right]\Big/T_{Y=0}$, skin friction $\tau_X=Gr^{3/4}\left(\frac{\partial F}{\partial Y}\right)_{Y=0}$, and Sherwood number $Sh_X=-\left[Gr^{1/4}X\left(\frac{\partial C}{\partial Y}\right)_{Y=0}\right]\Big/C_{Y=0}$ are given by

$$\overline{Nu}=-Gr^{1/4}\int_0^1\frac{\left(\frac{\partial T}{\partial Y}\right)_{Y=0}}{T_{Y=0}}dX,\quad \overline{\tau}=Gr^{3/4}\int_0^1\left(\frac{\partial U}{\partial Y}\right)_{Y=0}dX,\quad \overline{Sh}=-Gr^{1/4}\int_0^1\frac{\left(\frac{\partial C}{\partial Y}\right)_{Y=0}}{C_{Y=0}}dX \tag{11}$$

3 Results and Discussion

Equations (6) to (9) under the conditions (10) are solved by using the Crank–Nicolson finite difference scheme (Ganesan and Palani [9] and also citations therein). We have noticed that the present unsteady problem turns into a steady-state problem at $X = 1.0$ and the validation of present numerical results have been compared with previously published work of Ganesan and Palani [9] in the literature. Variations of physical quantities, namely, Nusselt number, Sherwood number, and skin friction in nondimensional local and average forms, are determined in Figs. 1, 2, 3, 4, 5 and 6 for thermal and solutal stratification parameters (ε_1 and ε_2), respectively. From Figs. 1 and 2, it can be seen that the τ_X and $\bar{\tau}$ diminish with an expansion in both ε_1 and ε_2. Changes in local and Nusselt number with respect to stratification parameters ε_1 and ε_2 are prescribed in Figs. 3 and 4, and these are referred that an enhancement in ε_1 leads to increase both local and average Nusselt numbers, and with an expansion in ε_2, the Nu_X declines close to the plate and far from the plate, it demonstrates a reverse trend, as shown in Fig. 3. Further, Fig. 4 reveals that there is no impressive impact on the average Nusselt number with respect to the variation of ε_2. Figures 5 and 6 uncover that both types of Sherwood numbers (i.e., local and average forms) improves with the upgrade of ε_2 in any case, whereas they show a reverse pattern with increment in ε_1.

Influence of Joule heating (b_*) and thermophoresis (τ) parameters on the above-mentioned physical quantities are projected through Figs. 7, 8, 9, 10, 11 and 12, and from Figs. 7 and 10, one can notice that both the skin friction and heat transfer gradients (for both local and average nondimensional quantities) diminish with the rise of b_*, whereas these two gradients show opposite trend with τ. Figures 11 and 12 portray that local and average Sherwood number improves with an increment of b_* while the contrary pattern is recognized for high estimations of τ.

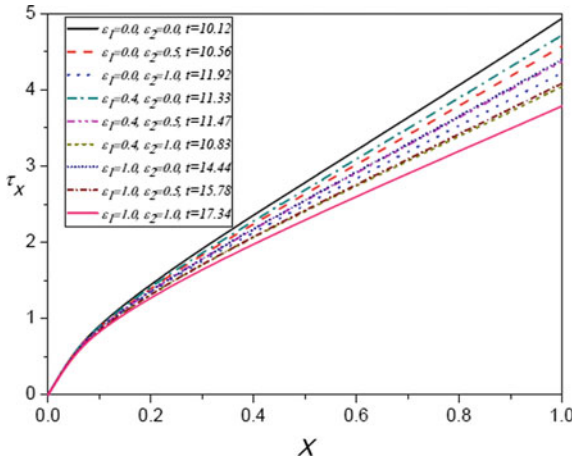

Fig. 1 Variation of τ_X for ε_1 and ε_2

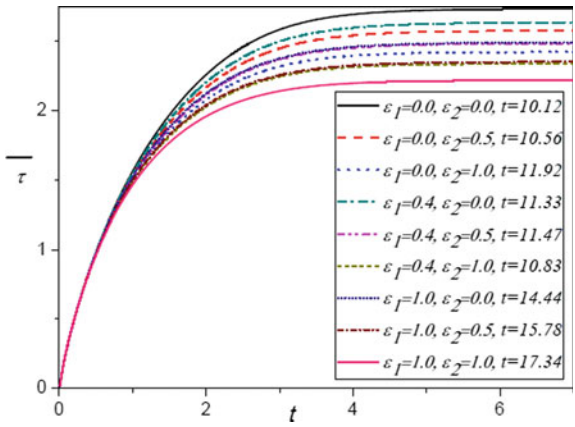

Fig. 2 Variation of $\bar{\tau}$ for ε_1 and ε_2

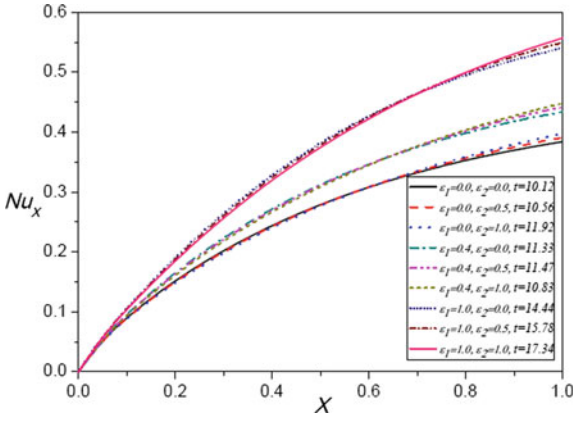

Fig. 3 Variation of Nu_X for ε_1 and ε_2

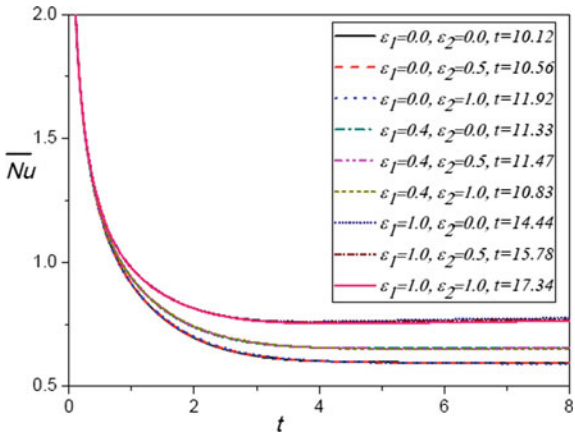

Fig. 4 Variation of $\overline{Nu}$ for ε_1 and ε_2

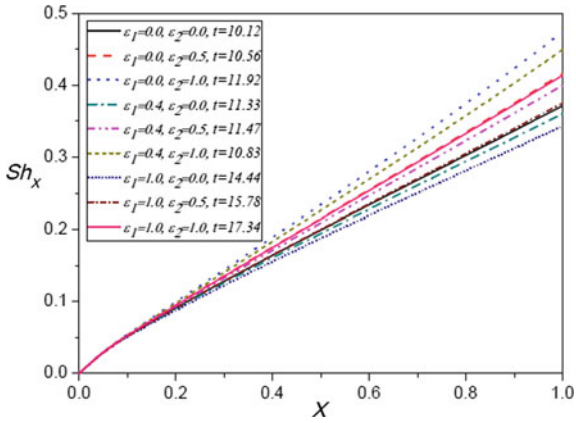

Fig. 5 Variation of Sh_X for ε_1 and ε_2

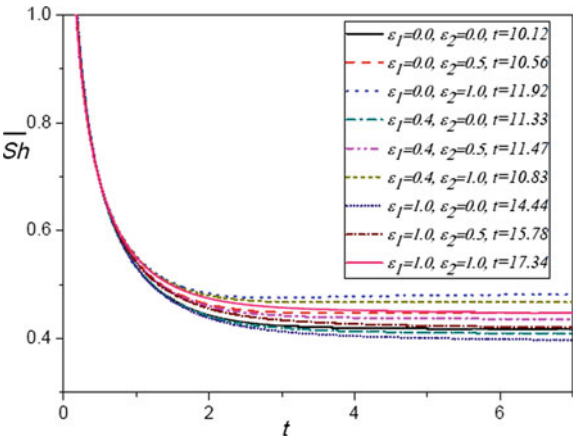

Fig. 6 Variation of $\overline{Sh}$ for ε_1 and ε_2

4 Conclusion

In the present work, the collective influence of Joule heating and thermophoresis on the unsteady free convective flow of an electrically conducting doubly stratified fluid along a vertical semi-infinite plate in a Darcy–Brinkman porous medium has been analyzed. Variations of nondimensional physical quantities skin friction, and Nusselt and Sherwood numbers are discussed in both local and average forms. For increasing values of ε_1, local and average skin friction, local and average Sherwood number uncover a similar trend but they appear inverse pattern for expanding estimations of ε_2. Further, the Nusselt numbers (in both local and average forms) improve with the rise in ε_1, while with an expansion in ε_2, there is no significant impact on the average Nusselt number.

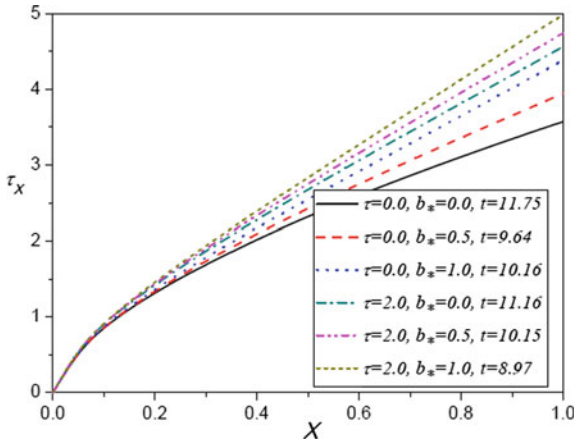

Fig. 7 Variation of τ_X for τ and b_*

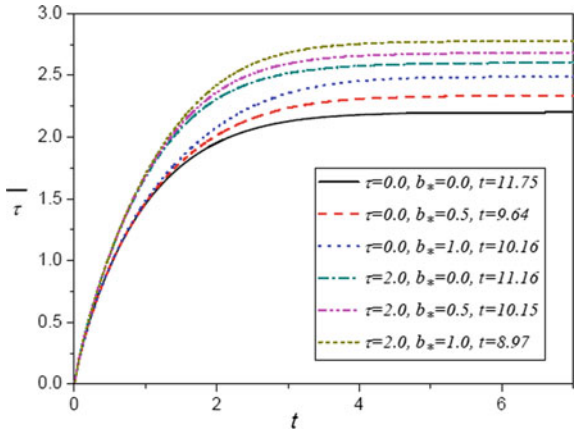

Fig. 8 Variation of $\bar{\tau}$ for τ and b_*

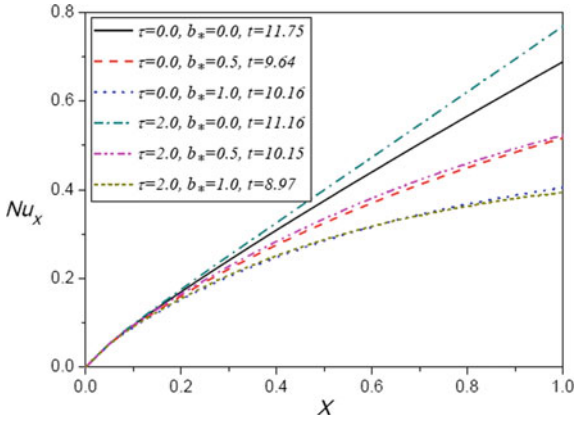

Fig. 9 Variation of Nu_X for τ and b_*

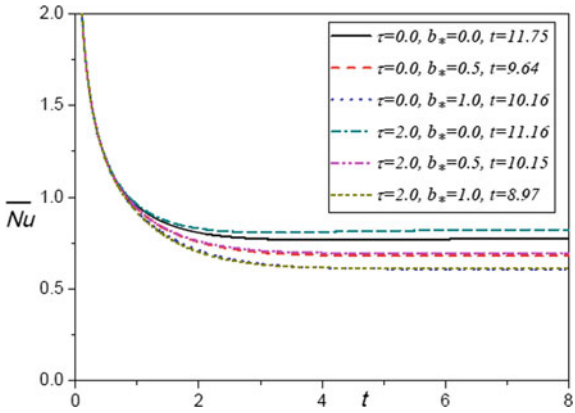

Fig. 10 Variation of $\overline{Nu}$ for τ and b_*

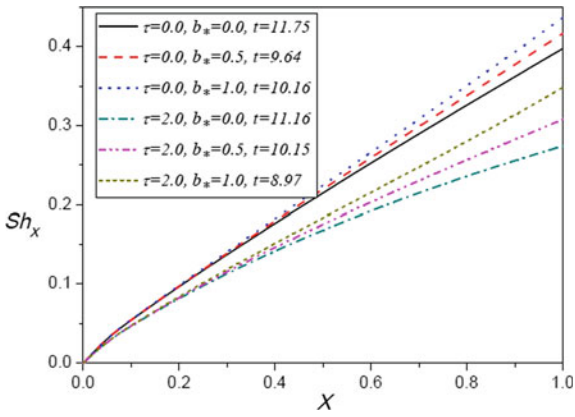

Fig. 11 Variation of Sh_X for τ and b_*

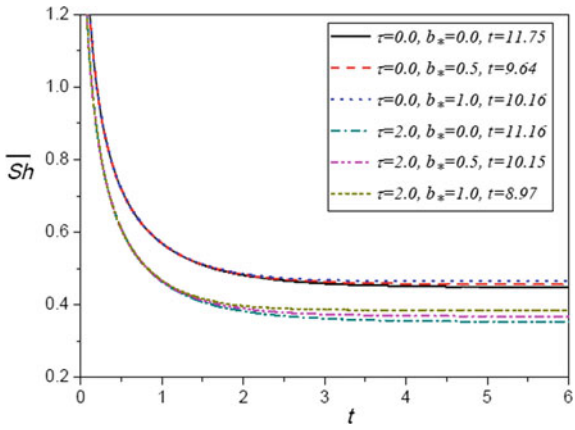

Fig. 12 Variation of $\overline{Sh}$ for τ and b_*

The increment in the estimations of prompts increment in local and average skin friction, Nusselt number but, the estimations of local and average Sherwood number abatements. The local and average skin friction, Sherwood improves with an upgrade of b_* while the Nusselt numbers (in both local and average forms) reductions

References

1. Poulikakos, D., Renken, K.: J. Heat Transf. **109**, 880 (1987)
2. Nield, D.A., Junqueira, S.L.M., Lage, J.L.: J. Fluid Mech. **322**, 201 (1996)
3. Murthy, P.V.S.N., Srinivasacharya, D., Krishna, P.V.S.S.S.R.: J. Heat Transf. **126**, 297 (2004)
4. Srinivasacharya, D., RamReddy, C.: Korean J. Chem. Eng. **28**, 1824 (2011)
5. Talbot, L.R.K.R.W.D.R., Cheng, R.K., Schefer, R.W., Willis, D. R.: J. Fluid Mech. **101**, 737 (1980)
6. Batchelor, G.K., Shen, C.: J. Colloid Interface Sci. **107**, 21 (1985)
7. Alam, M.S., Rahman, M.M., Sattar, M.A.: Int. J. Thermal Sci. **47**, 758 (2008)
8. Loganathan, P., Arasu, P.P.: Theor. Appl. Mech. **37**, 203 (2010)
9. Ganesan, P., Palani, G.: Int. J. Heat Mass Transf. **47**, 4449 (2004)
10. Alam, M.S., Rahman, M.M., Sattar, M.A.: Comm. Nonlinear Sci. Numer. Simul. **14**, 2132 (2009)
11. Chen, C.H.: J. Heat Transf. **132**, 064503 (2010)
12. Kawala, A.M., Odda, S.N.: Adv. Pure Math. **3**, 183 (2013)
13. Zaib, A., Shafie, S.: J. Franklin Inst. **351**, 1268 (2014)

Performance Analysis of Domestic Refrigerator Using Hydrocarbon Refrigerant Mixtures with ANN and Fuzzy Logic System

D. V. Raghunatha Reddy, P. Bhramara and K. Govindarajulu

Abstract This paper presents a new methodology for the performance prediction of domestic refrigeration system with hydrocarbon refrigerant mixture (R290/R600a), which is used as a working refrigerant at different weight combinations. Artificial neural network (ANN) and fuzzy logic system (FLS) techniques are used to predict the system performance of such as coefficient of performance (COP). This paper also describes the experimental test setup for collecting the required experimental test data the experimental values are calibrated at steady state conditions. While varying the input parameters like different masses of refrigerant charge, evaporator temperature and varying length of capillary tube. The ANN and FLS models are working under MATLAB toolbox. The back propagation algorithm with different variants and logistic sigmoid transfer function were used in the network. The outputs predicted from the ANN model agree with experimental values with help of coefficient of correlation ($R^2 > 0.9886$), and the percentage of error is less than 5%. In the comparison of performance, results obtained by experimentally and same has compared with the developed fuzzy model with COP are investigated, at all input variants in the system. This result gives that the ANN model gives good accuracy and reliability than the fuzzy logic system for predicting the performance of the domestic refrigeration system.

Keywords Artificial neural networks · Fuzzy logic model · VCR · Performance prediction · Absolute fraction of variance and COP

D. V. Raghunatha Reddy (✉)
Department of Mechanical Engineering, Faculty of Science and Technology, IFHE University, Hyderabad 501203, Telangana, India
e-mail: raghunathadvrr@ifheindia.org

P. Bhramara
Department of Mechanical Engineering, JNTUH College of Engineering Hyderabad, Hyderabad 500072, Telangana, India

K. Govindarajulu
Department of Mechanical Engineering, JNTUA College of Engineering Pulivendula, Pulivendula 516390, Andhra Pradesh, India

D. Srinivasacharya and K. S. Reddy (eds.), *Numerical Heat Transfer and Fluid Flow*, Lecture Notes in Mechanical Engineering,
https://doi.org/10.1007/978-981-13-1903-7_14

1 Introduction

Vapor compression refrigeration is a multidimensional problem such as to minimization of input power consumption and increasing refrigeration effect. Theoretical performance analysis of the vapor compression refrigeration system is too complex because equations of the performance of system with many equations are required. Refrigerator is main power-consuming unit in a domestic appliance [1] and chlorofluorocarbons are the most important refrigerant gas in household applications because it has excellent thermal as well as physical properties. Then, it may be phased out quickly to permitting the Kyoto protocol due to its great global warming potential (GWP) of 1300 advanced than CO_2. Ashford et al. [2–4] ensure that GWP of hydrofluorocarbon (HFC) refrigerants are most important than that of chlorofluorocarbon (CFC) refrigerants. As regards the above problem, alternative refrigerants can be investigated. Due to high GWP of R134a, the size of the system increases [5–7]. Various R134a refrigerant replacements that reach the requirements are an important method in this investigation. Various investigators have been described the mixed hydrocarbon refrigerants that are originated to be an excellent eco-friendly alternative refrigerant option in a household refrigerator.

The study of Fatouh and ElKafafy [8] reveals that single hydrocarbon refrigerants are not accurate to substitute the R134a since the thermal properties and operating pressures are very high. Jung et al. [9] done using R290/R600a (60/40 %wt.) as substitute to R12 in a 299L and 465L capacity of domestic refrigerators and also energy efficiency and coefficient of performance (COP) are enhanced by 4% & 2.3% over R12. Akash and Said [10] conducted experiments with LPG (60% of R290 and 40% R600a) as an alternative refrigerant to R12 in a household purpose at different weights like 50 g, 80 g, and 100 g. The results labeled from 80 g of LPG refrigerant as confirmed the outstanding substitute in the direction of R12. Lee and Chimres [11] presented an investigational report on the vapor compression refrigeration system using isobutene (R600a) as the retrofit for R12 and R134a, because the COP of the system was improved. Wongwises and Chimres [12] examined HC blends and HC/HFC refrigerants blends at various weight combinations, which are used in a 239L of home appliances worked at surrounding temperature 298 K to substitute for R134a. It concluded that the R290/R600 blend (60/40 wt%) is the ultimate alternative to R134a. Fatouh and Kafafy [13] conducted the test using LPG as a substitute to R134a in a 280L household refrigerator worked at 316 K surrounding temperature. The COP of the LPG refrigerator is improved by 7.6% than R134a. By using LPG as a refrigerant in a domestic refrigerator, the energy consumption also reduced by 10.8%. Mani and Selladurai [14] conducted the experiments on a domestic refrigeration system using different hydrocarbon refrigerant blends as alternative refrigerants to HFC refrigerants. The investigational significances presented that hydrocarbon refrigerant blends give 28.6–38.2% greater refrigerating capacity than R134a. The R290/R600a combination is a zoetrope mixture which does not act as a single constituent when it deviates from its segment. Stephan [15] find the zoetropic mixtures are evaporates restricted in the tubes are unstable element (R290). In the combina-

tion evaporates first in the liquid-based refrigerant and maintains a smaller amount of unstable constituent (R600a). For the reason that of less unstable constituent (R600a) in liquid, the saturation temperature becomes reduced. Colbourne et al. [16] have find out the challenging issue for the hydrocarbon combinations is to be present by chemically stable and nonreactive metallic constituents are used in compressor [17]. Subsequently the amount and weight of the hydrocarbon refrigerant mixtures are less than (about 50–55%) that of R134a. If any leakages happened in the hydrocarbon mixtures does not affect the system because the usage of refrigerant is less than 150 grams.

The above proposals disclose that most of the investigators [4–17] ensure that the different hydrocarbon refrigerant combinations are used as substitute to R134a in household appliances. However, the possibility of using HCM as R436A (54% R290 and 46% R600a) is a substitute to R134a at various evaporating and different ambient temperature settings. The aim of the current experimental work is to search the probability of using above HCM in a 175L household refrigerator through different mass charges (60, 80, and 100 g), evaporator temperature (T_e), and different capillary tube lengths (L_c) that are studied. To find the performance of a refrigerator with help of varying the evaporator temperatures and working at constant (29 °C) ambient temperature. This study focused on the independent variation of refrigerant charge (m_r) or capillary tube geometries (L_c), while a study on the effect of simultaneous variation of these parameters is still lacking. Therefore, this extent to investigational thermodynamic performance to household refrigerator was experimentally studied by simultaneously varying (m_r) and (L_c). Based on above experimental study the variation of input parameters, the performance of a domestic refrigerator can be improved by using R436A. So, the possibility of replacing of R134a with R436A. The primary objective of the experimental investigation is to find the finest combination of (L_e) and (m_r) to give minimum pull-down time (to reach evaporator temperature is −15 °C, according to IS1476 Part 1 [18]).

To optimize the domestic refrigeration system in a theoretical way we need so, many properties are required. But in a fuzzy logic system can be used to adaptive characteristics, which can achieve robust responses to uncertainties, parameter variations with a minimum values. Zadeh [18] introduced the fuzzy logic system in this system to resolve ill-defined, nonlinear problems. Adcock TA et al. [19] have investigated the fuzzy logic system are used in a variety of applications in a different fields, especially in a industrial process control and identified the best technique when compared to conventional system. Sugeno et al. [20] derived an application of medical diagnosis and security system. Lee et al. [21] used a fuzzy logic system to control nonlinear, time-varying, and ill-defined systems such as servomotor position control with dynamics applications. Scharf and Mandic [22] find a new technique for a robot-arm control. In this system, model predictions are compared with an experimental data available in the literature for the validation of fuzzy model.

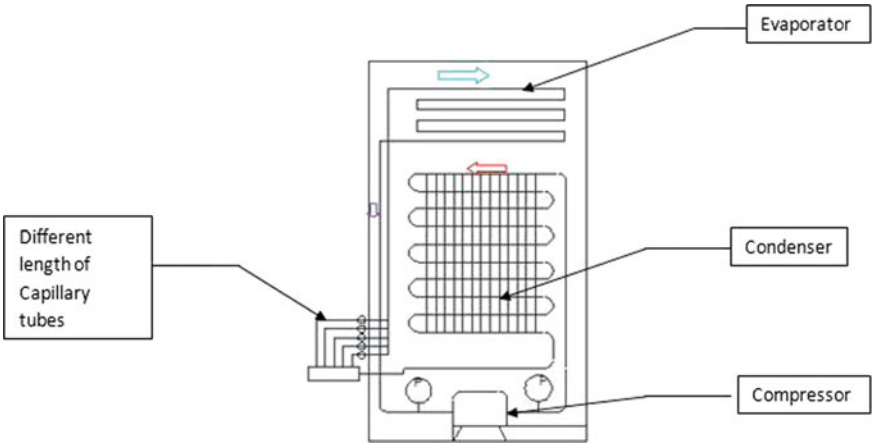

Fig. 1 Experimental test rig

2 Experimental Details

In this experimental setup, a single door household refrigerator works with R134a with the total capacity of 175L as shown in Fig. 1. It consists of deep freezer, hermetically sealed reciprocating compressor air-cooled condenser, strainer, and five capillary tubes with different lengths via ball valves. By using this experimental setup to conduct experiments and find the output parameters such as the refrigerating effect, power consumption and coefficient of performance of domestic refrigerator. In this context, ball valves are used to operate the capillary tubes with changed combinations. The capillary tube outlet is connected to evaporator and then the refrigerant flows through it. Two pressure gauges are connected with refrigerator at compressor inlet and outlet with a precision of $\pm 0.25\%$ to measure pressures. Seven thermocouple sensors are used for calibrating the (RTD Pt100) temperatures inside the freezer, refrigerator cabin, evaporator, compressor, and condenser inlets and outlets; the accuracy is ± 0.25 K. During the experimentation, the total experimental system is located in an open to atmosphere.

2.1 Experimental Setup and Testing Procedure

Initially, the system was evacuated by vacuum pump up to 30 PSI pressure. After that, 100 g of R600a/R290 (56/44 by wt%) mixture was used as an alternative to the system. Initially, fill the refrigerant charge R600a/R290 (56/44 by wt%) of 100 g mass in the system and calculate cooling capacity, compressor work, and COP for different length (4, 4.5,5 5.5, 6 m) and 0.036 inches diameter of capillary tube. The outcomes can be carried out as per the methodology followed by Sekhar and Lal [23].

For the period of testing, the ambient temperature to be maintained is around 29 °C for changing capillary tube and varying weight of refrigerant. Total experimental values are collected after reaching the steady-state conditions. The performance tests are to be carried out at different evaporator temperatures (−15, −9 and −3 °C). In this experimental analysis, there is no need to change major modification in a household refrigerator. Therefore, in the experimental work the HCM are used as a refrigerant without changing the compressor oils (polyesters). In this mixtures the weight of refrigerant can be calibrated with the help of electronic balancing machine and having the precision is ±0.01 g. The observation values are recorded for every 10 minutes. These HCMs are filled in a compressor in the form of liquid state and the observation values are recorded for every 10 minutes.

3 Development of ANN Model

Artificial neural network (ANN) can be defined as a system of processing units called neurons which are distributed over a finite number of layers and interconnected in a predetermined manner to accomplish the desired task. It resembles the brain in two respects; the interneuron connection strengths (also known as synaptic weights) are used to store knowledge just like the brain's neurons. Knowledge is acquired by the network through learning process. The network stores knowledge during the learning phase with the help of a learning algorithm. The objective of the learning rule is to capture the implicit relationships in the given set of input–output pattern pairs and store this knowledge by modifying the weights in an orderly design.

3.1 Modeling with the ANN

The performance parameters of domestic refrigerator is Refrigeration Effect, POWER Consumption of a compressor, and COP of system can be predicted by using Artificial Neural Network with back propagation Algorithm are used. The performance of ANN is affected by two important characteristics of the network such as number of hidden layers and number of neurons in the hidden layers. The output performance compared with the desired experimental values and errors is computed. These errors are back propagated to the neural network for adjusting the weight such that the errors decrease with each iteration. After different iterations with a combinations of different number of neurons in single hidden layer and changing the transfer functions (log-sig and tan-sig). It is finalized the the ANN model gives best results when compared with experimental values.

4 Design of Fuzzy Logic System for a Domestic Refrigeration System

Fuzzy logic system consists of fuzzifier, membership functions, fuzzy rule base inference engine, and defuzzifier. In this fuzzy logic techniques the performance of domestic system can be evaluated based on the input and desired outputs of the system. In the conception of fuzzy reasoning is described briefly based on the inputs and desired outputs of the system. In this work, a fuzzy controller has been developed with three inputs and three outputs. Three output parameters are Coefficient of Performance (COP), Refrigeration Effect (RE), and power consumption (P) are considered in this system. By using Mamdani fuzzy interface system with "if then" rules has been adopted to find the optimization of total system. The defuzzifier is used to convert fuzzy data to crisp response values. Fuzzy separation was performed on input and output variables by using triangular membership functions.

5 Results and Discussions

The results found from the experimentations conducted on the domestic refrigeration system performance evaluation and simulation with neural network and fuzzy logic system developed for modeling of the refrigeration system are summarized in this chapter. In this work, the effect of RE, POWER, and COP is studied on domestic refrigeration system with hydrocarbon refrigerant mixtures.

5.1 Prediction of COP by Using FlS and ANN for R134a

The predicted values from FLS and ANN models are compared with the experimental values. The validation is based on the data drawn from experimental runs of COP for R134a. The errors (%) for the predicted values are also calculated based on the deviation. The average error of fuzzy logic system is 2.4647%, whereas the error percentage of ANN model is as low as 1.466%. The lower error values indicate higher prediction ability. The ANN model prediction ability is higher compared to the fuzzy logic system. The details are shown in Fig. 2. Training with more data can make the prediction ability higher. Use of more data for training network process has been taken large time but not gives better prediction capabilities. Based on the error analysis, only the mass of refrigerant is a dominant parameter to increase the COP in optimized conditions.

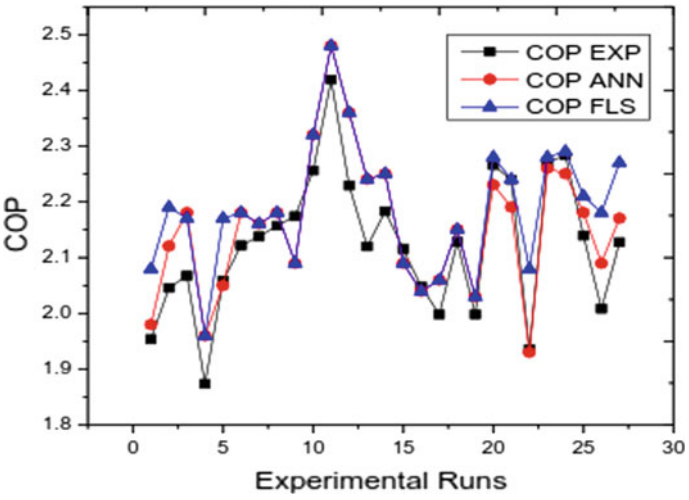

Fig. 2 Comparison of test data, FLS, and ANN values of COP for R134a

5.2 Prediction of COP by Using FlS and ANN for R436A

The predicted values from FLS and ANN models are compared with the experimental values. The validation is based on the data drawn from experimental runs of COP for R134a. The errors (%) for the predicted values are also calculated based on the deviation. The average error of fuzzy logic system is 2.836276%, whereas the error percentage of ANN model is as low as 1.467%. The ANN model prediction ability is higher compared to the fuzzy logic system based on the error analysis. The details are shown in Fig. 3. Use of more data for training network process has been taken large time but not gives better prediction capabilities are the capillary the percentage contribution of input parameters to calculated values are given to higher priority for capillary length and lower contribution for mass of refrigerant with increase in the COP of the system.

6 Conclusion

In this paper, FLS and ANN modeling techniques are used to optimize the performance of the domestic refrigeration system. Conventional modeling techniques are usually complicated because they required huge data and engineering effort and may be give incorrect results. To reduce above complications to propose FLS and ANN simulating techniques are used to optimize the domestic refrigeration system. The performance and optimization of total system can be evaluated based on input variables such as weight of refrigerant, different capillary tube length and varying

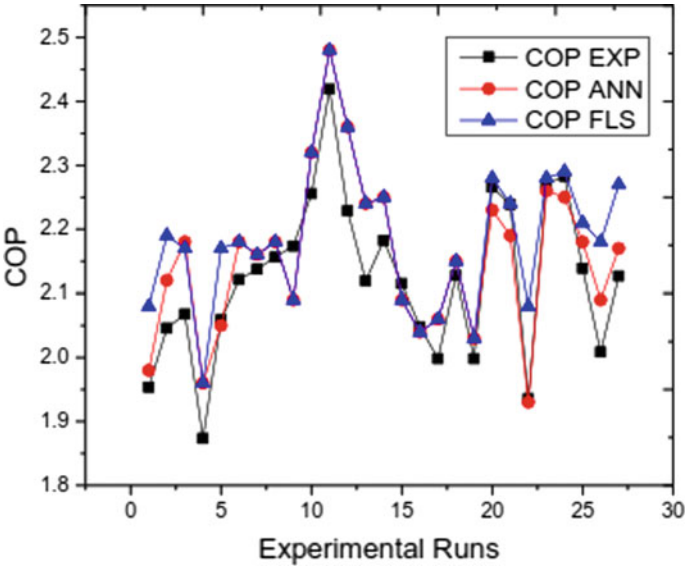

Fig. 3 Comparison of test data, FLS, and ANN values of COP for R436A

evaporator temperatures are considered. In order to collecting the data from a domestic refrigeration system operating at steady-state conditions with a constant ambient temperatures. The three input parameters are mass of refrigerant mixture weight, capillary tube length, and evaporator temperature. The output parameter is COP, which is to be predicted with ANN-based system and a back propagation algorithm can be developed, Whereas for FLS the Mamdani fuzzy inference system are used to finding optimization of total system. Finally, the performance of the ANN predictions was measured using average error with experimental values. The ANN modeling is good statistical performance with an average error when compared to FLS.

References

1. Radermacher, R., Kim, K.: Domestic refrigerators: recent developments. Int. J. Refrig. **19**(1), 61–69 (1996)
2. Ashford, P., Clodic, D., McCulloch, A., Kuijpers, L.: Emission from the foam and refrigeration sectors comparison with atmospheric concentrations. Int. J. Refrig. **27**, 701–716 (2004)
3. McCulloch, A., Lindley, A.: From mine to refrigeration alife cycle inventory analysis of the production of HFC134a. Int. J. Refrig. **26**, 865–872 (2003)
4. McCulloch, A., Midgley, P.M., Ashford, P.: Release of refrigerant gases (CFC12, HCFC22, HFC 134a) to the atmosphere. Atmos. Environ **37**, 889–902 (2003)
5. Li, G., Hwang, Y., Radermacher, R.: Review of cold storage materials for air conditioning application. Int. J. Refrig. **35**, 2053–2067 (2012)
6. Li, G., Liu, D., Xie, Y.: Study on thermal properties of TBAB-THF hydrate mixture for cold storage by DSC. J Therm. Anal. Calorim. **102**(2), 819–826 (2010)

7. Fatouh, M., ElKafafy, M.: Assessment of propane/commercial butane mixtures as possible alternatives to R134a in domestic refrigerators. Energy Convers. Manag. **47**, 2644–2658 (2006)
8. Jung, D.S., Kim, C.B., Song, K., Park, B.J.: Testing of propane/isobutene mixture in domestic refrigerators. Int. J. Refrig. **23**, 517–527 (2000)
9. Akash, B.A., Said, S.A.: Assessment of LPG as a possible alternative toR-12 in domestic refrigerator. Energy Convers. Manag. **44**, 381–388 (2003)
10. Lee, Y.S., Su, C.C.: Experimental studies of isobutene (R600a) as the refrigerant in domestic refrigeration system. Appl. Therm. Eng. **22**, 507–519 (2002)
11. Wongwises, S., Chimres, N.: Experimental study of hydrocarbon mixtures to replace HFC134a in domestic refrigerators. Energy Convers. Manag. **46**, 85–100 (2005)
12. Fatouh, M., ElKafafy, M.: Experimental evaluation of a domestic refrigerator working with LPG. Appl. Therm. Eng. **26**, 1593–1603 (2006)
13. Mani, K., Selladurai, V.: Experimental analysis of new refrigerant mixture as drop-in replacement for CFC12 and HFC134a. Int. J. Therm. Sci. **47**, 1490–5001 (2008)
14. Rajapaksha, L.: Influence of special attributes of zoetropic refrigerant mixtures on design and operation of vapor compression refrigeration and heat pump systems. Energy Convers. Manag. **48**, 539–545 (2007)
15. Stephan, K.: Two phase heat exchange for new refrigerants and their mixtures. Int. J. Refrig. **18**, 198–209 (1995)
16. Colbourne, D., Ritter,T.J.: Compatibility of Non-Metallic Materials with Hydrocarbon Refrigerants and Lubricant Mixtures. IIR Commission B1,B2, E1 and E2, Purdue University, USA (2000)
17. Domanski, P.A., Didion, D.A.: Evaluation of suction-line/liquid-line heat exchange in the refrigeration cycle. Int. J. Refrig. **17**, 487–493 (1994)
18. Zadeh, L.A.: Outline of a new approach to the analysis of complex systems and decision processes. IEEE Trans. Syst. Man Cybern. 270–280 (1973)
19. Adcock, T.A.: What is fuzzy logic: an overview of the latest control methodology. TI Application Report, pp. 1–7 (1993)
20. Sugeno, M.: Industrial applications of fuzzy control. North Holland, Amsterdam (1985)
21. Lee, C.C.: Fuzzy logic in control systems: fuzzy-logic controller Part I&II. IEEE Trans Syst. Man Cybern. **20**(2), 404–435 (1990)
22. Scharf, E.M., Mandic, N.J.: The application of a fuzzy controller to the control of a multi-degree-freedom robot arm. In: Industrial Applications of Fuzzy Control, pp. 41–62. Amsterdam, North-Holland (1985)
23. Didion, D.A., Bivens, D.B.: Role of refrigerant mixtures as alternatives to CFCs. Int. J. Ref. **13**, 163–175 (1990)
24. Performance of household refrigerating appliance-refrigerators with or without low temperature compartment-IS1476 part1 (2000)

Numerical Computation of the Blood Flow Characteristics Through the Tapered Stenotic Catheterised Artery with Flexible Wall

K. M. Surabhi, Dhiraj Annapa Kamble and D. Srikanth

Abstract This article explores the mathematical formulation of non-Newtonian fluid flow through an asymmetric tapered stenotic artery in the presence of catheter. Impact of the wall flexibility and pulsatile pressure is also considered. The governed model is solved by using the finite difference method. Effects of the various geometric parameters and the flow parameters are observed on the volumetric flow and velocity components. Further impact on physiological parameter, impedance is also estimated. This model is of significant importance in the pharmaceutical industry and also in medical field.

Keywords Power-law model · Stenotic artery · Resistance to the flow · Volumetric flow

1 Introduction

Over the past few decades, cardiovascular diseases (CVDs) have been the leading cause of death worldwide [1]. Most of the deaths occur because of heart attacks and strokes apart from conditions of atherosclerosis and thrombosis. Heart attacks and strokes are usually acute events, mainly caused by the blockages that prevent the flow of blood to the heart or brain. The abnormal narrowing of blood vessels in various locations of cardiovascular system, due to the deposition of the cholesterol and other fatty substances leads to a medical condition nomenclatured as stenosis.

The blood rheology when considered as Newtonian is acceptable when the blood flows through the larger arteries, and the same is not true in case the arterial radius is very small. Gijsen et al. [2] examined a comparison between Newtonian fluid and non-Newtonian fluid using Reynolds numbers. Based on literature survey, authors [3–6] demonstrated the impact of non-Newtonian fluid flow through the stenosed artery. Power-law paradigm [7] is very effective in extracting non-newtonian structure of

K. M. Surabhi · D. Annapa Kamble · D. Srikanth (✉)
Defence Institute of Advanced Technology (Deemed University), Pune 411025, India
e-mail: sri_dasari1977@yahoo.co.in

D. Srinivasacharya and K. S. Reddy (eds.), *Numerical Heat Transfer and Fluid Flow*, Lecture Notes in Mechanical Engineering,
https://doi.org/10.1007/978-981-13-1903-7_15

blood. Shear thickening and Shear thinning properties of the blood is well realised in the power-law model, as evident from the expression of stress. Nadeem et al. [8] and Ismail et al. [9] considered the power-law fluid model of blood flow in their analysis.

Based on the above literature survey, considered is the flow of power-law fluid, through an asymmetric stenosed tapered artery with flexible wall in the presence of catheter. The modelled governing equations are solved by using the finite difference method. We analysed flow parameters like volumetric flow, radial and axial velocities as well as the physiological parameter the resistance to the flow and the same are interpreted graphically.

2 Mathematical Modelling of the Problem

2.1 Schematic Representation of the Axisymmetric Stenosis

The schematic diagram of the asymmetric stenotic, tapered and flexible catheterised artery is as given in Fig. 1. Power-law equations are used to study the incompressible flow through the annular region that is formed between the coaxial cylinders represented by the catheter and an artery, across the arterial length L. Here, r_0 is the radius of the non-tapered and non-stenotic artery while r_c is the radius of the catheter which is fixed. $\zeta (= \tan(\phi))$ represents the tapering parameter with the taper angle ϕ. The converging, diverging and non-tapered nature of the artery accords with the taper angle $\phi < 0$, $\phi > 0$ and $\phi = 0$. The geometry of the asymmetric stenotic tapered artery with flexible wall is mathematically expressed as [3],

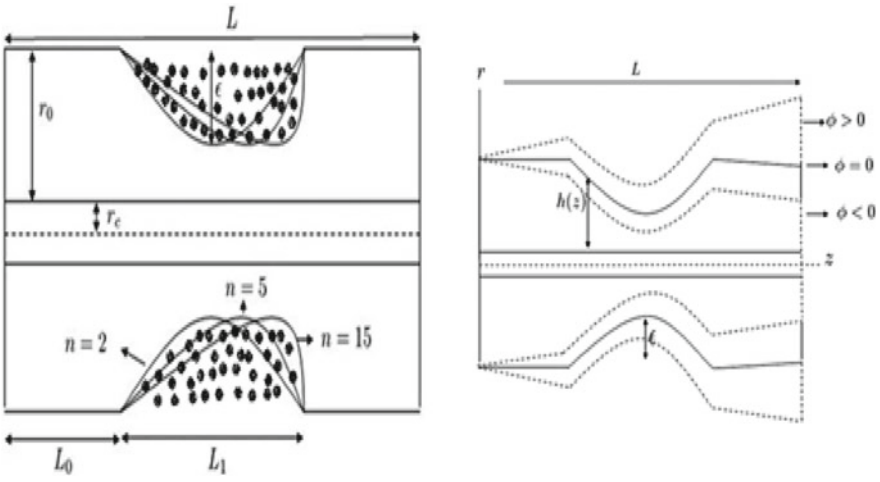

Fig. 1 Geometry of asymmetric stenosed artery

$$h(z,t)=\begin{cases}(r_0+z\zeta)\left[1-\frac{\varepsilon n^{n/(1-n)}}{L_1^n(n-1)}\left(L_1^{n-1}(z-L_0)-(z-L_0)^n\right)\right]f(t); & \text{if } L_0\le z\le L_0+L_1\\ (r_0+\zeta z)f(t); & \text{otherwise}\end{cases} \tag{1}$$

Here, L_0 and L_1 are the upstream length and stenotic length of the artery, respectively. $n(\geq 2)$ is the stenosis shape parameter (symmetric stenosis is obtained when $n=2$) of the artery. ε corresponds to the height of the stenosis. At $z=L_0+\frac{L_1}{n^{1/(n-1)}}$, the maximum height of the stenosis is located for non-tapered artery. The time variant parameter $f(t)$ is expressed as $f(t)=1-(b\cos\omega t-1)e^{-b\omega t}$.

2.2 Equations of the Governing Flow

For the fully developed unsteady, laminar, incompressible power-law fluid flow, the governing equations are given as under,

$$\frac{\partial v_r}{\partial r}+\frac{v_r}{r}+\frac{\partial v_z}{\partial z}=0 \tag{2}$$

$$\frac{\partial v_z}{\partial t}+\frac{\partial v_z}{\partial r}(v_r)+\frac{\partial v_z}{\partial z}(v_z)=-\frac{1}{\rho}\frac{\partial p}{\partial z}-\frac{1}{\rho}\left[\frac{\partial}{\partial r}(r\sigma_{rz}).\frac{1}{r}+\frac{\partial}{\partial z}(\sigma_{zz})\right] \tag{3}$$

$$\frac{\partial v_r}{\partial t}+v_r\frac{\partial v_r}{\partial r}+v_z\frac{\partial v_r}{\partial z}=-\frac{1}{\rho}\frac{\partial p}{\partial r}-\frac{1}{\rho}\left[\frac{1}{r}\frac{\partial}{\partial r}(r\sigma_{rr})+\frac{\partial}{\partial z}(\sigma_{zr})\right] \tag{4}$$

$$\sigma_{zz}=(-2)\left\{m\left|\left[\left(\frac{\partial v_r}{\partial r}\right)^2+\left(\frac{\partial v_z}{\partial z}\right)^2+\left(\frac{v_r}{r}\right)^2+\left(\frac{\partial v_r}{\partial z}+\frac{\partial v_z}{\partial r}\right)^2\right]^{\frac{1}{2}}\right|^{n-1}\right\}\left(\frac{\partial v_z}{\partial z}\right) \tag{5}$$

$$\sigma_{rz}=\sigma_{zr}=(-2)\left\{m\left|\left[\left(\frac{\partial v_r}{\partial r}\right)^2+\left(\frac{v_r}{r}\right)^2+\left(\frac{\partial v_z}{\partial z}\right)^2+\left(\frac{\partial v_r}{\partial z}+\frac{\partial v_z}{\partial r}\right)^2\right]^{\frac{1}{2}}\right|^{n-1}\right\}\left(\frac{\partial v_z}{\partial r}+\frac{\partial v_r}{\partial z}\right) \tag{6}$$

$$\sigma_{rr}=(-2)\left\{m\left|\left[\left(\frac{\partial v_r}{\partial r}\right)^2+\left(\frac{\partial v_z}{\partial z}\right)^2+\left(\frac{v_r}{r}\right)^2+\left(\frac{\partial v_r}{\partial z}+\frac{\partial v_z}{\partial r}\right)^2\right]^{\frac{1}{2}}\right|^{n-1}\right\}\left(\frac{\partial v_r}{\partial r}\right) \tag{7}$$

Here, $v_r(r, z, t)$ and $v_z(r, z, t)$ are the velocity components in the radial and axial direction, respectively. Density of the blood is ρ, and $\sigma's$ are the stress tensors while p is the pressure. The pressure gradient as observed from [9] is $-\partial p/\partial z = P_0 + P_1\cos(\omega t), t > 0$. In the pressure gradient, P_0 is considered as constant amplitude while the systolic and diastolic pressure in case of pulsatile flow occurs with the amplitude P_1 with $\omega = 2\pi f_p$, where f_p is the frequency of pulse. Non-dimensionalization is the partial or full removal of units from equations involving physical quantities by a suitable substitution of variables. Non-dimensional parameters introduced are as given under

$$z' = \frac{z}{r_0},\ r' = \frac{r}{r_0},\ v_z' = \frac{v_z}{u_0},\ v_r' = \frac{L_1 v_r}{u_0 \varepsilon},\ t' = \frac{\Omega t L_1}{r_0},\ p' = \frac{r_0 p}{u_0 \mu} \tag{8}$$

Equations (2)–(7) are transformed by using the non-dimensional parameters given above.

2.3 Boundary Conditions and Initial Condition

There is no radial flow and axial flow on the catheter wall as it is considered to be a rigid body and the same is mathematically expressed as

$$v_r(t, r, z) = 0 = v_z(t, r, z) \quad \text{on} \quad r = r_c \tag{9}$$

$$v_r = \frac{\partial h}{\partial t}; \ \text{on} \quad r = h(t, z) \tag{10}$$

$$\frac{\partial v_z}{\partial r} = \frac{\gamma}{\sqrt{D_a}}\left[u_b + \frac{D_a}{\mu}\frac{\partial p}{\partial z}\right]; \quad \text{on} \quad r = h(z, t); \quad \text{where} \quad L_0 \le z \le L_0 + L_1 \tag{11}$$

$$v_z = u_b; \quad \text{on} \quad r = h(t, z); \quad \text{where} \quad z \le L_0 \,\&\, z \ge L_0 + L_1 \tag{12}$$

Initial Condition is given as

$$v_z = \text{Real part of}\left\{\left[\frac{I_0\left(i^{1/2}\alpha r\right)}{I_1\left(i^{1/2}\alpha r\right)} - 1\right]\frac{\partial p}{\partial z}\frac{Re}{\beta}e^{it/\beta}\right\}; \text{ and } \quad v_r = 0 \tag{13}$$

Here, $\alpha = \frac{\rho a\sqrt{\Omega}}{\mu}$ is the Womersely number.

3 Solution Methodology

With the regard of this blood flow model, we are using finite difference method (FDM) to obtain velocity profiles and other flow characteristics are volumetric flow (Q) and the resistance to the flow (λ). FDM is relevant for the rectangular domain. Having such kind of limitation, we transform the irregular domain to the rectangular domain by introducing the radial co-ordinate transformation as given below

$$x = \frac{r - r_c}{h(t,z) - r_c} = \frac{r - r_c}{R(t,z)} \tag{14}$$

The radial transformation is applied to the non-dimensionalized equations and the boundary conditions. The discretized domain is $z_i = (i-1)\Delta z$, $x_j = (j-1)\Delta x$ and $t_k = (k-1)\Delta t$ where Δz, Δx and Δt are the discretization parameters in the z, x and t directions, respectively. The time derivative is discretized by the forward time difference first order accurate and space derivatives are discretized by central difference second order accurate methods, respectively. The flow characteristic volumetric flow as, $Q_k^i = 2\prod \int_0^1 x_j R_i (x_j R_i + r_c)(v_z)_{i.j}^k dx_j$ and resistance to the flow as $\lambda_i^k = \frac{|L(\partial p/\partial z)|}{Q_i^k}$

4 Results and Discussion

The resulting difference forms of the governing equations are explicit in nature. The discrete time period works as long as it satisfies CFL condition for difference schemes. The velocities and flow characteristics are generated by using the following values of various physical parameters a $r_0 = 0.152; r_c = 0.01; \varepsilon = 0.05; \varphi = 0.05; u_b = 0.05; \alpha = 2; \mathrm{Re} = 10; D_a = 0.1; \gamma = 0.1; \mu = 0.012$. From Figs. 2, 3 and 4, it is realised that the radial velocity and obstruction to the flow decreases while the axial velocity increases as the asymmetric nature of the artery increases in case of divergent artery. As depicted in Fig. 5, the volumetric flow is more in divergent artery which is proportional to the axial velocity, and hence, the results were simulated for the divergent case. In Fig. 6, it is shown that, as the height of the stenosis increases, resistance to the flow increases; it is because pressure drop is more dominant than the volumetric flow rate. Also as the catheter radius increases the values of the flow variables decrease. The same is depicted through Figs. 6 and 7. For the treatment of the cardiac patients we should focus on these parameters. Hence, such results are useful for the treatment of the CVDs.

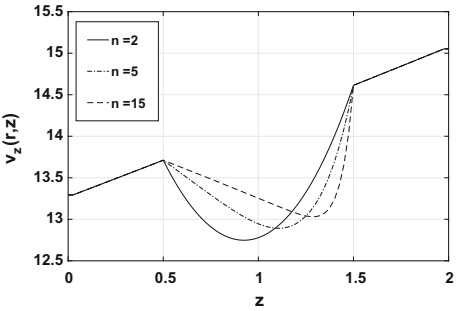

Fig. 2 Radial velocity for different n

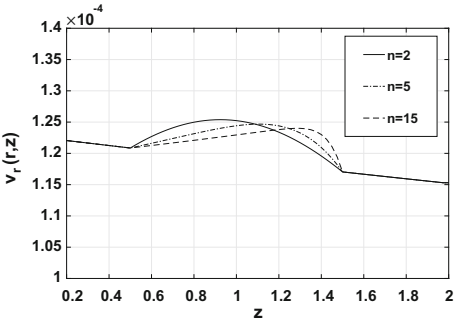

Fig. 3 Axial velocity for different n

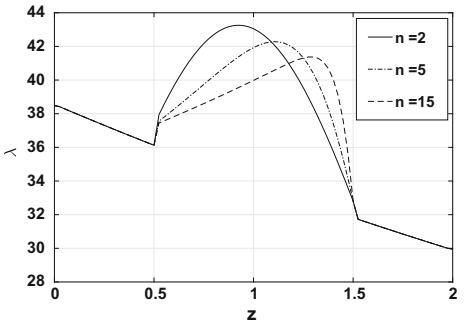

Fig. 4 Resistance to the flow

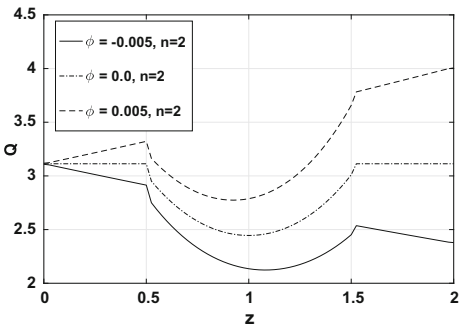

Fig. 5 Volumetric flow for varying taper angle

5 Conclusion

This paper presents the numerical computation of an unsteady power-law fluid flow in a tapered artery with stenosis. Tapering angle of blood vessel which is an important factor is considered. Stenosis height is proportional to the resistance to the flow in the

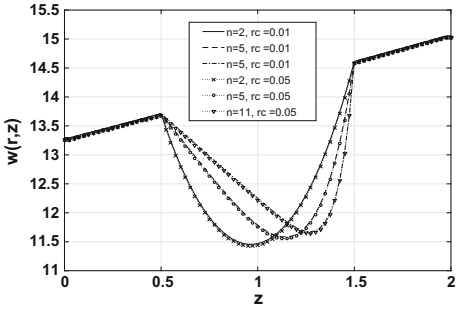

Fig. 6 Resistance to the flow at different heights of stenosis

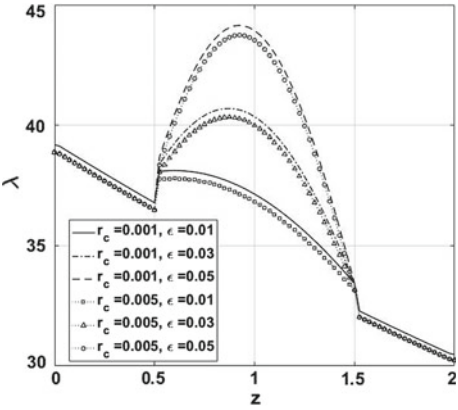

Fig. 7 Axial velocity at different r_c and n

arteries which results in the blood pressure. This model is applicable for the severe case of stenosis.

References

1. Lim, S.S., Vos, T., Flaxman, A.D., Danaei, G., Shibuya, K., Adair-Rohani, H., AlMazroa, M.A., Amann, M., Anderson, H.R., Andrews, K.G., Aryee, M.: A comparative risk assessment of burden of disease and injury attributable to 67 risk factors and risk factor clusters in 21 regions, 1990–2010: a systematic analysis for the global burden of disease study 2010. The lancet **380**(9859), 2224–2260 (2013)
2. Gijsen, F.J.H., Allanic, E., Vosse, F.N., Janssen, J.D.: The influences of the non-Newtonian properties of blood on the flow in large arteries: unsteady flow in a 90 degrees curved tube. J. Biomech. **32**, 705–713 (1999)
3. Reddy, J.V.R., Srikanth, D., Krishna Murthy, S.V.S.S.N.V.G.: Mathematical modelling of pulsatile flow of blood through catheterized unsymmetric stenosed artery—effects of tapering angle and slip velocity. Eur. J. Mech.-B/Fluids **48**, 236–244 (2014)

4. Chakravarty, S., Mandal, P.K.: An analysis of pulsatile flow in a model aortic bifurcation. Int. J. Eng. Sci. **35**, 409–422 (1997)
5. Reddy, J.V., Srikanth, D.: The polar fluid model for blood flow through a tapered artery with overlapping stenosis: effects of catheter and velocity slip. Appl. Bionics Biomech. (2015)
6. Chakravarty, S., Datta, A., Mandal, A.K.: Effect of body acceleration on unsteady flow of blood past a time-dependent arterial stenosis. Math. Comput. Model. **24**, 57–74 (1996)
7. Enderle, J., Susan, B., Bronzino, B.: Introduction to Biomedical Engineering. Academic Press, London (2000)
8. Nadeem, S., Akbar, N.S.: Power law fluid model for blood flow through a tapered artery with a Stenosis. J. Mech. Med. Biol. **11**, 1–30 (2010)
9. Ismail, Z., Abdullah, I., Mustapha, N., Amin, N.: A power-law model of blood flow through a tapered overlapping stenosed artery. Appl. Math. Comput. **195**(2), 669–680 (2008)

Combined Influence of Radiation Absorption and Hall Current on MHD Free Convective Heat and Mass Transfer Flow Past a Stretching Sheet

J. Deepthi and D. R. V. Prasada Rao

Abstract The present article investigates the combined influence of thermal radiation, radiation absorption, Soret and Dufour effect, and non-uniform heat source on the steady convective heat and mass transfer flow of a viscous incompressible fluid past a stretching sheet. The non-linear equations governing the flow, heat and mass transfer have been solved by using a Runge–Kutta fifth-order together with shooting technique. The influence of Sr/Du, A_1, B_1 on all flow characteristics has been analysed.

Keywords Non-uniform heat source/sink · Hall current · Cross diffusion Stretching sheet

1 Introduction

The analysis of boundary layer heat and flow transfer of fluids over a continuous stretching surface has gained much attention from numerous researchers. Stretching brings a one-sided direction to the extradite; due to this, the end product significantly relies upon the stream and heat and mass process. Many researchers have studied the flows with temperature-dependent viscosity in different geometries and under various flow conditions with Hall effects (1–8). Some of its applications in Industrial and Engineering domains are in polymeric sheets extraction, insulating materials, fine fiber matters, production of glass fibre and sticking of labels on surface of hot bodies. Some of the other applications are drawing of hot rolling wire, drawing of thin films of plastic and the study of crude oil spilling over the surface of seawater. In liquids-based applications such as petroleum, oils, glycerin, glycols and many more, viscosity exhibits a considerable variation with temperature. The viscosity

J. Deepthi (✉)
Department of Mathematics, IIIT, R.K.Valley, RGUKT-AP, Kadapa 516330, India
e-mail: dreddy075@gmail.com

D. R. V. P. Rao
Department of Mathematics, S.K. University, Anantapur 515003, India

D. Srinivasacharya and K. S. Reddy (eds.), *Numerical Heat Transfer and Fluid Flow*, Lecture Notes in Mechanical Engineering,
https://doi.org/10.1007/978-981-13-1903-7_16

of the water decreases by 240% when the temperature increases from 10 °C (μ = 0.0131 g/cm) to 50 °C (μ = 0.00548 g/cm). To estimate the heat transfer rate accurately, it is necessary to take the variation of viscosity with temperature into consideration.

2 Formulation of the Problem

The consequent equations, which are highly non-linear, are explained by using the fifth-order Runge–Kutta–Fehlberg method (denoted by RKF method) with shooting technique. Figure 1 explains the problem configuration of a stretching sheet having momentous convective stream of *Nu* and *Sh* of a viscous and electrically conducting liquid. A constant magnetic field B_0 is introduced across the y-axis considering Hall current effect. The temperature and the species concentration are maintained at prescribed constant values T_w, C_w at the sheet and T_∞, C_∞ are the fixed values far away from the sheet.

Taking Lai and Kulacki [1] proposition, μ the liquid viscosity is assumed to change as inversely proportional to the linear function of temperature is provided by

$$\frac{1}{\mu} = \frac{1}{\mu_\infty}\left[1 + \gamma_0(T - T_\infty)\right] \Rightarrow \frac{1}{\mu_\infty} = \alpha(T - T_\infty) \tag{1}$$

where $\alpha = \frac{\gamma_0}{\mu_\infty}$ and $T_r = T_\infty - \frac{1}{\gamma_0}$ in which α and T_r are constants, and their respective values are based on the liquid's thermal characteristic. Generally, $\alpha > 0$, $\alpha < 0$ represent for liquids and gases, respectively. The governing equations taking thermal radiating approximated by Rosseland approximation (Pal [2]) are

$$\frac{\partial u}{\partial x} + \frac{\partial v}{\partial y} = 0, \tag{2}$$

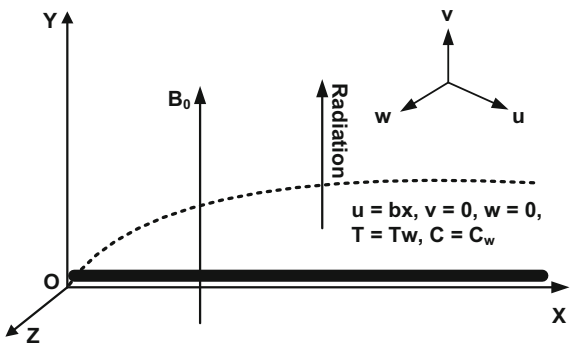

Fig. 1 Physical sketch of the problem

$$\left.\begin{aligned}\rho_m\left(u\frac{\partial u}{\partial x}+v\frac{\partial u}{\partial y}\right)&=\frac{\partial}{\partial y}\left(\mu\frac{\partial u}{\partial y}\right)+\rho_m g_0\beta_\tau(T-T_\infty)\\&\quad+\rho_m g_0\beta_c(C-C_\infty)-\frac{\sigma B_0^2}{1+m^2}(u+m\,w)\end{aligned}\right\}\tag{3}$$

$$\rho_m\left(u\frac{\partial w}{\partial x}+v\frac{\partial w}{\partial y}\right)=\frac{\partial}{\partial y}\left(\mu\frac{\partial w}{\partial y}\right)+\frac{\sigma B_0^2}{1+m^2}(m\,u-w)\tag{4}$$

$$\begin{aligned}\rho C_p\left(u\frac{\partial T}{\partial x}+w\frac{\partial T}{\partial z}\right)&=k_f\frac{\partial^2 T}{\partial y^2}+\mu\left(\frac{\partial^2 u}{\partial y^2}\right)^2\\&\quad+\frac{k_f u_w(x)}{\upsilon x}(A_1(T_w-T_\infty)u+B_1(T_w-T_\infty))\\&\quad+\frac{D_m K_T}{C_s C_p}\frac{\partial^2 C}{\partial y^2}+Q_1^1(C_w-C_\infty)+\frac{16\sigma^* T_\infty^3}{3\beta_R}\frac{\partial^2 T}{\partial y^2}\end{aligned}\tag{5}$$

$$u\frac{\partial C}{\partial x}+v\frac{\partial C}{\partial y}=D_m\frac{\partial^2 C}{\partial y^2}-k_0(C-C_\infty)+\frac{D_m K_T}{T_m}\frac{\partial^2 T}{\partial y^2}\tag{6}$$

The pertinent boundary conditions are

$$u\,(0)=u_w\,(x)=bx\,,\quad v\,(0)=w\,(0)=0,\quad T\,(0)=T_w,\quad C\,(0)=C_w\tag{7}$$

$$u\,(\infty)\to 0\,,\quad w\,(\infty)\to 0,\quad T\,(\infty)\to T_\infty,\quad C\,(\infty)\to C_\infty\tag{8}$$

where D_m, K_T, K_f, C_s and C_p denotes Mass diffusivity coefficient, thermal diffusion ratio, thermal conductivity coefficient, concentration susceptibility and specific heat at constant pressure. The below similarity transformations are introduced to study the stream adjoining the sheet.

$$\begin{aligned}&u=bxf'(\eta);v=-\sqrt{b\upsilon}f(\eta);w=bxg(\eta)\\&\eta=\sqrt{\frac{b}{\upsilon}}\,y;\theta(\eta)=\frac{T-T_\infty}{T_w-T_\infty};\varphi=\frac{C-C_\infty}{C_w-C_\infty}\end{aligned}\tag{9}$$

where f, h, θ and $\emptyset$ are non-dimensional stream function, similarity space variable and non-dimensional temperature and concentration, respectively. Equation (9) is satisfied by u and v in the continuity equation (Eq. 2). Substituting Eq. (9), Eqs. (2)–(6) reduce to

$$\begin{aligned}&\left(\frac{\theta-\theta_r}{\theta_r}\right)\left(f'-ff'\right)+f''-\left(\frac{\theta'}{\theta-\theta_r}\right)f'\\&-\left(\frac{\theta-\theta_r}{\theta_r}\right)G(\theta+N\varphi)+M^2\left(\frac{\theta'-\theta_r}{\theta_r}\right)\left(\frac{f'+mg}{1+m^2}\right)=0\end{aligned}\tag{10}$$

$$\left(\frac{\theta-\theta_r}{\theta_r}\right)(f'g-fg')+g''-\left(\frac{\theta'}{\theta-\theta_r}\right)g'-M^2\left(\frac{\theta-\theta_r}{\theta_r}\right)\left(\frac{mf'-g}{1+m^2}\right)=0 \tag{11}$$

$$\left(1+\frac{4N_{r_r}}{3}\right)\theta''+\Pr \mathrm{Ec}(f'')^2+\left(A_1f'+B_1\theta\right)+\Pr \mathrm{Du}\emptyset''+Q_1\emptyset=0 \tag{12}$$

$$\varphi''-\mathrm{Sc}(f\varphi'-\gamma\varphi)=-\mathrm{ScSr}\theta'' \tag{13}$$

Similarly, the transformed boundary conditions are given by

$$f'(\eta)=1,\ f(\eta)=0,\ g(\eta)=0,\ \theta(\eta)=1,\varphi(\eta)=1 \text{ at } \eta=0 \tag{14}$$

$$f'(\eta)\to 1,\ g(\eta)\to 0,\theta(\eta)\to 1,\varphi(\eta)\to 0 \text{ as } \eta\to\infty \tag{15}$$

3 Formulation of the Problem

The non-linear ordinary differential Eqs. (10–13) with boundary conditions (14–15) are solved numerically using Runge–Kutta–Fehlberg integration coupled with shooting technique. This method involves, transforming the equation into a set of initial value problems (IVP) which contain unknown initial values that need to be determined by first guessing, after which the Runge–Kutta–Fehlberg iteration scheme is employed to integrate the set of IVPs until the given boundary conditions are satisfied. The initial guess can be easily improved using the Newton–Raphson method.

4 Comparison

The results of this chapter are compared with the results of previously published paper of Shit et al. [3] as shown in Table 1, and the outcomes are in good concurrence.

5 Results and Discussion

An increase in heat source (A_1, $B_1 > 0$) generates energy in the thermal boundary layer, and as a consequence, the axial velocity rises. In the case of heat absorption (A_1, $B_1 < 0$), the axial velocity falls with decreasing values of A_1, $B_1 < 0$, an increase in the space-dependent/temperature-dependent heat generating source (A_1, $B_1 > 0$), and reduces in the case of heat absorbing source. The concentration increases with the increase of space-dependent heat/temperature-dependent generating source (A_1, $B_1 > 0$) and reduces in the case of heat absorbing source (A_1, $B_1 < 0$). And an increase

Table 1 Comparison of *Nu* and *Sh* at $\eta = 0$ with Shit et al. [3] with Sr = 0, Du = 0, $A_1 = 0$, $B_1 = 0$, Ec = 0, $Q_1 = 0$

M	Nr	γ	λ	θ_r	Shit et al. [3] Results		Present results	
					$Nu(0)$	$Sh(0)$	$Nu(0)$	$Sh(0)$
0.5	1	0.5	0.5	−2	−0.6912	0.6265	−0.69119	0.626499
1.5	1	0.5	0.5	−2	−0.6977	0.6543	−0.69765	0.654309
0.5	3	0.5	0.5	−2	−12.3751	0.9278	−12.7586	0.927799
0.5	1	1.5	0.5	−2	−0.6956	1.0959	−0.69559	1.095899
0.5	1	−0.5	0.5	−2	−0.6966	0.4898	−0.696599	0.489799
0.5	1	0.5	1.5	−2	−0.6968	0.4245	−0.696799	0.424489
0.5	1	0.5	1.5	−2	−0.5974	0.4071	−0.597399	0.407099

in A_1, B_1 enhances the skin friction component $|\tau_x|$ (Figs. 2, 3, 4, 5, 6, 7, 8 and 9).

An increase in the strength of space-dependent/temperature-dependent heat generating source (A_1, $B_1 > 0$) results in an enhancement in $|Nu|$ at $\eta = 0$ and we find that Sherwood number grows with $A_1, B_1 > 0$ and reduces with $A_1, B_1 < 0$ in the case of heat source absorption. It can be observed from the profiles that increase in Sr (or decrease in Du) smaller the axial velocity and cross flow velocity in the boundary layer. It is also found that higher the radiative heat flux smaller the axial velocity in the flow region and larger the cross flow velocity. It can be observed from the profiles that increase in Sr (or decreasing Du) reduces the temperature and concentration in the boundary layer. Increasing Soret parameter Sr (or decreasing Dufour parameter Du) leads to an enhancement in $|\tau_x|$ at the wall. $|\tau_z|$, $|Nu|$ and $|Sh|$ at $\eta = 0$ (Table 2).

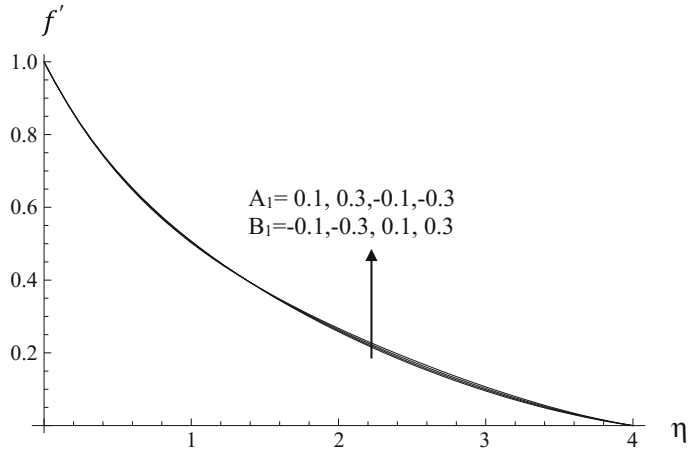

Fig. 2 Variation of f' with A_1, B_1: $G = 5$, $N = 1$, Nr = 0.5, Sc = 1.3, Sr = 2, Du = 0.04, $\theta_r = -2$, $Q_1 = 0.5$

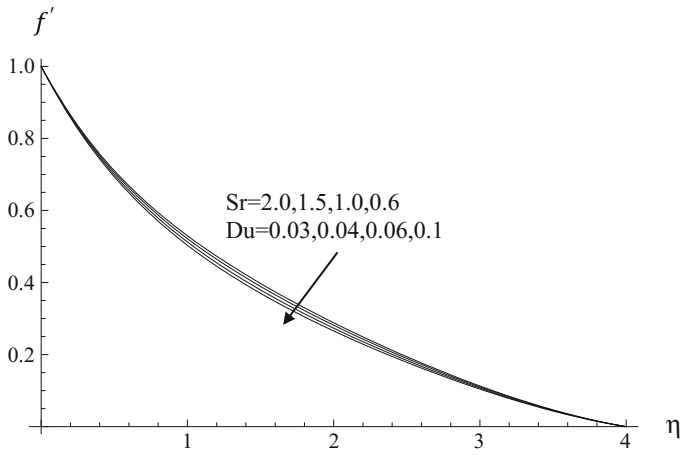

Fig. 3 Variation of f' with Sr and Du: $A_1 = 0.1$, $B_1 = 0.1$, $G = 5$, $N = 1$, Nr $= 0.5$, Sc $= 1.3$, $\theta_r = -2$, $Q_1 = 0.5$

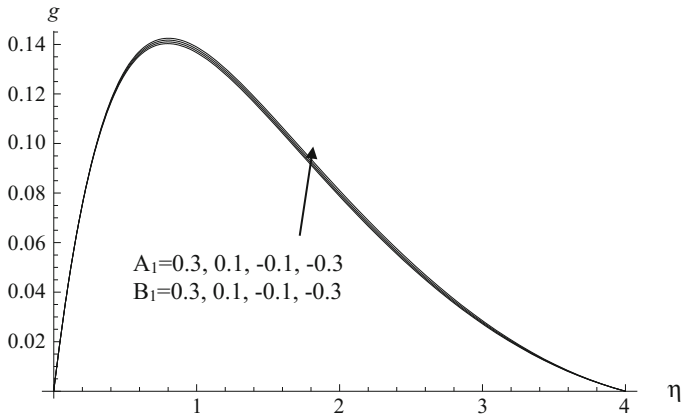

Fig. 4 Variation of g with A_1, B_1: $G = 5$, $N = 1$, Nr $= 0.5$, Sc $= 1.3$, Sr $= 2$, Du $= 0.04$, $\theta_r = -2$, $Q_1 = 0.5$

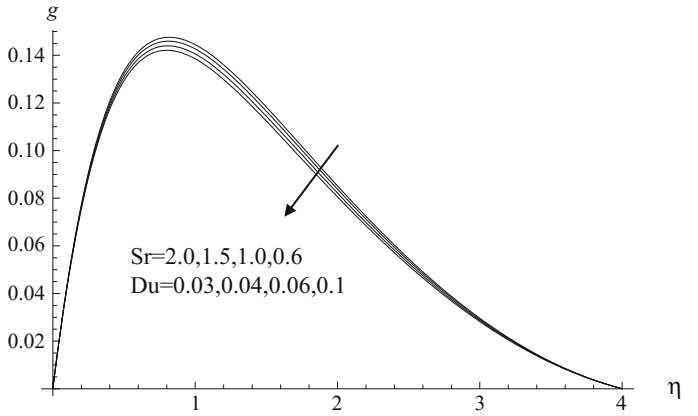

Fig. 5 Variation of g with Sr and Du: $A_1 = 0.1$, $B_1 = 0.1$, $G = 5$, $N = 1$, Nr $= 0.5$, Sc $= 1.3$, $\theta_r = -2$, $Q_1 = 0.5$

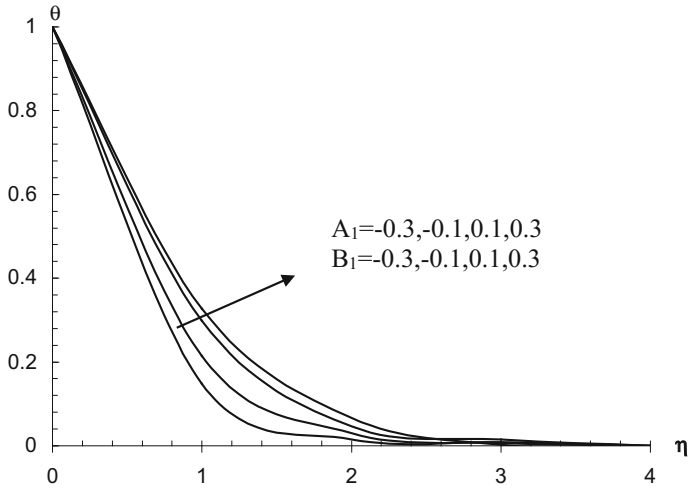

Fig. 6 Variation of θ with A_1, B_1 $G = 5$, $N = 1$, Nr $= 0.5$, Sc $= 1.3$, Sr $= 2$, Du $= 0.04$, $\theta_r = -2$, $Q_1 = 0.5$

6 Conclusions

This paper studies the influence of Soret and Dufour effects, non-uniform heat source, dissipation and radiation absorption and variable viscosity on mixed convective heat and mass transfer flow past stretching sheet. Influence of Soret and Dufour parameter on uniform heat source, dissipation and radiation absorption parameter on mixed convective heat and mass transfer flow has been explored in detail. Increasing Sr (or decreasing Du) reduces $|Nu|$ and $|Sh|$ at $\eta = 0$. $|Nu|$ reduces and $|Sh|$ enhances the

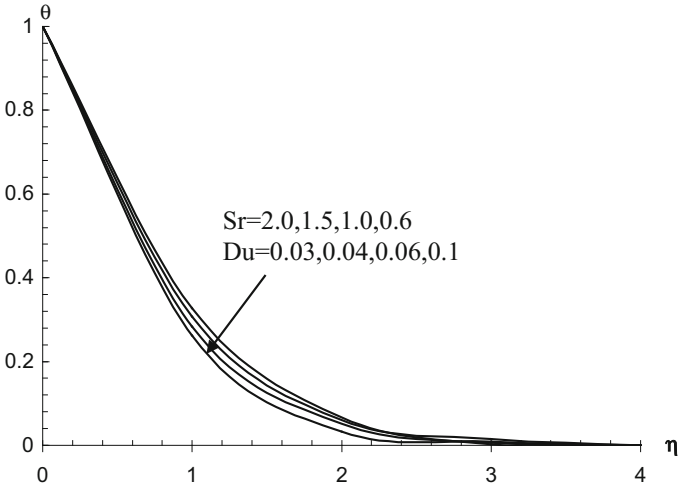

Fig. 7 Variation of θ with Sr and Du: $A_1 = 0.1$, $B_1 = 0.1$, $G = 5$, $N = 1$, Nr $= 0.5$, Sc $= 1.3$, $\theta_r = -2$, $Q_1 = 0.5$

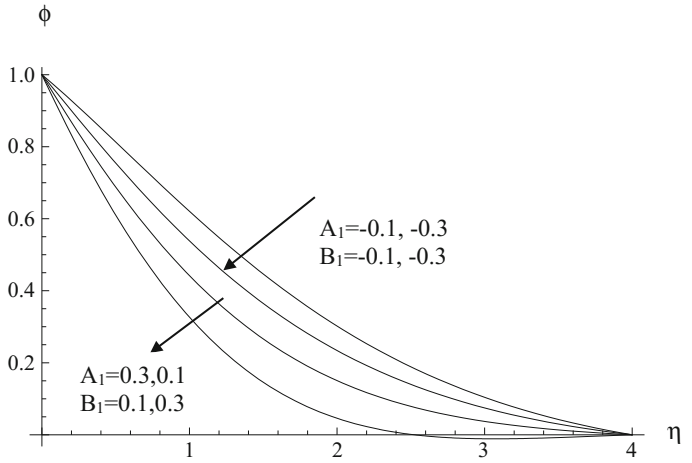

Fig. 8 Variation of θ with A_1, B_1: G $= 5$, N $= 1$, Nr $= 0.5$, Sc $= 1.3$, Sr $= 2$, Du $= 0.04$, $\theta_r = -2$, $Q_1 = 0.5$

increase in Ec. Nu and Sh at the wall grow with increase in the strength of A_1/B_1 and reduce with that of absorbing source. Excellent agreement with the present study and Shit et al. [3] has been obtained.

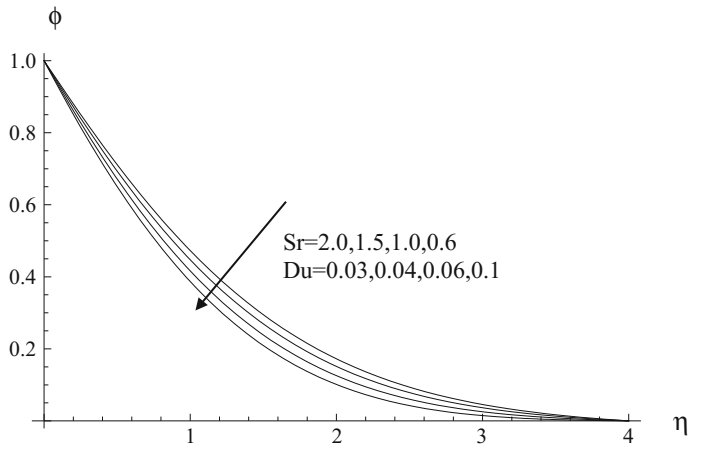

Fig. 9 Variation of ϕ with Sr and Du: $A_1 = 0.1$, $B_1 = 0.1$, $G = 5$, $N = 1$, Nr $= 0.5$, Sc $= 1.3$, $\theta_r = -2$, $Q_1 = 0$

Table 2 Shear stress, Nusselt number and Sherwood number at $h = 0$

Parameter	$\tau_x(0)$	$\tau_y(0)$	$Nu(0)$	$Sh(0)$
Sr/Du 2.0/0/03	−0.53308	0.458635	0.0584519	0.755636
1.5/0/04	−0.524227	0.46209	0.0548956	0.700006
1.0/0.06	−0.51499	0.465679	0.0508996	0.642667
0.6/0.1	−0.757774	0.493944	0.0451896	0.608179
$A1/B1$ 0.01/0.01	−0.53308	0.458635	0.0584519	0.755636
0.03/0.03	−0.534201	0.45682	−0.120486	0.987539
−0.01/−0.01	−0.532554	0.460894	0.326161	0.411181
−0.03/−0.03	−0.799178	0.488237	0.45532	0.25806

References

1. Theuri, D., Makind, O.D., Nancy, W.K.: Unsteady double diffusive magneto hydrodynamic boundary layer flow of a chemically reacting fluid over a flat permeable surface. Aust. J. Basic Appl. Sci. **7**(4), 78–89 (2013)
2. Lai, F.C., Kulacki, F.A.: The effect of variable viscosity on convective heat transfer along a vertical surface in a saturated porous medium. Int. J. Heat Mass Transfer **33**(5), 1028–1031 (1990)
3. Rahmanm, M., Salahuddin, K.M.: Study of hydro magnetic heat and mass transfer flow over an inclined heated surface with variable viscosity and electric conductivity. Commun. Nonliner Sci. Numer. Simul. **15**(8), 2073–2085 (2010)
4. Chamkha, A.J., El-Kabei, S.M.M., Rashad, A.M.: Unsteady coupled heat and mass transfer by mixed convection flow of a micro polar fluid near the stagnation point on a vertical surface in the presence of radiation and chemical reaction. Prog. Appl. Fluid Dyn. **15**, 186–196 (2015)

5. Pal, D., Mondal, H.: Soret and dufour effects on MHD Non-darcian mixed convection heat and mass transfer over a stretching sheet with non-uniform heat source/sink. Int. J. Phys. **13**(407), 642–651 (2012)
6. Shit, G.C., Haldar, R.: Combined effects of thermal radiation and hall current on MHD Free-convective flow and mass transfer over a stretching sheet with variable viscosity. J. Appl. Fluid Mech. **5**, 113–121 (2012)
7. Sarojamma, G., Mahaboobjan, S., Sreelakshmi, K.: Effect of hall current on the flow induced by a stretching surface. IJSIMR **3**(3), 1139–1148 (2015)
8. Das, S., Jana, R.N., Makinde, O.D.: MHD Boundary layer slip flow and heat transfer of nanofluid past a vertical stretching sheet with Non-uniform heat generation/absorption. Int. J. Nanosci. **13**(3), 1450019 (2014)

Numerical Study for the Solidification of Nanoparticle-Enhanced Phase Change Materials (NEPCM) Filled in a Wavy Cavity

Dheeraj Kumar Nagilla and Ravi Kumar Sharma

Abstract In this paper, the results of a numerical simulation of solidification phenomenon of nanoparticles mixed phase change materials are presented. The nanoparticles of copper dispersed in water were considered as nanofluid filled in a wavy cavity for this study. A parametric study concerning with the effect of nanoparticle volume fractions, initial temperature of nanofluid, and temperature of cold wall is carried out and findings are presented. Also, the effect of Grash of number on the solidification time is investigated. The results of this numerical investigation reveal that wavy cavity help to reduce the total solidification time of nanofluid over the square cavity. Also, the increasing volume of nanoparticles reduces the solidification time.

Keywords Solidification time · Nano-enhanced phase change materials
Cu nanoparticles · Wavy cavity

1 Introduction

Phase change materials (PCMs) use their latent heat for storing/releasing the energy which can be used when required. In most of the applications, PCMs are kept in a container. These containers help to avoid PCM leakage in their molten state and direct contact of environment to materials. The organic PCMs generally possess low thermal conductivity which is enhanced by the dispersion of nanosized metal particles in them. This mixture of nanoparticles and base fluid is known as nanofluid [1]. An aqueous solution of copper nanoparticles was prepared and filled in a square cavity by Khodadadi [2]. The results show that the addition of metal nanoparticles significantly enhances the heat transfer rate. The container's shape also significantly alters the heat transfer rate of nanofluid filled in it. Ostrach [3] presented a review of all such geometries to encapsulate the PCMs. Recently, Sharma [4] considered a trapezoidal

D. Kumar Nagilla · R. Kumar Sharma (✉)
Department of Mechanical Engineering, Manipal University Jaipur, Jaipur, Rajasthan, India
e-mail: ravipvb@gmail.com

D. Srinivasacharya and K. S. Reddy (eds.), *Numerical Heat Transfer and Fluid Flow*, Lecture Notes in Mechanical Engineering,
https://doi.org/10.1007/978-981-13-1903-7_17

cavity filled with a copper water nanofluid and carried out a parametric numerical investigation. Authors found that trapezoidal shape of cavity helps in enhancing the heat transfer performance of system. In the present work, solidification of a nanofluid filled in a wavy cavity is analyzed numerically using ANSYS Fluent. The effects of nanoparticle contents, initial temperature of nanofluid, temperature difference between hot and cold wall, and Grashof number on the freezing phenomenon of nanofluid are presented.

2 Methodology

2.1 Geometry and Boundary Conditions

A 2-D wavy cavity of 100 mm^2 internal area and 10 mm length (L) is used as shown in the Fig. 1. The height (H) and length (L) are adjusted in such way that area of cavity is always 100 mm^2.

It is assumed that the horizontal walls of this cavity are insulated and not allowing any heat transfer to take place across them. It is also assumed that the shape and size (10 nm) of nanoparticles are uniform and the thermophysical properties are given in Table 1. The nanofluid is assumed Newtonian and the flow is laminar and incompressible. Boussinesq approximation is being used for handling the density variation in momentum equation. The phase transition phenomenon in ANSYS Fluent is traced by the Enthalpy-Porosity technique proposed by Brent [5]. Hot left wall and cold right were considered as the boundary condition for this investigation. Also, horizontal walls are considered impermeable.

Mathematical Formulations

The set of equations used by FLUENT for modeling solidification process are as follows [6]:

Continuity:

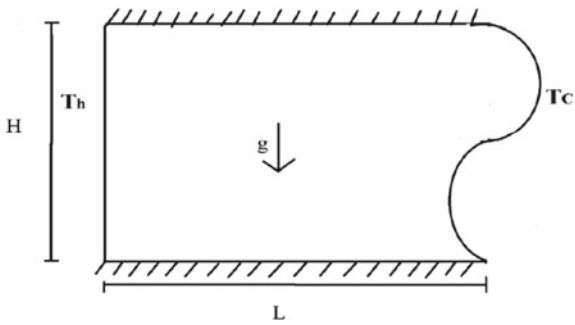

Fig. 1 2-D wavy cavity

Table 1 Thermophysical properties of basefluid (water), copper (Cu) nanoparticles, nanofluids

S. No.	Property	Cu-nano particles	Base fluid ($\emptyset = 0$)	Nanofluid ($\emptyset = 0.05$)	Nanofluid ($\emptyset = 0.1$)
1	ρ(kg/m^3)	8954	997.1	1394.95	1792.79
2	μ(pas)	–	8.9e^{-04}	1e^{-03}	1.158e^{-03}
3	C_P(J/kg.K)	383	4179	2960.67	2283.107
4	k(w/m.K)	400	0.6	0.698	0.8
5	β(1/K)	1.67e^{-05}	2.1e^{-04}	1.477e^{-04}	1.13e^{-04}
6	L(J/kg)	–	3.35e^{05}	2.27e^{05}	1.68e^{05}
7	Pr	–	6.2	4.755	3.31

$$\nabla . v = 0 \tag{1}$$

Momentum:

$$\rho\left(\frac{\partial u}{\partial t} + u.\nabla u\right) = -\nabla \bar{p} + \mu\nabla^2 u + \frac{1}{3}\mu\nabla(\nabla.u) + \rho g \tag{2}$$

Energy equation:

$$\frac{\partial}{\partial t}(\rho H) + \nabla.(\rho \vec{v} H) = \nabla.\left(\frac{k_t}{c_p}\nabla H\right) + S_h \tag{3}$$

The nanofluid's density is given by

$$\rho_{\text{nf}} = (1 - \emptyset)\rho_f + \emptyset\,\rho_s \tag{4}$$

Nanofluid's viscosity is given by

$$\mu_{\text{nf}} = \frac{\mu_f}{(1 - \emptyset)^{2.5}} \tag{5}$$

The latent heat of fusion of nanofluid is calculated by

$$(\rho L_h)_{\text{nf}} = (1 - \emptyset)(\rho L_h)_f \tag{6}$$

The thermal conductivity of the nanofluid is

$$\frac{k_{\text{nfo}}}{k_f} = \frac{k_s + 2k_s - 2\emptyset\left(k_f - k_s\right)}{k_s + 2k_f + 2\emptyset\left(k_f - k_s\right)} \tag{7}$$

The effective thermal conductivity of nanofluid is given by

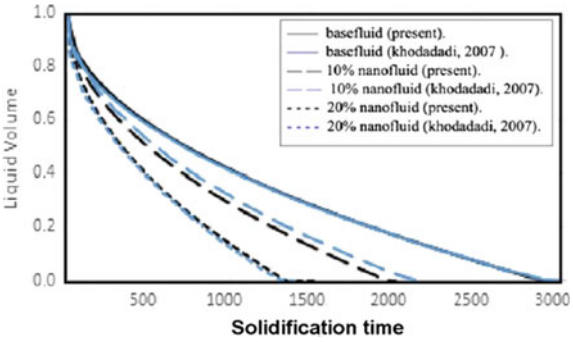

Fig. 2 Comparison of total solidification time in square cavity

$$k_{\text{eff}} = k_{\text{nfo}} + C(\rho c_P)_{\text{nf}}\sqrt{u^2 + v^2} \tag{8}$$

The constant C is obtained from the expression given by Wakao and Kaguei [7].

2.2 Numerical Methods

Initially, the nanofluid is maintained at 0 °C and this temperature was maintained uniformly by running steady-state simulation for some time. The hot wall was maintained at 10 °C and cold at 0 °C. After steady-state simulation, the temperature of both walls was reduced by 10 °C and nanofluid started solidifying from cold wall side and the solid–liquid interface start moving from cold to hot wall.

3 Results and Discussions

3.1 Validating the Numerical Model

The CFD findings of the current numerical model of square cavity of internal area 100mm^2 undergoing solidification process with nanofluid ($\emptyset = 0, 0.1, 0.2$) are compared with the numerical predictions of Khodadadi [3] in Fig. 2. The results show that the present numerical model validates the previously published results.

3.2 Solidification Time for Different Nanoparticle Volume Fraction

Left vertical and the right wavy walls of cavity were maintained at a different and constant temperature with the temperature difference ($\Delta T = 10$ °C). For all the numerical

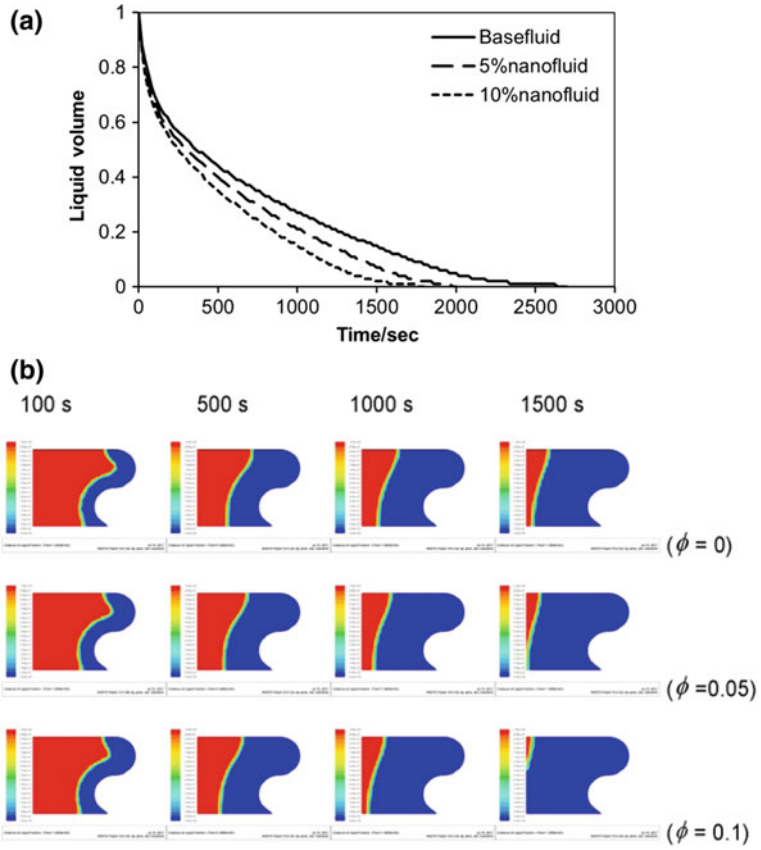

Fig. 3 **a** Instantaneous volume of nanofluid in the wavy cavity, **b** Colorized contours of nanofluid in the wavy cavity

simulations for this study, the internal area of cavity was kept constant, 100 mm^2. The results of the investigation on the solidification phenomenon of nanofluid with varied nanoparticles fractions ($\emptyset = 0, 0.05, 0.1$) in a wavy cavity as shown in Figs. 3a, b, reveal that the nanofluid's total solidification time is 33% lesser than that of base fluid. Results show that increase in the nanoparticle volume fraction decreases the solidification time. Colorized contours of the solidification of nanofluid ($\emptyset = 0, 0.05, 0.1$) at various time instants 100, 500, 1000, 1500s are shown in the Fig. 3b. The solidification starts from cold right wall and the solid region is shown by blue color and red color indicates the liquid region.

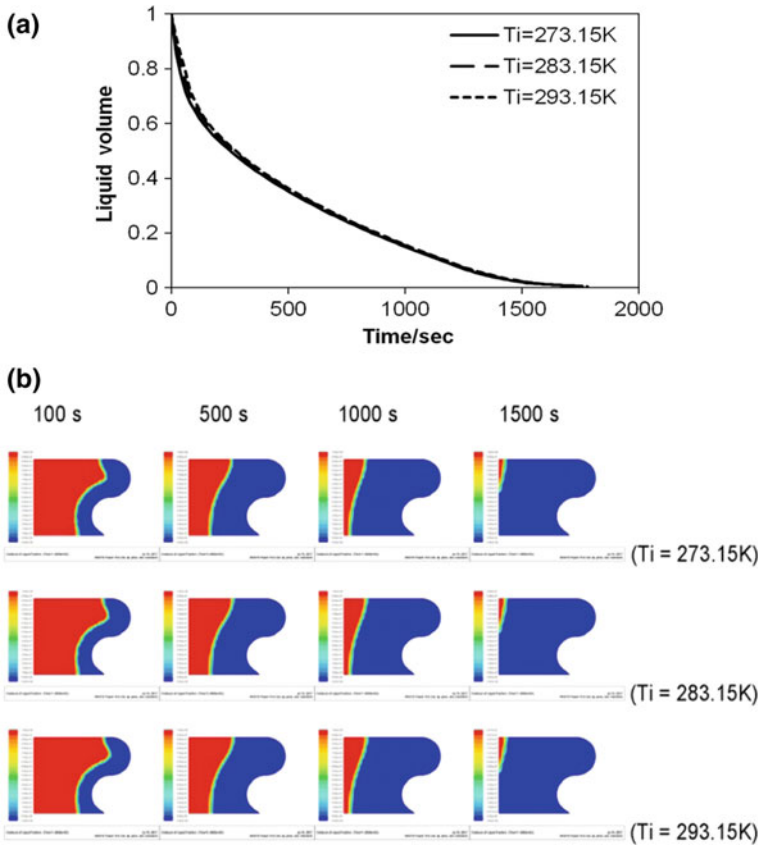

Fig. 4 **a** Instantaneous volume of nanofluid in the wavy cavity, **b** Colorized contours of nanofluid in the wavy cavity

3.3 Effect of Initial Temperature on the Total Solidification Time

The results of the investigation on the solidification process of nanofluid ($\emptyset = 0.1$) with different initial temperatures (T = 273.15, 283.15, 293.15 K) filled in a wavy cavity as shown in the Figs. 4a, b reveal that there is no change found in the solidification time of nanofluid due to the change in its initial temperature.

3.4 Effect of Hot and Cold Wall Temperature Difference

The effect of three wall temperature differences ($\Delta T = 10, 20, 30$ °C) between the left vertical and right wavy walls on solidification time is investigated. This effect is

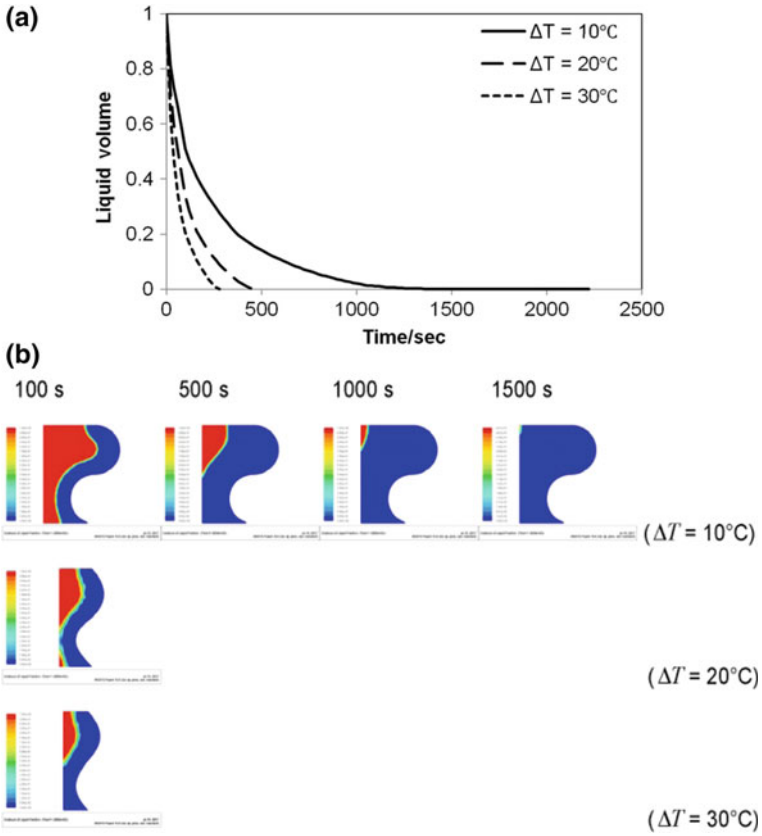

Fig. 5 **a** Instantaneous volume of nanofluid in the wavy cavity, **b** Colorized contours of nanofluid in the wavy cavity

investigated on nanofluid of 10% nanoparticles and findings are shown in Fig. 5a. The results show that increasing temperature difference decreases the solidification time, for example, for $\Delta T = 30°C$, the solidification time is 85% lesser in comparison of cavity subjected to $\Delta T = 10$ °C. Also, results indicate that increasing temperature difference does not deviate the profile of solid–liquid interface, which means the heat transfer is still being dominated by conduction phenomenon and shown in Fig. 5b.

*3.5 Investigation of Solidification Time for Different Grashof Number (*Gr*)*

The Grashof number was varied in the numerical model from $10^3 - 10^5$ and its effect on the total solidification time was investigated. For these simulation cases also, the nanofluid of 10% is considered and the results are shown in Fig. 6a. The figure

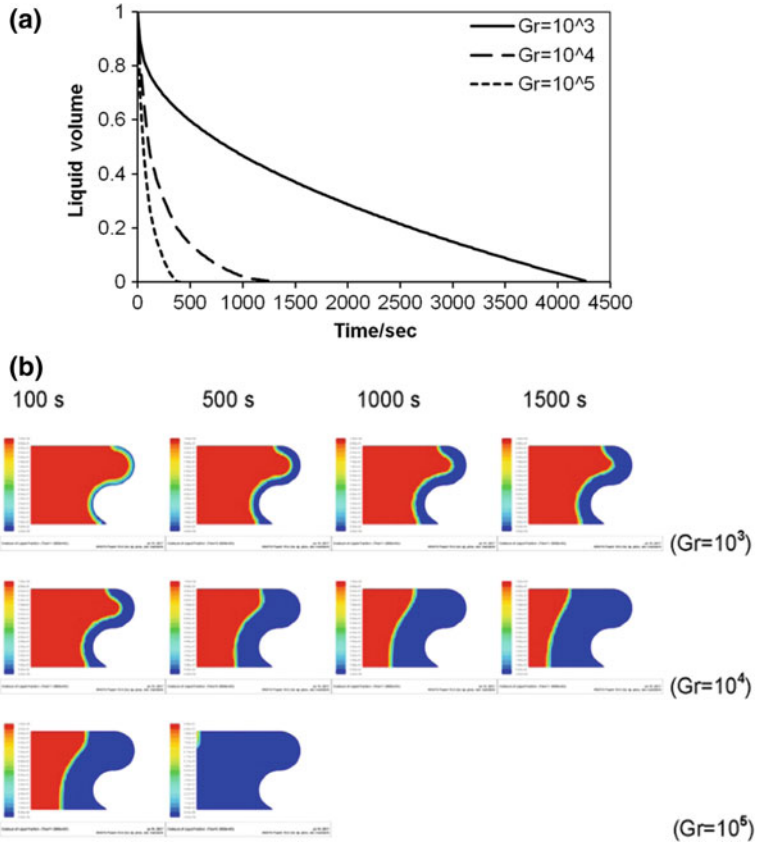

Fig. 6 **a** Instantaneous volume of nanofluid in the wavy cavity, **b**. Colorized contours of nanofluid in the wavy cavity

shows that increasing Grashof number significantly enhances the heat transfer which in turn decreases the total solidification time. For $(Gr \leq 10^5)$ as shown in the Fig. 6b, the conduction phenomenon dominates which can be understood by the appearance of solid–liquid interface that is straight in these cases. When the Grashof number increases beyond 10^5, the convection takes place and the phenomenon keeps exaggerating for higher values of *Gr*. Increasing the convection deflects the solid–liquid interface and it does not remain straight for higher values of *Gr*.

4 Conclusions

Present numerical investigation shows that wavy cavity is a potential geometrical structure for encapsulating the PCMs. Results show that higher nanoparticle fractions

reduce solidification time of nanofluid. Also, the Grashof number changes the heat transfer rate significantly. Heat transfer is higher for higher values of Grashof number. Higher *Gr* increases the convection phenomenon and solidification time decreases significantly.

References

1. Choi, S.U., Eastman, J.A.: Enhancing thermal conductivity of fluids with nanoparticles. Argonne National Lab, IL (United States) (1995)
2. Khodadadi, J., Hosseinizadeh, S.: Nanoparticle-enhanced phase change materials (NEPCM) with great potential for improved thermal energy storage. Int. Commun. Heat Mass Transfer **34**(5), 534–543 (2007)
3. Ostrach, S.: Natural convection in enclosures. J. Heat Transfer. **110**(4-B), 1175–21190 (1988)
4. Sharma, R.K., Ganesan, P., Sahu, J.N., Sandaram, S., Mahlia, T.M.I.: Numerical study for enhancement of solidification of phase change materials using trapezoidal cavity. Powder Technol. **268**, 38–47 (2014)
5. Brent, A., Voller, V., Reid, K.: Enthalpy-porosity technique for modeling convection-diffusion phase change: application to the melting of a pure metal. Numer. Heat Transfer Part A Appl. **13**(3), 297–318 (1988)
6. Khanafer, K., Vafai, K., Lightstone, M.: Buoyancy-driven heat transfer enhancement in a two-dimensional enclosure utilizing nanofluids. Int. J. Heat Mass Transf. **46**(19), 3639–3653 (2003)
7. Wakao, N., Kagei, S.: Heat and Mass Transfer in Packed Beds. Taylor & Francis (1982)

Analysis of Forced Convection Heat Transfer Through Graded PPI Metal Foams

Banjara Kotresha and N. Gnanasekaran

Abstract A forced convection heat transfer through high porosity graded Pores per inch (PPI) metal foam heat exchanger is numerically solved in this paper. The physical domain of the problem consists of a heat exchanger system attached to the bottom of a horizontal channel to absorb heat from the exhaust gas leaving the system. Two different pore densities of the metal foam 20 and 40 along with two different metal foam materials are considered for the enhancement of heat transfer in the present numerical investigation. The metal foam heat exchanger is considered as a homogeneous porous medium and is modeled using Darcy Extended Forchheimer model. The heat transfer through the metal foam porous media is solved by using local thermal equilibrium (LTE) model. The effect of graded pore density and graded thermal conductivity is investigated and compared with the nongraded PPI metal foam. The heat exchanger system is simulated over a velocity range of 6–30 m/s. The pressure drop decreases for the graded pore density metal foams compared to the higher PPI metal foam and also increases with increase in the fluid inlet velocity. The results of temperature and velocity distribution for the graded and nongraded metal foams are compared and discussed elaborately.

Keywords CFD · Heat exchanger · Metal foams · Graded PPI · LTE

1 Introduction

Metal foams are being widely used these days in thermal applications such as electronics cooling, refrigeration and air conditioning, etc. Mancin et al. [1] experimentally studied the flow and heat transfer through different copper metal foams with air as working fluid and concluded that the heat transfer coefficient increases with increase in the flow rate but it does not depend on the heat flux applied. Kim et al.

B. Kotresha · N. Gnanasekaran (✉)
Department of Mechanical Engineering, National Institute of Technology Karnataka, Surathkal, Mangaluru 575025, India
e-mail: gnanasekaran@nitk.edu.in

D. Srinivasacharya and K. S. Reddy (eds.), *Numerical Heat Transfer and Fluid Flow*, Lecture Notes in Mechanical Engineering,
https://doi.org/10.1007/978-981-13-1903-7_18

[2] experimentally studied the forced convection through aluminum metal foam in an asymmetrical heated channel. They reported that the low permeable foam gives significant improvement in the Nusselt number at the expense of friction factor. Lin et al. [3] numerically studied the performance of heat transfer through aluminum metal foams by applying both the LTE and LTNE (local thermal nonequilibrium) thermal models and concluded that the performance of LTE model and LTNE model was found the same at higher air velocities. Kamath et al. [4] carried out heat transfer experiments on high porosity aluminum metal foams filled in a vertical channel. Based on the Reynolds and Richardson numbers of the flow, they identified various regimes such as mixed and forced convections. Xu et al. [5] examined forced convection studies on metal foams partially filled in a parallel-plate channel. They reported that the friction factor can be reduced by increasing the porosity and decreasing the PPI. Bernardo et al. [6] conducted experimental and numerical studies on metal foam partially filled in a horizontal channel. They presented the results of temperature profiles for both with and without metal foam and calculated the amount of heat given to the surrounding. Sener et al. [7] carried out experiments on aluminum metal foam filled in a rectangular channel for calculating pressure drop and heat transfer. They concluded that the filling rate of the foam in the channel increases heat transfer. Lu et al. [8] carried out analytical studies on forced convection through horizontal plate channel partly filled with metallic foam. The effect of filling rate of the metal foam on velocity and temperature distribution is reported.

From the above literature review, it is clear that though there are numerous experimental and numerical studies on metal foams filled in channel, the authors found very few studies related to graded PPI metal foams employed in the channel for the enhancement of heat transfer. So, this paper presents the numerical study of forced convection through the partially filled highly porous graded PPI metal foams.

2 Problem Statement

The problem domain considered for the present simulation is shown in Fig. 1. A layer of graded metal foam is attached to the isothermal bottom wall to absorb heat leaving the exhaust system. The high-temperature air flows through the channel where the metal foam absorbs heat and then transfers to a cold fluid flowing in a secondary loop. The dimensions of the heat exchanger system are 195 mm long (L), 8 mm height (H), and 30 mm (W) in width, where H_f is total foam height which is half of H.

Aluminum and copper metal foams of two different pore densities 20 and 40 with porosity 0.937 is considered in the present study. The aluminum and copper metal foams possess thermal conductivity of 165 and 385 W/mK, respectively. The properties of the metal foam considered for the present simulations are tabulated in Table 1. In the present study, two types of graded pore density and graded thermal conductivity of the metal foams are studied, i.e., positive and negative gradients. The positive gradient PPI represents the increase in the pore density and negative

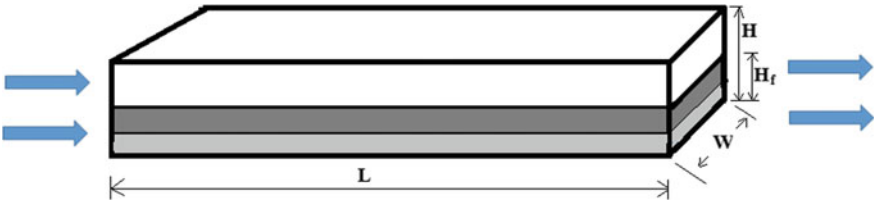

Fig. 1 Metal foam heat exchanger system

Table 1 Properties of metal foams

	Aluminum/Copper metal foam	
PPI	20	40
Permeability (K), m^2	3×10^{-7}	1×10^{-8}
C_F	0.1	0.2

gradient PPI represents the decrease of pore density along height of the channel. Similarly, positive gradient thermal conductivity represents the increase in thermal conductivity and negative gradient thermal conductivity represents the decrease of thermal conductivity along height of the 20PPI metal foam. The heights of the metal foams in the graded region are exactly half of the height of the metal foam of the nongraded.

3 Computational Domain and Boundary Conditions

A two-dimensional computational domain consisting of partially filled graded metal foam, upstream and downstream of the channel is considered for the computations. The inlet of the domain is defined with uniform velocity inlet boundary condition and the outlet is defined with zero pressure (see Fig. 2). The bottom wall of the channel is assigned with 300 K temperature while the top wall is adiabatic. Three different inlet velocities of the fluid are considered entering at a temperature of 523 K.

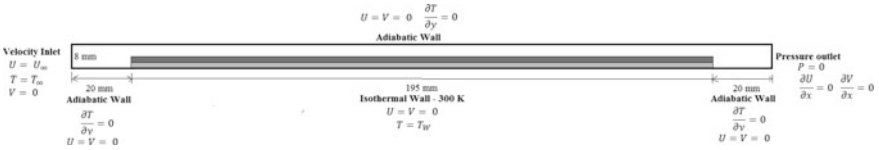

Fig. 2 Computational domain with boundary conditions

4 Numerical Details

The numerical computations are performed using the ANSYS FLUENT 15.0 software. As discussed earlier, three different inlet velocities of fluid considered ranging from 6 to 30 m/s, so the Reynolds number varies from 5000 to 26,000. To capture the turbulent characteristics of the flow, the well-known two equation k-ε model is used in both foam and open region of the channel. The metal foam region is considered as an isotropic homogeneous porous medium and modeled as the source term to the momentum equation using Darcy Extended Forchheimer model as given in Eq. (1).

$$-\frac{\mathrm{d}P}{\mathrm{d}x} = \frac{\mu_{\mathrm{eff}}}{K} u_x + C_F \frac{\rho}{\sqrt{K}} |U| u_x \tag{1}$$

where μ_{eff} is the effective viscosity equal to the fluid viscosity, K is the permeability (m^2), ρ is density of air (kg/m^3). The commonly used SIMPLE pressure–velocity coupling scheme considered in the present study and the convergence limit for continuity, momentum is set below $1e^{-4}$ and for energy is $1e^{-8}$.

5 Results and Discussion

5.1 Grid Independency and Validation of the Methodology

To solve the governing equations, optimum number of grids is required for effective computations. Hence, three different grids are considered in the numerical domain: 9200, 18,400 and 23,000. The variation of pressure drop and velocity distribution for 20PPI metal foam for an inlet velocity of 30 m/s is shown in Fig. 3a, b, respectively. From the figures, it has been noticed that the variation of pressure drop and velocity is almost the same for all the three grids considered, therefore a grid size of 18,400 is selected as the optimum grid for further investigations.

For the purpose of validation, the present numerical results are compared with theory and experimental results available in literature. Such an exercise is shown in Table 2 and the comparison of the exit air temperature and the pressure drop of the channel are validated against [9, 10]. The results of temperature and pressure show good agreement with the theory and experiments.

5.2 Hydrodynamic Results

The variation of pressure drop for the graded PPI metal foams is compared with the 20 PPI and 40 PPI metal foams and is shown in Fig. 4a. It is clear from the plot that the pressure drop decreases for both the graded PPI metal foam compared to the

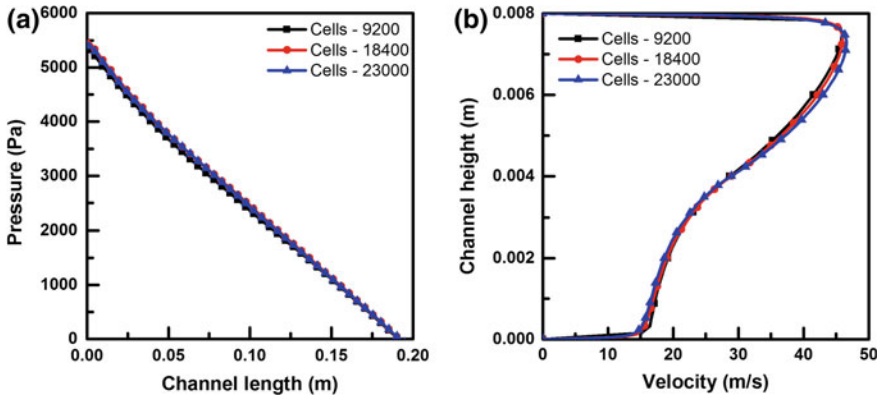

Fig. 3 Grid independency comparison **a** pressure drop **b** velocity distribution

Table 2 Validation of results

Inlet velocity (m/s)	Outlet temperature in K (nonporous channel)		Pressure drop dp–dp_{nf} in KPa (porous channel)	
	Theory [9]	Present study	Expt. [10]	Present study
10	496	477.38	0.53	0.572
30	501	492.14	5.5	4.38

40 PPI. The pressure drop increases as velocity increases for the all metal foams. Similarly, the friction factor also decreases for the graded PPI compared to the high pore density metal foam which can be seen in Fig. 4b. Figure 4c shows the velocity variation along the channel height for all the metal foams studied. The velocity in the metal foam region decreases and increases in the foam free region as PPI increases. The velocity in the open region for the graded PPI foam decreases compared to 40 PPI because the flow rate in the graded PPI foam region increases compared to 40 PPI. The effect of graded PPI can also be seen clearly from this plot.

5.3 Temperature Results

The variation of temperature along the height of the channel for graded PPI metal foam at the center and at the exit of the channel are shown in Fig. 5a, b. The temperature variation for both the graded PPI foam is almost similar to 40PPI metal foam. The heat absorption in the graded PPI foam region increases because more fluid flows through the metal foam region that performs similar to higher PPI metal foam. The effect of thermal conductivity gradient on the temperature results for 20PPI metal foam is shown in Fig. 5c. The temperature in the open region decreases for graded

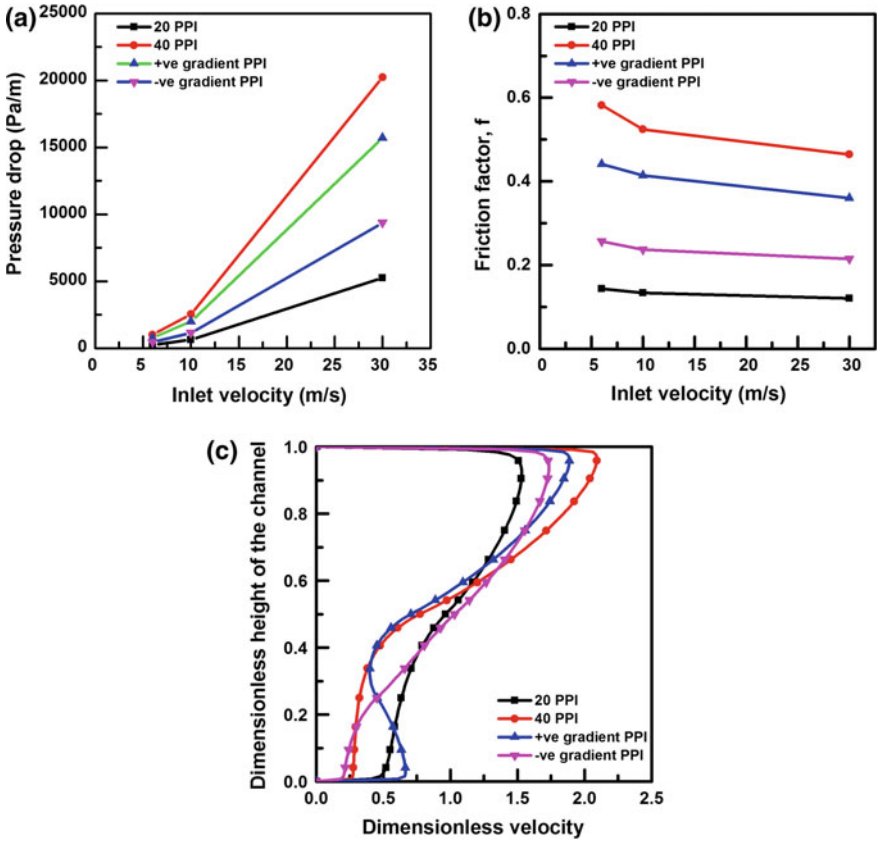

Fig. 4 Hydrodynamic results **a** Pressure drop **b** friction factor **c** velocity distribution

thermal conductivity metal foam compared to the aluminum metal foam as a result more heat is absorbed in the metal foam region.

6 Conclusion

Two-dimensional numerical simulations are carried out on graded PPI and graded thermal conductivity metal foam heat exchanger partially filled in the channel using the commercially available FLUENT software. The numerical results show that the pressure drop increases as PPI increases and further it increases with increase in the velocity of the fluid. The pressure drop for the graded PPI metal foams decreases compared to the higher pore density metal foam. The thermal performance of the graded PPI metal foams is similar to that of 40PPI metal foam. The effect of graded thermal conductivity has not shown any significant impact on the performance of

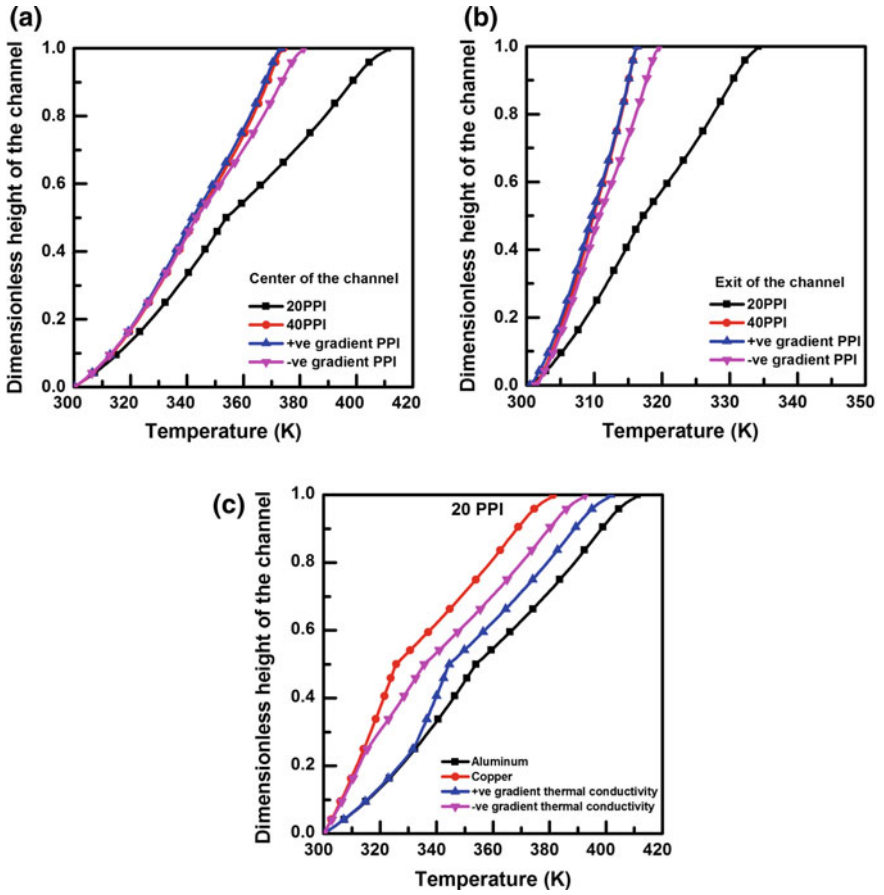

Fig. 5 Temperature variation along the height of the channel **a** at $x = 0.1$ m for all PPI **b** at $x = 0.195$ m for all PPI **c** effect of thermal conductivity gradient at $x = 0.1$ m of the channel

heat transfer. Eventually, it has been found that the graded PPI metal foam shows better performance in terms of pressure drop, friction factor, and thermal performance compared to the nongraded metal foam.

References

1. Mancin, S., Zilio, C., Diani, A., Rossetto, L.: Experimental air heat transfer and pressure drop through copper foams. Exp. Therm. Fluid Sci. **36**, 224–232 (2012)
2. Kim, S.Y., Kang, B.H., Kim, J.H.: Forced convection from aluminium foam materials in an asymmetrically heated channel. Int. J. Heat Mass Transf. **44**, 1451–1454 (2001)

3. Lin, W., Xie, G., Yuan, J., Sunden, B.: Comparison and analysis of heat transfer in aluminum foam using local thermal equilibrium or non-equilibrium model. Heat Transfer Eng. **34**(3–4), 314–322 (2016)
4. Kamath, P.M., Balaji, C., Venkateshan, S.P.: Experimental investigation of flow assisted mixed convection in high porosity foams in vertical channels. Int. J. Heat Mass Transf. **54**, 5231–5241 (2011)
5. Xu, H.J., Qu, Z.G., Lu, T.J., He, Y.L., Tao, W.Q.: Thermal modeling of forced convection in a parallel-plate channel partially filled with metallic foams. ASME J. Heat Transfer **133**, 1–9 (2011)
6. Bernardo, B., Ferraro, G., Manca, O., Marinelli, L., Nardini, S.: Mixed convection in horizontal channels partially filled with aluminium foam heated from below and with external heat losses on upper plate. J. Phys: Conf. Ser. **501**(012005), 1–10 (2014)
7. Sener, M., Yataganbaba, A., Kurtbas, I.: Forchheimer forced convection in a rectangular channel partially filled with aluminum foam. Experimental Thermal and Fluid Sciences **75**, 162–172 (2016)
8. Lu, W., Zhang, T., Yang, M.: Analytical solution of forced convection heat transfer in parallel-plate channel partially filled with metallic foams. Int. J. Heat Mass Transf. **100**, 718–727 (2016)
9. Incropera, F.P., DeWitt, D.P.: Fundamentals of Heat and Mass Transfer. Wiley, New-York (2007)
10. Ackermann, D.: Experimental Investigation of Fouling in Various Coolers. Ph.D. thesis, University of Stuttgart (2012)

Accelerating MCMC Using Model Reduction for the Estimation of Boundary Properties Within Bayesian Framework

N. Gnanasekaran and M. K. Harsha Kumar

Abstract In this work, Artificial Neural Network (ANN) and Approximation Error Model (AEM) are proposed as model reduction methods for the simultaneous estimation of the convective heat transfer coefficient and the heat flux from a mild steel fin subject to natural convection heat transfer. The complete model comprises of a three-dimensional conjugate heat transfer from fin whereas the reduced model is simplified to a pure conduction model. On the other hand, the complete model is then replaced with ANN model that acts as a fast forward model. The modeling error that arises due to reduced model is statistically compensated using Approximation Error Model. The estimation of the unknown parameters is then accomplished using the Bayesian framework with Gaussian prior. The sampling space for both the parameters is successfully explored based on Markov chain Monte Carlo method. In addition, the convergence of the Markov chain is ensured using Metropolis–Hastings algorithm. Simulated measurements are used to demonstrate the proposed concept for proving the robustness; finally, the measured temperatures based on in-house experimental setup are then used in the inverse estimation of the heat flux and the heat transfer coefficient for the purpose of validation.

Keywords ANN · AEM · Reduced model

1 Introduction

Many studies have been proposed to find out the thermophysical properties which are of great importance in engineering calculations. Because of the ill-posedness nature of the inverse problems, regularization of the objective function is required for a stable solution [1]. Many solution techniques for the inverse heat transfer problems have been discussed in [2]. Nowadays, Bayesian statistics is more popular in the field

N. Gnanasekaran (✉) · M. K. Harsha Kumar
Department of Mechanical Engineering, National Institute of Technology Karnataka, Surathkal, Mangaluru 575025, India
e-mail: gnanasekaran@nitk.edu.in

D. Srinivasacharya and K. S. Reddy (eds.), *Numerical Heat Transfer and Fluid Flow*, Lecture Notes in Mechanical Engineering,
https://doi.org/10.1007/978-981-13-1903-7_19

of inverse estimation because of the uncertainty quantification of the parameters. In addition, the kind of regularization provided by the Bayesian framework motivates researcher to work upon the estimation of unknown parameters involved in the mathematical formulation. The Prior Probability Density function in the Bayesian framework regularizes the Posterior Probability Density Function with the assumption that the "a priori" about the unknown parameters are known beforehand [3].

Markov chain Monte Carlo method has been adopted to simultaneously estimate the heat transfer coefficient and the thermal conductivity based on natural convection fin heat transfer experiments [4]. Transient one-dimensional heat conduction from fin was considered to estimate the thermal diffusivity and fin parameter simultaneously for the known measured data [5]. Wang and Zabaras proposed Posterior Probability Density Function for the estimation of boundary heat flux and also computed hierarchal parameters for the estimation of unknown function [6, 7].

Often researchers neglect the modeling error while proposing the model reduction to simplify the actual model which is much more complex to obtain the numerical solution. Subsequently, the solution to the inverse problem using Markov chain Monte Carlo methods is also expensive within the Bayesian framework. Therefore, it is more desirable to have a reduced or approximation model to unveil the complexity of the mathematical model and also to account for the modeling error. Lamien et al. [8] used Approximation error model in the solution of state estimation problem involving the laser heating of a subcutaneous tumor loaded with nanoparticles. To expedite the estimation process, a reduced model is used in the solution of the coupled radiation-bioheat transfer problem which resulted in large reduction of the computational time. Gugercin and Antoulas [9] presented a comparative study based on seven types of reduced model for four different dynamical systems. For the whole frequency range, approximation balanced reduction provided the best results. Arridge et al. [10] in their work showed that the accuracy of the computational model for the forward problem can be relaxed if the approximation error model is used with the optical diffusion tomography. They investigated the interplay between the mesh density and measurement accuracy in the case of optical diffusion tomography and concluded that with the application of approximation error model, it is possible to use mesh densities that would not be possible using conventional methods. Cesar et al. [11] used approximation error model for the simplification of three-dimensional and nonlinear heat conduction problem for the estimation of heat flux applied to the small region of the heat flux with transient temperature measurements measured on the opposite side.

Based on the literature, it has been found that the simultaneous estimation of the boundary properties for a conjugate heat transfer problem has not been adequately dealt with because of the complexity of the forward model and the computational cost involved in computing the inverse solution using MCMC. Therefore, this paper explores the possibilities of model reduction for the mathematical model combined with Bayesian framework in order to expedite the Markov chains for the estimation problem.

2 Mathematical Formulation of the Forward Problem

2.1 Description of the Complete Model

The complete model is a three-dimensional heat transfer from a mild steel fin of dimension 250 × 150 × 6 (all are in mm) exposed to a constant heat flux at the base. The numerical model is created using commercial software ANSYS. The problem is treated as a conjugate heat transfer from fin thereby Navier Stokes equation is incorporated to obtain the information of velocity. Several numerical computations are performed for the known boundary conditions to obtain the temperature distributions of the fin.

2.2 Description of the Reduced Model

The complete model shown in Fig. 1 is time consuming for the solution of the inverse estimation. Hence, the reduced models proposed in this work not only expedite the computational process but also accounts for all the statistical information of the complete model. Hence, two different models have been considered as model reduction in the present work based on the complete model.

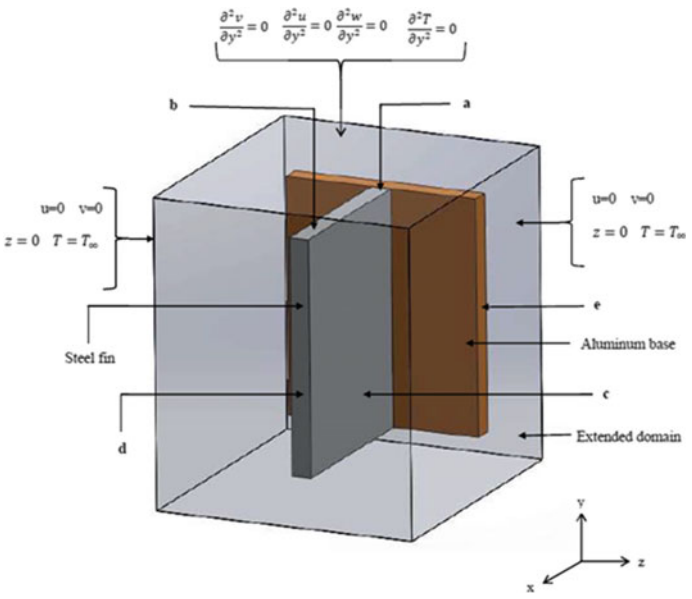

Fig. 1 Numerical model of the fin setup

2.2.1 Artificial Neural Network (ANN) Model

The ANN model is developed based on the complete model. The complete model is solved for a limited range of heat flux and the corresponding temperature distributions of the fin along with the surface heat transfer coefficient are obtained. Now, ANN model is developed based on the limited data set generated using complete model, therefore, a large data set between the input (heat flux and heat transfer coefficient) and the output (temperature distribution) is created based on training the network. This in turn acts as a fast forward model.

2.2.2 Approximation Error Model (AEM)

The complete model, which is based on the three-dimensional conjugate heat transfer, consumes more time for the numerical computations of temperature. Therefore, it is necessary to build up a reduced model which not only reduces the computation time but also includes all necessary statistical parameters. The modeling error is proposed as

$$Y = \Theta_{\mathrm{p}}(P) + e \tag{1}$$

where $\Theta_{\mathrm{p}}(P)$ represents the solution of the forward model. In Eq. (1), "e" represents the uncertainties in the measurement and is also assumed to be normally distributed with zero mean and known covariance matrix W. Hence, in the light of all these facts, the forward model can be written as

$$\pi(Y|P) = (2\pi)^{-\frac{D}{2}}|W|^{-\frac{1}{2}}\exp\left\{-\frac{1}{2}[Y - \Theta_p(P)]^{\mathrm{T}}W^{-1}[Y - \Theta_{\mathrm{p}}(P)]\right\} \tag{2}$$

In Eq. 2, D represents the total number of measurements and the forward solution is obtained from $\Theta_{\mathrm{p}}(P)$. Let the reduced model be given as $\Theta_{\mathrm{p}}^{\mathrm{r}}(P^{\mathrm{r}})$ and introducing the reduced model into Eq. (1), thus the resulting equation becomes

$$Y = \Theta_{\mathrm{p}}^{\mathrm{r}}(P^{\mathrm{r}}) + [\Theta_{\mathrm{p}}(P) - \Theta_{\mathrm{p}}^{r}(P^{\mathrm{r}})] + e \tag{3}$$

The difference between the accurate and reduced models can be given as

$$\varepsilon(P) = \Theta_{\mathrm{p}}(P) - \Theta_{\mathrm{p}}^{\mathrm{r}}(P^{\mathrm{r}}) \tag{4}$$

Equation (3) is rewritten as

$$Y = \Theta_{\mathrm{p}}^{\mathrm{r}}(P^{\mathrm{r}}) + \eta(P) \tag{5}$$

$$\eta(P) = \varepsilon(P) + e \tag{6}$$

The great difficulty associated in Eq. (6) is modeling of the error $\eta(P)$ that accounts for measurement uncertainties and modeling errors. Assuming $\eta(P)$ as normal random variable and the corresponding statistics can be computed from the knowledge of prior distribution. Now, the likelihood function is rewritten in terms of approximation error model

$$\tilde{\pi}(Y|P^{\mathrm{r}}) = (2\pi)^{-\frac{D}{2}}|\widetilde{W}|^{-\frac{1}{2}}\exp\left\{-\frac{1}{2}[Y - \Theta_{\mathrm{p}}^{\mathrm{r}}(P^{\mathrm{r}}) - \bar{\eta}_{\mathrm{p}^{\mathrm{r}}}]^{\mathrm{T}}\widetilde{W}^{-1}[Y - \Theta_{\mathrm{p}}^{\mathrm{r}}(P^{\mathrm{r}}) - \bar{\eta}_{\mathrm{p}^{\mathrm{r}}}]\right\} \tag{7}$$

3 Results and Discussion

The primary importance of the fin set up is to determine the heat flux supplied by the heater at the fin base. To account for the heat loss to the ambient and various other effects, a Gaussian prior with the information provided by the power source voltage (V) and current (I) is incorporated in the Bayesian framework. Subsequently, there is also a scope to estimate the heat transfer coefficient along with the heat flux based on the temperature data; hence the present estimation problem focuses on the simultaneous estimation of heat flux and heat transfer coefficient with the known temperature data.

Table 1 shows the values of the estimated parameters for the experimental temperature. The corresponding Markov chains and histograms are shown in Fig. 2a–d. The burn-in period has been adopted in order to avoid the disturbance of initial guess.

Table 1 Results of estimated parameters for measured temperature data

Standard deviation for the measurements	Parameters	Gaussian priors	Parameters estimated	
			Mean	Standard deviation
$\sigma = 0.02$	Heat flux, q(W/m^2)	$\mu = 500$ $\sigma = 0.02$	501.84	9.68
	Heat transfer coefficient (W/m^2 K)	$\mu = 3.5$ $\sigma = 0.05$	3.79	0.05

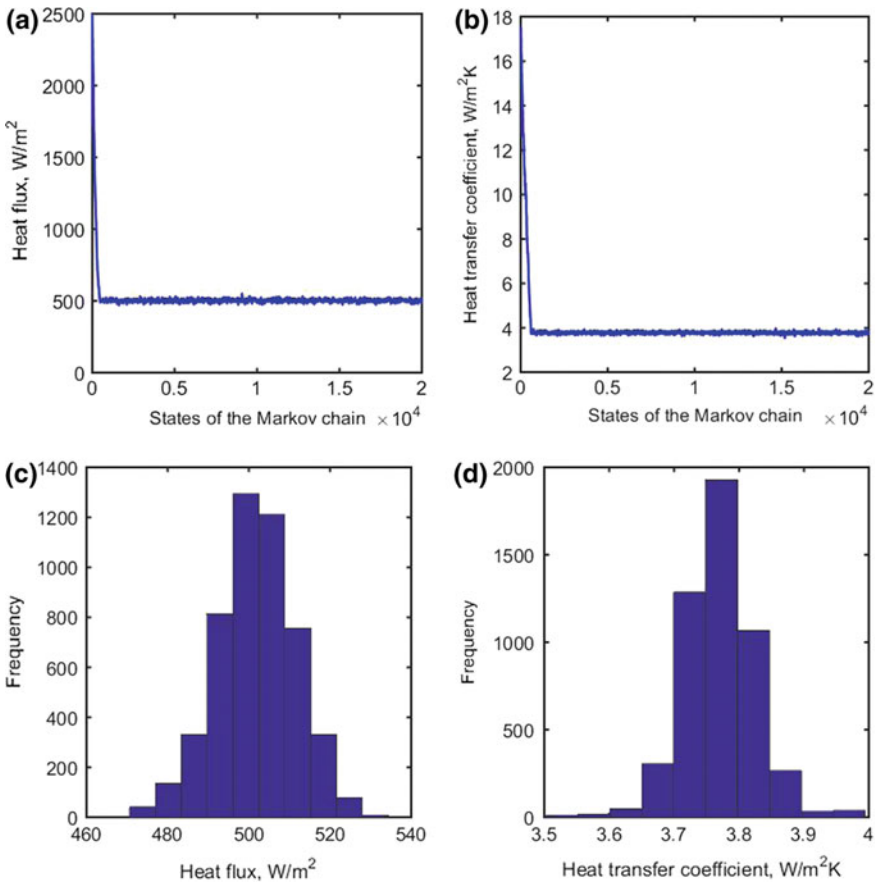

Fig. 2 **a** Markov states for heat flux. **b** Markov states for heat transfer coefficient. **c** Histogram of heat flux. **d** Histogram of heat transfer coefficient

4 Conclusion

An Approximation Error Model has been proposed in order to reduce the computational cost for the inverse estimation of the heat flux and the heat transfer coefficient. To accomplish this, complete and reduced models have been numerically solved using commercial software Ansys. The results obtained based on MCMC with the help of reduced model show good estimates of the unknown for the measured temperature data.

References

1. Beck, J.V., Blackwell, B., Clair, C.S.: Inverse Heat Conduction: Ill-Posed Problems. Wiley, New York (1985)
2. Ozisik, M.N., Orlande, H.R.B.: Inverse Heat Transfer: Fundamentals and Applications. Taylor and Francis, New York (2000)
3. Kaipio, J.P., Fox, C.: The Bayesian framework for inverse problems in heat transfer. Heat Transf. Eng. **32**(9) 718–751 (2011)
4. Gnanasekaran, N., Balaji, C.: A Bayesian approach for the simultaneous estimation of surface heat transfer coefficient and thermal conductivity from steady state experiments on fins. Int. J. Heat Mass Transf. **54**, 3060–3068 (2011)
5. Gnanasekaran, N., Balaji, C.: Markov Chain Monte Carlo (MCMC) approach for the determination of thermal diffusivity using transient fin heat transfer experiments. Int. J. Therm. Sci. **63**, 46–54 (2013)
6. Wang, J., Zabaras, N.: A Bayesian inference approach to the inverse heat conduction problem. Int. J. Heat Mass Transf. **47**, 3927–3941 (2004)
7. Wang, J., Zabaras, N.: Hierarchical Bayesian models in heat conduction. Inverse Prob. **21**(1) (2014)
8. Lamien, B., Orlande, H.R.B., Elicabe, G.E.: J. Heat Transf. 139/012001-1-11 (2017)
9. Gugercin, S., Antoulas, A.C.: A comparative study of 7 algorithms for model reduction. In: Proceedings of the 39th IEEE Conference on Decision and Control. Sydney, Australia, Dec 2000
10. Arridge, S.R., Kaipio, J.P., Kolehmainen, V., Schweiger, M., Somersalo, E., Tarvainen, T., Vauhkonen, M.: Approximation errors and model reduction with an application in optical diffusion tomography. Inverse Prob. **22**, 175–195 (2006)
11. Cesar, C., Orlande, H.R.B., Colaco, M.J., Dulikravich, G.S.: Estimation of a location and time dependent high magnitude heat flux in a heat conduction problem using the Kalman filter and the approximation error model. Numer. Heat Transf. Part A: Appl. **68**(11), 1198–1219 (2015)

Boundary Layer Flow and Heat Transfer of Casson Fluid Over a Porous Linear Stretching Sheet with Variable Wall Temperature and Radiation

G. C. Sankad and Ishwar Maharudrappa

Abstract A flow and heat transfer analysis is carried on non-Newtonian Casson fluid through the thermal boundary layer over previous linear stretching membrane with variable wall temperature and radiation. The governing equations for the present problem are deformed into nonlinear ordinary differential equations with the aid of similarity transformations. A regular perturbation method is applied to determine the solution for the energy equation. The variations of Prandtl number, Casson fluid parameter, suction parameter, and fluid thermal radiation parameter on temperature and velocity profile are discussed through graphs.

Keywords Thermal boundary layer · Stretching sheet · Casson fluid Perturbation method

1 Introduction

The study on boundary layer flow of non-Newtonian fluids is considered to be the most important in the physical science and engineering field due to their vast usage in the manufacturing industries and also, non-Newtonian fluid has more applications as compared to Newtonian fluid in industries such as extraction of petroleum products, polymer extrusion, manufacturing food products and paper production. Crane [1] was the initiator to study the steady boundary layer flows through linear stretching and shrinking surface. Further, he discussed the study on flow of boundary layer through stagnation point and heat conduction past a stretching sheet. Chakrabarti

G. C. Sankad (✉)
Department of Mathematics, VTU, Belagavi, Karnataka, India
e-mail: math.gurunath@bldeacet.ac.in

G. C. Sankad
Department of Mathematics, BLDEA's CET, Vijayapur, Karnataka, India

I. Maharudrappa
Department of Mathematics, Basaveshwar Engineering College, Bagalkot 587102, Karnataka, India

D. Srinivasacharya and K. S. Reddy (eds.), *Numerical Heat Transfer and Fluid Flow*, Lecture Notes in Mechanical Engineering,
https://doi.org/10.1007/978-981-13-1903-7_20

and Gupta [2] explained the flow and heat transfer analysis of electrically conducting incompressible fluid over stretching surface. Also, several researchers [3–8] analyzed boundary layer flow with different non-Newtonian fluids along with various situations by using either analytical or numerical methods.

Since, no attempt has been made to analyze the flow and heat conduction in porous medium with Casson fluid model over linear stretching sheet. So, in this paper, we have made an attempt to study the flow and heat transfer analysis on non-Newtonian Casson fluid through thermal boundary layer over permeable linear stretching membrane with variable wall temperature and radiation. The governing equations are solved by the regular perturbation method by reducing the partial differential equations to ordinary differential equation with similarity transformation.

2 Mathematical Formulation

Let us consider the boundary layer flow of non-Newtonian Casson fluid through porous linear stretching surface along x-axis and the fluid flow is restricted above $y > 0$.

The governing equations are

$$\frac{\partial u}{\partial x} + \frac{\partial v}{\partial y} = 0 \tag{1}$$

$$u\frac{\partial u}{\partial x} + v\frac{\partial u}{\partial y} = \upsilon\left(1 + \frac{1}{\beta}\right)\frac{\partial^2 u}{\partial y^2} - \frac{\upsilon}{k'}u \tag{2}$$

$$u\,\frac{\partial T}{\partial x} + v\frac{\partial T}{\partial y} = \frac{k}{\rho c_{\mathrm{p}}}\frac{\partial^2 T}{\partial y^2} - \frac{1}{\rho c_{\mathrm{p}}}\frac{\partial q_{\mathrm{r}}}{\partial y} \tag{3}$$

where u and v are the components of velocity in the x and y directions, respectively, T is the temperature of the liquid, ρ is the density of the fluid, C_{p} is the specific heat at constant pressure, and q_{r} is the radiative heat flux. The associated boundary conditions [8] are

$$\left.\begin{array}{l} u = bx\ , \quad v = v_c \quad \text{when y} = 0 \\ u \to 0 \quad \text{as} \quad y \to \infty \end{array}\right\}, \tag{4}$$

where $b > 0$ is stretching rate, and v_{c} is the mass suction velocity.

Using following similarity transformations:

$$u = bx\ f\prime(\eta)\,, \quad v = -\sqrt{b\upsilon}\ f(\eta) \,\text{and}\, \eta = \sqrt{\frac{b}{\upsilon}}\quad y, \tag{5}$$

in Eqs. (1) and (2), we obtain

$$\left(1+\frac{1}{\beta}\right)f'''(\eta)-\left[f'(\eta)\right]^2+f(\eta)f''(\eta)-P_{\mathrm{r}}k_1 f\prime[\eta]=0 \tag{6}$$

where $\upsilon=\frac{\mu}{\rho}$, $P_{\mathrm{r}}=\frac{\chi}{k'b}$, $k_1=\frac{\upsilon}{\chi}$.

Corresponding boundary conditions are

$$\left.\begin{aligned} &f(\eta)=-\tfrac{v_{\mathrm{c}}}{\sqrt{b\upsilon}}, \quad f\prime(\eta)=1 \quad \text{at} \quad \eta=0\\ &f'(\eta)\to 0 \quad \text{as} \quad \eta\to\infty. \end{aligned}\right\}, \tag{7}$$

On assuming $f(0)=v_{\mathrm{c}}$ and it is followed that $v_{\mathrm{c}}>0$ is for mass suction and $v_{\mathrm{c}}=0$ is for impervious surface. Solving Eqs. (5) and (6), we get

$$f(\eta)=v_{\mathrm{c}}+\frac{1-\mathrm{e}^{-\alpha\eta}}{\alpha}, \text{ where}\,\alpha=\frac{v_{\mathrm{c}}\pm\sqrt{v_{\mathrm{c}}^2+4\left(\frac{\beta+1}{\beta}\right)(P_{\mathrm{r}}k_1+1)}}{2\left(\frac{\beta+1}{\beta}\right)}. \tag{8}$$

Using Rosseland approximation for the radiative heat flux [6] is given by

$$q_{\mathrm{r}}=-\frac{4\sigma^*}{3k^*}\frac{\partial(T^4)}{\partial y} \text{ and } \frac{\partial q_{\mathrm{r}}}{\partial y}=\frac{-16\,\sigma^* T_\infty^*}{3k^*}\frac{\partial^2 T}{\partial y^2}, \tag{9}$$

where σ^* is the Stefan–Boltzmann constant and k^* is the mean absorption coefficient. On expanding T^4 about T_∞ using Taylor's series and neglecting the higher order terms beyond the first degree in $(T-T_\infty)$ and is approximated as

$$T^4\cong -3T_\infty^4+4T_\infty^3\,T \tag{10}$$

Hence, the energy equation can be rewritten as

$$u\frac{\partial T}{\partial x}+v\frac{\partial T}{\partial y}=\frac{1}{\rho c_{\mathrm{p}}}\frac{\partial}{\partial y}\left\{\left(k+\frac{16\,\sigma^* T_\infty^*}{3k^*}\right)\frac{\partial T}{\partial y}\right\}, \tag{11}$$

the subjected thermal boundary conditions for prescribed power law surface temperature are

$$\left.\begin{aligned} &T=T_{\mathrm{w}}=T_\infty+D\left(\tfrac{x}{l}\right)^2 \quad , \quad \text{at} \quad y=0\\ &T\to\infty \quad \text{as} \quad y\to\infty \end{aligned}\right\}, \tag{12}$$

where D is a constant, l is the characteristic length of the sheet, T_{w} is the wall temperature, and T_∞ is the temperature of the fluid at infinite distance from the membrane. Here, the degree of variable wall temperature is taken as 2.

Introducing nondimensional temperature $\theta(\eta)$ as

$$\theta(\eta) = \frac{T - T_\infty}{T_w - T_\infty}. \tag{13}$$

From Eqs. (11) and (13), we get

$$(1+ \in \theta + T_r)\theta''(\eta) + P_r f(\eta)\,\theta'(\eta) - 2P_r\theta(\eta) f'(\eta) + \in (\theta'(\eta))^2 = 0, \tag{14}$$

where

$$P_r = \frac{\mu C_p}{k_\infty},\ T_r = \frac{16\,\sigma^* T_\infty^4}{3k_\infty k^*}.$$

Using Eq. (13), the boundary conditions reduces to

$$\theta(\eta) = 1 \quad \text{at} \quad \eta = 0, \theta(\eta) \to 0 \quad \text{as} \quad \eta \to \infty. \tag{15}$$

3 Solution of the Problem

Let us assume that the exact solution of Eq. (14) in terms of a small parameter $\in$ be

$$\theta(\eta) = \theta_0(\eta) + \in \theta_1(\eta) + \in^2 \theta_2(\eta) + \in^{\backslash 3} \theta_3(\eta) + \cdots \tag{16}$$

where $\theta_0(\eta),\ \theta_1(\eta),\ \theta_2(\eta)\ , \theta_3(\eta) \ldots$ are to be determined.

Zeroth-order BVP and its solution:

$$(1 + T_r)\,\varepsilon\theta_0'' + \left\{1 + T_r - \frac{P_r v_c}{\alpha} - \frac{P_r}{\alpha^2} - \varepsilon\right\}\theta_0' + 2\theta_0 = 0 \tag{17}$$

The boundary conditions are:

$$\theta_0(\varepsilon) = 1 \quad \text{at} \quad \varepsilon_0 = -\frac{P_r}{\alpha^2} \text{ and } \theta_0(\varepsilon) \to 0 \quad \text{as} \quad \varepsilon_0 \to \infty.$$

Equation (17) can be transformed into confluent hypergeometric equation and its solution is

$$\theta_0(\eta) = C_0\, e^{-\alpha(B/A)\eta} M\left[B + (n-3)A, \quad B + nA, \quad \left(\frac{\varepsilon}{A}\right)\right] - a_1\left(\frac{P_r}{\alpha^2}\right)e^{-\alpha\eta} + a_2\left(\frac{P_r}{\alpha^2}\right)^2 e^{-2\alpha\eta} \tag{18}$$

where M is Kummer's function with its usual notation, $\varepsilon = -\left(\frac{P_r}{\alpha^2}\right)e^{-\alpha\eta}$,

$$A = (1 + T_{\mathrm{r}}),\ B = \frac{P_{\mathrm{r}} v_{\mathrm{c}}}{\alpha} + \frac{P_{\mathrm{r}}}{\alpha^2},\ a_1 = \frac{(B - 2A)}{A(A + B)}$$

$$a_2 = \frac{(B - 2A)(B - A)}{A^2(A + B)(2A + B)(2!)},\ C_0 = \frac{1 + a_1\left(\frac{P_{\mathrm{r}}}{\alpha^2}\right) - a_2\left(\frac{P_{\mathrm{r}}}{\alpha^2}\right)^2}{\mathrm{M}\left[B + (n - 3)A\ ,\quad B + nA\ ,\quad \left(\frac{-P_{\mathrm{r}}}{\alpha^2 A}\right)\right]}$$

First-order BVP and its solution

$$(1 + T_{\mathrm{r}})\,\varepsilon\theta_1'' + \left\{1 + T_{\mathrm{r}} - \frac{P_{\mathrm{r}} v_{\mathrm{c}}}{\alpha} - \frac{P_{\mathrm{r}}}{\alpha^2} - \varepsilon\right\}\theta_1' + 2\theta_1 = -\{\varepsilon\theta_0\theta_0'' + \theta_0\theta_0' + \varepsilon(\theta_0')^2\}, \tag{19}$$

The boundary conditions are

$$\theta_1(\varepsilon) = 1 \quad \text{at} \quad \varepsilon_1 = -\frac{P_{\mathrm{r}}}{\alpha^2},\ \text{and}\ \theta_1(\varepsilon) \to 0 \quad \text{as} \quad \varepsilon_1 \to \infty.$$

The solution of first-order equation for homogeneous part of the equation is given by

$$\theta_{11} = d_0 \mathrm{e}^{-\alpha(B/A)\eta} M\left[B + (n - 3)A\ ,\quad B + nA\ ,\quad \left(\frac{\varepsilon}{A}\right)\right] - a_1\left(\frac{P_{\mathrm{r}}}{\alpha^2}\right)\mathrm{e}^{-\alpha\eta} + a_2\left(\frac{P_{\mathrm{r}}}{\alpha^2}\right)^2 \mathrm{e}^{-2\alpha\eta}, \tag{20}$$

where

$$d_0 = \frac{-\sum d_{\mathrm{r}}(\varepsilon)^{2+\mathrm{r}}}{\mathrm{M}\left[B + (n - 3)A\ ,\quad B + nA\ ,\quad \left(\frac{-P_{\mathrm{r}}}{\alpha^2 A}\right)\right]}$$

The particular integral part of the equation has the solution in the form and is obtained by comparing various powers of ε on both the sides

$$\theta_{12} = \sum d_{\mathrm{r}}\,\varepsilon^{\mathrm{r}+2}$$

Therefore the solution of first order is

$$\theta_1 = \theta_{11} + \theta_{12}$$

The results of the higher solution are neglected due to small values in the magnitude and we seek the final solution for the energy equation in the form

$$\theta(\eta) = \theta_0(\eta) + \in \theta_1(\eta) \tag{21}$$

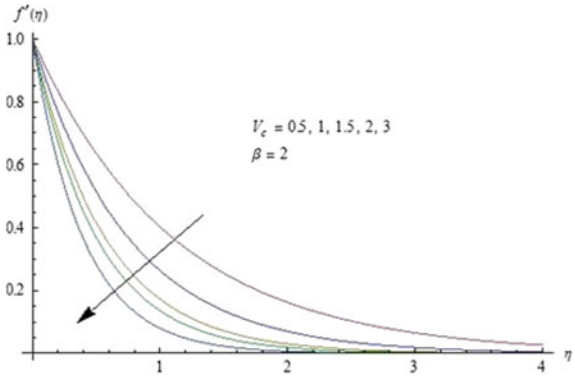

Fig. 1 Velocity profile for different values of suction parameter. Here we have taken $\beta = 2,\ k_1 = 1\ ,\ P_r = 1$

Table 1 **Values of** $-f''(0)$ for distinct values of the parameters

β	P_r	k_1	v_c	2	4	6	8	10
2	1	1		2.0	3.09717	4.3094	5.5726	6.861
	2			2.23014	3.27698	4.44949	5.68513	6.95426
	3			2.4305	3.44152	4.58199	5.79361	7.04518
	4			2.61032	3.59411	4.70801	5.89845	7.13392
		2		2.92744	3.87192	4.94392	6.09854	7.30546
		3		3.33333	4.23927	5.26599	6.37851	7.5497
		4		3.68513	4.56512	5.55903	6.63879	7.78055

4 Result and Discussion

In order to analyze the results of BVPs occurred in the study of boundary layer flow of Casson fluid and heat conduction with variable wall temperature and thermal radiation over stretching membrane has been carried out with the help of regular perturbation method. To visualize the effect of various parameters on the velocity and temperature distribution, graphs are plotted in Figs. 1, 2, 3, 4, 5, 6, and 7. From Figs. 1 and 2, it is observed that velocity of the boundary layer at the wall decreases with the increase in the suction parameter v_c and decreases with the increase in the Casson fluid parameter β for impermeable surface. Figure 3 visualizes the effect of Casson fluid parameter β with the local skin friction coefficient. It is found that skin friction coefficient $f''(0)$ increases with the increase in Casson fluid parameter and mass suction velocity and Prandtl number P_r. The temperature profile with the variations of distinct parameters is shown in Figs. 4, 5, 6 and 7. It is noticed that temperature decreases with increase of mass suction parameter, Casson fluid parameter, Prandtl number, and radiation parameter, respectively. Further, the values of the local skin coefficient and temperature gradient for the different values of pertinent parameters are shown through Tables 1 and 2. The results are found in good agreement with Bhattacharya [8] in absence of Prandtl number.

Table 2 Values of $-\theta'(0)$ for distinct values of the parameters. Here we assumed $\in = 0.1,\ k_1 = 1$

β	P_r	T_r	α	v_c	$-\theta'(0)$	β	P_r	T_r	α	V_c	$-\theta'(0)$
2	3	1	2.25733	2.5	4.40418	2	1	1	2.25733	2.5	1.69161
			2.36401	2.7	4.68432		2				3.03087
			2.52753	3	5.0937		3				4.47455
			3.09717	4	6.4581		4				6.09476
0.5			0.816497	0	1.49854		5				7.84656
1			1		1.36302		2	1			1.69161
1.5			1.09545		0.825758			2			3.03087
2			1.1547		1.39406			3			4.47455

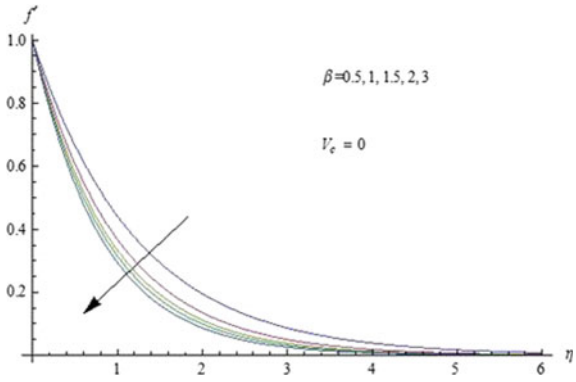

Fig. 2 Velocity profile for different values of Casson fluid parameter, assuming $v_c = 0,\ k_1 = 1\,,\ P_r = 1$

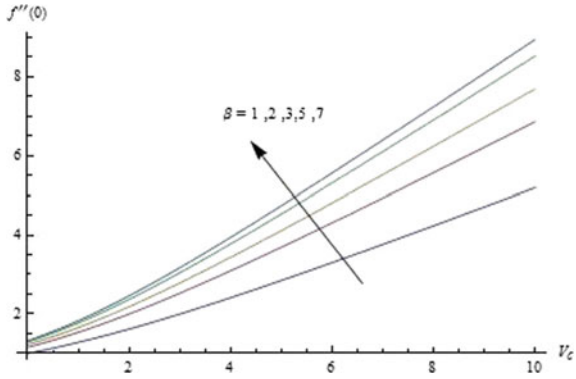

Fig. 3 The effect of Casson fluid and, suction parameter with local skin coefficient

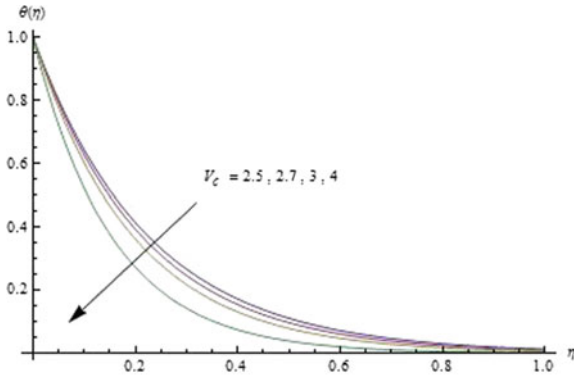

Fig. 4 Temperature profile for different values of suction velocity

5 Conclusion

The flow and heat conduction of Casson fluid over a stretching sheet with wall mass transfer and thermal radiation effects are discussed in the present work. The important outcomes in the present study are the boundary layer thickness decreases with the

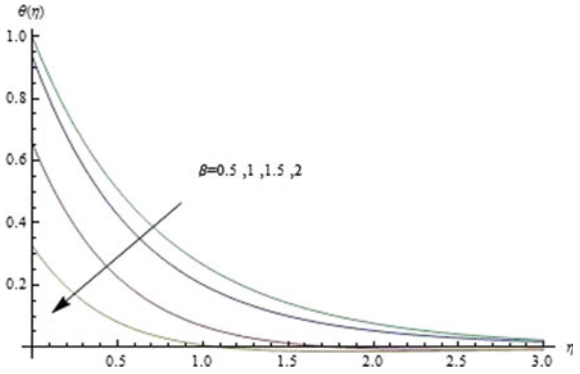

Fig. 5 Temperature profile for different values of Casson fluid parameter

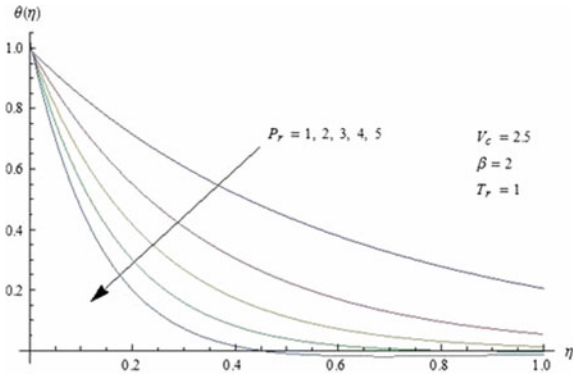

Fig. 6 Effect of Prandtl number on the temperature distribution

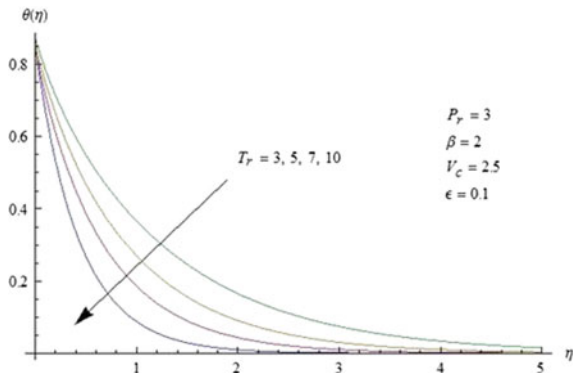

Fig. 7 Effect of thermal radiation parameter on temperature distribution

increase of Casson fluid parameter, Prandtl number, radiation and radiation can be reduced by maintaining the temperature of the system. Variable wall temperature also plays an important role in the temperature distribution and the small values of thermal conductivity ($\in$) must be chosen for the betterment of the cooling effect.

References

1. Crane, L.J.: Flow past a stretching plate. Z. Angrew. Math. Phys. **21**, 645–647 (1970)
2. Chakrabarti, A., Gupta, A.S.: Hydrodynamic flow and heat transfer over a stretching sheet. Q. Appl. Math. **12**, 73–78 (1979)
3. Anderson, H.I., Aarseth, J.B., Dandapat, B.S.: Heat transfer in a liquid film on an unsteady stretching surface. Int. J. Heat Mass Transf. **43**, 69–74 (2000)
4. Liu, I.-C.: Flow and heat transfer of viscous fluids saturated in porous media over a permeable non-isothermal stretching sheet. Transport Porous Media **64**, 375–392 (2006)
5. Pantokratoras, A.: Low adjacent to a stretching permeable sheet in a Darcy-Brinkman porous medium. Transp. Porous Media **80**, 223–227 (2009)
6. Pahlavan, A.A., Aliakbar, V., Farahani, F., Sadeghy, K.: MHD flows of UCM fluids above porous stretching sheets using two-auxiliary-parameter homotopy analysis method. Commun. Nonlinear Sci. Numer. Simul. **14**, 473–488 (2009)
7. Pramanik, S.: Casson fluid flow and heat transfer past an exponentially porous stretching surface in presence of thermal radiation. Ain Shams Eng. J. **5**, 205–212 (2014)
8. Bhattacharya, K., Uddin, M.S., Layek, G.C.: Exact solution for thermal boundary layer in Casson fluid over permeable shrinking sheet with variable wall temperature and thermal radiation. Alexandria Eng. J. **55**, 1703–1712 (2016)

Isogeometric Boundary Element Method for Analysis and Design Optimization—A Survey

Vinay K. Ummidivarapu and Hari K. Voruganti

Abstract Analysis of potential problems related to fluid flow and heat transfer can be solved effectively with Boundary Element Methods (BEMs) due to the reason that the interaction takes place at boundaries. BEMs too suffer the traditional problem of approximated geometry. A recent method called Isogeometric Analysis (IGA) was proposed for exact geometric analysis. The combination of the IGA and BEM leads to Isogeometric Boundary Element Method (IGBEM), which has the feature of exact boundary analysis. It suits well for the problems where boundaries of the domains are of interest like fluid structure interaction, shape optimization, etc. This paper provides a brief review on IGBEM by clearly explaining its methodology, applications, limitations and future directions.

Keywords IGA · BEM · Meshless · Shape optimization and potential flows

1 Introduction

As of today, there is a high need for integration of CAD and analysis modules. Many industries like aerospace, automotive, and others are focused on this. The recent research in the fields of design optimization, fluid structure interaction, and similar analysis problems observed the need for a unified framework of both analysis and geometric modeling. Among the available analysis tools, Computational Fluid Dynamics (CFD) and Finite Element Method (FEM) are the most widely used methods. They involve approximation of geometry and discretization of the domain which is computationally expensive [1]. BEM is an alternative method to FEM, in which only the boundary of the domain is considered, thus making it a perfect choice for the boundary interaction problems. BEM reduces the dimension of the problem by one. The only similarity between FEM and BEM are their basis functions. Both use the

V. K. Ummidivarapu · H. K. Voruganti (✉)
National Institute of Technology Warangal, Warangal 506004, Telangana, India
e-mail: harikumar@nitw.ac.in

D. Srinivasacharya and K. S. Reddy (eds.), *Numerical Heat Transfer and Fluid Flow*, Lecture Notes in Mechanical Engineering,
https://doi.org/10.1007/978-981-13-1903-7_21

same piecewise polynomial basis functions, thus making BEM also an approximated geometry based tool [2].

Isogeometric Analysis (IGA) is a recently developed tool as an alternative to FEM. Its advantages like use of splines and exact geometry representation made it attractive for the research community [3, 4]. It has integrated the geometric modeling with the analysis, hence removing the burden of meshing. Like FEM it is also a domain analysis tool. The combination of IGA and BEM is IGBEM method. It was proposed in 2009 and has become an emerging numerical tool. It inherits the advantages of both the IGA and BEM, making it an apt method for the problems of fluid structure interaction and shape optimization [2, 5]. The features like, no domain analysis, exact boundary representation, no meshing, and remeshing of the physical problem make IGBEM an effective choice among the available tools. But there are few limitations of IGBEM, confining the applicability of the method to certain problems. The theme of this paper is to explore these points, thus providing a brief survey on IGBEM.

The methodology of the IGBEM is explained in three parts: Fundamental solutions, Discretization, and Numerical integration.

2 Fundamental Solutions

The fundamental solutions form the basis of the BEM. In this context, these solutions are also called as kernels. Depending on the physics of the problem, the corresponding set of governing equations are considered, for example, Laplace's or Poisson's equation for potential problems, equilibrium equations of stresses for structural problems, etc. These equations are generally differential equations of field variables. Fundamental solutions are the complimentary functions of these differential equations [2]. In order to get actual solution to a particular problem, boundary conditions should be applied along with the dimensionality theorem to convert the domain problem into a boundary problem. For example, Greens second identity for the potential problems, Betti's reciprocal work theorem in the case of structural problems, etc. are used to convert a domain problem to a boundary problem. The displacement boundary integral equation for elastostatics is shown in Eq. (1).

$$C_{ij} * u_i(x') + \oint_{\Gamma} T_{ij}(x', x) * u_j(x) * d\Gamma(x) = \oint_{\Gamma} U_{ij}(x', x) * t_j(x) * d\Gamma(x) \tag{1}$$

where U_{ij} and T_{ij} are called fundamental solutions, C_{ij} is the jump term, Γ is the boundary and u_i, u_j and t_j are the corresponding displacement and traction field variables.

These fundamental solutions are well established only for some category of problems which is one of the drawbacks of BEM. And also, these fundamental solutions are of singular nature, i.e., discontinuous over the boundary. This is the main short-

coming of BEM during integration which will be dealt in the following sections. The fundamental solutions of various physical systems can be found in [6, 7].

2.1 Discretization

Using fundamental solutions along with the related theorems, the respective boundary integral equation is formed. In order to solve any problem numerically, the geometry of the problem should be discretized into elements using some CAD models. The traditional BEM employs the piecewise polynomials to discretize both the geometry and field variables. It is simple to apply, but is not efficient due to approximated boundary. To correct this, adaptive refinement is required, which of course is a tedious task [2]. In IGBEM, NURBS are used as the basis functions for representing both geometry and field variable variation. Here, the control points play the role of nodal points in the traditional BEM. NURBS is the most reliable CAD technique to generate any complex geometry exactly. These basis functions have advantages like local control, higher order continuity, etc. More details on NURBS can be found in [8, 9]. Figure 1 shows all the three parameterizations namely IGBEM, FEM, and IGBEM. Recently, T-splines which require much lesser control points to represent an equivalent NURBS curve or a surface are applied to IGBEM and shown much better results [5].

2.2 Numerical Integration of Kernels

As stated earlier, the kernels in the boundary integral equations are of singular type [11, 12]. They are not continuous over the entire boundary. When the field point (integration point) is coinciding with the source or load point (collocation point), the kernels are said to be strongly singular. Due to this, the renowned Gaussian-Legendre numerical integration is not suited for BEM. Several alternative methods were proposed to overcome this difficulty. Out of those, two robust and reliable methods are Subtraction of Singularity Technique (SST) and Tellas Transformation

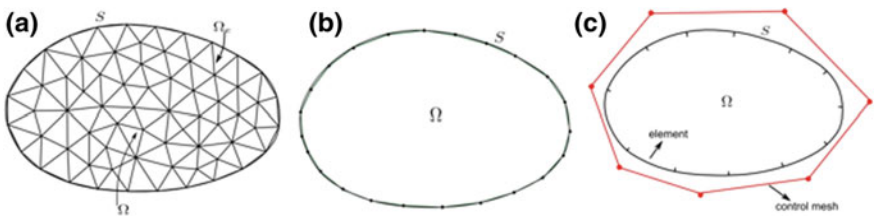

Fig. 1 **a** FEM, **b** BEM and **c** IGBEM discretization's [10]

Method (TTM). In the former, the singularity and non-singularity terms are separated and integrated. In the TTM technique, the integrand is converted to a continuous function using a transformation series. Among both, SST is more effective.

3 Applications

IGBEM has been applied to various applications. The trend in the applicability by researchers is shown in Fig. 2a. The major applications include fluid flow and shape optimization which are the most effective boundary based problems. The IGBEM features are shown in Fig. 2b.

Fluid flow: Fluid flow problems interact with the surroundings only at the boundary of the domain. The first work of IGBEM on fluid flow problem was carried out by [13]. It is also the first ever publication on IGBEM. Convergence tests on some problems were carried out to validate the method. Isogeometric boundary element analysis of steady incompressible viscous flow was performed by [14]. The work is on 2-D problems. The results of the simulation agree very well with the results available in the literature. Gong et al. [15] formulated IGBEM for solving 3-D potential problems. Few fluid flow problems of complex geometries were solved using IGBEM and compared with the available results.

Shape optimization: It is the process of obtaining the best shape while satisfying the given conditions. Change of shape involves only the boundary variation. The entire domain need not to be considered thus making shape optimization another best application for IGBEM. The primary work of shape optimization using IGBEM was presented by Li and Qian [16]. This work finds that the boundary integral based isogeometric analysis and optimization have many advantages like bypassing the need for domain parameterization and tight integration of CAD and analysis. Lian et al. [17] performed the sensitivity analysis for structural shape optimization. Kostas et al. [18] performed Ship-hull shape optimization using T-splines for geometric modeling. This work marks as a finest application of IGBEM.

Some of the other applications include Elastostatics, Crack growth etc. 2-D and 3-D structural problems were solved using IGBEM [2, 19]. The structural problems

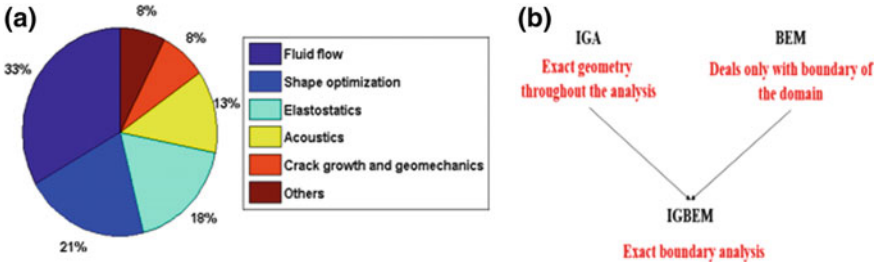

Fig. 2 **a** The trend in the applicability of IGBEM. **b** Features of IGBEM

were explored both with NURBS and T-splines. The elasto-plastic problems were dealt in [20, 21]. When cracks evolve, only the boundary surfaces are needed to be updated. IGBEM was also extended to solve crack growth problems [22, 23].

4 Research Groups and Other Information

Some of the active research groups of IGBEM are at University of Glasgow, Scotland, University of Luxembourg, Luxembourg, Nazarbayev University, Kazakhstan, Technological Educational Institute of Athens, Greece, Graz University of Technology, Austria, etc. There are some open source MATLAB codes for IGBEM available at [24].

5 Conclusions and Future Directions

The above brief literature review showed that the IGBEM has been applied to various problems even though it was proposed very recently. The reason is that the accuracy of the results produced by IGBEM is observed to be better than the existing results due to the exact geometry representation. The computational efficiency is increased as a result of meshless approach. Postprocessing does not take much efforts as the entire domain need not be considered. 3-Dimensional problems are also analysed in few applications. The IGBEM method could be much more improved to provide better results. In future, IGBEM could be used for real world design problems. A commercial package of IGBEM can accelerate the research and applicability of the method to boundary-based problems.

References

1. Hughes, T.J., Cottrell, J.A., Bazilevs, Y.: Isogeometric analysis: CAD, finite elements, NURBS, exact geometry and mesh refinement. Comput. Methods Appl. Mech. Eng. **194**(39–41), 4135–4195 (2005). https://doi.org/10.1016/j.cma.2004.10.008
2. Simpson, R.N., Bordas, S.P., Trevelyan, J., Rabczuk, T.: A two-dimensional isogeometric boundary element method for elastostatic analysis. Comput. Methods Appl. Mech. Eng. **209**, 87–100 (2012). https://doi.org/10.1016/j.cma.2011.08.008
3. Gondegaon, S., Voruganti, H.K.: Static structural and modal analysis using Isogeometric analysis. JTAM **46**(4), 36–75 (2016). https://doi.org/10.1515/jtam-2016-0020
4. Ummidivarapu, V.K., Voruganti, H.K.: Shape optimisation of two-dimensional structures using isogeometric analysis. IJESMS **9**(3), 169–176 (2017). https://doi.org/10.1504/IJESMS.2017.085080
5. Scott, M.A., Simpson, R.N., Evans, J.A., Lipton, S., Bordas, S.P., Hughes, T.J., Sederberg, T.W.: Isogeometric boundary element analysis using unstructured T-splines. Comput. Methods Appl. Mech. Eng. **254**, 197–221 (2013). https://doi.org/10.1016/j.cma.2012.11.001

6. Becker, A.A.: The Boundary Element Method in Engineering: A Complete Course. McGraw-Hill, London (1992)
7. Banerjee, P.K., Butterfield, R.: Boundary Element Methods in Engineering Science. McGraw-Hill, New York (1981)
8. Gondegaon, S., Voruganti, H.K.: Spline parameterization of complex planar domains for isogeometric analysis. JTAM **47**(1), 18–35 (2017). https://doi.org/10.1515/jtam-2017-0002
9. Rogers, D.F.: An Introduction to NURBS: With Historical Perspective. Academeic Press, Elsevier, Oxford (2000)
10. Lian, H., Kerfriden, P., Bordas, S.: Implementation of regularized isogeometric boundary element methods for gradient-based shape optimization in two-dimensional linear elasticity. Int. J. Numer. Meth. Eng **106**(12), 972–1017 (2016). https://doi.org/10.1002/nme.5149
11. Telles, J.C.F.: A self-adaptive co-ordinate transformation for efficient numerical evaluation of general boundary element integrals. Int. J. Numer. Meth. Eng. **24**(5), 959–973 (1987). https://doi.org/10.1002/nme.1620240509
12. Guiggiani, M., Casalini, P.: Direct computation of Cauchy principal value integrals in advanced boundary elements. Int. J. Numer. Meth. Eng. **24**(9), 1711–1720 (1987). https://doi.org/10.1002/nme.1620240908
13. Politis, C., Ginnis, A. I., Kaklis, P. D., Belibassakis, K., Feurer, C.: An isogeometric BEM for exterior potential-flow problems in the plane. In: SIAM/ACM Joint Conference on Geometric and Physical Modeling, pp. 349-354. ACM (2009). https://doi.org/10.1145/1629255.1629302
14. Beer, G., Mallardo, V., Ruocco, E., Dnser, C.: Isogeometric boundary element analysis of steady incompressible viscous flow, Part 1: plane problems. Comput. Methods in Appl. Mech. Eng. **326**, 51–69 (2017). https://doi.org/10.1016/j.cma.2017.08.005
15. Gong, Y.P., Dong, C.Y., Qin, X.C.: An isogeometric boundary element method for three dimensional potential problems. J. Comput. Appl. Math. **313**, 454–468 (2017). https://doi.org/10.1016/j.cam.2016.10.003
16. Li, K., Qian, X.: Isogeometric analysis and shape optimization via boundary integral. Comput.-Aided Des. **43**(11), 1427–1437 (2011). https://doi.org/10.1016/j.cad.2011.08.031
17. Lian, H., Kerfriden, P., Bordas, S.P.A.: Shape optimization directly from CAD: an isogeometric boundary element approach using T-splines. Comput. Methods Appl. Mech. Eng. **317**, 1–41 (2017). https://doi.org/10.1016/j.cma.2016.11.012
18. Kostas, K.V., Ginnis, A.I., Politis, C.G., Kaklis, P.D.: Ship-hull shape optimization with a T-spline based BEM isogeometric solver. Comput. Methods Appl. Mech. Eng. **284**, 611–622 (2015). https://doi.org/10.1016/j.cma.2014.10.030
19. Gu, J., Zhang, J., Sheng, X., Li, G.: B-spline approximation in boundary face method for three-dimensional linear elasticity. Eng. Anal. Bound. Elem. **35**(11), 1159–1167 (2011). https://doi.org/10.1016/j.enganabound.2011.05.013
20. Bai, Y., Dong, C.Y., Liu, Z.Y.: Effective elastic properties and stress states of doubly periodic array of inclusions with complex shapes by isogeometric boundary element method. Compos. Struct. **128**, 54–69 (2015). https://doi.org/10.1016/j.compstruct.2015.03.061
21. Beer, G., Marussig, B., Zechner, J., Dnser, C., Fries, T.P.: Isogeometric boundary element analysis with elasto-plastic inclusions. Part 1: plane problems. Comput. Methods Appl. Mech. Eng. **308**, 552–570 (2016). https://doi.org/10.1016/j.cma.2016.03.035
22. Peng, X., Atroshchenko, E., Kerfriden, P., Bordas, S.P.A.: Isogeometric boundary element methods for three dimensional static fracture and fatigue crack growth. Comput. Methods Appl. Mech. Eng. **316**, 151–185 (2017). https://doi.org/10.1016/j.cma.2016.05.038
23. Nguyen, B.H., Tran, H.D., Anitescu, C., Zhuang, X., Rabczuk, T.: An isogeometric symmetric Galerkin boundary element method for two-dimensional crack problems. Comput. Methods Appl. Mech. Eng. **306**, 252–275 (2016). https://doi.org/10.1016/j.cma.2016.04.002
24. https://sourceforge.net/projects/igabem/

Unsteady Boundary Layer Flow of Magneto-Hydrodynamic Couple Stress Fluid over a Vertical Plate with Chemical Reaction

Hussain Basha and G. Janardhana Reddy

Abstract The unsteady two-dimensional natural convective magneto-hydrodynamic non-Newtonian couple stress fluid flow over a vertical plate with homogenous first-order chemical reaction effect is addressed in this article. The thermodynamic study is executed in the presence of momentum, heat and mass transfer coefficients with chemical reaction. The highly nonlinear, coupled, time-dependent non-Newtonian fluid flow equations are simplified by using numerically stable Crank–Nicolson iteration method. For various flow parameter values, graphs are drawn and analysed. A related thermodynamic study with available numerical results is made.

Keywords Couple stress fluid · Magnetic field · Vertical plate

1 Introduction

In the modern days, the natural convection fluid flow with magneto-hydrodynamic, chemical reaction effects appealed the curiosity of many scientists and engineers. Due to the density differences in the fluid, the buoyancy forces will occur, and that causes the free convection fluid flow. This type of flows have important uses in various industrial applications such as nuclear reactors, solar collectors, producing electrical power, ignition systems, and counting the parching vaporisation at the exterior surface area of an aquatic body, energy transference in a showery refrigeration tower, solidification of twofold alloys, flow in a desert cool box, processing of food, in crystal growth, copses of fruit trees, dehydrating and drying up setups in food and chemical processing plants, and ignition of atomized liquefied fuels, crops injury because of freezing, etc. Many of the experimental diffusion processes show the species diffusion at molecular level with chemical reaction phenomena across the

H. Basha · G. Janardhana Reddy (✉)
Department of Mathematics, Central University of Karnataka,
Kalaburagi, Karnataka 585367, India
e-mail: gjr@cuk.ac.in

D. Srinivasacharya and K. S. Reddy (eds.), *Numerical Heat Transfer and Fluid Flow*, Lecture Notes in Mechanical Engineering,
https://doi.org/10.1007/978-981-13-1903-7_22

boundary layer. Having these uses and applications in mind, the present manuscript made an effort to analyse the chemically reacting free convective couple stress fluid flow past a vertical plate with MHD effects. More information can be found in Cussler [1]. For the first time, Ostrach [2] presented that for the determination of flow nature, the Grashof number is the dominant factor and for the big Grashof numbers, the flow is of boundary layer type. The theoretic improvement was made to deliberate the events of high Grashof number directly for the reason that, these are having the greatest importance in the field of aeronautics and engineering applications. Recently, many of the researchers [3–7] studied the special impacts of chemical reaction on heat and mass transfer with various circumstances in the boundary layer flow of couple stress fluid. The phenomena of transient free convective heat and mass transfer over a vertical plate, using finite difference method were studied by Soundalgekar and Ganesan [8]. Also, they showed that the species absorption with very small Schmidt number takes more time to reach the time-independent state as compared to high Schmidt number. More details about the couple stress fluid can be found in the available literature [9–12]. In the present manuscript, the species concentration dispersion in the flow region is investigated for various couple stress fluid parameter values. The time-dependent dimensionless governing equations of the motion are simplified numerically by employing Thomas as well as pentadiagonal algorithms [13]. For the different physical variable values, the thermodynamic behaviour of time-dependent and steady-state flow profiles are analysed in depth with physical interpretation.

2 Mathematical Statement of the Problem

The flow of two-dimensional, time-dependent, free convective, non-Newtonian MHD couple stress fluid over a vertical plate with homogenous first-order chemical reaction is discussed. Along the axial direction of the plate, x-coordinate is aligned in upward direction and y-axis is considered perpendicular to the plate. Since the magnitude of velocity in dominant flow region is negligible. Therefore, the influence of dissipation due to viscosity is omitted from the thermal equation. By considering the Boussinesq's approximation with the above assumptions, the flow of magnetohydrodynamic laminar viscous incompressible couple stress fluid with the thermal equation is given by the following nondimensional equations [3, 8, 9]:

$$\frac{\partial U}{\partial X} + \frac{\partial V}{\partial Y} = 0 \tag{1}$$

$$\frac{\partial U}{\partial t} + U\frac{\partial U}{\partial X} + V\frac{\partial U}{\partial Y} = \theta + \mathrm{BuC} + \frac{\partial^2 U}{\partial Y^2} - \mathrm{Co}\frac{\partial^4 U}{\partial Y^4} - MU \tag{2}$$

$$\frac{\partial \theta}{\partial t} + U\frac{\partial \theta}{\partial X} + V\frac{\partial \theta}{\partial Y} = \frac{1}{\mathrm{Pr}}\left(\frac{\partial^2 \theta}{\partial Y^2}\right) \tag{3}$$

$$\frac{\partial C}{\partial t} + U\frac{\partial C}{\partial X} + V\frac{\partial C}{\partial Y} = \frac{1}{\mathrm{Sc}}\left(\frac{\partial^2 C}{\partial Y^2}\right) - KC \tag{4}$$

The corresponding nondimensional boundary and initial conditions are given by

$$\left.\begin{array}{c} t \le 0 : \theta = 0, \quad C = 0, \quad U = 0, \quad V = 0 \quad \forall\, X \text{ and } Y \\ t > 0 : \theta = 1, \quad C = 1, \quad U = 0, \quad V = 0 \quad \text{at } Y = 0 \\ \theta = 0, \quad C = 0, \quad U = 0, \quad V = 0 \quad \text{at } X = 0 \\ \theta \to 0, \quad C \to 0, \quad U \to 0, \quad V \to 0 \quad \text{as } Y \to \infty \\ \frac{\partial U}{\partial Y} = \frac{1}{\mathrm{Gr}_T^2}\frac{\partial V}{\partial X} \quad \text{at} \quad Y = 0 \quad \text{and} \quad Y \to \infty \end{array}\right\} \tag{5}$$

The equivalent nondimensional numbers are given as follows:

$$\left.\begin{array}{c} X = \mathrm{Gr}_T^{-1}\frac{x}{L}, \quad Y = \frac{y}{L}, \quad U = \mathrm{Gr}_T^{-1}\frac{uL}{\vartheta}, \quad \mathrm{Co} = \frac{\eta}{\mu L^2} V = \frac{vL}{\vartheta}, \quad t = \frac{\vartheta t'}{L^2} \\ \theta = \frac{T'-T'_\infty}{T'_w - T'_\infty}, C = \frac{C'-C'_\infty}{C'_w - C'_\infty}, \quad M = \frac{\sigma \mathrm{Bo}^2 L^2}{\rho\vartheta}, \quad \mathrm{Sc} = \frac{\vartheta}{D}, \quad K = \frac{k_1 L^2}{\vartheta}, \mathrm{Bu} = \frac{\mathrm{Gr}_c}{\mathrm{Gr}_T} \\ \mathrm{Gr}_T = \frac{g\beta_T L^3 (T'_w - T'_\infty)}{\vartheta^2}, \quad \mathrm{Gr}_C = \frac{g\beta_C L^3 (C'_w - C'_\infty)}{\vartheta^2} \end{array}\right\} \tag{6}$$

It is important to evaluate momentum transport coefficient ($\overline{C}_f$), heat transport coefficient ($\overline{\mathrm{Nu}}$) and mass transport coefficient ($\overline{\mathrm{Sh}}$) because of their large number of industrial and engineering advantages. Thus, the dimensionless $\overline{C}_f$, $\overline{\mathrm{Nu}}$ and $\overline{\mathrm{Sh}}$ are defined as follows:

$$\overline{C}_f = \int_0^1 \left(\frac{\partial U}{\partial Y}\right)_{Y=0} \mathrm{d}X \tag{7}$$

$$\overline{\mathrm{Nu}} = -\int_0^1 \left(\frac{\partial T}{\partial Y}\right)_{Y=0} \mathrm{d}X \tag{8}$$

$$\overline{\mathrm{Sh}} = -\int_0^1 \left(\frac{\partial C}{\partial Y}\right)_{Y=0} \mathrm{d}X \tag{9}$$

where U, V, θ and C are the dimensionless velocity, temperature and concentration, respectively. Co is the couple stress fluid parameter, M is the magnetic number, Bu is the buoyancy variable, Prandtl number is denoted by Pr, Sc is the Schmidt number and K is the chemical reaction parameter and Gr is the Grashof number.

3 Solution Methodology

The governing unsteady Eqs. (1)–(4) along with the appropriate conditions Eq. (5) are highly nonlinear and coupled. Since there are no standard analytical techniques available to solve these flow equations, an unconditionally stable fast converging compatible implicit iterative method is applied, which is described in the reference [3]. The region of integration with $X_{\min} = 0$, $X_{\max} = 1$, $Y_{\min} = 0$ and $Y_{\max}(= \infty) = 20$ is considered with $Y_{\max}$ far from the boundary layers. It is observed that 100×500 grid compared with 50×250 and 200×1000 do not have considerable impact on the solutions of time-independent state flow variables. Therefore, with this remark, a uniform 100×500 grid size is chosen for the present analysis with the grid dimensions of 0.01 and 0.04, along x and y coordinates. Also, time step size Δt ($t = n\Delta t, n = 0, 1, 2, \ldots$) is fixed as 0.01.

4 Discussion of Numerical Results

To confirm the accuracy of current numerical method, the computer-generated numerical data is presented in terms of U, θ and C graphs and these profiles are compared with those of Soundalgekar and Ganesan [8] for $Pr = 0.73, Sc = 0.78, \mathrm{Bu} = 2.0, K = 0, \mathrm{Co} = 0, M = 0$. The present numerical results agree well with earlier results [8]. Figure 1a illustrates that, initially, the unsteady velocity profile upsurges with time (t) and reaches the maximum value, thereafter it decreases and over again slightly upsurges, later attains the time-independent state. Also, it is remarked that the transient behaviour of temperature profile at the other locations is almost same. From Fig. 1a, b, as Co increases the time-dependent and steady-state velocity decreases but the steady-state time increases. Also, the magnitude of the transient velocity overshoots decreases as Co increases. Figure 2a illustrates that initially all the temperature curves coincide with one another which indicates that at the starting time, conduction is dominant over the convection. From Fig. 2a, b, the unsteady and time-independent state temperature upsurges as Co rises. The steady-state time upsurges for the increasing Co values. Figure 3 indicates that the time-dependent and time-independent concentration increases as Co increases also the magnitude of the time-dependent concentration overshoots increases. The steady-state time upsurges as Co increases.

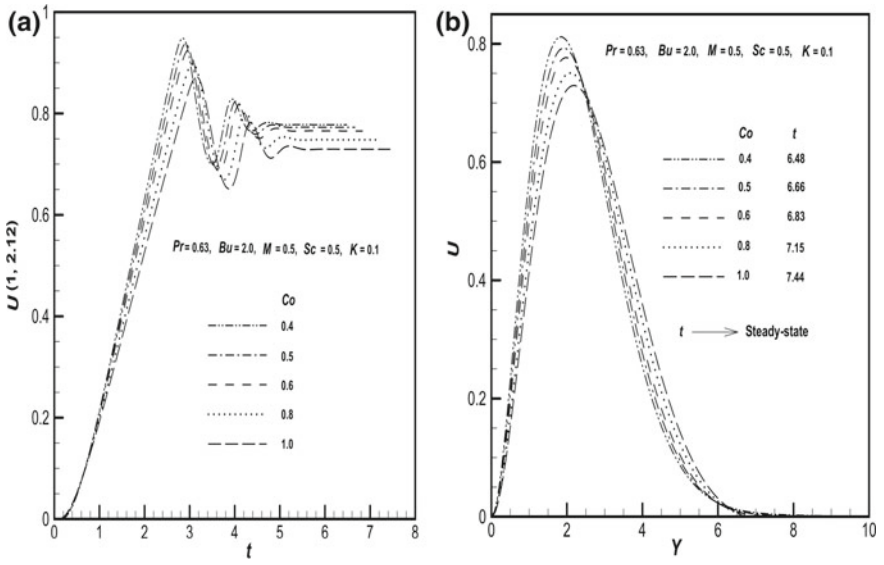

Fig. 1 **a** Unsteady U profile at (1, 2.12), **b** time-independent state profile at $X = 1.0$

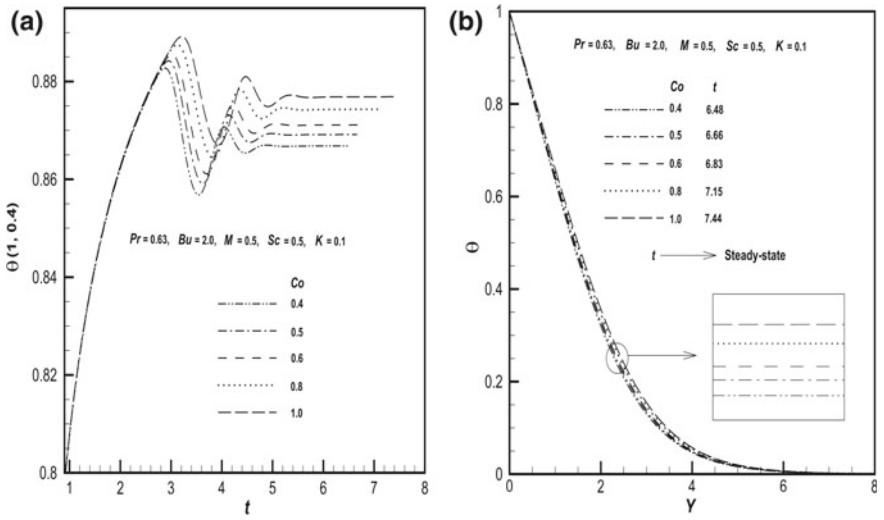

Fig. 2 **a** Unsteady temperature profile at (1, 0.4), **b** time-independent state profile at $X = 1.0$

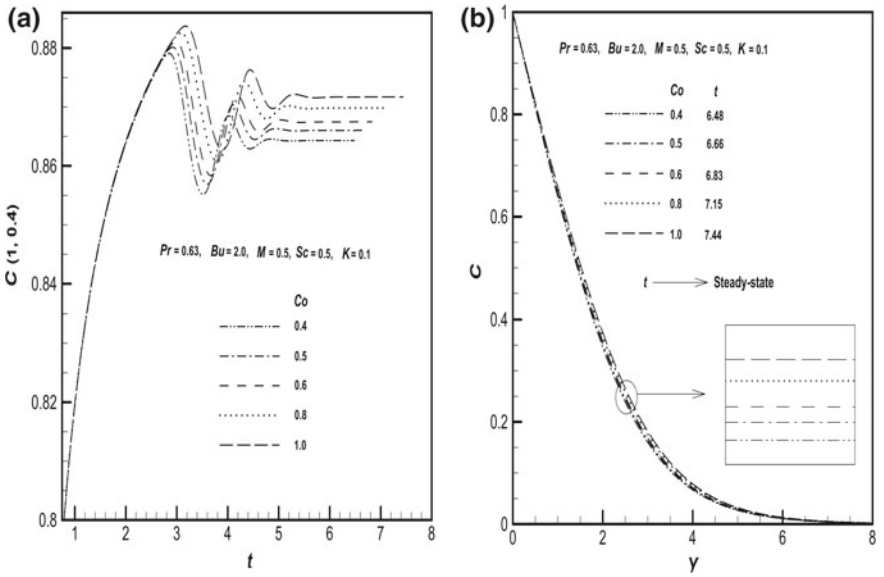

Fig. 3 **a** Unsteady concentration profile at (1, 0.4), **b** time-independent state profile at $X = 1.0$

At the beginning time, it is observed from Fig. 4a that, for all the Co values, the average wall shear stress upsurges with respect to t, reaches the highest value, decreases and later attains the asymptotic time-independent state. Figure 4a demonstrates that the $\overline{C_f}$ profiles decrease as Co increases also the steady-state time increases. Figure 4b illustrates that, during the early time intervals, each curve in the $\overline{\text{Nu}}$ profile coincides with one another and they deviate after some time. This observation clears that, in the beginning time, conduction process takes place and it dominates the convection heat transfer phenomena. The average $\overline{\text{Nu}}$ decreases as Co increases. From Fig. 4c it is remarked that the average $\overline{\text{Sh}}$ decreases as Co magnifies. Further, steady-state time upsurges for rising Co values.

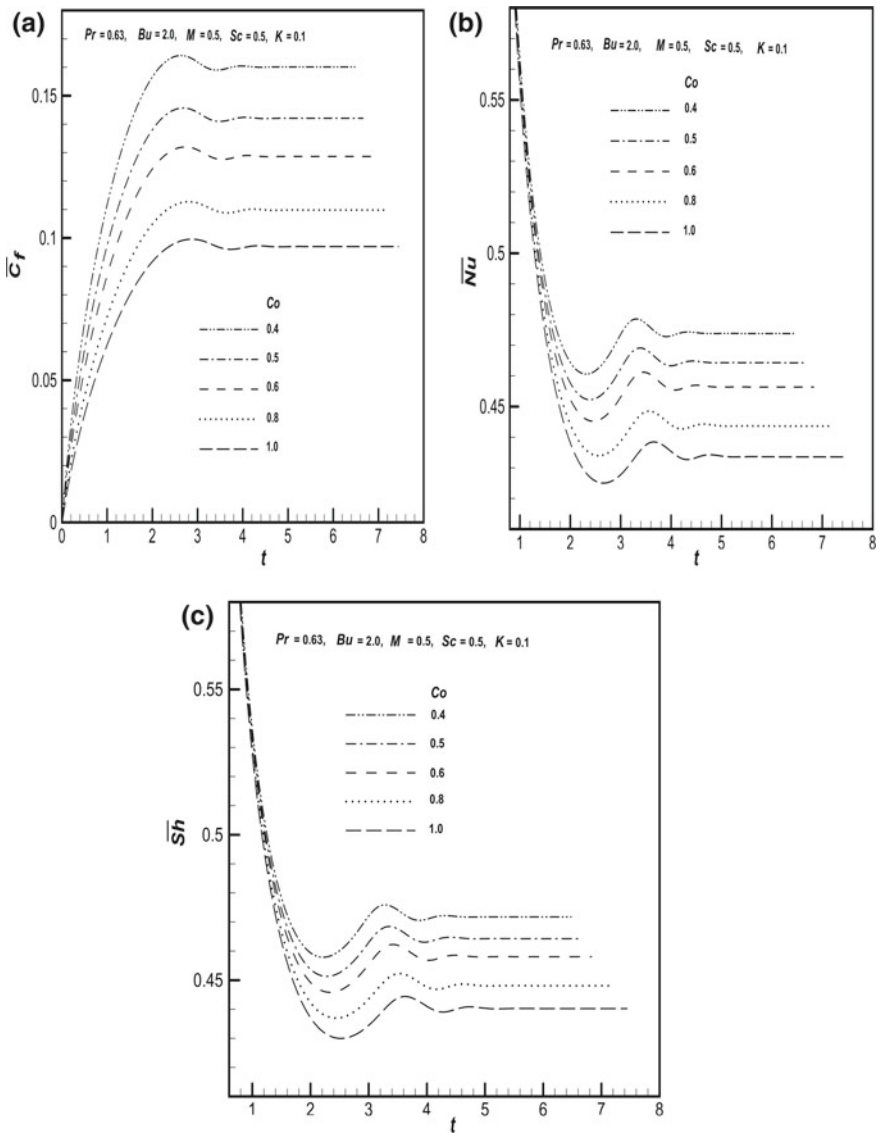

Fig. 4 Profiles of **a** average momentum transport coefficient ($\overline{C_f}$), **b** average Nusselt number ($\overline{\mathrm{Nu}}$) and **c** average Sherwood number ($\overline{\mathrm{Sh}}$) with time (t)

5 Conclusions

The contemporary article thermodynamically discussed the time-dependent viscous incompressible, free convective flow of non-Newtonian couple stress fluid over a vertical plate with magneto-hydrodynamic effect numerically with homogenous first-order chemical reaction. The present numerical simulations result in the following important observations.

(i) Time-dependent and time-independent state velocity decreases as Co increases.
(ii) Unsteady and steady-state temperature and concentration upsurges as Co increases.
(iii) The average momentum, Nusselt and Sherwood numbers decrease as Co upsurges.
(iv) The time required to reach the steady-state magnifies as Co increases.

Acknowledgements The first author Hussain Basha wishes to thank UGC-MANF for the research fellowship. Also, the corresponding author G. Janardhana Reddy acknowledges the financial support of UGC-BSR Start-Up Research Grant.

References

1. Cussler, E.L.: Diffusion mass Transfer in Fluid Systems, 3rd edn. Cambridge University Press, London (1988)
2. Ostrach, S.: An analysis of laminar free-convection flow and heat transfer about a flat plate parallel to the direction of the generating body force. Supersedes NACA (National Advisory Committee for Aeronautics) TN 2635, Report-1111 (1952)
3. Rani, H.P., Reddy, G.J., Kim, C.N.: Transient analysis of diffusive chemical reactive species for couple stress fluid flow over vertical cylinder. Appl. Math. Mech. (English Edition) **34**(8), 985–1000 (2013)
4. Hayata, T., Awaisa, M., Safdara, A., Hendi, A.A.: Unsteady three dimensional flow of couple stress fluid over a stretching surface with chemical reaction. Nonlinear Anal. Model. Control **17**(1), 47–59 (2012)
5. Kaladhar, K., Motsa, S.S., Srinivasacharya, D.: Mixed convection flow of couple stress fluid in a vertical channel with radiation and Soret effects. J. Appl. Fluid Mech. **9**(1), 43–50 (2016)
6. Srinivasacharya, D., Kaladhar, K.: Mixed convection flow of chemically reacting couple stress fluid in a vertical channel with Soret and Dufour effects. Int. J. Comput. Methods Eng. Sci. Mech. **15**, 413–421 (2014)
7. Chu, H.M., Li, W.L., Hu, S.Y.: Effects of couple stress on pure squeeze EHL motion of circular contacts. J. Mech. **22**, 77–84 (2006)
8. Soundalgekar, V.M., Ganesan, P.: Finite difference analysis of transient free convection with mass transfer on an isothermal vertical flat plate. Int. J. Eng. Sci. **19**, 757–770 (1981)
9. Stokes, V.K.: Couple stress in fluids. Phys. Fluids **9**, 1709–1715 (1966)
10. Lin, J.: Squeeze film characteristics of finite journal bearings: couple stress fluid model. Tribol. Int. **31**, 201–207 (1998)
11. Rani, H.P., Reddy, G.J., Kim, C.N.: Numerical analysis of couple stress fluid past an infinite vertical cylinder. Eng. Appl. Comput. Fluid Mech. **5**, 159–169 (2011)

12. Jian, C.W.C., Yau, H.T., Chen, J.L.: Nonlinear dynamic analysis of a hybrid squeeze-film damper-mounted rigid rotor lubricated with couple stress fluid and active control. Appl. Math. Model. **34**, 2493–2507 (2010)
13. Von Rosenberg, D.U.: Methods for the numerical solution of partial differential equations. American Elsevier Publishing Company, New York (1969)

A Mathematical Approach to Study the Blood Flow Through Stenosed Artery with Suspension of Nanoparticles

K. Maruthi Prasad and T. Sudha

Abstract The present paper deals with the effects of an overlapping stenosis of a micropolar fluid with nanoparticles in a uniform tube. The governing equations have been linearized. The expressions for impedance and shear stress at wall have been deduced. Effects of various parameters like coupling number, micropolar parameter, Brownian motion parameter, thermophoresis parameter, local temperature Grashof number, and local nanoparticle Grashof number on resistance to the flow and wall shear stress of the fluid are studied. Effect of these parameters on arterial blood flow characteristics are shown graphically and discussed briefly under the influence nanoparticles and streamline patterns have been studied with particular emphasis. It is noticed that impedance enhances with the increase of micropolar parameter, thermophoresis parameter, local temperature Grashof number and local nanoparticle Grashof number but reduces with the increase of coupling number and Brownian motion parameter. Shear stress at wall increases with coupling number and Brownian motion parameter but decreases with micropolar parameter, thermophoresis parameter, local temperature Grashof number and local nanoparticle Grashof number.

Keywords Micropolar fluid · Stenosis · Nanoparticles · Impedance
Shear stress at wall

1 Introduction

The Atherosclerosis or Stenosis is a serious medical issue because most of the deaths are occurred due to cardiovascular diseases. It realized that cardiovascular diseases are closely related with flow characteristics in the blood vessels. One of such diseases

K. Maruthi Prasad (✉) · T. Sudha
Department of Mathematics, School of Technology, GITAM University, Hyderabad 502329, Telangana, India
e-mail: maruthiprasad.karanamu@gitam.edu

T. Sudha
e-mail: sudhathulluri@gmail.com

D. Srinivasacharya and K. S. Reddy (eds.), *Numerical Heat Transfer and Fluid Flow*, Lecture Notes in Mechanical Engineering,
https://doi.org/10.1007/978-981-13-1903-7_23

is stenosis, which is defined as a partial blockage of the blood vessels due to the cholesterol, cellular waste products and deposits of fatty substances, calcium, and fibrin in the inner lining of an artery. These substances are causes for the blockage of blood flow in an artery. It leads to heart attack and stroke, etc. Mainly in this condition flow behavior is quite different from that in a normal artery and it results into significant changes in blood flow, pressure distribution, wall shear stress, and the impedance (flow resistance). In the view of this, blood flow through the stenosed arteries has become prominent and played a leading role of cardiovascular diseases. Based on this, several researchers investigated the characteristics of blood flow in an artery having stenosis by treating blood as non-Newtonian or Newtonian fluid [1, 2].

Micropolar fluid is a non-Newtonian fluid. Eringen [3] proposed the model of micropolar fluid. The main feature of this fluid is that it takes care of the rotation of fluid particles by means of independent kinematic vector known as micro rotation. Several researchers have investigated stenosis by considering blood as micropolar fluid [4, 5].

Present days, many researchers are concentrated on analysis of nanofluids for various flow geometries. A fluid containing nanoscaled particles is called as nanofluid. Nanofluid particles are added to the fluids having low thermal conductivity to increase the thermal conductivity of the fluids. Choi [6] was the first person to introduce the nanofluids. Micropolar fluid having nanoparticles through peristaltic transport in small intestines was studied by Akbar et al. [7].

It is realized that stenosis may develop in series like multiple stenosis or irregular shapes or overlapping. Based on this Srivastava and Shailesh [8] and Maruthi Prasad et al. [9] studied the non-Newtonian arterial blood flow through an overlapping stenosis. However, the effect of overlapping stenosis of a micropolar fluid with nanoparticles has not been studied.

Motivated by the above studies, an effort has been made in this paper to examine the effects overlapping stenosis of a micropolar fluid with nanoparticles has been investigated under the assumption of mild stenosis. The analysis is done analytically. The effect of different relevant parameters on flow variables has been observed through the graphs.

2 Mathematical Formulation

Consider the steady flow of blood through an axially symmetric but radially non-symmetric overlapping stenosed artery. The geometry of Stenosis can be taken as [8].

$$h = \frac{R(z)}{R_0} = \begin{cases} 1 - \frac{3\delta}{2R_0L_0^4}\left[11(z-d)L_0^3 - 47(z-d)^2L_0^2 + 72(z-d)^3L_0 - 36(z-d)^4\right] & d \le z \le d + L_0, \\ 1, & \text{otherwise.} \end{cases} \tag{1}$$

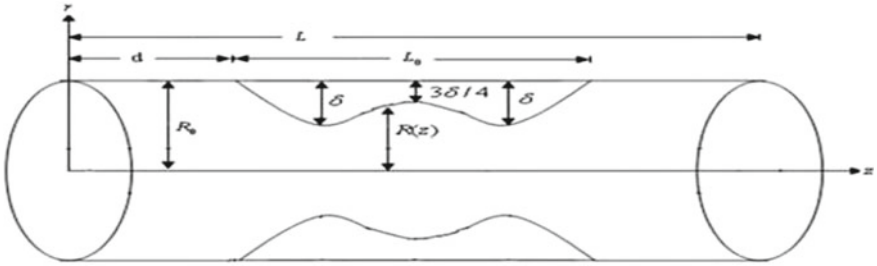

Fig. 1 Geometry of a uniform tube of circular cross section with overlapping stenosis

where $R_0(z)$ the tube radius without stenosis, $R(z)$ is tube radius with stenosis, L_0 is stenosis length and d indicates the location of stenosis, and δ is the maximum stenosis height. Projection of stenosis at the two positions is denoted by z as $z = d + \frac{L_0}{6}$, $z = d + \frac{5L_0}{6}$, respectively. The critical height is taken as $\frac{3\delta}{4}$ at $z = d + L_0/2$, from the origin (Fig. 1).

Using the following nondimensional quantities

$$\bar{z} = \frac{z}{L}, \overline{L} = \frac{L}{L_0}, \ \bar{u} = \frac{u}{U}, \overline{R}(z) = \frac{R(z)}{R_0}, \ \bar{\delta} = \frac{\delta}{R_0}, \ \bar{u}_z = \frac{u_z}{u_0},$$

$$\bar{u}_r = \frac{Lu_r}{u_0\delta}, \ \bar{v}_\theta = \frac{R_0 v_\theta}{u_0}, \overline{P} = \frac{P}{\mu U L/R_0^2}, \bar{q} = \frac{q}{\pi R_0^2 U}, R_e = \frac{\rho U R_0}{\mu},$$

$$\bar{h} = \frac{h}{h_0}, N_b = \frac{(\rho C)_P D_{\overline{B}} \overline{C}_0}{(\rho C)_f}, \quad N_t = \frac{(\rho C)_P D_T \overline{T}_0}{(\rho C)_f \beta}, G_r = \frac{g\beta \overline{T}_0 R_0^3}{\gamma^2}, \quad B_r = \frac{g\beta \overline{C}_0 R_0^3}{\gamma^2}.$$

The equations of an incompressible micropolar fluid with nanoparticle under assumption of mild stenosis approximation ($\frac{\delta}{R_0} \ll 1$, $R_e^*(2\delta/L_0) \ll 1$, and $2R_0/\widetilde{L_0}(1)$) are defined Maruthi Prasad et al. [10] as

$$\frac{\partial p}{\partial r} = 0 \tag{2}$$

$$\left(\frac{\partial^2 u_z}{\partial r^2} + \frac{1}{r}\frac{\partial u_z}{\partial r} + \frac{N}{r}\frac{\partial}{\partial r}(r v_\theta)\right) + (1-N)(G_r\theta_t + B_r\sigma) = (1-N)\frac{\partial p}{\partial z} \tag{3}$$

$$2v_\theta + \frac{\partial u_z}{\partial r} - \frac{2-N}{m^2}\frac{\partial}{\partial r}\left(\frac{1}{r}\frac{\partial}{\partial r}(r v_\theta)\right) = 0 \tag{4}$$

$$0 = \frac{1}{r}\frac{\partial}{\partial r}\left(r\frac{\partial \theta_t}{\partial r}\right) + N_b\frac{\partial \sigma}{\partial r}\frac{\partial \theta_t}{\partial r} + N_t\left(\frac{\partial \theta_t}{\partial r}\right)^2 \tag{5}$$

$$0 = \frac{1}{r}\frac{\partial}{\partial r}\left(r\frac{\partial \sigma}{\partial r}\right) + \frac{N_t}{N_b}\left(\frac{1}{r}\frac{\partial}{\partial r}\left(r\frac{\partial \theta_t}{\partial r}\right)\right) \tag{6}$$

In which N is the coupling number m is the micropolar parameter, u_z is the velocity in the axial direction, v_θ is the micro-rotation in the θ direction, θ_t is the temperature profile, σ is nanoparticle phenomena. N_t, N_b, B_r, and G_r denote thermophoresis

parameter, Brownian motion parameter, local nanoparticle Grashof number and local temperature Grashof number.

The relative nondimensional boundary conditions are

$$\frac{\partial u_z}{\partial r} = 0, \ \frac{\partial \theta_t}{\partial r} = 0, \ \frac{\partial \sigma}{\partial r} = 0 \quad at \ r = 0 \tag{7}$$

$$u_z = 0, \ \theta_t = 0, \sigma = 0, \ v_\theta = 0 \quad at \ r = h \tag{8}$$

$$u_z \text{ is finite}, \ v_\theta \text{ is flinite at } r = 0 \tag{9}$$

3 Solution

The solutions of the coupled Eqs. (5) and (6) have been solved by using homotropy perturbation method (HPM) as

$$H\left(q_t, \theta_t\right) = (1 - q_t)\left[L(\theta_t) - L\left(\theta_{t_{10}}\right)\right] + q_t\left[L(\theta_t) + N_b \frac{\partial \sigma}{\partial r}\frac{\partial \theta_t}{\partial r} + N_t\left(\frac{\partial \theta_t}{\partial r}\right)^2\right] \tag{10}$$

$$H(q_t, \sigma) = (1 - q_t)[L(\sigma) - L(\sigma_{10})] + q_t\left[L(\sigma) + \frac{N_t}{N_b}\left(\frac{1}{r}\frac{\partial}{\partial r}\left(r\frac{\partial \theta_t}{\partial r}\right)\right)\right]. \tag{11}$$

Where q_t is the embedding parameter which has the range $0 \leq q_t \leq 1$. For our convenience, $L = \frac{1}{r}\frac{\partial}{\partial r}\left(r\frac{\partial}{\partial r}\right)$ is taken as linear operator. The initial guesses $\theta_{t_{10}}$ and σ_{10} are defined as

$$\theta_{t_{10}}(r, z) = \left(\frac{r^2 - h^2}{4}\right), \quad \sigma_{10}(r, z) = -\left(\frac{r^2 - h^2}{4}\right) \tag{12}$$

Adopting the same procedure as done by Maruthi Prasad et al. [10], the solution for temperature and nanoparticle phenomena can be written for $q_t = 1$ as

$$\theta_t(r, z) = \left(\frac{r^4 - h^4}{64}\right)(N_b - N_t) \tag{13}$$

$$\sigma(r, z) = -\left(\frac{r^2 - h^2}{4}\right)\frac{N_t}{N_b}. \tag{14}$$

Substituting Eqs. (13) and (14) in Eq. (3), we get v_θ as,

$$v_\theta = AI_1(mr) + BK_1(mr) + \frac{(N-1)}{(2-N)}\frac{r}{2}\frac{dp}{dz} + \frac{G_r(1-N)(N_b-N_t)}{(2-N)}\left[\frac{r^5}{384} + \frac{r^3}{16m^2} + \frac{r}{2m^4} - \frac{h^4 r}{128}\right] + \frac{B_r(N-1)}{(2-N)}\frac{N_t}{N_b}\left[\frac{r^3}{16} + \frac{r}{2m^2} - \frac{h^2 r}{8}\right] \tag{15}$$

where $I_1(mr)$ and $K_1(mr)$ are the modified Bessel functions of first and second order, respectively. Substituting the value of v_θ and using the boundary conditions Eqs. (7)–(9) and expression for velocity u_z is

$$u_z = \frac{(1-N)}{(2-N)}\frac{dp}{dz}\left\{\frac{r^2-h^2}{2} + \frac{Nh}{2mI_1(mh)}[I_0(mh) - I_0(mr)]\right\} + \frac{G_r(1-N)(N_b-N_t)}{2(2-N)} \left\{\begin{array}{l} \frac{N}{I_1(mh)}\left(\frac{h^5}{96m} - \frac{h^3}{8m^3} - \frac{h}{m^5}\right)[I_0(mh) - I_0(mr)] \\ -\frac{r^6}{576} - \frac{h^6}{72} + \frac{h^4 r^2}{64} - \frac{N}{32m^2}\left(r^4 - h^4\right) - \frac{16N}{32m^4}\left(r^2 - h^2\right) \end{array}\right\} + \frac{B_r(N-1)}{2(2-N)}\frac{N_t}{N_b}\left\{\begin{array}{l} \frac{N}{I_1(mh)}\left(\frac{h^3}{8m} - \frac{h}{m^3}\right)[I_0(mh) - I_0(mr)] \\ -\frac{1}{16}\left(r^4 + 3h^4\right) - \frac{N}{2m^2}\left(r^2 - h^2\right) + \frac{h^2 r^2}{4} \end{array}\right\} \tag{16}$$

The dimension-less flux q is

$$q = \int_0^h 2ru_z\, dr. \tag{17}$$

By substituting Eq. (16) in Eq. (17), the flux is

$$q = \frac{(1-N)}{(2-N)}\frac{dp}{dz}\left\{\frac{-h^4}{4} + \frac{Nh^3 I_0(mh)}{2mI_1(mh)} - \frac{Nh^2}{m^2}\right\} + \frac{B_r(N-1)}{(2-N)}\frac{N_t}{N_b}\left\{\left(\frac{h^5}{16} - \frac{h^3}{2m^2}\right)\frac{NI_0(mh)}{mI_1(mh)} + \frac{Nh^2}{m^4} - \frac{h^6}{24}\right\} + \frac{G_r(1-N)(N_b-N_t)}{(2-N)}\left\{\begin{array}{l} \left(\frac{h^7}{192} - \frac{h^5}{16m^2} - \frac{h^3}{2m^4}\right)\frac{NI_0(mh)}{mI_1(mh)} \\ +\frac{Nh^4}{4m^4} + \frac{Nh^2}{m^6} - \frac{5h^8}{1536} \end{array}\right\} \tag{18}$$

From Eq. (18), $\frac{dP}{dz}$ can be given as

$$\frac{dp}{dz} = \frac{q(2-N)}{S(N-1)} + \frac{G_r(N_b - N_t)}{S}$$
$$\left\{\left(\frac{h^7}{192} - \frac{h^5}{16m^2} - \frac{h^3}{2m^4}\right)\frac{NI_0(mh)}{mI_1(mh)} + \frac{Nh^4}{4m^4} + \frac{Nh^2}{m^6} - \frac{5h^8}{1536}\right\}$$
$$- \frac{B_r N_t}{SN_b}\left\{\left(\frac{h^5}{16} - \frac{h^3}{2m^2}\right)\frac{NI_0(mh)}{mI_1(mh)} + \frac{Nh^2}{m^4} - \frac{h^6}{24}\right\} \tag{19}$$

where $S = \left[\frac{h^4}{4} - \frac{Nh^3 I_0(mh)}{2mI_1(mh)} + \frac{Nh^2}{m^2}\right]$

The pressure drop over one wavelength $p(0) - p(\lambda)$ is

$$\Delta p = -\int_0^1 \frac{dp}{dz} dz \tag{20}$$

The impedance λ is defined as

$$\lambda = \frac{\Delta p}{q} \tag{21}$$

The pressure drop without stenosis $h = 1$ is defined as

$$\Delta p_n = \left[-\int_0^1 \frac{dp}{dz} dz\right]_{h=1} \tag{22}$$

The impedance in the normal artery is defined as

$$\lambda_n = \frac{\Delta p_n}{q} \tag{23}$$

The normalized impedance defined as

$$\bar{\lambda} = \frac{\lambda}{\lambda_n} \tag{24}$$

And the wall shear stress τ_h is defined as

$$\tau_h = -\frac{h}{2}\frac{dp}{dz} \tag{25}$$

4 Result Analysis

Using MATHEMATICA 9.0 Software, computer codes are developed to evaluate analytical solutions for impedance $(\bar{\lambda})$ and shear stress at wall (τ_h). The effects of pertinent parameters on impedance, shear stress at wall and nanoparticle phenomena have been computed numerically for different values of height of the stenosis and are presented graphically in Figs. 2, 3, 4, 5, 6, 7, 8, and 9 by considering the parameter values as $d = 0.2,\ \mathrm{L}_0 = 0.4,\ m = 1,\ q = 0.1,\ L = 1, N = 0.1,\ \mathrm{N_b} = 0.3,\ N_\mathrm{t} = 0.8,\ B_\mathrm{r} = 0.3,\ G_\mathrm{r} = 0.5$ [9, 10].

In Figs. 2, 3, and 4, it is observed that impedance $(\bar{\lambda})$ increases with the heights of the stenosis (δ), micropolar parameter (m), thermophoresis parameter (N_t), local temperature Grashof number (G_r), and local nanoparticle Grashof number (B_r) but decreases with coupling number (N) and Brownian motion parameter (N_b).

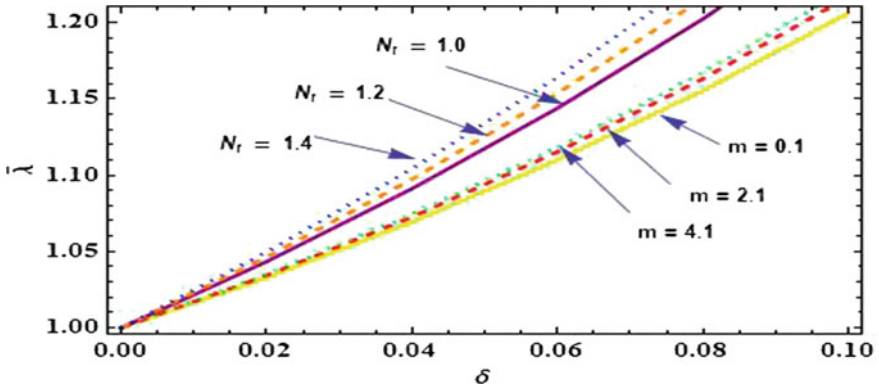

Fig. 2 Effect of δ and N_t, m on $\bar{\lambda}$

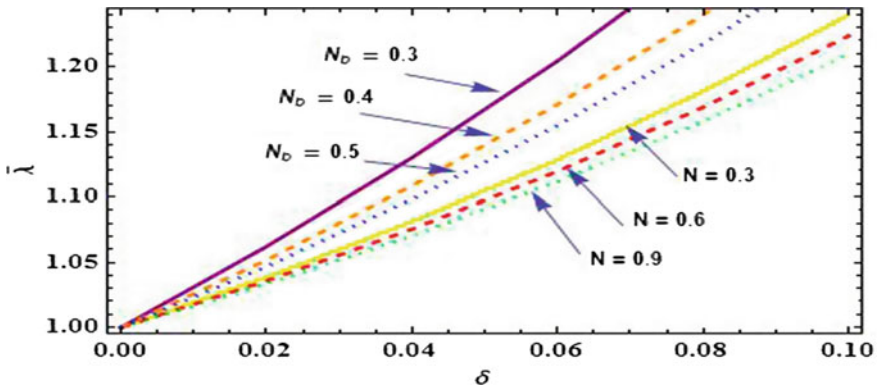

Fig. 3 Effect of δ and N_b, N on $\bar{\lambda}$

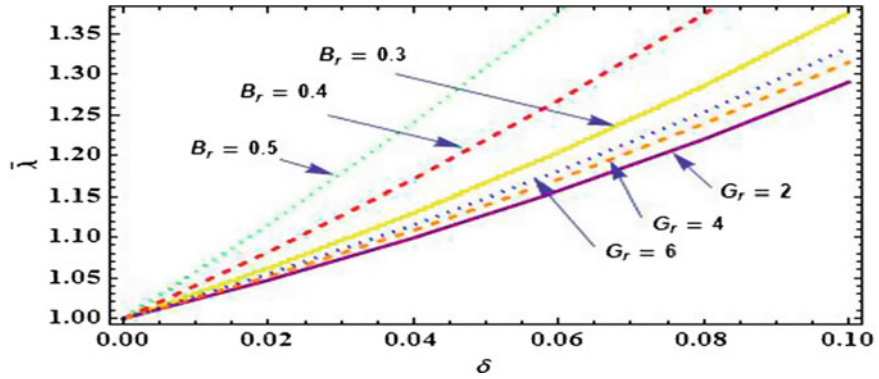

Fig. 4 Effect of δ and G_r, B_r on $\bar{\lambda}$

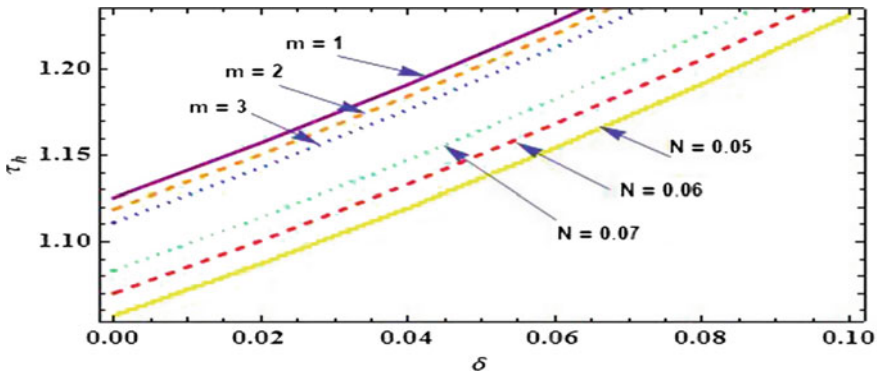

Fig. 5 Effect of δ and N, m on τ_h

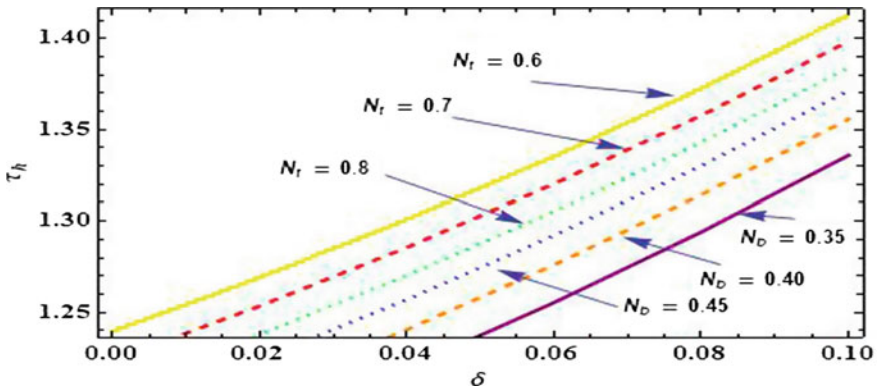

Fig. 6 Effect of δ and N_t, N_b on τ_h

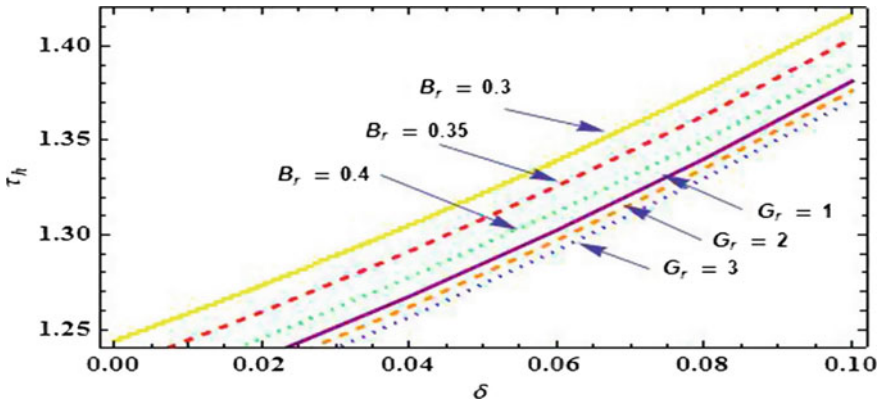

Fig. 7 Effect of δ and G_r, B_r on τ_h

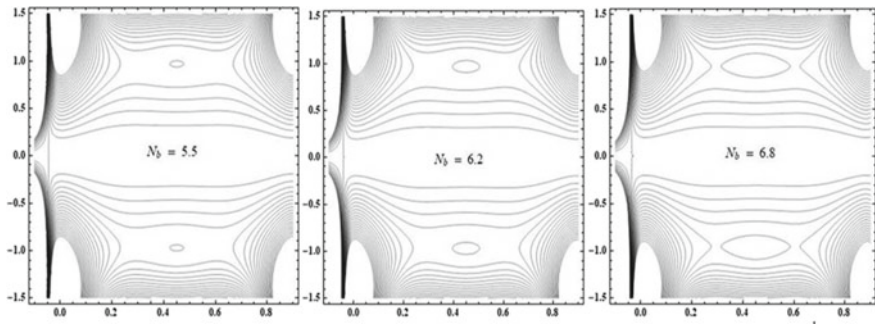

Fig. 8 Stream line patterns for different values of N_b

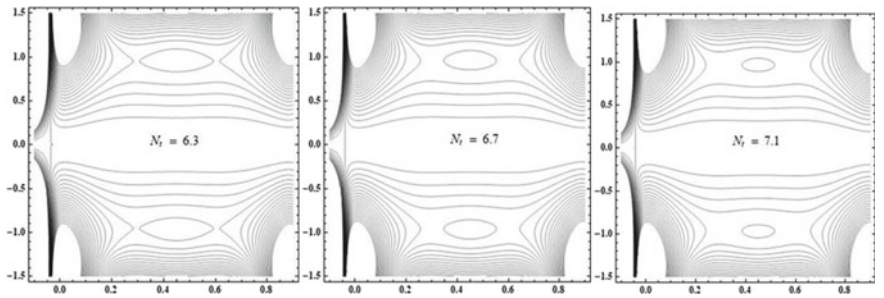

Fig. 9 Stream line patterns for different values of N_t

The shear stress at wall (τ_h) acting over the height of the stenosis (δ) is shown graphically in Figs. 5, 6 and 7, it is seen that shear stress at wall increases with the heights of the stenosis (δ), coupling number (N) and Brownian motion parameter

(N_b) but decreases with micropolar parameter (m), thermophoresis parameter (N_t), local temperature Grashof number (G_r), and local nanoparticle Grashof number (B_r).

Figures 8 and 9 illustrate the streamline patterns and it is noticed that size of bolus increases with the increase of Brownian motion parameter (N_b) and size of the bolus decreases with the increase in thermophoresis parameter (N_t).

5 Conclusion

A mathematical analysis for the steady flow of an incompressible micropolar fluid with nanoparticles in a tube having overlapping stenosis has been studied by assuming stenosis is to be mild. The analytical solutions of the governing equations are obtained by using Homotropy perturbation method. It is noticed that shear stress at wall increases with the stenotic heights, coupling number, and Brownian motion parameter but decreases with micropolar parameter, thermophoresis parameter, local temperature Grashof number and local nanoparticle Grashof number. Impedance increases with the heights of the stenosis, length of the stenosis, micropolar parameter, thermophoresis parameter, local temperature Grashof number, and local nanoparticle Grashof number but decreases with coupling number and Brownian motion parameter.

References

1. Young, D.F.: Effect of a time-dependent stenosis on flow through a tube. Trans. ASME J. Eng. Ind. **90**, 248–254 (1968). https://doi.org/10.1115/1.3604621
2. Shukla, J.B., Parihar, R.S., Rao, B.R.P.: Effects of stenosis on non-Newtonian flow of blood in an artery. Bull. Math. Biol. **42**(3), 283–294 (1980). https://doi.org/10.1007/BF02460787
3. Eringen, A.C.: Theory of micropolar fluids. J. Math. Mech. **16**, 1–18 (1966). https://doi.org/10.1512/iumj.1967.16.16001
4. Awgichew, G., Radhakrishnamacharya, G.: Effect of slip condition on micropolar fluid flow in a stenosed channel. J. Eng. Sci. **9**(1), 198–204 (2014)
5. Srinivasacharya, D., Madhava Rao, G.: Magnetic effects on Pulsatile flow of micropolar fluid through a bifurcated artery. World J. Model. Simul. **12**(2), 147–160 (2016)
6. Choi, S.U.S.: Enhancing thermal conductivity of fluids with nanoparticles. In: Siginer, D.A., Wang, H.P. (eds.) Developments and applications of Non-Newtonian flows, pp. 99–105. ASME, New York (1995)
7. Akbar, N.S., Nadeem, S.: Peristaltic flow of a micropolar fluid with nano particles in small intestine. Appl. Nanosci. **3**(1), 461–468 (2013). https://doi.org/10.1007/s13204-012-0160-2
8. Srivastava, V.P., Shailesh, M.: Non-Newtonian arterial blood flow through an overlapping stenosis. Appl. Appl. Math. **5**(1), 225–238 (2010)
9. Maruthi Prasad, K., Sudha, T., Phanikumari, M.V.: Investigation of blood flow through an artery in the presence of overlapping stenosis. J. Naval Architect. Marine Eng. **14**(1), 39–46 (2017). https://doi.org/10.3329/jname.v14i1.31165
10. Maruthi Prasad, K., Subadra, N., Srinivas, M.A.S.: Peristaltic motion of nano particles of a micropolar fluid with heat and mass transfer effect in an inclined tube. Procedia Eng. **127**(1), 694–702 (2015). https://doi.org/10.1016/j.proeng.2015.11.368

Non-Newtonian Fluid Flow Past a Porous Sphere Using Darcy's Law

M. Krishna Prasad

Abstract The present work describes the low Reynolds number flow of an incompressible micropolar fluid past and through a porous sphere placed in a uniform flow. Stokes equation is used for the flow outside the porous sphere and Darcy's law is used in the porous region. The boundary conditions used are the continuity of the normal velocity components, continuity of pressures, Beavers–Joseph slip boundary condition for tangential velocities and zero microrotation at the surface of the porous sphere. The drag force exerted on the porous sphere is determined and its variation versus permeability parameter is studied numerically. The limiting cases of micropolar fluid flow past a solid sphere in an unbounded medium and viscous fluid flow past a porous sphere are obtained from the present analysis.

Keywords Stokes' flow · Darcy's law · Sphere · Drag

1 Introduction

The study of motion of fluids with microstructure attracts the attention of several investigators due to its wide area of research in the fields of biomedical, engineering, and technology. Newtonian fluids fail to describe the correct behaviour of such fluids because it neglects the effect of microstructure. A theory that accounts for microstructure is the micropolar fluid theory introduced by Eringen [1, 2]. The review of microcontinuum theories with various applications has been presented by Ariman et al. [3]. The study of fluids within porous media is of great practical importance and has extensive applications, such as the filtration of solids from liquids, sedimentation, enhanced oil recovery and so on. Stokes flow past a Newtonian homogeneous porous sphere has been studied by many researchers [4–11]. Padmavathi et al. [12] discussed Stokes flow of Newtonian fluid past a porous sphere. Vainshtein et al. [13]

M. Krishna Prasad (✉)
Department of Mathematics, National Institute of Technology,
Raipur 492010, Chhattisgarh, India
e-mail: madaspra.maths@nitrr.ac.in; kpm973@gmail.com

D. Srinivasacharya and K. S. Reddy (eds.), *Numerical Heat Transfer and Fluid Flow*, Lecture Notes in Mechanical Engineering,
https://doi.org/10.1007/978-981-13-1903-7_24

investigated slow flow past a porous spheroid. Srinivasacharya [14] studied flow past a porous approximate spherical shell.

All the papers cited above are related viscous fluids, Rao and Rao [15], Ramkisson and Majumdar [16], Hoffmann et al. [17], Rao and Iyengar [18] and Iyengar and Srinivasacharya [19] discussed the Stokes flow of micropolar fluid past a solid sphere, spheroid and approximate sphere, respectively. Recently, Iyengar and Radhika [20] investigated flow past a porous prolate spheroidal shell with an impermeable core in an unbounded micropolar fluid. In this paper, the micropolar fluid flow past a porous sphere is studied using slip condition for tangential stress.

2 Statement of the Problem

Consider an axisymmetric translation of a porous sphere in an unbounded micropolar Stokes flow, moving in positive z-direction with uniform velocity U. The problem is concerned by dividing the flow into two regions (see Fig. 1): I is the region of the internal porous sphere and II is the region of the clear fluid.

The field equations governing the slow flow of an incompressible micropolar fluid in the absence of body force and body couples [1–3, 21] are given by

$$\nabla \cdot \mathbf{v}^{(1)} = 0, \tag{1a}$$

$$\nabla p^{(1)} + (\mu + \kappa)\, \nabla \times \nabla \times \mathbf{v}^{(1)} - \kappa\, \nabla \times \boldsymbol{\nu} = 0, \tag{1b}$$

$$-2\kappa\, \boldsymbol{\nu} + \kappa\, \nabla \times \mathbf{v}^{(1)} - \gamma_0\, \nabla \times \nabla \times \boldsymbol{\nu} + (\alpha_0 + \beta_0 + \gamma_0) \nabla \nabla \cdot \boldsymbol{\nu} = 0, \tag{1c}$$

The equations for the fluid motion within the porous sphere are

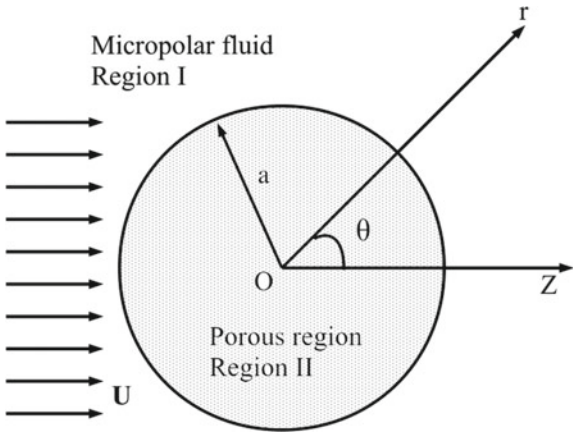

Fig. 1 Geometry of the problem

$$\nabla \cdot \mathbf{v}^{(2)} = 0, \tag{2a}$$

$$\mathbf{v}^{(2)} = -\frac{k}{\mu}\nabla p^{(2)}, \tag{2b}$$

where $\mathbf{v}^{(i)}$, $p^{(i)}, i = 1, 2$ are the velocity vector, pressure. $\boldsymbol{\nu}$, μ, κ, α_0 and β_0 and γ_0 are the microrotation vector, the dynamic viscosity, vortex viscosity, bulk spin viscosity and shear spin viscosity, respectively. k is the permeability of the porous medium.

Let $(\mathbf{e}_r, \mathbf{e}_\theta, \mathbf{e}_\phi)$ be the unit vectors in spherical coordinates system (r, θ, ϕ). For an axially symmetric translational steady motion, velocity vector and microrotation vector are independent of ϕ. Thus, we have

$$\mathbf{v}^{(i)} = v_r^{(i)}(r, \theta)\, \mathbf{e}_r + v_\theta^{(i)}(r, \theta)\, \mathbf{e}_\theta,\ i = 1, 2 \tag{3}$$

$$\boldsymbol{\nu} = \nu_\phi(r, \theta)\, \mathbf{e}_\phi. \tag{4}$$

It is convenient to introduce Stokes stream functions $\psi^{(i)}$, $i = 1, 2$ for both the regions. The related velocity components are given by

$$v_r^{(i)} = \frac{1}{r^2}\frac{\partial \psi^{(i)}}{\partial \xi},\ v_\theta^{(i)} = \frac{1}{r\sqrt{1-\xi^2}}\frac{\partial \psi^{(i)}}{\partial r},\ i = 1, 2. \tag{5}$$

Eliminating of the pressures from Eqs. (1) and (2), we get the fourth-order linear partial differential equations for the stream functions $\psi^{(i)}$, $i = 1, 2$ and the microrotation vector component ν_ϕ,

$$E^4 \left(E^2 - \lambda^2\right) \psi^{(1)} = 0, \tag{6}$$

$$\nu_\phi = \frac{1}{2r\sqrt{1-\xi^2}}\left(E^2 \psi^{(1)} + \frac{(2+\tau)}{\tau\, \lambda^2} E^4 \psi^{(1)}\right), \tag{7}$$

$$E^2 \psi^{(2)} = 0, \tag{8}$$

where

$$E^2 = \frac{\partial^2}{\partial r^2} + \frac{(1-\xi^2)}{r^2}\frac{\partial^2}{\partial \xi^2},$$

$$\lambda^2 = \left(\frac{\gamma_0}{a^2\, \kappa}\right)^{-1} \frac{(2+\tau)}{(1+\tau)},\ \tau = \kappa/\mu,\ \xi = \cos\theta.$$

The boundary conditions on the surface of the sphere $r = 1$

$$\frac{\partial \psi^{(1)}}{\partial \xi} = \frac{\partial \psi^{(2)}}{\partial \xi}, \tag{9}$$

$$p^{(1)} = p^{(2)}, \tag{10}$$

$$(2+\tau)\left[2\,r\frac{\partial}{\partial r}\left(\frac{1}{r}\frac{\partial \psi^{(1)}}{\partial r}\right) - E^2\psi^{(1)} - \frac{1}{\lambda^2}E^4\psi^{(1)}\right] = 2\,\alpha\,\sigma\left(\frac{\partial\,\psi^{(1)}}{\partial r} - \frac{\partial\,\psi^{(2)}}{\partial r}\right), \tag{11}$$

$$v_\phi = 0, \tag{12}$$

and uniform flow condition at infinity $\psi^{(1)} = \frac{1}{2}r^2(1-\xi^2)$ as $r \to \infty$, $\alpha^2 = \frac{a^2}{k}$

Using separation of variables, a solution to Eqs. (6)–(8) is

$$\psi^{(1)} = \left[r^2 + A\,r^{-1} + B\,r + C\,\sqrt{r}\,K_{3/2}(\lambda\,r)\right]\vartheta_2(\xi), \tag{13}$$

$$v_\phi = \frac{1}{r\sqrt{1-\xi^2}}\left[-B\,r^{-1} + \frac{\lambda^2(1+\tau)}{\tau}\,C\,\sqrt{r}\,K_{3/2}(\lambda\,r)\right]\vartheta_2(\xi), \tag{14}$$

$$\psi^{(2)} = D\,r^2\vartheta_2(\xi), \tag{15}$$

where the dimensionless constants A, B and C are found from Eqs. (9)–(12). $\vartheta_2(\xi), K_{n+1/2}(\lambda)$, $n = 0, 1$ are Gegenbauer function of the first kind and modified Bessel functions of the second kind, respectively.

The drag force exerted by the non-Newtonian fluid on the porous sphere is obtained by

$$\mathcal{D} = 2\,\pi\,a^2\int_0^\pi r^2\left(t_{rr}^{(1)} - t_{r\theta}^{(1)}\right)|_{r=1}\sin\theta d\theta = 2\,\pi\,a\,U\,\mu\,(2+\tau)\,B \tag{16}$$

$$B = -6\,K_{3/2}(\lambda)\,\lambda\,\alpha^2\,(1+\tau)\,w\,\Delta \tag{17}$$

$$\Delta^{-1} = \lambda\left(-2\,K_{1/2}(\lambda)\,\alpha^2\,\tau\,w + K_{3/2}(\lambda)\,\lambda\,(1+\tau)\left(4\,\alpha^3\,\sigma + 3\left(2\,\alpha^2 + w\right)(2+\tau)\right)\right)$$

$$w = (2 + \alpha\,\sigma + \tau).$$

Special cases

(i) If $\alpha \to \infty$,

$$\mathcal{D}_1 = -6\,\pi\,\mu\,a\,U\,(1+\lambda)\,(1+\tau)\,(2+\tau)[2+\tau+2\,\lambda+2\,\lambda\,\tau]^{-1} \tag{18}$$

this result is identical to the drag force obtained in Rao and Rao [15] and Ramkissoon and Majumdar [16].

(ii) When $\tau \to 0$ in (18),

$$\mathcal{D}_2 = -6\,\pi\,\mu\,a\,U \tag{19}$$

which is Stokes' law [22].

(iii) When $\tau \to 0$ in (16),

$$\mathcal{D}_3 = -6\,\pi\,\mu\,a\,U\left[\frac{3\,\alpha^2\,(2+\alpha\,\sigma)}{6+6\,\alpha^2+3\,\alpha\,\sigma+2\,\alpha^3\,\sigma}\right] \tag{20}$$

which agrees with the result obtained by Jones [9], Davis and Stone [11], and Srinivasacharya [14].

3 Results and Discussion

The normalized drag force $D_N(=\mathcal{D}/(6\,\pi\,\mu\,a\,U))$ versus permeability $k_1(=1/\alpha)$, is presented in Fig. 2 to study the effect of slip coefficient σ and micropolarity parameter τ. Computations are carried out for fixed value $\gamma_0/(\mu\,a^2) = 0.3$.

Figure 2a illustrates the influence of the micropolarity parameter τ on the drag coefficient with permeability k_1 keeping the slip coefficient $\sigma = 0.1$. It indicates the value of drag coefficient increases with an increase in the value τ and it is decreasing as k_1 is increasing. The drag force acting on the porous sphere in an unbounded micropolar fluid is more than that of a porous sphere in viscous fluid. Figure 2b shows the variation of drag coefficient with k_1 for different values of the slip coefficient σ for the case $\tau = 3$. It shows that drag coefficient decreases with an increase in the value of σ.

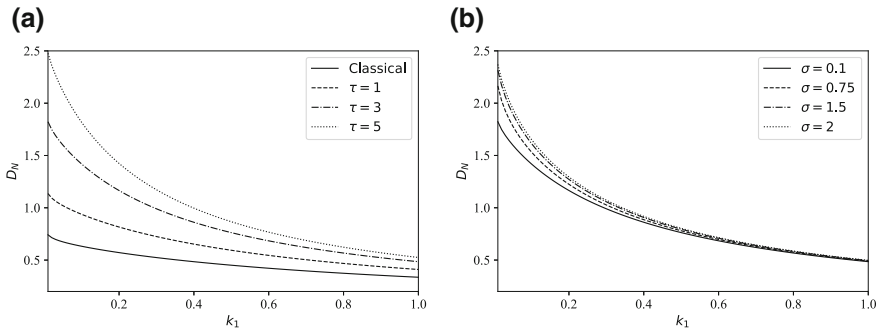

Fig. 2 Variation of D_N with k_1 **a** $\sigma = 0.1$, **b** $\tau = 3$

4 Conclusions

Analytical solution for non-Newtonian fluid past a porous sphere is presented. The drag force is obtained in the closed form and the dependence of the dimensionless drag on the permeability parameter, micropolarity parameter and slip coefficient is studied. It has been found that an increase in slip coefficient and micropolarity parameter increases the drag force.

Acknowledgements This work was supported by the Chhattisgarh Council of Science and Technology, Raipur (C.G), India.

References

1. Eringen, A.C.: Theory of micropolar fluids. J. Math. Mech. **16**, 1–18 (1966)
2. Eringen, A.C.: Microcontinuum Field Theories II: Fluent Media. Springer, New York (2001)
3. Ariman, T., Turk, M.A., Sylvester, N.D.: Applications of microcontinuum fluid mechanics. Int. J. Eng. Sci. **12**, 273–293 (1974). https://doi.org/10.1016/0020-7225(74)90059-7
4. Leonov, A.I.: The slow stationary flow of a viscous fluid about a porous sphere. J. App. Maths. Mech. **26**(3), 842–847 (1962). https://doi.org/10.1016/0021-8928(62)90050-3
5. Joseph, D.D., Tao, L.N.: The effect of permeability in the slow motion of a porous sphere in a viscous liquid. Z. Angew. Math. Mech. **44**, 361–364 (1964). https://doi.org/10.1002/zamm.19640440804
6. Sutherland, D.N., Tan, C.T.: Sedimentation of a porous sphere. Chem. Eng. Sci. **25**, 1948–1950 (1970). https://doi.org/10.1016/0009-2509(70)87013-0
7. Singh, M.P., Gupta, J.L.: The effect of permeability on the drag of a porous sphere in a uniform stream. Z. Angew. Math. Mech. **51**, 27–32 (1971). https://doi.org/10.1002/zamm.19710510103
8. Beavers, G.S., Joseph, D.D.: Boundary conditions at a naturally permeable wall. J. Fluid Mech. **30**(1), 197–207 (1967). https://doi.org/10.1017/S0022112067001375
9. Jones, I.P.: Low Reynolds number flow past a porous spherical shell. Proc. Camb. Phil. Soc. **73**, 231–238 (1973). https://doi.org/10.1017/S0305004100047642
10. Saffman, P.G.: On the boundary condition at the surface of a porous medium. Stud. Appl. Math. **50**, 93–101 (1971). https://doi.org/10.1002/sapm197150293
11. Davis, R.H., Stone, H.A.: Flow through beds of porous particles. Chem. Eng. Sci. **48**(23), 3993–4005 (1993). https://doi.org/10.1016/0009-2509(93)80378-4
12. Padmavathi, B.S., Amarnath, T., Palaniappan, D.: Stokes flow about a porous spherical particle. Arch. Mech. **46**, 191–199 (1994)
13. Vainshtein, P., Shapiro, M., Gutfinger, C.: Creeping flow past and within a permeable spheroid. Int. J. Multiphase flow. **28**, 1945–1963 (2002). https://doi.org/10.1016/S0301-9322(02)00106-4
14. Srinivasacharya, D.: Flow past a porous approximate spherical shell. Z. Angew. Math. Phys. 58, 646-658 (2007). https://doi.org/10.1007/s00033-006-6003-9
15. Rao, S.K.L., Rao, P.B.: The slow stationary flow of a micropolar liquid past a sphere. J. Eng. Math. **4**, 209–217 (1970). https://doi.org/10.1007/BF01534881
16. Ramkissoon, H., Majumdar, S.R.: Drag on an axially symmetric body in the Stokes' flow of micropolar fluid. Phys. Fluids **19**, 16–21 (1976). https://doi.org/10.1063/1.861320
17. Hoffmann, K.H., Marx, D., Botkin, N.D.: Drag on spheres in micropolar fluids with non-zero boundary conditions for microrotations. J. Fluid Mech. **590**, 319–330 (2007). https://doi.org/10.1017/S0022112007008099

18. Rao, S.K.L., Iyengar, T.K.V.: The slow stationary flow of incompressible micropolar fluid past a spheroid. Int. J. Eng. Sci. **19**, 189–220 (1981). https://doi.org/10.1016/0020-7225(81)90021-5
19. Iyengar, T.K.V., Srinivasacharya, D.: Stokes flow of an incompressible micropolar fluid past an approximate sphere. Int. J. Eng. Sci. **31**, 115–123 (1993). https://doi.org/10.1016/0020-7225(93)90069-7
20. Iyengar, T.K.V., Radhika, T.: Stokes flow of an incompressible micropolar fluid past a porous spheroidal shell. Bulletin of the Polish Academy of Sciences: Technical Sciences **59**(1), 63–74 (2011). https://doi.org/10.2478/v10175-011-0010-5
21. Lukaszewicz, G.: Micropolar Fluids: Theory and Applications. Birkhäuser, Basel (1999)
22. Happel, J., Brenner, H.: Low Reynolds Number Hydrodynamics. Prentice-Hall, Englewood Cliffs, NJ (1965)

Navier Slip Effects on Mixed Convection Flow of Cu–Water Nanofluid in a Vertical Channel

Surender Ontela, Lalrinpuia Tlau and D. Srinivasacharya

Abstract This article explores the steady laminar flow and mixed convection heat transfer of a nanofluid in a vertical channel under the influence of Navier slip and thermal radiation. The Tiwari–Das model has been employed for the Cu–water nanofluid. The governing equations of momentum and energy transports are solved analytically and the results are presented graphically. The slip parameter and nanoparticle volume fraction are found to have a strong influence on the skin friction coefficient, although the influence of radiation parameter was found to be minimal.

Keywords Mixed convection · Nanofluid · Vertical channel · Navier-slip Homotopy analysis method

1 Introduction

The term nanofluid was first introduced by Choi [1]. Since then rapid progress has been made in the field. The analysis of nanofluid flows has attracted several researchers due to their applications in cooling technology for high-performance thermal systems, biofluid mechanics, etc. Nanotechnology-based coolants, lubricants, hydraulic fluids, etc., are of great industrial importance.

The slip boundary condition was proposed by Navier [2], which states that slip effects are directly proportional to shear stress. It was then later studied by Mooney [3] extensively and even proposed a methodology to calculate the slip velocity. More recently, Rao and Rajagopal [4] proved that slip velocity depended strongly on the shear stress and even disproved traditional methods [3]. Further studies on the slip

S. Ontela (✉) · L. Tlau
Department of Mathematics, National Institute of Technology Mizoram, Aizawl 796012, India
e-mail: reddysurender3@gmail.com

D. Srinivasacharya
Department of Mathematics, National Institute of Technology Warangal, Warangal 506004, Telangana, India

D. Srinivasacharya and K. S. Reddy (eds.), *Numerical Heat Transfer and Fluid Flow*, Lecture Notes in Mechanical Engineering,
https://doi.org/10.1007/978-981-13-1903-7_25

flow of viscous fluids were done by Ebaid [5], Ullah et al. [6], Haq et al. [7], Sun et al. [8], Kaladhar and Makinde [9]. Effects of radiation on nanofluid flows were investigated by Alam et al. [10], Dogonchi et al. [11], Mohyud-Din et al. [12].

Previous investigations of radiation effects on nanofluid flows were done using the Buongiorno [13] model for nanofluid flows. There has been no evidence of any form of investigation on radiation effects on nanofluid flows with Navier slip effects using the Das–Tiwari model [14]. Motivated by the above works, in this paper, an attempt has been made to explore the flow of a nanofluid in a vertical channel with radiation and slip effects. The effects of thermal radiation, nanoparticle volume fraction, and slip parameters are of particular interest.

2 Mathematical Formulation

Consider a steady-state laminar flow of an incompressible Cu–water nanofluid in a vertical channel. The x-axis is taken vertically along the flow while the y-axis is taken normal to the x-axis. The channel walls are placed at $y = \pm d$ as shown in Fig. 1. The governing equations are

$$\frac{\partial v}{\partial y} = 0 \Rightarrow v = v_0 = \text{constant} \tag{1}$$

$$\rho_{nf} v_0 \frac{\partial u}{\partial y} = -\frac{dp}{dx} + \mu_{nf} \frac{\partial^2 u}{\partial y^2} + g(\rho\beta)_{nf}(T - T_0) \tag{2}$$

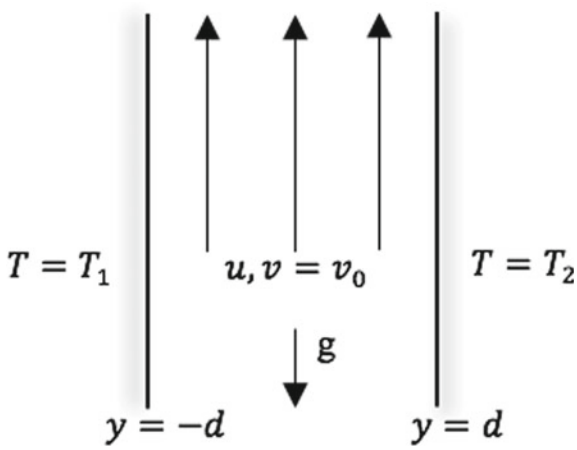

Fig. 1 Schematic diagram with coordinate axes

$$(\rho C_p)_{nf} v_0 \frac{\partial T}{\partial y} = K_{nf} \frac{\partial^2 T}{\partial y^2} - \frac{\partial q^r}{\partial y} \tag{3}$$

where u and v are the velocity components along the x and y axes, respectively, p is the pressure, g is the acceleration due to gravity, ρ_{nf} is the density, β_{nf} is the coefficient of thermal expansion, $(C_p)_{nf}$ is the specific heat capacity, μ_{nf} is the coefficient of viscosity and K_{nf} is the coefficient of thermal conductivity of the nanofluid, respectively, and q^r is the radiation heat flux. From the Rosseland approximation, q^r is taken as

$$q^r = -\frac{4\sigma}{3\chi} \frac{\partial T^4}{\partial y} \tag{4}$$

where σ is the the Stefan–Boltzmann constant, χ is the mean absorption coefficient. Assuming the temperature is sufficiently small and expanding T^4 using Taylor series and neglecting the higher order terms, we take

$$T^4 \approxeq 4T_\infty^3 T - 3T_\infty^4. \tag{5}$$

The associated boundary conditions are

$$y = -d : u = \beta_1 \frac{\partial u}{\partial y}, T = T_1 \tag{6a}$$

$$y = +d : u = \beta_2 \frac{\partial u}{\partial y}, T = T_2 \tag{6b}$$

Invoking the following dimensionless variables:

$$\eta = \frac{y}{d}; u = u_0 U; \theta = \frac{T - T_1}{T_2 - T_1}; p = \frac{\mu_f u_0}{d^2} P \tag{7}$$

in Eqs. (2) and (3), the dimesnsionless equations, thus, obtained are

$$U'' - A_1 R U' + A_2 \frac{Gr}{Re} \theta + A = 0 \tag{8}$$

$$\left(\frac{\alpha_{nf}}{\alpha_f} + \frac{4}{3} \frac{Rd}{B_1} \right) \theta'' - RPr\theta' = 0 \tag{9}$$

and boundary conditions in terms of dimensionless variables are

$$\eta = -1 : U - \beta_1 U' = 0; \theta = 0; \tag{10a}$$

$$\eta = +1 : U - \beta_2 U' = 0; \theta = 1 \tag{10b}$$

where the prime denotes differentiation with respect to η, $Gr = \frac{g\beta_f(T_2-T_1)d^3}{\nu^2}$ is the Grashof number, $Re = \frac{u_0 d}{\nu}$ is the Reynolds number, $R = \frac{v_0 d}{\nu}$ is the suction/injection parameter, $Rd = \frac{4\sigma T_\infty^3}{K_f \chi}$ is the radiation parameter, $Pr = \frac{\mu_f C_f}{K_f}$ is the Prandtl number, $A = -\frac{dP}{dx}$ is the constant pressure gradient, β_1, β_2 are the slip parameters on the left and right walls of the channel, respectively. α_{nf} and α_f are the thermal diffusivities of the nanofluid and base fluid, respectively, ϕ is the nanoparticle volume fraction, $A_1 = (1-\phi)^{2.5}\left[(1-\phi) + \phi\frac{\rho_s}{\rho_f}\right]$, $B_1 = \left[(1-\phi) + \phi\frac{(\rho\beta)_s}{(\rho\beta)_f}\right]$, $A_2 = (1-\phi)^{2.5}B_1$

The shearing stress and heat flux along the vertical channel walls can be calculated from

$$\tau_w = \mu_{nf}\left.\frac{\partial u}{\partial y}\right|_{y=\pm d}; q_w = \left.\left[-K_{nf}\frac{\partial T}{\partial y} + q^r\right]\right|_{y=\pm d}.$$

Thus, the skin friction coefficient $C_f = \frac{\tau_w}{\rho u_0^2}$ and the Nusselt number $Nu = \frac{q_w d}{K_f(T_2-T_1)}$ in non-dimensional form are given by

$$ReC_{f1} = U'(1); ReC_{f2} = U'(-1); Nu_{1,2} = -\left[\frac{K_{nf}}{K_f} + \frac{4}{3}Rd\right]\theta'(\eta)\Big|_{\eta=1,-1}$$

3 Results and Discussion

The non-dimensional Eqs. (8) and (9) along with boundary conditions (10) represent a system of coupled linear ordinary differential equations. The analytical solution has been found for this system of equations. A Copper– Water nanofluid is considered for the flow in the channel. The characteristic values of Cu nanoparticles are given in Table 1. The velocity $U(\eta)$ and temperature $\theta(\eta)$, skin friction coefficient and Nusselt number profiles are calculated and shown in Figs. 2, 3, 4, 5, 6, 7, 8, 9, 10, 11, 12, 13, 14, 15, 16, 17 and 18 for various values of ϕ, Rd, β_1, β_2.

Table 1 Thermophysical properties of base fluid and nanoparticles

Physical property	Base fluid (water)	Copper
C_p (J/kg K)	4179	385
ρ (kg/m^3)	997.1	8933
K (W/m K)	0.613	401
$\beta \times 10^{-5}$ (K^{-1})	21	1.67

Figures 2, 3 and 4 show the effects of nanoparticle volume fraction and slip parameters on the velocity profile. An increase in ϕ causes a decrease in velocity. This is due to the increase in density of the fluid, which is by an increase in concentration of nanoparticles. The slip parameter β_2 acts on the right wall of the channel and hence has a greater influence at $\eta = 1$, but its influence decreases near the left wall of the channel. A similar phenomenon is observed for β_1. The slip parameter β_1 acts on the left wall of the channel and hence, has a greater influence at $\eta = -1$, but its influence decreases near the right wall of the channel.

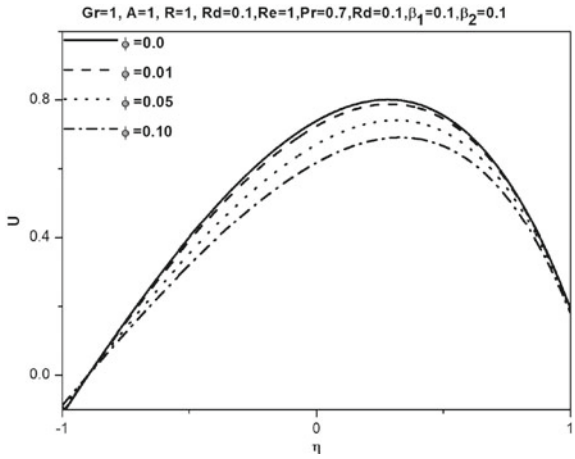

Fig. 2 Effect of ϕ on velocity

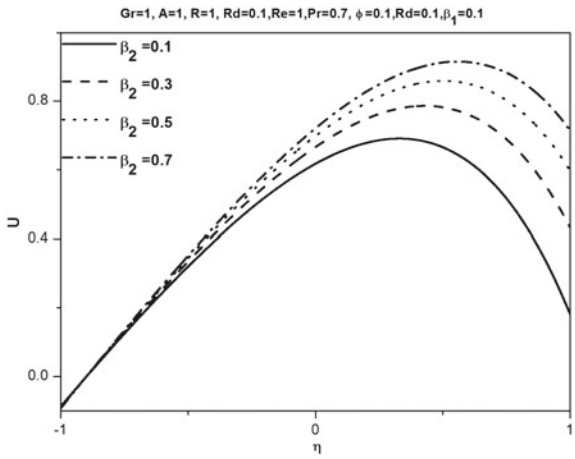

Fig. 3 Effect of β_2 on velocity

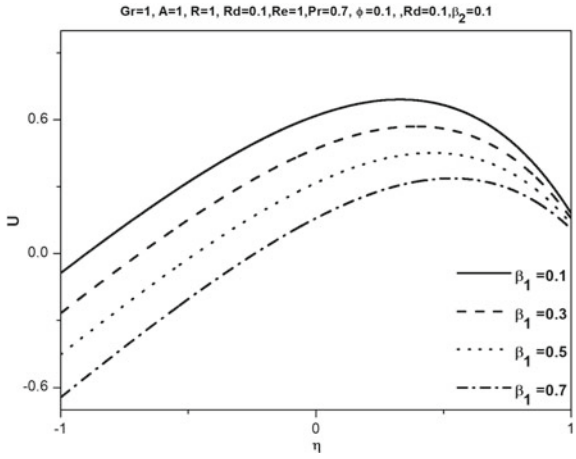

Fig. 4 Effect of β_1 on velocity

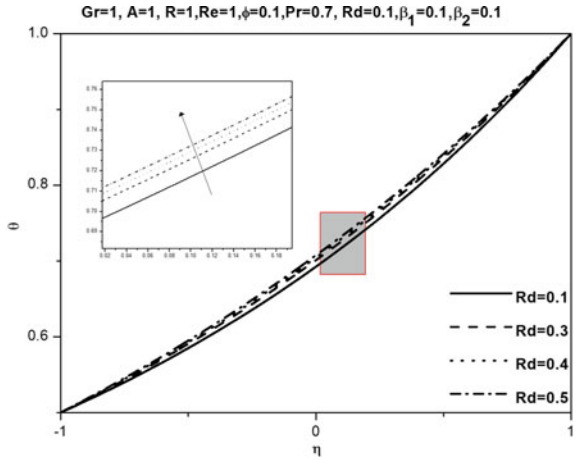

Fig. 5 Effect of Rd on temperature

Figures 5 and 6 depict the effects of radiation parameter and nanoparticle volume fraction on the temperature profile. An increase in the radiation parameter causes an increase in temperature profile. This is due to the increase in heat energy toward the fluid flow. An increase in nanoparticle volume fraction also causes an increase in temperature profile.

Figures 7, 8, 9 and 10 exhibit the influence of $Rd\phi$, β_1, β_2 on the skin friction on the left side of the channel wall. An increase in the radiation parameter causes the skin friction to increase. An increase in nanoparticle volume fraction also causes a decrease in skin friction. An increase in the slip parameters also causes skin friction to increase. This is due to the increase in drag at the wall.

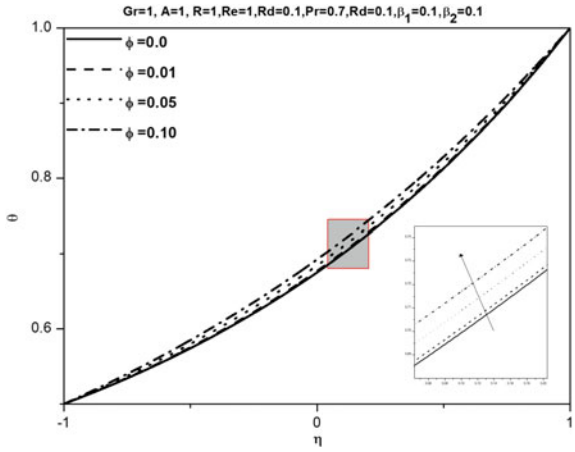

Fig. 6 Effect of ϕ on temperature

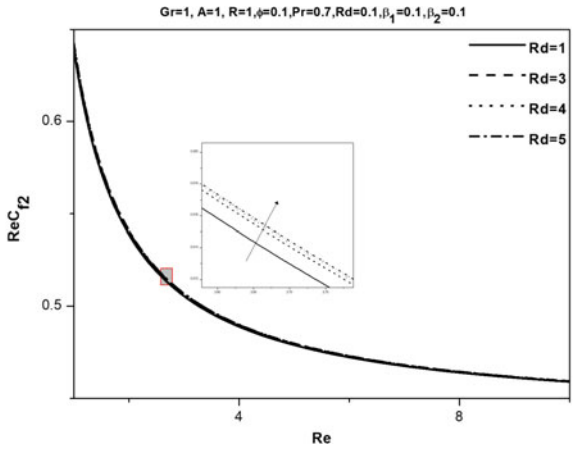

Fig. 7 Effect of Rd on skin friction

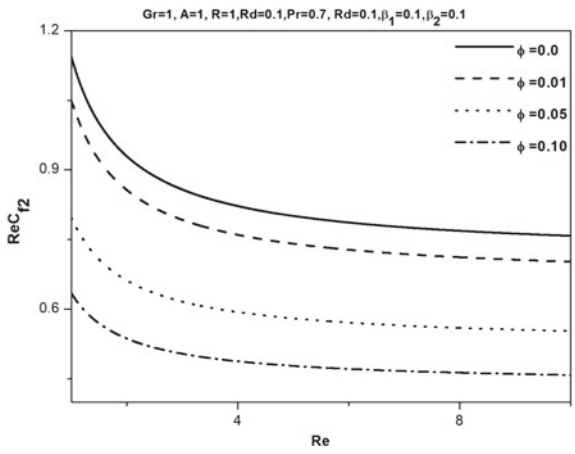

Fig. 8 Effect of ϕ on skin friction

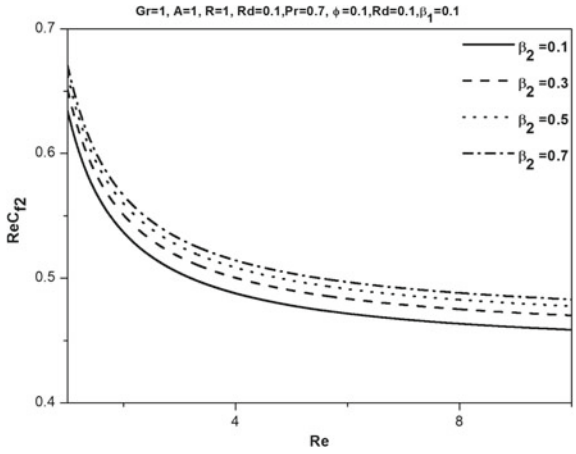

Fig. 9 Effect of β_2 on skin friction

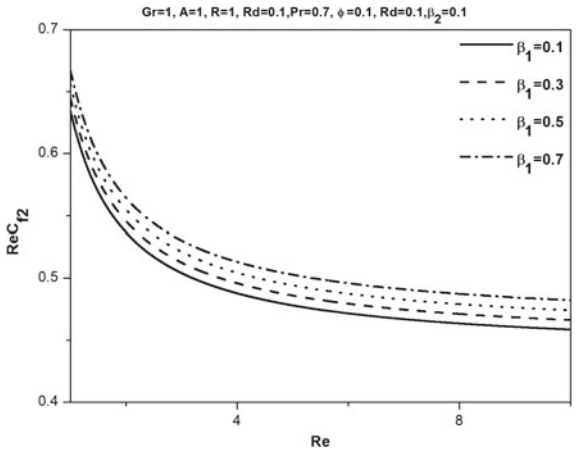

Fig. 10 Effect of β_1 on skin friction

Figures 11, 12, 13 and 14 show the effects of $Rd\phi$, β_1, β_2 on the skin friction on the right side of the channel wall. An increase in the radiation parameter causes a slight decrease in the skin friction. While an increase in nanoparticle volume fraction causes the skin friction to increase. An increase in the slip parameters also causes skin friction to increase. This is due to the increase in drag at the wall as well.

Figures 15, 16, 17 and 18 show the effects of radiation parameter and nanoparticle volume fraction on the Nusselt number. Both cause the Nusselt number to decrease, which is due to the increase in thermal conductivity with an increase in both the radiation parameter and nanoparticle volume fraction.

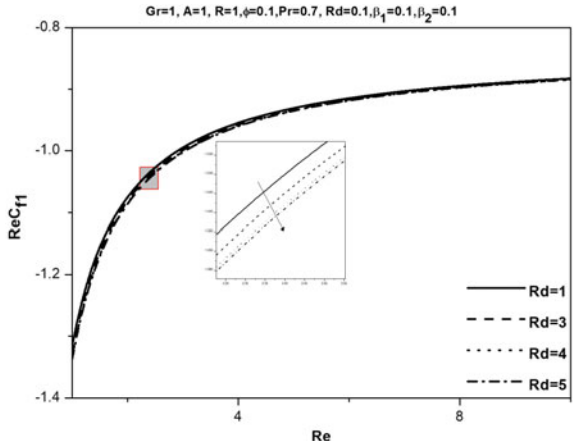

Fig. 11 Effect of Rd on skin friction

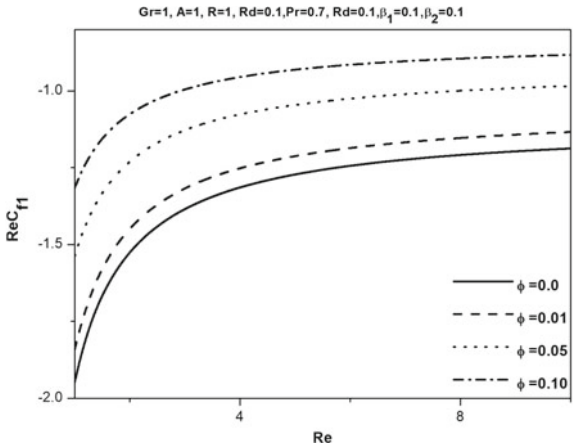

Fig. 12 Effect of ϕ on skin friction

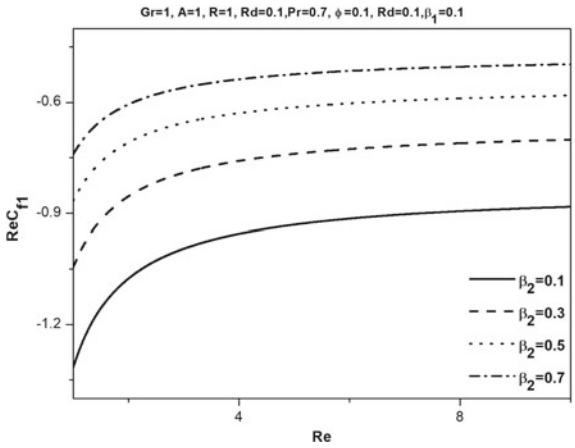

Fig. 13 Effect of β_2 on skin friction

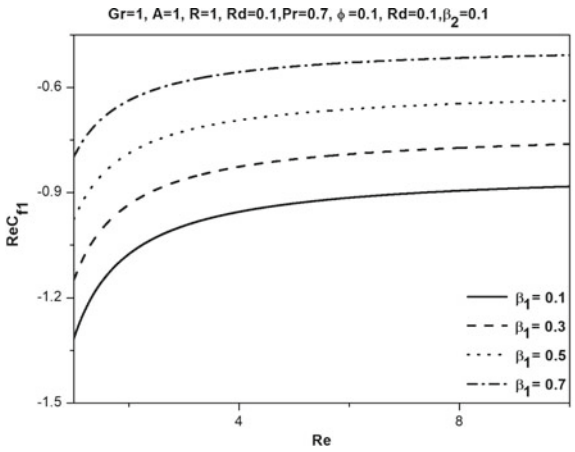

Fig. 14 Effect of β_1 on skin friction

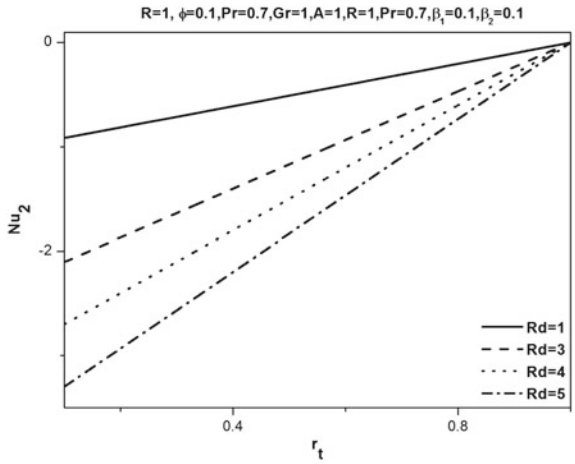

Fig. 15 Effect of Rd on Nusselt number

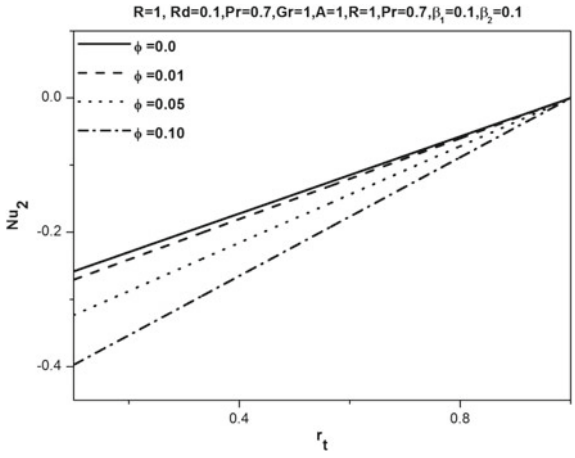

Fig. 16 Effect of ϕ on Nusselt number

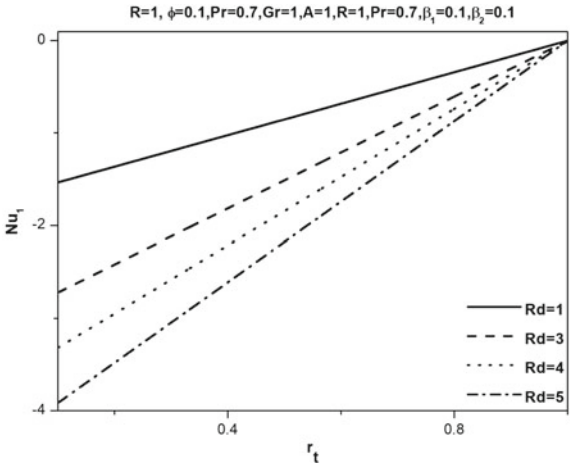

Fig. 17 Effect of Rd on Nusselt number

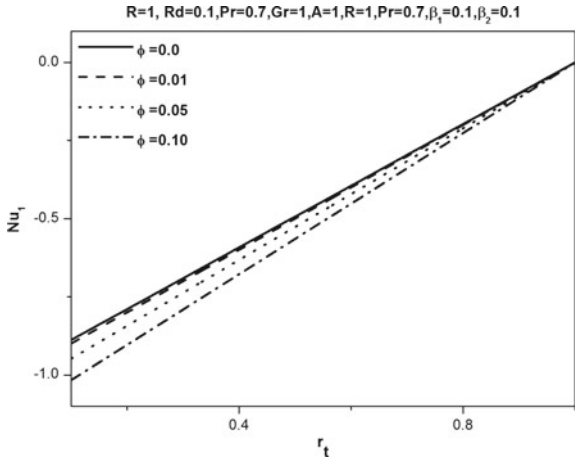

Fig. 18 Effect of ϕ on Nusselt number

4 Conclusion

In this paper, the flow of Cu–water nanofluid along a vertical channel has been studied. Special emphasis has been given to the effects of thermal radiation, nanoparticle volume fraction, and the Navier slips.

- It was seen that as the nanoparticle volume fraction increases, the velocity decreases.
- The dimensionless velocity profile increases on the left side of the wall, while it increases on the right side of the wall as the slip increases.
- The dimensionless temperature profile increases slightly as the radiation parameter and nanoparticle volume fraction are increased.

– The skin friction decreases on the left side of the wall, while it increases on the right side when an increase in the nanoparticle volume fraction is seen.
– The skin friction increases on the left side of the wall, while it decreases on the right side when the radiation parameter is increased.
– As the slip parameter is increased, the skin friction increased on the both sides of the wall.
– The Nusselt number decreases on the wall as the radiation parameter increases.
– When the nanoparticle volume fraction was increased, the Nusselt number was observed to decrease.

References

1. Choi, S.U.S.: Enhancing thermal conductivity of fluids with nanoparticles. Dev. Appl. Non-Newtonian Flows **231**(66), 99–105 (1995)
2. Navier, C.L.M.H.: M emoire sur les lois du mouvement des fluides. M emoires de l'Acad emie Royale des Sciences de l'Institute de France **VI**, 389–440 (1823)
3. Mooney, M.: Explicit formulas for slip and fluidity. J. Rheol. **2**, 210–222 (1931). https://doi.org/10.1122/1.2116364
4. Rao, I.J., Rajagopal, K.R.: The effect of the slip boundary condition on the flow of fluids in a channel. Acta Mechanica **135**, 113–126 (1999). https://doi.org/10.1007/BF01305747
5. Ebaid, A.: Effects of magnetic field and wall slip conditions on the peristaltic transport of a Newtonian fluid in an asymmetric channel. Phys. Lett. A **372**, 4493–4499 (2008). https://doi.org/10.1016/j.physleta.2008.04.031
6. Ullah, I., Shafie, S., Khan, I.: Effects of slip condition and Newtonian heating on MHD flow of Casson fluid over a nonlinearly stretching sheet saturated in a porous medium. J. King Saud Univ. Sci. **29**, 250–259 (2017). https://doi.org/10.1016/j.jksus.2016.05.003
7. Haq, S.U., Khan, I., Ali, F., Khan, A.,Abdelhameed, T.N.A.: Influence of slip condition on unsteady free convection flow of viscous fluid with ramped wall temperature. Abstr. Appl. Anal. **2015**(Article ID 327975), 7 pp. (2015). https://doi.org/10.1155/2015/327975
8. Sun, Q., Wu, Y., Liu, L., Wiwatanapataphee, B.: Study of a Newtonian fluid through circular channels with slip boundary taking into account electrokinetic effect. Abstr. Appl. Anal. **2013**(Article ID 718603), 9 pp. (2013). https://doi.org/10.1155/2013/718603
9. Kaladhar, K., Makinde, O.D.: Thermal radiation, Joule heating and Hall effects on mixed convective Navier slip flow in a channel with convective heating. Diffus. Found. **11**, 162–181 (2017). https://doi.org/10.4028/www.scientific.net/DF.11.162
10. Alam, Md.S., Alim, M.A., Khan, M.A.H.: Entropy generation analysis for variable thermal conductivity MHD radiative nanofluid flow through channel. J. Appl. Fluid Mech. **9**(3), 1123–1134 (2016). https://doi.org/10.18869/acadpub.jafm.68.228.24475
11. Dogonchi, A.S., Alizadeh, A., Ganji, D.D.: Investigation of MHD Go-water nanofluid flow and heat transfer in a porous channel in the presence of thermal radiation effect. Adv. Powder Technol. **28**(7), 1815–1825 (2017). https://doi.org/10.1016/j.apt.2017.04.022
12. Mohyud-Din, S.T., Jan, S.U., Khan, U., Ahmed, N.: MHD flow of radiative micropolar nanofluid in a porous channel: optimal and numerical solutions. Neural Comput. Appl. **29**(3), 793–801 (2018). https://doi.org/10.1007/s00521-016-2493-3
13. Buongiorno, B.: Convective transport in nanofluids. J. Heat Transf. **128**(3), 240–250 (2005). https://doi.org/10.1115/1.2150834
14. Tiwari, R.K., Das, M.K.: Heat transfer augmentation in a two-sided lid-driven differentially heated square cavity utilizing nanofluids. Int. J. Heat Mass Transf. **50**, 2002–2018 (2007). https://doi.org/10.1016/j.ijheatmasstransfer.2006.09.034

Heat Flow in a Rectangular Plate

M. Pavankumar Reddy and J. V. Ramana Murthy

Abstract Steady-state temperature distribution in a rectangular plane sheet with nonhomogeneous boundary conditions is solved using Fourier series. The results are compared with the numerical results. For different values of geometric ratio, the isothermal curves are obtained.

Keywords Temperature distribution · Isothermal lines · Fourier series

1 Introduction

The problem of steady-state temperature distribution is classical and very old, since the time of Laplace [1, 2]. Crank [3] in his treatise on Mathematics on diffusion has discussed some typical problems with homogeneous boundary conditions. The related problems involving the Laplacian equation in flow through channels of uniform cross-section were discussed by Langolois and Deville [4]. Recently analysis of heat flow in microchannels by theoretical and experimental studies is increasing due to their wide applications [5–8]. Lee et al. [9] presented the experimental study of heat flow in rectangular microchannels. Schmith and Kadlikar have discussed the pressure drop in a microchannel [10]. The problem of solving steady-state temperature when nonhomogeneous derivative boundary conditions are given, though classical, is not attempted by many analytically. Here, our aim is to solve this problem. The results of our paper are matched with the results of steady-state diffusion problem of Crank [3] when in the problem $q_2 = 0$, $T_2 = 0$ (pages 65–66).

M. Pavankumar Reddy (✉) · J. V. Ramana Murthy
Department of Mathematics, National Institute of Technology Warangal, Warangal 506004, Telangana, India
e-mail: mprnitw@gmail.com

D. Srinivasacharya and K. S. Reddy (eds.), *Numerical Heat Transfer and Fluid Flow*, Lecture Notes in Mechanical Engineering,
https://doi.org/10.1007/978-981-13-1903-7_26

2 Mathematical Formulation

Consider the case of conduction of heat in a rectangular plate with the two adjacent sides maintained at constant temperatures and with other two adjacent sides maintained at constant heat flux. The plate is insulated on the top and bottom surfaces so that heat will not escape. To find the temperature profiles in the plate, the Cartesian coordinate system is selected with origin at the left bottom corner of the plate with X and Y axes along the sides of the plate. The plate has sides of length a and H along X and Y directions. The temperature profiles in the plate follow heat conduction equation in steady state as given by

$$\nabla^2 T = 0 \tag{1}$$

subjected to the boundary conditions:

$$T = T_1 \text{ on } X = 0; T = T_2 \text{ on } Y = 0; k\frac{\partial T}{\partial X} = -Q_1 \text{ on } X = 1 \text{ and}$$
$$k\frac{\partial T}{\partial Y} = -Q_2 \text{ on } Y = \mathrm{H} \tag{2}$$

where T is the temperature in the plate at a point (x, y), k is the coefficient of thermal conductivity, and Q_1, Q_2 are heat fluxes imposed on the sides. The first two conditions in (2) are for constant temperatures and the last two conditions of (2) are for constant heat flux. We introduce the following non-dimensional scheme with capital on LHS as physical quantities and small letters on RHS as the corresponding nondimensional quantities:

$$X = ax; Y = ay;\ H = ha; Q_1 = \frac{q_1 k \Delta T}{a}; Q_2 = \frac{q_2 k \Delta T}{a} \text{ and } T = \Delta T.\theta + T_1$$
$$\text{where } \Delta T = T_2 - T_1 \tag{3}$$

Now, we have the non-dimensional equation as

$$\nabla^2 \theta = 0 \tag{4}$$
$$\text{subject to } \theta = 0 \text{ on } x = 0; \theta = 1 \text{ on } y = 0; \frac{\partial \theta}{\partial x} = q_1 \text{ on } x = 1 \text{ and}$$
$$\frac{\partial \theta}{\partial y} = q_2 \text{ on } y = h \tag{5}$$

Though it appears simple, it is difficult to solve (4) with conditions (5), since it involves an infinite system of equations. Again this method is useful in solving heat transfer with convection problems.

The solution of the problem can be obtained by two methods given below (Fig. 1).

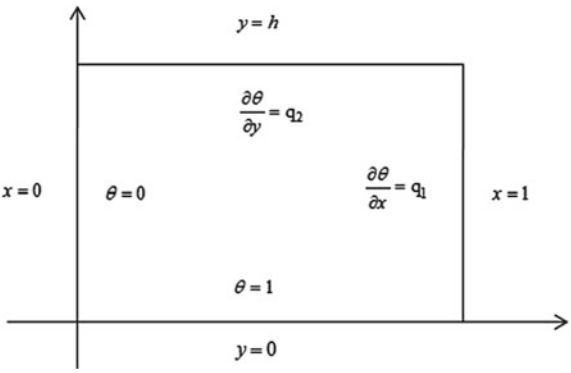

Fig. 1 Temperature distribution in a rectangular plate

3 Solution of the Problem

3.1 Method-1

We assume the solution in two parts such that the first part satisfies homogeneous conditions on $x = 0$ and $x = 1$ and the second part satisfies homogeneous conditions on $y = 0$ and $y = h$. The arbitrary constants in the general solution are adjusted such that the boundary conditions are satisfied for the solution. Hence, the solution is taken in the form as follows.

$$\theta = \sum_{n=1}^{\infty} \sin(n\pi x)[A_n \cosh(n\pi y) + B_n \sinh(n\pi y)] + \sin\left(\frac{n\pi y}{h}\right)\left[C_n \sinh\left(\frac{n\pi y}{h}\right) + D_n \cosh\left(\frac{n\pi y}{h}\right)\right] \tag{6}$$

From the condition (5), we get D_n=0
From the condition (5), we get $\sum_{n=1}^{\infty} A_n \sin(n\pi x) = 1$
Expanding $f(x) = 1$ on RHS in half range sine series over $0 \le x \le 1$, we get

$$A_n = \frac{4}{n\pi} \text{ if } n = (2m + 1) \text{ and } A_n = 0 \text{ if } n = 2m$$

From the condition (5), we have

$$\frac{\partial \theta}{\partial x} = \sum_{n=1}^{\infty} n\pi \left\{ \begin{array}{l} \cos(n\pi x)[A_n \cosh(n\pi y) + B_n \sinh(n\pi y)] \\ + \dfrac{C_n}{h} \sin\left(\dfrac{n\pi y}{h}\right) \cos h\left(\dfrac{n\pi x}{h}\right) \end{array} \right\} = q_1$$

This implies that

$$\sum_{n=1}^{\infty} n\pi \left\{ (-1)^n [A_n \cosh(n\pi y) + B_n \sinh(n\pi y)] + \frac{C_n}{h} \cosh(\frac{n\pi}{h}) \sin \frac{n\pi y}{h} \right\} = q_1 \tag{7}$$

Expanding q_1, $\cosh(n\pi y)$ and $\sinh(n\pi y)$ in half range sine series over $0 \le y \le h$, we get $q_1 = \sum_{n=1}^{\infty} A'_n \sin \frac{n\pi y}{h}$ which gives that $A'_n = q_1 A_n$ if n is odd and $A'_n = 0$ if n is even

$$\cosh(n\pi y) = \frac{2}{\pi} \sum_{m=1}^{\infty} \frac{m(1-(-1)^m \cosh(n\pi h))}{h^2 n^2 + m^2} \sin \frac{m\pi y}{h} = \sum_{m=1}^{\infty} c_{n,m} \sin \frac{m\pi y}{h}$$

$$\sinh(n\pi y) = \frac{2}{\pi} \sum_{m=1}^{\infty} \frac{m(-1)^{m+1} \sinh(n\pi h))}{h^2 n^2 + m^2} \sin \frac{m\pi y}{h} = \sum_{m=1}^{\infty} s_{n,m} \sin \frac{m\pi y}{h}$$

Substituting these above expressions in (7) and taking the coefficients of $\sin(n\pi y/h)$, we get

$$\frac{n\pi}{h} \cosh(\frac{n\pi}{h}) C_n = q_1 A_n - \sum_{m=1}^{\infty} (-1)^m m\pi (A_m c_{m,n} + B_m s_{m,n}) \tag{8}$$

Similarly, the condition (5) gives us

$$\frac{\partial \theta}{\partial y} = \sum_{n=1}^{\infty} n\pi \left\{ \sin n\pi x [A_n \sinh(n\pi h) + B_n \cosh(n\pi h)] + (-1)^n \frac{C_n}{h} \sinh\left(\frac{n\pi x}{h}\right) \right\} = q_2$$

Expanding q_2, $\sinh(n\pi x/h)$ in half range sine series, and collecting the coefficients of $\sin(n\pi x)$ on both sides we get

$$n\pi [A_n \sinh(n\pi h) + B_n \cosh(n\pi h)] = q_2 A_n - \sum_{m=1}^{\infty} m\pi (-1)^m \frac{C_m}{h} s1_{m,n} \tag{9}$$

where $\sinh\left(\frac{n\pi x}{h}\right) = \sum_{m=1}^{\infty} s1_{n,m} \sin(m\pi x)$

Equations (8) and (9) can be simplified by introducing the following notation:

$$A^*_n = \sinh(n\pi h) A_n,\ B^*_n = B_n \cosh(n\pi h),\ C^*_n = C_n \frac{n\pi}{h} \cosh\left(\frac{n\pi}{h}\right) \text{ and}$$

$$c^*_{m,n} = \frac{c_{m,n}}{\sinh(m\pi h)},\ s^*_{m,n} = \frac{s_{m,n}}{\cosh(m\pi h)},\ s1^*_{m,n} = \frac{s1_{m,n}}{\cosh(m\pi/h)}$$

Now, Eqs. (8) and (9) become

$$C^*_n = q_1 A_n - \sum_{m=1}^{\infty} (-1)^m m\pi (A^*_m c^*_{m,n} + B^*_m s^*_{m,n}) \tag{10}$$

and

$$q_2 A_n - n\pi\left(A_n^* + B_n^*\right) = \sum_{m=1}^{\infty} (-1)^m C_m^* s1_{m,n}^* \tag{11}$$

Substituting (10) in the Eq. (11), we get

$$\sum_{m=1}^{\infty} (-1)^m s1_{m,n}^* \left\{ q_1 A_m - \sum_{k=1}^{\infty} (-1)^k k\pi (A_k^* c_{k,m}^* + B_k^* s_{k,m}^*) \right\} = q_2 A_n - n\pi (A_n^* + B_n^*)$$

Rewriting this we get

$$\sum_{k=1}^{\infty} \left\{ \sum_{m=1}^{\infty} (-1)^{k+m} k\pi s_{k,m}^* s1_{m,n}^* \right\} B_k^* - \mathrm{n}\pi B_n$$
$$= -q_2 A_n + n\pi A_n^* + q_1 \sum_{m=1}^{\infty} (-1)^m s1_{m,n}^* A_m - \sum_{k=1}^{\infty} \sum_{m=1}^{\infty} (-1)^{k+m} k\pi c_{k,m}^* s1_{m,n}^* A_k^* \tag{12}$$

The first term on LHS within inner summation can be written as

$$bb_{k,n} = \sum_{m=1}^{\infty} (-1)^{k+m} k\pi s_{k,m}^* s1_{m,n}^*$$
$$= \frac{4knh^2}{\pi} \tanh(k\pi h) \sum_{m=1}^{\infty} \frac{(-1)^{k+n} \tanh\left(\frac{m\pi}{h}\right)}{\left(k^2h^2 + m^2\right)\left(m^2 + n^2h^2\right)} \text{ if } k \neq n$$

Thus Eq. (12) can be solved for B_n^* and then substituting B_n^* in (10) we get C_n^*. Now all the constants A_n, B_n, and C_n are known. Hence, the temperature can be computed from (6). By choosing $q_1 = 2$, $q_2 = 4$, the temperature profiles are obtained as below. We can observe that as n increases the solution converges more near to an exact solution. When we take only 5 terms (with each term containing 3 constants A_n, B_n, and C_n) in the series, we can find many discrepancies in the corners. As n increases, we get a good approximate solution at near to $n = 20$. But again, if n is more than 20, so many fluctuations will develop due to the multiplication of very large and very small numbers (Fig. 2).

3.2 Method-2

In this method, the solution is taken in two parts as $\theta = \theta_1 + \theta_2$. The part θ_1 satisfies Laplacian and boundary conditions on y. The conditions on x will be homogeneous. The part θ_2 satisfies the Laplacian and boundary conditions on x. The conditions on

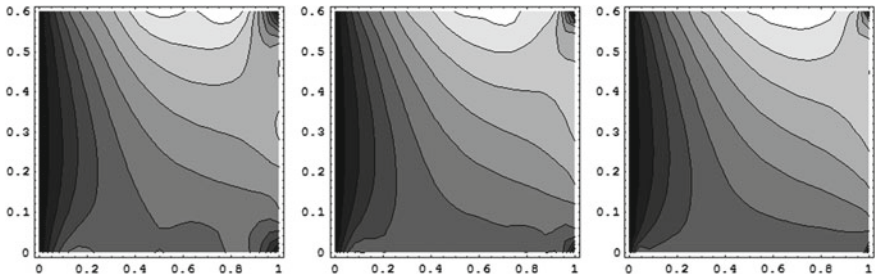

Fig. 2 Method-1 with 5, 10, and 20 terms

y will be homogeneous. Hence, θ satisfies all the boundary conditions. We assume the solution for

$$\nabla^2\theta = 0$$

with the conditions $\theta = 0$ on $x = 0; \theta = 1$ on $y = 0; \frac{\partial\theta}{\partial x} = q_1$ on $x = 1$ and $\frac{\partial\theta}{\partial y} = q_2$ on $y = h$ are split as

$$\begin{aligned} &\theta_1 = 0 \text{ on } x = 0 \quad \theta_2 = 0 \text{ on } x = 0 \\ &\tfrac{\partial\theta_1}{\partial x} = 0 \text{ on } x = 1 \quad \tfrac{\partial\theta_2}{\partial x} = q_1 \text{ on } x = 1 \\ &\theta_1 = 1 \text{ on } y = 0 \quad \theta_2 = 0 \text{ on } y = 0 \\ &\tfrac{\partial\theta_1}{\partial y} = q_2 \text{ on } y = h \quad \tfrac{\partial\theta_2}{\partial y} = 0 \text{ on } y = h \end{aligned}$$

The solution for θ_1, which satisfies homogeneous conditions on x, is taken as

$$\theta_1 = \sum_{n=1}^{\infty} \sin\frac{(2n+1)\pi x}{2}\left(A_n \cosh\frac{(2n+1)\pi y}{2} + B_n \sinh\frac{(2n+1)\pi y}{2}\right)$$

the constants A_n and B_n are found from the conditions on y as follows:

$$\theta_1 = 1 \text{ on } y = 0 \Rightarrow \sum_{n=1}^{\infty} A_n \sin\frac{(2n+1)\pi x}{2} = 1 \text{ for } 0 \le x \le 1$$

since $\sin((2n+1)\pi x/2)$ functions are orthogonal, we get

$$A_n = 2\int_0^1 \sin\frac{(2n+1)\pi x}{2} dx = \frac{4}{(2n+1)\pi}$$

again $\frac{\partial\theta_1}{\partial y} = q_2$ on $y = h$ which reduces to the following:

$$q_2 = \sum_{m=1}^{\infty} \frac{(2m+1)\pi}{2} \sin \frac{(2m+1)\pi x}{2} \left(A_m \sinh \frac{(2m+1)\pi h}{2} + B_n \cosh \frac{(2m+1)\pi h}{2} \right)$$

multiplying by $\sin((2n+1)\pi x/2)$ on both sides and then integrating with respect to x from 0 to 1, by orthogonal property of $\sin((2n+1)\pi x/2)$ functions, we get B_n as

$$B_n = \frac{q_2 A_n^2}{2} \operatorname{sech} \frac{(2n+1)\pi h}{2} - A_n \tanh \frac{(2n+1)\pi h}{2}$$

Now the solution for θ_2, which satisfies homogeneous conditions on y, is taken as

$$\theta_2 = \sum_{n=1}^{\infty} \sin \frac{(2n+1)\pi y}{2h} \left(C_n \sinh \frac{(2n+1)\pi x}{2h} + D_n \cosh \frac{(2n+1)\pi x}{2h} \right)$$

from the conditions on x, i.e., $\theta_2 = 0$ on $x = 0$ we get D_n=0 again since, $\frac{\partial \theta_2}{\partial x} = q_1$ on $x = 1$, we have

$$q_1 = \sum_{n=1}^{\infty} C_n \frac{(2n+1)\pi}{2h} \sin \frac{(2n+1)\pi y}{2h} \cosh \frac{(2n+1)\pi}{2h}$$

C_n's are obtained from the orthogonal property of $\sin((2n+1)\pi y/2h)$, as

$$C_n = \frac{h q_1 A_n^2}{2} \operatorname{sech} \frac{(2n+1)\pi}{2h}$$

Now combining the two solutions θ_1 and θ_2 we get the complete solution. It is computed numerically and presented below with n=20 number of terms in the solution. The solution is more close to the exact solution than the solution obtained in the first method. This problem is solved by five-point iterative formula by numerical method. The solution obtained at 3500 iterations is presented in Fig. 3.

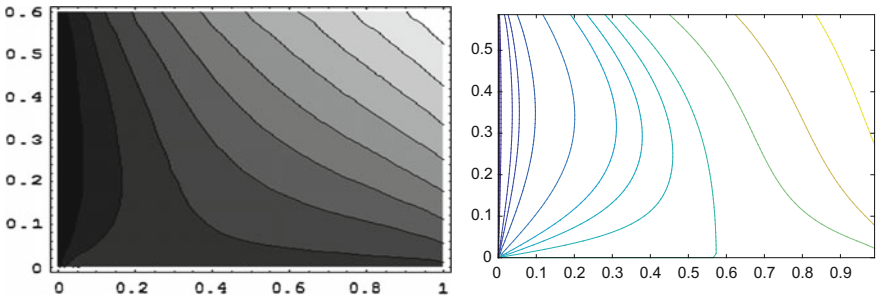

Fig. 3 Isothermal lines between Method-2 with 20 terms and by numerical method at 3500 iterations

4 Results and Discussions

The analytical solution is very fast converging with 20 terms and accurate enough whereas the numerical solution take hundreds of iterations even with Gauss-Seidel iterations and is not as accurate as an analytical solution. The effect of heat flux at the edges is shown below. When the ratio $q = q_1/q_2$ is very high as 200 (Fig. 4a), the isothermal lines are vertical. When $q = 0.1$ (Fig. 4b), the isothermal lines are

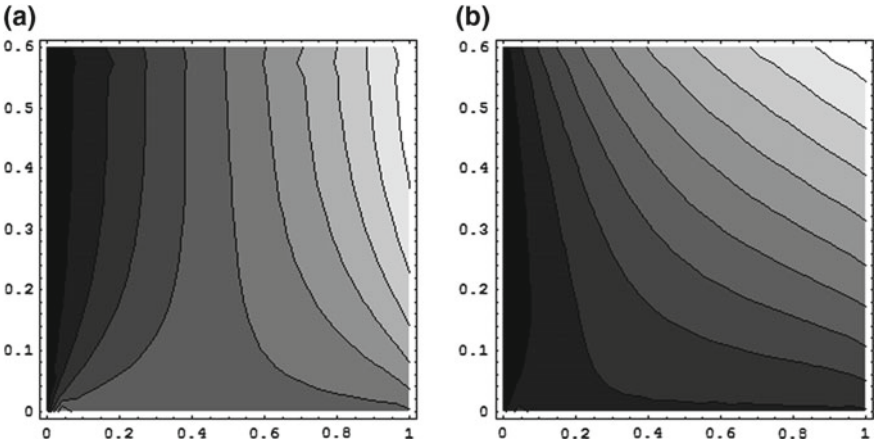

Fig. 4 **a** Isothermal lines for $q = 200$, **b** isothermal lines for and $q = 0.1$

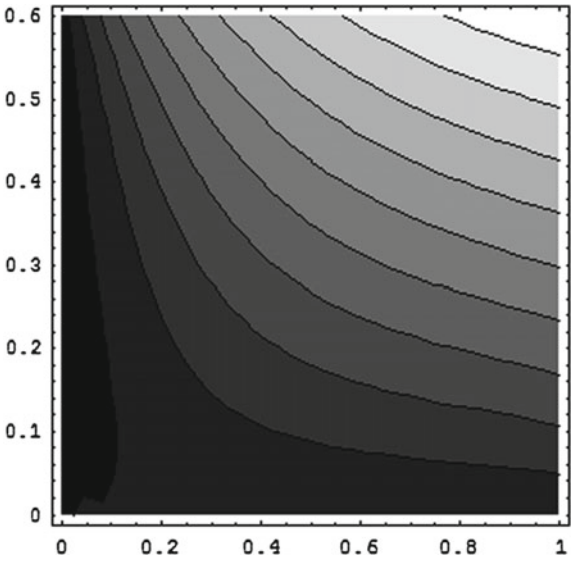

Fig. 5 Isothermal lines for $q = 0.001$

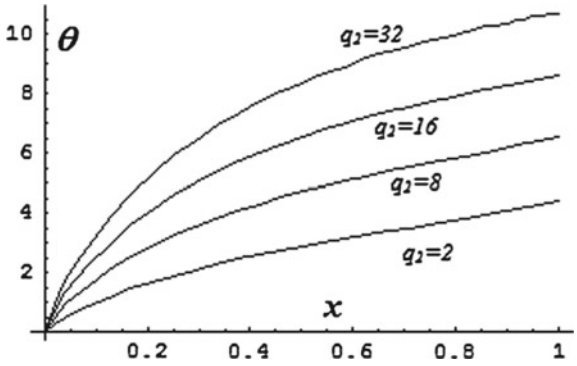

Fig. 6 Temperature at $y = h$

inclined with much variations near to down left corner and when $q = 0.001$ (Fig. 5), the isothermal lines are nearly parallel to the walls. In all the cases, there exists a small region of no heat flow zone at which the pattern changes its nature in direction of thermal flow.

In Fig. 6, temperature distribution at the top side of the plate is given. We notice that, as q_2, the heat flux increases, the temperature also increases.

References

1. Laplace, P.S.: Mémoire sur la théorie de l'anneau de Saturne. Academy of the History of Science, Paris (1787)
2. Laplace, P.S.: Méchanique Céleste, 4 vols. Bowditch, N. (trans.) Boston (1832)
3. Crank, J.: Mathematics of Diffusion Theory. Clarenden Press, Oxford University, Oxford (1975)
4. Langlois, W.E., Deville, M.O.: Slow Viscous Flows, 2nd edn. Springer, Switzerland (2014)
5. Van Male, P., de Croon, M.H.J.M., Tiggelaar, R.M., Van den Berg, A., Schouten, J.C.: Int. J. Heat Mass Transf. **47**, 87–99 (2004)
6. Shokouhmand, H., Jomeh, S.: In: Proceedings of the World Congress on Engineering, vol II (2007)
7. Khan, W.A., Yovanovich, M.M.: In: Proceedings of IPACK 2007. InterPACK'07. ASME (2007)
8. Mirmanto, D.B.R., Kenning, J.S.L., Karayiannis, T.G.: J. Phys.: Conf. Ser. **395,** 012085 (2012)
9. Lee, P.-S., Garimella, S.V., Liu, D.: CTRC Research Publications Paper 7, vol. 48, Issue 9, pp. 1688–1704, April 2005
10. Schmitt, D.J., Kandlikar, S.G.: In: Proceedings of ICMM 2005. Toronto, Ontario, Canada (2005)

Flow of Blood Through a Porous Bifurcated Artery with Mild Stenosis Under the Influence of Applied Magnetic Field

G. Madhava Rao, D. Srinivasacharya and N. Koti Reddy

Abstract The effect of porous medium on blood flow through an artery with bifurcation and a mild stenosis in the parent lumen under the influence of an applied magnetic field is investigated in the present work. Blood is taken to be couple stress fluid. The arterial division is assumed to be symmetrical. The governing equations for flow of blood are reduced to non-dimensional and a particular mapping is used to make a well-shaped boundary. The developed system of equations is solved numerically using the finite difference scheme. The variation of physical quantities near the apex is analyzed graphically with pertinent parameters.

Keywords Blood flow · Stenosis · Bifurcated artery · Porous medium

1 Introduction

The main cause to develop cardiovascular diseases is related to the characteristics of blood flow and the mechanical behaviour of the arterial walls. The formation of fatty material on the inner wall of the artery is medically termed as "stenosis". The deposition of fatty material, in general, occurs at the entrances of bifurcation of the arteries [1]. Gupta [2] studied the fluid–structure interaction in the carotid artery. The couple stress fluids theory was introduced by Stokes [3]. Srinivasacharya and

G. Madhava Rao (✉)
Department of Mathematics, KL University, R.V.S Nagar, Moinabad Road, Near AP Police Academy, Aziz Nagar, Hyderabad 500075, Telangana, India
e-mail: rao.gmr.madhav@gmail.com

D. Srinivasacharya
Department of Mathematics, National Institute of Technology, Warangal 506004, Telangana, India

N. Koti Reddy
Department of Mathematics, Anurag Engineering College, Kodad 508206, Telangana, India

D. Srinivasacharya and K. S. Reddy (eds.), *Numerical Heat Transfer and Fluid Flow*, Lecture Notes in Mechanical Engineering,
https://doi.org/10.1007/978-981-13-1903-7_27

Madhava Rao [4] studied the effect of couple stress fluid parameters on blood flow through bifurcated artery.

The behaviour of fluid flow through porous media is an important one because some mass of the fluid is stored in the pores present in the media. Chaturvedi et al. [5] investigated the flow of blood through a porous medium with the influence of the magnetic field.

The liquid carriers work as magnetic particles, which are suspended in blood flow serve as drug carriers to the diseased place. The influence of magnetic field on the couple stress fluid flow through bifurcated artery has been studied by Srinivasacharya and Madhava Rao [6]. The influence of suction and injection on saturated micropolar fluid flow through the porous medium has been investigated by Ram Reddy and Pradepa [7].

This article deals with the flow of couple stress fluid through a bifurcated artery by treating walls as porous plates.

2 Mathematical Formulation

Consider the flow of blood in a bifurcated artery with mild stenosis in its parent artery by treating the walls of the artery as porous plates. Blood is treated to be couple stress fluid. The stenosis and bifurcation of the artery are taken to be in an axisymmetric manner as shown in Fig. 1. The cylindrical polar coordinate system is considered for frame of reference in which z-axis is taken along the central line of the parent artery. In order to eliminate the flow separation zones, deflection is initiated at the start of the lateral junction and the apex.

The governing equations for the flow of incompressible couple stress fluid under the influence of uniform transverse magnetic field in the porous medium is given by

$$\nabla \cdot \boldsymbol{q} = 0 \tag{1}$$

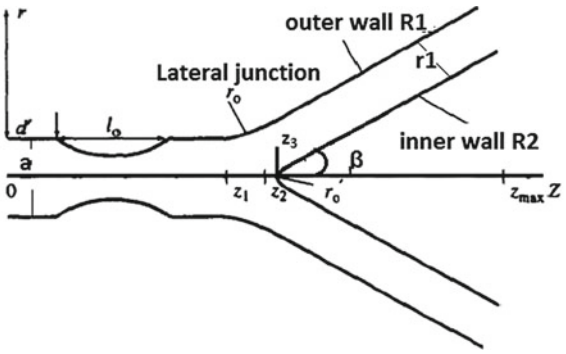

Fig. 1 Oversimplified diagram of the bifurcated artery with stenosis

$$\rho(\boldsymbol{q}\cdot\nabla)\boldsymbol{q} = -\nabla p + \mu\nabla^2\boldsymbol{q} - \eta\nabla^4\boldsymbol{q} - \frac{\mu}{k}\boldsymbol{q} + \bar{J}\times\bar{B} \tag{2}$$

where η—couple stress viscosity parameter, μ—dynamic viscosity of blood, ρ—density of blood, $\boldsymbol{q}$—velocity vector, $\bar{B}$—strength of magnetic field, $\bar{J}$—current density, κ—permeability parameter of porous medium and the body force and body moments are neglected.

Simplified bifurcated artery with stenosis mathematically given by Murthy [8] is as follows:

$$R_1(z) = \begin{cases} a, \quad 0 \le z \le d' \quad \text{and} \quad d' + l_0 \le z \le z_1 \\ (a - \frac{4\varepsilon}{l_0^2}(l_0(z-d') - (z-d')^2),\ d' \le z \le d' + l_0 \\ (a + r_0 - \sqrt{r_0^2 - (z-z_1)^2}), \qquad z_1 \le z \le z_2 \\ (2r_1 \sec\beta + (z-z_2)\tan\beta), \qquad z_2 \le z \le z_{\max} \end{cases} \tag{3}$$

$$R_2(z) = \begin{cases} 0, & 0 \le z \le z_3 \\ \sqrt{(r_o')^2 - (z - z_3 - r_o')^2}, & z_3 \le z \le z_3 + r_o'(1-\sin\beta) \\ (r_o'\cos\beta + z_4), & z_3 + r_o'(1-\sin\beta) \le z \le z_{\max} \end{cases} \tag{4}$$

where $R_1(z), R_2(z)$ represents the outer and inner walls, r_1 and a, respectively, stands for the radius of daughter and parent artery, β is the 50% of the bifurcation angle, l_0 is length of the stenosis at a distance d' from the origin, ε denotes the maximum height of the stenosis at $z = d' + \frac{l_0}{2}$, and $z_{\max}$ represents the maximum length of the artery.

The associated boundary conditions are

$$\left.\begin{array}{l} \frac{\partial w}{\partial r} = 0,\ \frac{\partial^2 w}{\partial r^2} - \frac{\sigma}{r}\frac{\partial w}{\partial r} = 0,\ \text{on } r = 0 \text{ for } 0 \le z \le z_3 \\ w = 0,\ \frac{\partial^2 w}{\partial r^2} - \frac{\sigma}{r}\frac{\partial w}{\partial r} = 0,\ \text{on } r = R_1(z) \text{ for all } z \\ w = 0,\ \frac{\partial^2 w}{\partial r^2} - \frac{\sigma}{r}\frac{\partial w}{\partial r} = 0,\ \text{on } r = R_2(z) \text{ for } z_3 \le z \le z_{\max} \end{array}\right\} \tag{5}$$

where $\sigma = \eta'/\eta$—couple stress fluid parameter which is liable for the consequence of local viscosity of particles apart from the bulk viscosity of the fluid μ. If $\eta' = \eta$, the influence of couple stresses will be absent in the fluid, which signify that couple stress tensor is symmetric. In this case, the couple stresses are absent on the inner and outer walls of the bifurcated artery (Eq. 5).

All the variables are not dependent of θ, because the flow is treated to be symmetric about *z-axis*. Therefore, velocity is $\boldsymbol{q} = (u(r,z), 0, w(r,z))$. Now Eq. (2) in nondimensional form as

$$\left[\frac{\partial^2}{\partial r^2}+\frac{1}{r}\frac{\partial}{\partial r}\right]w-\frac{1}{\alpha^2}\left[\frac{\partial^2}{\partial r^2}+\frac{1}{r}\frac{\partial}{\partial r}\right]^2 w+\left(\frac{1}{k}+H^2\right)w=\frac{dp}{dz} \tag{6}$$

where $\alpha^2=\frac{\mu a^2}{\eta}\alpha^2=\frac{\mu a^2}{\eta}$ is couple stress fluid parameter, $H=B_0 a\sqrt{\frac{\sigma_1}{\mu}}$ is Hartmann number. The effect of outer and inner walls of the boundary can be conveyed into the ruling equations and boundary conditions by the following radial coordinate transformation by $\xi=\frac{r-R_2}{R}$, where $R=R_1-\mathrm{R}_2$. Therefore, Eqs. (5) and (6) take the form

$$\left.\begin{aligned}&\tfrac{1}{\alpha^2}\tfrac{\partial^4 w}{\partial\xi^4}+\tfrac{2R}{\alpha^2(\xi R+R_2)}\tfrac{\partial^3 w}{\partial\xi^3}-\left[1+\tfrac{1}{\alpha^2(\xi R+R_2)^2}\right]R^2\tfrac{\partial^2 w}{\partial\xi^2}\\&+\left[\tfrac{1}{\alpha^2(\xi R+R_2)^3}-\tfrac{1}{(\xi R+R_2)}\right]R^3\tfrac{\partial w}{\partial\xi}+(\tfrac{1}{k}+H^2)R^4 w=-R^4\tfrac{dp}{dz}\end{aligned}\right\} \tag{7}$$

The reduced boundary condition in the new coordinate system is

$$\left.\begin{aligned}&\tfrac{\partial w}{\partial\xi}=0,\ \ \tfrac{\partial^2 w}{\partial\xi^2}-\tfrac{\sigma R}{(\xi R+R_2)}\tfrac{\partial w}{\partial\xi}=0,\ \ \text{on } \xi=0 \text{ for } 0\le z\le z_3\\&w=0,\ \ \tfrac{\partial^2 w}{\partial\xi^2}-\tfrac{\sigma R}{(\xi R+R_2)}\tfrac{\partial w}{\partial\xi}=0,\ \ \text{on } \xi=1 \text{ for all } z\\&w=0,\ \ \tfrac{\partial^2 w}{\partial\xi^2}-\tfrac{\sigma R}{(\xi R+R_2)}\tfrac{\partial w}{\partial\xi}=0,\ \ \text{on } \xi=0 \text{ for } z_3\le z\le z_{max}\end{aligned}\right\} \tag{8}$$

The rate of flow along the parent (Q_p) and daughter arteries (Q_d) are calculated by using

$$Q_\mathrm{p}=2\pi R\left[R\int_0^1 \xi w d\xi+R_2\int_0^1 w d\xi\right] \text{ and } Q_\mathrm{d}=\pi R\left[R\int_0^1 \xi d\xi+R_2\int w d\xi\right] \tag{9}$$

The resistance to the flow in both the arteries is determined using

$$(\lambda_\mathrm{p})_i=\left|\frac{z_3\frac{dp}{dz}}{Q_\mathrm{p}}\right| \text{for } z<z_3 \quad \text{and} \quad (\lambda_\mathrm{d})_i=\left|\frac{(z_{\max}-z_3)\frac{dp}{dz}}{Q_\mathrm{d}}\right| \text{for } z\ge z_3 \tag{10}$$

The shear stress is determined by using

$$\tau_{ij}=\frac{1}{R}\frac{\partial w}{\partial\xi}+\frac{1}{4R\alpha^2(\xi R+R_2)^2}\frac{\partial w}{\partial\xi}-\frac{1}{4\alpha^2R^3}\frac{\partial}{\partial\xi}\left(\frac{\partial^2 w}{\partial\xi^2}\right)-\frac{1}{4R^2\alpha^2(\xi R+R_2)}\frac{\partial^2 w}{\partial\xi^2} \tag{11}$$

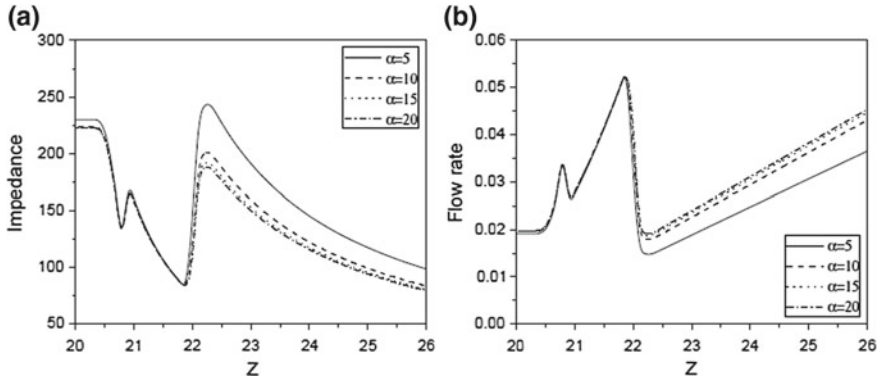

Fig. 2 Influence of α on **a** resistance to the flow and **b** rate of flow on both sides of the apex for fixed values of other parameters

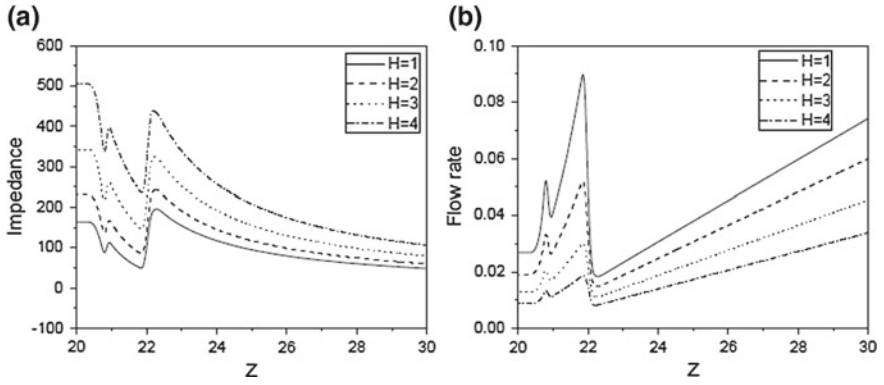

Fig. 3 Influence of H on **a** resistance to the flow and **b** rate of flow on both sides of the apex for fixed values of other parameters

3 Results and Discussion

Equations (7) and (8) are solved numerically using the finite difference scheme. We used the following data: $a = 0.5$ cm, $d' = 1$ cm, $l0 = 0.5$ cm, $\beta = \pi/10$, $r_1 = 0.51$a, $\varepsilon = 2$.

The effect of α on resistance to the flow and rate of flow in both sides of the flow divider is shown in Fig. 2a, b. It is noticed from these figures that resistance to the flow is low and rate of flow is more for greater values of α on both sides of the apex.

Figure 3a, b illustrates the effect of magnetic parameter H on resistance to the flow and rate of flow on both sides of the apex. From these figures, it is identified that resistance to the flow is rising and the rate of flow is falling with an enhancement in the value of H.

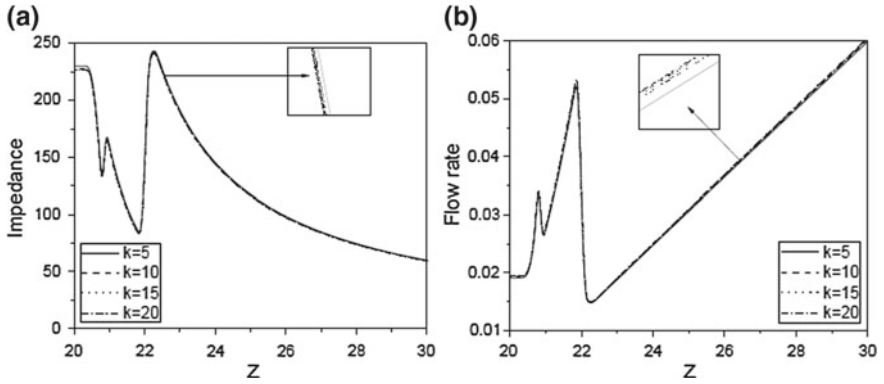

Fig. 4 The effect of κ on **a** resistance to the flow and **b** rate of flow on both sides of the apex for fixed values of other parameters

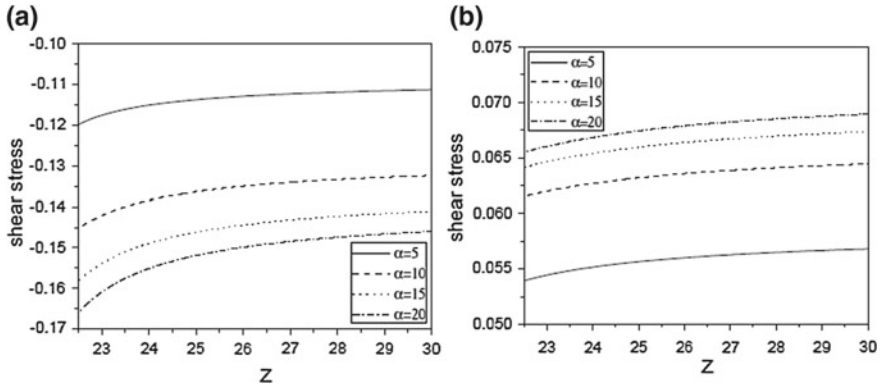

Fig. 5 The effect of α on shear stress along the **a** inner and **b** outer walls of the daughter artery for fixed values of other parameters

The variations of resistance to the flow and flow rate with κ near the flow divider are depicted in Fig. 4a, b. It is noticed from these figures that resistance to the flow is low and flow rate is more with an increased value of κ near the apex.

Figures 5a, b illustrates the effect of α on shear stress along the inner and outer walls of the daughter artery. These figures explore that shear stress is diminishing and advancing along the inner and outer walls of the daughter artery with an increase in the value of α.

Figure 6a, b, respectively, explore the effect of Knudsen number κ on shear stress along the walls of the daughter artery. It is seen from these figures that shear stress is reducing along the inner wall and increasing along the outer wall with an advanced value of κ.

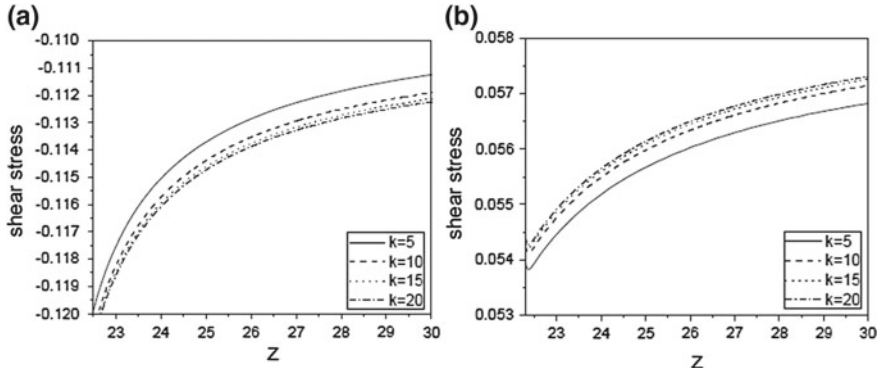

Fig. 6 Influence of Knudsen number κ on shear stress along the **a** inner and **b** outer walls of the daughter artery

4 Conclusions

The results of the work concluded the following points, which are important in biomedical engineering and medical sciences.

1. The rate of flow raised with a raise in the value of α, H and diminished with an increase in the value of κ.
2. The resistance to the flow decreased with a raise in the value of α, H and increased with a raise in the value of κ.
3. The shear stress is getting down with better values of α and κ along the inner wall of daughter artery. But, along the outer wall of the daughter artery shear stress getting better for increased values of α and κ.

References

1. Mlneo Motomiya, M.D., Karino, T.: Flow patterns in the human carotid artery bifurcation. Stroke 15(1), 50–56 (1984)
2. Gupta, A.K.: Performance and analysis of blood flow through carotid artery. Int. J. Eng. Bus. Manag. **3**, 1–6 (2011)
3. Stokes, V.K.: Couple stesses in fluids. Phys. Fluids **9**, 1709–1715 (1966)
4. Srinivasacharya, D., Madhava Rao, G.: Mathematical model for blood flow through a bifurcated artery using couple stress fluid. Math. Biosci. **278**, 37–47 (2016)
5. Chaturvedi, R., Shrivastav, R.K., Vinay Kumar, J.: Blood flow in presence of magnetic field through porous medium and its effect on heat transfer rate. Int. J. Adv. Comput. Math. Sci. **3**(2), 266–271 (2012)
6. Srinivasacharya, D., Madhava Rao, G.: Computational analysis of magnetic effects on pulsatile flow of couple stress fluid through a bifurcated artery. Comput. Methods Programs Biomed. **137**, 269–279 (2016)

7. RamReddy, Ch., Pradeepa, T.: The effect of suction/injection on free convection in a micropolar fluid saturated porous medium under convective boundary condition. Procedia Eng. **127**, 235–243 (2015)
8. Sachin, S., Rama SubbaReddy, G., Murthy, P.V.S.N., Ng, C.O.: Pulsatile Casson fluid flow through a stenosed bifurcated artery. Int. J. Fluid **36**(1), 43–63 (2009)

Finite Element Model to Study the Effect of Lipoma and Liposarcoma on Heat Flow in Tissue Layers of Human Limbs

Mamta Agrawal and K. R. Pardasani

Abstract Heat transfer processes play a very important role in the thermal control system of the human body in order to maintain the structure and function of human body organs. Any physical or physiological disorder can influence the heat transfer processes leading to disorder in the thermal control system. The impact of various disorders on heat transfer processes in human body organs is still not well understood. In this paper, a model is proposed to study the effect of benign and malignant disorders on heat transfer processes in an elliptical-shaped human limb. The processes like heat conduction, metabolic heat generation, and convective heat transfer by blood perfusion are incorporated in the model. A tumor is considered to be present in the human limb which may be benign or malignant. The benign and malignant tumors considered here are lipoma and liposarcoma, respectively. The finite element method has been employed to obtain the solution. The numerical results have been obtained by using MATLAB and are used to compute the temperature profiles in the region.

Keywords Finite element method · Human limb · Heat transfer · Benign · Malignant · Fat tissues

1 Introduction

The assessment of heat transfer processes in human body organs in terms of thermal response due to various physical and physiological conditions is of vital interest to biomedical technologists and scientists for its applications in real-world problems of mining, deep sea mining, space mission, sports, military operations, and health and medical sciences. In view of the above, modeling of heat transfer processes in human body tissues has gained interest among the mathematicians, scientists, and engineers

M. Agrawal (✉)
SASL, Mathematics Department, VIT Bhopal University, Bhopal 466114, MP, India
e-mail: mamta_agrawal2311@yahoo.co.in

K. R. Pardasani
Department of Mathematics, MANIT, Bhopal 462051, MP, India

D. Srinivasacharya and K. S. Reddy (eds.), *Numerical Heat Transfer and Fluid Flow*, Lecture Notes in Mechanical Engineering,
https://doi.org/10.1007/978-981-13-1903-7_28

since the past few decades. Various physical and physiological processes like blood flow, metabolic activity, thermal conduction, convection, radiation, and evaporation are responsible for the thermal behavior of tissues and thermoregulation as a whole, which regulates the thermal response of the body with the environment. The heat control system of a human body maintains the body core at an almost uniform temperature of 37 °C by achieving a balance between heat generation within the body cells and heat loss from body surface to the environment. The skin and deep tissues play an important role in the transport of heat from the body core to the body surface from where the heat is lost to the environment. Any abnormality like the presence of tumors in the skin and deep tissues of human body organs can cause thermal disturbances in the body organs.

Several investigations have been made by various research workers to study one-dimensional heat flow in human organs [1, 2]. Also, attempts have been made to study the temperature distribution in dermal regions of spherical and cylindrical human organs for two-dimensional cases [3, 4]. Many researchers [5, 6] have studied temperature distribution in the skin and subcutaneous region of human organs with and without tumor. Agrawal et al. [7, 8] have studied temperature distribution in elliptical-shaped human limbs for two-, and three-dimensional steady-state cases by using FEM, seminumerical, and cubic splines approaches under normal and abnormal conditions.

No attempt is reported for the study of thermal disturbances due to tumors of fat tissues like lipoma and liposarcoma in deep tissues of a human limb. In this paper, a model is proposed to study the heat flow in tissue layers of a human limb due to benign and malignant tumors in fat tissue layers.

2 Mathematical Model

The human limb has been modeled as a layered structure, consisting of a bone layer, a muscle layer, a fat layer, and a skin layer as shown in Fig. 1. The bone layer has been assumed as a core of the human limb. The FEM analysis is carried out for a two-dimensional model by dividing the whole region into 24 coaxial sectoral elements. The lipoma tumor (0.005 m) is assumed in the fat layer of about 0.0401 m above the core (bone) of the limb between $\upsilon = \pi/4$ to $\nu = \pi/2$ near the trunk. It is also assumed that after some period of time, fat layer thickness increases by 0.01 m and lipoma grows in size and forms a cancerous tumor liposarcoma, twice that of lipoma [9].

In an elliptical-shaped limb, the bioheat equation [10] for a two-dimensional steady-state case is given by

$$K_i \frac{1}{d_i^2\left(\sin h^2 \mu_i + \sin h^2 \mathrm{v}_i\right)}\left[\frac{\partial}{\partial \mu_i}\left(\frac{\partial T_i}{\partial \mu_i}\right) + \frac{\partial}{\partial \upsilon_i}\left(\frac{\partial T_i}{\partial \upsilon_i}\right)\right] + \rho_{\mathrm{b}} c_{\mathrm{b}} m_{\mathrm{b}}(T_{\mathrm{b}} - T_i) + \bar{S}_i + W = 0 \tag{1}$$

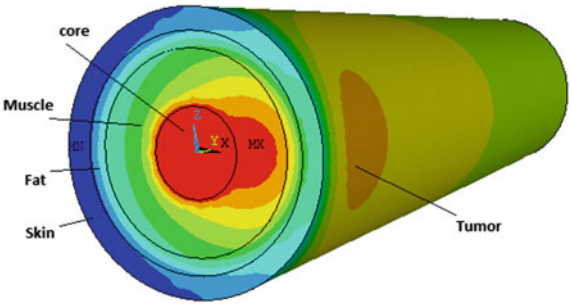

Fig. 1 Layered model of human limb with liposarcoma tumor in the fat layer

where ρ_b, c_b, m_b, T_b, and S denote the density, specific heat, blood perfusion rate, the temperature of the blood and metabolic heat generation, respectively. In Eq. (1), i denotes the specific skin layer.

Here, d_i is the eccentricity of the outer layer which is the function of radius of tissue layers, i.e., $d_i = f(\mu_i)$ and $\bar{S}_i$ is the self-controlled metabolic heat generation rate per unit volume and W is the rate of uncontrolled metabolic heat generation. Also, $W = 0$ for the normal tissues and $W = \eta S_1$ for the malignant tissues. The η denotes the ratio of metabolic heat generation in malignant and normal tissues. The malignant tissues have higher rates of metabolic heat generation. Here, blood perfusion and metabolic heat generation are assumed to be 3 times for benign lipoma and 6 times for malignant liposarcoma than that in the normal skin tissues [11].

The initial and boundary conditions are as follows.

Along angular (ν) direction [7],

$$T_{i0} = a_1 + a_2\nu + a_3\nu^2;\ i = \alpha \text{ when } \nu = 0 \text{ and } \nu = 2\pi;\ i = \beta \text{ when } \nu = \pi \tag{2}$$

where $T_{\alpha 0}$ and $T_{\beta 0}$, respectively, are the temperatures of the sides of the limb where major arteries and veins are present.

At the outer surface of the limb [12].

$$-K\frac{\partial T}{\partial \eta} = h(T - T_a) + LE \tag{3}$$

where h, T_a, L, E, and $\frac{\partial T}{\partial \eta}$ are heat transfer coefficient, atmospheric temperature, latent heat, rate of evaporation, and partial derivatives of T along the normal to the skin surface, respectively. The variational form of Eq. (1) with boundary conditions in Eqs. (2) and (3) are evaluated and assembled to obtain the following:

$$I = \sum_{e=1}^{24} I^{(e)} \tag{4}$$

Equation (4) can be written as follows in the linear system of equations:

Table 1 The thermal properties of body tissues before and after increasing fat layer thickness [14]

Tissue layer	μ_n (m)	K_n (W m^{-1} K^{-1})	ρ (kg/m^3)	c (J kg^{-1} K^{-1})	$m_b(10^{-3})$ (1/s)	S_n (W/m^3)
Bone	0.0153	0.75	1357	1700	0.0	0.0
Muscle	0.0343	0.42	1085	3768	2.7	684
Fat	0.0401	0.16	850	2300	0.08	58
Skin	0.0418	0.47	1085	3680	1.26	368
Tumor (benign) (malignant)	0.005 (0.010)	0.558	1030	3582	3.00 (6.00)	1104 (2208)

$$XT = Y \tag{5}$$

where X, T, Y are matrices of order 32×32, 32×1 and 32×1, respectively.

3 Results and Discussion

The metabolic activity in tumors varies with type and size of tumors which may be benign or malignant. The metabolic activity in tumor varies between 0 and 7 times than in normal tissues [8]. Some investigators have reported that metabolic activity in a malignant tumor is 3–20 times [13]. Further, for the larger tumor, the metabolic activity in a malignant tumor is found to be 20–200 times of that in normal tissues [13]. The present study is performed for the two types of uniformly perfused tumors of fat namely lipoma a benign tumor and liposarcoma a malignant tumor. We initially assume that fat layer contains lipoma of metabolic activity 0–3 times that of normal tissues and the same tumor after some period of time becomes malignant as liposarcoma with metabolic activity 5–10 times that of normal tissues. The purpose here is to differentiate between lipoma and liposarcoma. A computer program has been developed and the system of Eq. (5) is solved using the Gaussian elimination method to obtain nodal temperatures $T_k = 1(1)32$. The thermal properties of tissue layers are presented in Table 1 [14].

The different graphs have been plotted for the temperature distribution in various tissue layers of human limbs with and without tumor. In Figs. 2 and 3, we observe elevation in temperature profiles between $v = \pi/4$ and $v = \pi/2$ due to presence of lipoma tumor for $T_a = 15\,^{\circ}\text{C}$, $\eta = 3$ and $E = 0.0\,\text{kg/m}^2$ min. We also observe the change in the slope of the curve at the junction of normal and benign tissue is at $v = \pi/4$ to $v = \pi/2$. The maximum elevation is observed between $v = \pi/4$ and $v = \pi/2$. The elevation in temperature profiles is observed in the tumor region and the effect of tumor on temperature distribution decreases as we move away from the tumor to the outer surface. In Fig. 4, we observe an elevation in temperature profiles between $v = \pi/4$ and $v = \pi/2$ due to the presence of liposarcoma tumor for $\text{T}_\text{a} = 15^{\circ}\,\text{C}$,

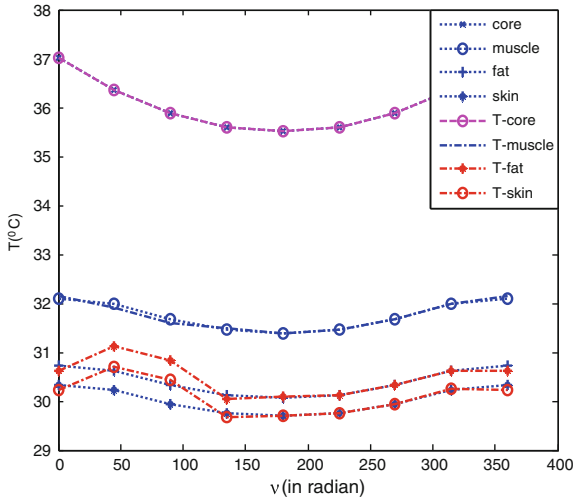

Fig. 2 Temperature distribution angular direct for $T_a = 15\,^{\circ}\mathrm{C}$, $E = 0.0\,\mathrm{kg/m^2\,min}$ $\eta = 3$

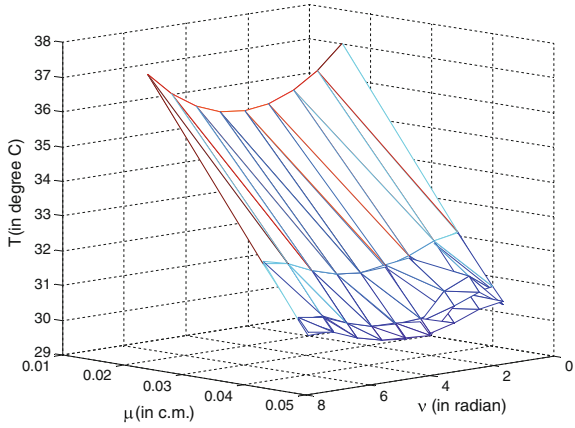

Fig. 3 Temperature distribution along radial and angular direction for $T_a = 15\,^{\circ}\mathrm{C}$, $\eta = 3$

$\eta = 10$ and $E = 0.0\,\mathrm{kg/m^2}$ min. We also observe the change in the slope of curves at the junction of normal and malignant tissues at $\nu = \pi/4$ to $\nu = \pi/2$. The maximum elevation is observed between $\upsilon = \pi/4$ and $\upsilon = \pi/2$. Figure 5 shows radial and angular temperature distribution due to the presence of malignant liposarcoma tumor for $T_a = 15\,^{\circ}\mathrm{C}$ and $\eta = 10$. The elevation in temperature profile is observed in the tumor region and the effect of tumor on temperature distribution decreases as we move away from the tumor to the outer surface.

Thus, the results obtained here give us the clear picture about the distinction between benign (lipoma) and malignant (liposarcoma) tumors on the basis of thermal information generated from the proposed model. Further, the change in the slope of the curves at the boundaries of the tumor gives us the idea about boundary, location,

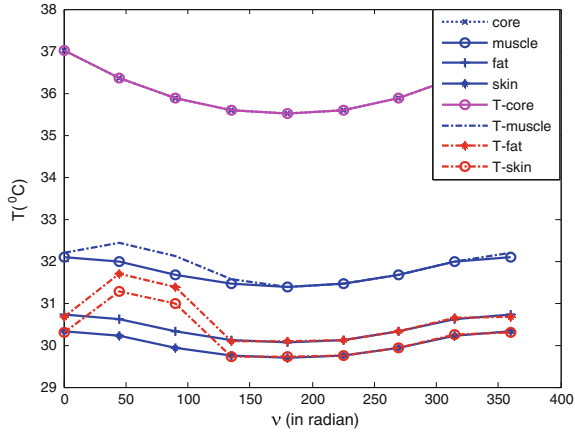

Fig. 4 Temperature distribution along the angular direction for $T_a = 15\,^{\circ}\mathrm{C}$, $\eta = 10$

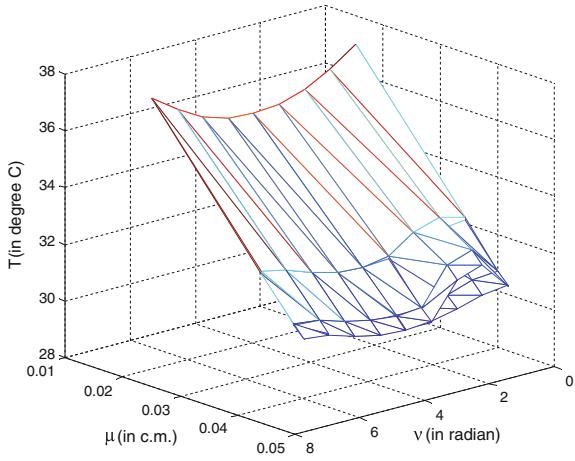

Fig. 5 Temperature distribution along radial and angular direction for $T_a = 15\,^{\circ}\mathrm{C}$, $\eta = 10$

and size of the tumor. This information is useful to biomedical scientists for the development of protocols and diagnosis of malignant tumors.

4 Conclusion

The proposed thermal model is able to predict temperature distribution in the normal and abnormal deep tissues of elliptical-shaped human limb. The model is also able to generate the thermal responses due to fat thickness below the skin layer, heat exchange with the environment, heat generation rate, blood perfusion, and fatty-tumor-like lipoma and liposarcoma in human limbs. The finite element method has proved to be quite versatile and effective in the present study. The thermal responses

by the proposed model are able to provide a clear distinction between lipoma and liposarcoma in human limbs.

Acknowledgements We are highly thankful to the Department of Science and Technology (DST), New Delhi for providing financial support under the Women Scientist-A (WOS-A) project no. SR/WOS-A/MS-04/2012 (G). DST, New Delhi for carrying out this work.

References

1. Saxena, V.P., Arya, D.: Steady state heat distribution in epidermis, dermis and sub dermal tissues. J. Theor. Biol, **89**, 423–432 (1981)
2. Saxena, V.P.: Temperature distribution in human skin and subdermal tissues. J. Theor. Biol **102**, 277–286 (1983)
3. Gurung, D.B., Saxena, V.P., Adhikary, P.R.: Transient temperature in human dermal part with protective layer at low atmospheric temperature. Int. J. Biomath. **3**(4), 439–451 (2009)
4. Akshara, M., Adlakha, N.: Two dimensional finite element model of temperature distribution in dermal tissues of extended spherical organs of a human body. Int. J. Biomath. **6**(1), 1250065–1250074 (2013)
5. Saxena, V.P., Pardasani, K.R.: Effect of dermal tumor on temperature distribution in skin with variable blood flow. Bull. Math. Biol. **53**(4), 525–536 (1991) (USA)
6. Adlakha, N., Pardasani, K.R.: Exact solution to a heat flow problem in peripheral tissue layers with a solid tumor in dermis. Ind. J. Pure Appl. Math. **22**(8), 679–682 (1991)
7. Agrawal, M., Adlakha, N., Pardasani, K.R.: Finite element model to study thermal effect of uniformly perfused tumor in dermal layers of elliptical shaped human limb. Int. J. Biomath. **4**(2), 241–254 (2011)
8. Agrawal, M., Adlakha, N., Pardasani, K.R.: Finite element model to study the thermal effect of tumors in dermal regions of irregular tapered shaped human limbs. Int. J. Thermal Sci. **98**, 287–295 (2015)
9. Krandorf, M.J., Bancroft, L.W., Peterson, J.J., Murphey, M.D., Foster, W.C., Temple, H.T.: Imaging of fatty tumors distinction of lipoma and well-differentiated liposarcoma. Radiology, **224**, 99–104 (2002)
10. Pennes, H.: Analysis of tissue and arterial blood temperature in the resting human forearm. J. Appl. Physiol. **1**(2), 93–122 (1948)
11. Kandala, S.K., Deng, D., Herman, C.: Simulation of discrete blood vessel effects on the thermal signature of a melanoma lesion. In: ASME Proceeding, Biomedical and Biotechnology Engineering, vol. 3B, pp. 15–21. San Diego, California, USA, Nov 2013
12. Mitchell, J.W., Galvez, T.L., Hengle GEM, J., Siebercker, K.L.: Thermal response of human legs during cooling. J. Appl. Physiol. **29**(6), 859–865 (1970) (USA)
13. Agyingi, E., Wiandt, T., Maggelakis, S.: Thermal detection of a prevascular tumor embedded in breast tissue. Math. Biosci. Eng. MBE **12**(5), 907–915 (2015)
14. Fiala, D., Lomas, K.J., Stohrer, M.: A computer model of human thermoregulation for a wide range of environmental conditions, the passive system. J. Appl. Physiol. **87**(5), 1957–1972 (1999)

Effects of Thermal Stratification and Variable Permeability on Melting over a Vertical Plate

M. V. D. N. S. Madhavi, Peri K. Kameswaran and K. Hemalatha

Abstract In the present paper, we studied the effect of thermal stratification with variable permeability and melting on mixed convective heat transfer from a vertical plate in a non-Darcy porous medium. The various physical parameters entering into the problem on dimensionless velocity, temperature, and Nusselt number were discussed graphically. Using similarity variables, the partial differential equations are transformed to ordinary differential equations and are solved using MATLAB bvp4c solver numerically.

Keywords Melting · Thermal stratification · Variable permeability · Heat transfer · Mixed convection

1 Literature Review

The various aspects of convective flow and heat transfer from a vertical plate in a non-Darcy porous medium with the effects of melting and variable permeability were explored by many researchers [1–11] owing to lot of industrial and biological applications such as magma solidification, energy storage systems, geothermal extraction, oil recovery, nuclear reactors, and hyperthermia treatment and so on. In this context, Kameswaran et al. [12] found that the heat transfer rate increases with an increase in the values of melting with variable permeability.

M. V. D. N. S. Madhavi (✉)
Department of Mathematics, Krishna University, Machilipatnam 521002, Andhra Pradesh, India
e-mail: mvdnsmadhavi71@gmail.com

P. K. Kameswaran
Department of Mathematics, School of Advanced Sciences, VIT, Vellore 632014, Tamil Nadu, India

K. Hemalatha
Department of Mathematics, V. R. Siddhartha Engineering College, Vijayawada 520007, Andhra Pradesh, India

D. Srinivasacharya and K. S. Reddy (eds.), *Numerical Heat Transfer and Fluid Flow*, Lecture Notes in Mechanical Engineering,
https://doi.org/10.1007/978-981-13-1903-7_29

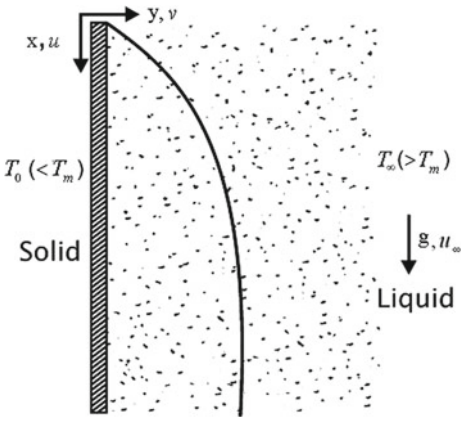

Fig. 1 Schematic diagram

Also, the effect of thermal stratification of the medium plays an important role in heat transport process but much work is not published. Researchers [13–17] studied convective transport from a vertical plate in a thermally stratified porous medium with different power function forms. Most of the researchers mentioned the above-presented effect of thermal stratification without considering the effect of variable permeability. Hence, in this paper, we made an attempt to analyze the effects of thermal stratification on melting with variable permeability in a non-Darcy porous medium.

2 Mathematical Formulation

Consider a vertical melting front at the melting point T_m. Coordinate system x-y is attached to the melting front as shown in Fig. 1. The melting front is modeled as a vertical plate. This plate constitutes the interface between the liquid and solid phases during melting inside the porous matrix. The temperature of the solid region is T_0 and liquid phase temperature is T_∞. A vertical boundary layer smoothens the transition from T_m to T_∞. By taking into consideration, the effects of thermal stratification and melting with Variable permeability, the governing equations with boundary conditions for steady non-Darcy flow in a porous medium can be stated as follows:

$$\frac{\partial u}{\partial x} + \frac{\partial v}{\partial y} = 0 \tag{1}$$

$$u + \frac{C_f \sqrt{K}}{\nu} u^2 = -\frac{K}{\mu}\left(\frac{\partial P}{\partial x} + \rho g\right) \tag{2}$$

$$v + \frac{C_f \sqrt{K}}{\nu} v^2 = -\frac{K}{\mu}\frac{\partial P}{\partial y} \tag{3}$$

$$u\frac{\partial T}{\partial x}+v\frac{\partial T}{\partial y}=\frac{\partial}{\partial y}\left(\alpha\frac{\partial T}{\partial y}\right), \tag{4}$$

where density

$$\rho=\rho_\infty\beta(T-T_\infty) \tag{5}$$

$$T=T_m, k_{\text{eff}}\frac{\partial T}{\partial y}=\rho\left[h_{sf}+C_s(T_m-T_0)\right]v \text{ at } y=0\, u=u_\infty,\ T\to T_\infty \text{ at } y\to\infty, \tag{6}$$

where u and v are velocity components in x and y directions, respectively. C_f is the Forchheimer constant, K is the permeability of porous medium, v is the kinematic viscosity, g is the acceleration due to gravity, β is the thermal expansion coefficient, T is temperature, α is the effective thermal diffusivity of the porous medium, and C_p is the specific heat at constant pressure. The subscripts, m is the melting and ∞ is the ambient condition).

Under these assumptions, invoking the Boussinesq approximations, Eqs. (2)–(5) become

$$\frac{\partial u}{\partial y}+\frac{C_f}{\upsilon}\left[2\sqrt{K}u\frac{\partial u}{\partial y}+\frac{u^2}{2\sqrt{K}}\frac{\partial K}{\partial y}\right]\pm\frac{g\beta}{\upsilon}\left[K\frac{\partial T}{\partial y}+(T_\infty-T_m)(\theta-1)\frac{\partial K}{\partial y}\right]=0 \tag{7}$$

$$u\frac{\partial T}{\partial x}+v\frac{\partial T}{\partial y}=\frac{\partial}{\partial y}\left(\alpha\frac{\partial T}{\partial y}\right). \tag{8}$$

The variation of permeability $K(\eta)$ and the porosity $\varepsilon(\eta)$ are taken as

$$K(\eta)=K_\infty\left(1+be^{-\eta}\right) \text{ and } \varepsilon(\eta)=\varepsilon_\infty\left(1+de^{-\eta}\right) \tag{9}$$

By Chandrasekhara et al. [8], the permeability and porosity are, respectively, K_∞, ε_∞ and b, d are constants $\eta=\frac{y}{x}\sqrt{Pe_x}$,

$$\alpha=\lambda_m/\left(\rho_\infty C_p\right)_f \tag{10}$$

where

$$\lambda_m=\lambda_f\varepsilon+(1-\varepsilon)\lambda_s. \tag{11}$$

Using Eqs. (9) and (11)

$$\alpha=\alpha_\infty\left[\varepsilon_\infty\left(1+d\mathrm{e}^{-\eta}\right)+\sigma\left\{1-\varepsilon_\infty\left(1+de^{-\eta}\right)\right\}\right]. \tag{12}$$

Introduce the stream function $\psi(x, y)$ such that $u = \frac{\partial \psi}{\partial y}$, $v = -\frac{\partial \psi}{\partial x}$, where $\psi = \alpha_\infty \sqrt{Pe_x} f(\eta)$,

$$u = u_\infty f' \text{ and } v = -\frac{\alpha_\infty}{2x}\sqrt{Pe_x}\left[f - \eta f'\right]. \tag{13}$$

The temperature is represented by $T = T_m + (T_\infty - T_m)\theta(\eta)$,

$$T_\infty = T_{\infty,0} + Ax^{\frac{1}{3}}. \tag{14}$$

Using Eqs. (7), (8), (13) and (14) are transformed into the following boundary value problem.

$$f'' + F\sqrt{1 + be^{-\eta}} f' f'' - \frac{F}{4}\frac{be^{-\eta}}{\sqrt{1 + be^{-\eta}}} f'^2 \pm \frac{Ra}{Pe}\left[\left(1 + be^{-\eta}\right)\theta' - be^{-\eta}(\theta - 1)\right] = 0 \tag{15}$$

$$\left[\varepsilon_\infty(1 - \sigma)\left(1 + de^{-\eta}\right) + \sigma\right]\theta'' + \varepsilon_\infty de^{-\eta}(\sigma - 1)\theta' + \frac{1}{2} f\theta' - f'\theta\varepsilon_1 = 0 \tag{16}$$

$$f(0) + 2M\theta'(0) = 0,\ f'(\infty) \to 1,\ \theta(0) = 0,\ \theta(\infty) \to 1, \tag{17}$$

where dash represents differentiation with respect to η. The involved variables in the above expressions (15)–(17) are non-Darcy parameter F, Local Rayleigh number Ra_x, Local Peclet number Pe_x, and thermal stratification parameter ε_1, which are defined as

$$F = \frac{2C_f\sqrt{K_\infty u_\infty}}{\nu},\ Ra_x = \frac{K_\infty \rho_\infty g\beta\Delta T x}{\mu\alpha_\infty},$$
$$Pe_x = \frac{u_\infty x}{\alpha_\infty},\ \varepsilon_1 = \frac{1}{\Delta T}\frac{A}{3}x^{\frac{1}{3}},\ \varepsilon_1 = \frac{A}{3n},$$

where $T_\infty - T_m = nx^{\frac{1}{3}}$.

3 Heat Transfer Coefficient

$$q_w = -k_{\text{eff}}\left(\frac{\partial T}{\partial y}\right)_{y=0}. \tag{18}$$

The rate of transfer from the surface of the plate is given by

$$N\,u_x = \frac{x\,q_w}{k_{\text{eff}}(T_\infty - T_m)}. \tag{19}$$

Using Eqs. (18) and (19), the local Nusselt number is defined as $\frac{N\,u_x}{\sqrt{Pe_x}} = -\theta'(0)$.

4 Graphs and Discussions

In this problem, we studied, the effects of melting and thermal stratification with variable permeability on convective heat transfer from a vertical plate in a non-Darcy porous medium.

Figure 2 depicts velocity profiles for melting values ranging from $M = 0$ to 2 with variable permeability. Increase in velocity profile is observed with and without stratification parameter. But the increment is more in the absence of stratification parameter. The effects of thermal stratification and melting on temperature profile with variable permeability are shown in Fig. 3. It can be noted that with the increase in melting values, the temperature near the plate decreases in the presence and absence of stratification parameter. But the increase in temperature is high in the presence of stratification parameter than in its absence. Figure 4 illustrates the effect of thermal stratification on velocity profile with melting and variable permeability. We noted that an increase in stratification parameter decreases the velocity profile. In Fig. 5 with variable permeability and melting, the effect of thermal stratification on temperature profile is shown. It is observed that by increasing the stratification parameter, the temperature profile also increases. The variation of heat transfer rate with melting in the presence and absence of variable permeability is presented in Figs. 6 and 7.

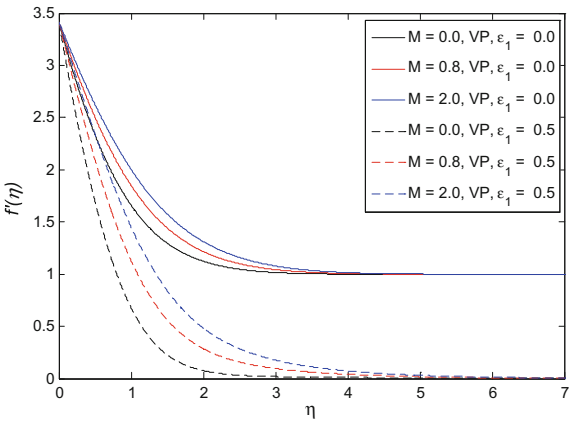

Fig. 2 Thermal stratification and melting effects on velocity profile for $F = 0.5$, $Ra/Pe = 2$, $\varepsilon_\infty = 0.4$, $\sigma = 2$, $b = 3$, $d = 1.5$

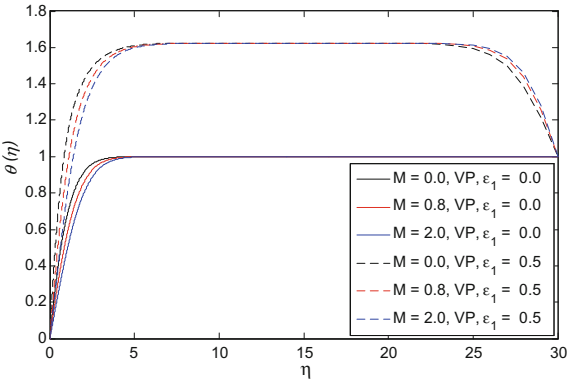

Fig. 3 Thermal stratification and melting effects on temperature profile for $F = 0.5$, $Ra/Pe = 2$, $\varepsilon_\infty = 0.4$, $\sigma = 2$, $b = 3$, $d = 1.5$, $M = 2$

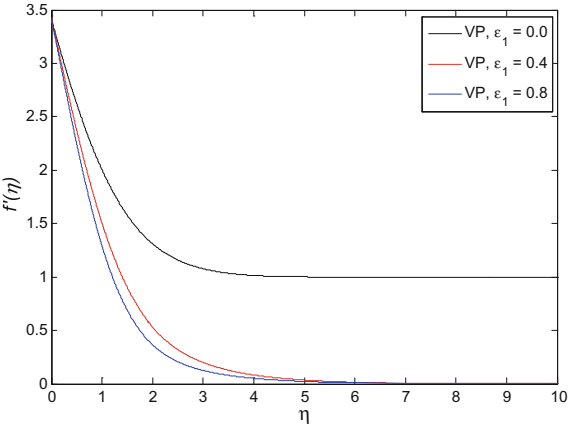

Fig. 4 Thermal stratification and variable permeability effects on velocity profile for $F = 0.5$, $Ra/Pe = 2$, $\varepsilon_\infty = 0.4$, $\sigma = 2$, $b = 3$, $d = 1.5$, $M = 2$

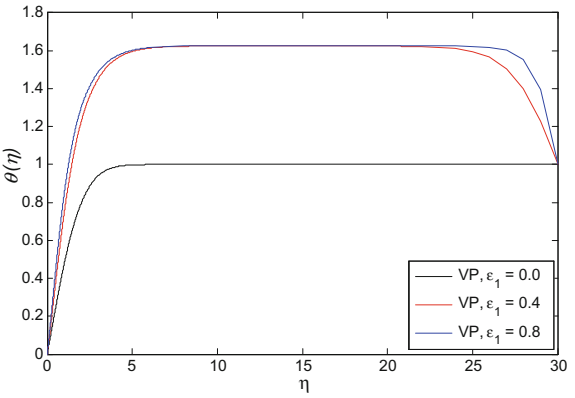

Fig. 5 Thermal stratification and variable permeability effects on temperature profile for $F = 0.5$, $Ra/Pe = 2$, $\varepsilon_\infty = 0.4$, $\sigma = 2$, $b = 3$, $d = 1.5$, $M = 2$

We found that in both the cases, the heat transfer rate increases with stratification parameter but the increment is significant with variable permeability.

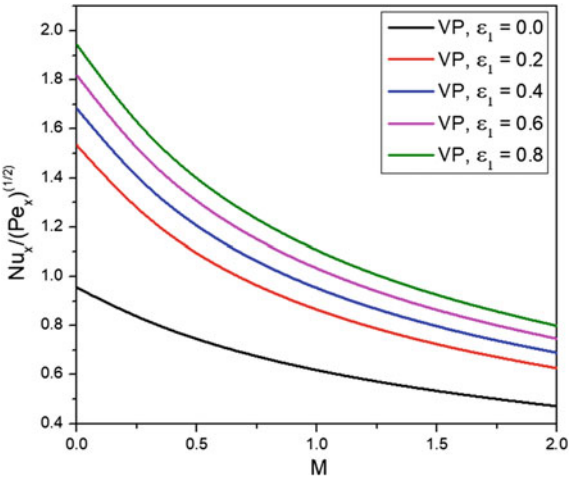

Fig. 6 Thermal stratification and variable permeability effects on Heat transfer for $F = 0.5$, $Ra/Pe = 2$, $\varepsilon_\infty = 0.4$, $\sigma = 2$, $b = 3$, $d = 1.5$,

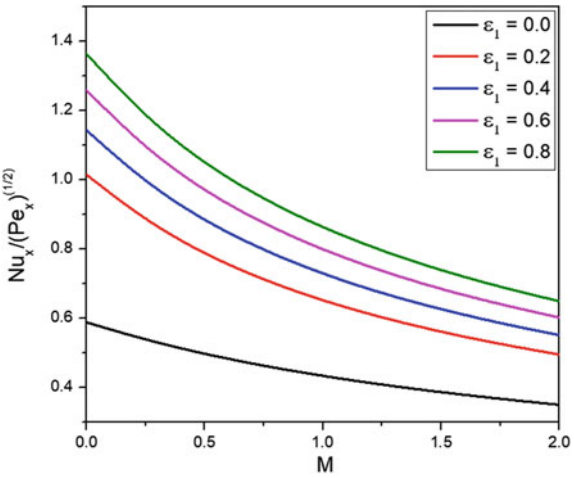

Fig. 7 Effect of Thermal stratification on Heat transfer for $F = 0.5$, $Ra/Pe = 2$, $\varepsilon_\infty = 0.4$, $\sigma = 2$, $b = 0$, $d = 0$

References

1. Epstein, M., Cho, D.H.: Laminar film condensation on a vertical melting surface. ASME J. Heat Transf. **98**, 108–113 (1976)
2. Tien, C.: The effect of melting on forced convection heat transfer. J. Appl. Meteorol. 523–527 (1965)
3. Bakier, A.Y.: Aiding and opposing mixed convection flow in melting from a vertical flat plate embedded in a porous medium. Transp. Por. Med. **29**, 127–139 (1997)
4. Gorla, R.S.R., Mansour, M.A., Hassanien, I.A., Bakier, A.Y.: Mixed convection effect on melting from a vertical plate in a porous medium. Transp. Por. Med. **36**, 245–254 (1999)
5. Cheng, W.T.: Melting effect on mixed convective heat transfer with aiding and opposing external flows from the vertical plate in a liquid-saturated porous medium. Int. J. Heat Mass Transf. **50**, 3026–3034 (2007)

6. Sobha, V.V., Vasudeva, R.Y., Ramakrishna, K., HemaLatha, K.: Non-darcy mixed convection with thermal dispersion in a saturated porous medium. ASME J. Heat Transf. **132**(1–4), 014501 (2010)
7. Ahmad, S., Pop, I.: Melting effect on mixed convection boundary layer flow about a vertical surface embedded in a porous medium opposing flows case. Transp. Por, Med (2014)
8. Chandrasekhara, B.C., Namboodiri, P.M.S., Hanumanthappa, A.R.: Similarity solutions for buoyancy induced flows in a saturated porous medium adjacent to impermeable horizontal surfaces. Warmeund Toffeubertragung **18**, 17–23 (1984)
9. Hassanien, I.A., Salama, A.A.: The onset of longitudinal vortices in mixed convection flow over an inclined surface in a porous medium with variable permeability. Appl. Math. Comput. **154**, 313–333 (2004)
10. Satya Narayana, P.V.: Effects of variable permeability and radiation absorption on magneto hydrodynamic (MHD) mixed convective flow in a vertical wavy channel with traveling thermal waves. Propul. Power Res. **4**, 150–160 (2015)
11. Bejan, A., Poulikakos, D.: The non-darcy regime for vertical boundary layer natural convection in a porous medium. Int. J. Heat Mass. Transfer. **24**, 717–722 (1984)
12. Kameswaran, P.K., Hemalatha, K., Madhavi, M.V.D.N.S.: Melting effect on convective heat transfer from a vertical plate embedded in a non-darcy porous medium with variable permeability. Adv. Powder Technol. (2016)
13. Singh, P., Sharma, K.: Integral method for free convection in thermally stratified porous medium. Acta Mech. **83**, 157–163 (1990)
14. Kalpana, T., Singh, P.: Natural convection in a thermally stratified fluid saturated porous medium. Int. J. Eng. Sci. **30**, 1003–1007 (1992)
15. Nakayama, A., Koyama, H.: Effect of thermal stratification on free convection with a porous medium. AAIA J. Thermophys. Heat Transfer. **1**, 282–285 (1987)
16. Srinivasacharya D., Reddy, S.: Effect double stratification on mixed convection in a power-law fluid saturated porous medium. Int. J. Heat Tech. **30**, 141–146 (2012)
17. Kandasamy, R., Dharmalingam, R.: Thermal and solutal startification on MHD nanofluid flow over a porous vertical plate. Alexandria Eng. J. https://doi.org/10.1016/j.aej.2016.02.029

Effect of Chemical Reaction and Thermal Radiation on the Flow over an Exponentially Stretching Sheet with Convective Thermal Condition

D. Srinivasacharya and P. Jagadeeshwar

Abstract The present work addresses the influence of thermal radiation and chemical reaction effects on the viscous fluid flow over a porous sheet stretching exponentially by employing convective boundary condition. The numerical solutions to the governing equations are evaluated using succesive linearization procedure together with Chebyshev collocation method. The variation of fluid flow, temperature, concentration and rate of heat, and mass transfers in presence of physical parameters are portrayed graphically.

Keywords Chemical Reaction · Thermal Radiation · Velocity Slip · Heat and Mass transfer

1 Introduction

The investigation of flow over an exponentially stretching sheet is of considerable interest because of its applications in industrial and technological processes such as fluid film condensation process, aerodynamic extrusion of plastic sheets, crystal growth, the cooling process of metallic sheets, design of chemical processing equipment and various heat exchangers, and glass and polymer industries. The pioneering works of Sakiadis [1, 2] motivated the several researchers to investigate the flow due to stretching sheet under various physical conditions.

Radiative heat transfer on convective flows has applications in areas of engineering and physics such as solar power technology, space technology, and other industrial areas. Yasir et al. [3] studied the influence of radiation on the heat transfer analysis of the boundary layer flow toward exponentially shrinking sheet. Recently, Adeniyan

D. Srinivasacharya (✉) · P. Jagadeeshwar
Department of Mathematics, National Institute of Technology,
Warangal 506004, Telangana State, India
e-mail: dsrinivasacharya@yahoo.com

P. Jagadeeshwar
e-mail: jagadeeshwar.pashikanti@gmail.com

D. Srinivasacharya and K. S. Reddy (eds.), *Numerical Heat Transfer and Fluid Flow*, Lecture Notes in Mechanical Engineering,
https://doi.org/10.1007/978-981-13-1903-7_30

and Adigun [4] investigated the influence of thermal radiation on heat transfer past an exponentially stretching sheet. On the other hand, the study of heat and mass transfer with chemical reaction has received considerable attention because of its importance in chemical and hydrometallurgical industries such as the design of chemical processing equipment, the manufacturing of ceramics or glassware, polymer production, etc. Gorla and Mukhopadhyay [5] studied the flow and mass transfer analysis of Casson fluid over an exponentially stretching surface with first-order homogeneous chemical reaction. Recently, Srinivasacharya and Jagadeeshwar [6] investigated the influence of Hall currents together with thermal radiation and chemical reaction effects on the laminar slip flow of viscous fluid over an exponentially stretching surface.

A novel technique for the heating process by providing the heat with a finite capacity to the convecting fluid through the bounding surface has attracted numerous researchers. This type of thermal boundary condition, called convective boundary condition, results in the rate of exchange of heat across the boundary being proportional to the difference in local temperature with the ambient conditions [7]. Due to the realistic nature of the convective thermal condition, the investigation of heat transfer with this condition has rich significance in mechanical and designing fields, for example, heat exchangers, atomic plants, gas turbines, and so forth. Hayat et al. [8] investigated the importance of convective-type boundary conditions in modeling the heat transfer process of MHD flow of viscous nanofluid over an exponentially stretching surface in a porous medium. Khan et al. [9] analyzed the convective thermal condition on the boundary layer flow of nanofluid past a bidirectional exponentially stretching sheet. Recently, Srinivasacharya and Jagadeeshwar [10] investigated the slip flow of viscous fluid over a sheet stretching exponentially with convective thermal condition.

Therefore, the motto of the present work is to analyze the thermal radiation, chemical reaction effects, and velocity slip on the convective flow of viscous fluid over an exponentially stretching permeable sheet. In addition to these physical conditions, fluid suction/injection is also considered.

2 Mathematical Formulation

Consider a stretching sheet in a laminar slip flow of incompressible viscous fluid with a temperature T_∞ and concentration C_∞. The Cartesian framework is selected by taking positive $\tilde{x}-$axis along the sheet and $\tilde{y}-$axis orthogonal to the sheet. The stretching velocity of the sheet is assumed as $U_*(\tilde{x}) = U_0\, e^{\frac{\tilde{x}}{L}}$, where $\tilde{x}$ is the distance from the slit. Assume that the sheet is either cooled or heated convectively through a fluid with temperature T_f and, thus induces a heat transfer coefficient h_f, where $h_f = h\sqrt{U_0/2L}e^{\frac{\tilde{x}}{2L}}$. $(\tilde{u}_x, \tilde{u}_y)$ is the velocity vector, $\tilde{C}$ is the concentration, and $\tilde{T}$ is the temperature. The suction/injection velocity of the fluid through the sheet is $V_*(\tilde{x}) = V_0\, e^{\frac{\tilde{x}}{2L}}$, where V_0 is the strength of suction/injection. The slip velocity of the fluid is assumed as $N_*(\tilde{x}) = N_0\, e^{\frac{\tilde{x}}{2L}}$, where N_0 is the velocity slip factor. The

fluid is considered to be gray, absorbing/emitting radiation, but is a non-scattering medium. The Rosseland approximation [11] is used to describe the radiative heat flux in the energy equation. Also, it is assumed that there exists a homogenous chemical reaction of the first order with rate constant $k_1 = k_0 e^{\frac{\tilde{x}}{L}}$, where k_0 is constant, between the diffusing species and the fluid. Hence, the governing equations for the present flow problem are given by

$$\frac{\partial \tilde{u}_x}{\partial \tilde{x}} + \frac{\partial \tilde{u}_y}{\partial \tilde{y}} = 0 \tag{1}$$

$$\tilde{u}_x \frac{\partial \tilde{u}_x}{\partial \tilde{x}} + \tilde{u}_y \frac{\partial \tilde{u}_x}{\partial \tilde{y}} = \nu \frac{\partial^2 \tilde{u}_x}{\partial \tilde{y}^2} \tag{2}$$

$$\tilde{u}_x \frac{\partial \tilde{T}}{\partial \tilde{x}} + \tilde{u}_y \frac{\partial \tilde{T}}{\partial \tilde{y}} = \alpha \frac{\partial^2 \tilde{T}}{\partial \tilde{y}^2} + \frac{16 T_\infty^3 \sigma^*}{3 k^* \rho c_p} \frac{\partial^2 \tilde{T}}{\partial \tilde{y}^2} \tag{3}$$

$$\tilde{u}_x \frac{\partial \tilde{C}}{\partial \tilde{x}} + \tilde{u}_y \frac{\partial \tilde{C}}{\partial \tilde{y}} = D \frac{\partial^2 \tilde{C}}{\partial \tilde{y}^2} - k_1 (\tilde{C} - C_\infty) \tag{4}$$

where D is the mass diffusivity, α is the thermal diffusivity, ρ is density, ν is the kinematic viscosity of the fluid, k^* is mean absorption coefficient, σ^* is Stefan-Boltzmann constant and c_p is specific heat capacity at the constant pressure.

The conditions on the surface of the sheet are

$$\left.\begin{array}{l} \tilde{u}_x = U_* + N_* \nu \frac{\partial \tilde{u}_x}{\partial \tilde{y}}, \;\; \tilde{u}_y = -V_*(\tilde{x}), \\ h_f (T_f - \tilde{T}) = -\kappa \frac{\partial \tilde{T}}{\partial \tilde{y}}, \;\; \tilde{C} = C_w \;\; \text{at} \;\; \tilde{y} = 0 \\ \tilde{u}_x \to 0, \;\; \tilde{T} \to T_\infty, \;\; \tilde{C} \to C_\infty \;\; \text{as} \;\; \tilde{y} \to \infty \end{array}\right\} \tag{5}$$

Introducing the stream functions through $\tilde{u}_x = -\frac{\partial \psi}{\partial \tilde{y}}$ and $\tilde{u}_y = \frac{\partial \psi}{\partial \tilde{x}}$ and then the following dimensionless variables:

$$\left.\begin{array}{l} y = \tilde{y} \sqrt{U_0 / 2\nu L} e^{\frac{\tilde{x}}{2L}}, \quad \psi = \sqrt{2\nu L U_0} e^{\frac{\tilde{x}}{2L}} F(x, y), \\ \tilde{T} = T_\infty + (T_f - T_\infty) T(x, y), \quad \tilde{C} = C_\infty + (C_w - C_\infty) C(x, y) \end{array}\right\} \tag{6}$$

into Eqs. (1)–(4), we obtain

$$F''' + FF'' - 2F'^2 = 0 \tag{7}$$

$$\frac{1}{Pr} \left(1 + \frac{4R}{3}\right) T'' + FT' = 0 \tag{8}$$

$$\frac{1}{Sc} C'' + FC' - \gamma\, C = 0 \tag{9}$$

The conditions at the boundary reduces to

$$\left.\begin{array}{l} F(0)=S,\quad F'(0)=1+\lambda F''(0),\quad T'(0)=-Bi(1-T(0)),\quad C(0)=1 \text{ at } y=0 \\ F'(\infty)\to 0,\quad T(\infty)\to 0,\quad C(\infty)\to 0 \text{ as } y\to\infty \end{array}\right\} \tag{10}$$

where $Bi=\frac{h}{\kappa}\sqrt{\nu}$ is the Biot number, $\gamma=\frac{2Lk_0}{U_0}$ is the chemical reaction parameter, $S=V_0\sqrt{2L/\nu U_0}$ is the suction/injection parameter according as S > 0 or S < 0, respectively, $Sc=\frac{\nu}{D}$ is the Schmidt number, $R=\frac{4\ \sigma^*\ T_\infty^3}{\kappa\ \kappa^*}$ is the radiation parameter, $\lambda=N_0\sqrt{\nu U_0/2L}$ is the velocity slip parameter, $Pr=\frac{\nu}{\alpha}$ is the Prandtl number, and the prime denotes derivative with respect to y.

The nondimensional skin friction $C_f=\frac{2\tau_w}{\rho U_*^2}$, the local Nusselt number $Nu_{\tilde{x}}=\frac{\tilde{x}q_w}{\kappa(T_f-T_\infty)}$, and the local Sherwood number $Sh_{\tilde{x}}=\frac{\tilde{x}q_m}{\kappa(C_w-C_\infty)}$, are given by

$$\frac{\sqrt{Re_{\tilde{x}}}\,C_f}{\sqrt{2\tilde{x}/L}}=F''(0),\quad \frac{Nu_{\tilde{x}}}{\sqrt{\tilde{x}/2L}\sqrt{Re_{\tilde{x}}}}=-\left(1+\frac{4R}{3}\right)T'(0)\ \text{ and }\ \frac{Sh_{\tilde{x}}}{\sqrt{\tilde{x}/2L}\sqrt{Re_{\tilde{x}}}}=-C'(0) \tag{11}$$

where $Re_{\tilde{x}}=\frac{\tilde{x}U_*(\tilde{x})}{\nu}$ is the local Reynolds number.

3 Numerical Solution

The system of Eqs. (7)–(9) is linearized using successive linearization method (SLM) [12, 13]. In this method, the functions $F(y)$, $T(y)$, and $C(y)$ are expressed as

$$F(y)=F_r(y)+\sum_{i=0}^{r-1}F_i(y),\ \ T(y)=T_r(y)+\sum_{i=0}^{r-1}T_i(y),\ \ C(y)=C_r(y)+\sum_{i=0}^{r-1}C_i(y) \tag{12}$$

where $F_r(y)$, $T_r(y)$, and $C_r(y)$ $(r=1,2,3,\ldots)$ are functions, which are not known and $F_i(y)$, $T_i(y)$ and $C_i(y)$ $(i\geq 1)$ are approximations. Substituting Eq. (12) in Eqs. (7) to (9) and taking the linear part, we get

$$F_i'''+\chi_{11,i-1}F_i''+\chi_{12,i-1}F_i'+\chi_{13,i-1}F_i=\zeta_{1,i-1} \tag{13}$$

$$\chi_{21,i-1}F_i+\frac{1}{Pr}\left(1+\frac{4R}{3}\right)T_i''+\chi_{22,i-1}T_i'=\zeta_{2,i-1} \tag{14}$$

$$\chi_{31,i-1}F_i+\frac{1}{Sc}C_i''+\chi_{32,i-1}C_i'-yC_i=\zeta_{3,i-1} \tag{15}$$

where the coefficients $\chi_{lk,r-1}$ and $\zeta_{k,i-1}$, $(l,k=1,2,3)$ are in terms of the approximations F_i, T_i, and C_i, $(i=1,2,3,\ldots,r-1)$ and their derivatives.

The boundary-associated conditions are

$$F_r(0) = \lambda F_r''(0) - F_r'(0) = F_r'(\infty) = T_r'(0) - BiT_r(0) = T_r(\infty) = C_r(0) = C_r(\infty) = 0 \tag{16}$$

Choosing the initial approximation $F_0(y)$, $T_0(y)$ and $C_0(y)$ satisfy the conditions (10) and solving Eqs. (13)–(16) recursively, we get the solutions for $F_r(y)$, $T_r(y)$, and $C_r(y)$ $(r \geq 1)$, and hence $F(y)$, $T(y)$, and $C(y)$. To solve Eqs. (13)–(15) along with the boundary conditions (16), Chebyshev collocation is used (see for reference [13]).

4 Results and Discussions

Numerical values for $-T'(0)$ of Magyari and Keller [14] are compared with the results of current method for particular values of $R = 0$, $\lambda = 0$, $\gamma = 0$, $S = 0$ and for large value of Bi, shown in Table 1 and found to be in good agreement.

To elucidate the significance of relevant parameters, the numerical calculations are carried out by taking $S = 0.5$, $\gamma = 0.5$, $Sc = 0.22$, $\lambda = 1.0$, $Pr = 1.0$, $R = 0.5$, $Bi = 1.0$, N = 100, and L = 20 unless otherwise mentioned.

The influence of slip and suction/injection parameters on the fluid velocity is portrayed in Fig. 1a and b. It is evident from the Fig. 1a and b that the rise in the slipperiness and the fluid suction diminish the velocity, while injection enhances the velocity. On the other hand, the skin friction is enhancing with the slipperiness and reducing with the suction of the fluid as depicted in Fig. 1c.

The variation of temperature distribution with S, R, and Bi is plotted through Fig. 2a– c. It is a well-known that wall suction reduces the thickness of thermal boundary layer, and hence reduction in temperature. This phenomenon is graphically presented in Fig. 2a. However, the wall injection produces the exactly contradictory nature.

Table 1 Comparative analysis for $-T'(0)$ by the current method for $\lambda = 0$, $R = 0$, $\gamma = 0$, $S = 0$, and $Bi \to \infty$

Nusselt number $-T'(0)$		
Pr	Magyari and Keller [14]	Present
0.5	0.330493	0.33053741
1	0.549643	0.54964317
3	1.122188	1.12208592
5	1.521243	1.52123757
8	1.991847	1.99183597
10	2.257429	2.25742182

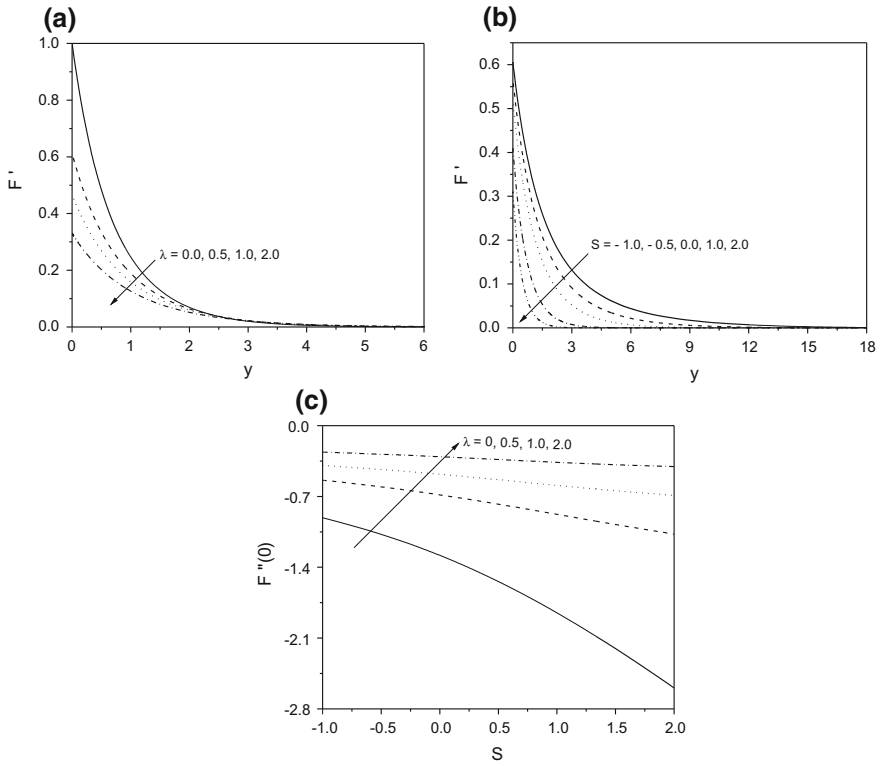

Fig. 1 Effect of **a** λ on F' **b** S on F' and **c** λ on $F''(0)$ against S

Figure 2b illustrates that the temperature is enhancing with a rise in the value of thermal radiation, and hence there is a gain in thickness of thermal boundary layer. The variation of temperature with Bi is presented in Fig. 2c. With the rise in Biot number, the temperature is enhancing. Further, for large value of Biot number, the convective thermal condition from (10) transforms to $T(0) \to 1$, which signifies the constant wall condition, i.e., stronger convection leads to the higher surface temperatures which appreciably increases the temperature.

The fluctuation of rate of heat transfer with S for diverse values of R, Bi, and λ is portrayed through Fig. 3a–c. The rate of heat transfer is enhancing with the rise in the radiation parameter as shown in Fig. 3a. Figure 3b demonstrates that the rate of heat transfer is enhancing with an increase in the value of Bi. On the other hand, Fig. 3c shows that increase in λ diminishes the rate of heat transfer. Further, it is noticed from these figures that the fluid suction enhances the rate of heat transfer.

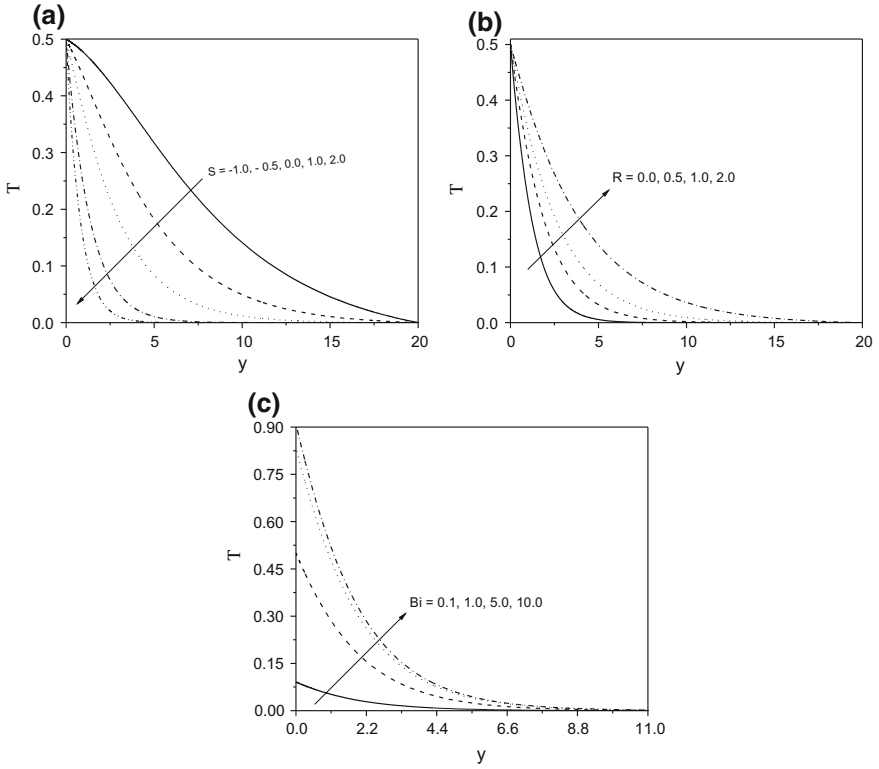

Fig. 2 Effect of **a** S, **b** R, and **c** Bi on T

The influence of λ, S, and γ on the concentration of the fluid is shown graphically in Fig. 4a–c. It is clear from Fig. 4a that an increase in the slipperiness rises the concentration. while, the wall injection is enhancing the fluid concentration as shown in Fig. 4b. It is noticed from Fig. 4c that concentration of the fluid is increasing for constructive reaction($\gamma < 0$) and reducing for destructive reaction($\gamma > 0$).

The variation of rate of mass transfer with S for different values of λ and γ is shown in Fig. 5a and b. It is observed from Fig. 5a that an increase in slipperiness reduces the rate of mass transfer. On the other hand, when there is an increase in the chemical reaction parameter (positive values of γ), the rate of mass transfer is enhancing as shown in Fig. 5b. Further, the rate of mass transfer is increasing with the fluid suction.

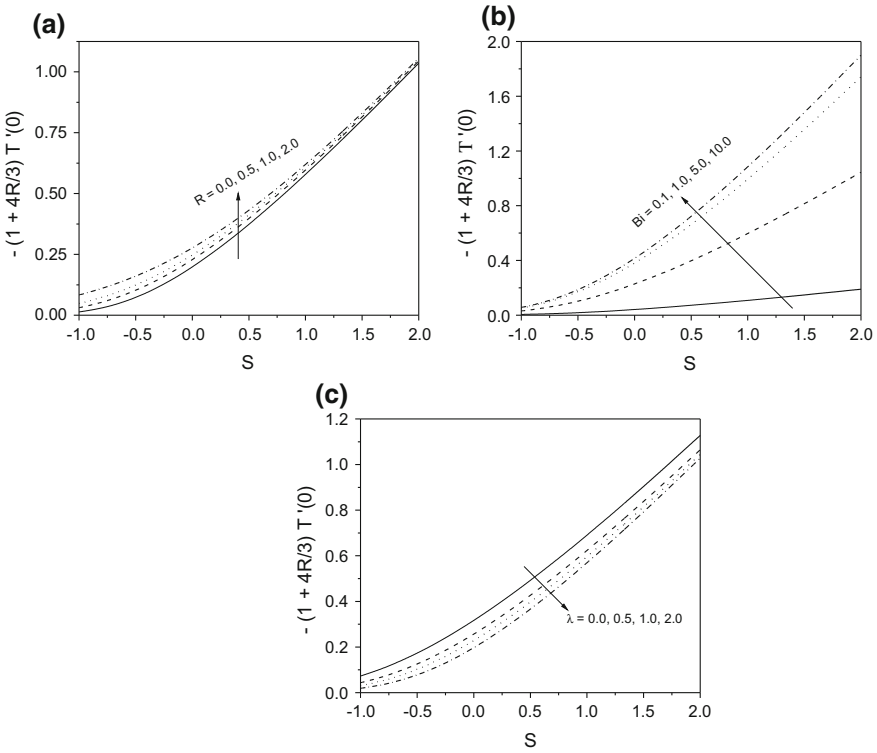

Fig. 3 Effect of **a** R, **b** Bi, and **c** λ on $-(1+\frac{4R}{3})T'(0)$ against S

5 Conclusions

The influence of thermal radiation and chemical reaction on the laminar slip flow of viscous fluid over an exponentially stretching sheet in the presence of fluid suction/injection at the boundary of the stretching surface with the convective thermal condition has been investigated. Successive linearization method along with the Chebyshev spectral collocation method is used to solve the governing equations. The following are the important findings from this study:

- The velocity of the fluid reduces with an increase in the velocity slip and fluid suction. The skin friction diminishes with a rise in the fluid suction and enhances with slipperiness.
- The fluid temperature escalates with the rise in R and Bi and falls with fluid suction.
- The concentration increases with the rise in slip parameter and reduces with the enhancement in the suction and chemical reaction parameters.

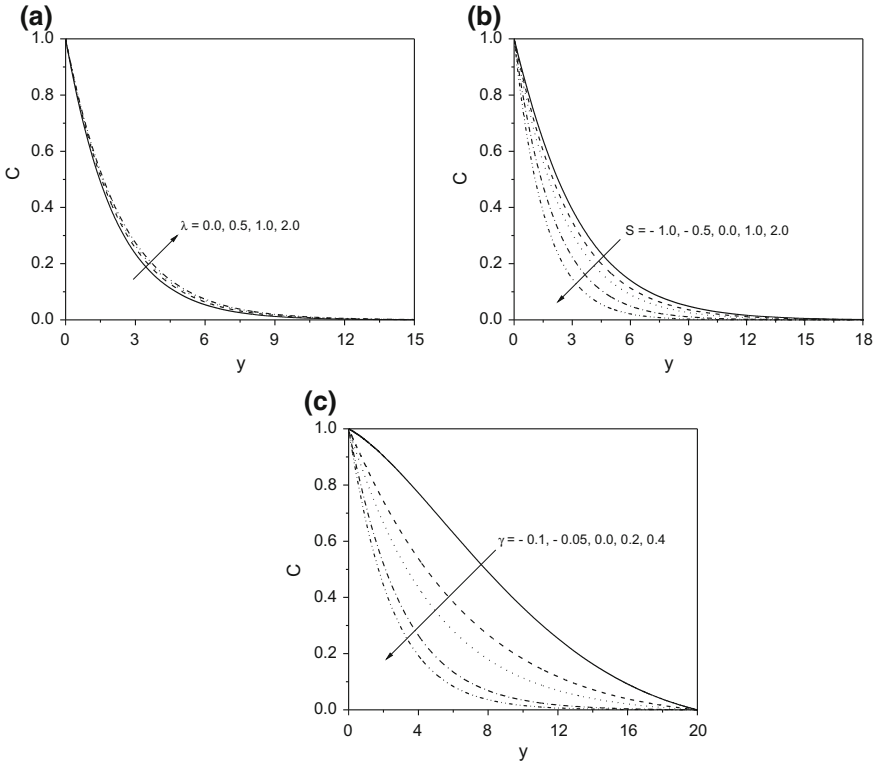

Fig. 4 Effect of **a** λ, **b** S, and **c** γ on C

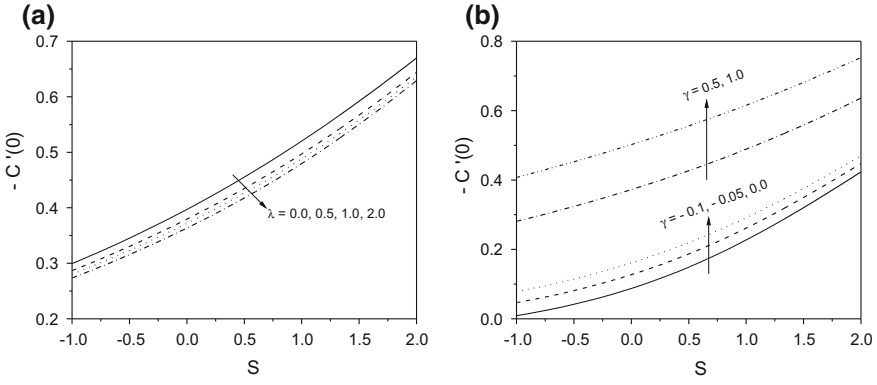

Fig. 5 Effect of **a** λ and **b** γ on $-C'(0)$ against S

– The rate of heat transfer escalates with the rise in R, S, and Bi, while it reduces with slipperiness. The rate of mass transfer is enhancing as the suction and chemical reaction parameters increase but reducing with an increase in the velocity slip.

References

1. Sakiadis, B.C.: Boundary-layer equations for two-dimensional and axisymmetric flow. A. I. Ch. E. J. **7**, 26–28 (1961)
2. Sakiadas, B.C.: The boundary layer on a continuous flat surface. A. I. Ch. E. J. **7**, 221–225 (1961)
3. Khan, Y., Smarda, Z., Faraz, N.: On the study of viscous fluid due to exponentially shrinking sheet in the presence of thermal radiation. Ther. Sci. **19**, 191–196 (2015)
4. Adeniyan, A., Adigun, J.A.: Similarity solution of hydromagnetic flow and heat transfer past an expoentially stretching permeable vertical sheet with viscous dissipation, Joulean and viscous heating effects. Anns. of the Fac. of Engg. Hun. **14**, 113–119 (2016)
5. Mukhopadhyay, S., Gorla, R.S.R.: Diffusion of chemically reactive species of a Casson fluid flow over an exponentially stretching surface. Ther. Ener. Pow. Engg. **3**, 216–221 (2014)
6. Srinivasacharya, D., Jagadeeshwar, P.: Flow over an exponentially stretching sheet with Hall, thermal radiation and chemical reaction effects. Fron. Heat Mass Tranf. **9**, 1–10 (2017). https://doi.org/10.5098/hmt.9.37
7. Merkin, J.H.: Natural-convection boundary-layer ow on a vertical surface with newtonian heating. I. J. Heat Flu. Fl. **15**, 392–398 (1994)
8. Hayat, T., Imtiaz, M., Alsaedi, A., Mansoora, R.: MHD flow of nanofluids over an exponentially stretching sheet in a porous medium with convective boundary conditions. Chin. Phy. B. **23**, 054701 (2014)
9. Khan, J.A., Mustafa, M., Hayat, T., Alsaedi, A.: Numerical study on three-dimensional flow of nanofluid past a convectively heated exponentially stretching sheet. Can. J. Phy. **93**, 1131–1137 (2015)
10. Srinivasacharya, D., Jagadeeshwar, P.: Slip viscous flow over an exponentially stretching porous sheet with thermal convective boundary conditions. I. J. Appl. Compl. Math. **3**, 3525–3537 (2017). https://doi.org/10.1007/s40819-017-0311-y
11. Sparrow, E. M., Cess, R. D.: Radiation Heat Transfer. Ser. in Ther. and Flu. Engg, Augmented ed. 1, McGraw-Hill (1978)
12. Motsa, S.S., Shateyi, S.: Successive linearisation solution of free convection non-darcy flow with heat and mass transfer. Adv. Tops. Mass Tranf. **19**, 425–438 (2011)
13. Canuto, C., Hussaini, M. Y., Quarteroni, A., Zang, T. A.: Spectral Methods-Fundamentals in Single Domains. J. Appd. Math. Mech. **87** (2007)
14. Magyari, E., Keller, B.: Heat and mass transfer in the boundary layers on an exponentially stretching continuous surface. J. Phy D: Appd. Phy. **32**, 577–585 (1999)

Soret and Viscous Dissipation Effects on MHD Flow Along an Inclined Channel: Nonlinear Boussinesq Approximation

P. Naveen and Ch. RamReddy

Abstract In this study, we investigate the Soret and viscous dissipation effects on the mixed convective flow of an electrically conducting fluid inside an inclined channel. In addition, nonlinear Boussinesq approximation (i.e., nonlinear convection) is taken into account to address thermal and solutal transport phenomena in some thermal and solutal systems, which are performed at high-level temperatures. Initially, the set of governing equations and the related boundary conditions are transformed into dimensionless form under suitable transformations and after that homotopy analysis method is used to obtain semi-analytic solutions of flow equations. The behavior of flow characteristics with pertinent flow parameters is discussed through graphs.

Keywords Nonlinear Boussinesq approximation · Soret effect · Viscous dissipation effect · Inclined channel

1 Introduction

Many of thermal systems are processed at high-level temperatures and in such situations, the density relation with temperature and concentration may become nonlinear. This nonlinear variation in temperature–concentration-dependent density relation (to be specific, nonlinear Boussinesq approximation or nonlinear convection) gives a strong influence on the fluid flow characteristics (for more details see Barrow and Sitharamarao [1], Vajravelu and Sastri [2]) and the Soret and viscous dissipation effects are of immense importance. The early writing and applications of nonlinear convection can be seen in the paper by Partha [3]. A Darcy–Forchheimer model is considered in the analysis of nonlinear convection and convective boundary condition in a micropolar fluid by Ramreddy et al. [4].

P. Naveen (✉) · Ch. RamReddy
Department of Mathematics, National Institute of Technology, Warangal 506004, India
e-mail: naveenpadi09@gmail.com

Ch. RamReddy
e-mail: chittetiram@gmail.com

D. Srinivasacharya and K. S. Reddy (eds.), *Numerical Heat Transfer and Fluid Flow*, Lecture Notes in Mechanical Engineering,
https://doi.org/10.1007/978-981-13-1903-7_31

Analysis of mixed convective flow problems in vertical or horizontal channels is the most relevant topic in engineering and industrial fields such as fluid transport, chemical processing units, heat exchangers, etc. The earliest discussions on a fully developed mixed convective flow along a vertical channel can be found in the works of Tao [5]. Barletta [6] utilized the heat flux condition instead of the wall condition to examine viscous dissipation effect in the combined free and forced convective flows through vertical channels. Magnetohydrodynamic (MHD) effects have been a topic of great interest in the problems of free and mixed convective flows. Due to this attention, Umavathi and Malashetty [7] addressed the effect of MHD in forced and free convective flows along the vertical channels. Applications and early literature of MHD and Soret effect can be found in the work of Afify [8]. Surender and Ramreddy [9] (also see the citations therein) analyzed the significance of cross-diffusion and viscous dissipation effects on the natural convective flow of a nanofluid through the vertical channel.

Much attention has not been given to the problem of mixed convective flow, a regular fluid over an inclined geometry in the presence of a nonlinear Boussinesq approximation, even though the study is useful in the mechanism of combustion, solar collectors which are performed at high-level temperatures. Thus, the object of this work is to examine the Soret and viscous dissipation effects on the MHD fully developed flow in an inclined channel with the consideration of nonlinear Boussinesq approximation. The homotopy analysis method is used to explore the impact of pertinent parameters on the fluid flow characteristics through graphs and the salient features are discussed in detail.

2 Mathematical Modeling

Consider the steady, laminar flow of an electrically conducting incompressible regular fluid in an inclined channel. The distance between the walls, i.e., the channel width is $2L$ and the channel is inclined at an angle Ω to the vertical direction. Choose the coordinate system such that x-axis is along the inclined channel and y-axis normal to the channel. A fluid flow rises in the channel driven by external forces. In this study, the lower plate (i.e, at $y = L$) of the channel is maintained at a constant heat and mass fluxes q_w and q_m, respectively, while the upper plate (i.e, at $y = -L$) of the channel is kept at constant temperature T_1 and constant concentration C_1, respectively. Further, the following assumptions are assumed in the analysis: (i) a uniform magnetic field of constant strength $B = B_0$ is applied, (ii) flow is assumed to be fully developed so that the transverse velocity is zero, i.e, $v = 0$, $\frac{\partial v}{\partial y} = 0$, $\frac{\partial p}{\partial y} = 0$, $\frac{\partial T}{\partial x} = 0$, $\frac{\partial C}{\partial x} = 0$, and (iii) the viscous dissipation and Soret effects are included.

Under the consideration of the above said assumptions, the governing equations for the fluid flow are given by

$$\mu\frac{d^2u}{dy^2} + \rho g\cos\Omega - \sigma {B_0}^2 u = \frac{dP}{dx} \tag{1}$$

$$\frac{k}{\rho C_P}\frac{d^2T}{dy^2} + \frac{\mu}{\rho C_P}\left(\frac{du}{dy}\right)^2 = 0 \tag{2}$$

$$D_m\frac{d^2C}{dy^2} + \frac{D_m K_T}{T_m}\frac{d^2T}{dy^2} = 0 \tag{3}$$

by considering the nonlinear Boussinesq approximation (see ref. Parth [3]), the density can be written as

$$\rho = \rho_0\left[1 - \beta_0\,(T - T_1) - \beta_1(T - T_1)^2 - \beta_2\,(C - C_1) - \beta_3(C - C_1)^2\right] \tag{4}$$

The subject to the boundary conditions are

$$\begin{aligned} u(-L) = 0,\ T(-L) = T_1,\ C(-L) = C_1,\\ u(L) = 0,\ \left.\frac{dT}{dy}\right|_{y=L} = \frac{q_w}{k},\ \left.\frac{dC}{dy}\right|_{y=L} = \frac{q_m}{D}. \end{aligned} \tag{5}$$

Here, u, P, μ, ρ, B_0, σ, D_m, T, C, C_p, k, and K_T denotes the velocity component, pressure, dynamic viscosity, density, transverse magnetic field, coefficient of electric conductivity, coefficient of mass diffusivity, dimensional temperature, dimensional concentration, specific heat, thermal conductivity of the fluid, and thermal diffusion ratio, respectively.

We define the nondimensional variables as

$$\eta = \frac{y}{L}\ ,\ f = \frac{u}{U_0}\ ,\ \theta = \frac{T - T_1}{\frac{q_w L}{k}}\ ,\ \phi = \frac{C - C_1}{\frac{q_m L}{D}}\ ,\ \alpha = \frac{L^2}{\mu U_0}\frac{dp}{dx} \tag{6}$$

Substituting Eq. (6) into Eqs. (1)–(5), we obtain the following equation:

$$\frac{d^2f}{d\eta^2} + \lambda\left[\theta(1 + \chi_1\theta) + \mathcal{B}\phi(1 + \chi_2\phi)\right]\cos\Omega - M^2 f = \alpha \tag{7}$$

$$\frac{d^2\theta}{d\eta^2} + Br\left(\frac{df}{d\eta}\right)^2 = 0 \tag{8}$$

$$\frac{1}{Sc}\frac{d^2\phi}{d\eta^2} + Sr\frac{d^2\theta}{d\eta^2} = 0 \tag{9}$$

The boundary conditions (5) in terms of f, θ, ϕ become

$$f(-1) = 0,\ \theta(-1) = 0,\ \phi(-1) = 0,\ f(1) = 0,\ \left.\frac{d\theta}{d\eta}\right|_{\eta=1} = 1,\ \left.\frac{d\phi}{d\eta}\right|_{\eta=1} = 1 \tag{10}$$

In the above equations: B, G_r, R_e, λ, χ_1, χ_2, M, α, Br, Sr, and Sc represents the Buoyancy ratio parameter, Grashof number, Reynolds number, mixed convection parameter, nonlinear density-temperature (NDT) parameter, Schmidt number, Hartmann number, constant pressure gradient, Brinkman number, Soret number, and nonlinear density concentration (NDC) parameter, respectively. Mathematically, these parameters are expressed in the following manner:

$$B = \frac{\beta_C q_m K_p}{D\beta_T q_w},\ G_r = \frac{g\beta_T q_w L^3}{\upsilon^2},\ R_e = \frac{U_0 K_P}{\upsilon},\ \lambda = \frac{G_r}{R_e},\ \chi_1 = \frac{\beta_2}{\beta_1}\frac{q_w L}{k}, Sc = \frac{D}{D_m},$$
$$M^2 = \frac{\sigma {B_0}^2 L^2}{\mu},\ \alpha = \frac{L^2}{\mu U_0}\frac{dP}{dx},\ Br = \frac{\mu {U_0}^2 K_P}{LKq_w},\ Sr = \frac{D_m K_T q_w}{K_P T_m q_m},\ \chi_2 = \frac{\beta_3}{\beta_2}\frac{q_m L}{D}$$

3 Results and Discussion

Numerical solution of Eqs. (7)–(9) together with the boundary conditions (10) has been assessed with a homotopy analysis method (HAM) (Wang and Kao [10], Liao [11]). This method has been used successfully by Srinivasacharya and Kaladhar [12], and others in different problems.

The effects of various pertinent parameters on the characteristics of fluid flow (specifically, the velocity (f), temperature (θ), and concentration (ϕ) have been presented graphically. The graphs are drawn by taking the value of the auxiliary parameter h, at which the average residual error is minimized. The influence of Sr and Br on the boundary layer profiles is determined for both the presence and absence of nonlinear convection parameters in Figs. 1, 2 and 3. From Figs. 1 and 2, one can notice that the velocity and temperature of the fluid flow increased for the rise of Brinkman number, whereas these profiles have opposite change with Soret number Sr. The enhancement of Soret and Brinkman numbers leads to the decrease in the concentration profile for both cases of linear and nonlinear Boussinesq approximations, as shown in Fig. 3. Additionally, these two parameters are giving more influence on the boundary layer profiles in the presence of χ_1 and χ_2. It means the rate of change (either increasing or decreasing) is more in the case of nonlinear convection when compared to the results of linear convection.

The results presented in Figs. 4, 5 and 6 indicate the behavior of Hartmann number (M) and inclination of angle (Ω) on the flow, thermal, and concentration profiles of the fluid. These illustrations are considered for both linear and nonlinear Boussinesq approximation cases. By increasing the value of M, velocity decreases in the right

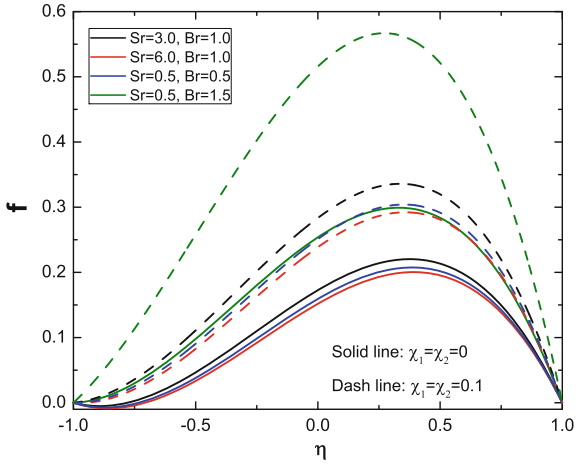

Fig. 1 Effect of *Sr* and *Br* on the velocity profile

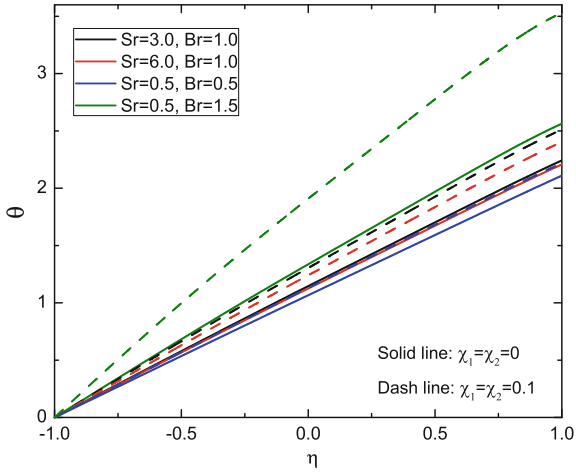

Fig. 2 Effect of *Sr* and *Br* on the temperature profile

half of the channel but the reverse trend can be noticed in the left half of the channel. Moreover, the magnitude of the velocity is a decreasing function of M and the same effect is projected in Fig. 4. Also, Fig. 4 reveals the influence of Ω on the velocity, and magnitude of the velocity is a decreasing function of Ω. The variation of M is magnifying the concentration profile gradually and this variation gives an opposite impact on temperature profile. However, the thermal boundary layer thickness decreases and solutal boundary layer thickness is increased when the channel moves from vertical to horizontal position, as displayed in Figs. 5 and 6. Here again, the individual impact of M and Ω (i.e., when M varies, Ω is fixed, and vice versa) is more provoking in the case of nonlinear convective flow over an inclined channel. Physically, $\chi_1 > 0$ and $\chi_2 > 0$ imply that there will be a supply of heat and mass to the flow region from the surface of the channel. Similarly, when $\chi_1 < 0$ and $\chi_2 < 0$

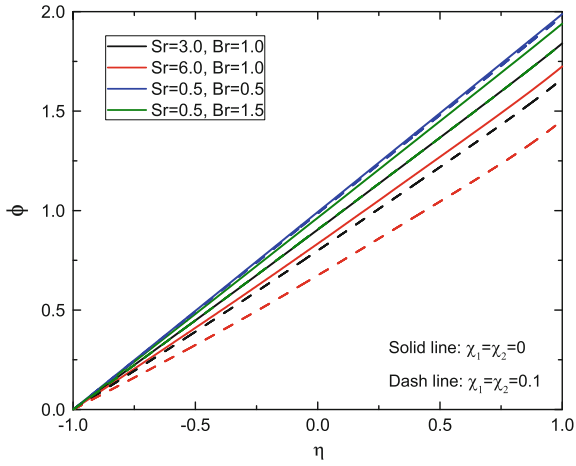

Fig. 3 Effect of Sr and Br on the concentration profile

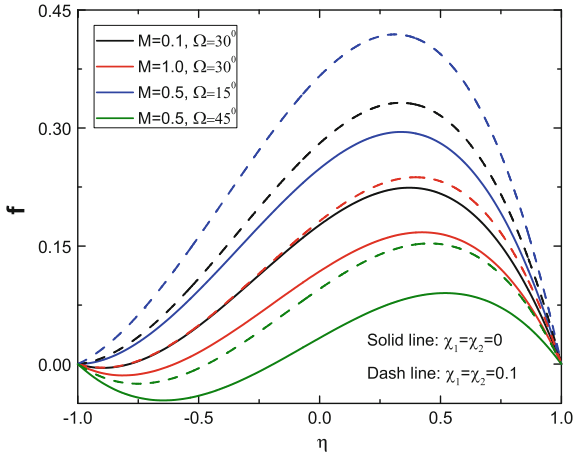

Fig. 4 Effect of M and Ω on the velocity profile

there will be a transfer of heat and mass from the fluid to the surface of the channel. This nonlinear convection gives a strong influence on the fluid flow characteristics, and then the impact of Sr, Br, M, and Ω is more prominent on the physical quantities, compared therewith results of linear convection.

4 Conclusion

In the present work, the collective influence of thermal diffusion and viscous dissipation, on a fully developed mixed convective flow between inclined channels in an electrically conducting fluid in the presence of nonlinear Boussinesq approximation has been analyzed. The major notice is that the impact of pertinent parameters on

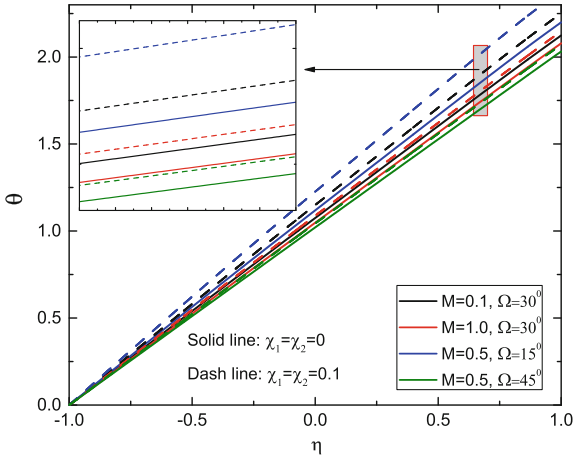

Fig. 5 Effect of M and Ω on the temperature profile

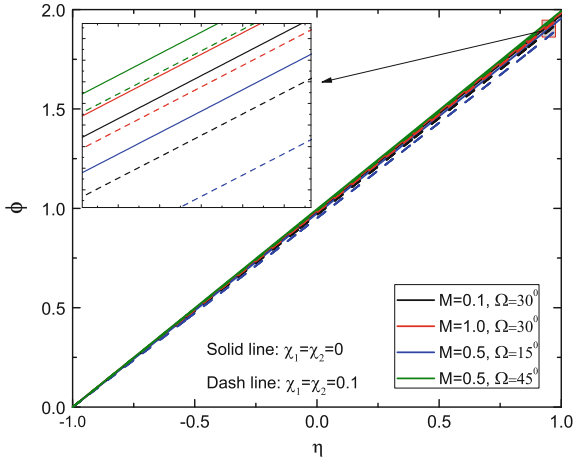

Fig. 6 Effect of M and Ω on the concentration profile

the physical quantities is prominent with the consideration of nonlinear convection, compared therewith results of linear convection. The influence of magnetic parameter and angle of inclination leads to decrease in both the velocity and temperatures of fluid but these increases the concentration profile. Brinkman number increases the thickness of the thermal and momentum boundary layers within the channel, whereas it decreases the concentration boundary layer thickness. The profiles of fluid flow are declined with the rise of the Soret parameter in both linear and nonlinear convective flow cases. Due to the flux conditions considered at a lower plate $\eta = 1$, the changes in the temperature and concentration profiles are more at $\eta = -1$ as compared with that of the upper plate.

References

1. Barrow, H., Sitharamarao, T.L.: Effect of variation in volumetric expansion coefficient on free convection heat transfer. British Chem. Eng. **16**(8), 704–709 (1971)
2. Vajravelu, K., Sastri, K.S.: Fully developed laminar free convection flow between two parallel vertical walls-I. Int. J. Heat Mass Transf. **20**(6), 655–660 (1977)
3. Partha, M.K.: Nonlinear convection in a non-Darcy porous medium. Appl. Math. Mech. **31**(5), 565–574 (2010)
4. RamReddy, C., Naveen, P., Srinivasacharya, D.: Quadratic convective flow of a micropolar fluid along an inclined plate in a non-Darcy porous medium with convective boundary condition. Nonlinear Eng. **6**(2), 139–151 (2017)
5. Tao, L.N.: On combined free and forced convection in channels. J. Heat Transf. **82**(3), 233–238 (1960)
6. Barletta, A.: Heat transfer by fully developed flow and viscous heating in a vertical channel with prescribed wall heat fluxes. Int. J. Heat Mass Transf. **42**(20), 3873–3885 (1999)
7. Umavathi, J.C., Malashetty, M.S.: Magnetohydrodynamic mixed convection in a vertical channel. Int. J. Non-Linear Mech. **40**(1), 91–101 (2005)
8. Afify, A.A.: Similarity solution in MHD: effects of thermal diffusion and diffusion thermo on free convective heat and mass transfer over a stretching surface considering suction or injection. Comm. Nonlinear Sci. Numer. Simu. **14**(5), 2202–2214 (2009)
9. Surender, O., Ramreddy, C.H.: Significance of viscous dissipation on fully developed natural convection flow of a nanofluid in vertical channel with cross-diffusion effects. Adv. Sci. Eng. Med. **8**(7), 579–588 (2016)
10. Wang, Z.K., Gao, T.: An Introduction to Homotopy Methods. Chongqing Publishing House, Chongqing (1991)
11. Liao, S.: Beyond Perturbation: An Introduction to the Homotopy Analysis Method. CRC Press (2003)
12. Srinivasacharya, D., Kaladhar, K.: Mixed convection flow of couple stress fluid between parallel vertical plates with Hall and Ion-slip effects. Comm. Nonlinear Sci. Numer. Simu. **17**(6), 2447–2462 (2012)

Optimization of Temperature of a 3D Duct with the Position of Heat Sources Under Mixed Convection

V. Ganesh Kumar and K. Phaneendra

Abstract We consider a numerical investigation of a problem to determine the optimal arrangement of ten discrete heat sources, mounted on a bottom wall of a three-dimensional horizontal duct under turbulent mixed convection heat transfer using finite volume method (FVM). The standard $k-\varepsilon$ turbulence model modified by including buoyancy effects with physical boundary conditions has been used for the analysis. The objective is to find the configuration of ten heat sources so that the total temperature of the duct is minimum at this configuration. The governing equations are solved by FVM using FLUENT. Finally, an exhaustive search has been made to determine the optimum.

Keywords $k-\varepsilon$ turbulence model · FVM · Horizontal duct

1 Introduction

Making a better and better design plays an important role to improve the global performance of electronic packages under the given constraints. da Silva et al. [1, 2] addressed the optimal distribution of discrete heat sources on a wall cooled by forced convection and natural convection separately to maximize the global conductance between the wall and the coolant. Premachandran and Balaji [3, 4] investigated the effect of buoyancy and surface radiation in a horizontal channel with four heat sources under conjugate mixed convection. They also studied numerically about mixed convection heat transfer from converging, parallel, and diverging channels

V. G. Kumar
Department of Mathematics, VNR Vignana Jyothi Institute of Engineering and Technology, Hyderabad 500090, Telangana, India
e-mail: ganeshkumar68@gmail.com

K. Phaneendra (✉)
Department of Mathematics, University College of Science Saifabad, Osmania University, Hyderabad 500004, Telangana, India
e-mail: kollojuphaneendra@yahoo.co.in

D. Srinivasacharya and K. S. Reddy (eds.), *Numerical Heat Transfer and Fluid Flow*, Lecture Notes in Mechanical Engineering,
https://doi.org/10.1007/978-981-13-1903-7_32

with uniform volumetric heat generating plates. Sudhakar et al. [5] investigated an optimal heat distribution among the five protruding heat sources under laminar conjugate mixed convection heat in a vertical duct using the artificial neural network.

2 Mathematical Formulation

Normal to the flow direction, conjugate mixed convection in a 3D horizontal duct is considered. Ten identical finite heat sources with uniform heat rate are placed on the bottom wall of the duct at arbitrary positions. The dimensions of this duct are 30 cm length, 15 cm width, and 5 cm height. Each heat source has the dimensions 10 mm length, 10 mm width, and 5 mm height. The schematic view of the geometry considered is shown in Fig. 1.

Air is considered as the medium, which is initially at 303 K. The flow is considered to be unsteady, incompressible, and turbulent with constant fluid properties except for density for which Boussinesq approximation [6] is assumed to be valid. Radiation heat transfer, compressibility effects, and contact resistance between the substrate and the heat source are considered to be negligible. The objective is to locate ten discrete heat sources so that the total temperature in the duct is under the target temperature. The upper limit is usually 353 K, above which the reliability of electronic equipment goes down drastically. Based on these assumptions, the governing Eq. (5) in nondimensional form are as follows:

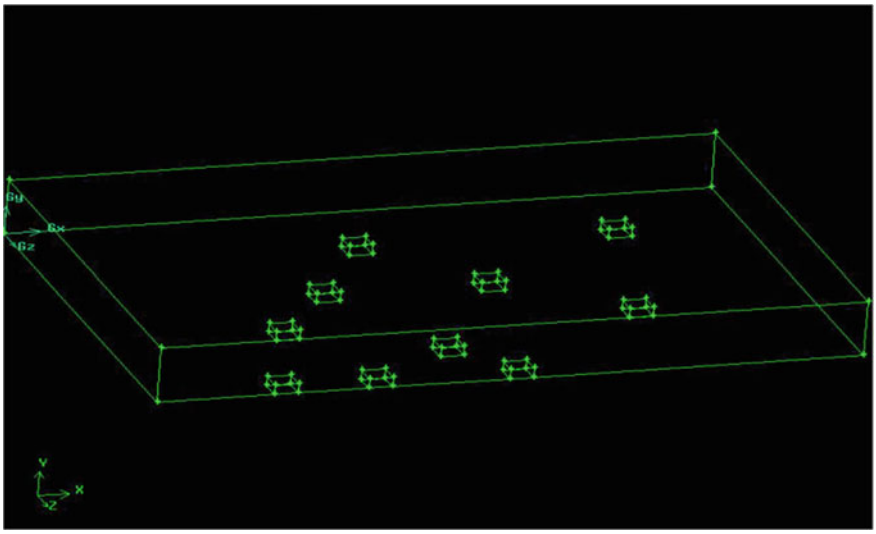

Fig. 1 Schematic view of discrete heat sources

Continuity

$$\frac{\partial U}{\partial X}+\frac{\partial V}{\partial Y}+\frac{\partial W}{\partial Z}=0 \tag{1}$$

X-momentum

$$\frac{\partial U}{\partial \tau}+U\frac{\partial U}{\partial X}+V\frac{\partial U}{\partial Y}+W\frac{\partial U}{\partial Z}=-\frac{\partial P}{\partial X}+\frac{1}{\mathrm{Re}_s}\frac{\partial}{\partial X}\left[2\left(1+\nu_t^*\right)\frac{\partial U}{\partial X}\right]+\frac{1}{\mathrm{Re}_s}\frac{\partial}{\partial Y}\left[\left(1+\nu_t^*\right)\left(\frac{\partial U}{\partial Y}+\frac{\partial V}{\partial X}\right)\right]+\frac{1}{\mathrm{Re}_s}\frac{\partial}{\partial Z}\left[\left(1+\nu_t^*\right)\left(\frac{\partial U}{\partial Z}+\frac{\partial W}{\partial X}\right)\right] \tag{2}$$

Y-momentum

$$\frac{\partial V}{\partial \tau}+U\frac{\partial V}{\partial X}+V\frac{\partial V}{\partial Y}+W\frac{\partial V}{\partial Z}=-\frac{\partial P}{\partial X}+\frac{1}{\mathrm{Re}_s}\frac{\partial}{\partial X}\left[\left(1+\nu_t^*\right)\left(\frac{\partial V}{\partial X}+\frac{\partial U}{\partial Y}\right)\right]+\frac{1}{\mathrm{Re}_s}\frac{\partial}{\partial Y}\left[2\left(1+\nu_t^*\right)\left(\frac{\partial V}{\partial Y}\right)\right]+\frac{1}{\mathrm{Re}_s}\frac{\partial}{\partial Z}\left[\left(1+\nu_t^*\right)\left(\frac{\partial W}{\partial Y}+\frac{\partial V}{\partial Z}\right)\right] \tag{3}$$

Z-momentum

$$\frac{\partial W}{\partial \tau}+U\frac{\partial W}{\partial X}+V\frac{\partial W}{\partial Y}+W\frac{\partial W}{\partial Z}=-\frac{\partial P}{\partial X}+\frac{1}{\mathrm{Re}_s}\frac{\partial}{\partial X}\left[\left(1+\nu_t^*\right)\left(\frac{\partial W}{\partial X}+\frac{\partial U}{\partial Z}\right)\right]+\frac{1}{\mathrm{Re}_s}\frac{\partial}{\partial Y}\left[\left(1+\nu_t^*\right)\left(\frac{\partial W}{\partial Y}+\frac{\partial V}{\partial Z}\right)\right]+\frac{1}{\mathrm{Re}_s}\frac{\partial}{\partial Z}\left[2\left(1+\nu_t^*\right)\frac{\partial W}{\partial Z}\right] \tag{4}$$

Energy

$$\frac{\partial \theta}{\partial \tau}+U\frac{\partial \theta}{\partial X}+V\frac{\partial \theta}{\partial Y}+W\frac{\partial \theta}{\partial Z}=-\frac{\partial P}{\partial X}+\frac{1}{\mathrm{Re}_s}\frac{\partial}{\partial X}\left[\left(\frac{1}{\mathrm{Pr}}+\frac{\nu_t^*}{\sigma_T}\right)\frac{\partial \theta}{\partial X}\right]+\frac{1}{\mathrm{Re}_s}\frac{\partial}{\partial Y}\left[\left(\frac{1}{\mathrm{Pr}}+\frac{\nu_t^*}{\sigma_T}\right)\frac{\partial \theta}{\partial Y}\right]+\frac{1}{\mathrm{Re}_s}\frac{\partial}{\partial Z}\left[\left(\frac{1}{\mathrm{Pr}}+\frac{\nu_t^*}{\sigma_T}\right)\frac{\partial \theta}{\partial Z}\right] \tag{5}$$

Here,

$$X=\frac{x}{S},\ Y=\frac{y}{S},\ Z=\frac{z}{S},\ U=\frac{uS}{\alpha},\ V=\frac{vS}{\alpha},\ W=\frac{wS}{\alpha},\ \mathrm{Pr}=\frac{\nu}{\alpha},\ P=\frac{pS^2}{\rho\alpha^2},$$

$$\mathrm{Re}_s=\frac{u_\infty S}{\nu},\ \theta=\frac{T-T_\infty}{T_{\max}-T_\infty}$$

2.1 *Standard* k−ε *Turbulence Model*

The viscosity multiplied by the fluctuating vorticity gives the rate of dissipation of kinetic energy ε at high Reynolds numbers. Using Navier–Stokes equation, one can derive exact transport equation for the fluctuating vorticity and thus the dissipation rate. The $k-\varepsilon$ model consists of the following two equations:

The turbulent kinetic energy equation is

$$\begin{aligned}\frac{\partial k^*}{\partial \tau} + U\frac{\partial k^*}{\partial X} + V\frac{\partial k^*}{\partial Y} + W\frac{\partial k^*}{\partial Z} &= \frac{1}{\mathrm{Re}_s}\frac{\partial}{\partial X}\left[\left(1+\frac{\nu_t^*}{\sigma_k}\right)\frac{\partial k^*}{\partial X}\right] \\ &+ \frac{1}{\mathrm{Re}_s}\frac{\partial}{\partial Y}\left[\left(1+\frac{\nu_t^*}{\sigma_k}\right)\frac{\partial k^*}{\partial Y}\right] \\ &+ \frac{1}{\mathrm{Re}_s}\frac{\partial}{\partial Z}\left[\left(1+\frac{\nu_t^*}{\sigma_k}\right)\frac{\partial k^*}{\partial Z}\right] + P_k^* + G_k^* - \varepsilon^* \end{aligned} \tag{6}$$

Equation for dissipation rate of turbulent kinetic energy is

$$\begin{aligned}\frac{\partial \varepsilon^*}{\partial \tau} + \mathrm{U}\frac{\partial \varepsilon^*}{\partial \mathrm{X}} + \mathrm{V}\frac{\partial \varepsilon^*}{\partial \mathrm{Y}} + \mathrm{W}\frac{\partial \varepsilon^*}{\partial \mathrm{Z}} &= \frac{1}{\mathrm{Re}_s}\frac{\partial}{\partial \mathrm{X}}\left[\left(1+\frac{\nu_t^*}{\sigma_\varepsilon}\right)\frac{\partial \varepsilon^*}{\partial \mathrm{X}}\right] \\ &+ \frac{1}{\mathrm{Re}_s}\frac{\partial}{\partial \mathrm{Y}}\left[\left(1+\frac{\nu_t^*}{\sigma_\varepsilon}\right)\frac{\partial \varepsilon^*}{\partial \mathrm{Y}}\right] \\ &+ \frac{1}{\mathrm{Re}_s}\frac{\partial}{\partial Z}\left[\left(1+\frac{\nu_t^*}{\sigma_\varepsilon}\right)\frac{\partial \varepsilon^*}{\partial Z}\right] + [C_{\varepsilon 1}P_k^* + C_{\varepsilon 3}G_k^* - C_{\varepsilon 2}\varepsilon^*]\frac{\varepsilon^*}{k^*} \end{aligned} \tag{7}$$

Here,

$$\begin{aligned}P_k^* = \frac{\nu_t^*}{\mathrm{Re}_s}\Bigg[&2\left(\frac{\partial U}{\partial X}\right)^2 + 2\left(\frac{\partial V}{\partial Y}\right)^2 + 2\left(\frac{\partial W}{\partial Z}\right)^2 + \left(\frac{\partial U}{\partial Y} + \frac{\partial V}{\partial X}\right)^2 \\ &+\left(\frac{\partial W}{\partial Y} + \frac{\partial V}{\partial Z}\right)^2 + \left(\frac{\partial U}{\partial Z} + \frac{\partial W}{\partial X}\right)^2\Bigg]\end{aligned}$$

$$G_k^* = -\frac{\nu_t^*}{\sigma_T}\frac{Ri^+}{\mathrm{Re}_s}\left(\frac{\partial \theta}{\partial X} + \frac{\partial \theta}{\partial Y} + \frac{\partial \theta}{\partial Z}\right),\ \nu_t^* = C_\mu \mathrm{Re}_s \frac{k^{*2}}{\varepsilon^*},\ C_{\varepsilon 3} = \tanh\left(\frac{\nu_t^*}{U}\right)\ Ri^+ = \frac{Gr^*}{\mathrm{Re}_s^2}.$$

Here, $C_\mu, \sigma_k, \sigma_\varepsilon, \sigma_T, C_{\varepsilon 1}, C_{\varepsilon 2}$ are all taken to be constants and are given, respectively, the values 0.09, 1.0, 1.3, 1.0, 1.44, 1.92.

2.2 Boundary Conditions

For all fluid–solid surface interfaces, no-slip conditions are applied $U = V = W = 0$ and the other solid surfaces are assumed to be adiabatic $\frac{\partial T}{\partial n} = 0$. At the inlet $V = W = 0, U = u_\infty, T = T_\infty$.

3 Method of Solution

The finite volume method (FVM) is used to solve the governing Eqs. (1)–(7) with the associated boundary conditions. The FVM can accommodate any type of grid when compared to FDM. It uses the integral form of the conservation equations as its starting point. The solution domain is divided into a finite number of sub-volumes for which the conservation equations are applied. To handle the pressure–velocity coupling, the numerical procedure called SIMPLEC is used. As the convergence criteria, a residual of 10^{-6} for the continuity and momentum, and 10^{-2} for the energy have been employed. When the maximum relative change between two consecutive iteration levels fall below 10^{-4}, then the convergence at a given time step is declared for U, V, W, and θ.

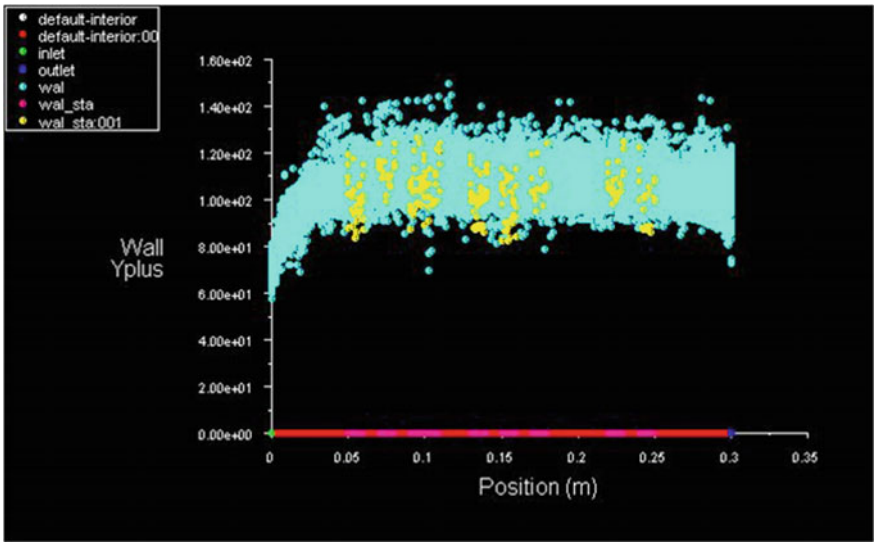

Fig. 2 Values of wall y_p^+

4 Validation of the Numerical Scheme

The location of the first cell adjacent to the wall is determined based on the region of the turbulent boundary layer. Standard wall functions can be employed when the flow resolution starts from the log-layer region. When the standard wall function is considered, then the value of wall is $y_p^+ \geq 30 - 300$ for high Reynolds flow. Mesh should be generated in such a way that the first cell adjacent to the wall does not fall in buffer layer, i.e.,$y_p^+ = 5 - 30$.

It can be observed from Fig. 2 that all values y_p^+ are above the 40. It does not fall between the buffer layers. So, the given numerical scheme is valid.

5 Results and Discussion

At high Reynolds number under mixed convection heat transfer, a detailed numerical study has been carried out. Initially, a heat flux input of 25×10^4 W/m^2 was given to all the heat sources. In our study, 40 configurations are made arbitrarily. In every configuration, each heat source is located at prescribed location. Table 1 represents the location of all heat sources at prescribed configurations and Figs. 3, 4, 5, 6, and 7 show the contours of temperature in the duct with the heat sources at those configurations.

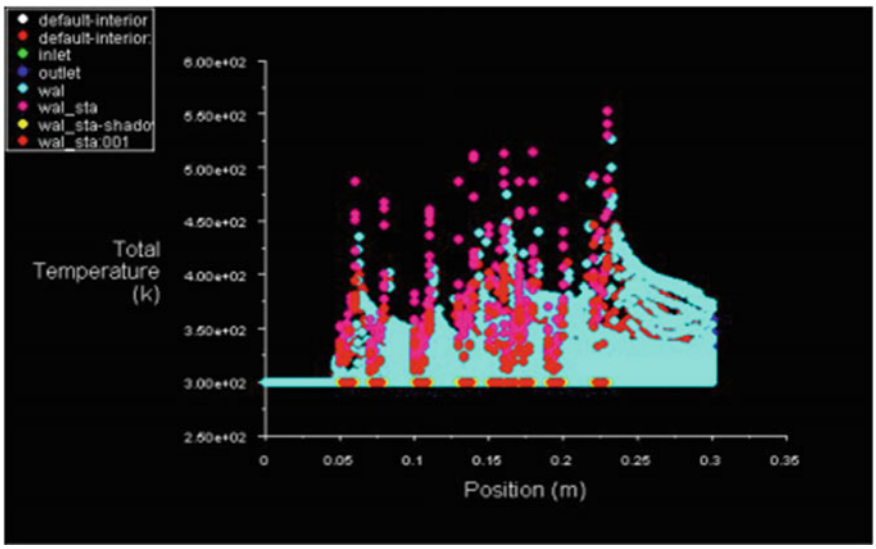

Fig. 3 Total temperature at configuration 1

Table 1 Location of all heat sources at prescribed configurations

Conf. no.	Chip no. →	1	2	3	4	5	6	7	8	9	10
1	Distance from +ve x-axis	0.19	0.19	0.19	0.19	0.19	0.19	0.19	0.19	0.19	0.19
	Distance from +ve z-axis	0.19	0.19	0.19	0.19	0.19	0.19	0.19	0.19	0.19	0.19
2	Distance from +ve x-axis	0.18	0.18	0.16	0.16	0.14	0.14	0.13	0.11	0.06	0.04
	Distance from +ve z-axis	0.16	0.19	0.22	0.26	0.17	0.21	0.25	0.27	0.18	0.20
3	Distance from +ve x-axis	0.16	0.16	0.16	0.12	0.12	0.11	0.09	0.08	0.06	0.04
	Distance from +ve z-axis	0.11	0.13	0.16	0.12	0.12	0.11	0.09	0.08	0.06	0.04
4	Distance from +ve x-axis	0.19	0.19	0.19	0.13	0.13	0.09	0.09	0.04	0.04	0.16
	Distance from +ve z-axis	0.05	0.09	0.15	0.07	0.22	0.10	0.17	0.13	0.24	0.13
5	Distance from +ve x-axis	0.17	0.17	0.16	0.14	0.13	0.14	0.08	0.08	0.08	0.05
	Distance from +ve z-axis	0.03	0.11	0.18	0.05	0.15	0.22	0.07	0.12	0.25	0.01

Finally, Table 2 shows the values of the total temperature in the duct at prescribed configurations when the constant heat flux is given to all heat sources. By observing the temperature contours at configuration 4 in Fig. 6, the total temperature in the duct is less than the target temperature (353 K). So, this configuration is one of the required configurations to control the total temperature in the duct. This optimum configuration is not unique. There are several near-optimal configurations for the present problem. Among them, one is at configuration 5. The worst configuration is at configuration 2.

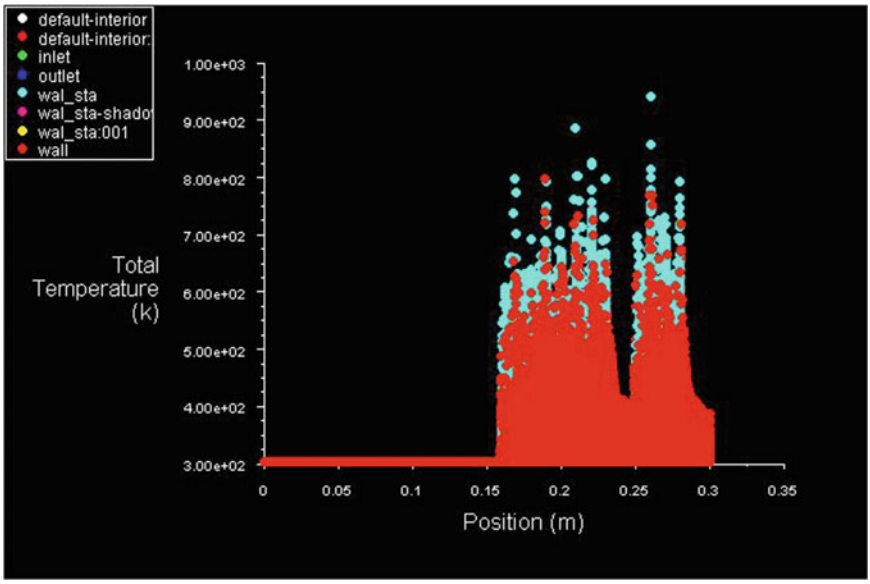

Fig. 4 Total temperature at configuration 2

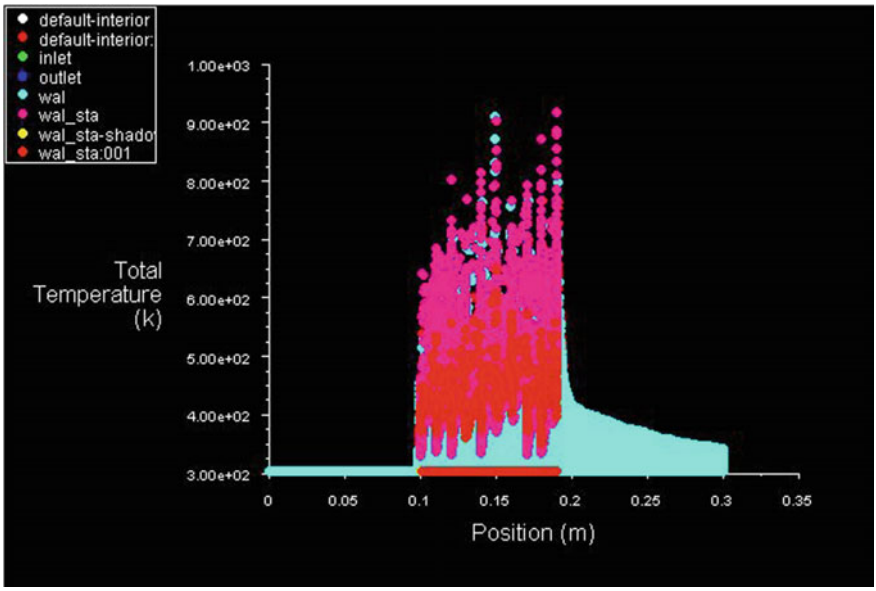

Fig. 5 Total temperature at configuration 3

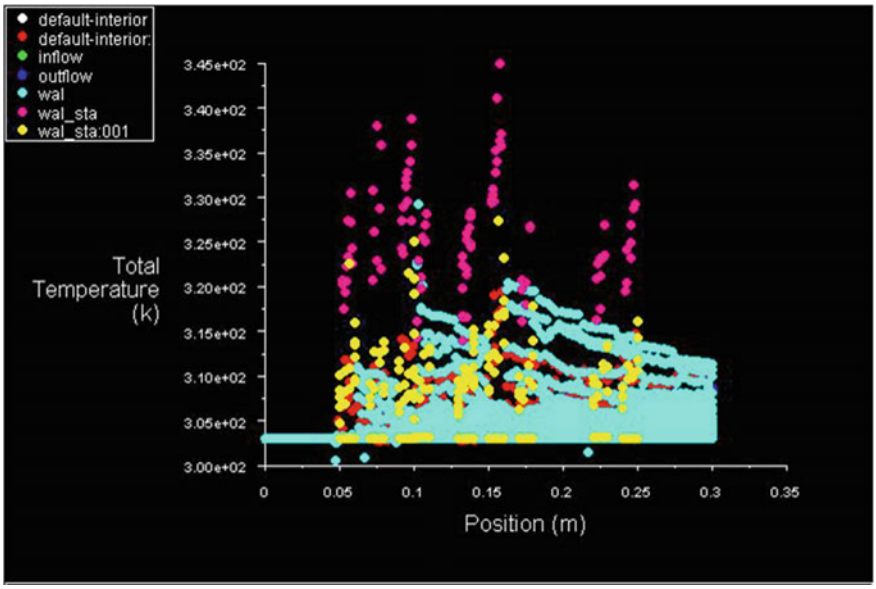

Fig. 6 Total temperature at configuration 4

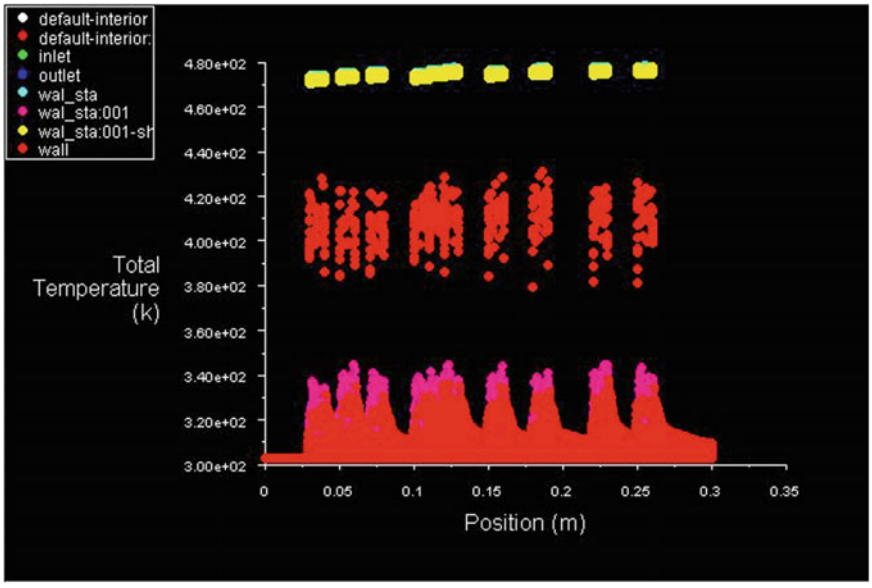

Fig. 7 Total temperature at configuration 5

Table 2 Total temperature in the duct at prescribed configurations

Configuration no.	1	**2**	3	**4**	5
Total temperature in *K*	552	**965**	946	**348**	478

6 Conclusion

The following conclusions are drawn from the above study:

(i) The temperature increases when the chips are placed close to each other due to which there is an interaction of the boundary layers, and the cooling efficiency comes down while the temperature decreases when the chips are placed away from each other.
(ii) The temperature decreases when the chips are placed near the inlet face due to the flow.
(iii) The heat source which is placed near the outlet face has the maximum temperature due to heated fluid flow.

References

1. da Silva, A.K., Lorente, S., Bejan, A.: Optimal distribution of discrete heat sources on a plate with laminar forced convection. Int. J. Heat Mass. Transfer. **47**, 2139–2148 (2004)
2. da Silva, A.K., Lorente, S., Bejan, A.: Optimal distribution of discrete heat sources on a wall with natural convection. Int. J. Heat Mass. Transfer. **47**, 203–214 (2004)
3. Premachendran, B., Balaji, C.: Conjugate Mixed convection with surface radiation from a horizontal channel with protruding heat sources. Heat Mass. Transf. **49**, 3568–3582 (2006)
4. Premachendran, B., Balaji, C.: Mixed convection Heat transfer from a horizontal channel with protruding heat sources. Heat Mass. Transf. **41**, 510–518 (2005)
5. Sudhakar, T.V.V., Balaji, C., Venkateshan, S.P.: Optimal configuration of discrete heat sources in a vertical duct under conjugate mixed convection using artificial neural networks. Int. J. Therm. Sci. **48**, 881–890 (2009)
6. Mathews, R.N., Balaji, C., Sundararajan, T.: Computation of conjugate heat transfer in the turbulent mixed convection regime in a vertical channel with multiple heat sources. Int. J. Heat Mass. Transfer **43**, 1063–1074 (2007)

Viscous Fluid Flow Past a Permeable Cylinder

P. Aparna, N. Pothanna and J. V. Ramana Murthy

Abstract Uniform flow of a viscous fluid past a permeable circular cylinder is considered. The flow across the surface of permeable cylinder is possible due to jump in the pressure at the surface. The flow pattern for the outer and inner regions of the cylinder is obtained in terms of stream function. The bounds for the permeability parameter are estimated. For various values of permeability parameter, the streamline pattern is drawn. The effect of permeability parameter on the drag is studied numerically and the results are presented in the form of graphs.

Keywords Viscous fluid · Permeable cylinder

1 Introduction

The classical problem of flow past axi-symmetric bodies has been attracting many researchers even in modern times. There is a vast literature available for the case of sphere, spheroid and circular cylinder for the particular case of Stokesian flows and non-Stokesian flows. But the attention paid by researchers towards flow past permeable bodies is very less. The first work in this direction was presented by Leonov [1] for the case of sphere. Wolfersdorf [2], Padmavathi et al. [3], and Usha [4] studied viscous fluid flows past permeable sphere in different situations. It is observed that the drag due to permeable body is lesser than the impervious body. The work of Padmavathi [5] is worth mentioning for the case of permeable cylinder. In the case of cylinders filled with porous medium similar problems were attempted by many researchers. For the numerical solutions of the flow of fluids past cylinder, one can refer the works of Rajani and Majumdar [6] and Catalano et al. [7]. Experimental and analytical analysis of flow past D-shaped cylinder was studied by Mhalungekar et al.

P. Aparna (✉) · N. Pothanna
VNR Vignana Jyothi Institute of Engineering & Technology, Hyderabad 500090, India
e-mail: aparnapodila@gmail.com

J. V. Ramana Murthy
National Institute of Technology Warangal, Warangal 506002, India

D. Srinivasacharya and K. S. Reddy (eds.), *Numerical Heat Transfer and Fluid Flow*, Lecture Notes in Mechanical Engineering,
https://doi.org/10.1007/978-981-13-1903-7_33

[8]. They studied the flow past bluff body. The D-shaped cylinder is one of the bluff bodies, which serve some vital operational function in aerodynamics. They calculated analytically and experimentally the dimensions of D-shaped circular cylinder and obtained the drag coefficient for different values of Reynolds's number. Numerical study of a viscous fluid flow past a circular cylinder was studied by Kawaguti and Jain [9]. They calculated the pressure distribution and coefficient of drag. In this, we consider the viscous fluid flow past a permeable circular cylinder.

2 Statement and Formulation of the Problem

The equations of motion for an incompressible viscous fluid under slow flow of Stokesian assumption are given by

$$\nabla.\overline{Q} = 0 \tag{1}$$

$$0 = -\nabla P - \mu\nabla \times (\nabla \times \overline{Q}), \tag{2}$$

where $\overline{Q}$ is the velocity vector, P is pressure, ρ is density and μ is the viscosity coefficient.

We consider slow uniform flow with velocity U_0 of an incompressible viscous fluid past a fixed permeable cylinder of radius a (see Fig. 1). A cylindrical polar coordinate system with $(e_r,\ e_\theta,\ e_z)$ as unit base vectors with origin at the centre of the cylinder and with X-axis along the direction of the flow is considered. Since the flow is two dimensional, velocity is taken independent of z as

$$\overline{Q} = U(R,\theta)\bar{e}_r + V(R,\theta)\bar{e}_\theta. \tag{3}$$

We introduce the following non-dimensional variables:

$$R = ar,\ \Psi = U_0 a\psi,\ U = U_0 u,\ V = U_0 v,\quad P = p\,\rho U_0^2 \text{ and } Re = \frac{\rho U_0 a}{\mu}, \tag{4}$$

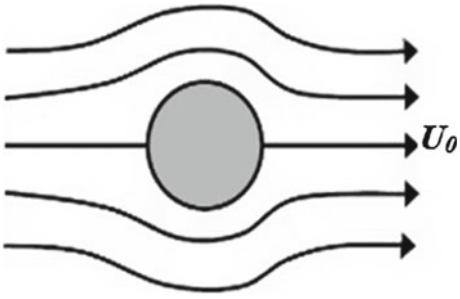

Fig. 1 Physical view of flow past cylinder

where Re is the Reynolds number. Since the flow is two dimensional, the stream function $\psi(r, \theta)$ can be introduced as

$$u = \frac{1}{r}\frac{\partial \Psi}{\partial \theta}, v = -\frac{\partial \Psi}{\partial r}. \tag{5}$$

Substituting (5) in Eq. (2), we get the following three equations along base vectors:

$$Re\,\frac{\partial p}{\partial r} = \frac{1}{r}\frac{\partial E^2\psi}{\partial \theta} \tag{6}$$

$$Re\frac{1}{r}\,\frac{\partial p}{\partial \theta} = -\frac{\partial E^2\psi}{\partial r} \tag{7}$$

$$Re\,\frac{\partial p}{\partial z} = 0, \tag{8}$$

where

$$E^2 = \frac{\partial^2}{\partial r^2} + \frac{1}{r}\frac{\partial}{\partial r} + \frac{1}{r^2}\frac{\partial^2}{\partial \theta^2} = \nabla^2$$

Eliminating pressure p from (6) and (7), we get

$$E^4\psi = 0. \tag{9}$$

3 Boundary Conditions

The stream function ψ can be obtained under the boundary conditions: *(i) Regularity condition, (ii) Continuity of normal velocity on the boundary and (iii) No slip condition.* These can be stated mathematically as

$$\lim_{r\to\infty} \bar{q} = \bar{i} \quad \text{i.e} \lim_{r\to\infty} \psi_e = r\sin\theta \tag{10}$$

$$\frac{\partial \psi_e}{\partial \theta} = \frac{\partial \psi_i}{\partial \theta} \text{on } r = 1 \tag{11}$$

$$\frac{\partial \psi_e}{\partial r} = \frac{\partial \psi_i}{\partial r} \text{on } r = 1. \tag{12}$$

4 Solution of the Problem

By the method of separation of variables, we observed that the stream function for external flow and internal flow is given by

$$\psi_e = \left(r + \frac{a_1}{r} + b_1 \mathrm{r} \log \mathrm{r}\right) \sin\theta \tag{13}$$

$$\psi_i = \left(a_2 r + b_2 r^3\right) \sin\theta. \tag{14}$$

The constants a_1, b_1, a_2, b_2 are obtained using the boundary conditions in (11) and (12) as stated above. After finding the constants, the internal and external solutions are obtained as

$$\psi_e = \left\{r + \left(\frac{2a_2}{3} - 1\right)\frac{1}{r} + \left(\frac{2a_2}{3} - 2\right) r \ \log r\right\} \sin\theta \tag{15a}$$

$$\psi_i = a_2 \left\{r - \frac{r^3}{3}\right\} \sin\theta. \tag{15b}$$

The constant a_2 is arbitrary and we can define it as permeability parameter since when $a_2 = 0$, then $\psi_i = 0$, which implies the impermeability of the surface.

5 Pressure

Now, from Eqs. (6) and (7), the pressure can be obtained as follows:

$$P = \int \left(\frac{\partial p}{\partial r}\mathrm{d}r + \frac{\partial p}{\partial \theta}\mathrm{d}\theta\right)$$

$$= \frac{1}{Re} \int \left(-\frac{1}{r}\frac{\partial E^2 \psi}{\partial \theta}\mathrm{d}r + r\frac{\partial}{\partial r}E^2\psi \mathrm{d}\theta\right) = \frac{1}{\mathrm{Re}} \int \left(\frac{g}{r}\cos\theta \, \mathrm{d}r - r g' \sin\theta \, d\theta\right)$$

$$\mathrm{P} = \frac{1}{Re}(r g') \cos\theta. \tag{16}$$

This is obtained by taking $D^2 f = -\mathrm{g}$ and $D^2 g = 0$.

From the above equations, we obtain the external pressure P_e and the internal pressure P_i as

$$P_e = 2b_1 \frac{\cos\theta}{Re.r} = 4\left(\frac{\tau}{3} - 1\right)\frac{\cos\theta}{Re.r} \text{ and } P_i = -8b_2 r \frac{\cos\theta}{Re} = 8\tau.r\frac{\cos\theta}{3Re}. \tag{17}$$

6 Bounds for Permeability Parameter

On the surface of the cylinder for $0 \leq \theta \leq \pi/2$, the filtration velocity u_0 must be positive and for $\pi/2 \leq \theta \leq \pi$, u_0 must be negative. If $\Delta P = P_e - P_i$ at $r = 1$, then for $0 \leq \theta \leq \pi/2$, $\Delta P \leq 0$ and for $\pi/2 \leq \theta \leq \pi$, $\Delta P \geq 0$ at $r = 1$. The condition that filtration velocity $u_0 \geq 0$ gives $u \geq 0$ at $r = 1$ or $a_2 + b_2 \geq 0$, which implies that $2a_2/3 \geq 0$ or $a_2 \geq 0$. The condition that $\Delta P \leq 0$ gives the condition that $b_1 + 4b_2 \leq 0$.

This implies that $a_2 \leq 3$. We now introduce permeability parameter τ as a_2. Hence, the bounds for permeability parameter τ are given by $0 \leq \tau \leq 3$.

7 Drag Acting on the Cylinder

Drag on the cylinder per length

$$L = L \int_0^{2\pi} (T_{11}\cos\theta - T_{21}\sin\theta) R|_{R=a} \mathrm{d}\theta \tag{18}$$

$$T_{11} = -P + \mu . \frac{\partial U}{\partial R} \quad \text{and} \quad T_{21} = \frac{\mu}{2}\left\{ \frac{\partial V}{\partial R} + \frac{1}{R}\frac{\partial U}{\partial \theta} - \frac{V}{R} \right\}. \tag{19}$$

Substituting the above expressions for T_{11} and T_{21} in drag, the reduced expression for drag in non-dimensional form is given by (p and ψ are non-dimensional in (20a, 20b))

$$\text{Drag} = \mathrm{D} = \pi U_0 \mu L \left\{ -Re.\bar{p} + D^2 f \right\}_{r=1} = \pi U_0 \mu L \left(g' - g\right)_{r=1} = \frac{2\pi\rho U_0^2 aL}{Re}\left(1 - \frac{a_2}{3}\right) \tag{20a}$$

$$\text{Coefficient of Drag} = \mathrm{C_f} = \mathrm{D}/(1/2a\mathrm{L}\rho\mathrm{U}_0^2) = \frac{4}{Re}\left(1 - \frac{a_2}{3}\right). \tag{20b}$$

8 Results and Discussions

8.1 Streamlines

The streamline pattern for the viscous fluid flow past permeable cylinder at low Reynolds numbers is drawn based on Eq. (16). We can notice that in the flow region, a fluid cylinder is formed in concentric to the permeable cylinder. Within this fluid cylinder, flow reversal takes place and fluid passes through the permeable cylinder. This flow circulation takes place due to the permeable nature of the cylinder. Note that *this is one novel feature for flow past a permeable body.* This type of flow reversal will not occur for flow past impermeable body or for a body filled with porous medium. The flow past a porous cylinder at low Reynolds numbers is different from this. The radius of the fluid cylinder increases as the value of the permeability parameter τ increases. When $\tau = 0$, the flow is exactly similar to the flow past an impermeable cylinder. When $\tau = 3$ (this is the maximum value of τ), then flow collapses to uniform flow, i.e. free flow. This is shown in Fig. 2 for four different values of τ. In Fig. 5, the radius of the circle in which we observe the flow reversal at various values of permeability parameter τ is shown. This is in conformity with above observations as in Figs. 3 and 4. As τ increases, the radius of the circle increases slowly but

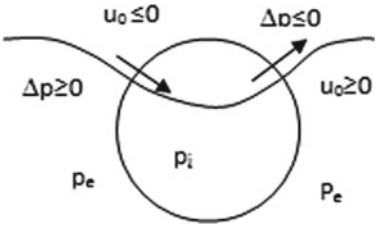

Fig. 2 Pressure changes in and out of the body

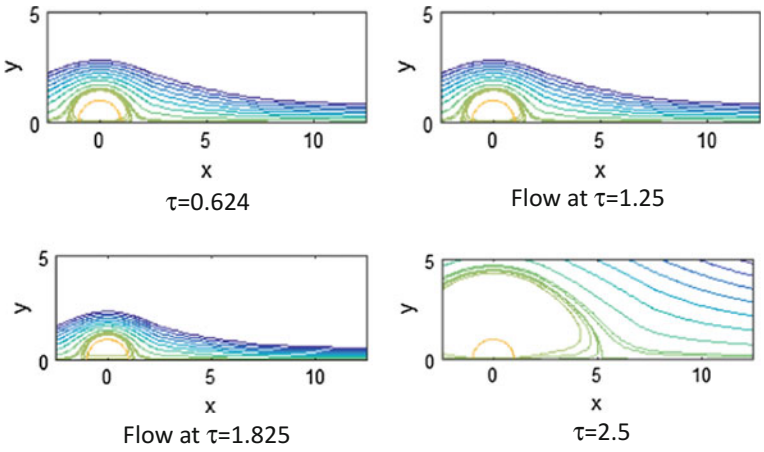

Fig. 3 Streamline pattern for different values of permeability parameter τ

when τ is more than 2.7, the radius shoots to very big values. In Fig. 6, pressure is shown at different Reynolds numbers and various permeability values based on the expression (17). For $Re = 1$, $\tau = 0$, the pressure is approximately in agreement with the results of Nieuwstadt and Keller [10]. This is the case of impermeable cylinder at low Reynolds numbers.

8.2 Drag

It can be observed from Eqs. (20a and 20b) that the drag decreases as permeability parameter increases. This result is exactly the same as that of Nieuwstadt and Keller [10], when nonlinear terms are deleted. Drag attains minimum value zero, when permeability parameter is maximum, i.e. $\tau = 3$ and drag is maximum, when $\tau = 0$, i.e. the case of impermeable cylinder. The formula for drag as given by Lamb [11] is

$$D = \frac{4\pi}{\mathrm{Re}\left(0.5 - \gamma - \log\left(\frac{\mathrm{Re}}{4}\right)\right)}.$$

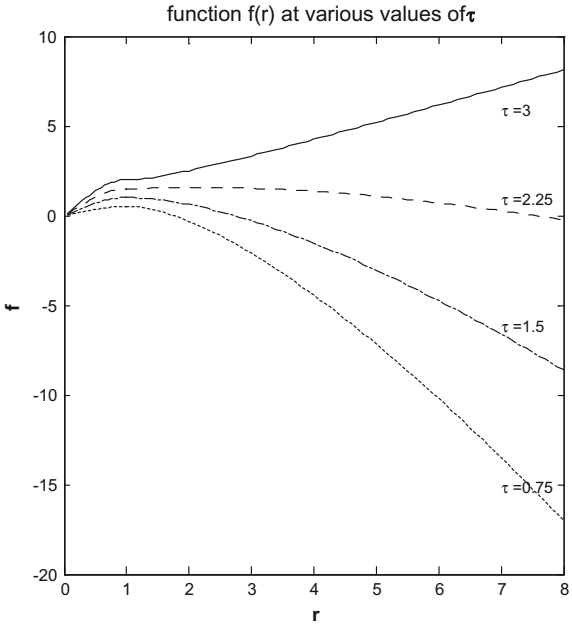

Fig. 4 Stream function f versus distance r

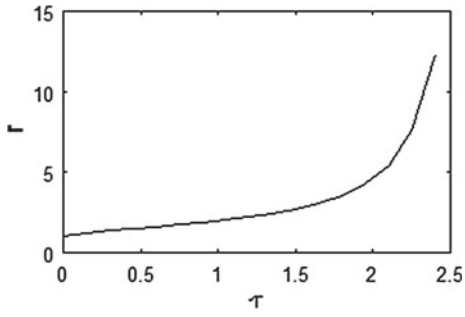

Fig. 5 Radius of fluid cylinder formed versus τ

The above formula is obtained by considering that at distance r, $\nabla^2 \vec{q}$ is comparable with $1/Re$. Barring this, our results are in agreement with Nieuwstadt and Keller [10] for $Re = 1$. As in the case of impermeable cylinder, here also the drag is inversely proportional to Reynolds number. From this, we can conclude that the permeability of the body decreases the drag acting on the body. This result is similar to flow past porous bodies, which reduce the drag.

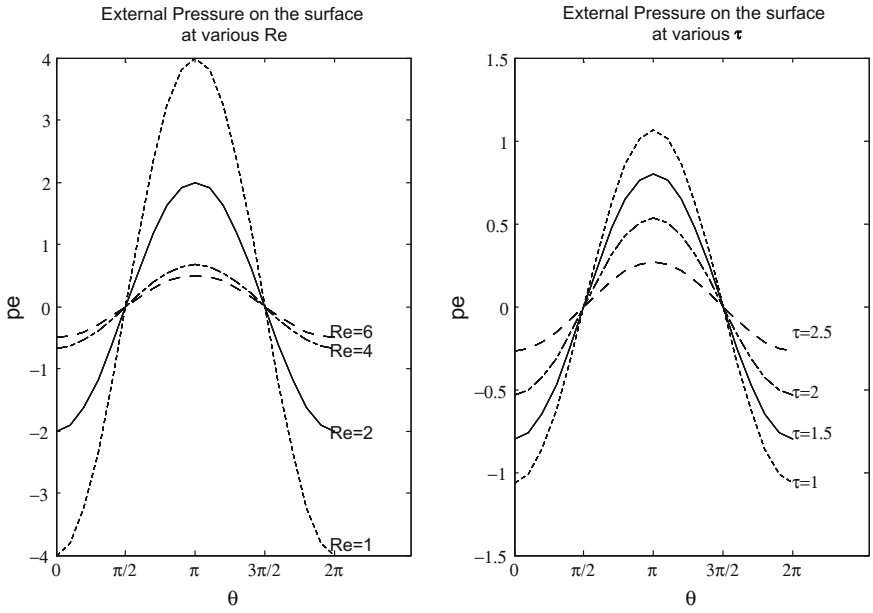

Fig. 6 Pressure at different values of Reynolds numbers and permeabilities τ

9 Conclusions

9.1 Drag

It is observed by mathematical analysis that at low Reynolds numbers the flow past a permeable cylinder experiences reduction of drag and pressure on the surface. This reduction is quite observable and can be comparable with impermeable case. This has wide applications in aerospace research and industries.

Acknowledgements First, author gratefully acknowledges UGC–SERO, Hyderabad, India for the financial support in carrying out this work. No.F MRP-6736/16 (SERO/UGC).

References

1. Leonov, A.I.: The slow stationary flow of a viscous fluid about a porous sphere. J. App. Maths. Mech. **26**, 564–566 (1962)
2. Wolfersdorf, L.V.: Stokes flow past a sphere with permeable surface. ZAMM **69**, 111 (1989)
3. Padmavathi, B.S., Amarnath, T., Palaniappan, P.: Stokes flow past a permeable sphere-non-axisymmetric case. ZAMM **74**, 290–292 (1994)
4. Usha, R.: Creeping flow with concentric permeable spheres in relative motion. ZAMM **75**, 644–646 (1995)

5. Padmavathi, B.S.: Stokes flow past a permeable circular cylinder. Mech. Res. Comm. **26**, 107–113 (1999)
6. Rajani, B.N., Majumdar, S.: Numerical simulation of laminar flow past a circular cylinder. Appl. Math. Model. **33**, 1228–1247 (2009)
7. Catalano, P., Wang, M., Iaccarino, G., Moin, P.: Numerical simulation of the flow around a circular cylinder at high Reynolds numbers. Int. Jr of Heat Fluid Flow **24**, 463–469 (2003)
8. Mhalungekar, C.D., Kothavale, B.S., Wadkar, S.P.,: Experimental and analytical analysis of flow past d-shaped cylinder. IJIRAE **1**, 218–223 (2014)
9. Kawaguti, M., Jain, P.: Numerical Study of a viscous Fluid flow past a Circular Cylinder. J. Phys. Soc. Japan **21**, 2055–2062 (1966)
10. Nieuwstadt, F., Keller, H.B.: Viscous flow past a circular cylinder. Comput. Fluids **1**, 59–71 (1973)
11. Lamb, H.: Hydrodynamics, 6th edn. Cambridge University Press, Cambridge (1932)

Numerical Solution of Load-Bearing Capacity of Journal Bearing Using Shape Function

Pooja Pathak, Vijay Kumar Dwivedi and Adarsh Sharma

Abstract The increasing demand of high speed with high reliability for longer life and noiseless operation requires a compact size bearing. For the exact calculation of load-bearing capacity requires mathematical expertise to solve two-dimensional fluid flow Reynolds equation. In this chapter, Gauss–Legendre numerical integration is used to calculate the load-carrying capacity of bearing.

Keywords Journal bearing · Shape function · Load bearing capacity

1 Introduction

Machine speed increased dramatically and bearings were central to rotary and linear movements. Lubrication theory only gave its first step at the end of nineteenth century though Hirn [1] and Petrov [2] verified experimentally that the drag was actually caused by the shear rate within the fluid rather than by direct interaction between two surfaces in relative motion. Sommerfeld [3] derived an analytical solution for the Reynolds equation, which neglects the effect of bearing edges as well as occurrence of film rupture. Gumbel [4] improved Sommerfeld solution by presenting the half-Sommerfeld theory. In this approach, the negative pressure obtained at the divergent portion of the gap is turned to zero. In the same context, Ockvirk [5] proposed the short bearing theory and an approximate method to predict the behaviour of narrow bearings, which are more commonly used in industry because the long bearing theory results were poor. Dwivedi et al. [6, 7] proposed a computer program for one-dimensional journal bearing problem to find out journal trajectory as well as the stability of bearing in different flow zones. To get the more realistic calculation of

P. Pathak (✉)
Department of Mathematics, GLA University, Mathura 281406, UP, India
e-mail: pooja.pathak@gla.ac.in

V. K. Dwivedi · A. Sharma
Mechanical Engineering Department, GLA University, Mathura 281406, India

D. Srinivasacharya and K. S. Reddy (eds.), *Numerical Heat Transfer and Fluid Flow*, Lecture Notes in Mechanical Engineering,
https://doi.org/10.1007/978-981-13-1903-7_34

static and dynamic characteristics of journal bearing, the author proposed a two-dimensional quadrilateral element for numerical integration in this chapter.

2 Analysis

Consider a journal bearing system as shown in Fig. 1, which shows the journal centre O_j eccentric to bearing centre O_b by eccentricity, e. External load W is acting through the journal centre Oj. Figure 2 is the expanded form of the bearing along the centre line O_b-O_j.

The Reynolds equation which governs the flow of lubricating oil in the clearance space of a journal bearing using linearized turbulence theory of Constantinescu [8] is given by Eq. (1)

$$\frac{\partial}{\partial x}\left[\frac{h^3}{\mu K_X}\frac{\partial p}{\partial X}\right]+\frac{\partial}{\partial Y}\left[\frac{h^3}{\mu K_Y}\frac{\partial p}{\partial Y}\right]=\frac{1}{2}U\frac{\partial h}{\partial X}+\frac{\partial h}{\partial t} \tag{1}$$

where K_X and K_Y are turbulent coefficients, and h can be expressed in terms of journal centre (X_j, Z_j) as

$$h = c - X_j \cos\alpha - Z_j \sin\alpha \tag{2}$$

where $\overline{h}=\frac{h}{c};\overline{X}_j=\frac{X_j}{c};\overline{Z}_j=\frac{Z_j}{c}$

Or

$$\overline{h} = 1 - \overline{X}_j \cos\alpha - \overline{Z}_j \sin\alpha \tag{3}$$

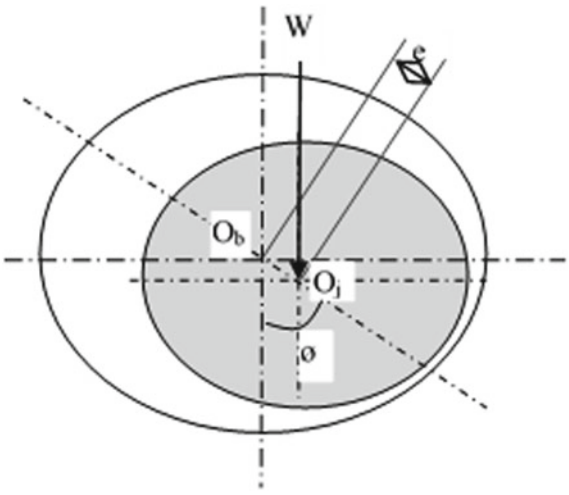

Fig. 1 Journal bearing system with bearing eccentricity, e

For non-dimensionalization of Eq. (1), different terms of Eq. (1) are non-dimensionalized as

$$\overline{h} = \frac{h}{c}; \overline{p} = \frac{p}{\mu_r \omega_r}\left(\frac{c}{R}\right)^2; \alpha = \frac{X}{R}; \beta = \frac{Y}{R}; \overline{\mu} = \frac{\mu}{\mu_r}$$

$\overline{\Omega} = \overline{\Omega}_r + \overline{a}_g\left(\overline{t} - \overline{t_r}\right)$, where $\overline{t} = \omega t; \overline{t_r} = \omega_r t_r; \overline{\Omega}_r = \frac{\Omega_r}{\omega_r}; \bar{a}_g = \frac{a_g}{\omega_r^2}$.
After non-dimensionalization, Eq. (1) reduces to Eq. (4)

$$\frac{\partial}{\partial \alpha}\left[\frac{\bar{h}^3}{\bar{\mu}\bar{K}_\alpha}\frac{\partial \bar{p}}{\partial \alpha}\right] + \frac{\partial}{\partial \beta}\left[\frac{\bar{h}^3}{\bar{\mu}\bar{K}_\beta}\frac{\partial \bar{p}}{\partial \beta}\right] = \frac{1}{2}\bar{\Omega}\frac{\partial \bar{h}}{\partial \alpha} + \frac{\partial \bar{h}}{\partial \bar{t}} \tag{4}$$

After the substitution of $\bar{h}$ from Eq. (3) into Eq. (4), the Reynolds equation reduces to

$$\frac{\partial}{\partial \alpha}\left[\frac{\bar{h}^3}{\bar{\mu}\bar{K}_\alpha}\frac{\partial \bar{p}}{\partial \alpha}\right] + \frac{\partial}{\partial \beta}\left[\frac{\bar{h}^3}{\bar{\mu}\bar{K}_\beta}\frac{\partial \bar{p}}{\partial \beta}\right] = \frac{1}{2}\bar{\Omega}\left(\bar{X}_j \sin\alpha - \bar{Z}_j \cos\alpha\right) - \dot{\bar{X}}_j \cos\alpha - \dot{\bar{Z}}_j \sin\alpha \tag{5}$$

If the approximation is made that the bearing is infinitely short such that the pressure gradient in the circumferential direction is much smaller than the axial direction, i.e.

$$\frac{\partial \bar{p}}{\partial \alpha} \ll \frac{\partial \bar{p}}{\partial \beta} \tag{6}$$

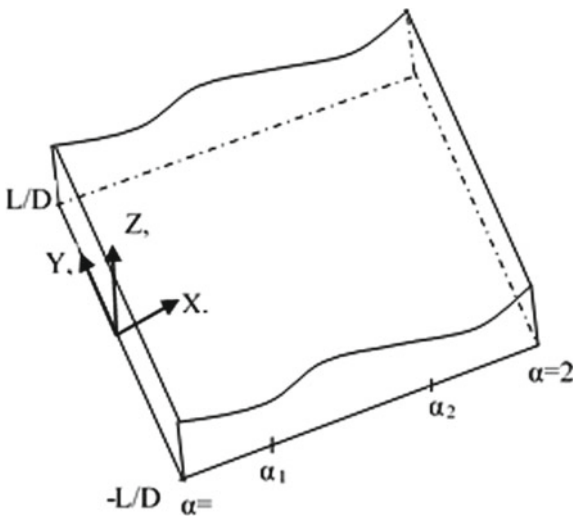

Fig. 2 Development of fluid film between journal surfaces

The Reynolds equation reduces to

$$\frac{\partial}{\partial\beta}\left[\frac{\bar{h}^3}{\bar{\mu}\bar{K}_\beta}\frac{\partial\bar{p}}{\partial\beta}\right] = f(\alpha) \tag{7}$$

$$f(\alpha) = \frac{1}{2}\bar{\Omega}\left(\bar{X}_j\sin\alpha - \bar{Z}_j\cos\alpha\right) - \dot{\bar{X}}_j\cos\alpha - \dot{\bar{Z}}_j\sin\alpha \tag{8}$$

Equation (7) is solved using boundary condition which is given as

$$(i)\quad \frac{\partial\bar{p}}{\partial\beta} = 0\,\text{at}\,\beta = 0 \qquad (ii)\quad \bar{p} = 0\,\text{at}\,\beta = \pm\frac{L}{D} = \pm\lambda \tag{9}$$

Integrating Eq. (7) with respect to β and using boundary conditions

$$\int\frac{\partial}{\partial\beta}\left[\frac{\bar{h}^3}{\bar{\mu}\bar{K}_\beta}\frac{\partial\bar{p}}{\partial\beta}\right]\partial\beta = f(\alpha)\int\partial\beta \;\text{ i.e. }\; \frac{\bar{h}^3}{\bar{\mu}\bar{K}_\beta}\frac{\partial\bar{p}}{\partial\beta}$$
$$= f(\alpha)\beta + A_1,\ \frac{\partial\bar{p}}{\partial\beta} = \frac{\bar{\mu}\bar{K}_\beta}{\bar{h}^3}f(\alpha)\beta + A_2$$

Integrating again the above equation with respect to β

$$\int\frac{\partial\bar{p}}{\partial\beta} = \int\left(\frac{\bar{\mu}\bar{K}_\beta}{\bar{h}^3}f(\alpha)\beta + A_2\right)\partial\beta\ \text{so},\ \bar{p} = \frac{\bar{\mu}\bar{K}_\beta}{\bar{h}^3}f(\alpha)\beta^2 + A_2\beta + A_3 \tag{10}$$

Constant of integration A_2 and A_3 are obtained by using boundary condition $\bar{p} = 0$, at $\beta = \pm\lambda$

$A_2 = 0$ and $A_2 = 0$ and $A_3 = -\frac{\bar{\mu}\bar{K}_\beta}{\bar{h}^3}f(\alpha)\frac{\lambda^2}{2}$

Now, by substituting values of A_2 and A_3 in Eq. (10), the pressure distribution is obtained as

$$\bar{p} = \left(\frac{\bar{\mu}\bar{K}_\beta}{\bar{h}^3}\right)\left(\frac{1}{2}f(\alpha)\left(\beta^2 - \lambda^2\right)\right) \tag{11}$$

The fluid film pressure is computed using Eq. (11) and to establish positive pressure zone, all negative pressures are made zero.

The load-carrying capacity of journal bearing is found by integrating the pressure over the positive pressure zone. Load-carrying capacity in circumferential and radial direction is given by

$$F_X = -\int_{-L/2}^{L/2}\int_{\alpha_1 R}^{\alpha_2 R} p\,\cos\alpha\,\mathrm{d}X\mathrm{d}Y; \tag{12}$$

$$F_Z = -\int_{-L/2}^{L/2}\int_{\alpha_1 R}^{\alpha_2 R} p \sin\alpha \, \mathrm{d}X\mathrm{d}Y \tag{13}$$

Substituting $X = \alpha \,.\, R$, $Y = \beta \,.\, R$ and $p = \bar{p}\mu_r\omega_r\left(\frac{R}{c}\right)^2$ in Eqs. (12) and (13), then the load-carrying capacity F_X and F_Y is obtained in non-dimensional form as given by Eqs. (14a, b) and (15)

$$F_X = -\int_{-\lambda}^{\lambda}\int_{\alpha_1}^{\alpha_2} \bar{p}\mu_r\omega_r\left(\frac{R}{c}\right)^2 . \cos\alpha \; R\mathrm{d}\alpha \,.\, R\mathrm{d}\beta \tag{14a}$$

or

$$\frac{F_X c^2}{\mu_r\omega_r R^4} = -\int_{-\lambda}^{\lambda}\int_{\alpha_2}^{\alpha_1} \bar{p}.\cos\alpha \,\mathrm{d}\alpha.\mathrm{d}\beta; \quad \text{or} \quad \bar{F}_X = -\int_{-\lambda}^{\lambda}\int_{\alpha_1}^{\alpha_2} \bar{p}.\cos\alpha \,\mathrm{d}\alpha.\mathrm{d}\beta \tag{14b}$$

and similarly load-carrying capacity in Z direction is given as

$$\bar{F}_Z = -\int_{-\lambda}^{\lambda}\int_{\alpha_1}^{\alpha_2} \bar{p}.\sin\alpha \,\mathrm{d}\alpha.\mathrm{d}\beta \tag{15}$$

Now, substituting the value of $\bar{p}$ from Eq. (11) in Eq. (14a, b), the non-dimensional load-carrying capacity $\bar{F}_X$ is given by

$$\bar{F}_X = -\int_{-\lambda}^{\lambda}\int_{\alpha_1}^{\alpha_2} \left(\frac{\bar{\mu}\bar{K}_\beta}{\bar{h}^3}\right)\left(\frac{1}{2}f(\alpha)\left(\beta^2 - \lambda^2\right)\right).\cos\alpha \,\mathrm{d}\alpha.\mathrm{d}\beta$$

let

$$f_1(\alpha) = \frac{\bar{\mu}\bar{K}_\beta}{\bar{h}^3}\left(\frac{f(\alpha)}{2}\right); \tag{16}$$

So,

$$\bar{F}_X = -\int_{-\lambda}^{\lambda}\int_{\alpha_1}^{\alpha_2} \left(\beta^2 - \lambda^2\right) f_1(\alpha)\cos\alpha \,\mathrm{d}\alpha.\mathrm{d}\beta \tag{17}$$

Similarly, for Z direction, the load-carrying capacity in non-dimensional form is written as

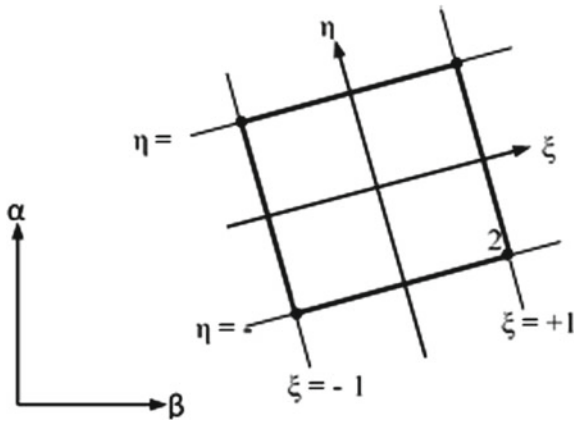

Fig. 3 Element in global coordinates (α, β) and the natural coordinates (ξ, η)

$$\bar{F}_Z = -\int_{-\lambda}^{\lambda}\int_{\alpha_1}^{\alpha_2} \left(\beta^2 - \lambda^2\right) f_1(\alpha) \sin\alpha \, \mathrm{d}\alpha.\mathrm{d}\beta \tag{18}$$

Equations (17) and (18) are solved numerically using Gauss–Legendre numerical integration over positive pressure zone. Implementation of numerical integration is given below

For numerical integration, iso-parametric element equations are formulated using natural coordinate system ξ and η that is defined by element geometry and not by the element orientation in the global coordinate system, α and β as shown in Fig. 3. There are four nodes at the corners of the quadrilateral element. In the natural coordinate system (ξ, η), the shape function can be generalized as follows:

$$N_i = \frac{1}{4}(1 + \xi\xi_i)(1 + \eta\eta_i) \quad \text{where } i = 1, 2, 3, 4$$

Hence,

$$\begin{aligned} N_1 &= \frac{1}{4}(1 - \xi)(1 - \eta);\ N_2 = \frac{1}{4}(1 + \xi)(1 - \eta); \\ N_3 &= \frac{1}{4}(1 + \xi)(1 + \eta);\ N_4 = \frac{1}{4}(1 - \xi)(1 + \eta) \end{aligned} \tag{19}$$

The transformation from global coordinate to natural coordinate is given as

$$\int\int f(\alpha, \beta)\mathrm{d}\alpha \, \mathrm{d}\beta = \int_{-1}^{1}\int_{-1}^{1} f(\xi, \eta) J \mathrm{d}\xi \, \mathrm{d}\eta \tag{20}$$

where J is Jacobian matrix of (α, β) with respect to (ξ, η), represented as

$$\begin{bmatrix} d\alpha \\ d\beta \end{bmatrix} = \begin{bmatrix} \frac{\partial\alpha}{\partial\xi} & \frac{\partial\alpha}{\partial\eta} \\ \frac{\partial\beta}{\partial\xi} & \frac{\partial\beta}{\partial\eta} \end{bmatrix} \begin{bmatrix} d\xi \\ d\eta \end{bmatrix} = J^T \begin{bmatrix} d\xi \\ d\eta \end{bmatrix}; \tag{20a}$$

$$\begin{bmatrix} d\xi \\ d\eta \end{bmatrix} = \begin{bmatrix} \frac{\partial\xi}{\partial\alpha} & \frac{\partial\xi}{\partial\beta} \\ \frac{\partial\eta}{\partial\alpha} & \frac{\partial\eta}{\partial\beta} \end{bmatrix} \begin{bmatrix} d\alpha \\ d\beta \end{bmatrix} = J^{-T} \begin{bmatrix} d\alpha \\ d\beta \end{bmatrix} \tag{20b}$$

where J^{-1} is inverse of the Jacobian matrix of (ξ, η) with respect to (α, β). For numerical integration, $f_1(\alpha)\cos\alpha$ and $f_1(\alpha)\sin\alpha$ of Eqs. (17) and (18) are computed at Gauss points after converting the equations in natural coordinate $d\alpha$ and $d\beta$ can be obtained from Eq's. (20a) and (20b) as

$$d\alpha = \frac{\partial\alpha}{\partial\xi}.d\xi + \frac{\partial\alpha}{\partial\eta}.d\eta \tag{21}$$

$$d\beta = \frac{\partial\beta}{\partial\xi}.d\xi + \frac{\partial\beta}{\partial\eta}.d\eta \tag{22}$$

Global coordinates (α, β) and the natural coordinates (ξ, η) are related with each other by the help of shape functions (N_1, N_2, N_3 and N_4) as follows:

$$\frac{\partial\alpha}{\partial\xi} = \alpha_1\frac{\partial N_1}{\partial\xi} + \alpha_2\frac{\partial N_2}{\partial\xi} + \alpha_2\frac{\partial N_3}{\partial\xi} + \alpha_1\frac{\partial N_4}{\partial\xi}; \tag{23a}$$

$$\frac{\partial\alpha}{\partial\eta} = \alpha_1\frac{\partial N_1}{\partial\eta} + \alpha_2\frac{\partial N_2}{\partial\eta} + \alpha_2\frac{\partial N_3}{\partial\eta} + \alpha_1\frac{\partial N_4}{\partial\eta} \tag{23b}$$

$$\frac{\partial\beta}{\partial\xi} = -\lambda\frac{\partial N_1}{\partial\xi} + \lambda\frac{\partial N_2}{\partial\xi} + \lambda\frac{\partial N_3}{\partial\xi} - \lambda\frac{\partial N_4}{\partial\xi}; \tag{23c}$$

$$\frac{\partial\beta}{\partial\eta} = -\lambda\frac{\partial N_1}{\partial\eta} + \lambda\frac{\partial N_2}{\partial\eta} + \lambda\frac{\partial N_3}{\partial\eta} - \lambda\frac{\partial N_4}{\partial\eta} \tag{23d}$$

Derivatives of shape function with respect to natural coordinates can be obtained by partially differentiating Eq. (19) which is given as

$$\frac{\partial N_1}{\partial\xi} = -\frac{(1-\eta)}{4}; \frac{\partial N_2}{\partial\xi} = \frac{(1-\eta)}{4}; \frac{\partial N_3}{\partial\xi} = \frac{(1+\eta)}{4}; \frac{\partial N_4}{\partial\xi} = -\frac{(1+\eta)}{4} \tag{24}$$

$$\frac{\partial N_1}{\partial\eta} = -\frac{(1-\xi)}{4}; \frac{\partial N_2}{\partial\eta} = -\frac{(1+\xi)}{4}; \frac{\partial N_3}{\partial\eta} = \frac{(1+\xi)}{4}; \frac{\partial N_4}{\partial\eta} = \frac{(1-\xi)}{4} \tag{25}$$

The values of $\frac{\partial\alpha}{\partial\xi}$, $\frac{\partial\alpha}{\partial\eta}$, $\frac{\partial\beta}{\partial\xi}$ and $\frac{\partial\beta}{\partial\eta}$ can be obtained by substituting the values of the derivatives of shape function from Eqs. (24) and (25) into Eqs. (23a–23d) as

$$\frac{\partial\alpha}{\partial\xi} = \frac{\alpha_2 - \alpha_1}{2}; \frac{\partial\alpha}{\partial\eta} = 0, \frac{\partial\beta}{\partial\xi} = 0, \frac{\partial\beta}{\partial\eta} = \lambda \tag{26}$$

The values of $\mathrm{d}\alpha$ and $\mathrm{d}\beta$ can be obtained by substituting Eq. (26) into Eqs. (21) and (22) as

$$\mathrm{d}\alpha = \frac{1}{2}(\alpha_2 - \alpha_1).\mathrm{d}\xi \tag{27a}$$

and

$$\mathrm{d}\beta = \lambda.\mathrm{d}\eta \tag{27b}$$

Forces $\bar{F}_X$ and $\bar{F}_Z$ can be obtained by substituting the value of $\mathrm{d}\alpha$ and $\mathrm{d}\beta$ from Eq. (27a) and (27b) into Eqs. (17) and (18), respectively. Now, Eq. (17) can be written as Eq. (28a)

$$\bar{F}_X = -\int_{\xi=-1}^{\xi=1} f(\xi)\frac{1}{2}(\alpha_2 - \alpha_1)\left(\int_{\eta=-1}^{\eta=1}\left(\beta^2 - \lambda^2\right)\lambda \mathrm{d}\eta\right)\mathrm{d}\xi \tag{28a}$$

where $f(\xi) = f_1(\alpha)\cos\alpha$

or

$$\bar{F}_X = \sum_{e=1}^{n_e}\left[\sum_{i=1}^{N_{\text{Gauss point}}} W_i f(\xi_i)\frac{1}{2}(\alpha_2 - \alpha_1)\left(\sum_{j=1}^{N_{\text{Gauss point}}} W_j\left(\beta^2 - \lambda^2\right)\lambda\right)\right] \tag{28b}$$

where W_i and W_j are weights, depending on number of Gauss points selected for integration.

Equation (18) can be written as Eq. (29a)

$$\bar{F}_Z = -\int_{\xi=-1}^{\xi=1} f'(\xi)\frac{1}{2}(\alpha_2 - \alpha_1)\left(\int_{\eta=-1}^{\eta=1}\left(\beta^2 - \lambda^2\right)\lambda \mathrm{d}\eta\right)\mathrm{d}\xi \tag{29a}$$

where $f'(\xi) = f_1(\alpha)\sin\alpha$

or

$$\bar{F}_Z = \sum_{e=1}^{n_e}\left[\sum_{i=1}^{N_{\text{Gauss point}}} W_i f'(\xi_i)\frac{1}{2}\left(\alpha_2^e - \alpha_1^e\right)\left(\sum_{j=1}^{N_{\text{Gauss point}}} W_j\left(\beta^2 - \lambda^2\right)\lambda\right)\right] \tag{29b}$$

3 Conclusion

The investigations in this chapter were concerned with the theoretical study of load-carrying capacity of the journals in laminar as well as super laminar regime with short bearing approximation. The analysis and numerical solution algorithm were used to compute the load-carrying capacity of a bearing. These studies were conducted by taking 0.5 aspect ratio, assuming bearing and journal axes parallel and ratio of nominal clearance to the journal radius 0.001 (C/R = 0.001). By using Gauss–Legendre numerical integration method, the forces in X as well as Z direction are easily found out with the help of a computer program. The output of the computer program is further used to find out other static and dynamic characteristics of journal bearing.

References

1. Hirn, G.: Ind. Soc. Mulhouse **26**, 188 (1854)
2. Petrov, N.P.: Theoretical and experimental study of mediate friction: parts I, II, II and IV. Reprinted in: Rohde et al. (eds.) Fluid film Lubrication: A century of Progress, pp. 107–134. American Society of Mechanical Engineers (1983)
3. Sommerfeld, A.: Zeitschrif Mathematik Phisik **50**, 97 (1904)
4. Gumbel, L.: Das problem derlagerreibung. Monotsblatter. Berliner Biezirks Verein Deutscher Ing, VDI No. **5**, 97–104 (1914)
5. Ockvirk, F.W.: Short bearing approximation for full journal bearings. NACA Tech. Note 2808 (1952)
6. Dwivedi, V.K., Chand, S., Pandey, K.N.: Int. J. Des. Eng. **5**(3), 256 (2014)
7. Dwivedi, V.K., Chand, S., Pandey, K.N., J. Appl. Fluid Mech. **9**(6), 2763 (2016)
8. V.N. Constantinescu, Proc. IMechE. **182**(3A), 383 (1967)

A Numerical Scheme for Solving a Coupled System of Singularly Perturbed Delay Differential Equations of Reaction–Diffusion Type

Trun Gupta and P. Pramod Chakravarthy

Abstract In this work, a coupled system of singularly perturbed delay differential equations of reaction–diffusion type is solved by applying a fitted numerical scheme based on cubic spline in tension. Numerical examples are provided to illustrate the efficiency and applicability of the method.

Keywords Singular perturbation · Coupled system · Delay differential equation Reaction–diffusion problem

1 Introduction

If the future state of the system is dependent of past states, the governing differential equations contain delay arguments. A subclass of these equations consists of singularly perturbed delay differential equations. These types of equations arise frequently in modelling of the human pupil light reflex [1], model of HIV infection [2, 3] and many other areas in applied mathematics. The difference between the non-delay and delay singularly perturbed problems is that sometimes delay problems exhibit extra interior layers. Numerical analysis of singularly perturbed problems is a matured mathematical research area but numerical analysis of singularly perturbed problems with delay terms is in initial stage. Kadalbajoo and Sharma [4], Pramod Chakravarthy et al. [5] proposed fitted operator schemes for solving singularly perturbed delay differential equations. Only a few results are reported in the literature for solving system of singularly perturbed delay differential equations. Subburayan and Ramanujam [6] suggested initial value technique for solving these types of problems. For the numerical solution of coupled system of singularly perturbed delay differential equations, Selvi and Ramanujam [7, 8] proposed iterative numerical methods. In this work, we studied a fitted operator scheme to solve the coupled system of singularly perturbed reaction–diffusion delay differential equations.

T. Gupta · P. P. Chakravarthy (✉)
Visvesvaraya National Institute of Technology, Nagpur 440010, Maharashtra, India
e-mail: pramodpodila@yahoo.co.in

D. Srinivasacharya and K. S. Reddy (eds.), *Numerical Heat Transfer and Fluid Flow*, Lecture Notes in Mechanical Engineering,
https://doi.org/10.1007/978-981-13-1903-7_35

2 Statement of the Problem

Consider the following coupled system of singularly perturbed delay differential equations:

$$\begin{cases} -\varepsilon y_1''(x) + \sum_{k=1}^{2} a_{1k}(x) y_k(x) \\ \qquad\qquad + \sum_{k=1}^{2} b_{1k}(x) y_k(x-1) = f_1(x), x \in \Omega, \\ -\varepsilon y_2''(x) + \sum_{k=1}^{2} a_{2k}(x) y_k(x) \\ \qquad\qquad + \sum_{k=1}^{2} b_{2k}(x) y_k(x-1) = f_2(x), x \in \Omega, \\ y_1(x) = \phi_1(x),\ x \in [-1, 0],\ y_1(2) = l_1, \\ y_2(x) = \phi_2(x),\ x \in [-1, 0],\ y_2(2) = l_2, \end{cases} \tag{1}$$

where $0 < \varepsilon \ll 1$, l_1, l_2 are real constants.

$$\begin{aligned} &a_{11}(x) > 0, a_{22}(x) > 0, a_{12}(x) \le 0, a_{21}(x) \le 0, \\ &a_{i1}(x) + a_{i2}(x) \ge \alpha_i \ge \alpha > 0, i = 1, 2, \\ &b_{ij}(x) \le 0, i = 1, 2, j = 1, 2, \\ &-\beta \le -\beta_i \le b_{i1}(x) + b_{i2}(x) < 0, i = 1, 2, \end{aligned}$$

$\alpha - \beta > 0$, the functions $a_{ik}, b_{ik}, f_i \in C^4(\bar{\Omega})$, $i = 1, 2$, $k = 1, 2$, $\Omega = (0, 2)$, $\bar{\Omega} = [0, 2]$ and ϕ_i, $i = 1, 2$ is smooth function on $[-1, 0]$. Here, $C^n(\Omega)$ stands for class of n times continuously differentiable functions in Ω.

3 Derivation of Method

A difference scheme based on cubic spline in tension is derived in this section.
Let $x_0 = 0, x_{2N} = 2, x_i = ih, i = 1, 2, ... 2N - 1$, where h is step size.
The functions $S_j(x, \tau) = S_j(x), j = 1, 2$ satisfying the differential equations

$$S_j''(x) - \tau S_j(x) = [S_j''(x_i) - \tau S_j(x_i)]\frac{(x_{i+1} - x)}{h} + [S_j''(x_{i+1}) - \tau S_j(x_{i+1})]\frac{(x - x_i)}{h} \tag{2}$$

in $[x_i, x_{i+1}]$, where $S_j(x_i) = Y_j(x_i) \simeq y_j(x_i),\ j = 1, 2$ and $\tau > 0$ are termed as cubic spline in tension.

Equation (2) is a linear second-order differential equation. On solving, we get

$$S_j(x) = A_j e^{\frac{\lambda}{h}x} + B_j e^{-\frac{\lambda}{h}x} + \left(\frac{M_{j,i} - \tau Y_{j,i}}{\tau}\right)\left(\frac{x - x_{i+1}}{h}\right) + \left(\frac{M_{j,i+1} - \tau Y_{j,i+1}}{\tau}\right)\left(\frac{x_i - x}{h}\right).$$

Here, A_j and B_j are the arbitrary constants which can be determined by using interpolatory conditions
$S_j(x_{i+1}) = Y_{j,i+1}$, $S_j(x_i) = Y_{j,i}$ for $j = 1, 2$.
Writing $\lambda = h\tau^{\frac{1}{2}}$ and $M_{j,i} = S_j''(x_i)$, we get

$$S_j(x) = \frac{h^2}{\lambda^2 \sinh\lambda}[M_{j,i+1}\sinh\frac{\lambda(x - x_i)}{h} + M_{j,i}\sinh\frac{\lambda(x_{i+1} - x)}{h}] - \frac{h^2}{\lambda^2}[\frac{(x - x_i)}{h}(M_{j,i+1} - \frac{\lambda^2}{h^2}Y_{j,i+1}) + \frac{(x_{i+1} - x)}{h}(M_{j,i} - \frac{\lambda^2}{h^2}Y_{j,i})]. \quad (3)$$

Differentiating Eq. (3) and taking limit $x \to x_i$, we get

$$S_j'(x_i^+) = \frac{Y_{j,i+1} - Y_{j,i}}{h} - \frac{h}{\lambda^2}[(1 - \frac{\lambda}{\sinh\lambda})M_{j,i+1} - (1 - \lambda\coth\lambda)M_{j,i}].$$

Similarly, we can find

$$S_j'(x_i^-) = \frac{Y_{j,i} - Y_{j,i-1}}{h} + \frac{h}{\lambda^2}[-(1 - \lambda\coth\lambda)M_{j,i} + (1 - \frac{\lambda}{\sinh\lambda})M_{j,i-1}].$$

By equating both in the above and simplifying, we get a tridiagonal system

$$h^2(\lambda_1 M_{j,i-1} + 2\lambda_2 M_{j,i} + \lambda_1 M_{j,i+1}) = Y_{j,i+1} - 2Y_{j,i} + Y_{j,i-1},\ i = 1, 2, \ldots 2N - 1 \quad (4)$$

for $j = 1, 2$, where $\lambda_1 = \frac{1}{\lambda^2}(1 - \frac{\lambda}{\sinh\lambda})$, $\lambda_2 = \frac{1}{\lambda^2}(\lambda\coth\lambda - 1)$ and $M_{j,i} = S_j''(x_i)$, $i = 1, 2, ..., 2N - 1$.
We can solve the differential Eq. (4), provided it is consistent. This condition is satisfied, when $\lambda_1 + \lambda_2 = \frac{1}{2}$.
We write the boundary conditions as $Y_{j,i} = \phi_{j,i}$, $-N \le i \le 0$,
$Y_{j,2N} = \beta_j$, where $\phi_{j,i} = \phi_j(x_i)$.
We consider the notation
$a_{1j}(x_i) = a_{1j,i}$, $a_{2j}(x_i) = a_{2j,i}$, $b_{1j}(x_i) = b_{1j,i}$, $b_{2j}(x_i) = b_{2j,i}$ and $f_j(x_i) = f_{j,i}$.
From Eq. (1), we have

$$\varepsilon M_{1,k} = a_{11,k}Y_{1,k} + a_{12,k}Y_{2,k} + b_{11,k}Y_1(x_k - 1) + b_{12,k}Y_2(x_k - 1) - f_{1,k}$$

$$\varepsilon M_{2,k} = a_{21,k}Y_{1,k} + a_{22,k}Y_{2,k} + b_{21,k}Y_1(x_k - 1) + b_{22,k}Y_2(x_k - 1) - f_{2,k}.$$

Substituting $M_{1,k}$ and $M_{2,k}$ with $k = i, i \pm 1$ in Eq. (4), we get the following linear system of equations for $Y_{1,i}$ and $Y_{2,i}$:

$$\begin{cases} (-\varepsilon + \lambda_1 h^2 a_{11,i-1})Y_{1,i-1} + (2\varepsilon + 2\lambda_2 h^2 a_{11,i})Y_{1,i} + (-\varepsilon + \lambda_1 h^2 a_{11,i+1})Y_{1,i+1} \\ +h^2(\lambda_1 a_{12,i-1}Y_{2,i-1} + 2\lambda_2 a_{12,i}Y_{2,i} + \lambda_1 a_{12,i+1}Y_{2,i+1}) \\ = h^2[\{\lambda_1 f_{1,i-1} + 2\lambda_2 f_{1,i} + \lambda_1 f_{1,i+1}\} \\ -\{\lambda_1 b_{11,i-1}Y_1(x_{i-1-N}) + 2\lambda_2 b_{11,i}Y_1(x_{i-N}) + \lambda_1 b_{11,i+1}Y_1(x_{i+1-N})\} \\ -\{\lambda_1 b_{12,i-1}Y_2(x_{i-1-N}) + 2\lambda_2 b_{12,i}Y_2(x_{i-N}) + \lambda_1 b_{12,i+1}Y_2(x_{i+1-N})\}], \end{cases}$$

$$\begin{cases} (-\varepsilon + \lambda_1 h^2 a_{22,i-1})Y_{2,i-1} + (2\varepsilon + 2\lambda_2 h^2 a_{22,i})Y_{2,i} + (-\varepsilon + \lambda_1 h^2 a_{22,i+1})Y_{2,i+1} \\ +h^2(\lambda_1 a_{21,i-1}Y_{1,i-1} + 2\lambda_2 a_{21,i}Y_{1,i} + \lambda_1 a_{21,i+1}Y_{1,i+1}) \\ = h^2[\{\lambda_1 f_{2,i-1} + 2\lambda_2 f_{2,i} + \lambda_1 f_{2,i+1}\} \\ -\{\lambda_1 b_{22,i-1}Y_2(x_{i-1-N}) + 2\lambda_2 b_{22,i}Y_2(x_{i-N}) + \lambda_1 b_{22,i+1}Y_2(x_{i+1-N})\} \\ -\{\lambda_1 b_{21,i-1}Y_1(x_{i-1-N}) + 2\lambda_2 b_{21,i}Y_1(x_{i-N}) + \lambda_1 b_{21,i+1}Y_1(x_{i+1-N})\}] \end{cases}$$

$$\text{for } i = 1, 2, \ldots 2N - 1. \qquad (5)$$

To obtain the solution of (1), we introduce a fitting factor (c.f. [9])

$$\sigma_j(\rho) = \frac{\rho^2 b_{jj}(x)}{4\sinh^2(\frac{1}{2}\rho\sqrt{b_{jj}(x)})}, \quad j = 1, 2,$$

where $\rho = \frac{h}{\varepsilon}$ in system (5).
By using the fitting factor, scheme (5) can be rewritten as

$$\begin{cases} (-\varepsilon\sigma_1 + \lambda_1 h^2 a_{11,i-1})Y_{1,i-1} + (2\varepsilon\sigma_1 + 2\lambda_2 h^2 a_{11,i})Y_{1,i} + (-\varepsilon\sigma_1 + \lambda_1 h^2 a_{11,i+1})Y_{1,i+1} \\ +h^2(\lambda_1 a_{12,i-1}Y_{2,i-1} + 2\lambda_2 a_{12,i}Y_{2,i} + \lambda_1 a_{12,i+1}Y_{2,i+1}) \\ = h^2[\{\lambda_1 f_{1,i-1} + 2\lambda_2 f_{1,i} + \lambda_1 f_{1,i+1}\} \\ -\{\lambda_1 b_{11,i-1}Y_1(x_{i-1-N}) + 2\lambda_2 b_{11,i}Y_1(x_{i-N}) + \lambda_1 b_{11,i+1}Y_1(x_{i+1-N})\} \\ -\{\lambda_1 b_{12,i-1}Y_2(x_{i-1-N}) + 2\lambda_2 b_{12,i}Y_2(x_{i-N}) + \lambda_1 b_{12,i+1}Y_2(x_{i+1-N})\}], \end{cases}$$

$$\begin{cases} (-\varepsilon\sigma_2 + \lambda_1 h^2 a_{22,i-1})Y_{2,i-1} + (2\varepsilon\sigma_2 + 2\lambda_2 h^2 a_{22,i})Y_{2,i} + (-\varepsilon\sigma_2 + \lambda_1 h^2 a_{22,i+1})Y_{2,i+1} \\ +h^2(\lambda_1 a_{21,i-1}Y_{1,i-1} + 2\lambda_2 a_{21,i}Y_{1,i} + \lambda_1 a_{21,i+1}Y_{1,i+1}) \\ = h^2[\{\lambda_1 f_{2,i-1} + 2\lambda_2 f_{2,i} + \lambda_1 f_{2,i+1}\} \\ -\{\lambda_1 b_{22,i-1}Y_2(x_{i-1-N}) + 2\lambda_2 b_{22,i}Y_2(x_{i-N}) + \lambda_1 b_{22,i+1}Y_2(x_{i+1-N})\} \\ -\{\lambda_1 b_{21,i-1}Y_1(x_{i-1-N}) + 2\lambda_2 b_{21,i}Y_1(x_{i-N}) + \lambda_1 b_{21,i+1}Y_1(x_{i+1-N})\}] \end{cases}$$

$$\text{for } i = 1, 2, \ldots 2N - 1. \qquad (6)$$

Gauss elimination method with partial pivoting is used to solve the above system of equations.

4 Numerical Examples

To check the robustness of the proposed method, it is tested on two examples. Numerical results are presented for $\lambda_1 = \frac{1}{12}$, $\lambda_2 = \frac{5}{12}$. To find the maximum absolute pointwise errors, we use the double mesh principle given in Doolan et al. [9]

$$E_{i,\varepsilon}^{N} = \max_{0 \le j \le N} |Y_{i,j}^{N} - Y_{i,2j}^{2N}|,$$

for $i = 1, 2$. Here, $Y_{i,j}^{N}$ and $Y_{i,2j}^{2N}$ denote the jth and $2j$th components of the numerical solutions with mesh points N and $2N$, respectively.

Example 1 Consider the system of delay differential equation with the boundary conditions as follows [6]:

$$\begin{cases} -\varepsilon y_1''(x) + 11y_1(x) - (x^2+1)y_1(x-1) - (x+1)y_2(x-1) = exp(x), \\ -\varepsilon y_2''(x) + 16y_2(x) - xy_1(x-1) - xy_2(x-1) = exp(x), \\ y_1(x) = 1, x \in [-1, 0], \ y_1(2) = 1, \\ y_2(x) = 1, x \in [-1, 0], \ y_2(2) = 1. \end{cases}$$

The maximum absolute errors are tabulated in Tables 1 and 2 for different values of perturbation parameter ε. The numerical solution for this example is plotted in Fig. 1 for $\varepsilon = 2^{-8}$, $N = 128$.

Example 2 Consider the system of delay differential equation with the boundary conditions as follows [6]:

Table 1 Maximum absolute errors of Example 1 for different values of ε for Y_1

ε/M	64	128	256	512	1024	2048
2^{-4}	1.9055e−003	1.0824e−003	6.3655e−004	3.5180e−004	1.8562e−004	9.5420e−005
2^{-6}	9.8148e−003	1.8815e−003	1.0747e−003	6.3428e−004	3.5118e−004	1.8546e−004
2^{-8}	3.3235e−002	9.8070e−003	1.8763e−003	1.0726e−003	6.3356e−004	3.5097e−004
2^{-10}	5.3896e−002	3.3120e−002	9.7970e−003	1.8753e−003	1.0719e−003	6.3330e−004
2^{-12}	7.3776e−002	5.3626e−002	3.3057e−002	9.7905e−003	1.8752e−003	1.0716e−003
2^{-14}	8.0605e−002	7.3775e−002	5.3488e−002	3.3024e−002	9.7868e−003	1.8752e−003
2^{-16}	8.0891e−002	8.0605e−002	7.3774e−002	5.3418e−002	3.3007e−002	9.7849e−003

Table 2 Maximum absolute errors of Example 1 for different values of ε for Y_2

ε/M	64	128	256	512	1024	2048
2^{-4}	2.7328e−003	6.7631e−004	2.6633e−004	1.4628e−004	7.7040e−005	3.9576e−005
2^{-6}	1.1435e−002	2.7313e−003	6.7593e−004	2.6562e−004	1.4607e−004	7.6984e−005
2^{-8}	3.8907e−002	1.1434e−002	2.7310e−003	6.7584e−004	2.6544e−004	1.4601e−004
2^{-10}	7.5940e−002	3.8906e−002	1.1434e−002	2.7309e−003	6.7582e−004	2.6540e−004
2^{-12}	9.9406e−002	7.5939e−002	3.8905e−002	1.1434e−002	2.7309e−003	6.7582e−004
2^{-14}	1.0417e−001	9.9406e−002	7.5938e−002	3.8905e−002	1.1434e−002	2.7309e−003
2^{-16}	1.0427e−001	1.0417e−001	9.9406e−002	7.5938e−002	3.8905e−002	1.1434e−002

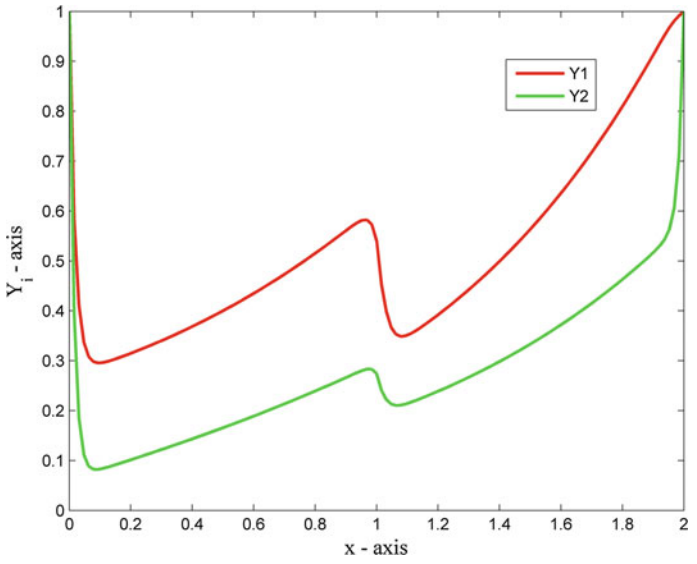

Fig. 1 Numerical sol. of Example 1

$$\begin{cases} -\varepsilon y_1''(x) + 11y_1(x) - (x^2+1)y_1(x-1) - (x+1)y_2(x-1) = \begin{cases} -1 & 0 < x < 1 \\ 1 & 1 < x < 2 \end{cases} \\ -\varepsilon y_2''(x) + 16y_2(x) - xy_1(x-1) - xy_2(x-1) = \begin{cases} 1 & 0 < x < 1 \\ -1 & 1 < x < 2 \end{cases} \\ y_1(x) = 1, x \in [-1, 0], \ y_1(2) = 1, \\ y_2(x) = 1, x \in [-1, 0], \ y_2(2) = 1, \end{cases}$$

The maximum absolute errors are tabulated in Tables 3 and 4 for different values of perturbation parameter ε. The numerical solution for this example is plotted in Fig. 2 for $\varepsilon = 2^{-8}, N = 128$.

Table 3 Maximum absolute errors of Example 2 for different values of ε for Y_1

ε/M	64	128	256	512	1024	2048
2^{-4}	8.4748e−03	5.0222e−03	2.7915e−03	1.4784e−03	7.6160e−04	3.8662e−04
2^{-6}	1.4385e−02	8.4814e−03	5.0225e−03	2.7912e−03	1.4783e−03	7.6156e−04
2^{-8}	2.9969e−02	1.4403e−02	8.4872e−03	5.0233e−03	2.7913e−03	1.4783e−03
2^{-10}	6.4678e−02	2.9913e−02	1.4414e−02	8.4906e−03	5.0238e−03	2.7913e−03
2^{-12}	9.2219e−02	6.4674e−02	2.9888e−02	1.4420e−02	8.4924e−03	5.0241e−03
2^{-14}	1.0075e−01	9.2218e−02	6.4673e−02	2.9875e−02	1.4423e−02	8.4934e−03
2^{-16}	1.0111e−01	1.0075e−01	9.2218e−02	6.4673e−02	2.9869e−02	1.4424e−02

Table 4 Maximum absolute errors of Example 2 for different values of ε for Y_2

ε/M	64	128	256	512	1024	2048
2^{-4}	7.8748e−03	3.6345e−03	1.7272e−03	8.3931e−04	4.1335e−04	2.0507e−04
2^{-6}	1.7163e−02	7.8617e−03	3.6326e−03	1.7269e−03	8.3927e−04	4.1334e−04
2^{-8}	4.0925e−02	1.7117e−02	7.8546e−03	3.6316e−03	1.7268e−03	8.3924e−04
2^{-10}	8.1107e−02	4.0923e−02	1.7094e−02	7.8509e−03	3.6310e−03	1.7267e−03
2^{-12}	1.0651e−01	8.1109e−02	4.0923e−02	1.7082e−02	7.8490e−03	3.6307e−03
2^{-14}	1.1166e−01	1.0652e−01	8.1111e−02	4.0923e−02	1.7076e−02	7.8481e−03
2^{-16}	1.1176e−01	1.1166e−01	1.0652e−01	8.1112e−02	4.0923e−02	1.7073e−02

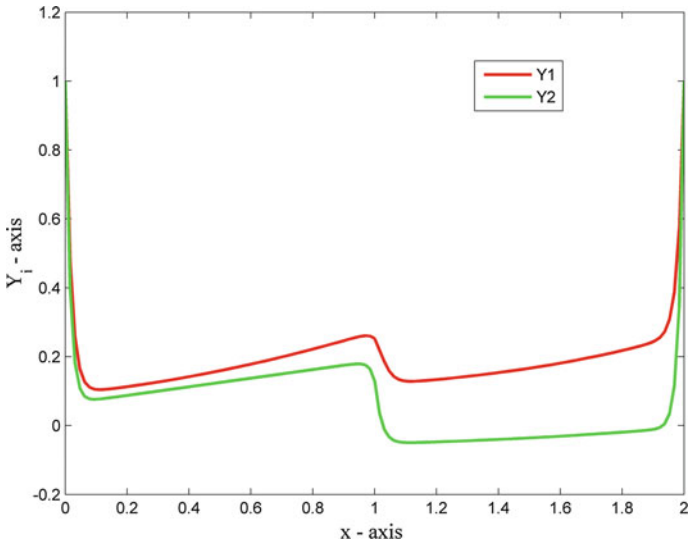

Fig. 2 Numerical sol. of Example 2

5 Conclusions

In this work, we proposed a fitted numerical scheme for a coupled system of singularly perturbed delay differential equations of reaction–diffusion type. The method is based on cubic spline in tension. The proposed method is tested on two numerical examples and the results are presented in tables. Numerical experiments show that the proposed method produces oscillation-free solution everywhere in the domain of integration. It can also be observed that maximum absolute errors are decreasing with the decrease of mesh parameter h. It shows the convergence of the computed solution.

References

1. Longtin, A., Milton, G.J.: Complex oscillations in the human pupil light reflex with mixed and delayed feedback. Math. Biosci. **90**, 183–199 (1988)
2. Culshaw, R.V., Ruan, S.: A delay differential equation model of HIV infection of CD4 + T-cells. Math. Biosci. **165**(1), 27–39 (2000)
3. Nelson, P.W., Perelson, A.S.: Mathematical analysis of delay differential equation models of HIV - 1 infection. Math. Biosci. **179**, 73–94 (2002)
4. Kadalbajoo, M.K., Sharma, K.K.: An -uniform fitted operator method for solving boundary-value problems for singularly perturbed delay differential equations: Layer behavior. Int. J. Comput. Math. **80**(10), 1261–1276 (2003)
5. Chakravarthy, P.P., Kumar, S.D., Ragi, N.R. : Numerical solution of second order singularly perturbed delay differential equations via cubic spline in tension. Int. J. Appl. Comput. Math. **3**(3), 1703–1717 (2016)
6. Subburayan, V., Ramanujam, N.: An initial value method for singularly perturbed system of reaction - diffusion type delay differential equations. J. Korea Soc. Indust. Appl. Math. **17**(4), 221–237 (2013)
7. Selvi, P.A., Ramanujam, N.: An iterative numerical method for singularly perturbed reaction diffusion equations with negative shift. J. Comput. and Appl. Math. **296**, 10–23 (2016)
8. Selvi, P.A., Ramanujam, N.: A numerical method for a system of singularly perturbed differential equations of reaction-diffusion type with negative shift. Diff. Eq. and Numer. Anal. **172**, 99–116 (2016)
9. Doolan, E.P., Miller, J.J.H., Schilders, W.H.A.: Uniform Numerical Methods for Problems with Initial and Boundary layers. Boole Press, Dublin (1980)

A Computational Study on the Stenosis Circularity for a Severe Stenosed Idealized Artery

B. Prashantha and S. Anish

Abstract Narrowing of blood vessels (stenosis) changes the nature of blood flow through the arteries. The altered flow structures at the downstream of stenosis may generate adverse effects on the arterial wall. Hence, an understanding of the effect of stenosis circularity on the flow behavior at the downstream of stenosis is clinically beneficial. The present study has been carried out on idealized stenosed artery model with severe case of stenosis (75% area reduction) but with the same cross-sectional area that has been selected for the study. The effect of different physiological states (pulse rates) study has been examined through using FLUENT Inc. solver by finite volume method, controlled through user-defined functions. The results indicate that the velocity profiles, oscillatory shear stress, and fluid residence time are significantly affected by the shape of the stenotic region. Fluid residence time in the downstream plays a significant role in understanding the hotspots for the secondary deposition/plaque.

Keywords Stenosis · Atherosclerosis · Streamlines · Oscillatory shear index (OSI)

1 Introduction

Several autopsy studies have demonstrated 70–80% of cardiovascular diseases (atherosclerosis/plaque) that occur at complex geometries [1]. Continuous development of plaque causes narrowing of the vessel lumen (known as stenosis) and looses its flexibility. These plaques/stenoses resist the blood flow in the vessels and create significant flow disturbances. Quite often, the adhesion of new cells on the vessels' wall occurs at regions where the wall shear stress is lower [2]. Large plaque formation/uneven manner of plaque buildup in the artery changes the wall shear stress

B. Prashantha (✉) · S. Anish
Centre for Biomedical Engineering, Department of Mechanical Engineering, National Institute of Technology, Surathkal 575025, Karnataka, India
e-mail: Prashanthb.mech@gmail.com

D. Srinivasacharya and K. S. Reddy (eds.), *Numerical Heat Transfer and Fluid Flow*, Lecture Notes in Mechanical Engineering,
https://doi.org/10.1007/978-981-13-1903-7_36

distribution on the arterial walls. In a normal healthy person, blood flow through the artery is laminar. However, the presence of new cells in the blood flow and its adhesion on the arterial wall make the flow transitional to turbulence [3]. Nature of deposition of new cells on the arterial wall will not be uniform, resulting in an asymmetric [4]. Plaque nature will vary from patient to patient [1]. Some plaque curvature and/or arterial wall avoid accumulation of cells or secondary plaques on the arterial wall [5]. A study on accurate prediction of plaque formation/development with pulsatile flow has been more essential.

Blood flow through the stenotic arteries has been extensively studied in the past few decades; however, up to the author knowledge, not much work has been reported on pulsatile blood flow through the stenosed artery having different circularity shapes. The objective of the present work is to numerically analyze the blood flow through the idealized stenotic arteries, in the presence of different stenosis circularity effects on the flow stability. Consider plaques with a different curved nature of elliptical shapes and maintain the same percentage of area reduction (75% area reduction). The study has been mainly focused on being adhesion of platelets/new cells in the post-stenotic region through OSI, RRT, and WSS. Recognizing the features of downstream flow behavior contributes to the clinicians to make early interventions in patients.

2 Methods

Patient-specific model is too irregular and unique for each subject. Hence, the simulations with patient-specific geometry create difficulties in identifying and separating out the effect of any single parameter on the flow behavior. Hence, the present study has followed the idealized Ahmed and Giddens models [6]. The idealized stenotic geometry models were constructed with keeping the same degree of stenosis (75% by area reduction). The geometry of an idealized artery model has been scaled up keeping the dynamic similarity. Inlet and outlet diameters (D) are 2 in. Upstream length will be 94D, and downstream region has length of 36D that is considered from the throat section shown in Fig. 1. Different circularities at the stenosis models have been constructed by increasing the percentage of minor axis distance of ellipse and maintained the same percentage of area blockage (stenosis) for all the cases. Three-dimensional model has been generated, and the grid generation is carried out using ICEMCFD.

2.1 Problem Setup

Blood is treated as continuous fluid; time-averaged Navier–Stokes equation was solved by means of using Pressure Implicit Splitting of Operators (PISO) algorithm. The turbulence methodology adopted for this study is the traditional RANS simulation with standard *k-omega* model, which incorporates low Reynolds number effects

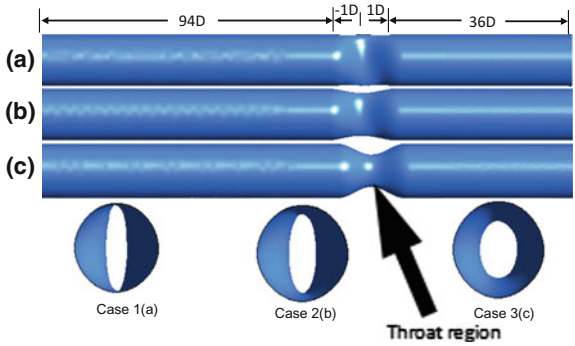

Fig. 1 Asymmetric stenosis geometry with different circularities at the throat region

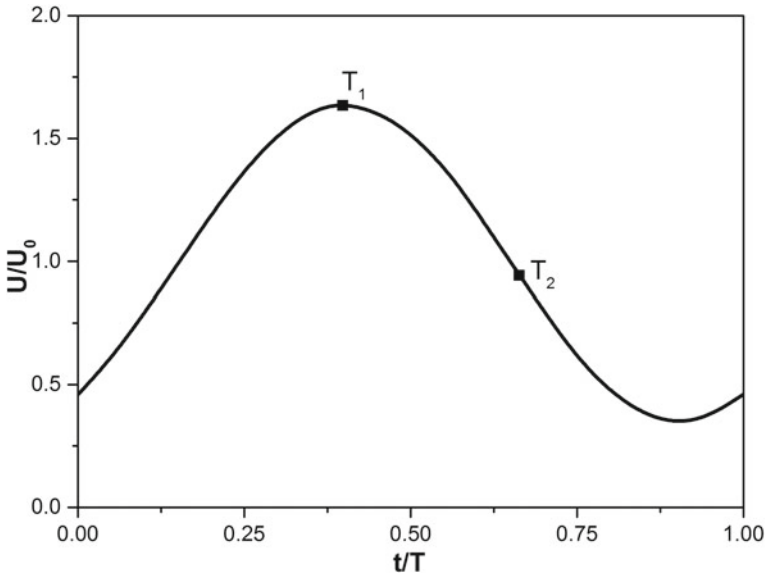

Fig. 2 The pulsatile inflow velocity profile obtained from Ahmed and Giddens [6]. Where U/U_0 is the normalized velocity and t/T is the normalized cardiac pulse. T_1 and T_2, are the peak and decelerating time instances

and shear flow spreading. The turbulence intensity of 7.2% and a length scale of 0.003556 m are used. The simulation was carried out by finite volume method using FLUENT. Time-varying velocity profile was used as inlet boundary condition one used by Ahmed and Giddens for the in vitro analysis shown in Fig. 2, and the velocity profile as a function of time (t) may be expressed in Eq. (1). At the outlet, outflow boundary condition is applied. The range of Reynolds number 200–1000 used in the idealized artery model simulation is similar to the human non-bifurcating artery [6]. The boundary wall is assumed to be rigid, and no-slip condition is specified [5, 7].

$$V(t) = \left[\frac{0.85}{20} + \frac{0.56}{20} \times \cos(2 \times \pi \times \frac{t}{20}) - \frac{50.6}{20}\right]. \quad (1)$$

2.2 Validation

The present computational study has been validated with Ahmed and Giddens [6] experimental result as shown in Fig. 3. The results obtained by the present simulation are compared with experimental results obtained by the Ahmed and Giddens [6]. Plotted results in the post-stenotic region at 1D and 1.5D show that the computed values are in good agreement with the experimental results.

Grid independence studies are one of the most important steps in the computational work. It has been carried out to arrive at an optimum number of grid elements for the numerical study. The study was carried out for four different mesh elements (3.5, 6.4, 7.8, and 8.7 lakh). Comparing the velocity profiles at proximal to the stenosis (−1D) predicts 6.4 and 7.8 lakh elements that follow the same trend of fine-mesh plot (8.7 lakh), and a discrepancy of less than 0.5% can be observed. Hence, further simulations are carried out for grids with 6.8 lakh elements and the same number of elements can be adopted for all the models.

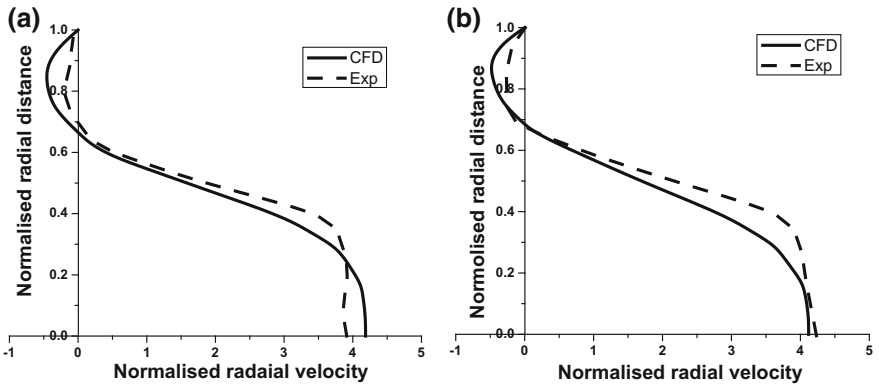

Fig. 3 Axial velocity comparison during peak time step in the post-stenosis region **a** Plane at 1D location **b** Plane at 1.5D location

3 Results and Discussion

3.1 Flow Behavior in the Downstream

The stenosis circularity in a diseased artery causes the flow scattering in the downstream during cardiac cycle [8]. Figure 4 represents the behavior of axial velocity during peak and decelerating time instances. Circularity of stenosis is visible primarily along the XY-plane, and hence it is worth to study the flow behavior along the XY-plane. The results are plotted at different time instances (systolic, peak, and decelerating) along the axial direction. The percentage variation in the minor axis of stenotic region (ellipse) generates significant flow disturbances in the downstream. Case-3 exhibits a symmetric pattern in the velocity distribution, similar to a fully developed velocity profile. However, for the other two cases, where the stenosis is more elliptic, the velocity profiles are far from symmetry.

Diseased artery with case-1 and case-2 types of stenoses follows similar trends than case-3, which carries set of multiple vortices along the stream. However, in case-1 and case-2, the reverse flows can be observed near to the wall region with low magnitude of axial velocity at one side of the wall shown in Fig. 4. Shifting of peak velocity from one end of the wall toward other predicts swaying motion of jet in the cardiac cycle. The newly formed shear layers, by stenotic jet, fluctuate the

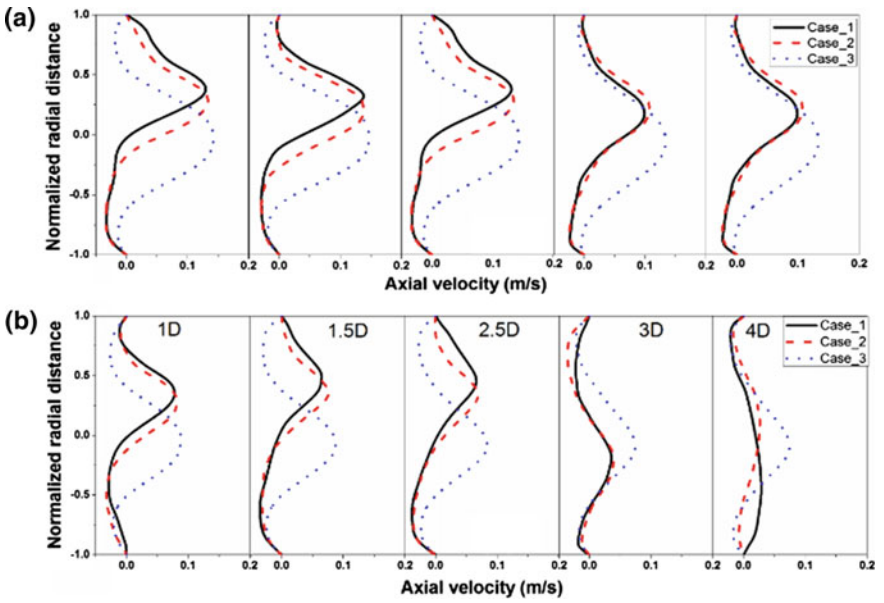

Fig. 4 Comparison of streamwise velocity profile with different stenosis circularities **a** Peak time step **b** Deceleration time step

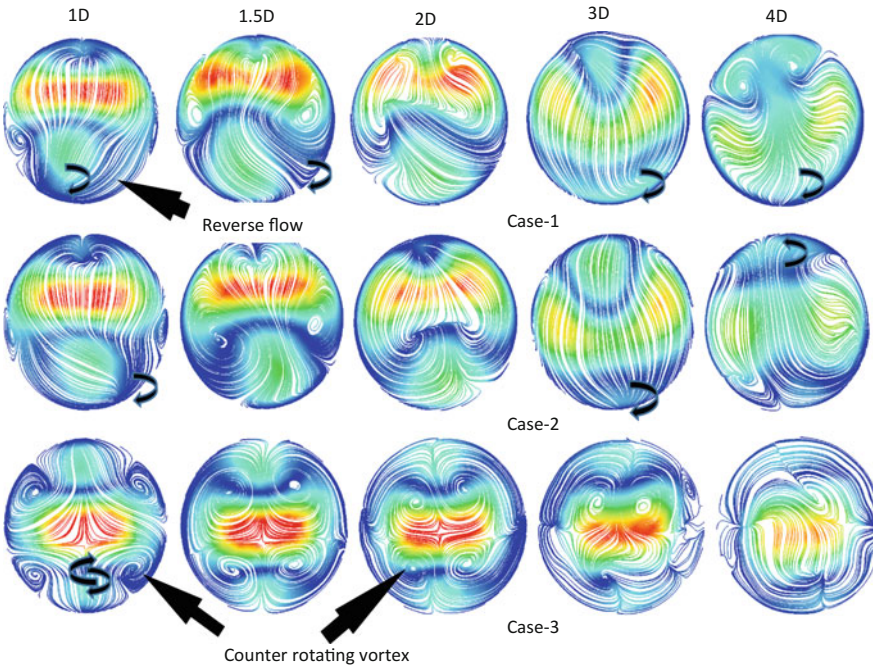

Fig. 5 Distributed surface streamlines in the downstream during deceleration time step

flow of streamlines in the post-stenotic region. Swaying motion of plug flow in the downstream side is an evidence for the presence of secondary flows [9], and this can be observed in case-1 and case-2 types of stenoses.

The presence of transformational vortices and/or reverse flow in the downstream can be analyzed with the help of surface streamlines shown in Fig. 5. Streamlines' plot in the downstream clearly describing case-3 carries set of liked multiple vortices and swirl nature of flow along the wall side. However, in case-1 and case-2 near to the wall, reverse flow can be observed. Linge [5] and Zovatto [9] stated that swirl/helical flow nature in the post-stenotic region slow downs the occlusion rate and improves self-cleaning. Multiple linked vortices provoke fluid to move at faster rate, and hence there will be less chances of occlusion in case-3.

3.2 Oscillatory Shear Index (OSI)

Atherosclerotic regions are widely observed in the complex geometries with high-oscillatory and low-wall shear stress [4]. OSI measures the cyclic departure of the wall shear stress vectors from its predominant flow direction. OSI values vary from 0

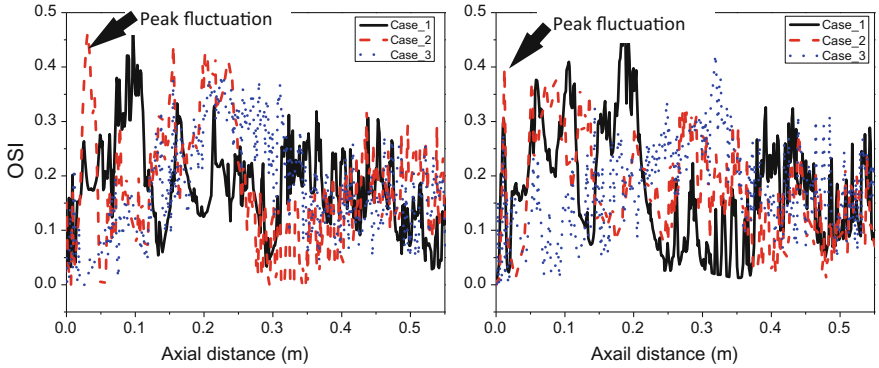

Fig. 6 Spatial variation of oscillatory shear index along outer wall of the XY-plane

to 0.5; high values of OSI predict rupture and/or further localization of atherosclerosis (plaque) [1, 10], and it can be defined as

$$OSI = 0.5\left[1 - \frac{\left|\int_0^T \overrightarrow{wss}\right|}{\int_0^T \left|\overrightarrow{wss}\right|}\right], \tag{2}$$

where T is the pulse period and $\underset{\text{WSS}}{\rightarrow}$ is the instantaneous wall shear stress. Figure 6a and b represents the OSI values on the inner and outer walls of the lumen, starting from throat to 11D. Sadeghi [11] stated that the larger oscillating nature of flow and low WSS in the cardiac pulse represent the major plaque development in the post-stenotic region. During pulsatile flow, stenosed artery with case-1 and case-2 shows high values of OSI. Oscillated shear stress predicts that there will be more chances of secondary plaque progression in the downstream.

4 Conclusion

The present study investigates the simulation of pulsatile blood flow through an idealized artery with different elliptical stenosis curvatures. A thorough understanding of flow behavior streamlines, vortices, and OSI in the artery concluded major clinical interventions. An artery with circular (case-3) type of stenosis at the throat generates more helical structures (spinning). Spinning nature of flow carries deoxygenated blood away from the stenosis region, which leads to lower residence time of atherogenic particles. However, in case-1 and case-2, the presence of primary and secondary recirculation zones in the downstream accumulates deoxygenated blood.

Insufficient oxygen (mass transfer) in the blood makes the particles inactive and later on the particles stick to the wall. Presence of multiple linked vortices (swirling nature) in the flow improves self-cleaning in the arterial passage. Patients with complex circularity in the stenotic region may have further chances of plaque deposition. Hence, they may be advised for an early clinical intervention.

References

1. Ethier, C.R.: Computational modeling of mass transfer and links to atherosclerosis. Ann. Biomed. Eng. **30**(4), 461–471 (2002)
2. Razavi, A., Shirani, E., Sadeghi, M.R.: Numerical simulation of blood pulsatile flow in a stenosed carotid artery using different rheological models. J. Biomech. **44**(11), 2021–2030 (2011)
3. Varghese, S.S., Frankel, H.S., Fischer, P.S.: Direct numerical simulation of stenotic flows. Part 2. Pulsatile flow. J. Fluid Mech. **582**, 281–318 (2007)
4. Basavaraja, P., Surendran, A., Gupta, A., Saba, L., Laird, J.R., Nicolaides, A., Mtui, E.E., Baradaran, H., Lavra, F., Suri, J.S.: Wall shear stress and oscillatory shear index distribution in carotid artery with varying degree of stenosis: a hemodynamic study. J. Mech. Med. Biol. **17**(02), 1750037 (2017)
5. Linge, F., Hye, M.A., Paul, M.C.: Pulsatile spiral blood flow through arterial stenosis. Comput. Methods in biomechanics and biomedical engineering **17**(15), 1727–1737 (2014)
6. Ahmed, S.A., Giddens, D.P.: Pulsatile post stenotic flow studies with laser Doppler anemometry. J. Biomech. **17**(9), 695–705 (1984)
7. Lee, S.W., Steinman, D.A.: On the relative importance of rheology for image-based CFD models of the carotid bifurcation. J. Biomech. Eng. **129**(2), 273–278 (2007)
8. Zhang, C., Xie, S., Li, S., Pu, F., Deng, X., Fan, Y., Li, D.: Flow patterns and wall shear stress distribution in human internal carotid arteries: the geometric effect on the risk for stenoses. J. Biomech. **45**(1), 83–89 (2012)
9. Zovatto, L., Pedrizzetti, G.: Fluid flow in a helical vessel in presence of a stenosis. Meccanica **52**(3), 1–9 (2017)
10. LoGerfo, F.W., Nowak, M.D., Quist, W.C., Crawshaw, M., Bharadvaj, B.K.: Flow studies in a model carotid bifurcation. Arterio- sclerosis **1**, 235–241(1981)
11. Sadeghi, M.R., Shirani, E., Tafazzoli-Shadpour, M., Samaee, M.: The effects of stenosis severity on the hemodynamic parameters—assessment of the correlation between stress phase angle and wall shear stress. J. Biomech. **44**(15), 2614–2626 (2011)

Flow and Heat Transfer of Carbon Nanotubes Nanofluid Flow Over a 3-D Inclined Nonlinear Stretching Sheet with Porous Media

Shalini Jain and Preeti Gupta

Abstract A numerical study of boundary layer flow of carbon nanotubes (CNTs) nanofluid over a three-dimensional inclined nonlinear stretching sheet in the presence of seawater with porous medium under the convective boundary conditions have been investigated. In this paper, we have considered both single-wall carbon nanotube (SWCNT) and multiwall carbon nanotube (MWCNT). Using suitable similarity transformations, the governing equations are changed into ordinary differential equations. The reduced equations are solved numerically by applying Runge–Kutta fourth-order method with shooting technique. The influence of the relevant parameters on the fluid velocity and temperature is discussed and presented graphically.

Keywords CNTs · Porous media · Nonlinear stretching sheet

1 Introduction

Boundary layer flow through a nonlinear stretching surface has wide applications in engineering and industrial process such as aerodynamics, extrusion of plastic sheets, paper and glass fiber production, etc. Hayat et al. [1] studied three-dimensional nanofluid flow with convective boundary conditions over a stretching MHD nonlinear surface. Jain and Parmar [2] studied radiative Williamson fluid flow over stretching cylinder in the presence of porous medium with heat source. Gopal et al. [3] studied Joule's and viscous dissipation on Casson fluid flow with inclined magnetic field over a chemical reacting stretching sheet. Kandasamy et al. [4] discussed MHD

S. Jain (✉)
Department of Mathematics and Statistics,
University of Rajasthan, JLN Marg, Jaipur, India
e-mail: drshalinijainshah@gmail.com

P. Gupta
Department of Mathematics,
Manipal University Jaipur, Jaipur 303007, Rajasthan, India
e-mail: pritimbgupta@gmail.com

D. Srinivasacharya and K. S. Reddy (eds.), *Numerical Heat Transfer and Fluid Flow*, Lecture Notes in Mechanical Engineering,
https://doi.org/10.1007/978-981-13-1903-7_37

SWCNT-type nanofluid flow in the occurrence of the base fluids: water and seawater. Among the usual nanoparticles, carbon nanotubes have attracted special interest due to high thermal conductivity and hexagonally shaped arrangements of carbon atoms that have been rolled into tubes. CNTs are used in several devices such as gas storage, radar-absorbing coating, ultra-capacitors, batteries with improved lifetime, conductive plastics, and also used in biosensors, medical devices due to their higher chemical compatibility with biomolecules, i.e., DNA, proteins, and purification of contaminated drinking water. First, nanofluids were introduced by Choi [5]. Hayat et al. [6] discussed three-dimensional flow of CNTs for homogenous–heterogeneous reactions in the presence of porous media. Jain and Choudhary [7] studied the impact of boundary layer flow due to shrinking exponentially sheet with MHD, porous media, and slip.

Convective boundary condition represents heat transfer rate across the surface. In other words, the convective boundary condition increases the thermal conductivity and the temperature of nanofluids. Many researchers Mahanthesh et al. [8], Jain and Bohra [9], Das et al. [10], Junaid et al. [11], and Nayak [12] discussed radiative heat transfer in 3D MHD flow of nanofluid over a stretching sheet with convective boundary conditions.

This paper aimed to study flow and heat transfer of seawater-based CNT's nanofluid over an inclined 3D nonlinear stretching sheet under convective surface boundary conditions. The governing inclined nonlinear system is evaluated through Runge–Kutta fourth-order method with shooting technique. Velocity and temperature profiles are obtained and presented through figures.

2 Formulation of the Problem

Consider flow and heat transfer of seawater-based carbon nanotubes over a nonlinear inclined 3-D stretching sheet with porous media under the convective boundary condition. Velocities along x- and y-directions are $U_w = c(x+y)^n$, $V_w = \mathrm{d}(x+y)^n$, where $n > 0$, where c and d are positive constants (see Fig. 1).

The governing equations of continuity, momentum, and energy of nanofluid flow are as follows:

$$\frac{\partial u}{\partial x} + \frac{\partial v}{\partial y} + \frac{\partial w}{\partial z} = 0 \tag{1}$$

$$u\frac{\partial u}{\partial x} + v\frac{\partial u}{\partial y} + w\frac{\partial u}{\partial z} = \upsilon_{nf}\frac{\partial^2 u}{\partial z^2} - \frac{\upsilon_{nf}}{k_p}u + g[\beta_T(T - T_\infty)]\cos\alpha, \tag{2}$$

$$u\frac{\partial v}{\partial x} + v\frac{\partial v}{\partial y} + w\frac{\partial v}{\partial z} = \upsilon_{nf}\frac{\partial^2 v}{\partial z^2} - \frac{\upsilon_{nf}}{k_p}v + g[\beta_T(T - T_\infty)]\sin\alpha, \tag{3}$$

$$u\frac{\partial T}{\partial x} + v\frac{\partial T}{\partial y} + w\frac{\partial T}{\partial z} = \frac{k_{nf}}{(\rho c_p)_{nf}}\frac{\partial^2 T}{\partial z^2} - \frac{1}{(\rho c_p)_{nf}}\frac{\partial q_r}{\partial z}, \tag{4}$$

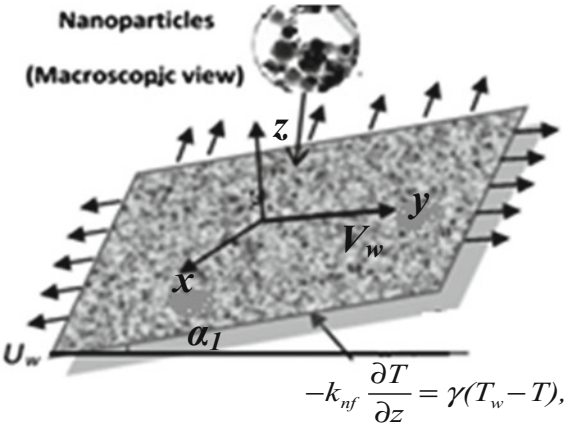

Fig. 1 Schematic diagram

under the boundary conditions

$$\text{at } z = 0,\ u = c(x+y)^n,\ v = d(x+y)^n,\ w = 0$$

$$-k_{nf}\frac{\partial T}{\partial z} = \gamma(T_w - T) \tag{5}$$

$$\text{at } z \to \infty,\ u \to 0,\ T \to T_\infty, \tag{6}$$

where u, v, w are fluid velocities along x-, y-, and z-directions, respectively; $k_p v \to 0$ is the permeability of porous medium; β_T is the thermal expansion. Also, μ_{nf}, υ_{nf}, ϕ, ρ_{nf}, ρ_{CNT} are the viscosity, kinematic viscosity, volume fraction, density, and carbon nanotube, respectively. Thermophysical properties of fluid and nanoparticles are given in Table 1

$$\mu_{nf} = \frac{\mu_f}{(1-\phi)^{2.5}},\ \upsilon_{nf} = \frac{\mu_{nf}}{\rho_{nf}},\ (\rho Cp)_{nf} = (1-\varphi)^{2.5}(\rho Cp)_f + \varphi(\rho Cp)_{CNT}. \tag{7}$$

Table 1 Thermophysical properties of base fluid and nanoparticles

Physical characteristics	Seawater (Basefluid)	SWCNT (nanoparticle)	MWCNT (nanoparticle)
ρ (kg/m^3)	1021	2600	1600
C_p(J/kg K)	4000	425	796
k(W/m K)	0.6015	6600	3000

The thermal conductivity of nanofluid is expressed as

$$\frac{k_{nf}}{k_f} = \left(\frac{1 - \phi + 2\phi\left(\frac{k_{CNT}}{k_{CNT} - k_f}\right) \ln\left(\frac{k_{CNT} + k_f}{2k_f}\right)}{1 - \phi + 2\phi\left(\frac{k_f}{k_{CNT} - k_f}\right) \ln\left(\frac{k_{CNT} + k_f}{2k_f}\right)} \right). \tag{8}$$

The Rosseland approximation is expressed as

$$q_r = -\frac{4\sigma^*}{3k^*} \frac{\partial T^4}{\partial z}, \tag{9}$$

where k^* is the mean absorption coefficient and σ^* is the Stefan–Boltzmann constant. The temperature difference has been considered very small, so that T^4 may be communicated as a linear function of temperature.

$$T^4 \approx 4T_\infty^3 T - 3T_\infty^4 \tag{10}$$

Similarity transformations are $u = c(x + y)^n f'(\eta)$, $v = c(x + y)^n g'(\eta)$,

$$w = -\left(\frac{c\upsilon_f(n+1)}{2}\right)^{1/2} (x+y)^{\frac{n-1}{2}} \left\{ (f+g) + \frac{n-1}{n+1}\eta\left(f' + g'\right) \right\},$$
$$\eta = \left(\frac{c(n+1)}{2\upsilon_f}\right)^{1/2} (x+y)^{\frac{n-1}{2}} z, T - T_\infty = (T_w - T_\infty)\theta, \tag{11}$$

On substituting Eq. (11) in Eqs. (1)–(4), Eq. (1) is identically satisfied and Eqs. (2)–(4) are converted into the following form:

$$f''' + (1-\phi)^{2.5} A_1 \left\{ (f+g)f'' - \frac{2n}{n+1}\left(f' + g'\right)f' + \frac{2}{n+1}\delta\cos\alpha_1\theta \right\} - \frac{2K}{n+1}f' = 0 \tag{12}$$

$$g''' + (1-\phi)^{2.5} A_1 \left\{ (f+g)g'' - \frac{2n}{n+1}\left(f' + g'\right)g' + \frac{2}{n+1}\delta\sin\alpha_1\theta \right\} - \frac{2K}{n+1}g' = 0 \tag{13}$$

$$\frac{1}{A_2 \Pr}\left(A_3 + \frac{4}{3}R\right)\theta'' + (f+g)\theta' = 0, \tag{14}$$

under the boundary condition

$$\text{at } \eta = 0\, f(0) = g(0) = 0,\ f'(0) = 1,\ g'(0) = \alpha,\ \theta(0) = 1 + \frac{A_3}{B_i}\theta'(0),$$
$$\text{at } \eta \to \infty\, f'(\infty) \to 0,\ g'(\infty) \to 0,\ \theta(\infty) \to 0, \tag{15}$$

where $K = \frac{\upsilon_f}{k_p c(x+y)^{n-1}}$ is the local porosity parameter, $\alpha = \frac{d}{c}$ is the ratio parameter, $R = \frac{4\sigma^* T_\infty^3}{k^* k_f}$ is the radiation parameter, and $\Pr = \frac{\mu_f (c_p)_f}{k_f}$ is the Prandtl number. Assuming $A_1 = (1-\phi) + \phi\frac{\rho_{CNT}}{\rho_f}$, $A_2 = (1-\phi) + \phi\frac{(\rho C_p)_{CNT}}{(\rho C_p)_f}$, $A3 = \frac{k_{nf}}{k_f}$.

Converted nondimensional ordinary differential Eqs. (12–14) under the boundary conditions (15) are solved by Runge–Kutta fourth-order method accompanied by shooting technique.

3 Results and Discussion

The numerical results have been obtained for two different cases of CNTs, i.e., SWCNTs and MWCNTs and are presented graphically. Effects of relevant parameters like ratio parameter α, porosity parameter K, radiation parameter R, Biot number Bi, and nanoparticle volume fraction ϕ, on velocity and temperature are obtained and presented through graphs. Consider $\alpha = 0.3, K = 0.1, R = 0.2, Bi = 0.5, \phi = 0.2, \alpha_1 = \frac{\pi}{4}$, as fix values during computation.

Figure 2 shows the variation of stretching ratio parameter on the axial velocity. It is noted that rises in stretching ratio parameter lead to reduce the boundary layer thickness along the x-direction (axis), whereas it increases along the y-direction (transverse). Figure 3 depicts that the velocity profile reduces when nanoparticle volume fraction increases for SWCNT and MWCNT. Figure 4 shows that a rise in K shows decreasing trend for velocity profile and boundary layer thickness. Figure 5 shows that temperature increases when porosity parameter increases for both SWCNT and MWCNT. Figure 6 shows the influence of Biot number and stretching ratio parameter of the temperature distribution. It is noted that an increase in Biot number causes enhancement in the temperature profile. Physically speaking, an enhance in Biot

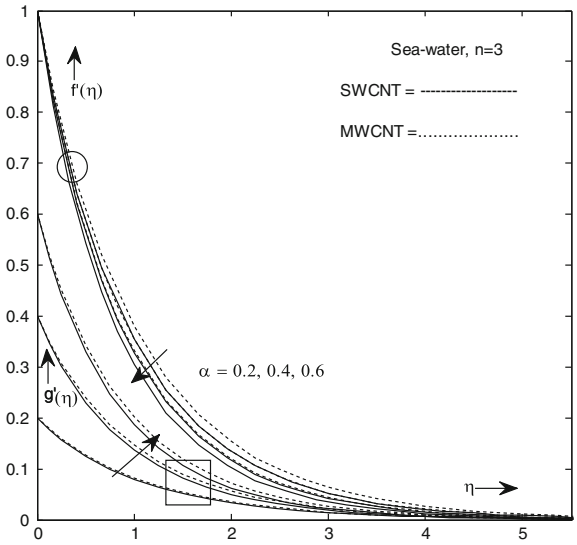

Fig. 2 Velocity for different values of α

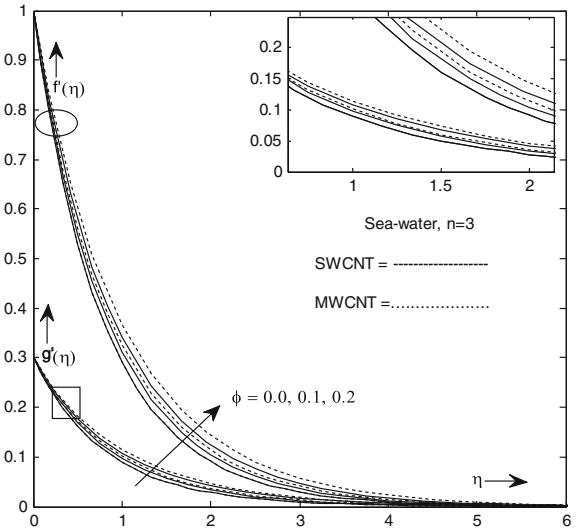

Fig. 3 Velocity for different values of ϕ

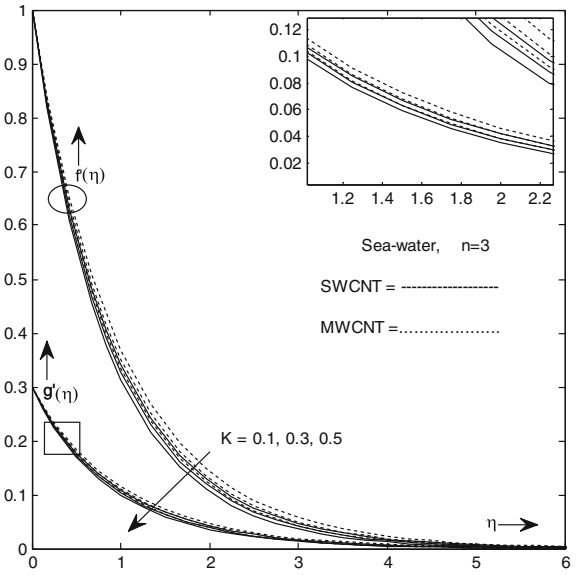

Fig. 4 Velocity for different values of K

number decreases sheet's thermal resistance and also an improves convective heat transfer to the fluid on the sheet. While stretching ratio parameter decreases, the temperature increases.

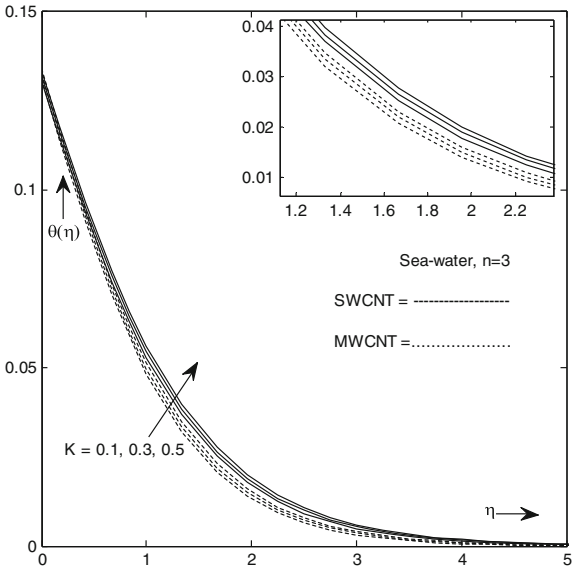

Fig. 5 Temperature for different values of K

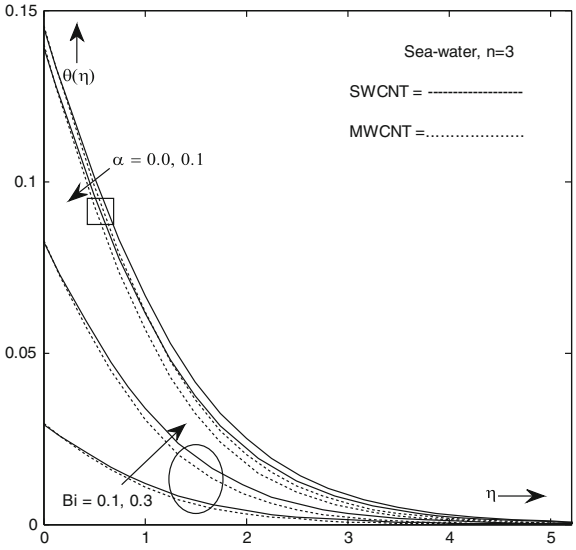

Fig. 6 Temperature for Bi and α

Figure 7 shows that the temperature is enhanced in the boundary layer with an enhance in radiation parameter. The higher radiative heat transfer is responsible for the enhancement of thermal boundary layer growth. Further, the temperature profile

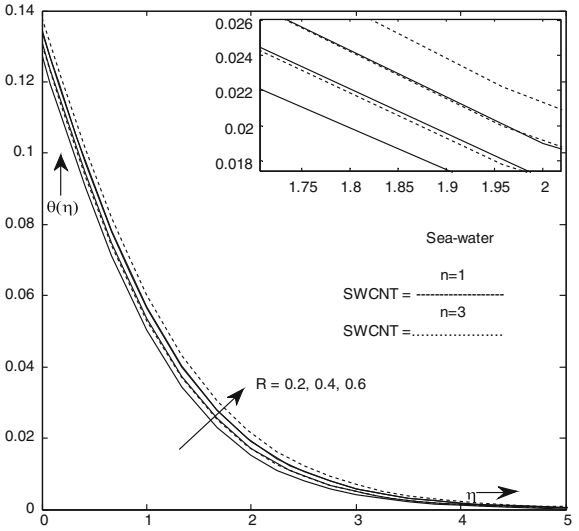

Fig. 7 Temperature for different values of R

is lower for linear thermal radiation as compared with nonlinear thermal radiation. Therefore, the nonlinear thermal radiation is more suitable for heating processes.

4 Conclusion

Analysis of seawater-based carbon nanotubes over a nonlinear inclined 3-D stretching sheet with porous media is studied. The results obtained are as follows:

- Velocity components decay for higher local porosity parameter K.
- Both velocity components are lower for SWCNTs when compared with MWCNTs.
- The nonlinear thermal radiation has high impact on flow fields as compared with linear thermal radiation.

References

1. Hayat, T., Aziz, A., Muhammad, T., Alsedi, A.: On magnetohydrodynamic three-dimensional flow of nanofluid over a convectively heated nonlinear stretching surface. Int. J. Heat and Mass Transf. **100**, 566–572 (2016)
2. Jain, S., Parmar, A.: Numerical study of unsteady inclined MHD casson fluid flow and heat transfer through porous medium along a vertical sheet. Global Sto. Analy. 41–50 (2017)

3. Gopal, D., Kishan, N., Raju, C.S.K.: Viscous and joule's dissipation on Casson fluid over a chemically reacting stretching sheet with inclined magnetic field and multiple slips. Inform. Med. Unlocked **9**, 154–160 (2017)
4. Kandasamy, R., Vignesh, V., Kumar, A., Hasan, S.H., Isa, N.M.: Thermal radiation energy due to SWCNTs on MHD nanofluid flow in the presence of seawater/water: lie group transformation. Ain Shams Eng. J. (2016)
5. Choi, S.U.S., Zhang, Z.G., Yu, W.: Anomalous thermal conductivity enhancement in nanotube suspension. Appl. Phys. Lett. **231**, 99–105 (1995)
6. Hayat, T., Ahmed, S., Muhammad, T., Alsedi, A., Ayub, M.: Computational modeling for homogenous-heterogeneous reactions in three-dimensional flow of carbon nanotubes. Res. In Phy. **7**, 2651–2657 (2017)
7. Jain, S., Choudhary, R.: Effects of MHD on boundary layer flow in porous medium due to exponentially shrinking sheet with slip. Proc. Eng. **127**, 1203–1210 (2015)
8. Mahanthesh, B., Gireesha, B.J., Gorla, R.S.R.: Nonlinear radiative heat transfer in MHD 3-D flow of water based nanofluid over a non-linearly stretching sheet with convective boundary condition. J. Nige. Math. Soc. **35**, 178–198 (2016)
9. Jain, S., Bohra, S.: Hall current and radiation effects on unsteady MHD squeezing nanofluid flow in a rotating channel with lower stretching permeable wall. Appl. Fluid Dyna. 127–141 (2018)
10. Das, S., Chakraborty, S., Jana, R.N., Makinde, O.D.: Entropy analysis of unsteady magneto-nanofluid flow past accelerating stretching sheet with convective boundary condition. Appl. Math. Mech. Engl. Ed. **36**(12), 1593–1610 (2015)
11. Khan, J.A., Mustafa, M., Hayat, T., Alsedi, A.: Three-dimensional flow of nanofluid over a non-linearly stretching sheet: an application to solar energy. Int. J. Heat and Mass Trans. **86**, 158–164 (2015)
12. Nayak, M.K.: MHD 3D flow and heat transfer analysis of nanofluid by shrinking surface inspired by thermal radiation and viscous dissipation. Int. J. of Mech. Sci. **124–125**, 185–193 (2017)

MHD Boundary Layer Liquid Metal Flow in the Presence of Thermal Radiation Using Non-similar Solution

S. Mondal, P. Konar, T. R. Mahapatra and P. Sibanda

Abstract In this paper, we have studied the effects of thermal radiation parameters on an incompressible boundary layer liquid metal (e.g., Mercury) flow over a flat plate in the presence of magnetic field. The governing nonlinear partial differential equations have been transformed using Görtler transformation on coupled non-similar ordinary differential equations, which are solved numerically by the use of finite difference technique together with Thomas algorithm. We have discussed and interpreted the effects of thermal radiation parameters and streamwise pressure gradient in the boundary layer on the fluid and the Görtler transformation in our current study. A detailed comparison with previously published results is given.

Keywords Liquid metal · Thermal radiation · Non-similar solution

1 Introduction

The non-similarity boundary layer flows of Newtonian fluids over a plate have important engineering applications such as polymer processing unit in a chemical plant, working process of metals in metallurgy, and aerodynamic extrusion of plastic sheets. The laminar boundary layer equations were first introduced by Prandtl [1], and the boundary layer theory has been developing greatly and applied in nearly all regions of fluid mechanics. Later, Minkowycz, and Cheng [2] performed local non-similar

S. Mondal · P. Konar (✉)
Department of Mathematics, Amity University, Kolkata 700135, West Bengal, India
e-mail: pulakkonar@gmail.com

T. R. Mahapatra
Department of Mathematics, Visva Bharati (A Central University),
Santiniketan 731235, West Bengal, India

P. Sibanda
School of Mathematics, Statistics and Computer Science,
University of KwaZulu-Natal, Pietermaritzburg Private Bag X01,
Scottsville 3209, South Africa

D. Srinivasacharya and K. S. Reddy (eds.), *Numerical Heat Transfer and Fluid Flow*, Lecture Notes in Mechanical Engineering,
https://doi.org/10.1007/978-981-13-1903-7_38

solutions for free convective flow with uniform lateral mass flux in a porous medium. Recently, Beg et al. [3] studied non-similar, laminar, steady, electrically conducting forced convection liquid metal boundary layer flow with induced magnetic field effects. All these non-similar boundary problems had been solved using local non-similarity method. In the present paper, we have investigated the effects of thermal radiation on the plate considering the liquid metal flow in the presence of magnetic field using Görtler transformation [4]. Blasius [5] presented a result for the boundary layer flow over a plate. By the use of Görtler transformation [4], the governing nonlinear partial differential equations have been transformed into the coupled non-similar ordinary differential equations and solved numerically by applying finite difference method along with Thomas algorithm [6]. Our results have been shown graphically and discussed quantitatively.

2 Mathematical Formulations

The magnetic field is investigated in this paper considering two-dimensional, steady, incompressible, laminar, Newtonian boundary layer flow over a plate in the presence of liquid metal (e.g., Mercury). The buoyancy effects are negligible here. The governing equations under these conditions are

$$\frac{\partial u}{\partial x} + \frac{\partial v}{\partial y} = 0, \tag{1}$$

$$u\frac{\partial u}{\partial x} + v\frac{\partial u}{\partial y} = U_e\frac{\partial U_e}{\partial x} + \nu\frac{\partial^2 u}{\partial y^2} - \frac{\sigma B_0^2}{\rho}(u - U_e), \tag{2}$$

$$u\frac{\partial T}{\partial x} + v\frac{\partial T}{\partial y} = \lambda\frac{\partial^2 T}{\partial y^2} - \frac{1}{\rho c_p}\frac{\partial q_r}{\partial y} + \frac{Q_o}{\rho c_p}(T - T_\infty). \tag{3}$$

B_0, ν, λ, q_r, Q_0, and c_p denote magnetic field strength, kinematic viscosity, thermal diffusivity, the radiation heat flux, heat generation constant, and specific heat at constant pressure of the fluid. In addition, the radiation heat flux q_r is considered according to Rosseland approximation such that

$$q_r = -\frac{4\sigma^*}{3K^*}\frac{\partial T^4}{\partial y}, \tag{4}$$

where σ^* and K^* are the Stefan–Boltzmann constant and the mean absorption coefficient, respectively.

2.1 Görtler Transformation

In order to solve the boundary layer equations more efficiently, Görtler [4] described a transformation that converts the equations of continuity and momentum into a single differential equation. After considerable algebraic transformations similar to Görtler [4], we get the new nondimensional form of the equation

$$f''' + ff'' + \beta(\xi)[1 - f'^2] = 2\xi[f' f'_\xi - f_\xi f'' - Mf' + M], \tag{5}$$

$$(1 + N_R)\theta'' + P_r f\theta' = 2P_r\xi[\theta_\xi f' - f_\xi\theta' - \mathrm{He}\theta], \tag{6}$$

depending on ξ and η. Here, β represents the streamwise pressure gradient in the boundary layer and M, N_R, and He represent the uniform magnetic field, where

$$\beta(\xi) = \frac{2U'_e \int_0^x U_e \mathrm{d}x}{U_e^2} = \frac{2\nu U'_e \xi}{U_e^2}. \tag{7}$$

Other nondimensional parameters are

$$M = \frac{\nu\sigma B_0^2}{U_e^2\rho}, N_R = \frac{16\sigma^* T_\infty^3}{3K^*\lambda\rho c_p}, \mathrm{He} = \frac{Q_o\nu}{U_e^2\rho c_p}, P_r = \frac{\nu}{\lambda}. \tag{8}$$

The transformed boundary conditions

$$f(\xi, 0) = f'(\xi, 0) = 0, \lim_{\eta\to\infty} f'(\xi, \eta) = 1, \tag{9}$$

$$\theta(\xi, 0) = 1, \lim_{\eta\to\infty} \theta(\xi, \eta) = 0. \tag{10}$$

3 Method of Solution

3.1 Discretization and Grid

Now, the following steps are applied for discretization of Eq. (5). The first step was to discretizing the Görtler equation. This was done using central differences for the derivatives in the η direction and backward differences in the ξ direction. As the f' values in the Görtler equation represent the velocity relation $u(x) = Ue(x)$, and with most of the boundary conditions being with respect to f', it makes sense to introduce the mapping $G = f'$ and to solve the equation for G. The non-discretized equation now presents itself as

$$G'' + G' \int_0^\eta G \, \mathrm{d}\eta + \beta(\xi)[1 - G^2] = 2\xi \left[GG_\xi - G' \frac{\partial}{\partial\xi} \left(\int_0^\eta G \mathrm{d}\eta \right) - M(G - 1) \right], \tag{11}$$

are discretized as

$$\frac{2}{\eta_{j+1}-\eta_{j+1}}\left[\frac{G_{i,j+1}-G_{i,j}}{\eta_{j+1}-\eta_j}-\frac{G_{i,j}-G_{i,j-1}}{\eta_j-\eta_{j-1}}\right]+f_{i,j}\frac{G_{i,j+1}-G_{i,j-1}}{\eta_{j+1}-\eta_{j-1}}$$
$$+\beta(\xi)\left[1-2G_{i,j}G_{i,j\mathrm{OLD}}+G_{i,j\mathrm{OLD}}^2\right]$$
$$=2\xi_i\left[G_{i,j\mathrm{OLD}}\frac{G_{i,j}-G_{i-1,j}}{\xi_i-\xi_{i-1}}-\frac{f_{i,j}-f_{i-1,j}}{\eta_j-\eta_{j-1}}\frac{G_{i,j+1}-G_{i,j-1}}{\eta_{j+1}-\eta_{j-1}}-MG_{i,j}+M\right]. \tag{12}$$

The index in the ξ direction is i, and in the η direction is j. After the mapping, $G = f^{'}$, all appearances of f itself are replaced with the integral over G from 0 to η, and the integral is calculated using the trapezoidal rule. In the η direction, a nonuniformly spaced grid is used and a uniform grid is used in the ξ direction. The nonuniform grid was conceived by starting off with an initial Δ_η at the wall, which is then multiplied with an amplification factor $k > 1$ at each step (e.g., $k = 1.1$). The distance between two grid points gradually increases with greater distance from the wall. With this strategy, it is possible to get good results with as little as 25 grid points in the η direction over the whole domain. The downside to this approach is that it becomes more difficult to use higher order schemes for the discretization. Since the boundary condition is defined for $\eta \to \infty$, a value of $\eta = 10$ is chosen as the numerical value for infinity. Now, the similar procedure is applied for discretization temperature equation as in Eq. (5) and then non-discretized equation of temperature equation [see Eq. (6)] is

$$(1+N_R)\theta'' + P_r f\theta' = 2P_r\xi\left[\theta_\xi G - \frac{\partial}{\partial\xi}\left(\int_0^\eta G\mathrm{d}\,\eta\right)\theta' - \mathrm{He}\,\theta\right]. \tag{13}$$

We get discretization form as follows:

$$\frac{2(1+N_R)}{\eta_{j+1}-\eta_{j-1}}\left(\frac{\theta_{i,j+1}-\theta_{i,j}}{\eta_{j+1}-\eta_j}-\frac{\theta_{i,j}-\theta_{i,j-1}}{\eta_j-\eta_{j-1}}\right)+P_r f_{i,j}\left(\frac{\theta_{i,j+1}-\theta_{i,j-1}}{\eta_{j+1}-\eta_{j-1}}\right)$$
$$=2P_r\xi\left[\left(\frac{\theta_{i,j}-\theta_{i-1,j}}{\xi_i-\xi_{i-1}}\right)G_{i,j}-\frac{\partial}{\partial\xi}\left(\int_0^\eta G\mathrm{d}\eta\right)\left(\frac{\theta_{i,j+1}-\theta_{i,j-1}}{\eta_{j+1}-\eta_{j-1}}\right)-\mathrm{He}\,\theta_{i,j}\right]. \tag{14}$$

Here, central differences are used for the derivatives in the η direction and backward differences are used in the ξ direction. The index in the ξ direction is i, and in the η direction is j; and in the η direction, a nonuniformly spaced grid was used and a uniform grid in the ξ direction.

4 Results and Discussions

We choose $P_r = 0.06$ which is small. Therefore, the heat will diffuse very quickly compared to velocity (momentum). This means that for the liquid metals, the thickness of the thermal boundary layer is much bigger than the velocity boundary layer. For this paper, the Blasius solution is used as the initial values at $\xi = 0.01$.

In Table 1 using same initial step size and the amplification factor for the step size for various values of η and β. This table shows good agreement between the numerical values and the results of the existing literature [7]. What can be nicely shown in Fig. 1 is that how the velocity profiles increase for the increasing value of β, when $\xi = 0.11$ near the boundary. As one would expect from boundary layer observations, for higher values of β, the boundary layer becomes thinner. Figure 2 shows that the temperature profile decreases with the increasing thermal radiation parameter. This is because the divergence of the radiation heat flux $\frac{\partial q_r}{\partial y}$ decreases with the increase in the Rosseland radiative absorption coefficient K^* [see Eq. (4)], which in turn decreases the rate of radiative heat transfer to the fluid, which causes the fluid temperature to decrease. From these figures, it is noteworthy that the thermal boundary layer thickness increased with an increase in He as η.

Table 1 Comparison table of numerical values for the Blasius and Falkner–Skan solution

	White [7]		Present result		White [7]	Present result	White [7]	Present result
β	0.0		0.0		0.3	0.3	10.0	10.0
η	f	f'	f	f'	f'	f'	f'	f'
0.0	0.0	0.0	0.0	0.0	0.0	0.0	0.0	0.0
0.1	0.00235	0.04696	0.00235	0.04719	0.07597	0.07634	0.31843	0.31843
0.2	0.00939	0.09391	0.00939	0.09389	0.14894	0.14891	0.54730	0.54730
0.3	0.02113	0.14081	0.02113	0.14100	0.21886	0.21914	0.70496	0.70496
0.4	0.03755	0.18761	0.03755	0.18749	0.28569	0.28553	0.81043	0.81043
0.5	0.05864	0.23423	0.05864	0.23426	0.34938	0.34943	0.87954	0.87954
0.6	0.08439	0.28058	0.08439	0.28071	0.40988	0.41006	0.92414	0.92413
0.7	0.11474	0.32653	0.11475	0.32672	0.46713	0.46735	0.95259	0.95259
0.8	0.14967	0.37196	0.14968	0.37213	0.52107	0.52127	0.97057	0.97057
0.9	0.18911	0.41672	0.18912	0.41680	0.57167	0.57176	0.98185	0.98185
1.0	0.23299	0.46063	0.23299	0.46056	0.61890	0.61882	0.98888	0.98887

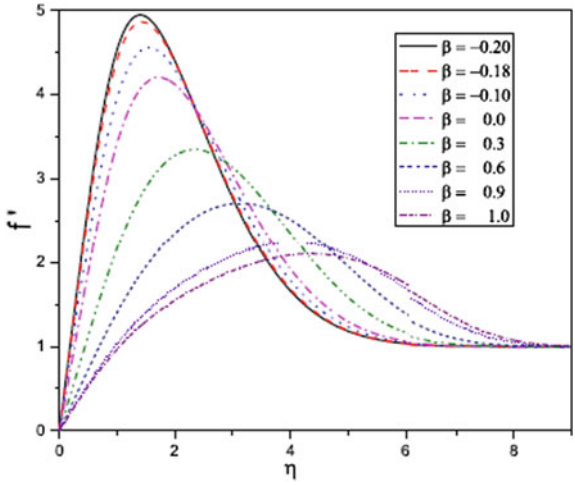

Fig. 1 Variation of $f'(\eta)$ with η for several values of β, when $P_r = 0.06$, $M = 1.0$, and $\xi = 0.11$

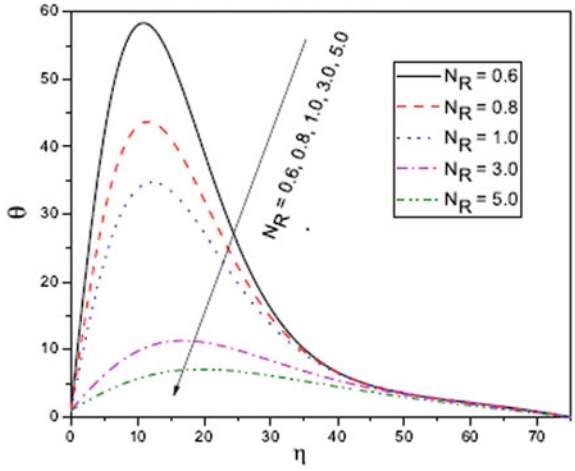

Fig. 2 Variation of $\theta(\eta)$ with η for different values of N_R, when $P_r = 0.06$, $\beta = 0.3$, $M = 1.0$, He $= 1.0$, and $\xi = 0.05$

5 Conclusion

The main objective of the current investigation is to study the non-similar solution procedure for magnetohydrodynamic boundary layer liquid metal flow over a plate in the presence of thermal radiation and heat generation. From the study, the following conclusions can be made:

- Velocity profiles increase for the increasing value of β, when $\xi = 0.11$ exists near the boundary. But opposite trend of velocity profiles can be found away from the wall.
- Temperature profile decreases with the increasing thermal radiation parameter.

References

1. Prandtl, L.: über Flüssigkeitsbewegung bei sehr kleiner Reibung, vol. 2, p. 484. Verhandl III, Intern. Math. Kongr. Gesammelte Abhandlungen, Heidelberg (1904)
2. Minkowycz, W.J., Cheng, P.: Local non-similar solutions for free convective flow with uniform lateral mass flux in a porous medium. Lett. Heat Mass Transf. **9**(3), 159 (1982)
3. Beg, O.A., Bakier, A.Y., Prasad, V.R., Zueco, J., Ghosh, S.K.: Nonsimilar, laminar, steady, electrically-conducting forced convection liquid metal boundary layer flow with induced magnetic field effects. Int. J. Therm. Sci. **48**, 1596 (2009)
4. Görtler, H.: A new series for the calculation of steady laminar boundary layer flows. Indiana Univ. Math. J. **6**, 1 (1982)
5. Blasius, H.: Grenzschichten in Flussigkeiten mit kleiner Reibung. Zeitschr. f. Math. u. Phys. **56**, 1 (1908)
6. Tannehill, J.C., Anderson, D.A., Pletcher, R.H.: Computational Fluid Mechanics, and Heat Transfer. Taylor and Francis, Washington, D.C. (1997)
7. White, F.M.: Viscous Fluid Flow. McGraw-Hill, New York (2006)

Similarity Analysis of Heat Transfer and MHD Fluid Flow of Powell–Eyring Nanofluid

Govind R. Rajput and M. G. Timol

Abstract In this present analysis, the heat transfer for the flow of Powell–Eyring nanofluid under the magnetic effects considering stretching sheet are derived. The governing model is transformed to ODE using similarity analysis. The obtained system of equation is then solved numerically using the MATLAB package. The various effects of the different parameters like magnetic parameter M, δ, ε Prandtl number Pr, suction parameter S and Schmidt number Sc on all profiles are plotted and discussed through graphs.

Keywords Powell–Eyring model · Nanofluid · Similarity analysis

1 Introduction

Flow of fluid past a stretching surface has a great application in various sectors of engineering and the industries. Production of papers and gas fibres, food manufacture, crystal growing and metallic plate cooling are some of the examples of such processes. In these processes, the fluids get interacted with the stretching surface. A large number of problems considering heat and fluid flow past stretching surface are taken into account by the researchers with Newtonian and non-Newtonian under the influence of magnetic fields and radiation effects with different models. A lot of work has been done by the researchers over different flow geometries with a stretching surface which is shown in the references [1–5].

Nowadays, the nature of the fluids used by several industries is the non-Newtonian fluids. Blood, ketchup, toothpaste, honey, mud and biological foods are some exam-

G. R. Rajput (✉)
Department of Applied Mathematics, SVKMs, NMIMS, Mukesh Patel School of Technology Management and Engineering, Shirpur Campus, Shirpur 425405, Maharashtra, India
e-mail: g.rajput7@gmail.com

M. G. Timol
Department of Mathematics, Veer Narmad South Gujarat University, Magdulla Road, Surat 395007, Gujarat, India

D. Srinivasacharya and K. S. Reddy (eds.), *Numerical Heat Transfer and Fluid Flow*, Lecture Notes in Mechanical Engineering,
https://doi.org/10.1007/978-981-13-1903-7_39

ples of this fluid. Non-Newtonian fluids are divided into different classes like power law, Prandtl–Eyring, Sisko fluid, Reiner–Philippoff, Powell–Eyring, etc. Out of these models, the Powell–Eyring [6] is very important and useful as compared to other models. This model plays a vital role almost in all chemical engineering operations and also has benefits over the above said models. This model is derived from the kinetic theory of liquids, and it acts as Newtonian fluids when the shear rate is high and low [1]. Most of the researchers have contributed a lot for the Powell–Eyring model which is found in the literature. Akbar et al. [7] analysed the model of Powell–Eyring with a magnetic effect numerically past stretching surface. Hayat et al. [8–10] discussed the Eyring–Powell model over different flow geometries. Khan et al. [11] explained the Eyring–Powell MHD fluid flow over homogeneous and heterogeneous reactions with Newtonian heating. Patel and Timol [12] presented the numerical solution of the model of the Powell–Eyring. Recently, Ramazan et al. [13] analysed the model of Powell–Eyring with magnetic field and radiation. Panigrahi et al. [14] reported the influence of MHD mixed convection of flow of Powell–Eyring fluid past a non-linear stretching sheet. The Eyring–Powell flow of unsteady nanofluid past stretching sheet is addressed by Khan et al. [15].

2 Problem Formulation

Consider the two-dimensional, steady incompressible flow of Eyring–Powell nanofluid past a stretching surface having velocity $u_w(\bar{x})$ and $v_w(\bar{x})$ which the velocity of suction/injection over the surface. We assumed that the temperature and the nanoparticles fraction, i.e. T and C, respectively, have T_w and C_w as constant values, respectively. On the other hand, these values are denoted by T_∞ and C_∞, respectively, when $y \to \infty$.

Consider the flow model for Eyring–Powell

$$\frac{\partial \bar{u}}{\partial \bar{x}} + \frac{\partial \bar{v}}{\partial \bar{y}} = 0 \tag{1}$$

$$\bar{u}\frac{\partial \bar{u}}{\partial \bar{x}} + \bar{v}\frac{\partial \bar{u}}{\partial \bar{y}} = \frac{\mu_{nf}}{\rho_{nf}}\frac{\partial^2 \bar{u}}{\partial \bar{y}^2} - \sigma B^2(\bar{x})\,\bar{u} + \frac{1}{\rho_{nf}}\frac{\partial \tau_{\bar{x}\,\bar{y}}}{\partial \bar{y}} \tag{2}$$

$$\bar{u}\frac{\partial T}{\partial \bar{x}} + \bar{v}\frac{\partial T}{\partial \bar{y}} = \alpha_{nf}\frac{\partial^2 T}{\partial \bar{y}^2} \tag{3}$$

$$\bar{u}\frac{\partial C}{\partial \bar{x}} + \bar{v}\frac{\partial C}{\partial \bar{y}} = D_m\frac{\partial^2 C}{\partial \bar{y}^2} \tag{4}$$

and

$$\begin{aligned} &\bar{y} = 0 : \bar{u} = \lambda \bar{u}_w(\bar{x}),\ \bar{v} = \bar{v}_w(\bar{x}),\ T = T_w,\ C = C_w \\ &\bar{y} \to \infty : \bar{u} = 0,\ T \to \infty,\ C \to \infty, \end{aligned} \tag{5}$$

where $(\bar{u}, \bar{v})$ are the components of velocity along coordinate axis, ρ_{nf} is the base fluid density, σ is the electrical conductivity, $\lambda > 0$ is the stretching parameter and τ is the stress tensor, which can be expressed as $\tau = \mu \frac{\partial \bar{u}}{\partial \bar{y}} + \frac{1}{B} \sinh^{-1}\left(\frac{1}{C}\frac{\partial \bar{u}}{\partial \bar{y}}\right)$, where μ is the viscosity, and B and C are the parameters of the fluid material. Following [16], we have $\frac{1}{B}\sinh^{-1}\left(\frac{1}{C}\frac{\partial \bar{u}}{\partial \bar{y}}\right) \cong \frac{1}{C}\frac{\partial \bar{u}}{\partial \bar{y}} - \frac{1}{6}\left(\frac{1}{C}\frac{\partial \bar{u}}{\partial \bar{y}}\right)^3, \quad \left|\frac{1}{C}\frac{\partial \bar{u}}{\partial \bar{y}}\right| \ll 1.$

By putting above value in Eq. (2),

$$\bar{u}\frac{\partial \bar{u}}{\partial \bar{x}} + \bar{v}\frac{\partial \bar{u}}{\partial \bar{y}} = \frac{\mu_{nf}}{\rho_{nf}}\frac{\partial^2 \bar{u}}{\partial \bar{y}^2} - \sigma B^2(\bar{x})\,\bar{u} + \left(v + \frac{1}{\rho BC}\right)\frac{\partial^2 \bar{u}}{\partial \bar{y}^2} - \frac{1}{2\rho BC^3}\left(\frac{\partial \bar{u}}{\partial \bar{y}}\right)^2 \frac{\partial^2 \bar{u}}{\partial \bar{y}^2}. \tag{6}$$

Introducing the dimensionless quantities

$$x = \frac{\bar{x}}{L}, y = \frac{\bar{y}\sqrt{Re}}{L}, u = \frac{\bar{u}}{u_\infty}, v = \frac{\bar{v}\sqrt{Re}}{u_\infty}, \theta = \frac{T - T_\infty}{T_w - T_\infty},$$
$$\phi = \frac{C - C_\infty}{C_w - C_\infty}, S(x) = \frac{L}{u_\infty}\bar{S}(\bar{x}).$$

Here, L is the characteristic length, $S(x)$ is the magnetic parameter, Re is the Reynolds number and u_∞ is the reference velocity. Using above dimensionless quantities and the stream functions $u = \frac{\partial \psi}{\partial y}$ and $v = -\frac{\partial \psi}{\partial x}$, Eqs. (1), (3) and (6) become

$$\frac{\partial \psi}{\partial y}\frac{\partial^2 \psi}{\partial y \partial x} - \frac{\partial \psi}{\partial x}\frac{\partial^2 \psi}{\partial y^2} = (1+\varepsilon)\frac{\partial^3 \psi}{\partial y^3} - \varepsilon\delta\left(\frac{\partial^2 \psi}{\partial y^2}\right)^2 \frac{\partial^3 \psi}{\partial y^3} - S(x)\left(\frac{\partial \psi}{\partial y}\right) \tag{7}$$

$$\frac{\partial \psi}{\partial y}\frac{\partial \theta}{\partial x} - \frac{\partial \psi}{\partial x}\frac{\partial \theta}{\partial y} = \frac{1}{\mathrm{Pr}}\frac{\partial^2 \theta}{\partial y^2} \tag{8}$$

$$\frac{\partial \psi}{\partial y}\frac{\partial \phi}{\partial x} - \frac{\partial \psi}{\partial x}\frac{\partial \phi}{\partial y} = \frac{1}{Sc}\frac{\partial^2 \phi}{\partial y^2}, \tag{9}$$

with boundary conditions

$$y = 0 : u = \lambda u_w(x), v = v_w(x), T = T_w, C = C_w$$
$$y \to \infty : u = 0, T \to \infty, C \to \infty. \tag{10}$$

3 Problem Formulation

We introduced the following group G:

$$G : \overline{Q} = \wp^Q(\omega)Q + \aleph^Q(\omega), \tag{11}$$

where Q represents $x, y, \psi, S, \theta, \varphi$ also $\wp$'s and $\aleph$'s are real valued, which are at least differentiable in the real argument ω.

The given differential equations are transformed via chain rule operations from group G

$$\left.\begin{aligned}\overline{S_{\bar{i}}} = \left(\frac{\wp^{Q}}{\wp^{i}}\right) Q_i, \overline{Q}_{\bar{i}\,\bar{j}} = \left(\frac{\wp^{Q}}{\wp^{i}\wp^{j}}\right) Q_{ij}\end{aligned}\right\} \quad Q = \psi, S, \theta, \phi; \quad i, j = x, y. \tag{12}$$

The system of Eqs. (7)–(10) remains invariant by applying the group (11), and the application of chain rule and can be written as

$$\begin{aligned}
&\frac{\partial\bar{\psi}}{\partial\bar{y}}\frac{\partial^2\bar{\psi}}{\partial\bar{y}\partial\bar{x}} - \frac{\partial\bar{\psi}}{\partial\bar{x}}\frac{\partial^2\bar{\psi}}{\partial\bar{y}^2} - (1+\varepsilon)\frac{\partial^3\bar{\psi}}{\partial\bar{y}^3} + \varepsilon\delta\left(\frac{\partial^2\bar{\psi}}{\partial\bar{y}^2}\right)^2\frac{\partial^3\bar{\psi}}{\partial\bar{y}^3} + \overline{S}(\bar{x})\left(\frac{\partial\bar{\psi}}{\partial\bar{y}}\right)\\
&= N_1(\omega)\left[\frac{\partial\psi}{\partial y}\frac{\partial^2\psi}{\partial y\partial x} - \frac{\partial\psi}{\partial x}\frac{\partial^2\psi}{\partial y^2} - (1+\varepsilon)\frac{\partial^3\psi}{\partial y^3} + \varepsilon\delta\left(\frac{\partial^2\psi}{\partial y^2}\right)^2\frac{\partial^3\psi}{\partial y^3} + S(x)\left(\frac{\partial\psi}{\partial y}\right)\right]\\
&\frac{\partial\bar{\psi}}{\partial\bar{y}}\frac{\partial\bar{\theta}}{\partial\bar{x}} - \frac{\partial\bar{\psi}}{\partial\bar{x}}\frac{\partial\bar{\theta}}{\partial\bar{y}} - \frac{1}{\mathrm{Pr}}\frac{\partial^2\bar{\theta}}{\partial\bar{y}^2} = N_2(\omega)\left[\frac{\partial\psi}{\partial y}\frac{\partial\theta}{\partial x} - \frac{\partial\psi}{\partial x}\frac{\partial\theta}{\partial y} - \frac{1}{\mathrm{Pr}}\frac{\partial^2\theta}{\partial y^2}\right]\\
&\frac{\partial\bar{\psi}}{\partial\bar{y}}\frac{\partial\bar{\phi}}{\partial\bar{x}} - \frac{\partial\bar{\psi}}{\partial\bar{x}}\frac{\partial\bar{\phi}}{\partial\bar{y}} - \frac{1}{Sc}\frac{\partial^2\bar{\phi}}{\partial\bar{y}^2} = N_2(\omega)\left[\frac{\partial\psi}{\partial y}\frac{\partial\phi}{\partial x} - \frac{\partial\psi}{\partial x}\frac{\partial\phi}{\partial y} - \frac{1}{Sc}\frac{\partial^2\phi}{\partial y^2}\right].
\end{aligned}$$

By putting Eqs. (11)–(12) in the system of equations discussed above, we get

$$\begin{aligned}
&\frac{\left(\wp^{\psi}\right)^2}{\wp^{x}(\wp^{y})^2}\left(\frac{\partial\psi}{\partial y}\frac{\partial^2\psi}{\partial y\partial x} - \frac{\partial\psi}{\partial x}\frac{\partial^2\psi}{\partial y^2}\right) - \left(\frac{\wp^{\psi}}{\wp^{y^3}}\right)(1+\varepsilon)\frac{\partial^3\psi}{\partial y^3}\\
&+\left(\frac{\wp^{\psi}}{\wp^{y^2}}\right)^2\varepsilon\delta\left(\frac{\partial^2\psi}{\partial y^2}\right)^2\frac{\partial^3\psi}{\partial y^3} + \wp^{S}S(x)\left(\frac{\partial\psi}{\partial y}\right)\\
&\left(\frac{\wp^{\psi}}{\wp^{y}}\right)\frac{\partial\psi}{\partial y}\left(\frac{\wp^{\theta}}{\wp^{x}}\right)\frac{\partial\theta}{\partial x} - \left(\frac{\wp^{\psi}}{\wp^{x}}\right)\frac{\partial\psi}{\partial x}\left(\frac{\wp^{\theta}}{\wp^{y}}\right)\frac{\partial\theta}{\partial y} - \frac{1}{P_r}\left(\frac{\wp^{\theta}}{\wp^{y^2}}\right)\frac{\partial^2\theta}{\partial y^2}\\
&\left(\frac{\wp^{\psi}}{\wp^{y}}\right)\frac{\partial\psi}{\partial y}\left(\frac{\wp^{\phi}}{\wp^{x}}\right)\frac{\partial\phi}{\partial x} - \left(\frac{\wp^{\psi}}{\wp^{x}}\right)\frac{\partial\psi}{\partial x}\left(\frac{\wp^{\phi}}{\wp^{y}}\right)\frac{\partial\phi}{\partial y} - \frac{1}{S_c}\left(\frac{\wp^{\phi}}{\wp^{y^2}}\right)\frac{\partial^2\phi}{\partial y^2}.
\end{aligned}$$

The above system remains invariant if we summarize the group G as

$$G:\begin{cases} G_S:\begin{cases}\bar{x} = (\wp^{y})^3 x + \aleph^{x} \\ \bar{y} = \wp^{y} y\end{cases}, \quad \bar{\psi} = (\wp^{y})^2\psi + \aleph^{x}. \\ \overline{S} = \frac{1}{\wp^{y^2}}S,\ \bar{\theta} = \frac{1}{\wp^{y}}\theta,\ \bar{\phi} = \frac{1}{\wp^{y}}\phi \end{cases} \tag{13}$$

Also, a function $g(x, y : \psi, S, \theta, \phi)$ is an absolute invariant only if it satisfies the following equation:

$$\sum_{i=1}^{6} (\alpha_i Q_i + \beta_i) \frac{\partial g}{\partial Q_i} = 0,\ Q_i = x, y, \psi, S, \theta, \phi, \tag{14}$$

where $\alpha_i = \left.\frac{\partial \wp^i}{\partial \omega}\right|_{\omega=\omega^0}$ and $\beta_i = \left.\frac{\partial \aleph^i}{\partial \omega}\right|_{\omega=\omega^0} i = 1, 2, \ldots 6.$

Here, ω^0 is the value of 'ω', which is the identity element in the group G.

The generator (14) and Eq. (13) give the relation between all α's and β's. Hence, we obtained the following similarity variables:

$$\eta = y(x+\beta)^{-1/3}, \psi = (x+\beta)^{2/3} f(\eta), \theta = (x+\beta)^{-1/3} g(\eta)$$
$$\text{and } \varphi = (x+\beta)^{-1/3} h(\eta), \text{ where } \beta = \frac{\beta_1}{\alpha_1}.$$

Using above similarity variables, Eqs. (7)–(9) become

$$(1+\varepsilon) f''' - \varepsilon\delta\, f''^2 f''' - \frac{1}{3} f'^2 + \frac{2}{3} f f'' - M f' = 0 \tag{15}$$

$$\frac{1}{P_r} g'' + \frac{2}{3} f g' + \frac{1}{3} f' g = 0 \tag{16}$$

$$\frac{1}{S_c} h'' + \frac{2}{3} f h' + \frac{1}{3} f' h = 0. \tag{17}$$

To obtain the similarity solutions, we assume the free steam velocity and the mass flux velocity as $u_w = (x+\beta)^{\frac{1}{3}}$ and $v_w = -\frac{2}{3}(x+\beta)^{-1/3} S$, where S is the mass flux velocity parameter which causes suction when $S > 0$ and injection when $S < 0$. Since $S(x)$ is a function of x only, which is free from the terms of y, it must be treated as a constant which is given by $S(x) = M(x+\beta)^{-2/3}$.

And the transformed boundary conditions are

$$f(0) = S, \quad f'(0) = \lambda, \quad \theta(0) = 1, \quad \phi(0) = 1$$
$$f(\infty) = 0, \quad \theta(\infty) = 0, \quad \phi(\infty) = 0. \tag{18}$$

4 Results and Discussions

Here, we have discussed the impact of the parameters like S, Pr, ε, δ and M on all profiles considering the constant value of $\lambda = 2$ (stretching sheet). Equations (15)–(18) are numerically obtained. The obtained outcomes and computations are plotted graphically and presented in Figs. 1, 2, 3, 4, 5, 6 and 7.

Figures 1, 2 and 3 illustrate the effect of the suction parameter S on the velocity, the temperature and the nanoparticle volume fraction profile. It is clearly observed from these figures that as S increases (i) the fluid is forced towards the surface of the plate and this in turn causes a decrease in the boundary layer thickness as well

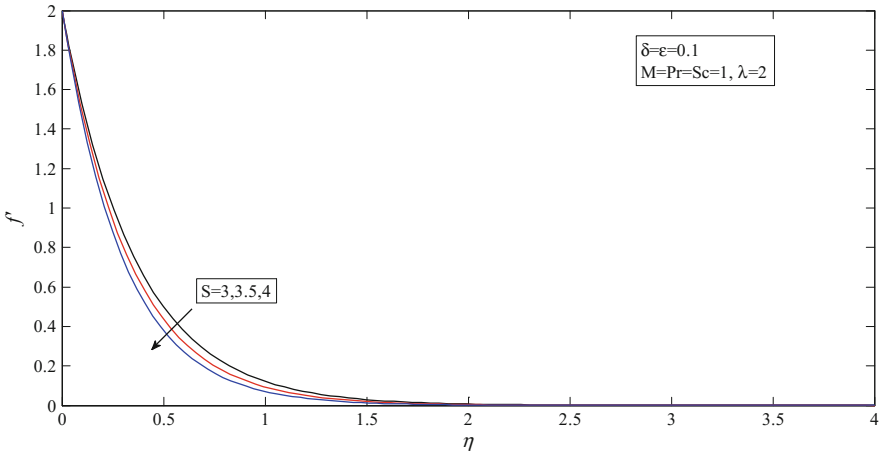

Fig. 1 Effect of suction parameter S on velocity profile

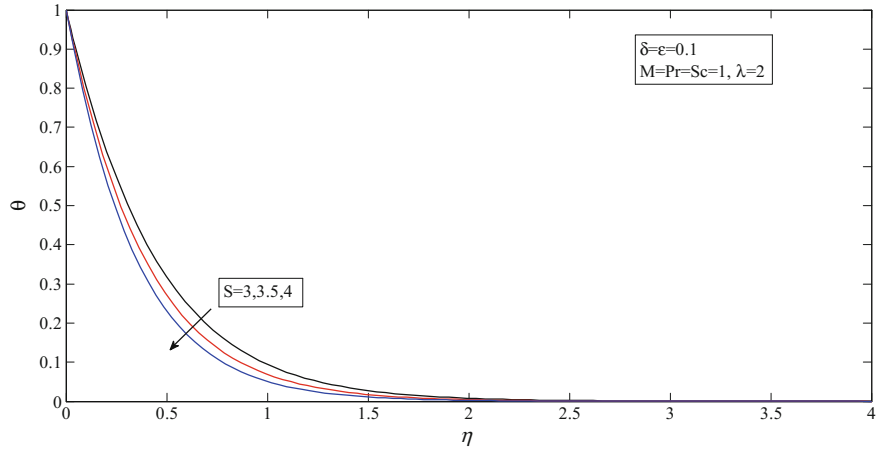

Fig. 2 Effect of S on temperature profile

as the velocity of fluid, (ii) nanofluid is sucked out, and hence it causes a decrease in the temperature and the thickness of the thermal boundary layer and finally (iii) it decreases the mass fraction of nanoparticles in the boundary layer due to which the mass diffusivity also decreases.

Figure 4 reveals the impact of the magnetic parameter M on the velocity profile. The fluid velocity falls down as the magnetic influence increases. High magnetic field creates the Lorentz force due to which the velocity of fluid decreases. Figures 5 and 6 reveal the effect of the parameter ε and δ on the profile of temperature. It is shown from Fig. 5 that as parameter δ increases, the fluid temperature as well as thickness decreases, whereas the effect of ε is totally opposite which is shown in Fig. 6.

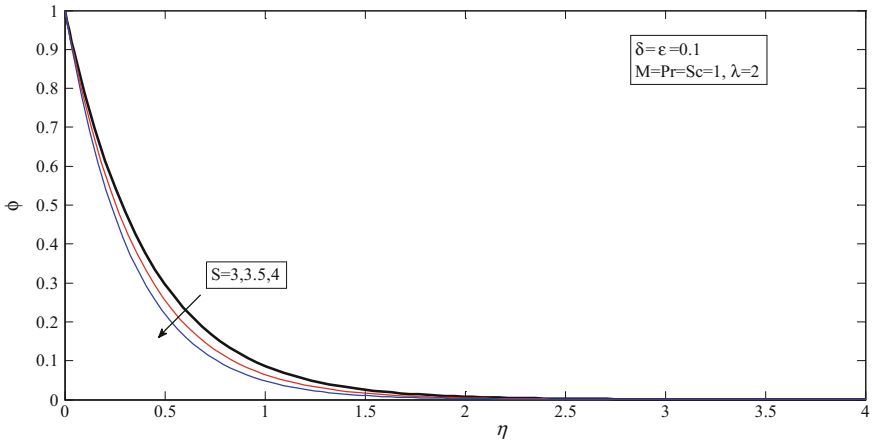

Fig. 3 Effect of suction parameter S on nanoparticle volume fraction profile

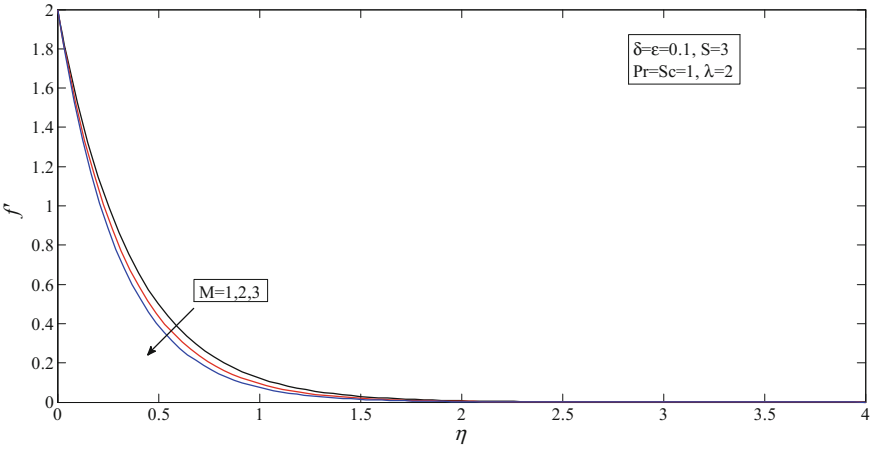

Fig. 4 Effect of M on velocity profile

Figures 7 and 8 show the impact of the Pr and Sc on the temperature and the nanoparticle volume fraction profile. Keeping on increasing both the values cause a decrease in both the (i) temperature and thickness of the thermal boundary layer and (ii) the mass fraction of nanoparticles in the boundary layer.

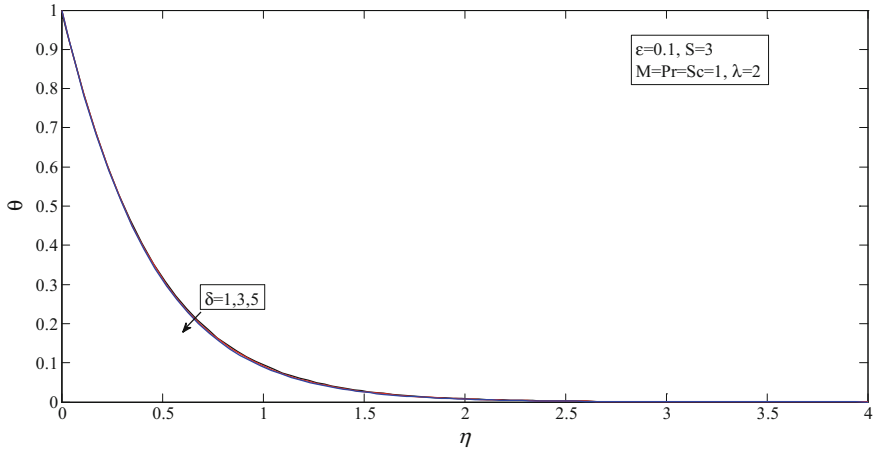

Fig. 5 Effect of parameter δ on temperature profile

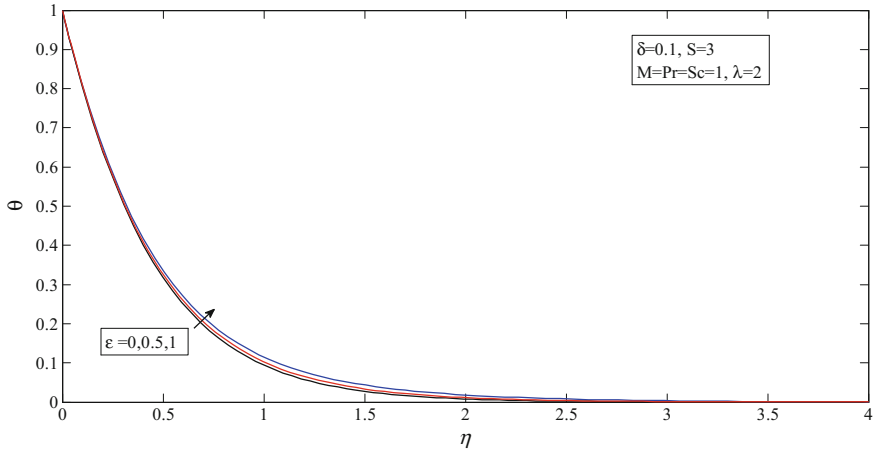

Fig. 6 Effect of parameter ε on temperature profile

5 Conclusion

The model of Powell–Eyring nanofluid flow with magnetic field considering stretching sheet is derived. The present investigation is done using the similarity analysis, which transforms the system of PDEs to ODEs. Numerical solution is obtained for different parameters. It is found that the velocity, temperature and the nanoparticle fraction are decreases as suction parameter increases. Also, the parameter δ increases, which decreases the fluid temperature and as ε increases, it causes an increase in temperature of fluid.

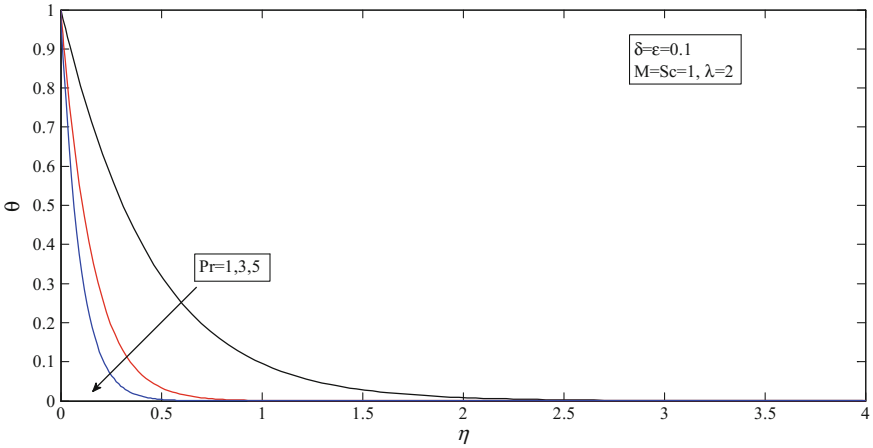

Fig. 7 Effect of Prandtl number Pr on temperature profile

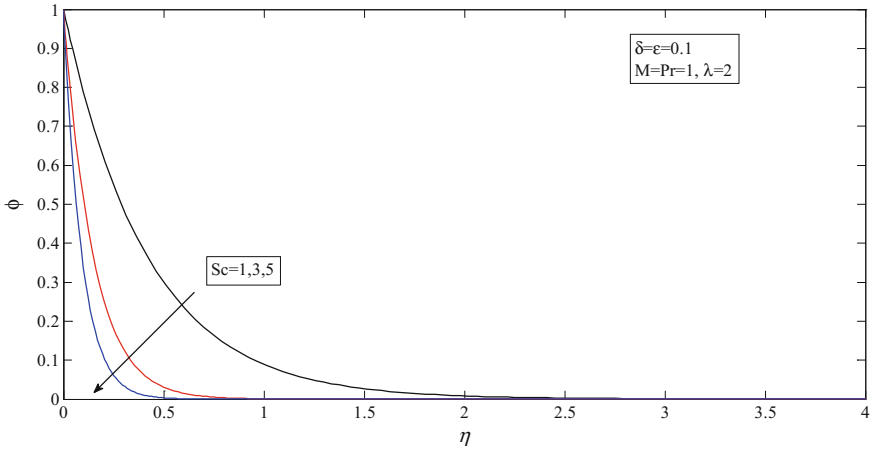

Fig. 8 Effect of Schmidt number Sc on nanoparticle volume fraction profile

References

1. Crane, L.J.: Flow past a stretching plate. J. Appl. Math. Phys. ZAMP **21**(4), 645–647 (1970)
2. Ibrahim, W., Shankar, B., Nandeppanavar, M.M.: MHD stagnation point flow and heat transfer due to nanofluid towards a stretching sheet. Int. J. Heat Mass Transf. **56**(1–2), 1–9 (2013)
3. Jalil, M., Asghar, S.: Flow and heat transfer of Powell-Eyring fluid over a stretching surface: a lie group analysis. J. Fluids Eng. **135**(12), 121201 (2013)
4. Ishak, A., Nazar, R., Pop, I.: Mixed convection stagnation point flow of a micropolar fluid towards a stretching sheet. Meccanica **43**(4), 411 (2008)
5. Banks, W.H.: Similarity solutions of the boundary-layer equations for a stretching wall. J. de Mecanique theorique et appliquee **2**, 375–392 (1983)

6. Powell, R.E., Eyring, H.: Mechanisms for the relaxation theory of viscosity. Nature **154**(3909), 427 (1944)
7. Akbar, N.S., Ebaid, A., Khan, Z.H.: Numerical analysis of magnetic field effects on Eyring-Powell fluid flow towards a stretching sheet. J. Magn. Magn. Mater. **382**, 355–358 (2015)
8. Hayat, T., Saeed, Y., Alsaedi, A., Asad, S.: Effects of convective heat and mass transfer in flow of Powell-Eyring fluid past an exponentially stretching sheet. PLoS ONE **10**(9), e0133831 (2015)
9. Hayat, T., Hussain, Z., Farooq, M., Alsaedi, A.: MHD flow of Powell-Eyring fluid by a stretching cylinder with newtonian heating. Therm. Sci. **00**, 162 (2016)
10. Hayat, T., Waqas, M., Shehzad, S.A., Alsaedi, A.: Mixed convection stagnation-point flow of Powell-Eyring fluid with Newtonian heating, thermal radiation, and heat generation/absorption. J. Aerosp. Eng. **30**(1), 04016077 (2016)
11. Khan, I., Malik, M.Y., Salahuddin, T., Khan, M., Rehman, K.U.: Homogenous–heterogeneous reactions in MHD flow of Powell–Eyring fluid over a stretching sheet with Newtonian heating. Neural Comput. Appl. 1–8 (2017)
12. Patel, M., Timol, M.G.: Numerical treatment of Powell-Eyring fluid flow using method of satisfaction of asymptotic boundary conditions (MSABC). Appl. Numer. Math. **59**(10), 2584–2592 (2009)
13. Ramzan, M., Bilal, M., Chung, J.D.: Radiative flow of Powell-Eyring magneto-nanofluid over a stretching cylinder with chemical reaction and double stratification near a stagnation point. PLoS ONE **12**(1), e0170790 (2017)
14. Panigrahi, S., Reza, M., Mishra, A.K.: MHD effect of mixed convection boundary-layer flow of Powell-Eyring fluid past nonlinear stretching surface. Appl. Math. Mech. **35**(12), 1525–1540 (2014)
15. Khan, S.U., Ali, N., Abbas, Z.: Influence of heat generation/absorption with convective heat and mass conditions in unsteady flow of Eyring Powell nanofluid over porous oscillatory stretching surface. J. Nanofluids **5**(3), 351–362 (2016)
16. Hayat, T., Iqbal, Z., Qasim, M., Obaidat, S.: Steady flow of an Eyring Powell fluid over a moving surface with convective boundary conditions. Int. J. Heat Mass Transf. **55**(7–8), 1817–1822 (2012)

Entropy Generation Analysis of Radiative Rotating Casson Fluid Flow Over a Stretching Surface Under Convective Boundary Conditions

Shalini Jain and Rakesh Choudhary

Abstract The three-dimensional radiative flow of rotating Casson fluid over a stretching surface with magnetohydrodynamics and convective boundary conditions has been analyzed. The entropy generation analysis is also done. Governing PDEs are transformed into nondimensional ODEs using appropriate similarity transformations and are solved numerically by using *R–K* fourth-order method with shooting technique. Influence of diverse parameters such as Casson fluid parameter β, radiation parameter R, Biot number Bi, rotation parameter λ, magnetic field parameter M, and Prandtl number Pr on temperature profile and local entropy generation Ns is analyzed and depicted through graphs.

Keywords Casson fluid · MHD · Convective boundary condition

1 Introduction

The flow due to stretching surfaces has many scientific and engineering applications such as wire and fiber cutting process, extraction and manufacturing of rubber and polymer sheets, and design of chemical and foodstuff processing equipment. Initially, Crane [1] and Sakiadis [2] examined the boundary layer flow due to continuous stretching surface and moving surface, respectively. Later, Wang [3] investigated the effects of 3D flow over a stretching flat surface. Many researchers such as Najar et al. [4] and Jain and Choudhary [5] studied boundary layer phenomena over various geometries. Design of turbines and rotating heat exchangers, industrial processes, cosmic fluid dynamics, biomechanics , and astrophysical process are some

S. Jain (✉)
University of Rajasthan, Jaipur 303007, Rajasthan, India
e-mail: drshalinijainshah@gmail.com

R. Choudhary
Manipal University Jaipur, Jaipur-Ajmer Expressway, Jaipur 303007, Rajasthan, India

D. Srinivasacharya and K. S. Reddy (eds.), *Numerical Heat Transfer and Fluid Flow*, Lecture Notes in Mechanical Engineering,
https://doi.org/10.1007/978-981-13-1903-7_40

applications of rotating fluid flow. Movement of oil and migration of underwater are also observed as a significant application of rotating flows. Authors such as Rajeswari and Nath [6] and Zaimi et al. [7] analyzed the rotating fluid over a stretching surface. Entropy generation plays a significant role in the improvement of the heat exchanger industry. Bejan [8] investigated the entropy generation minimization. San and Laven [9] discussed the second law analysis of convective heat and mass transfer. Further, Jain et al. [10], Makinde and Osalusi [11] and Butt and Ali [12] examined the entropy generation characteristic with different aspects of boundary layer flow.

The Casson fluid model is a non-Newtonian fluid model, which has an infinite viscosity at zero rate of shear. Casson [13] explained that the Casson fluid behaves like a solid elastic fluid and had yield shear stress in the consecutive equation. Authors such as Pramanik [14], Jain and Parmar [15], Butt et al. [16] and Jain and Choudhary [17] have been analyzed the effects of Casson fluid flow over various geometries. The current study is aimed to find out the radiative heat transfer effects and second law analysis of rotating Casson fluid under convective boundary conditions.

2 Flow Analysis

We consider the steady, 3D flow of an incompressible rotating Casson fluid with MHD and radiation over a stretching surface under convective boundary conditions. The considered surface is stretching in the x-direction. Assume that the velocity components u, v, and w are in the direction of x, y, and z axis, correspondingly with an angular velocity ω in the z-direction as seen in Fig. 1. Magnetic field B_0 is applied normal to the surface. Due to the Coriolis force, the fluid is rotating in three-dimensional structure with an angular velocity ω. Let T_f is the surface temperature of the structure and T_∞ is the temperature of the fluid at far away.

Rheological model that describes Casson fluid is defined as follows:

$$\tau_{ij} = \begin{cases} 2(\mu_B + p_y/\sqrt{2\pi})e_{ij}, \pi > \pi_c \\ 2(\mu_B + p_y/\sqrt{2\pi_c})e_{ij}, \pi < \pi_c \end{cases}, \tag{1}$$

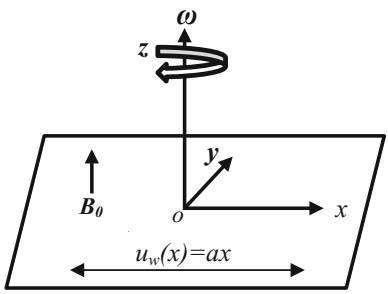

Fig. 1 Physical diagram of the problem

where p_y is the yield stress of the fluid, τ_{ij} is the component of the stress tensor, π_c is a critical value of this product based on the non-Newtonian model, π is the product of the component of the deformation rate with itself, and μ_B is plastic dynamic velocity of the non-Newtonian fluid.

Under the above assumptions, the governing equations (follow Butt and Ali [12]) are given as

$$\frac{\partial u}{\partial x}+\frac{\partial v}{\partial y}+\frac{\partial w}{\partial z}=0 \tag{2}$$

$$u\frac{\partial u}{\partial x}+v\frac{\partial u}{\partial y}+w\frac{\partial u}{\partial z}-2\omega v=-\frac{1}{\rho}\frac{\partial p}{\partial x}+v\left(1+\frac{1}{\beta}\right)\nabla^2 u-\frac{\sigma B_0^2 u}{\rho} \tag{3}$$

$$u\frac{\partial v}{\partial x}+v\frac{\partial v}{\partial y}+w\frac{\partial v}{\partial z}+2\omega u=-\frac{1}{\rho}\frac{\partial p}{\partial y}+v\left(1+\frac{1}{\beta}\right)\nabla^2 v-\frac{\sigma B_0^2 v}{\rho} \tag{4}$$

$$u\frac{\partial w}{\partial x}+v\frac{\partial w}{\partial y}+w\frac{\partial w}{\partial z}=-\frac{1}{\rho}\frac{\partial p}{\partial z}+v\left(1+\frac{1}{\beta}\right)\nabla^2 w-\frac{\sigma B_0^2 w}{\rho} \tag{5}$$

$$u\frac{\partial T}{\partial x}+v\frac{\partial T}{\partial y}+w\frac{\partial T}{\partial z}=\frac{k}{\rho C_p}\nabla^2 T+\frac{v}{C_p}\left(1+\frac{1}{\beta}\right)\left[\left(\frac{\partial u}{\partial z}\right)^2+\left(\frac{\partial v}{\partial z}\right)^2\right]+\frac{1}{\rho C_p}\frac{\partial q_r}{\partial z}. \tag{6}$$

The boundary conditions for this particular problem are given as

$$\begin{aligned}&\text{at } z=0, u=u_w(x)=ax, \quad v=0, \quad w=0, \quad -k\frac{\partial T}{\partial z}=h_f(T_f-T)\\ &\text{at } z\to\infty, \quad u\to 0, \quad v\to 0, \quad T\to T_\infty,\end{aligned} \tag{7}$$

where ν is the kinematic viscosity, $\beta=\frac{\mu_B\sqrt{2\pi_c}}{p_y}$ is the Casson fluid parameter, $a>0$ is a constant, ρ is the density of the fluid, C_p is the specific heat of the fluid at a constant pressure, k is thermal conductivity, h_f is the heat transfer coefficient, and T is the temperature of the fluid. The radiative heat flux in energy equation is $q_r=-\frac{4\sigma_1}{3k_1}\frac{\partial T^4}{\partial z}$, where σ_1 is the Stephan–Boltzmann constant and k_1 is the mean absorption constant. T^4 may be defined in terms of T that is given as $T^4\cong 4T_\infty^3 T-3T_\infty^4$. Now introducing similarity transformation

$$\eta=\sqrt{\frac{a}{v}}z, \quad \theta=\frac{T-T_\infty}{T_f-T_\infty}, u=axf'(\eta), \quad v=axg(\eta), w=-\sqrt{av}f(\eta). \tag{8}$$

Using Eqs. (3)–(6), Eq. (8) under the boundary conditions of Eq. (7) is converted into nondimensional ordinary differential equations, which are as follows:

$$\left(1+\frac{1}{\beta}\right)f'''+ff''+2\lambda g-Mf'-f'^2=0 \tag{9}$$

$$\left(1+\frac{1}{\beta}\right)g'' - f'g + fg' - 2\lambda f' - \mathrm{Mg} = 0 \tag{10}$$

$$(1+R)\theta'' + \mathrm{Pr}\ f\theta' + \left(1+\frac{1}{\beta}\right)\mathrm{Pr}\ \mathrm{Ec}\,(f''^2 + g'^2) = 0. \tag{11}$$

Subjected to boundary conditions

$$\begin{aligned} &\text{at } \eta = 0,\ f'(0) = 1, \quad f(0) = 0, \quad g(0) = 0, \quad \theta'(0) = -\mathrm{Bi}[1-\theta(0)], \\ &\text{at } \eta \to \infty,\ f'(\infty) = 0, \quad g(\infty) = 0, \quad \theta(\infty) = 0, \end{aligned} \tag{12}$$

where $\lambda = \frac{\omega}{a}$ is the ratio of rate of rotation to stretching rate, $R = \frac{16\sigma_1 T_\infty^3}{3k_1 k}$ is the radiation parameter, $\mathrm{Pr} = \frac{\mu C_p}{k}$ is Prandtl number, $M = \frac{\sigma B_0^2}{\rho a}$ is the magnetic field parameter, $\mathrm{Ec} = \frac{u_w^2}{C_p(T_f - T_\infty)}$ is local Eckert number, and $\mathrm{Bi} = \frac{h_f}{k}\sqrt{\frac{\nu}{a}}$ is the Biot number.

3 Numerical Solution

Converted nondimensional coupled ordinary differential Eqs. (9)–(11) under the boundary conditions (12) are solved by Runge–Kutta fourth-order method (RK4) with shooting technique. Initially, we find out the guesses $f''(0)$, $g'(0)$, and $\theta'(0)$, respectively. Secant method is used to find out the approximate correct guesses. Runge–Kutta fourth-order method needs a finite domain $0 \le \eta \le \eta_\infty$; therefore, in this study, we have chosen $\eta_\infty = 10$.

4 Entropy Generation Analysis

Local entropy generation rate per unit volume S^G of Casson fluid follows Bejan [8], which is defined as

$$S^G = \frac{k}{T_\infty^2}(1+R)\left(\frac{\partial T}{\partial z}\right)^2 + \frac{\mu}{T_\infty}\left(1+\frac{1}{\beta}\right)\left[\left(\frac{\partial u}{\partial z}\right)^2 + \left(\frac{\partial v}{\partial z}\right)^2\right] + \frac{\sigma B_0^2}{T_\infty}(u^2+v^2). \tag{13}$$

The characteristic entropy generation rate is given as

$$S_0^G = \frac{k\Delta T^2}{T_\infty^2 x^2}. \tag{14}$$

Using Eqs. (13) and (14), nondimensional local entropy generation rate is given as

$$N_S = \frac{S^G}{S_0^G} = \mathrm{R}_e(1+R)\theta'^2 + \left(1+\frac{1}{\beta}\right)\frac{1}{\Omega}\mathrm{Br}\, R_e(f''^2 + g'^2) + \frac{1}{\Omega}\mathrm{Br}\, R_e M(f'^2 + g^2), \tag{15}$$

where $\mathrm{Br} = \frac{\mu u_w^2}{k(T_w - T_\infty)}$ is the Brinkmann number, $R_e = \frac{u_w x}{\nu}$ is the local Reynolds number, and $\Omega = \frac{\Delta T}{T_\infty}$ is dimensionless temperature difference. Bejan number is described as $\mathrm{Be} = \frac{N_H}{N_H + N_F}$.

5 Results and Discussion

Table 1 shows that the results obtained in the present study by taking $M = 0$, $\mathrm{Ec} = 0$, $R = 0$, $\mathrm{Bi} \to \infty$, and $\beta \to \infty$ as a special case are very well in agreement with the results obtained by Butt et al. [16].

Figure 2 shows that an increase in Lorentz force offers greater resistance to the flow, and therefore to an increase in magnetic field M that causes an increase in the temperature profile. Figure 3 exhibits that higher Prandtl number declines the temperature profile. Prandtl number can be used to upsurge the rate of chilling in fluid flows. The higher Prandtl number signifies that the fluid is more viscous and with less velocity. The fluid with smaller Prandtl number is effective in monitoring the heat transfer.

Figures 4 and 5 display that the temperature profile is the growing function of radiation parameter and Biot number. Generally, the rise in the value of radiation parameter produces more heat to the fluid flow and due to this reason, an improvement in the temperature field takes place . The Biot number contains the heat transfer

Table 1 Comparison of the values of $\theta'(0)$ when $M = 0$, $\mathrm{Ec} = 0$, $R = 0$, $\mathrm{Bi} \to \infty$, and $\beta \to \infty$

λ	Pr = 0.7		Pr = 2.0		Pr = 7.0	
	Butt et al. [16]	Present work	Butt et al. [16]	Present work	Butt et al. [16]	Present work
0.0	−0.454	−0.453933	−0.911	−0.911359	−1.895	−1.895409
1.0	−0.321	−0.322178	−0.770	−0.770303	−1.788	−1.787645
2.0	−0.242	−0.248103	−0.638	−0.637760	−1.664	−1.664369

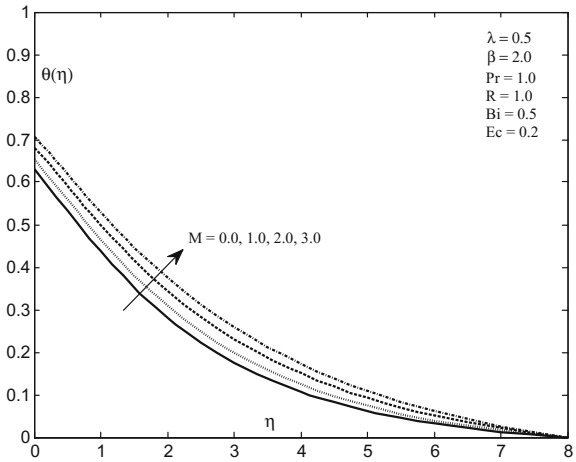

Fig. 2 Temperature profile for variation in M

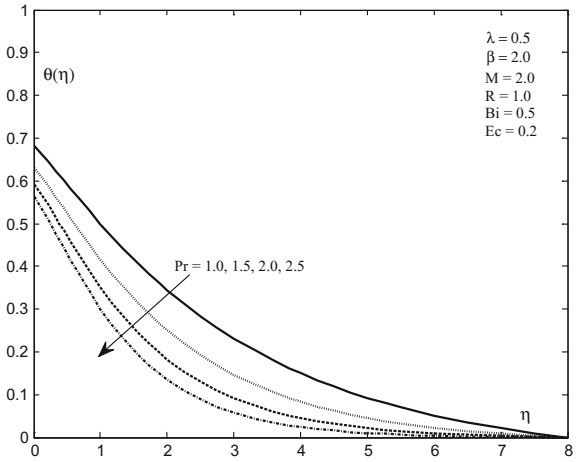

Fig. 3 Temperature profile for variation in Pr

coefficient, which rises the thermal conductivity of the fluid, and hence, higher Biot number upsurges the temperature profile. Figure 6 demonstrates that by enhancing the group parameter $\mathrm{Br}\Omega^{-1}$, the fluid friction irreversibility becomes dominant at the stretching surface when the impacts of viscous dissipation are also applied in the fluid flow, and hence, the entropy generation rate rises. Figure 7 depicts that as rotation parameter λ increases, Bejan number declines.

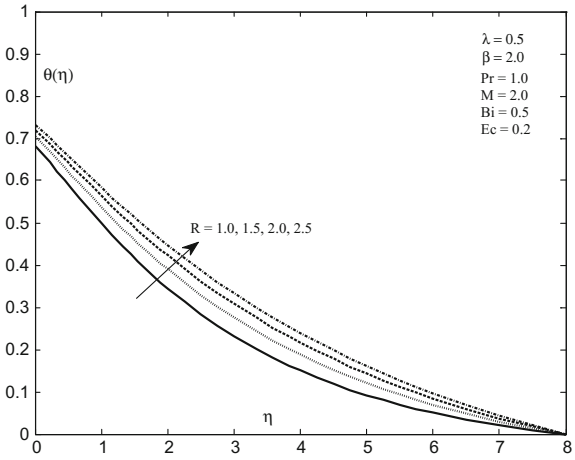

Fig. 4 Temperature profile for variation in *R*

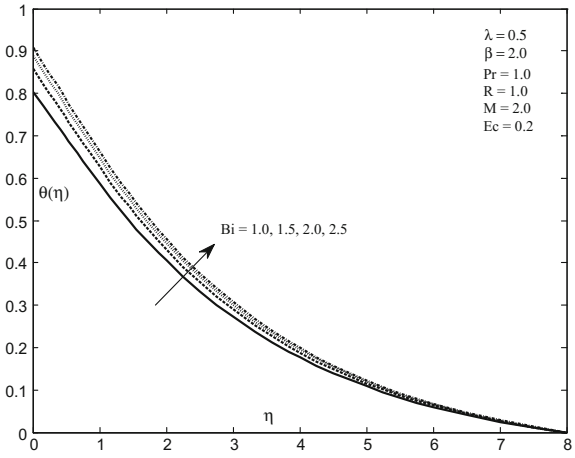

Fig. 5 Temperature profile for variation in Bi

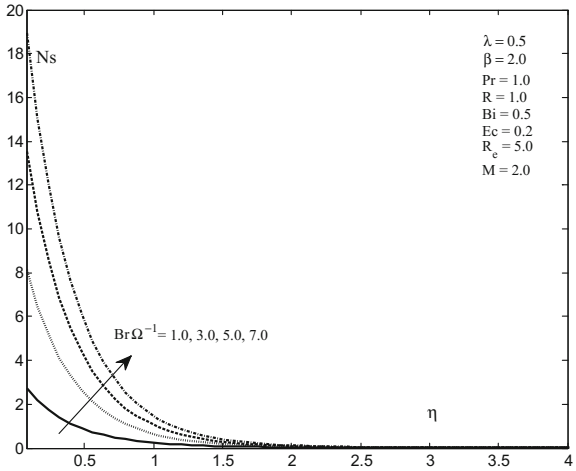

Fig. 6 Entropy effects of *Ns* for variation in $\mathrm{Br}\Omega^{-1}$

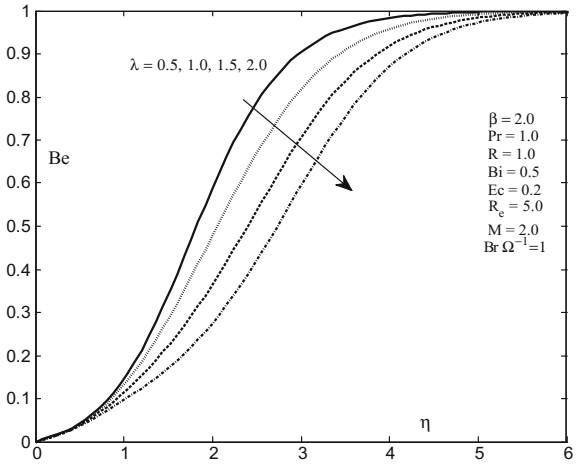

Fig. 7 Entropy effects of Be for variation in λ

6 Conclusion

The current study focuses on the investigation of entropy generation for three-dimensional MHD boundary layer flow and radiative heat transfer due to the stretching surface in a rotating Casson fluid with the convective boundary condition. The following results have been obtained:

1. Temperature profile is the rising function of magnetic field parameter, radiation parameter, and Biot number.
2. Temperature profile reduces as the value of Prandtl number rises.
3. Entropy generation number enhances with group parameter $\mathrm{Br}\Omega^{-1}$.
4. Bejan number falls down for rotation parameter.

References

1. Crane, L.J.: Flow past a stretching sheet. Zeitschriftfur Angewandte Mathemactik und Physik **21**, 645–647 (1970)
2. Sakiadis, B.C.: Boundary layer behaviour on continuous solid surfaces. AIChE J. **7**, 26–28 (1961)
3. Wang, C.Y.: The three-dimensional flow due to stretching flat surface. Phys. Fluids **27**, 1915–1917 (1984)
4. Najar, R., Amin, N., Pop, I.: Unsteady boundary layer flow due to a stretching surface in a rotating fluid. Mech. Res. Commun. **31**, 121–128 (2004)
5. Jain, S., Choudhary, R.: Combined effects of suction/injection on MHD boundary layer flow of nanofluid over a horizontal permeable cylinder with radiation. J. Adv. Res. Dyn. Control Syst. **11**, 88–98 (2017)
6. Rajeswari, V., Nath, G.: Unsteady flow over a stretching surface in a rotating fluid. Int. J. Eng. Sci. **30**, 121–128 (2004)
7. Zaimi, K., Ishak, A., Pop, I.: Stretching surface in rotating viscoelastic fluid. Appl. Math. Mech. Eng. Ed. **34**, 945–952 (2013)
8. Bejan, A.: Entropy Generation Minimization. CRC Press, Boca Raton, FL (1996)
9. San, J.Y., Laven, Z.: Entropy generation in convective heat transfer and isothermal mass transfer. J. Heat Transf. **109**, 647–652 (1987)
10. Jain, S., Kumar, V., Bohra, S.: Entropy generation for MHD radiative compressible fluid flow in a channel partially filled with porous medium. Global Stoch. Anal. 13–31 (2017)
11. Makinde, O.D., Osalusi, E.: Second law analysis of laminar flow in a channel filled with saturated porous media. Entropy **7**(2), 148–160 (2005)
12. Butt, A.S., Ali, A.: Investigation of entropy generation effects in MHD three-dimensional flow and heat transfer of viscous fluid over a stretching surface. J. Braz. Soc. Mech. Sci. Eng. **37**, 211–219 (2015)
13. Casson, N.A.: A Flow Equation for Pigment Oil Suspension of Printing Ink Type. Pergamon Press, Oxford (1959)
14. Pramanik, S.: Casson fluid flow and heat transfer past an exponentially porous stretching surface in presence of thermal radiation. Ain Shams Eng. J. **5**, 205–212 (2014)
15. Jain, S., Parmar, A.: Entropy generation of unsteady radiative Casson fluid flow through porous medium over a permeable stretching surface with inclined magnetic field. Frontiers Heat Mass Transf. **9**, 40 (2017)
16. Butt, A.S., Ali, A., Mehmood, A.: Study of flow and heat transfer on a stretching surface in a rotating Casson fluid. Proc. Natl. Acad. Sci. India **85**, 421–426 (2015)
17. Jain, S., Choudhary, R.: Second law analysis in MHD flow and heat transfer of a rotating Casson fluid over a stretching surface. Ind. J. Pure Appl. Phys. **56**(1), 56–62 (2018)

Study on Effects of Slots on Natural Convection in a Rectangular Cavity Using CFD

Rakesh Kumar, Jyotshnamoyee Behera and Prabir Kumar Jena

Abstract This paper investigates those characteristic convection wonders on a rectangular nook hosting pit with separate opening proportion need to be investigated utilizing CFD. The straight divider confronting those opening with slots is heated by uniform heat flux and sides perpendicular to the heated side are insulated. Conservation of mass, momentum, and energy equations are solved considering the constant value of fluid properties and Boussinesq approximation. The isotherms and streamlines are produced and heat transfer is calculated for Rayleigh number that varies for a different number of slots from 2 to 5. Two different pit perspective proportions, $A = L/H > 1$ and $A = L/H < 1$ are taken with constant Prandtl number value of 0.7. The influence of *Ra*, *N*, and OR on the Nusselt number is investigated. The results obtained reveal that the value of *Nu* increases with the increase in the value of *Ra* and OR. The results show that at lower Rayleigh number the heat transfer across the fluid layer is dominant by conduction due to the absence of circulation of air inside the cavity.

Keywords Rectangular nook · Opening proportion · Slots · Cavity

1 Introduction

The investigation of characteristic convection in a fenced-in area gives a valuable depiction of the kept fluid in numerous down-to-earth applications. In this present period, open depressions are experienced in many building applications, for example, twofold sheet window, warm exchanger [1], open cavity warm recipients, revealed level plate sun-based gatherers having columns of vertical strips, electronic chips, warm sinks, inactive framework, and so on. Numerical investigations on open holes with spaces in a walled-in area have been likewise the subject of many examinations as spaces with various opening proportions can fundamentally influence the

R. Kumar (✉) · J. Behera · P. K. Jena
Mechanical Engineering, VSSUT Burla, Sambalpur 768018, Odisha, India
e-mail: Yashram1993@gmail.com

D. Srinivasacharya and K. S. Reddy (eds.), *Numerical Heat Transfer and Fluid Flow*, Lecture Notes in Mechanical Engineering,
https://doi.org/10.1007/978-981-13-1903-7_41

stream field and in this manner the execution of the general fenced-in areas [2–5]. Warmth expulsion of a hot body from a fenced area is a testing issue nowadays. So, it is critical that the cooling framework ought to be composed such that the power prerequisite for this procedure is to be least. So, for this reason, natural convection is preferred over forced convection. For some situations because of the little size of the equipment, it is not conceivable to present a fan or blower in the framework as it will make the framework complex and now and again it is for all intents and purposes additionally unrealistic. Therefore, characteristic convection is the main possible method of cooling of warmth source in various applications.

As for the distinctive writing regarding the matter, another strategy is acquainted by showing the numerous information of the warm execution of the nooks utilizing the overall Nusselt number. For some particular relevant situations, the flow field, the thermal field, and the heat transfer process are also presented and analyzed using the isotherms, the heatlines, and the streamlines [6].

The present work is to study the laminar natural convection in open rectangular cavity with multiple slots at one side proposed by Bejan [7–9]. The divider confronting the open side is warmed by uniform transition and two flat dividers are insulated. We want to decide the cooling attributes as an element of overseeing warm and geometrical parameters.

2 Physical and Mathematical Demonstration

Two-dimensional rectangular enclosure of negligible wall thickness is shown in Fig. 1. A uniform heat flux "q" is applied on the inner surface of the left wall, the top and bottom (i.e., Horizontal) dividers would be aggravated similarly as insulated, which prompts the adiabatic state and the dividers on the right side are aggravated likewise the slots because of which the climatic air enters to prepare some cooling impact for diverse opening proportion for separate warm state. Under the influence of vertical gravitation field and presence of different temperature fields on the right wall (i.e., vertical), it prompts an instance of natural convection inside the fenced-in area.

The walled-in area is thought to be loaded with Newtonian liquid and there is no impact of third measurement in the present issue. Due to pressure changes, there is no impact on the fluid density (i.e., incompressible) yet it changes with temperature changes. The density of the buoyancy term is temperature-subordinate. The remaining thermophysical properties of the fluid are thought to be constant, aside from this density showing up in the convective term that will likewise stay constant. The stream is thought to be laminar. Following conservation Eqs. (1)–(4) are spoken to in the dimensionless frame with a specific goal to reduce the number of parameters.

$$\frac{\partial U}{\partial X} + \frac{\partial V}{\partial Y} = 0 \tag{1}$$

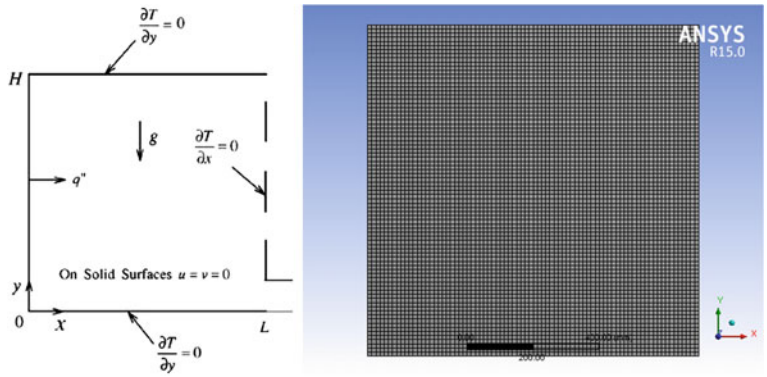

Fig. 1 Physical geometry is on the left and the corresponding meshed body on the right

$$\frac{\partial U}{\partial T} + U\frac{\partial U}{\partial X} + V\frac{\partial U}{\partial Y} = -\frac{\partial P}{\partial X} + Pr\,\nabla^2 U \tag{2}$$

$$\frac{\partial V}{\partial T} + U\frac{\partial V}{\partial X} + V\frac{\partial V}{\partial Y} = -\frac{\partial P}{\partial Y} + Pr\,\nabla^2 V + Ra\ Pr\theta \tag{3}$$

$$\frac{\partial \theta}{\partial T} + U\frac{\partial \theta}{\partial X} + V\frac{\partial \theta}{\partial Y} = \nabla^2\theta. \tag{4}$$

Boundary conditions:
On the solid surface, velocities are assumed to be null

$$U = 0, V = 0 \tag{5}$$

The best and base walls are assumed to be insulated, i.e.,

$$\frac{\partial T}{\partial Y} = 0. \tag{6}$$

On right wall,

$$\frac{\partial T}{\partial X} = 0. \tag{7}$$

The temperature at the interfaces between the solid wall and the fluid enclosure is assumed to have same temperature, i.e., they follow the conservation of energy and continuity of temperature, or mathematically it can be represented as

$$T_s = T_f. \tag{8}$$

Visualization of fluid flow can be obtained from the contours (streamlines) and at the same time, it can be figured from its definition as

$$U = -\frac{\partial \varphi}{\partial Y}, V = \frac{\partial \varphi}{\partial X}. \tag{9}$$

The governing heat transfer parameters are Rayleigh number *Ra*, Prandtl number *Pr*, aspect ratio, and total opening ratio. Here, the overall heat transferred through the cavity is given by the overall Nusselt number along the wall, which is given by

$$Nu = \frac{-\int_0^1 \frac{\partial T}{\partial X}\partial Y}{\int_0^1 (T_0 - T_A)\partial Y} \; Ra = \frac{g\beta q'' H^4}{\vartheta \alpha k} \; Pr = \frac{\vartheta}{\alpha}.$$

3 Numerical Modeling

We have taken a two-dimensional laminar flow in this system, which is based on the finite element method and which will be utilized to define the numerical arrangement of the given issue. A broadly useful computational liquid flow (CFD) code, ANSYS FLUENT 15.0, is chosen for the analysis of fluid flow and heat transfer from a rectangular cavity having slots of different opening ratios. The code used here is semi-implicit method for pressure-linked equations (SIMPLE) algorithm based on control-volume application and using a pressure-based solver. A second-order upwind implicit scheme is used as discretization tool here. Convergence criteria for continuity, momentum, and energy equation are set to be 10^{-3}, 10^{-3} and 10^{-4} respectively. Convergence connects the computed solution to the differential equation.

4 Results and Discussion

See Figs. 2 and 3.

5 Conclusion

Isotherms and streamlines for the instance of $N = 3$, for the vent proportion OR = 0.1, 0.2, 0.4, and 0.6 are got. The case with OR = 0.1 demonstrates a conduction overwhelmed administration and for OR = 0.2, the convection is prevailing. As the aggregate open territory proportion OR is expanded to 0.1 and 0.6, the convection is additionally expanded. With expanding *Ra*, the depression air gets significantly cooler, and furthermore at high Ra there is some stratification and thus warm exchange might be made strides.

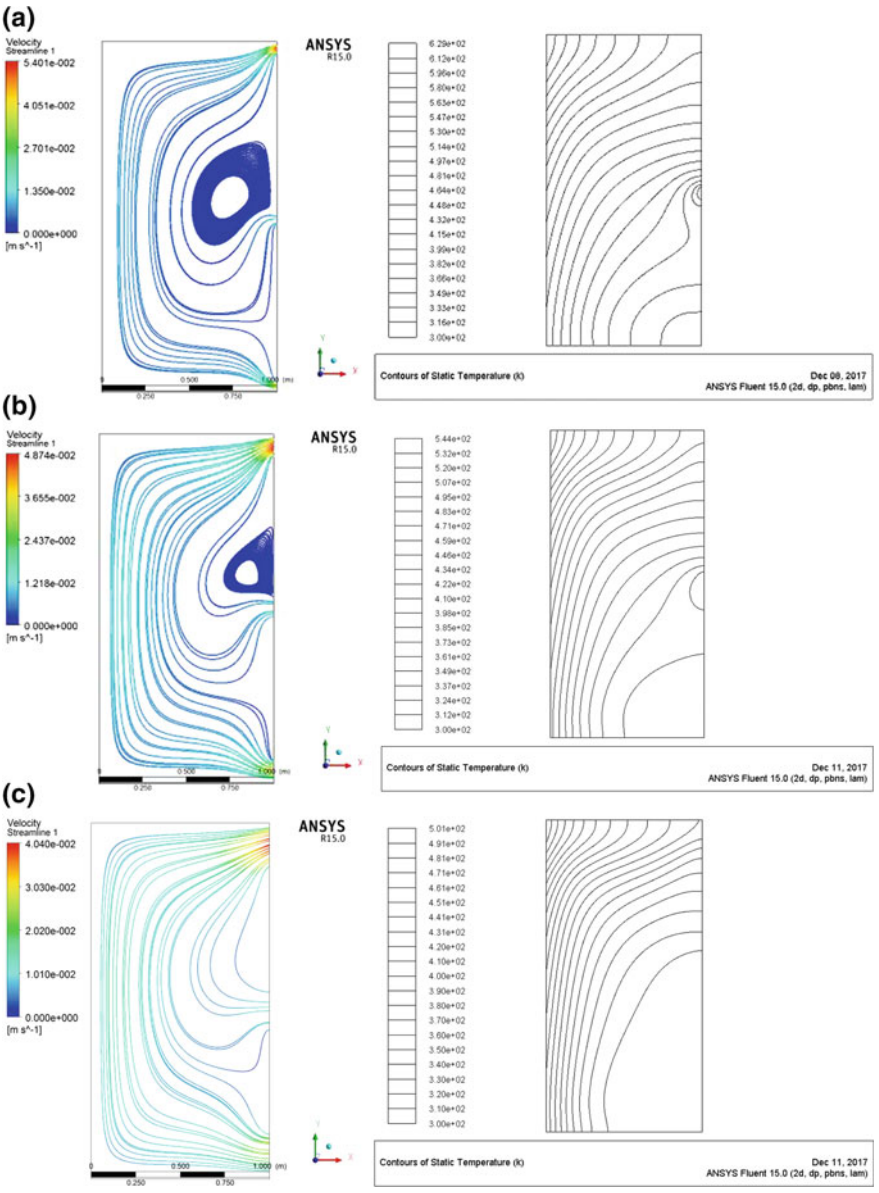

Fig. 2 Isotherms on the top and streamlines at the bottom for $N = 3$; **a** OR = 0.1, **b** OR = 0.2, **c** OR = 0.4, and **d** OR = 0.6

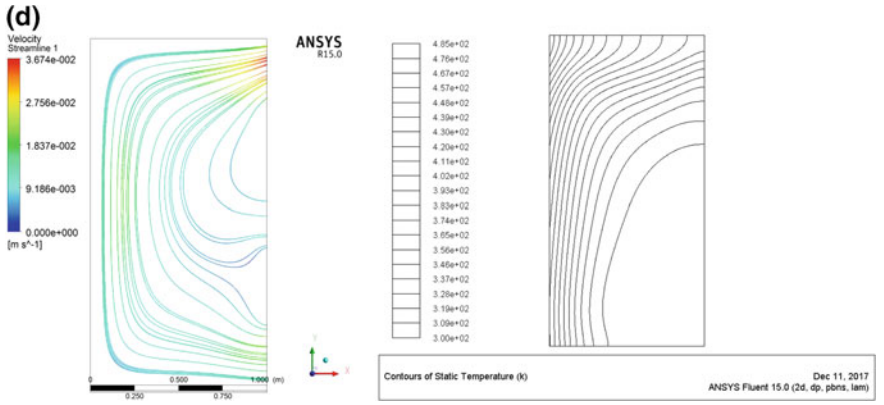

Fig. 2 (continued)

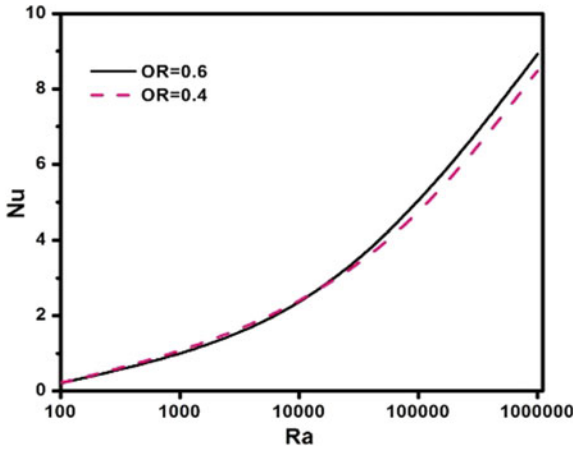

Fig. 3 Variation of Nusselt number as a component of Rayleigh number

References

1. Ostarch, S.: J. Heat Transf. ASME (1988)
2. Polat, O., Bilgen, E.: Laminar natural convection in shallow open cavities. Int. J. Therm. Sci. **41**, 360–368 (2002)
3. Mohamad, A.A.: Natural convection in open cavities and slots. Numer. Heat Transf. **27**, 705–716 (1995)
4. De Vahl Davis, G.: Natural convection of air in a square cavity, a benchmark numerical solution. Int. J. Numer. Meth. Fluids **3**, 249–264 (1983)
5. Hasnaoui, M., Bilgen, E., Vasseur, P.: Natural convection heat transfer in rectangular cavities partially heated from below. J. Thermophys. Heat Transf. **6**, 255–264 (1992)
6. Costa, V.A.F.: Bejan's heatlines and masslines for convection visualization and analysis. Appl. Mech. Rev. **59**(3), 126–145 (2006)

7. Corcione, M.: Effects of the thermal boundary conditions at the side walls upon natural convection in rectangular enclosures heated from below and cooled from above. Int. J. Therm. Sci. **42**, 199–208 (2003)
8. Ciofalo, M., Karayiannis, T.G.: Natural convection heat transfer in partially-or completely-partitioned vertical rectangular enclosure. Int. J. Heat Mass Transf. **34**, 167–169 (1991)
9. Bejan, A.: Convection Heat Transfer, 3rd edn. Wiley, New York (2004)

Numerical Investigation on Heat Transfer and Fluid Flow Characteristics of Natural Circulation Loop with Parallel Channels

Ramesh Babu Bejjam and K. Kiran Kumar

Abstract The main objective of the present study is to numerically investigate heat transfer and fluid flow characteristics of natural circulation loop (NCL) with parallel channels. By imparting temperature difference to the fluid, the density gradient is developed which causes to circulate the fluid flow in a loop. In the current study, the steady-state analysis has been carried out on NCL with parallel channel at different power inputs. For this study, a three-dimensional geometry of NCL with parallel channel is developed and simulated using ANSYS-FLUENT 14.5. This kind of parallel channel NCL model would be useful in various heat transfer applications such as geothermal heat extraction, solar energy, electronics cooling, etc. The results of parallel channel NCL are compared to single channel NCL. The results show that the steady-state mass flow rate is increased by 17.26% and average Nusselt number is enhanced by 10.74% when compared to single channel NCL. All the simulation results are validated with open literature.

Keywords Heat transfer · Natural circulation · Parallel channel

1 Introduction

Natural circulation loop (NCL) is a passive heat transfer arrangement to transfer heat from one place to another place without any mechanical aid. The absence of mechanical elements, NCLs gives advantages such as low maintenance cost, safety, and high reliability. Therefore, it offers some applications such as solar water heaters, geothermal heat extraction systems, electronic cooling systems, nuclear reactor core cooling, etc. Vijayan et al. [1] studied the effect of uniform and nonuniform diameter NCLs on the stability of the NCL and developed new correlations in terms of modified Grashof number and Reynolds number. Basu et al. [2] have been proposed

R. B. Bejjam (✉) · K. Kiran Kumar
Department of Mechanical Engineering, National Institute of Technology, Warangal 506004, Telangana, India
e-mail: rameshbabubejjam@gmail.com

D. Srinivasacharya and K. S. Reddy (eds.), *Numerical Heat Transfer and Fluid Flow*, Lecture Notes in Mechanical Engineering,
https://doi.org/10.1007/978-981-13-1903-7_42

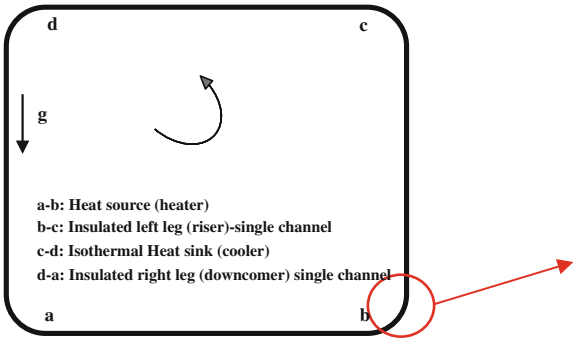

Fig. 1 Single channel NCL configuration

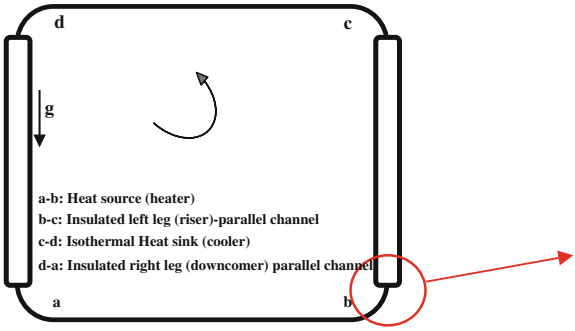

Fig. 2 Parallel channel NCL configuration

an analytical solution for different shapes of NCLs they concluded that the rectangular NCL model has a stable flow. Kumar et al. [3] developed new relation for the suitability of various fluids in NCL.

In the current study, two types of NCL configurations are studied. They are: one is single channel type NCL and another is parallel channel type NCL and the performance of both configurations are compared with each other. Single-channel type NCL consists of one riser and one down comer. Parallel channel type NCL consists of two risers and two downcomers and these are parallel to each other. The detailed diagrams of these configurations are shown in Figs. 1 and 2.

2 Numerical Methodology

The schematic diagrams of NCL with single channel and parallel channel are shown in Figs. 1 and 2, respectively. The geometrical specifications are given in Table 1.

Table 1 Geometrical specifications of the NCL configurations

Parameter	Single channel NCL (m)	Parallel channel NCL (m)
Loop pipe diameter	0.015	0.015
Pipe wall thickness	0.0016	0.0016
Total length of the loop	5.44	8.44
Length of the heat source and heat sink each	1.4	1.4
Height of the loop	1.26	1.26
Loop width	1.46	1.56

2.1 Governing Equations

The standard conservation equations are solved using the ANSYS -FLUENT 14.5. For the simulations, power input over the range of 500–2500 W with an increment of 500 W at heat source and isothermal wall temperature of 293 K at the heat sink are applied as thermal boundary conditions. The riser and downcomers are considered as insulated. The continuity, momentum, and energy equation are as follows [4], respectively:

$$\nabla \cdot \left(\rho \vec{V}\right) = 0 \tag{1}$$

$$\nabla \cdot \left(\rho \vec{V} \vec{V}\right) = -\nabla p + \nabla \cdot \left[\mu\left(\nabla \vec{V} + \nabla \vec{V}^{T}\right)\right] + (\rho \vec{g}) \tag{2}$$

$$\nabla \cdot \left(\left(\vec{V}(\rho E + p)\right)\right) = \nabla \cdot (k \nabla T) + \bar{\bar{\tau}}_{\text{eff}} \cdot \vec{V} \tag{3}$$

2.2 Solution Method and Grid Independency Test

The entire simulations are carried out at steady-state condition. REFPROP tool is used to get the water properties. The implicit coupled condition is imposed. The governing equations are discretized by the finite volume method. The moment and energy equations are iterated by using the second-order upwind scheme. The continuity, moment equations are converged by reaching the velocity and pressure residuals to 10^{-3} and energy equation is converged when its residual reaches to 10^{-6}.

Meshing of a loop fluid at the bend of a single channel NCL and a parallel channel NCL is shown in Figs. 3 and 4, respectively. Gird independency test has been carried out with different grid sizes (varied in mm) and they are $1 \times 1 \times 1$, $2 \times 2 \times 2$, $3 \times 3 \times 3$ and $4 \times 4 \times 4$. The influence of grid size on Reynolds number is presented in Table 2. The maximum deviation in the values of Reynolds number for the present simulation case with input power of 500 W is 0.25%. Therefore, the mesh with $2 \times$

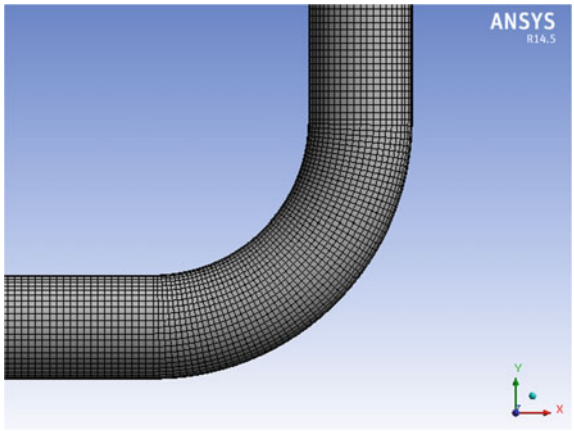

Fig. 3 Mesh of the loop fluid at bend

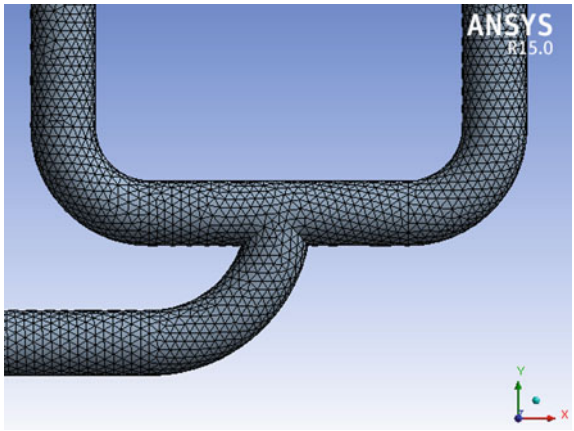

Fig. 4 Mesh of loop fluid at bend of the parallel channel NCL

Table 2 Grid independency test result

Power input (500 W)	4 × 4 × 4	3 × 3 × 3	2 × 2 × 2 (present study)	1 × 1 × 1
Number of elements	48,000	72,350	150,920	782,784
Reynolds number	854.5	925.81	1052.6	1055.2

2 × 2 grid size is considered for the simulations in order to save the computational time and utilization of the resources.

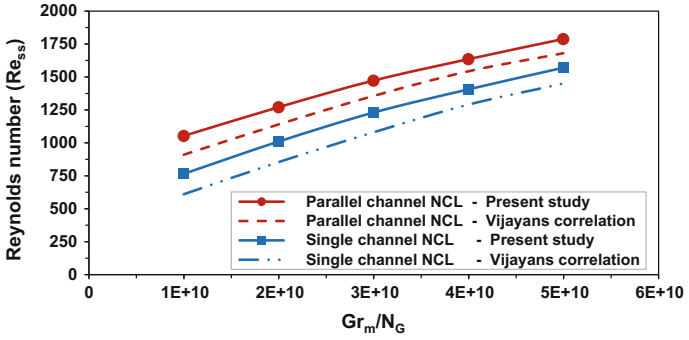

Fig. 5 Validation

3 Results and Discussion

In the present study, the two types of NCL configurations (single channel type and parallel channel type) are investigated with water as working fluid. Both NCLs are operated at different power inputs. As part of the validation, the simulation results are compared with the analytical results calculated from Vijayan's correlation Eq. (4) [1].

$$\mathrm{Re}_{\mathrm{ss}} = 0.1768\left[\frac{\mathrm{Gr}_m}{N_G}\right]^{0.5} \tag{4}$$

$$\mathrm{Gr}_m = \frac{g\beta d^3\rho^2 QZ}{A_{\mathrm{cs}}\mu^3 C_p} \tag{5}$$

Figure 5 illustrates that the simulation results are well matched with analytical results over a range of Reynolds number for both configurations of NCL. The maximum difference between the analytical and simulation results is less than 9% for single channel NCL and 7% for parallel channel NCL. Therefore, further analysis is carried out with the developed model. Figures 6 and 7 show the temperature contours of loop fluid in single and parallel channel configurations respectively. High temperatures are observed in case of parallel channel configuration at given power input condition.

Figure 8 explicits the variation of mass of flow rate with power input. By increasing the power input to heat source, the higher density gradient is developed between the source and sink which causes for enhanced mass flow rate. It is noticed from Fig. 8, the mass flow rate of parallel channel NCL is more than the single channel NCL due to improved buoyancy forces. From Fig. 8, it is observed that the steady-state mass flow rate of the loop fluid in parallel channel NCL is enhanced by 17.26% when compared to single channel configuration. The average Nusselt number at the heat source is calculated based on the wall function average heat transfer coefficient which is obtained from the simulation results. As can be seen in Fig. 9, the average Nusselt

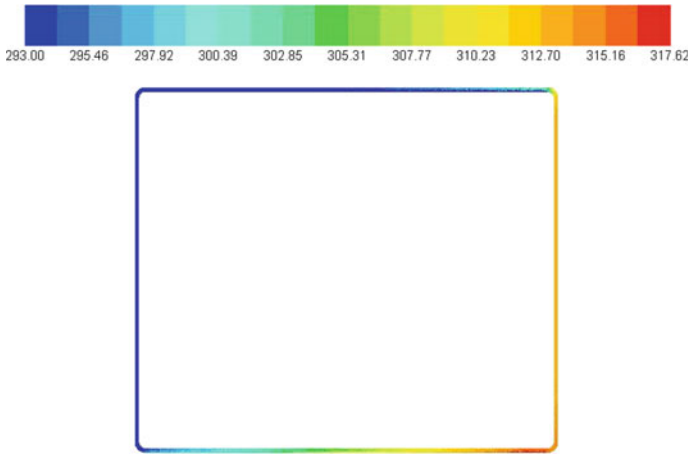

Fig. 6 Temperature contour profile of loop fluid in single channel NCL

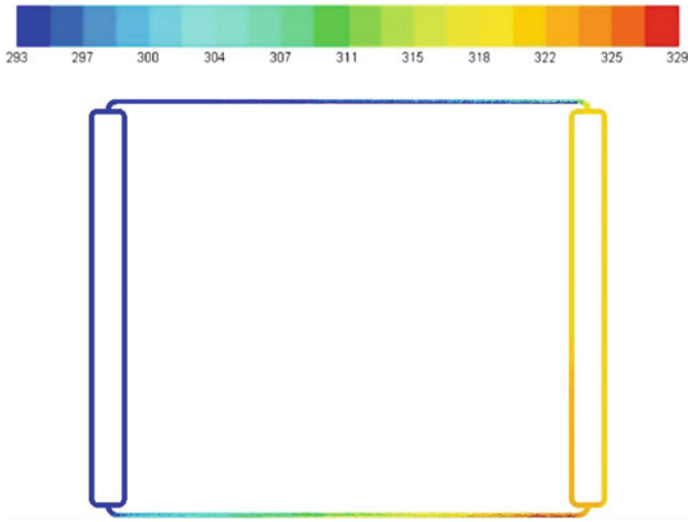

Fig. 7 Temperature contour profile of loop fluid in parallel channel NCL

number increases with increase in the power input. From the Fig. 9 it is observed that the average Nusselt number of parallel channel configuration is enhanced by 10.74% when compared to single channel configuration.

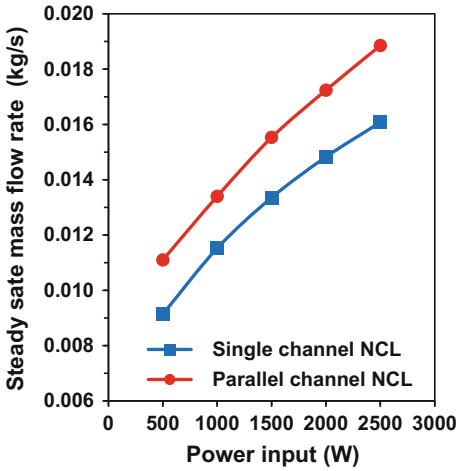

Fig. 8 Variation of steady-state mass flow rate with power input

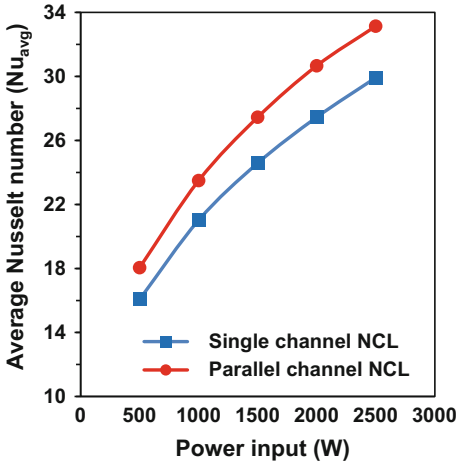

Fig. 9 Variation of average Nusselt number with power input

4 Conclusions

In the present study, the steady-state analysis has been carried out on different Natural Circulation Loop (NCL) configurations with water as working fluid. A three-dimensional geometry of the rectangular NCL model is developed and simulated using Ansys-Fluent 14.5. The simulation results follow the same trend with the published data. The mass flow rate and average Nusselt number increases with power input. The mass flow rate of the loop fluid in parallel channel NCL is enhanced when compared to single channel configuration. The average Nusselt number is enhanced by adding channels to the NCL.

Acknowledgements The financial support offered by DST-MHRD India is gratefully acknowledged.

References

1. Vijayan, P.K.: Nuclear Engineering and Design, vol. 215 (2002)
2. Basu, D.N. Bhattacharyya, S., Das, P.K.: Int. J. Heat Mass Tran. **62** (2013)
3. Kiran Kumar, K., Ram Gopal, M.: Appl. Therm. Eng. **29** (2009)
4. ANSYS-Fluent 15 Theory Guide (2013)

Numerical Study of Heat Transfer Characteristics in Shell-and-Tube Heat Exchanger

Ravi Gugulothu, Narsimhulu Sanke and A. V. S. S. K. S. Gupta

Abstract The heat exchangers are essential elements in a wide range of thermal systems including automobiles, computers, power plants, etc. The most commonly used type of heat exchanger is the shell-and-tube heat exchangers. In paper has been made an attempt with shell and tube heat exchanger that has been designed based on TEMA code to improve the performance of shell side fluid with the help of helical baffles of 40° helix angle and the Reynolds numbers are considered for shell side 2,500–16,500 and tube side 3,000–22,000 respectively. The variation of heat transfer coefficient and the friction factor with the increase of Reynolds number is studied and noticed that heat transfer coefficient is increasing while the friction factor is reduced.

Keywords Shell-and-tube heat exchanger · Helical baffle · Helix angle Reynolds number · Pressure drop · Overall heat transfer coefficient

1 Introduction

The shell-and-tube heat exchangers are commonly used in petroleum and power generation industries because of their relatively simple manufacturing technology and adaptability to different operating conditions; their robustness and shape make them well suitable for high-pressure operations. The baffles may be mainly used in shell-and-tube heat exchangers for inducing cross-flow over the tubes for improving the heat transfer performance and also to reduce the pressure drop. The segmental baffles are used in shell-and-tube heat exchanger, which forces the shell-side fluid

R. Gugulothu (✉) · N. Sanke
Department of Mechanical Engineering, University College of Engineering, Osmania University, Hyderabad 500007, Telangana, India
e-mail: ravi.gugulothu@gmail.com

A. V. S. S. K. S. Gupta
Department of Mechanical Engineering, JNTUH College of Engineering Hyderabad, Kukatpally 500085, Hyderabad, India

D. Srinivasacharya and K. S. Reddy (eds.), *Numerical Heat Transfer and Fluid Flow*, Lecture Notes in Mechanical Engineering,
https://doi.org/10.1007/978-981-13-1903-7_43

into a zigzag manner. But due to some drawbacks in these baffles such as larger pressure drop in the shell side, fouling problem, and high risk of vibration failure on the tube bundles, a number of new methods were proposed to overcome these drawbacks in shell-and-tube heat exchanger with segmental baffles.

2 Literature Review

Many experimental and numerical investigations on the structure parameters of heat exchangers with segmental baffles and helical baffles have been performed in the past, and those are listed out here. In the world market, the shell-and-tube heat exchangers are more served by process industries like power generation, oil refineries, etc., because of their robust geometry construction, possible upgrades, and reliability. Over the years, more significant research and development efforts are devoted by academicians, scientists, and researchers to understand the geometry of the shell-and-tube heat exchangers. The pioneering work published by Gao et al. [1], Lutcha and Nemcansky [2], Wang et al. (2007), and Zhang et al. [3] on helical baffles proved the way to shift from a conventional/clear understanding of baffles' role in a shell-and-tube heat exchanger.

Gao et al. [1] experimentally studied the effects on baffle helix angles (8°, 12°, 20°, 30°, and 40°) on shell-and-tube heat exchangers. The heat exchanger with helical baffles at 40° helix angle presents the best comprehensive performance among all the five testing heat exchangers. Zhang et al. [4] experimentally studied and compared the segmental baffle heat exchanger with four different helix angles (20°, 30°, 40°, and 50°) based on the same shell-side flow rate and found that the 40° helix angle gives the best performance. Zhang et al. [5] numerically studied three different helix angles (30°, 40°, and 50°) and found that the 40° helix angle of helical baffle is the best one.

Wen et al. [6, 7] experimentally studied the performance of shell-and-tube heat exchangers with different baffles (ladder-type baffles and helical baffles) and found that the helical-type baffles have shown great improvement in heat exchanger when compared with the ladder-type baffle. Wen et al. [8] studied the flow and heat transfer characteristics of shell-and-tube heat exchanger with helical baffles using multi-objective genetic algorithms (MOGA). In this study, helix angle and overlapped degree of helical baffles were chosen as the optimization parameters, while overall heat transfer coefficient and pressure drop of the shell-and-tube heat exchanger with helical baffle were optimized using MOGA. They found that the helix angle 40° was considered as an optimum angle.

Gugulothu et al. [9] studied the different types of baffles used in shell and tube heat exchangers along with helix angles (8°, 12°, 20°, 30°, 40° and 50°) and found that the 40° helix angle is the optimum angle for designing a shell and tube heat exchangers.

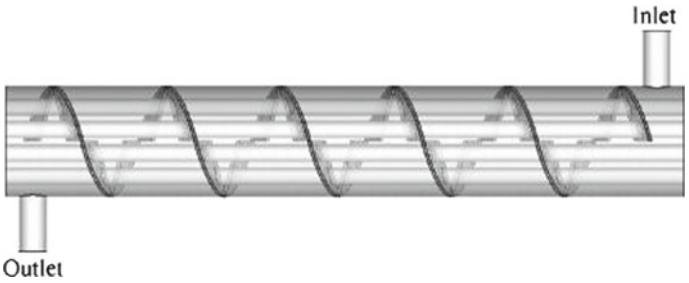

Fig. 1 Shell-and-tube heat exchanger with helical baffle

3 Mathematical Model and Analysis

The heat exchangers are devices that transfer heat between two fluids which are at different temperatures. A shell-and-tube heat exchanger consists of a bundle of tubes enclosed within a cylindrical shell. One fluid flows through the shell and another fluid flows through the tubes. The fluid flow and heat transfer processes are turbulent in nature and assumed as steady state. The shell-and-tube heat exchanger considered in the present study with helical baffles is shown in Fig. 1.

4 Formulations

The heat exchanger has 2000 mm length, and 114.3 and 102.10 mm of shell's outer and inner diameters are chosen with four numbers of tubes with outer diameter as 25.4 mm, arranged in an angle of 45° rotating square arrangement. From the literature, the optimum helix angle (β) is 40° and the same has been considered for the present work and thickness of the baffle is 3 mm. Hot fluid is considered in shell side at a temperature of 343.15 K, and cold fluid is considered in tube side at a temperature of 298.15 K. In this study, the shell-side flow rate ($\dot{Q}_S$) and the tube-side flow rate ($\dot{Q}_t$) are considered as 20–60 and 10–30 lpm.

$$\text{Baffle spacing } (S) = 0.2 \times D_i \text{ or } 51 \text{ mm (Whichever is greater)} \tag{1}$$

$$\text{Tube outer diameter } (d0) = 25.4 \text{ mm from Table RCB-4.52} \tag{2}$$

$$p = 1.25 \times d0 \tag{3}$$

$$B_{\text{helical}} = \sqrt{2} D_i \tan(\beta) \tag{4}$$

Number and size of tie rods: No fewer than four tie rods and not less than 9.5 mm of diameter are chosen. Any baffle segment requires a minimum of three points of support.

5 Shell-Side Calculation

$$\dot{m} = Q_s \times \rho_s \tag{5}$$

$$A_s = 0.25\pi\left(D_i^2 - \left(N \times d_0^2\right)\right) \tag{6}$$

$$V_s = \frac{\dot{m_s}}{\rho_s A_s} \tag{7}$$

$$D_e = \frac{4\left(P_t^2 - \left(0.25\pi - d_0^2\right)\right)}{\pi d_0} \tag{8}$$

Equivalent/Effective diameter varies with the flow arrangements.

$$\mathrm{Re}_S = \frac{V_S \times D_e}{\nu} \tag{9}$$

$$\mathrm{Pr}_S = \frac{\mu C_p}{k_{\text{Shell Fluid}}} \tag{10}$$

$$h_S = 0.023 \times \left(\frac{k_{\text{Shell Fluid}}}{D_e}\right) \times (\mathrm{Re})^{0.8} \times (\mathrm{Pr})^{0.3} \tag{11}$$

$$Nu_S = \frac{h_S \times D_e}{k_{Shell\,Fluid}} \tag{12}$$

$$f_S = 0.184 \times (\mathrm{Re})^{-0.2} \tag{13}$$

$$\Delta p_S = \frac{\rho \times f_S \times L_S \times V_S^2}{2 \times B} \tag{14}$$

6 Tube-Side Calculation

$$\dot{m}_t = \dot{Q}_t \times \rho_t \tag{15}$$

$$A_t = N \times A_o \tag{16}$$

$$V_t = \frac{\dot{m}_t}{\rho_t \times A_t} \tag{17}$$

$$\mathrm{Re}_t = \frac{V_t \times d_i}{\nu} \tag{18}$$

$$\mathrm{Pr}_t = \frac{\mu C_p}{k_{\text{tube fluid}}} \tag{19}$$

$$h_t = 0.023 \times \left(\frac{k_{\text{tube fluid}}}{d_i}\right) \times (\mathrm{Re})^{0.8} \times (\mathrm{Pr})^{0.4} \tag{20}$$

The heat transfer coefficient can be calculated by the Nusselt number equation.

$$\mathrm{Nu}_t = \frac{h_t \times d_i}{k_{\text{tube fluid}}} \tag{21}$$

$$f_t = 0.184 \times (\mathrm{Re})^{-0.2} \tag{22}$$

$$\Delta p_t = \frac{\rho \times f_t \times L \times V_t^2}{2 \times d_i} \tag{23}$$

7 Results and Discussions

Numerical analysis has been done on the shell-and-tube heat exchangers with helical baffles of helix angle 40° based on Zhang et al. [5].

Figure 2 indicates the variation of Reynolds number for different mass flow rates. It is observed that the Reynolds number increasing with the increasing of mass flow rate in shell side as well as tube side. It indicates that higher mass flow rate gives the higher Reynolds number.

Figure 3 predicts the variation of pressure drop for different Reynolds numbers ranging from 2500 to 16,500 in shell side and 3000 to 22,000 in tube side. It is being observed from the figure that the pressure drop is increasing with increase in Reynolds number and this may be due to an increase in the density of the fluid at given Reynolds number.

Figure 4 shows the increasing heat transfer coefficient with the increasing Reynolds number ranging from 2500 to 16,500 in shell side and 3000 to 22,000 in tube side. This is caused by the increasing mass flow rates within the range of Reynolds number.

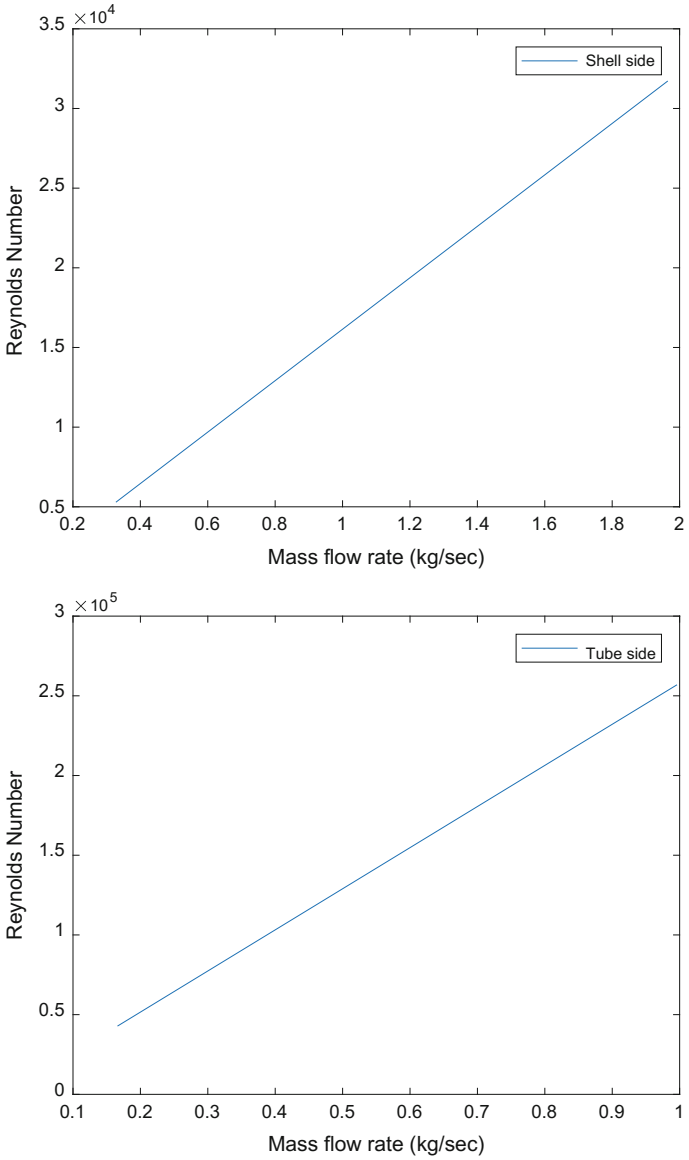

Fig. 2 Mass flow rate versus Reynolds number (shell side and tube side)

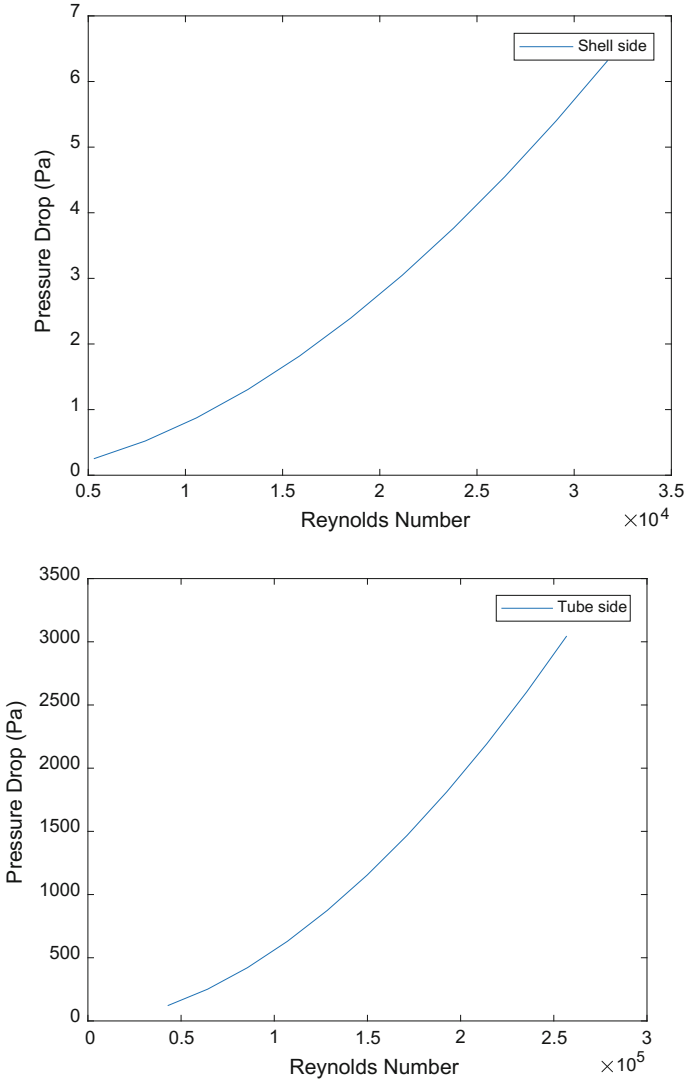

Fig. 3 Reynolds number versus pressure drop (shell side and tube side)

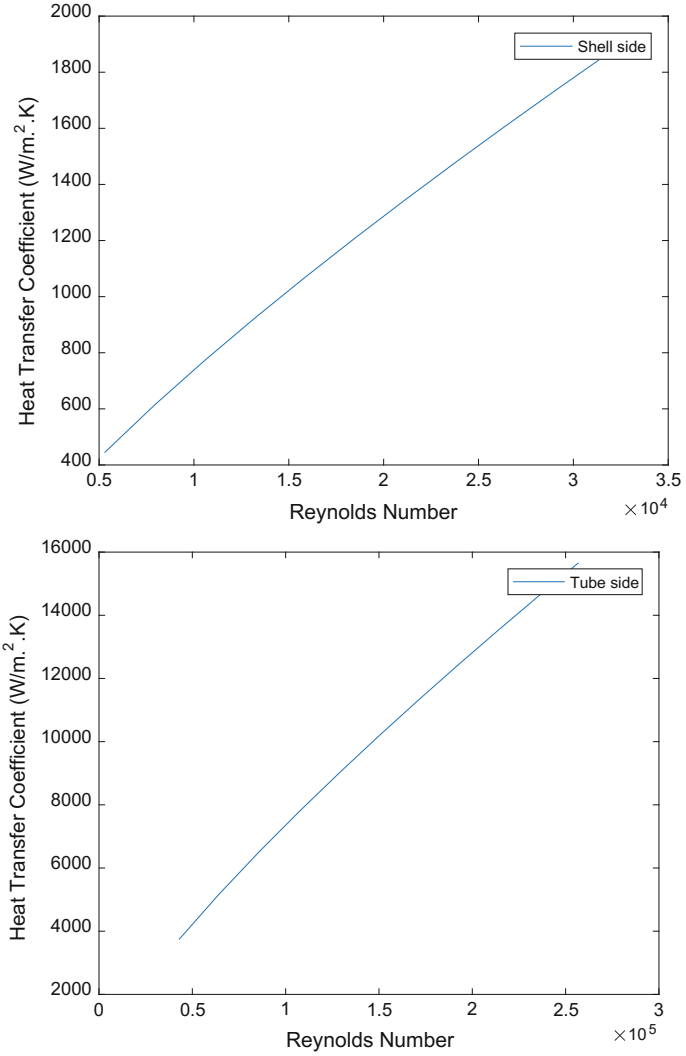

Fig. 4 Reynolds number versus heat transfer coefficient (shell side and tube side)

8 Conclusion

In this present work, flow, pressure drop, and heat transfer characteristics were performed for different mass flow rates of shell-and-tube heat exchanger with helical baffle of 40° helix angle. Both the pressure drop and heat transfer coefficients are the major parameters of heat exchanger performance. The shell-side and tube-side Reynolds number, pressure drop, and heat transfer coefficient are increasing with the increase in inlet mass flow rate in shell side and tube side. Increasing the flow velocities will cause a rise in the heat transfer coefficient and more pressure drop in the heat exchanger.

Acknowledgements Authors would like to thanks Dr. P.A Deshpande, Dr. Debasis Sarkar and their research scholars (Phanikumar Pentyala, Stutee Bhoi and V. Sai Phani Kumar) Department of Chemical Engineering, IIT Kharagapur, West Bengal, India for conducting Short Term Course on "Numerical Techniques for Chemical Process Simulations" funded by AICTE and cleared all the doubts in simulation of mathematical models during course work time. JNTUH College of Engineering Hyderabad, TEQIP-III is funded to present this research paper.

References

1. Gao, B., Bi, Q., Nie, Z., Wu, J.: Exp. Thermal Fluid Sci. **68**, 48–57 (2015)
2. Lutcha, J., Nemcansky, J.: Chem. Eng. Res. Des. **68**, 263–270 (1990)
3. Zhang, J.F., Li, B., Huang, W.J., Lei, Y.G., He, Y.L., Tao, W.Q.: Chem. Eng. Sci. **64**, 1643–1653 (2009a)
4. Zhang, J.F., He, Y.L., Tao, W.Q.: Int. J. Heat Mass Transf. **52**, 5371–5380 (2009b)
5. Zhang, J.F., He, Y.L., Tao, W.Q.: Int. J. Heat Mass Transf. **52**, 5381–5389 (2009c)
6. Wen, J., Yang, H., Wang, S., Xue, Y., Tong, X.: Int. J. Heat Mass Transf. **84**, 990–997 (2015)
7. Wen, J., Yang, H., Wang, S., Xu, S., Xue, Y., Tuo, H.: Energy Convers. Manage. **89**, 438–448 (2015)
8. Wen, J., Gu, X., Wang, M., Wang, S., Tu, J.: Int. Commun. Heat Mass Transf. **89**, 91–97 (2017)
9. Gugulothu, R., Somanchi, N.S., Reddy, K.V.K., Tirkey, J.V.: In: Proceedings of the Asian Congress on Gas Turbines (ACGT-2016). Department of Aerospace Engineering, Indian Institute of Technology Bombay, during 14th to 16th November (2016)

Application of Green's Function to Establish a Technique in Predicting Jet Impingement Convective Heat Transfer Rate from Transient Temperature Measurements

Ritesh Kumar Parida, Anil R. Kadam, Vijaykumar Hindasageri and M. Vasudeva

Abstract Jet impingement heat transfer has gained attention of the researchers due to its very high rate of convective heat transfer. The objective of this study is to establish an analytical technique to predict the convective heat transfer coefficient and the reference temperature over a surface being impinged. This technique is based on the fundamental mathematical concept of Green's function. A code in MATLAB is developed to predict both local convective heat transfer coefficient and reference temperature over the impinging surface, which requires the transient temperature data at both faces of the impinging plate as input. Radiation correction is also considered to incorporate radiation losses in high-temperature applications. This code works on the principle of one-dimensional heat transfer across the impinging plate, for known dimensions, thermal diffusivity, and surface emissivity. A numerical simulation of hot jet at Reynolds number equal to 1000, over a cold plate of thickness 10 mm, is carried out for a given set of spatially varying convective heat transfer coefficient and reference temperature values, along the impinging surface. The impinging plate is considered to be orthotropic to ensure one-dimensional heat conduction across the plate thickness. Transient temperature at both the faces for a duration of 10 s with an interval of one second was recorded and used as input to the code to validate the proposed technique. Local heat transfer coefficient and the reference temperature predicted are in good agreement with those input values for numerical analysis

R. K. Parida · A. R. Kadam · M. Vasudeva
National Institute of Technology Karnataka, Surathkal 755025, Karnataka, India
e-mail: ritesh.parida@gmail.com

V. Hindasageri (✉)
K.L.S's Vishwanathrao Deshpande Rural Institute of Technology, Haliyal 581329, Karnataka, India
e-mail: vkhnitk@gmail.com

D. Srinivasacharya and K. S. Reddy (eds.), *Numerical Heat Transfer and Fluid Flow*, Lecture Notes in Mechanical Engineering,
https://doi.org/10.1007/978-981-13-1903-7_44

using ANSYS, having a maximum deviation of 2 and 10%, respectively. Further, it is observed that estimated values of convective heat flux at a given location on the impinging surface varies linearly with temperature at the same location, which confirms Newton's law of cooling.

Keywords Jet impingement · Greens function · Convective heat transfer coefficient

1 Introduction

Principle of jet impingement heat transfer is extensively studied for industrial, military as well as space technology applications, because of its very high convective heat transfer rate, faster heating response time, possibility to heat or cool locally, thereby improving product quality or process efficiency. A very high rate of heat transfer occurs at stagnation point, which creates dynamism in temperature change within the object being impinged. Numerous fundamental experiments have been undertaken to understand the heat transfer characteristics of jet impingement heat transfer [1–5].

Qualitative as well as quantitative analysis of heat transfer due to impinging jets have been summarized in the review papers [6–10]. Dependence of convective heat transfer coefficient on various parameters like turbulence, induced swirl, nozzle-to-plate spacing, orientation of nozzle, arrays of jets, jet-to-jet spacing, jet shape and size, Reynolds number, and equivalence ratio has been reported in literature [11–13]. Empirical correlations for convective heat transfer distributions are developed based on analytical and semi-analytical studies. Predicting exact heat transfer rate associated with jet impingement heat transfer is very complex [14–20]. Researcher has attempted to express the exact heat transfer rate analytically using mathematical tools like Duhamel's theorem, Laplace transform technique and inverse heat transfer technique, which have their own limitations to handle practical problems holistically. For example, inverse heat transfer algorithm is multifaceted and hence computationally complex.

With reference to the literature, it is concluded that most of the research articles on jet impingement heat transfer are experimental in nature, and are based on parametric studies. Fluid flow pattern over the impinging surface being very complex and turbulent, it is difficult to quantify the exact heat transfer rate. It is pertinent to mention that, because of turbulent fluid flow over the impinging surface, the nature of heat transfer within the impinging surface is transient in nature. Therefore, formulating a standard, reliable, and accurate technique to estimate rate of heat transfer from or to impinging jet is very essential.

In this paper, an alternative approach to predict the convective heat transfer coefficient using Green's function is presented. Green's function is a mathematical tool capable of dealing transient heat transfer problems with transient boundary conditions and spatially varying initial condition. Orthotropic material is considered to

ensure one-dimensional transient heat conduction for easy validation and confirmation of the solutions numerically. The objectives of the present work are as follows:

(a) To present the application of Green's function to solve problems on jet impingement heat transfer.
(b) To predict local convective heat transfer coefficient and corresponding reference temperature over impinging surface from transient surface temperature measurements.

2 Methodology and Mathematical Formulation

With reference to the objectives of this paper listed in the last paragraph, the problem statement is to solve a case of one-dimensional transient heat conduction problem with transient temperature boundary conditions (BCs) at both front and rear face of the plate under consideration, which is impinged by hot jet at front face. The material of impinging plate is considered to be orthotropic. The required BCs are derived from the numerical analysis (ANSYS) of one-dimensional transient heat conduction within an orthotropic material with known boundary heat flux at the impinging face, and the other face being insulated [21].

Governing equation for one-dimensional transient conduction problem is given by, $\frac{\partial^2 T}{\partial x^2} = \frac{1}{\alpha}\frac{\partial T}{\partial t}$ for $0 < x < L$ and $t > 0$ where BCs are $T_{x=0} = f_1(t)$ and $T_{x=L} = f_2(t)$ and initial condition is $T_{t=0} = F(x)$. Corresponding Green's function is given by $G\left(x, t : x^I, \tau\right) = \frac{2}{L}\sum_{n=1}^{\infty} \sin\lambda_n x \sin\lambda_n x^I \mathrm{e}^{-\alpha\lambda_n(t-\tau)}$ and hence the temperature distribution is given by,

$$T(x,t) = \frac{2}{L}\sum_{n=1}^{\infty} \sin\lambda_n x \mathrm{e}^{-\alpha\lambda_n t} \int_{x^I=0}^{L} \sin\lambda_n x^I F(x^I)\mathrm{d}x^I + \alpha\frac{2}{L}\sum_{n=1}^{\infty} \sin\lambda_n x \mathrm{e}^{-\alpha\lambda_n t} \int_{\tau=0}^{t} \mathrm{e}^{\alpha\lambda_n \tau} f_1(\tau)\mathrm{d}\tau$$
$$- \alpha\frac{2}{L}\sum_{n=1}^{\infty}(-1)^n \sin\lambda_n x \mathrm{e}^{-\alpha\lambda_n t} \int_{\tau=0}^{t} \mathrm{e}^{\alpha\lambda_n \tau} f_2(\tau)\mathrm{d}\tau \quad (1)$$

where the eigenvalues are given by, $\lambda_n = \frac{n\pi}{L}$.

Equation (1) is valid in the open interval "$0 < x < L$". Such phenomenon occurs when the solution derives its basis from the orthogonal expansion technique with the BC being utilized to develop the eigen condition [22]. In this study, both BCs are expressed in terms of quadratic polynomials as $T_{x=0} = at^2 + bt + c$ and $T_{x=L} = pt^2 + qt + r$; and the IC as $T_{t=0} = T_{\text{initial}}$. On simplifying further, using integration by parts in second and third term of Eq. (1) and applying the limits of integration, transient temperature profile is expressed as

$$T(x,t) = \frac{2}{L}\sum_{n=1}^{\infty}\sin\lambda_n x\mathrm{e}^{-\alpha\lambda_n t}\left[1-(-1)^n\right]\frac{T_{\text{initial}}}{\lambda_n} + \alpha\frac{2}{L}\sum_{n=1}^{\infty}\sin\lambda_n x\left[\frac{at^2+bt+c-c\mathrm{e}^{-\alpha\lambda_n t}}{\alpha\lambda_n} - \frac{2at+b-b\mathrm{e}^{-\alpha\lambda_n t}}{(\alpha\lambda_n)^2} + \frac{2a-2a\mathrm{e}^{-\alpha\lambda_n t}}{(\alpha\lambda_n)^3}\right] - \alpha\frac{2}{L}\sum_{n=1}^{\infty}(-1)^n\sin\lambda_n x\left[\frac{pt^2+qt+r-r\mathrm{e}^{-\alpha\lambda_n t}}{\alpha\lambda_n} - \frac{2pt+q-q\mathrm{e}^{-\alpha\lambda_n t}}{(\alpha\lambda_n)^2} + \frac{2r-2r\mathrm{e}^{-\alpha\lambda_n t}}{(\alpha\lambda_n)^3}\right] \tag{2}$$

It is clear from Eq. (2) that all the terms converge. This equation is handled using a computer code, for $0 < x < L$ and $t > 0$. The temperature at an infinitely small distance (Δl) from the impinging surface and at an interval of 1 s is evaluated.

2.1 *Procedure to Calculate Heat Transfer Coefficient and Reference Temperature*

Using Eq. (2), the conductive heat flux at the impinging face $Q_{\text{cond}} = \frac{T_{x=0}-T_{x=\Delta l}}{\Delta l}$ can be estimated. Further, convective heat flux over the surface being impinged upon can be estimated by adding radiative heat flux leaving the surface to conductive heat flux (i.e., $Q_{\text{conv}} = Q_{\text{rad}} + Q_{\text{cond}}$). Here, radiative heat flux leaving the surface is given by $Q_{rad} = \varepsilon\sigma T_w^4$, where T_w is nothing but the measured temperature at impinging face. The method of calculating convective heat transfer coefficient and reference temperature is based on Newton's law of cooling. As we know, convective heat transfer coefficient is expressed as, $h = \frac{Q_{\text{conv}}}{(T_w - T_{\text{ref}})}$, which can also be rewritten as $T_w = \frac{Q_{\text{conv}}}{h} + T_{\text{ref}}$, a form of an equation of line having slope, $\frac{1}{h}$ and y-intercept, T_{ref}. With estimated value of Q_{conv} and corresponding known T_w, the variation of Q_{conv} along x-axis with T_w along y-axis can be plotted. Ideally, this plot must be a straight line, which is the first indication that the method is valid.

3 Results and Discussions

The convective heat transfer coefficient and reference temperatures at impinging zone are estimated analytically. Comparison of estimated convective heat transfer coefficient with the input convective heat transfer coefficients to the ANASYS software is presented in Fig. 1a. The convective heat transfer coefficient profiles are in agreement with each other, with a maximum deviation of 2%. Similarly, the comparison of predicted reference temperatures with the input reference temperature profile is shown in Fig. 1b. Maximum difference between predicted and input reference temperatures is 10%. Since the trend of both predicted as well as input convective heat transfer coefficient profile follow each other, it can be concluded that the technique

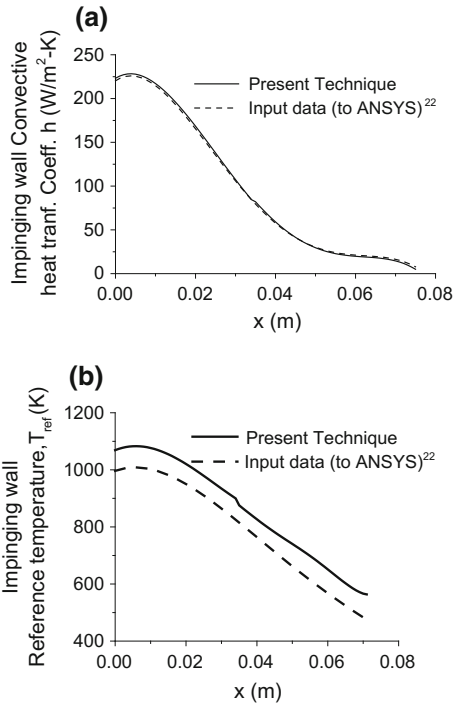

Fig. 1 **a** Comparison of estimated convective heat transfer coefficient with those input data (to ANSYS), **b** Comparison of estimated reference temperature with the input (to ANSYS) reference temperature

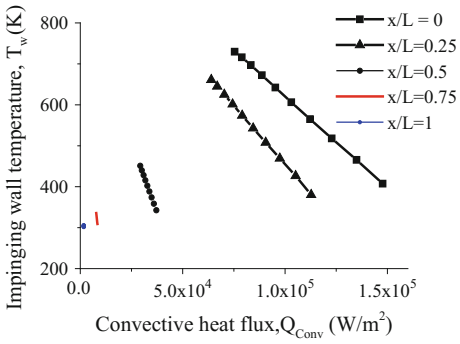

Fig. 2 Variation of front wall temperature with estimated heat flux for different *x*/*L* ratio

is useful in estimation of local convective heat transfer coefficients over impinging surface.

A linear trend of front wall temperature versus predicted convective heat flux at the impinging face is observed and presented in Fig. 2. Since this linear trend is expected from the principle of Newton's law of cooling, it can strongly be stated that the proposed mathematical technique for estimation of local convective heat transfer coefficient at the impinging zone is valid.

4 Conclusion

In this paper, an analytical technique to predict heat transfer rate over an impinging surface of an orthotropic material using Green's function is discussed. Linear trend of front wall temperature versus predicted convective heat flux at the front face confirms the validity and reliability of the technique. Since the multidimensional Green's function formulations are available in literature, and radiation corrections are incorporated, it would be easy to extend this technique for analysis of jet impingement heat transfer for a real material even at higher temperature. Computational time in the proposed technique as compared to existing analytical techniques is much lesser. The proposed method of determining heat transfer coefficient offers flexibility in designing an experiment to study phenomenon relating to jet impingement heat transfer. Instead of requiring direct measurements of heat flux and temperature at the surface where heat transfer coefficient is to be determined, the experiment can be designed so that temperature measurements are taken at locations where sensors can be conveniently placed and the sensors do not disturb the fluid flow field.

References

1. Kilham, J.K., Purvis, M.R.I.: Heat transfer from normally impinging flames. Combust. Sci. Technol. **18**(3–4), 81–90 (1978)
2. Milson, A., Chigier, N.A.: Studies of methane and methane-air flames impinging on a cold plate. Combust. Flame **21**(3), 295–305 (1973)
3. Conolly, R., Davies, R.M.: A study of convective heat transfer from flames. Int. J. Heat Mass Transf. **15**(11), 2155–2172 (1972)
4. Popiel, C.O., Van der Meer, T.H., Hoogendoorn, C.J.: Convective heat transfer on a plate in an impinging round hot gas jet of low Reynolds number. Int. J. Heat Mass Transf. **23**(8), 1055–1068 (1980)
5. Remie, M.J., Särner, G., Cremers, M.F.G., Omrane, A., Schreel, K.R.A.M., Aldén, L.E.M., De Goey, L.P.H.: Heat-transfer distribution for an impinging laminar flame jet to a flat plate. Int. J. Heat Mass Transf. **51**(11–12), 3144–3152 (2008)
6. Chander, S., Ray, A.: Flame impingement heat transfer: a review. Energy Convers. Manage. **46**(18–19), 2803–2837 (2005)
7. Zuckerman, N., Lior, N.: Jet impingement heat transfer: physics, correlations, and numerical modeling. Adv. Heat Transf. **39**, 565–631 (2006)
8. Baukal, C.E., Gebhart, B.: A review of semi-analytical solutions for flame impingement heat transfer. Int. J. Heat Mass Transf. **39**(14), 2989–3002 (1996)
9. Baukal Jr., C.E., Gebhart, B.: A review of empirical flame impingement heat transfer correlations. Int. J. Heat Fluid Flow **17**(4), 386–396 (1996)
10. Arganbright, D.G., Resch, H.: A review of basic aspects of heat transfer under impinging air jets. Wood Sci. Technol. **5**(2), 73–94 (1971)
11. Gulati, P., Katti, V., Prabhu, S.V.: Influence of the shape of the nozzle on local heat transfer distribution between smooth flat surface and impinging air jet. Int. J. Therm. Sci. **48**(3), 602–617 (2009)
12. Katti, V., Prabhu, S.V.: Influence of spanwise pitch on local heat transfer distribution for in-line arrays of circular jets with spent air flow in two opposite directions. Exp. Therm. Fluid Sci. **33**(1), 84–95 (2008)

13. Garimella, S.V., Nenaydykh, B.: Nozzle-geometry effects in liquid jet impingement heat transfer. Int. J. Heat Mass Transf. **39**(14), 2915–2923 (1996)
14. Baughn, J.W.: Liquid crystal methods for studying turbulent heat transfer. Int. J. Heat Fluid Flow **16**(5), 365–375 (1995)
15. Sagheby, S.H., Kowsary, F.: Experimental design and methodology for estimation of local heat transfer coefficient in jet impingement using transient inverse heat conduction problem. Exp. Heat Transf. **22**(4), 300–315 (2009)
16. Kant, M.A., von Rohr, P.R.: Determination of surface heat flux distributions by using surface temperature measurements and applying inverse techniques. Int. J. Heat Mass Transf. **99**, 1–9 (2016)
17. Hindasageri, V., Vedula, R.P., Prabhu, S.V.: A novel concept to estimate the steady state heat flux from impinging premixed flame jets in an enclosure by numerical IHCP technique. Int. J. Heat Mass Transf. **79**, 342–352 (2014)
18. Taler, J.: A General Method for the Experimental Determination of Local Transient Heat Transfer, vol. 23, pp. 283–289. Springer, Berlin (1988)
19. Frankel, J.I., Keyhani, M., Arimilli, R.V.: New orthotropic, two-dimensional, transient heat-flux/temperature integral relationship for half-space diffusion. J. Thermophys. Heat Transf. **24**(1), 215–218 (2010)
20. Fernandes, A.P., Sousa, P.F., Borges, V.L., Guimaraes, G.: Use of 3D-transient analytical solution based on Green's function to reduce computational time in inverse heat conduction problems. Appl. Math. Model. **34**(12), 4040–4049 (2010)
21. Hindasageri, V., Vedula, R.P., Prabhu, S.V.: A novel method of estimation of adiabatic wall temperature for impinging premixed flame jets. Int. J. Heat Mass Transf. **77**, 185–193 (2014)
22. Hahn, D.W., Ã–zisik, M.N.: Heat Conduction, 3rd edn. Wiley, Hoboken (2012)

Mathematical Simulation of Cavitation with Column Separation in Pressurized Pump Pipeline Systems

Nerella Ruben and Erva Venkatarathnam

Abstract Hydraulic transient analysis is important in design stage as well as the execution stage of pipeline systems for diagnosis of problems arises due to pipe burst, pipe collapses and leakages. The calculations necessary to analyse transient conditions must be very precise, more realistic and less time consuming. To fulfill this objective, a suitable mathematical model incorporating different components that simulates the real physical phenomenon is the need of hour. In this paper, column separation model called Discrete Vapour Cavitation Model (DVCM) is described and applied to a reference problem that consists of pump pipeline system. The calculations of this model are compared with calculations of the reference problem by conventional Method of Characteristics (MOC) approach. The results show that MOC could not able to capture the real physical phenomenon of cavitation with water column separation due to drawbacks in basic modelling.

Keywords Hydraulic transients · Water column separation · Method of characteristics

1 Introduction

In the water field, mathematical modelling of water distribution systems has become a necessary component to analyse, design and diagnose the systems. The numerical representation of the water installation components leads to optimized and efficient safe design of the systems. Thus, the numerical models allow greater reliability and command over the entire system operation. Nowadays, the simulations of hydraulic

N. Ruben (✉)
Vignan's Foundation for Science, Technology and Research,
Guntur 522213, AP, India
e-mail: rubennerella2512@gmail.com

E. Venkatarathnam
National Institute of Technology Warangal, Warangal 506001, TS, India
e-mail: e.venkatarathnam@gmail.com

D. Srinivasacharya and K. S. Reddy (eds.), *Numerical Heat Transfer and Fluid Flow*, Lecture Notes in Mechanical Engineering,
https://doi.org/10.1007/978-981-13-1903-7_45

transients or water hammer analysis in complex pipe system are a real need. In this era of powerful computers, many mathematical models were developed or devoted to simulate the hydraulic transients. The numerical model used must be reliable, efficient, and must solve wide range of problems encountered in real field. Many notable works were performed in the realm of this component.

Izquierdo and Iglesias [1] developed a mathematical model called DYAGATS which uses elastic model, also known as water hammer, to model the behaviour of fluid within the pipeline. The Method of Characteristic (MOC) and the wave plan methods were used and applied to simple pipe systems. The same authors [2] extended the model and applied it to complex systems. A review on water hammer equations [3] suggests that the governing 1D water hammer can be solved analytically by using most popular technique called MOC which has the desirable advantages of simplicity and numerical efficiency. Other than MOC technique, the wave plan [4], finite difference [5], and finite volume [6] methods have been applied to governing equations. Many MOC-based schemes were developed to solve numerical solutions of hyperbolic equations. A fixed grid MOC also called method of fixed time intervals was applied to a reservoir-pipe-valve system [7]. It was found that fixed grid MOC was easier and gives user full control of the grid selection. Similarly, pressure fluctuations were captured at the middle and at the valve of simple reservoir systems by using the MOC method [8]. In addition, the recent knowledge that negative pressure phases of transients can result in contamination of potable water systems, meaning that the need to understand and deal effectively with transient phenomena is more acute than ever [9]. The negative phase in a pipeline results from column separations and cavitation when pressure drops to vapour pressure of the liquid.

Much theoretical and experimental analysis have been done in the realm of cavitation and water column separation which was first identified by JouKowsky early in the twentieth century [10, 11]. The intensity of water column separation and its associated pressure valve system was studied and analysed by three numerical models namely, Discrete Vapour Cavity Model (DVCM), Discrete Gas Cavity Model (DGCM), and Generalized Interface Vapour Cavity Model (GIVCM) [12]. It reveals that DVCM involves simple algorithm and takes smaller computational time. Similarly, a laboratory test was conducted and the numerical prediction of pressure changes during water hammer with liquid column separation by DVCM were compared with experimental results [13]. In this experiment, visualization of cavities and its associated pressures were observed not only at the vicinity of the shutoff valve but along some discrete points of the pipeline. Numerical prediction of water hammer and column separation with DVCM and GIVCM approach for the simple reservoir-pipe-valve system and simple pump pipeline was analysed [14]. The pressure heads predicted by both models show no difference and the effect of various hydraulic and geometric parameters like pipe diameter, pump-motor inertia, and specific speed were investigated.

2 Methodology

The water hammer equations Eqs. (1) and (2) are one-dimensional hyperbolic partial differential equations that describe transient state flows in closed conduits are derived by

$$gA\frac{\partial H}{\partial t} + a^2\frac{\partial Q}{\partial x} = 0 \tag{1}$$

$$gA\frac{\partial H}{\partial x} + \frac{\partial Q}{\partial t} + f\frac{Q|Q|}{2DA} = 0 \tag{2}$$

where H, t, a, and g are the piezometric pressure head, time, wave speed, and gravitational acceleration, respectively, and A, Q, x, f, and D are the pipe area, discharge, distance, Darcy–Weisbach friction factor and inner diameter of pipe, respectively. The method of characteristics (MOC) is a widely used numerical method which can transform the partial differential equations of Eqs. (1) and (2) into of ordinary differential equations valid along two characteristic lines. These equations are then converted into compatibility equations Eqs. (3) and (4) by finite difference approach.

Along the $C+$ characteristic line $(\Delta x/\Delta t = a)$:

$$gA\left(H_{i,t} - H_{i-1,t_0}\right) + a\left((Q_u)_{i,t} - Q_{i-1,t_0}\right) + \frac{f\Delta x}{2gDA^2}(Q_u)_{i,t}\left|Q_{i-1,t_0}\right| = 0 \tag{3}$$

Along the $C-$ characteristic line $(\Delta x/\Delta t = a)$:

$$gA\left(H_{i,t} - H_{i+1,t_0}\right) + a\left((Q)_{i,t} - (Q_u)_{i+1,t_0}\right) + \frac{f\Delta x}{2gDA^2}Q_{i,t}\left|(Q_u)_{i+1,t_0}\right| = 0 \tag{4}$$

3 Discrete Vapour Cavitation Model

In DVCM model, a vapour cavity can form in computational grids and the head should be set to saturated vapour pressure head

$$H_{\text{abs}} = H^{v}_{\text{abs}} \tag{5}$$

The variation of discharge in the system can be simulated at ith computational node by assigning upstream discharge as $(Q_u)_i$ and downstream discharge as (Q_i) to include discrete vapour cavity model. In conventional MOC model they are made equal and identical, i.e. $Q_u \equiv Q$. Conversely in discrete vapour model $Q_u \not\equiv Q$ at points where liquid becomes vapour. The staggered grid is used to get the unknown values at computation grids (Fig. 1). Along with Eqs. (3) and (4), continuity equation

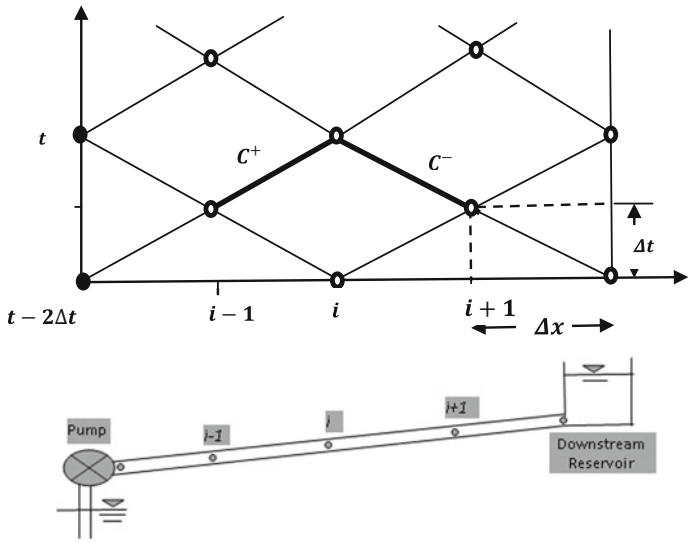

Fig. 1 Staggered grid in (x, t) plane

Eq. (6) is required to solve for variables along at each time step and Eq. (6) must be integrated to be used in DVCM model. The integration yields Eq. (7)

$$\frac{\mathrm{d}V_v^*}{\partial t} = Q_u - Q \tag{6}$$

$$V^{n+1} = V^{n-1} + \left\{\psi\left(Q^{n+1} - Q_u^{n+1}\right) + (1-\psi)\left(Q^{n-1} - Q_u^{n-1}\right)\right\} 2\Delta t \tag{7}$$

where V^{n+1}, V^{n-1} are the vapour volumes at the new time and $2\Delta t$ earlier respectively and ψ is a weighting factor ($\psi = \Delta t'/2\Delta t$) used in time direction.

4 Numerical Simulation—Results and Discussions

A simple pumping system is adopted from a reference article [1] and numerical simulations were performed to validate the conventional MOC model with the column separation model. This pumping system delivers water from lower reservoir to upper reservoir through a pump. The nominal parameters of the pump given are: Pump Rated discharge $Q_R = 0.1$ m^3/s, Pump Head $H_R = 37$ m, Specific speed $N_s = 0.46$ (SI Units). Similarly, the geometrical dimensions of pipe 1 consist of length $L_1 =$ 400 m, diameter, $D_1 = 250$ mm, thickness of pipe, $e_1 = 20$ mm and wave speed, $a_1 = 919$ m/s. Similarly, the dimensions of pipe 2 are length $L_2 = 100$ m, diameter, $D_2 = 250$ mm, thickness of pipe, $e_2 = 20$ mm and wave speed, $a_2 = 919$ m/s. The

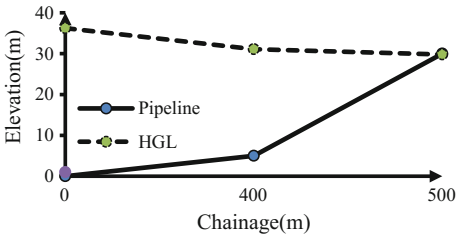

Fig. 2 Pipeline and steady-state HGL along the pipeline

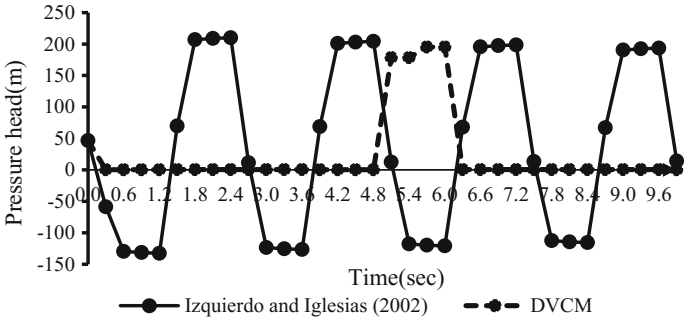

Fig. 3 Comparison between the reference results of MOC with DVCM

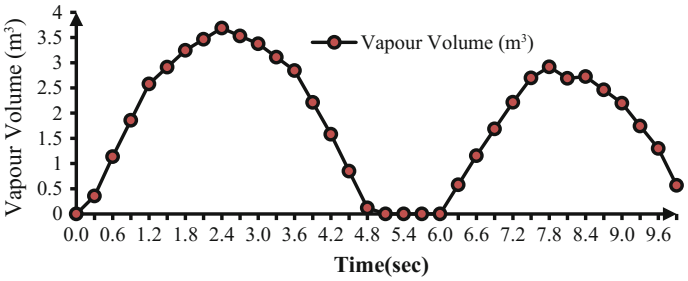

Fig. 4 Vapour volume calculations at pump valve by DVCM

steady-state analysis, i.e. when the pump runs its rated speed were performed and the results are shown in Fig. 2.

Numerical simulations were performed after sudden pump trip or power failure to pumps. The results show that the maximum pressure head simulated at pump locations are 205 m by MOC and 195 m by DVCM as shown in Fig. 3. It is observed that through the results are similar, but the time of occurrence of these pressure heads is different. The vapour volumes formed at appropriate times due to local pressure are shown in Fig. 4. The total vapour volumes calculated at pump location is 61 m^3 where the maximum vapour volume is 3.54 m^3.

5 Conclusions

Mathematical model used to simulate the cavitation with column separation in a simple pump pipeline system has been described. To model the hydraulic transients in pipe systems, use is made of conventional MOC method. The main emphasis in this paper is put on use of DVCM model in pressurized pump pipeline systems rather than simple reservoir-pipe-valve systems. For a reference case of pump system, the DVCM could able to capture the physical phenomenon of cavitation and column separation than MOC has been theoretically proved. The model uses staggered grid computations that can compute unknowns at every $2\Delta t$ time step. This helps, in principle, to obtain more realistic pressures.

References

1. Izquierdo, J., Iglesias, P.L.: Mathematical modelling of hydraulic transients in simple systems. Math. Comput. Model. **35**, 801–812 (2002)
2. Izquierdo, J., Iglesias, P.L.: Mathematical modelling of hydraulic transients in complex systems. Math. Comput. Model. **39**, 529–540 (2004). https://doi.org/10.1016/S0895-7177(04)90524-9
3. Ghidaoui, M.S., Zhao, Z., McInnis, D.A., Axworthy, D.H.: A review of water hammer theory and practice. Appl. Mech. Rev. **58**, 49–76 (2005). https://doi.org/10.1115/1.1828050
4. Wood, D.J., Lingireddy, S., Boulos, P.F., Karney, B.W., McPherson, D.L.: Numerical methods for modeling transient flow in distribution systems. Urban Water J. **97**(7), 104–110 (2005)
5. Islam, M.R., Chaudhry, M.H.: Modeling of constituent transport in unsteady flows in pipe networks. J. Hydraul. Eng. **124**(11), 1115–1124 (1998). https://doi.org/10.1061/(ASCE)0733-9429(1998)124:11(1115)
6. Bourdarias, C., Gerbi, S.A.: A conservative model for unsteady flows in deformable closed pipes and its implicit second-order finite volume discretisation. Comput. Fluids **37**, 1225–1237 (2008). https://doi.org/10.1016/j.compfluid.2007.09.007
7. Chaudhry, M.H.: Applied Hydraulic Transients, 3rd edn. Springer Publishers, New York (2014)
8. Ruben, N., Rathnam, E.V.: Fluid transients and wave propagation in pressurized conduits due to valve closure. Procedia Eng. **127**, 1158–1164 (2015)
9. Bergant, A., Simpson, A.R., Tijsseling, A.S.: Water hammer with column separation: a historical review. J. Fluids Struct. **22**, 135–171 (2006). https://doi.org/10.1016/j.jfluidstructs.2005.08.00
10. Ghidaoui, M.S.: On the fundamental equations of water hammer. Urban Water J. **1**(2), 71–83 (2004). https://doi.org/10.1080/15730620412331290001
11. Simpson, A.R., Bergant, A.: Numerical comparison of pipe-column-separation models. J. Hydraul. Eng. **120**(3), 361–377 (1994). https://doi.org/10.1061/(ASCE)0733-9429(1994)120:3(361)
12. Adamkowski, A., Lewandowski, M.: Investigation of hydraulic transients in a pipeline with column separation. J. Hydraul. Eng. **138**(11), 935–944 (2012). https://doi.org/10.1061/(ASCE)HY.1943-7900.0000596
13. Sadafi, M., Riasi, A., Nourbakhsh, S.A.: Cavitating flow during water hammer using a generalized interface vaporous cavitation model. J. Fluids Struct. **34**, 190–201 (2012). https://doi.org/10.1016/j.jfluidstructs.2012.05.014
14. Malekpour, A., Karney, B.W.: Profile-Induced column separation and rejoining during rapid pipeline filling. J. Hydraul. Eng. **140**, 1–12 (2014)

MHD Flow of Micropolar Fluid in the Annular Region of Rotating Horizontal Cylinders with Cross Diffusion, Thermophoresis, and Chemical Reaction Effects

G. Nagaraju, S. Shilpa and Anjanna Matta

Abstract The influence of magnetic field, thermophoresis, and the first-order reaction of a dissipative micropolar flow involving two coaxial inner rotating horizontal cylinders are studied both analytically and numerically. The motion of the fluid is generated due to the rotation of the inside cylinder with a constant angular velocity. The internal and external cylinders are kept maintained at different uniform temperatures and concentrations. The transformed systems of differential equations are solved systematically using modified Bessel functions and numerically with the fourth-order Runge–Kutta scheme along with a shooting method. The temperature and concentration are examined for a variety of parameters which govern the flow through graphical illustrations. The results obtained are in very good agreement with benchmark solutions for a particular case.

Keywords MHD flow · Micropolar fluid · Hyper-stick condition · Soret parameter · Chemical reaction

1 Introduction

The studies of fluid involving two horizontal cylinders through inner rotating walls have received the topic of a vast interest for its significance as an idealization of numerous industrial applications. In the design of cooling systems for electric

G. Nagaraju
Department of Mathematics, GITAM, Hyderabad Campus, Rudraram, Medak 502329, Telangana, India

S. Shilpa (✉)
Department of Mathematics, BVRIT Narsapur, Narsapur 502313, Telangana, India
e-mail: msc009_shilpa@yahoo.com

A. Matta
Department of Mathematics, ICFAI Foundation for Higher Education, Hyderabad 501203, Telangana, India

D. Srinivasacharya and K. S. Reddy (eds.), *Numerical Heat Transfer and Fluid Flow*, Lecture Notes in Mechanical Engineering,
https://doi.org/10.1007/978-981-13-1903-7_46

machines, information of such fluid flow is desired to limit the rotor temperature to less than the highest permitted value. Besides other applications in drilling, rotating machinery, swirl nozzles, porous bearings, the ballistics of projectiles with spin and electrical motors [1] and combustion chambers. Richard et al. [2] investigated the viscous flow through the annular gap between vertical concentric cylinders with the internal rotation and an imposed axial pressure gradient. The problem of non-Newtonian fluid flow between two coaxial cylinders has been studied by different authors [3–5]. The magnetohydrodynamic (MHD) study has received more interest for its broad range of industrial applications in geophysics, MHD pumps, fire engineering, the extraction of geothermal energy, nuclear reactors. The MHD flow of viscous fluid through coaxial cylinders was examined by many researchers [6–10]. The Soret effect (thermophoresis) mass flux through a temperature gradient is ignored in many cases related to cross diffusions due to a lower order magnitude than the properties given by Fick's and Fourier law. Eringen [11] initiated the theory of micropolar fluids, in which the fluid molecules can experience microrotation. This theory allows two independent vectors, velocity and microrotation vectors for each fluid particle. Micropolar fluid can exhibit couple stresses in addition to the usual stresses and can have micro-inertia. These fluids consist of elongated molecules such as polymeric fluids, Ferrofluid, liquid crystals, bubbly liquids, animal blood, etc. Comprehensive list of studies on micropolar fluids can be seen in [12–15]. Very recently Gajjela et al. [16] studied Soret, Dufour, and chemical reaction effects in the magnetized micropolar rotating annular flow.

The main of the current work is investigating the double-diffusive micropolar flow through the rotating annular region between two horizontal coaxial cylinders.

2 Problem Statement

The geometry of the problem under this study is steady, incompressible, and unidirectional (see Fig. 1); therefore the axial and radial velocity components are functions of radial distance r only. A uniform magnetic field B_0 is working in Z-direction. The internal and external cylinders are kept at temperatures T_1 and $T_{2,}$ concentrations C_1 and $C_{2,}$ respectively. Additionally, the Soret effect with first-order chemical reaction is considered. Under the above hypothesis, the governing flow equations for an incompressible magnetized micropolar fluid in the annular region are as follows:

$$\frac{\mathrm{d}P}{\mathrm{d}R} = \rho \frac{V^2}{R} \tag{1}$$

$$-\kappa \frac{\mathrm{d}N_1}{\mathrm{d}R} + (\mu + \kappa)\left(\frac{\mathrm{d}^2 V}{\mathrm{d}R^2} + \frac{1}{R}\frac{\mathrm{d}V}{\mathrm{d}R} - \frac{V}{R^2}\right) - \sigma B_0^2 V = 0 \tag{2}$$

$$-2\kappa N_1 + \kappa\left(\frac{\mathrm{d}V}{\mathrm{d}R} + \frac{V}{R}\right) + \gamma\left(\frac{\mathrm{d}^2 N_1}{\mathrm{d}R^2} + \frac{1}{R}\frac{\mathrm{d}N_1}{\mathrm{d}R}\right) = 0 \tag{3}$$

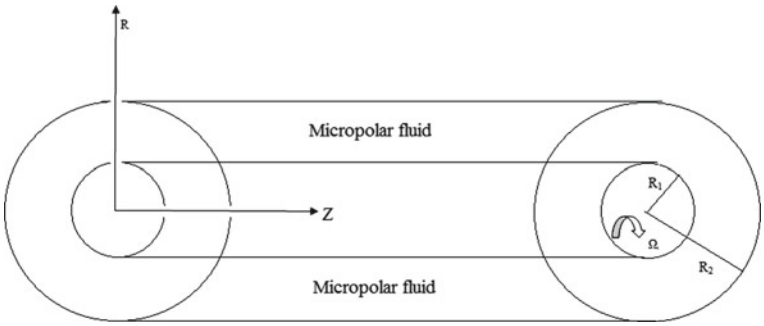

Fig. 1 Physical diagram of the concentric inner rotating annulus

$$\alpha\left(\frac{\mathrm{d}^2T}{\mathrm{d}R^2}+\frac{1}{R}\frac{\mathrm{d}T}{\mathrm{d}R}\right)+\mu\left(\frac{\mathrm{d}V}{\mathrm{d}R}-\frac{V}{R}\right)^2+4\kappa\left(\frac{1}{2}\left(\frac{\mathrm{d}V}{\mathrm{d}R}+\frac{V}{R}\right)-N_1\right)^2+\beta\left(\frac{\mathrm{d}N_1}{\mathrm{d}R}\right)^2=0 \tag{4}$$

$$D\left(\frac{\mathrm{d}^2C}{\mathrm{d}R^2}+\frac{1}{R}\frac{\mathrm{d}C}{\mathrm{d}R}\right)+\frac{DK_T}{T_m}\left(\frac{\mathrm{d}^2T}{\mathrm{d}R^2}+\frac{1}{R}\frac{\mathrm{d}T}{\mathrm{d}R}\right)-k_1C=0 \tag{5}$$

The boundary conditions considering for internal and external cylinders are taken as follows:

$$\begin{aligned}&\text{(i)}\quad V=R\Omega, N_1=\Omega, T=T_1, C=C_1 \text{ at } R=R_1 \quad \text{and}\\ &\text{(ii)}\quad V=0, N_1=0, T=T_2, C=C_2 \text{ at } R=R_2\end{aligned} \tag{6}$$

We introduce the following nondimensional scheme:

$$\begin{aligned}&V=vR_1\Omega, R=rR_2, \quad N_1=N\Omega, \quad R_1=\eta R_2, \quad P=p\rho\Omega^2R_1^2,\\ &T=\theta(T_1-T_2)+T_2, \quad C=\phi(C_1-C_2)+C_2\end{aligned}$$

The basic equations together with boundary conditions are given in the nondimensional form:

$$\frac{\mathrm{d}p}{\mathrm{d}r}=\frac{v^2}{r} \tag{7}$$

$$-\frac{c}{\eta}\frac{\mathrm{d}N}{\mathrm{d}r}+\left(\frac{\mathrm{d}^2v}{\mathrm{d}r^2}+\frac{1}{r}\frac{\mathrm{d}v}{\mathrm{d}r}-\frac{v}{r^2}\right)-Ha^2(1-\eta)^{-2}v=0 \tag{8}$$

$$-2sN+s\eta\left(\frac{\mathrm{d}v}{\mathrm{d}r}+\frac{v}{r}\right)+\left(\frac{\mathrm{d}^2N}{\mathrm{d}r^2}+\frac{1}{r}\frac{\mathrm{d}N}{\mathrm{d}r}\right)=0 \tag{9}$$

$$\frac{\mathrm{d}^2\theta}{\mathrm{d}r^2}+\frac{1}{r}\frac{\mathrm{d}\theta}{\mathrm{d}r}+EcPr\left[\left(\frac{\mathrm{d}v}{\mathrm{d}r}-\frac{v}{r}\right)^2+\frac{4c}{1-c}\left(\frac{1}{2}\left(\frac{\mathrm{d}v}{\mathrm{d}r}+\frac{v}{r}\right)-\frac{N}{\eta}\right)^2+\delta\left(\frac{\mathrm{d}N}{\mathrm{d}r}\right)^2\right]=0 \tag{10}$$

$$\left(\frac{\mathrm{d}^2\phi}{\mathrm{d}r^2}+\frac{1}{r}\frac{\mathrm{d}\phi}{\mathrm{d}r}\right)+\mathrm{ScSr}\left(\frac{\mathrm{d}^2\theta}{\mathrm{d}r^2}+\frac{1}{r}\frac{\mathrm{d}\theta}{\mathrm{d}r}\right)-(K_1+Cr\phi)=0 \tag{11}$$

$$(i)\quad v=N=\theta=\phi=1 \text{ at } r=\eta \text{ and}$$

$$(ii)\quad v=N=\theta=\phi=0 \text{ at } r=1 \tag{12}$$

Coupling number c, Hartmann number Ha, couple stress parameter s, couple stress parameter δ, Eckert number Ec, Prandtl number Pr, Schmidt number Sc, chemical reaction parameter Cr, Soret number Sr, and modified Reynolds number Re are given by

$$c=\frac{\kappa}{\kappa+\mu},\ Ha=B_0(R_2-R_1)\sqrt{\frac{\sigma}{\mu+\kappa}},\ s=\frac{\kappa R_2^2}{\gamma},\ \delta=\frac{\beta}{\mu R_1^2},$$

$$Ec=\frac{\Omega R_1^2}{\upsilon c_p(T_1-T_2)},\ Pr=\frac{\upsilon}{\alpha},\ Sc=\frac{\upsilon}{D},\ Cr=\frac{k_1R_1^2}{D},\ K_1=\frac{C_2R_2^2}{D(C_1-C_2)},$$

$$Sr=\frac{DK_T(T_1-T_2)}{\upsilon T_m(C_1-C_2)},\ \text{and}\ Re=\frac{\rho\Omega R_1^2}{\mu+\kappa}$$

The dimensionless coefficient of skin-friction, Nusselt as well as Sherwood numbers are taken as

$$C_f=\frac{2\eta}{Re}\left(\frac{\mathrm{d}v}{\mathrm{d}r}-(1-c)\frac{v}{r}-\frac{c}{\eta}N\right),\ Nu=-\eta\frac{\mathrm{d}\theta}{\mathrm{d}r}\text{and}$$

$$Sh=-\eta\frac{\mathrm{d}\phi}{\mathrm{d}r}\text{at } r=\eta \text{ and } r=1 \tag{13}$$

Eliminating $\frac{\mathrm{d}N}{\mathrm{d}r}$ from Eqs. (8) and (9), we get the subsequent equation for v as

$$D^4v-\left(Ha^2(1-\eta)^{-2}+(2-c)s\right)D^2v+2sHa^2(1-\eta)^{-2}v=0 \tag{14}$$

which can be expressed as $\left(D^2-\lambda_1^2\right)\left(D^2-\lambda_2^2\right)v=0$

Where $D^2=\frac{\mathrm{d}^2}{\mathrm{d}r^2}+\frac{1}{r}\frac{\mathrm{d}}{\mathrm{d}r}-\frac{1}{r^2}$, $\lambda_1^2+\lambda_2^2=Ha^2(1-\eta)^{-2}+(2-c)s$ and $\lambda_1^2\lambda_2^2=2sHa^2(1-\eta)^{-2}$

The velocity v *is* finite in $\eta<r<1$, the solution of Eq. (14) can be taken as

$$v=a_1I_1(\lambda_1r)+a_2K_1(\lambda_1r)+a_3I_1(\lambda_2r)+a_4K_1(\lambda_2r) \tag{15}$$

The constants a_1, a_2, a_3, a_4 could be established by using the no-slip condition on v and hyper-stick condition on microrotation N.

Table 1 Comparison of test results of variation of velocity (v), temperature (θ), concentration (φ) for 'r' at $c = 0.4$, $s = 1.4$, and $\eta = 0.2$

r	Velocity (v)		Temperature (θ)		Concentration (φ)	
	Analytical	Numerical	Analytical	Numerical	Analytical	Numerical
$Ha = 2$						
0.25	0.79195	0.79195	1.10798	1.10798	0.811847	0.811847
0.3	0.649151	0.649151	1.11272	1.11272	0.675011	0.675011
0.4	0.461357	0.461357	0.994953	0.994953	0.482536	0.482536
0.5	0.338812	0.338812	0.818814	0.818814	0.349045	0.349045
0.6	0.248304	0.248304	0.63352	0.63352	0.248315	0.248315
$Ha = 4$						
0.25	0.703419	0.703419	1.15253	1.15253	0.80803	0.80803
0.3	0.514152	0.514152	1.16249	1.16249	0.672217	0.672217
0.4	0.296583	0.296583	1.02669	1.02669	0.483103	0.483103
0.5	0.183414	0.183414	0.851523	0.851523	0.35142	0.35142
0.6	0.118527	0.118527	0.634307	0.634307	0.251352	0.251352

3 Numerical Method for Solution

The coupled collection of nonlinear differential Eqs. (8)–(11) with boundary conditions (12) formed a boundary value problem of second order and it is solved by a shooting with Runge–Kutta scheme through an initial value problem.

4 Comparison of Analytical and Numerical Solutions

To test the accuracy of shooting method calculations, the outcomes of v, θ, φ, Cf, Nu, and Sh profiles in Tables 1, 2 and 3 are compared by the analytical solutions. It is precisely seen from Tables 1, 2 and 3 that the results are smart admirable agreement. It shows that the efficiency concerning the numerical solutions is excellent for the analytical and numerical computations of v, θ, and φ are close to each other.

5 Results and Discussions

On the way to understand the behavior of the fluid characteristics, velocity (v), microrotation (N), temperature (θ), and concentration (ϕ) are calculated for different parameters like aspect ratio, Hartmann number, coupling number, Prandtl number, Eckert number, Schmidt number, Soret, and first-order reaction parameter. The influence of Hartmann number (Ha) on v and N are presented in Fig. 2a, b. Hartmann

Table 2 Comparison of test results of skin-friction coefficients at $c = 0.4$, $s = 1.5$, $\eta = 0.2$, Ha = 4

		Analytical results		Numerical results	
c	Re	Cf (η)	Cf (1)	Cf (η)	Cf (1)
0.2	100	0.0416478	0.00053881	0.0416478	0.00053881
0.4	100	0.0300744	0.000643984	0.0300744	0.000643984
0.6	100	0.0192766	0.000588999	0.0192766	0.000588999
0.5	200	0.0122893	0.000318244	0.0122893	0.000318244
0.5	300	0.00819888	0.000212163	0.00819888	0.000212163
0.5	400	0.00614466	0.000159122	0.00614466	0.000159122

Table 3 Validation of test results of heat and mass transfer coefficients at $c = 0.4$, $s = 1.5$, $\eta = 0.2$, $\delta = 0.05$, $k1 = 0.1$, Ha = 4

Ec	Pr	Sc	Sr	Cr	Analytical results				Numerical results			
					Nu (η)	Nu (1)	Sh (η)	Sh (1)	Nu (η)	Nu (1)	Sh (η)	Sh (1)
0.25	0.5	0.22	0.5	0.25	0.1690	0.178	0.6972	0.1062	0.1699	0.1781	0.6982	0.1082
0.5	0.5	0.22	0.5	0.25	0.2811	0.2313	0.7475	0.1014	0.2814	0.2318	0.7475	0.1024
0.5	**0.75**	0.22	0.5	0.25	0.7322	0.2853	0.7963	0.0963	0.7328	0.2856	0.7967	0.0966
0.5	0.5	**0.66**	0.5	0.25	0.2813	0.2310	0.9441	0.0790	0.2811	0.2318	0.9446	0.0792
0.5	0.5	0.22	**1.5**	0.25	0.2811	0.2312	0.9442	0.0796	0.2812	0.2319	0.9446	0.0792
0.5	0.5	0.22	0.5	**0.35**	0.2812	0.2311	0.7521	0.1011	0.2813	0.2318	0.7529	0.1012

The number in bold indicates the different values of parameters

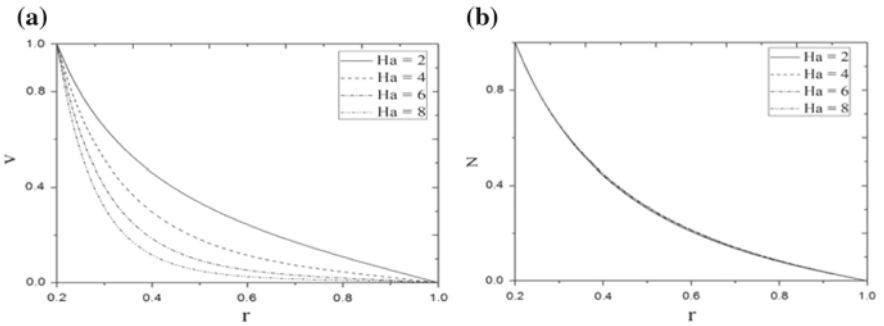

Fig. 2 **a**, **b** Effect of Hartmann number on velocity v, microrotation N for $c = 0.4$, $s = 1.5$, $\eta = 0.2$

number for flow profiles characterizes the proportion of electromagnetic force to viscous force. Presently, it is a well-recognized case that the magnetic field allows a damping reaction on velocity through generating drag force that resists the motion, lead to velocity decrease. The effect of Ha on micro-rotation (N) is insignificant for small values of Ha < 10. Figure 3a, b displays the control of coupling number (c) on v and N, is given for stipulated values of alternative parameters. The coupling

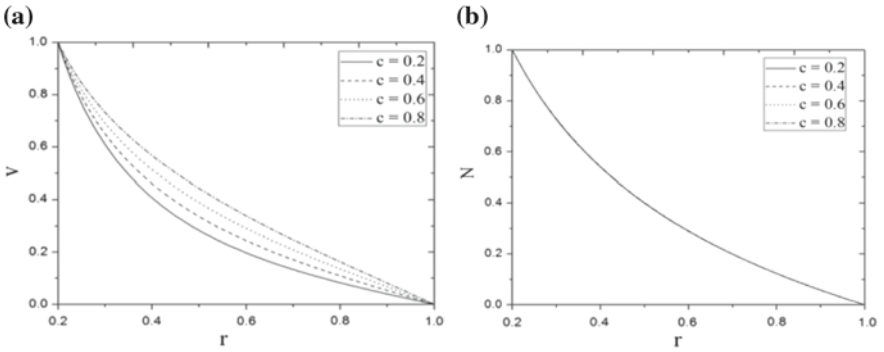

Fig. 3 **a**, **b** Effect of Coupling number on velocity (v), microrotation (N) for Ha $= 4$, $s = 1.5$, $\eta = 0.2$

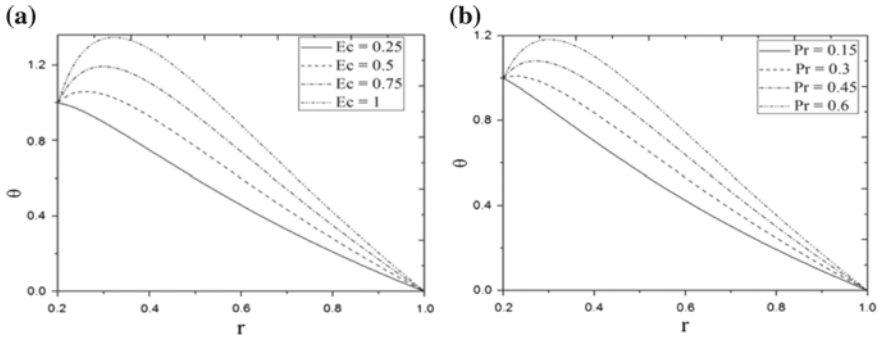

Fig. 4 **a**, **b** Effect of Eckert number (Ec) and Prandtl number (Pr) on temperature (θ) for $s = 1.5$, Ha $= 4$, $c = 0.5$, $\eta = 0.2$, Ec $= 0.5$, $\delta = 0.05$, Pr $= 0.7$

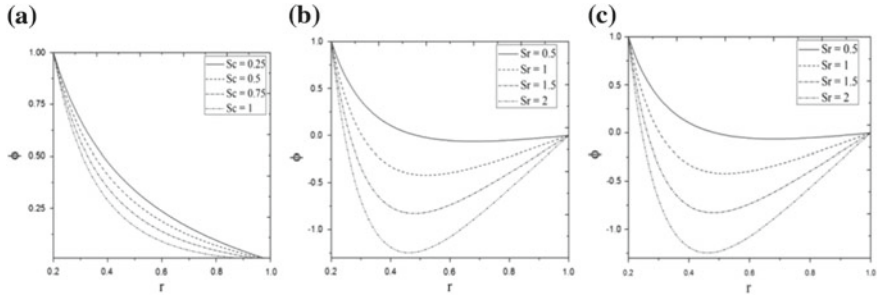

Fig. 5 **a**, **b**, **c** Effect of Schmidt number (Sc), Soret parameter (Sr), and chemical reaction parameter (Cr) on concentration (ϕ) for $s = 1.5$, Ha $= 4$, $c = 0.5$, $\eta = 0.2$, Ec $= 0.5$, $\delta = 0.05$, Pr $= 0.7$, $K_1 = 0.1$

number (c) describes the combination of rotational and linear movement originating from the micro-motion of the flow particles. Therefore, c represents the coupling

involving the rotational Newtonian viscosities. It is clear that in presence of c, tangential velocity profiles increase. The flow velocity in case of micropolar fluid has fewer analyses toward Newtonian fluid. The increasing values of c have an insignificant effect on microrotation (N). The rise in temperature profiles due to enhancing of the Eckert number and Prandtl number is observed in Fig. 4a, b. The response of Schmidt number (Sc), Soret number (Sr), and chemical reaction parameter (Cr) on φ for constant values of various alternative parameters are shown in Fig. 5a–c. Figure 5a shows the increase in Schmidt number increases the concentration. The Soret parameter indicates the contribution of the temperature gradient to the mass flux in the fluid flow. Figure 5b displays that the rise in Sr decelerates the concentration. Figure 5c displays the responses of chemical reaction (Cr) on dimensionless concentration φ. The concentration (φ) decelerate as Cr increases. Large values of Cr amount to a decrease in molecular diffusivity, i.e., small diffusion. Hence, the rise in Cr will suppress species concentration.

6 Conclusions

The following specific conclusions were derived from the above study:

1. The fluid velocity increases with the rise in coupling number; and is pragmatic to decelerate with an increase in Hartmann number.
2. The temperature of the fluid increases with the enhancement in Prandtl and Eckert numbers.
3. The concentrations of the fluid decelerate with the rise in Schmidt number, Soret, and reaction parameters.
4. The numerical (shooting) results are in excellent agreement with analytical solutions.

References

1. Maron, D.M., Cohen, S.: Hydrodynamics and heat/mass transfer near rotating surfaces. Adv. Heat Transf. **21**, 141–183 (1991)
2. Richard, M.L., Andreas, D., Kyungyoon, M.: Stability of axial flow in an annulus with a rotating inner cylinder. Phys. Fluids **4**, 2446 (1992)
3. Maia, M.C.A., Gasparetto, C.A.: A numerical solution for entrance region of non-Newtonian flow in annuli. Braz. J. Chem. Eng. **20**, 201–211 (2003)
4. Ravanchi, M.T., Mirzazadeh, M., Rashidi, F.: Flow of Giesekus viscoelastic fluid in a concentric annulus with inner cylinder rotation. Int. J. Heat Fluid Flow **28**, 838–845 (2007)
5. Kumari, M., Nath, G.: Unsteady natural convection from a horizontal annulus filled with a porous medium. Int. J. Heat Mass Transf. **51**, 5001–5007 (2008)
6. Omid, M., Shohel, M., Pop, I.: Analysis of first and second laws of thermodynamics between two isothermal cylinders with relative rotation in the presence of MHD flow. Int. J. Heat Mass Transf. **55**, 4808–4816 (2012)

7. Sofiane, A., Mourad, M., Malika, I., Abderahmane, G.: Effect of magnetic field on the heat and mass transfer in a rotating horizontal annulus. In: Proceedings of the International Conference on Heat Transfer and Fluid Flow Prague 2014, vol. 67, pp. 1–9, Czech Republic (2014)
8. Mohsen, S., Shirley, A.: Two-phase simulation of nanofluid flow and heat transfer in an annulus in the presence of an axial magnetic field. IEEE Trans. Nanotechnol. **14**(3), 561–569 (2015)
9. Srinivas, J., Nagaraju, G., Beg, O.A.: Mathematical modeling of entropy generation in magnetized micropolar flow between co-rotating cylinders with internal heat generation. Alexandria Eng. J. **55**, 1969–1982 (2016)
10. Eringen, A.C.: The theory of micropolar fluids. J. Math. Mech. **16**, 1–18 (1966)
11. Ariman, T., Cakmak, A.S., Hill, L.R.: Flow of micropolar fluids between two concentric cylinders. Phys. Fluids **10**, 2545–2550 (1967)
12. Ramkissoon, H., Majumdar, S.R.: Unsteady flow of a micropolar fluid between two concentric circular cylinders. Can. J. Chem. Eng. **55**, 408–413 (1977)
13. Aparna, P., Ramana Murthy, J.V.: Uniform flow of an incompressible micropolar fluid past a permeable sphere. IEEMS **8**, 1–10 (2010)
14. Ramanamurthy, J.V., Nagaraju, G., Muthu, P.: Micropolar fluid flow generated by a circular cylinder subject to longitudinal and torsional oscillations with suction/injection. Tamkang J. Math. **43**(3), 339–356 (2012)
15. Nagaraju, G., Kaladhar, K., Sai, K.S.: Magnetohydrodynamic effect on rotating free surface flow of micropolar fluid in a cylindrical container with porous lining. Int. J. Dyn. Syst. Differ. Equ. **5**(3), 191–205 (2015)
16. Nagaraju, G., Anjanna, M., Kaladhar, K.: The effects of Soret and Dufour, chemical reaction, Hall and ion currents on magnetized micropolar flow through co-rotating cylinders. AIP Adv. **7**(115201), 1–16 (2017)

Numerical and CFD Analysis of Joints in Flow-Through Pipe

Rupesh G. Telrandhe and Ashish Choube

Abstract The present work is aimed at performing experimental, CFD, and mathematical investigations on the fluid flow and the flow characteristics of the fluid (water) through gradual expansion and gradual contraction joint of pipes. Head loss suffered by the flow after passing through Gradual Contraction and Gradual Expansion junction and to study the reliability of the classical engineering formulas, and to find the head loss for gradual contraction and gradual expansion junction of pipes were used. In this, we have compared our results with CFD software packages with classical formula and made an attempt to determine optimum cone angle. The experimentation is also carried out for measurement of pressure and further, the CFD result is compared with experimentation. In this work, the CFD software is used to simulate the flow at gradual contraction and gradual expansion junction of pipe with FLUENT and observed flow properties inside the junction and analyzed the head loss suffered by fluid flow after passing through the gradual contraction and gradual expansion junction. One of the purposes of this study is also to study the change in pressure loss with change in a cone angle of gradual contraction and gradual expansion junction and to find out an optimum cone angle.

Keywords Pipe · Gambit · Fluent · CFD

1 Introduction

Pipe networks are mainly used for transportation and supply of fluids and gases. These networks vary from fewer pipes to thousands of pipes (e.g., water supply network of

R. G. Telrandhe (✉)
Department of Mechanical Engineering, Datta Meghe Institute
of Engineering, Technology & Research, Wardha 442001, Maharashtra, India
e-mail: telrandherupesh@gmail.com

A. Choube
Department of Mechanical Engineering, Jawaharlal Darda Institute
of Engineering and Technology, Yavatmal 445001, Maharashtra, India

D. Srinivasacharya and K. S. Reddy (eds.), *Numerical Heat Transfer and Fluid Flow*, Lecture Notes in Mechanical Engineering,
https://doi.org/10.1007/978-981-13-1903-7_47

Fig. 1 Water distribution in industries

a large city, see in Fig. 1). In addition to pipes, the network also consists of elbows, T-junctions, bends, contractions, expansions, valves, meters, pumps, turbines, and many other components. All these components cause a loss in pressure due to change in momentum of the flow caused due to friction and pipe components. This means conversion of flow energy into heat due to friction or energy lost due to turbulence.

Pipe networks are very common in industries, where fluid or gases are to be transported from one location to the other. The head loss (pressure loss) may vary depending on the type of components occurring in the network, material of the pipe, and the type of fluid transported through the network. In industries, the networks are usually large and require very precise pressure at certain points of the network. It is also sometimes essential to place valves, pumps, or turbines of a certain capacity to control the pressure in the network. The placement of valves, pumps, and turbines is important to overcome pressure loses caused by other components in the network. This is one of the important reasons why this study was conducted.

2 Experimental Setup and Operating Procedure

The design and fabrication of the experimental setup used to generate the sufficient data to measure the heat loss and the fluid flow characteristics at different pressure for gradual contraction and gradual expansion joints through circular Pipe. Extensive data was generated by varying different parameters over wide ranges. This experimentation was carried out in the fluid mechanics laboratory of the institute.

Fig. 2 Experimental setup

2.1 Experimental Setup

The schematic of the experimental setup used for the present investigation is shown Fig. 2. The setup consisted of the following components

(1) PVC Pipes
(2) Water tanks
(3) Centrifugal pump (0.5 Hp)
(4) Stop Watch
(5) Pressure Gauges
(6) Discharged measuring device.

A schematic of the experimental setup is shown in Fig. 2. It consists of a long PVC pipe connected to the centrifugal pump, for the circulation of water through the pipe. In order to measure discharge at different pressures, a pressure gauge of range 0–100 kg/cm^2 has been used. The gradual contraction joint with the ratio of 2 and 1.3 and gradual expansion joint with the ratio of 1.5 and 2 has been taken into consideration to measure the heat loss at these ratios and find out optimum cone angle.

2.2 Operating Procedure

Adjust the pipe at the desired height.

Set the water tank on the adjustable stand.

Fill the water tank.

Adjust discharge measuring tank at the outlet.

Placed the flow regulator valve on the certain distance before and after gradual contraction and gradual expansion joint of pipe.

Switch on the power supply.

Table 1 Experimental results of gradual expansion ratio = 1.5

Inlet pressure	Discharge (Q)	Inlet velocity	Outlet velocity	Head loss ($h_L = k(v_1^2/2\ g)10^{-5}$)					
P_1	ml/min	v_1 (m/sec)	v_2 (m/sec)	600	400	300	200	150	100
10	170	0.023	0.01	1.56	1.29	1.05	0.67	0.35	0.17
15	142	0.019	0.0085	1.06	0.88	0.71	0.45	0.23	0.12
20	106	0.014	0.0063	0.58	0.48	0.4	0.25	0.13	0.07
25	100	0.013	0.006	0.5	0.41	0.34	0.22	0.11	0.06
30	68	0.009	0.0041	0.24	0.2	0.16	0.1	0.053	0.03

Table 2 Experimental results of gradual contraction ratio = 2

Inlet pressure	Discharge (Q)	Inlet velocity	Outlet velocity	Head loss ($h_L = k(v_1^2/2\ g)10^{-5}$)						
P_1	ml/min	v_1 (m/sec)	v_2 (m/sec)	1500	1200	1050	900	760	500–600	150–400
10	120	0.004	0.016	0.45	0.34	0.28	0.22	0.16	0.08	0.052
15	100	0.0033	0.013	0.298	0.29	0.2	0.15	0.11	0.051	0.034
20	90	0.003	0.012	0.25	0.19	0.16	0.12	0.09	0.04	0.02
25	70	0.023	0.009	0.14	0.11	0.091	0.07	0.05	0.02	0.016

While taking the reading for gradual contraction joint keep the gradual expansion joint closed and vice versa.

Measure the discharge 'Q' for 60 s at different inlet pressures, i.e., on 10, 15, 20, 25, and 30 kg/cm^2 for gradual contraction and expansion joint.

3 Results and Discussion

3.1 Experimental Results

The followings results are obtained after conducting the experiment for different pressure and different diameter ratios of gradual contraction and gradual expansion joint of pipe (Tables 1 and 2).

Case 1. Gradual Expansion Ratio = 1.5, Inlet Pipe Diameter (d_1) = 12.5 mm, Outlet Pipe Diameter (d_2) = 18.75 mm, Length = 1 m.

Case 2. Gradual Contraction Ratio = 2, Inlet Pipe Diameter (d_1) = 25 mm, Outlet Pipe Diameter (d_2) = 12.5 mm, Length = 1 m.

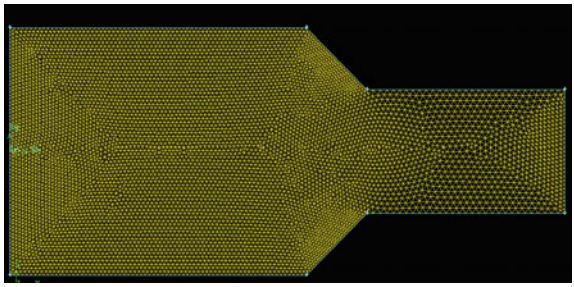

Fig. 3 Gradual contraction joint

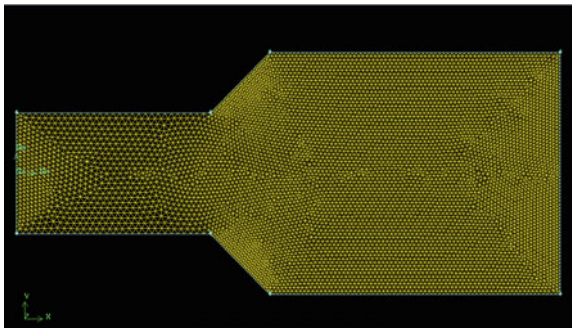

Fig. 4 Gradual expansion joint

4 CFD Analysis

CFD is concerned with the study of fluid flow problems using computational techniques, as opposed to analytical or experimental methods. For this particular geometry and problem, GAMBIT and FLUENT software were used to analyze the flow. Gambit is a Geometry and Mesh Building Intelligent Toolkit. It is a preprocessing unit in which create a geometry. FLUENT is the general name for the collection of Computational Fluid Dynamics (CFD) programs.

4.1 Modeling Details

The gradual expansion joint and gradual contraction joints are represented in 2D. The joint geometries of gradual expansion and contraction are displayed in Figs. 3 and 4.

The geometry and mesh consists of a joint of various dimension created by joining the coordinates. There are some boundary conditions applied for the above geometry like velocity inlet and pressure outlet and fixed wall with no-slip condition.

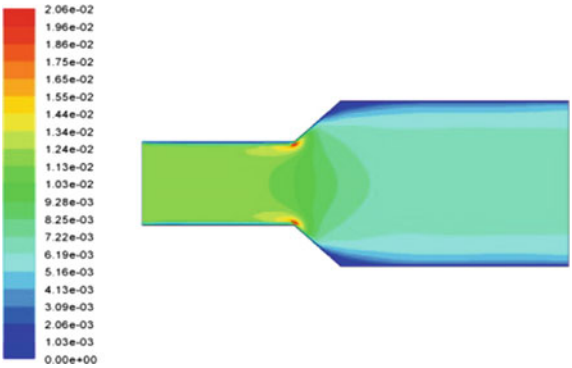

Fig. 5 Velocity contours for gradual expansion ratio = 1.5

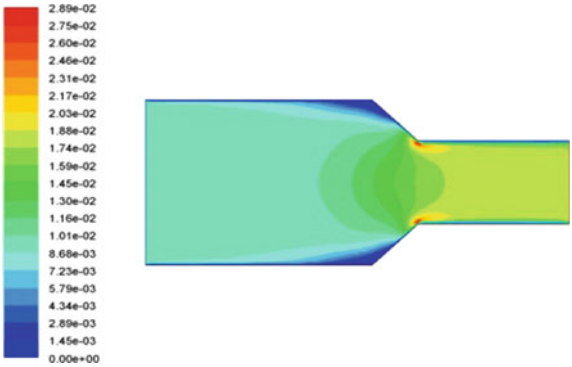

Fig. 6 Velocity contours for gradual contraction ratio = 2

4.2 Post-processing

This section consists of the final steps of FLUENT, which contains the results to be plot and shows the various contours of a pipe.

Figure 5 shows the Contour of velocity of flow of pipe having inlet diameter 12.5 mm & outlet diameter 25 mm. The color contours shows that how the velocity gets decrease at the entrance edges of expandable pipe due to which velocity loss occurred in pipe.

Figure 6 shows the contour of velocity of flow of pipe having inlet diameter 12.5 mm and outlet diameter 25 mm. The color contours show that how the velocity gets increased at the entrance edges of expandable pipe due to which velocity loss occurred in pipe. The details of velocity losses in pipe are quoted in Table 3.

Table 3 Case 1: comparison of the CFD results with the experimental results

Gradual expansion ratio = 1.5					
Inlet pressure	Discharge (Q)	Inlet velocity	Outlet velocity	CFD result	% Error
P_1	ml/min	v_1 (m/sec)	Exp. result v_2 (m/sec)	v_2 (m/sec)	
10	170	0.023	0.01	0.0059	0.41
15	142	0.019	0.0085	0.0049	0.36
20	106	0.014	0.0063	0.0039	0.24
25	100	0.013	0.006	0.0034	0.26
30	68	0.009	0.0041	0.0019	0.22

5 Comparison of the CFD Results with the Experimental Results

The following comparative results were obtained after conducting the experimentation and CFD analysis for different pressure and different diameter ratio of gradual contraction and gradual expansion joint of pipe. The following Table 3 shows the comparative results.

Case 1 Gradual Expansion Ratio = 1.5, Inlet Pipe Diameter (d_1) = 12.5 mm, Outlet Pipe Diameter (d_2) = 18.75 mm, Length = 1 m.

Case 2 Gradual Contraction Ratio = 2, Inlet Pipe Diameter (d_1) = 25 mm, Outlet Pipe Diameter (d_2) = 12.5 mm, Length = 1 m.

6 Conclusion

The main conclusions of the present work are as follows:

1. The velocity of water flow is strongly influenced by gradual contraction and gradual expansion joint of pipe.
2. The head loss can be decreased by decreasing the cone angle of gradual expansion and gradual contraction joint of pipe.
3. In case of gradual expansions joint for the diameter ration of 1.5 and 2 the optimum cone angle would be 100.
4. The experimental results and CFD results have very less percentage of error as shown in Tables 3 and 4.

Table 4 Case 2: comparison of the CFD results with the experimental results

Gradual contraction ratio = 2					
Inlet pressure	Discharge (Q)	Inlet velocity	Outlet Velocity	CFD result	% Error
P_1	ml/min	v_1 (m/sec)	Exp. result v_2 (m/sec)	v_2 (m/sec)	
10	120	0.004	0.016	0.015	0.01
15	100	0.0033	0.013	0.013	0
20	90	0.003	0.012	0.01	0.02
25	70	0.023	0.009	0.008	0.01

References

1. Roy, V., Majumder, S., Sanyal, D.: Analysis of the turbulent fluid flow in an axi-symmetric sudden expansion. Int. J. Eng. Sci. Technol. **2**(6), 1569–1574 (2010)
2. Florescu, I., Florescu, D., Nedelcu, D.I.: Study about the fluid losses in the branching pipes. Proc. Manuf. Syst. **7**(4) (2012)
3. Satish, G., Ashok Kumar, K., VaraPrasad, V., Pasha, Sk.M.: Comparison of flow analysis of a sudden and gradual change of pipe diameter using fluent software. Int. J. Res. Eng. Technol. **02**(12) (2013)
4. Mandal, D.K., Bandyopadhyay, S., Chakrabarti, S.: A numerical study on the flow through a plane symmetric sudden expansion With a fence viewed as a diffuser. Int. J. Eng. Sci. Technol. **3**(8), 210–233 (2011)
5. Narayane, A.V., Pathade, V.C., Telrandhe, R.: CFD analysis of water flow through gradual contraction joint. Int. J. Eng. Res. Technol. (IJERT) **3**(6) (2014). ISSN: 2278-0181

2D Numerical Analysis of Natural Convection in Vertical Fins on Horizontal Base

Sunirmal Karmakar and Aurovinda Mohanty

Abstract Natural convection heat transfer from a finned horizontal flat plate at a constant temperature has been studied in this work. It analyzes the fin performance and; natural convection behavior of the finned horizontal flat plate. A complete picture of heat transfer on the horizontal finned surface (temperature and velocity contours) is captured. Then behaviors of multi-number of fins (2, 4, 6, 8, 10 and 12 fins) were analyzed in the current progressed work. The base body is subjected to constant temperature difference from the surrounding $\Delta T = 40$ K for all cases in the laminar range, i.e., Raleigh number $5 < \text{Ra} < 10^8$. The types of plumes caused are pictorially viewed. This work is progressed by comparing the graphical relation between Q (heat transfer) to $S^* = S/L$.

Keywords Natural convection heat transfer · Constant temperature difference Raleigh number · Nusselt number

Nomenclature

A	Area of fins for convection m^2
G	Gravitational acceleration m/s^2
H_b	Height of base surface mm
H_{fin}	Height of the fin mm
h_c	Average heat transfer coefficient W/m^2 K
K	Conductivity of fin apparatus W/m K
L	Length of the cylinder mm
N	Number of fins
Nu	Average Nusselt number

S. Karmakar · A. Mohanty (✉)
Department of Mechanical Engineering, VSSUT, Burla 768017, Odisha, India
e-mail: aurovindam@gmail.com

S. Karmakar
e-mail: skarch1994@rediffmail.com

D. Srinivasacharya and K. S. Reddy (eds.), *Numerical Heat Transfer and Fluid Flow*, Lecture Notes in Mechanical Engineering,
https://doi.org/10.1007/978-981-13-1903-7_48

P	Pressure N/m^2
P_{atm}	Atmospheric pressure N/m^2
Q	Convected heat transfer W
R	Specific gas constant J/kg K
Ra	Raleigh Number
S	Spacing between fins mm
S/L	Nondimensional fin spacing
T	Thickness of the fin mm
T_s	Surface temperature K
T_∞	Ambient temperature K
u, v, w	Velocity components of fluid m/s
x, y, z	Cartesian spatial Coordinates m

Greek Letters

α	Thermal diffusivity m^2/s
β	Thermal expansion coefficient 1/K
ΔT	Temperature difference K
ν	Kinematic viscosity m^2/s
ρ	Density kg/m^3

1 Introduction

Longevity of devices made engineers to come up with the concept of fins. Researchers came up with ideas improving the performance of these fins. This study also deals with the thermal performance of the fins at different condition(s) varying various factors which usually affect the heat transfer rate of the fins. These factors are spacing between the fins; length of the fins; thermal conductivity of the fun apparatus made material; Alignment of the fins; Cross section of fins; temperature of the base surface, etc. Churchill and Chu [1] have developed a general correlation of Nusselt number (Nu) depending on the Raleigh number (Ra) and Prandtl number (Pr). This correlation can be used in both natural convection in laminar and turbulent regime. Leung et al. [2, 3], Sara [4] and Nada [5] encountered that natural convection by horizontal and vertical fin(s); for high range of Ra, heat dissipation Q from a flat surface in a rectangular channel flow by attaching array of staggered pin fins or continuous fins is varied keeping base area constant. And it was experimentally elaborated by modifying the array of such pattern, resulting decrement in clearance with enclosure and fin spacing on a constant base due to which Nusselt number was increased keeping every other factor(s) constant to constrained measures. An empirical relation was developed making Nu depending on C/H [4]. Some authors also gave a slight variation by giving interruption in the fin array resulting drastic changes in natural

convection of fins on a surface. Narasimha et al. [6] explained the compact ratio of fin in an enclosure to its own base surface and the fin performance was stated in pictures. Senapati et al. [7–9] experimented numerically a finned cylinder on wide range of Ra in vertical and horizontal setup and modifying it by applying annular heating and eccentric fin arrangement from the base cylinder axis and correlation is developed to find the optimum spacing and annular displacement. Considering all covered areas of study done before by above authors, this led to addition to the curiosity of fin performance on fins installed on a horizontal base surface. This numerical study has encapsulated the study of vertical fins performance on the horizontal surface on constant temperature surface from the same base with visualized behaviors extracted numerically.

2 Problem Description

On a 2D Rectangular horizontal surface of length L shown in Fig. 1 containing array of vertical fins equidistant to each other is taken for 2D analysis. The length (L) along horizontal axis is about 190 mm with fins of height ($H = 30$ mm) installed of thickness ($t = 3$ mm) with inter-fin spacing as (S). The fin is mounted on a base surface of thickness ($t_{\text{base}} = 30$mm). The fin apparatus is made of aluminum due to higher conductivity of material. The setup is encapsulated in an enclosure of height $5H_{\text{total}}$ and a width of $3L$ filled with air in it. For the enclosure, the behavior of the enclosure fluid is to be Bossenique Approximation. The analysis of the fluid is done in multi-fin of number of fins $n = 2$, 4, 6, 8, 10, 12 and 14. The inter-fin spacing is dependent on the number of fins on a constant horizontal surface. The main task of this project is Nusselt number (Nu) is a function of Raleigh number (Ra), S^* and H^*. Thereafter now, the base body surface is kept at a constant surface temperature (T_S) of 340 K. The operating condition of the enclosure fluid air (T_∞) is 300 K. The pressure at the edge of the enclosure is at P_{atm}. The project is progressed by analyzing the heat transfer of the fin setup on one side of the base body. The mesh contains 35,505 cells with 36,906 nodes when taken in symmetry form and mesh grid is aligned structured and fine to analyze the natural convection with very low skewness of grid of order of 10^{-10}.

2.1 Mathematical Model

For the type of flow around fins in the setup above is within Ra less than 10^8 that is laminar flow and the fluid properties are assumed under Bossenique's Approximation. The governing equation for this flow is listed below.

$$\frac{\partial u}{\partial x} + \frac{\partial v}{\partial y} = 0 \tag{1}$$

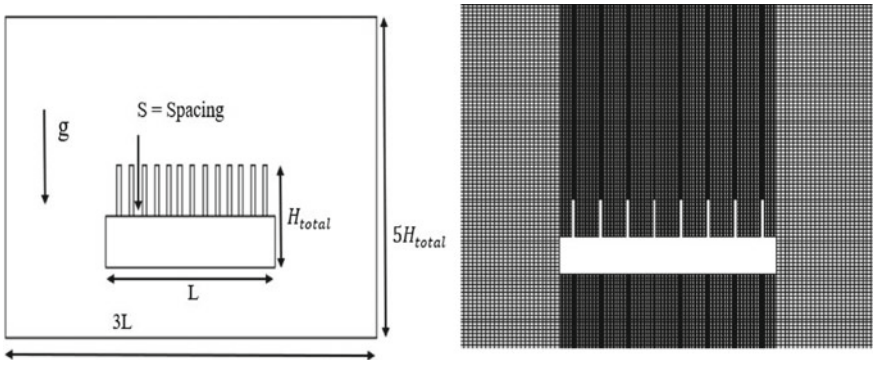

Fig. 1 (Left) Shows the geometrical view of fin setup; (Right) shows the computational grid of analysis of the fin apparatus setup in ANSYS R16

$$u\frac{\partial u}{\partial x} + v\frac{\partial u}{\partial y} = \nu\left(\frac{\partial^2 u}{\partial x^2} + \frac{\partial^2 u}{\partial y^2}\right) \tag{2}$$

$$u\frac{\partial T}{\partial x} + v\frac{\partial T}{\partial y} = \alpha\left(\frac{\partial^2 T}{\partial x^2} + \frac{\partial^2 T}{\partial y^2}\right) \tag{3}$$

$$Q = h_c A \Delta T \tag{4}$$

The above-listed equation(s) is the governing equation while Eq. (1) is continuity equation; Eq. (2) is the NS momentum equation for x-velocity; Eq. (3) is heat equation considering no heat generation and Eq. (4) is the convected heat equation.

Boundary Condition(s).

In the flow around fins, characteristic is found to be steady ($\mathrm{d}/\mathrm{d}t = 0$) no-slip boundary condition on the walls at the fin fluid interface (u, v) = 0. The numerical calculation is assumed to have the density characteristics as flow in Bossenique approximation(s). The flow encountered to be Laminar flow [$\mathrm{Ra} < 10^8$] The apparatus is set to enclosure with ambient pressure: P_{out} The temperature of base body set to $T_s = 340$ K. In a mesh design in Fig. 2 of the setup, fin wall and fin tip are coupled to the base and fluid region. Enclosure fluid temperature: $T_\infty = 300$ K. The equation of steady-state heat transfer in the base body taking no heat generation into account gives the temperature of the base body $\nabla^2 T = 0$. From the geometry perspective, the inter-fin spacing between the fins

$$S = \{L - (nt)\}/n \text{ and } A_{\text{total}} = 2(L + H_{\text{base}}) + 2nH_{\text{fin}}$$

At the interface, the heat conducted by the fin body is the convected heat transfer

$$Q = h_c * A * \Delta T = -k\frac{\mathrm{d}T}{\mathrm{d}x} \tag{5}$$

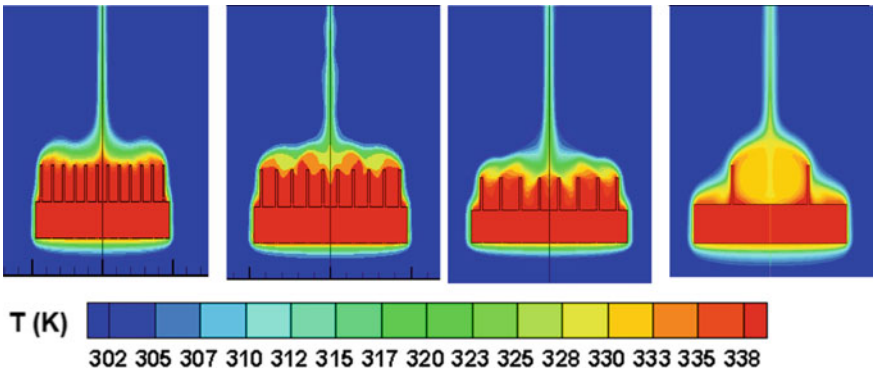

Fig. 2 Shows the temperature contour of 12, 10, 8, and 2 fins

The analysis is carried by nondimensionalizing the equations which rose to various nondimensional numbers. The flow in which regime laminar or turbulent is given by Raleigh number (Ra) where (Ra) $= \frac{\beta * g * \Delta T * H^3}{\alpha \nu}$. In the above analysis, the Raleigh number is less than 10^8 so it is in laminar range of flow condition. Nusselt number helps in knowing whether conduction is dominant on convection phenomenon or the vice versa. Nusselt number is given by (Nu) $= \frac{Q * S}{k * A * (T_s - T_\infty)}$.

Numerical modeling

The governing differential equations were integrated over a control volume and then discretized using the finite volume technique. The resulting algebraic equations were solved by the algebraic multigrid solver of FLUENT R16 in an iterative manner by imposing the boundary conditions. Second-order upwind scheme for the x-momentum, y-momentum, and continuity were considered for the momentum and energy equations. SIMPLE (Semi Implicit Momentum and Pressure Linked Equation) algorithm scheme was used for coupling the pressure and the velocity terms for the pressure correction equation. The relative convergence criterion for the energy equation was set to 10^{-6} and the continuity; x-momentum and y-momentum were set to 10^{-3}. The cells vertical along with fins are made smaller and also the fin till the end of the base body have been made of small cell. It results in very small computation calls near the fins and larger cell away from the fin setup. The case of computation grid for 8 fins is shown in Fig. 2 in the enclosure. The dense cells are in the vertical direction because the variation in heat flux temperature is encultured near the fins in vertical direction.

Analysis Parameters.

During analysis done in FLUENT R16 environment, it is very necessary to converge the solution to find a significant result. To converge it takes a minimum under-relaxation factors for pressure, density, body force, momentum, and energy. Table 1 indicates the set of under-relaxation factors were mostly used in all cases of multi-number fins having cases where $n = 2, 4, 6, 8, 10, 12, 14$.

Table 1 Under-relaxation factors used in FLUENT R16

Pressure	Density	Body force	Momentum	Energy
0.8	1	0.7	0.01	1

Table 2 Quantitative record of heat flux (Q) and S^* (S/L) for different cases of fins

No. of fins	S/L	Q (W)
2	0.4862	51.88
4	0.2342	53.48
6	0.1508	54.14
8	0.1089	54.28
10	0.08421	56.7
12	0.06754	51.62
14	0.05563	48.34

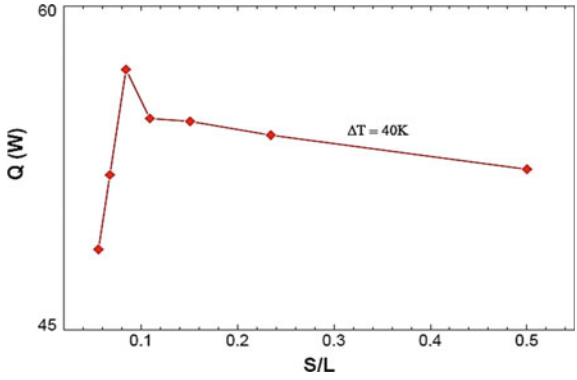

Fig. 3 Graph plotted of Q (heat Flux) and S^* (S/L)

3 Results

On a same base body surface, the number of fins is increased lowering the spacing in different cases. When at constant $\Delta T = 40$ K, less number of fins the heat transfer is low, as the fin number is increased, the heat transfer increases until, it is decreased to optimum spacing. Later if the spacing is decreased further, the heat transfer will decrease again. It is given by the graph in Fig 3 showing the variation of heat transfer with respect to spacing. The records of the heat transfer have been tabulated in Table 2. If observed keenly the contours presented below in Fig. 2, the red region indicated is conduction. It increases with increase in fin number later becomes responsible for less heat transfer (Fig. 3).

By constraining others factors like height, Ra, etc., graphically the optimum number of fins for this case is obtained to be 10 fins with a heat transfer of 56.7 W. 12 and 14 fins decrease the heat transfer from the base surface according to the information extracted from the graph.

4 Conclusion

The heat transfer first increases with the more fins and decreases with further added fins. The visualization of the temperature contour can make the reader know the behavior of the temperature distribution. It deduces the *S*/*L* (opt) among these cases is 0.08421. These fins performance can be tested when installed on both sides and different alignments and can be used in plate heat exchangers used in different thermodynamic cycles. This can be used as heat dissipation mechanism from ducts of large sides acting as horizontal base.

References

1. Churchill, S.W., Chu, H.H.S.: Correlating equation of laminar and turbulent flow in natural convection in vertical plates. Int. J. Heat Mass Transf. **18**, 1323–1329 (1975)
2. Leung, C.W., Probert, S.D., Shilston, M.J.: Heat exchanger design: optimal uniform separation between rectangular fins protruding from a rectangular base. Appl. Energy **19**, 287–299 (1985)
3. Leung, C.W., Probert, S.D., Shilston, M.J.: Heat exchanger design: thermal performance of rectangular fins protruding from a vertical or horizontal base. Appl. Energy **20**, 123–140 (1985)
4. Sara, O.N.: Performance Analysis of rectangular ducts with ducts with staggered pin fin. Energy Conserv. Manage. **44**, 1787–1803 (2003)
5. Nada, S.A.: Natural convection heat transfer in horizontal and vertical closed narrow enclosure with heated rectangular fin base plate. Int. J. Heat Mass Transf. **50**, 667–679 (2007)
6. Narasimha, S., Majdalani, J.: Characterization of compact heat sink models in natural convection. IEEE Trans. Compon. Packag. Technol. **25**, 78–86 (2002)
7. Senapati, J.R., Dash, S.K., Roy, S.: Numerical investigation of natural convection heat transfer from horizontal cylinder with annular fins. Int. J. Therm. Sci. **96**, 330–345 (2016)
8. Senapati, J.R., Dash, S.K., Roy, S.: 3D numerical study of the effect of eccentricity on heat transfer characteristic over horizontal cylinder fitted with annular fins. Int. J. Therm. Sci. **108**, 28–39 (2016)
9. Senapati, J.R., Dash, S.K., Roy, S.: Numerical investigation of natural convection heat transfer from vertical cylinder with annular fins. Int. J. Therm. Sci. **111**, 146–159 (2017)
10. Goshayeshi, H.R., Ampofo, F.: Heat transfer by natural convection from a vertical and horizontal surface using vertical fins. Energy Power Eng. **01**, 85–89 (2009)

Effect of Loop Diameter on Two-Phase Natural Circulation Loop Performance

S. Venkata Sai Sudheer, K. Kiran Kumar and Karthik Balasubramanian

Abstract This paper aims to present the effect of loop diameter on steady-state performance of the two-phase rectangular natural circulation loop. A one-dimensional homogeneous equilibrium model is developed to estimate the two-phase pressure drop across each section of the loop. Thermophysical properties and state properties are considered at local pressure. Uniform heat flux is applied at both evaporator and condenser sections. Mass flux is obtained by solving loop momentum equation using iterative procedure. Results are presented for different loop diameters under same heat load, gravitational head, and fluid quantity. The effect of the loop diameter on the mass flow rate is also analyzed.

Keywords Two-phase NCL · Loop diameter · Quality

1 Introduction

In the present scenario, effective utilization of energy plays a prominent role in day to day life. Versatile needs of energy, demanding various energy transporting mechanisms. Forced Circulation Loops (FCLs) and Natural Circulation Loops (NCLs) play a key role, in the vicinity of energy transport for different industrial and commercial applications. The fluid circulation can be attained either by external power sources like pumps in case of FCLs or by buoyancy in NCLs. In natural circulation, thermally developed density gradients are the driving force. In precise and safety apparatus, one cannot rely on the external source to run the loop for longer period. Therefore, NCL is a lucrative choice. In NCL, riser and downcomer connect the source and sink for energy transfer. Simplicity in configuration and reliability in performance grabs the attention of researchers to make use of NCL for diversified applications like cooling of nuclear reactor, gas turbine blades, solar heaters, waste heat recovery boilers, and so on [1–3].

S. Venkata Sai Sudheer (✉) · K. Kiran Kumar · K. Balasubramanian
National Institute of Technology, Warangal 506004, Telangana, India
e-mail: svssnitw@gmail.com

D. Srinivasacharya and K. S. Reddy (eds.), *Numerical Heat Transfer and Fluid Flow*, Lecture Notes in Mechanical Engineering,
https://doi.org/10.1007/978-981-13-1903-7_49

Based on the state of working fluid, NCLs can be either single or two phases. Larger density gradient of working fluid across the loop is the inherent advantage of two-phase NCL over single-phase NCL. From the past few decades, different analytical approaches are reported in the literature to study the performance of two-phase NCL. Few of them which are giving closer prediction to the experimental results are homogeneous model [4, 5], drift flux model [5, 6], and one-dimensional two-fluid model with thermodynamic nonequilibrium [7]. The present work aims to develop a model to study the performance of two-phase NCL with one-dimensional approach. Pressure drop in two-phase regions is estimated by using homogeneous equilibrium model. The effect of diameter on loop performance is also analyzed.

2 Mathematical Modeling

A uniform cross-sectional rectangular loop is considered for the analysis. Evaporator and condenser sections are positioned on horizontal arms at an elevated distance to add the favorable gravity gradients to the loop fluid. These two sections are connected by two vertical arms called riser and downcomer. Constant heat flux boundary condition is considered at evaporator and condenser sections. Schematic representation of two-phase NCL is as shown in Fig. 1. Based on the state of loop fluid, the loop is divided into six regions, which are represented in Fig. 1 and Table 1.

The following assumptions are made to simplify the solution:

1. The bulk temperature of the loop fluid reaches saturation temperature in the evaporator section.
2. Thermophysical properties are considered at a local pressure only instead of system pressure.
3. Loop is perfectly insulated.
4. Minor losses in the loop are neglected.
5. Quality in the loop linearly varies.
6. The flow is in counterclockwise direction.

Table 1 Loop regions

S. No.	Regions	Zone description
1	a–b	Subcooled heating region
2	b–c	Vaporization region
3	c–d	Adiabatic two-phase region
4	d–e	Condensation region
5	e–f	Subcooled cooling region
6	f–a	Adiabatic single-phase region

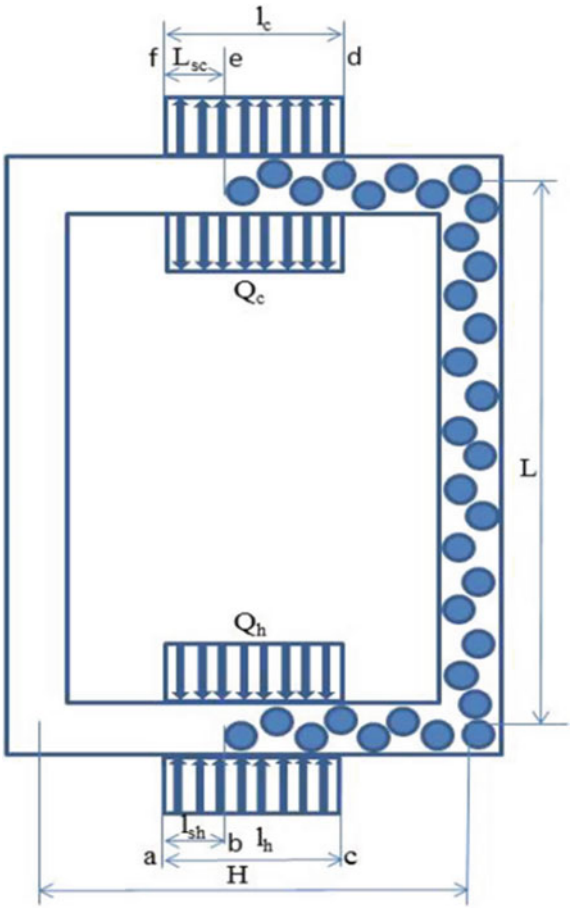

Fig. 1 Schematic diagram of a two-phase NCL

2.1 Governing Equations

One-dimensional steady-state continuity equation at any section in the loop is given by

$$\frac{\mathrm{d}(\rho u A)}{\mathrm{d}s} = 0 \tag{1}$$

The total loop momentum equation is given by

$$\oint \frac{2fG^2}{D\bar{\rho}}\mathrm{d}s + \oint \bar{\rho} g \sin\theta \mathrm{d}s + \oint \frac{\mathrm{d}\bar{\vartheta}}{\mathrm{d}s}\mathrm{d}s = 0 \tag{2}$$

The governing equation for energy in the loop at any section is given by

For single-phase region:

$$\frac{\mathrm{d}(h)}{\mathrm{d}s} = \frac{QP}{A_{\mathrm{cs}}} \tag{3.a}$$

For two-phase region:

$$\frac{\mathrm{d}x}{\mathrm{d}s} = \frac{QP}{A_{\mathrm{cs}}} \tag{3.b}$$

where Q is amount of heat interaction with evaporator, condenser and this value will be zero in adiabatic riser and downcomer sections.

Loop is filled with two-phase mixture as well as single-phase fluid; hence, the pressure drop at every section is given by

For single-phase fluid:

$$\frac{\mathrm{d}p}{\mathrm{d}s} = \frac{2fG^2}{D\rho} \pm g\rho \sin\theta \tag{4}$$

For two-phase mixture

$$\frac{\mathrm{d}p}{\mathrm{d}s} = \frac{2f_{\mathrm{tp}}G^2}{D\bar{\rho}} + G^2\vartheta_f\left(\frac{\vartheta_{fg}}{\vartheta_f}\right)\frac{\mathrm{d}x}{\mathrm{d}s} \pm \frac{g\sin\theta}{\vartheta_f\left(1+x\left(\frac{\vartheta_{fg}}{\vartheta_f}\right)\right)} \tag{5}$$

where f_{tp} is the two-phase friction factor, and it is estimated as for laminar flow $f_{\mathrm{tp}} = \frac{16}{\mathrm{Re}_{\mathrm{tp}}}$, for turbulent flow $f_{tp} = \frac{0.079}{Re_{tp}^{0.25}}$.

The two-phase Reynolds number can be estimated by $\mathrm{Re}_{\mathrm{tp}} = \frac{GD}{\mu_{\mathrm{tp}}}$.

The pressure drop in the loop is evaluated by using Eq. (4) for single-phase fluid and Eq. (5) for two-phase mixture. The two-phase pressure drop is estimated by using homogenous equilibrium model. The different zone lengths are evaluated by using the energy equation (3.a, 3.b). A suitable iterative procedure is applied to solve the total loop momentum equation for estimating the final mass flow rate.

3 Result and Discussion

By keeping the mass of the loop and height of the loop constant, the required diameter, horizontal section length, and heat section length are derived. These values are shown in Table 2. Figure 2 shows the effect of diameter on loop mass flow rate for different heat inputs. As the heat flux increases, mass flow rate increases up to certain limit and then after decreases. As the diameter increases, mass flow rate increases and the peak value is shifted to right. This happens because of the quality and pressure drop in the riser section.

Table 2 Two-phase NCL configuration

Diameter (m)	Horizontal section length (m)	Height of the loop (m)	Heating section length (m)
0.01225	1.5098	2	0.5408
0.01325	1	2	0.5
0.01425	0.5937	2	0.4649

Figure 2b shows the variation of quality in the loop. In homogeneous 1D modeling, quality is estimated as the area averaged value. As diameter increases, the evaporator length decreases, even though the fluid quantity in the evaporator increases. Thus, for the same amount of heat flux supplied at evaporator, exit quality of loop fluid decreases and higher quality can be obtained at higher heat fluxes. Figure 3 shows the two-phase pressure drop in the loop for different diameters. As loop diameter increases, the friction loss and quality reduce. The decrease in quality provokes gravitational head in the riser. Hence, the overall two-phase pressure drop increases.

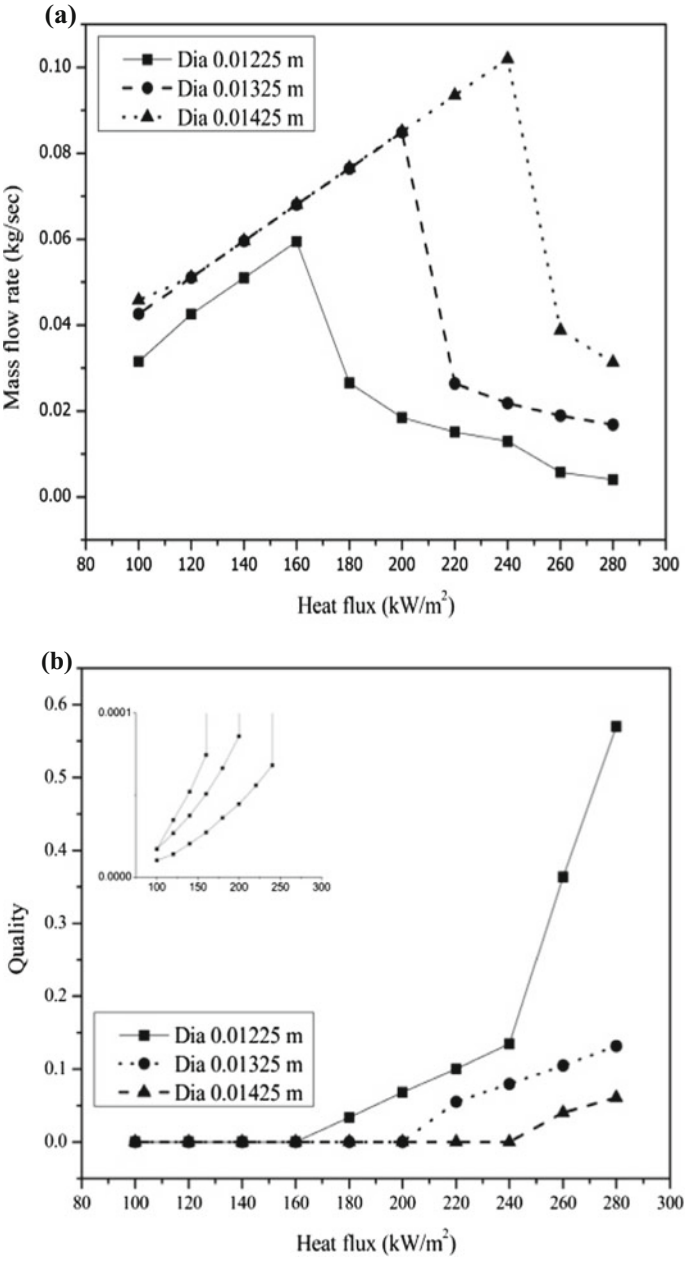

Fig. 2 **a** Effect of diameter on loop mass flow rate and **b** effect of diameter on loop quality

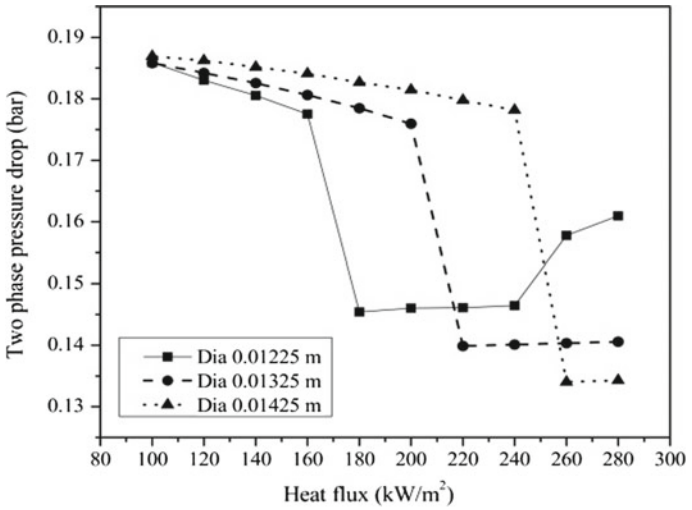

Fig. 3 Two-phase pressure drop in the loop at different heat flux

4 Conclusions

The steady-state performance of a two-phase natural circulation loop by varying loop diameter is analyzed. One-dimensional homogeneous model is used. Loop steady-state solution is obtained in terms of mass flux by solving the momentum equation. The following important findings are noted during the analysis.

- The performance of the NCL is strongly affected by loop diameter.
- For a particular loop height and quantity of loop fluid, loop diameter has a significant influence on quality.
- There is an optimum value of heat flux for any configuration of the loop.

Acknowledgements The present work is carried out under a project sponsored by the Department of Atomic Energy, Board of Research in Nuclear sciences (BRNS), and Government of India. The financial support offered by BRNS is gratefully acknowledged.

References

1. van der Hagen, T.H.J.J., van Bragt, D.D.B., van der Kaa, F.J., Killian, D., Wouters, J.A.A., Karuza, J., Nissen, W.H.M., Stekelenburg, A.J.C.: Exploring the Dodewaard Type-I and Type-II stability: from start-up to shut-down, from stable to unstable. Ann. Nucl. Energy **28**, 659–669 (1997)
2. Heisler, M.P.: Development of scaling requirements for natural convection liquid-metal fast breeder reactor shutdown heat removal test facilities. Nucl. Sci. Eng. **80**, 347–359 (1982)

3. Shitzer, A., Kalmanoviz, D., Zvirin, Y., Grossman, G.: Experiments with a flat plate solar water heating system in thermosyphonic flow. Sol. Energy **22**, 27–35 (1979)
4. Chen, K.S., Chang, Y.R.: Steady-state analysis of two-phase natural circulation loop. Int. J. Heat Mass Transf. **31**, 931–940 (1988)
5. Rao, N.M., Sekhar, C.C., Maiti, B., Das, P.K.: Steady-state performance of a two-phase natural circulation loop. Int. Commun. Heat Mass Transf. **33**, 1042–1052 (2006)
6. Jeng, H.R., Pan, C.: Analysis of two-phase flow characteristics in a natural circulation loop using the drift-flux model taking flow pattern change and subcooled boiling into consideration. Ann. Nucl. Energy **26** (1999)
7. Basu, D.N., Bhattacharyya, S., Das, P.K.: Steady-State Behavior of a Two-Phase Natural Circulation Loop with Thermodynamic Non-equilibrium. 131, 1–12 (2009)

Studies on Heat and Mass Transfer Coefficients of Pearl Millet in a Batch Fluidized Bed Dryer

D. Yogendrasasidhar and Y. Pydi Setty

Abstract Drying is the mechanism for separation of moisture content from the solids. The heat transfer mechanism in dryers is by several modes such as conduction, convection, and radiation and sometimes in the combination of two or three of them. Fluidized bed dryer is adapted to process industries like pharmaceuticals, food, and cement due to a wide range of applications. Generally, fluidized bed dryers are operated with preheated air at high temperatures. The bed particles behave like a fluid with hot air. Heat and mass transfer plays a main role in fluidized bed dryer. In the process of drying, heat and mass transfer coefficients of particles in the bed changes rapidly. India is one of the major producers of grains in the world. Fluidized bed dryer is widely used in particulate drying. In this study, experiments were performed to determine heat and mass transfer coefficients of pearl millet varying different parameters in fluidized bed dryer.

Keywords Pearl millet · Heat transfer coefficient · Mass transfer coefficient

1 Introduction

Drying is one of the traditional moisture separation processes in pharmaceutical, food, and fertilizer industries. Dryers are classified mostly by the mode of heat supplied to the wet solids, which may be conduction, convection, and radiation and sometimes in the combination of two or three of them. The disadvantage with other conventional dryers is nonuniform drying and material property changes that leads to damage of product quality. To get uniform quality of the product, the fluidized bed dryers are adapted in the process industries. In fluidized beds, the solids are suspended in the hot gas stream, which is the heating medium that results in high heat and mass transfer rates in the fluidized beds [1]. Fluidized bed dryers have many

D. Yogendrasasidhar · Y. Pydi Setty (✉)
Department of Chemical Engineering, National Institute of Technology Warangal, Warangal 506004, Telangana, India
e-mail: psetty@nitw.ac.in

D. Srinivasacharya and K. S. Reddy (eds.), *Numerical Heat Transfer and Fluid Flow*, Lecture Notes in Mechanical Engineering,
https://doi.org/10.1007/978-981-13-1903-7_50

advantages compared to other conventional dryers such as uniform drying due to high solids mixing, uniform moisture distribution due to very high particle circulation rate and very high rates of heat and mass transfer because of good gas-to-solid contact in the bed. Generally, in fluidized beds, different types of heat transfer phenomena takes place, like wall-to-particle, gas-to-particle, and particle-to-particle heat transfer. The gas-to-particle heat transfer plays a major role because of carryover of the moisture from the particle. The mass transfer coefficient of particles is based on moisture removal rate in fluidized bed dryer. Previously, some of the researchers conducted drying studies on different food grains [2]. The heat and mass transfer studies were conducted with sand, grains, porous materials, and ammonium chloride, etc., in fluidized bed dryer by many researchers [3–5]. Srinivasakannan and Balasubramanian have studied the drying behavior of pearl millet in fluidized bed dryer [6]. In the present study, experiments were carried out to determine the mass transfer coefficient of pearl millet varying air velocity, temperature, and initial moisture content. Also, studies were conducted on heat transfer to determine the heat transfer coefficient of pearl millet in fluidized bed dryer.

2 Experimental Setup and Procedure

Fluidized bed dryer was designed with a cylindrical column having a fluidization column of 1 m, calming section of 1 m, and diameter of 0.083 m. Distributor plate with 5 mm orifices was used for the uniform distribution of gas. Air is drawn from the compressor and passed through air heater, followed by the calming section. The air inlet temperature is controlled by a rheostat, the air flow rate was controlled using a bypass valve, and measured using rotameter of range 0–120 kg/h. Insulation is provided over the air heater to prevent heat losses. Thermocouples connected to a temperature indicator were used to measure the air and solid temperatures. In the present study, pearl millet having a diameter of 2.2 mm and density of 1350 kg/m^3 was used. Experimental setup of fluidized bed dryer is presented in Fig. 1. A known amount of millet with known initial moisture content has been used inside the fluidized bed dryer. After attaining the experimental conditions, airflow has been initiated and the samples were collected at the top of the bed at regular intervals. The collected sample's moisture was analyzed using hot air oven and microbalance.

3 Results and Discussion

3.1 Heat Transfer Studies

Generally, heat transfer environment created for fluidized bed dryer is by solar heating, microwave heating, or by manual heating using heating coils. The moisture

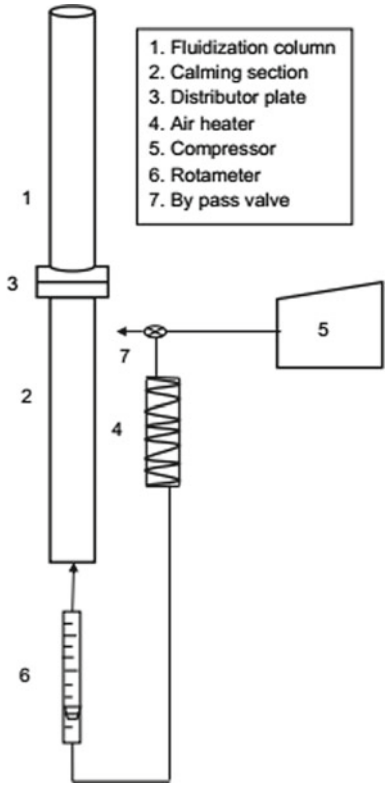

Fig. 1 Batch fluidized bed dryer

removal rate mainly depends on heat transfer between gas-to-solid and gas-to-solid contact ratio. Many authors studied and developed heat transfer correlation between gas to solid in fluidized bed dryer [3, 7]. Minimum fluidization velocity and Reynolds number of pearl millet were calculated using Eqs. (1) and (2) [8]. Based on experimental air velocities presented, Reynolds numbers of pearl millet are presented in Fig. 2. Initially, gas was sent through the bed of particles and bed porosity changes with air velocity. Due to this, the heat transfer between gas to solid also changes with bed porosity. Here, heat transfer coefficient of pearl millet in fluidized bed dryer is calculated based on bed porosity and the Nusselt number are presented in Eqs. (3)–(6) given [3, 8]. The Nusselt number of pearl millet varying with air velocity is presented in Fig. 3. It can be observed from the figure that heat transfer coefficient is increased with increasing air velocity in fluidized bed dryer. From Fig. 4, it can be observed that the drying rate of pearl millet increased with increasing air velocity, as moisture removal rate of particles in bed increases due to increasing air velocity.

$$\frac{d_p u_{mf} \rho_g}{\mu} = \left[(28.7)^2 + 0.0494 \left(\frac{d_p^3 \rho_g (\rho_s - \rho_g) g}{\mu^2} \right) \right]^{1/2} - 28.7 \qquad (1)$$

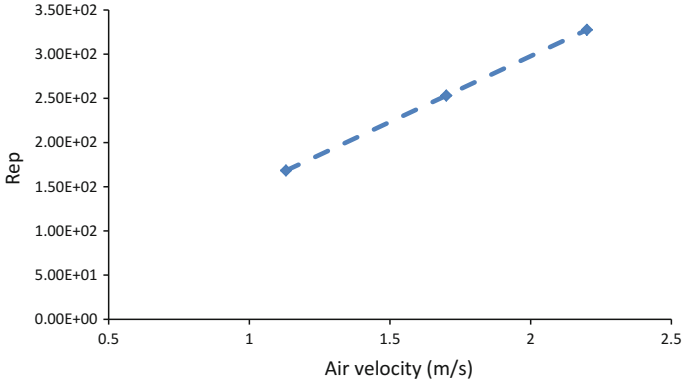

Fig. 2 Reynolds number of pearl millet

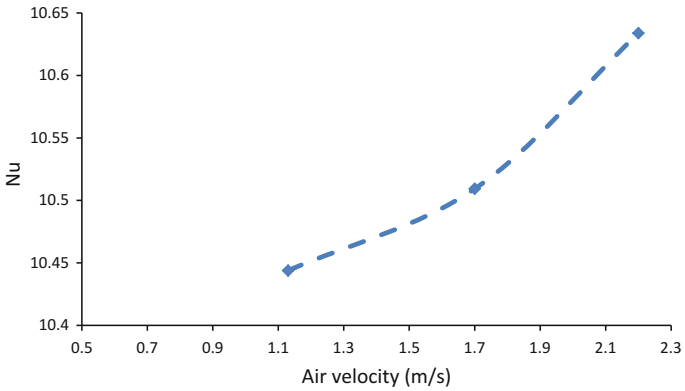

Fig. 3 Nusselt number of pearl millet

$$Re_p = \frac{d_p u \rho}{\mu} \tag{2}$$

$$\varepsilon_{\mathrm{mf}} = 0.586 \times \left(\emptyset^{-0.72}\right) \times \left[\frac{\mu^2}{\rho_s\left(\rho_s - \rho_g\right) g d_p^3}\right]^{0.029} \left(\frac{\rho_g}{\rho_s}\right)^{0.021} \tag{3}$$

$$\delta = 0.534 - 0.534 \times \exp\left(-\frac{u_0 - u_{\mathrm{mf}}}{0.413}\right) \tag{4}$$

$$\varepsilon_f = \delta + (1 - \delta)\varepsilon_{\mathrm{mf}} \tag{5}$$

$$\begin{aligned} Nu =& \left(7 - 10\varepsilon_f + 5\varepsilon_f^2\right)\left(1 + 0.7 Re_p^{0.2} Pr^{\frac{1}{3}}\right) \\ &+ \left(1.33 - 2.4\varepsilon_f + 1.2\varepsilon_f^2\right) Re_p^{0.7} Pr^{1/3} \end{aligned} \tag{6}$$

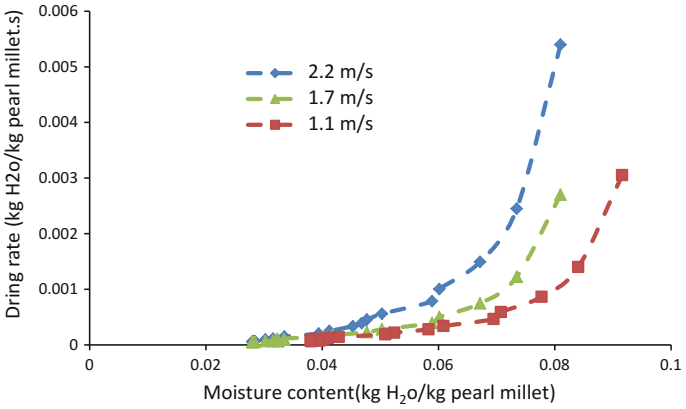

Fig. 4 Effect of air velocity on drying characteristics of pearl millet (Air temperature—55 °C, bed height—4 cm, and initial moisture content—10%)

3.2 Mass Transfer Studies

In a fluidized bed dryer, moisture transport generally occurs from solid to gas. It is influenced by different parameters of the dryer. Many authors estimated diffusion coefficients of several materials with the help of Fick's law [6]. In the present study, experiments were performed by changing air velocity from 1.1 to 2.2 m/s, temperature from 40 to 70 °C, and bed height from 3 to 5 cm with 10% moisture content of pearl millet.

The mass transfer coefficient, K was calculated using Eq. (7) incorporating the experimental moisture content of pearl millet at different air velocity, air temperature, and bed height [9].

$$K = \frac{\text{Rw}}{M_t - M_e} \tag{7}$$

Here, M_t is transient moisture content of pearl millet, R_w is drying rate, and M_e is equilibrium moisture content.

Effect of air velocity on the mass transfer coefficient
Experiments were performed with air velocity from 1.1 to 2.2 m/s, and the remaining parameters are kept constant in fluidized bed dryer. From Fig. 5, it can be noticed that the mass transfer coefficient of pearl millet increased with increasing air velocity.

Effect of air temperature on the mass transfer coefficient
Experiments were performed with air temperature from 40 to 70 °C, and the remaining parameters are kept constant in fluidized bed dryer. From Fig. 6, it can be observed that the mass transfer coefficient of pearl millet increased with increasing air temperature.

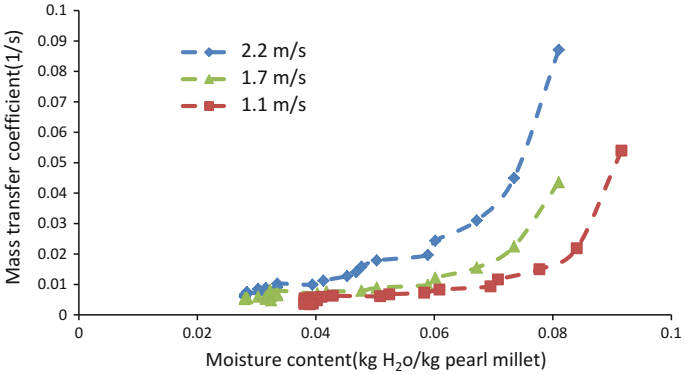

Fig. 5 Effect of air velocity on the mass transfer coefficient of pearl millet (Air temperature—55 °C, bed height—4 cm, and initial moisture content—10%)

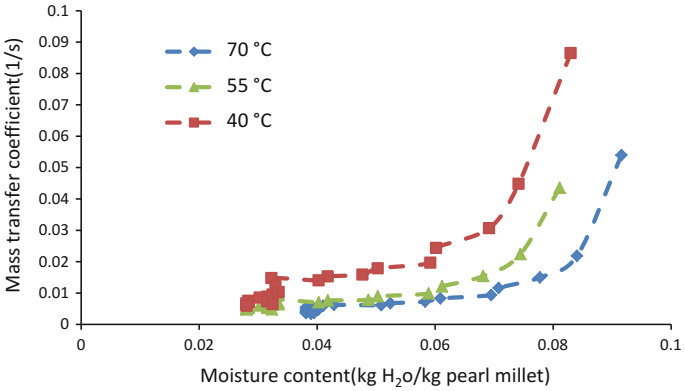

Fig. 6 Effect of air temperature on the mass transfer coefficient of pearl millet (Air velocity—1.7 m/s, bed height—4 cm, and initial moisture content—10%)

Effect of bed height on the mass transfer coefficient

Experiments were performed with bed height from 3 to 5 cm, and the remaining parameters are kept constant in fluidized bed dryer. From Fig. 7, it can be observed that the mass transfer coefficient of pearl millet decreased with increasing bed height.

From the results, the highest mass transfer coefficient is found to be 0.87 s^{-1} at air velocity 2.2 m/s, air temperature of 50 °C, and bed height of 4 cm.

4 Conclusion

Experiments were performed with pearl millet using fluidized bed dryer. Heat transfer studies were carried out using pearl millet. The Nusselt number and Reynolds number

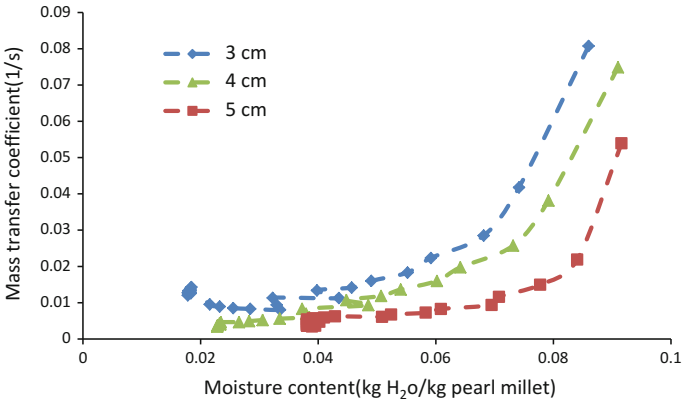

Fig. 7 Effect of bed height on the mass transfer coefficient of pearl millet (Air velocity—1.7 m/s, Air temperature—55 °C, and initial moisture content—10%)

of pearl millet were presented at different velocities in fluidized bed dryer. It can be observed that the heat transfer coefficient of pearl millet increased with increasing air velocity in fluidized bed dryer. Studies were also conducted on mass transfer changing air velocity, air temperature, and bed height in fluidized bed dryer. From the results, it was observed that mass transfer coefficient increased with increasing air temperature, velocity, and decreased with increasing bed height. In these studies, the highest Nusselt number was found to be 10.65 at 2.2 m/s and highest mass transfer coefficient of pearl millet was observed as 0.087 s^{-1} at air velocity of 2.2 m/s, air temperature of 50 °C, and bed height of 4 cm.

References

1. Mujumdar, A.S.: Handbook of Industrial Drying. Marcel Dekker, New York (2014)
2. Srinivasakannan, C., Balasubramanian, N.: An analysis on modeling of fluidized bed drying of granular material. Adv. Powder Technol. **19**, 73–82 (2008)
3. Wang, H., Chen, G.: Heat and mass transfer in batch fluidized-bed drying of porous particles. Chem. Eng. Sci. **55**, 1857–1869 (2000)
4. Srinivas, G., Pydi Setty, Y.: Heat and mass transfer studies in a batch fluidized bed dryer using Geldart group D particles. Heat Mass Transf. **50**, 1535–1542 (2014)
5. Hideo, I., Syahrul, H., Akihiko, H., Naoto, H.: Heat and mass transfer analysis of fluidized bed grain drying. Mem. Fac. Eng. Okayama Univ. **41**, 52–62 (2007)
6. Srinivasakannan, C., Balasubramanian, N.: An investigation on drying of millet in fluidized beds. Adv. Powder Technol. **20**, 298–302 (2009)
7. Kumaresan, R., Viruthagiri, T.: Simultaneous heat and mass transfer studies in drying ammonium chloride in a batch-fluidized bed dryer. Indian J. Chem. Technol. **13**, 440–447 (2006)
8. Kunii, D., Levenspiel, O.: Fluidization Engineering, 2nd edn. Butterworth Heinemann, Botson (1991)
9. Luz, G.R., Estadual, U., Uem, D.M., Paraíso, P.R.: Mass transfer coefficient in the drying of soybean meal. Braz. J. Food Technol. **12**, 92–96 (2009)

Effect of Channel Confinement and Hydraulic Diameter on Heat Transfer in a Micro-channel

D. Sathishkumar and S. Jayavel

Abstract The study of fluid flow and heat transfer in a micro-channel plays a major role in electronic cooling. The effect of micro-channel confinement and hydraulic diameter on heat transfer characteristics is investigated. Three-dimensional numerical simulation is carried out using ANSYS Fluent 15 for a wide range of hydraulic diameter ranging from 0.1 to 1 mm. Further, the simulations are extended for various Reynolds numbers. Water is the working fluid. The present numerical results are validated with those available in literature. The computational results are presented in the form of temperature contours and Nusselt number variation. The results show that the Nusselt number increases with increasing hydraulic diameter.

Keywords Rectangular micro-channel · Hydraulic diameter
Thin-walled model

1 Introduction

Today, all the machines engaged in diverse fields such as computing, communication, mechanical, etc., involve electronic devices. Thermodynamically, all electronic devices undergo irreversible process with the net result being the generation of heat. The main basis for this concern is the increasing cost and complexity of thermal management in electronic systems. The air cooling strategy is still a viable option in some areas although other factors such as operating costs, chip reliability, and waste heat recovery may still encourage the use of liquid cooling [1]. Subsequent paragraphs, however, are indented.

The micro-channel investigation is first introduced by Tuckerman and Pease et al. [2]. They considered rectangular micro-channel to dissipate high heat flux value using laminar water flow. Peng et al. [3] experimentally investigated the rectangular

D. Sathishkumar · S. Jayavel (✉)
Department of Mechanical Engineering, IIITDM Kancheepuram, Chennai 600127, Tamil Nadu, India
e-mail: sjv@iiitdm.ac.in

D. Srinivasacharya and K. S. Reddy (eds.), *Numerical Heat Transfer and Fluid Flow*, Lecture Notes in Mechanical Engineering,
https://doi.org/10.1007/978-981-13-1903-7_51

micro-channels with the range of hydraulic diameter from 0.113 to 0.367 mm. The critical Reynolds number value was found to depend on channel hydraulic diameter. Mokrani et al. [4] experimentally investigated the fluid flow and convective heat transfer in rectangular micro-channels by varying both channel height (0.05–0.5 mm) and the hydraulic diameter (0.1–1 mm). They concluded that the micro-channel hydraulic diameter has no effect on the Nusselt number and for the micro-channel having hydraulic diameter greater than 1, the conventional laws and correlations are applicable. On the other hand, Liu and Garimella [5] explained that conventional correlations are giving same predictions for the laminar flow in rectangular micro-channels over a hydraulic diameter range of 0.244–0.974 mm. There are few methods to predict the effect of wall boundary.

Sahar et al. [6] conducted a numerical study on heat transfer in micro-channels considering different models for simulation such as 2D, 3D thin-walled, and 3D full conjugate model. They concluded that 3D thin-walled model gives results that match with experimental data. Based on the literature study, in the present study, 3D thin-walled model is used with constant heat flux boundary conditions. Gunnasegaran et al. [7] explained the effect of channel size and shape on heat transfer in different multi-micro-channels. They considered three different geometries and all three cases simulated for a wide range of hydraulic diameter and aspect ratio. They concluded that rectangular micro-channel with small hydraulic diameter gives high heat transfer coefficient values than triangular and trapezoidal geometries. This claim is also supported by the results due to Wang et al. [8].

2 Model Description

In this present numerical investigation, the geometry considered is rectangular micro-channel with the channel length of $L = 62$ mm as shown in Fig. 1. In order to avoid the conjugate effect, 3D thin-walled model is selected for the numerical study. To study the effect of channel confinement and hydraulic diameter on heat transfer, the Dh is varied from 0.1 to 1 mm while keeping aspect ratio as constant, $(W/H) = 1$. Further, Reynolds number effect is studied in the range, $300 \leq Re \leq 2000$.

ICEM CFD is used for grid generation as shown in Fig. 1 while ANSYS Fluent 15 is used for simulation. Uniform inlet velocity condition is imposed at the inlet of channel and a zero static pressure is given to the outlet of the channel. Constant heat flux is applied at three walls except for top wall. The shaded top wall as shown in Fig. 1 is considered adiabatic as applicable to most of the electronics cooling. Using 10^{-6} as convergence criterion indicates the level of accuracy maintained in the study. Both momentum and energy equations are solved by first-order upwind scheme. To solve pressure–velocity coupling, a SIMPLE scheme is applied. In order to save the computation time, constant grid size of $20 \times 15 \times 400$ is chosen.

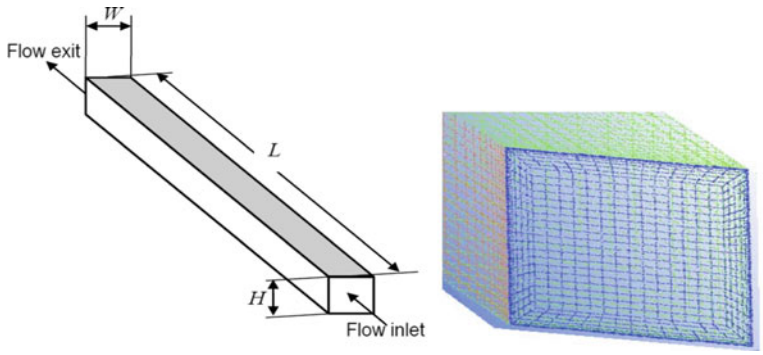

Fig. 1 Schematic representation of computational domain and enlarged view of mesh near the inlet

3 Mathematical Formulations

The general governing equations applicable to the present study are given in Eqs. (1)–(3). Further, the following assumptions are imposed: (1) Incompressible laminar steady flow and (2) negligible radiation heat transfer. Parameters used in the present study are listed in Eqs. (4)–(7).

Continuity equation is

$$\nabla\left(\rho\vec{V}\right) = 0 \tag{1}$$

Momentum equation is

$$\vec{V}.\nabla\left(\rho\vec{V}\right) = -\nabla p + \nabla.\left(\mu\nabla\vec{V}\right) \tag{2}$$

Energy equation is

$$\vec{V}.\nabla\left(\rho C_p T_f\right) = \nabla.(K_f \nabla T_f) \tag{3}$$

Nondimensional Reynolds number is defined as

$$\mathrm{Re} = \frac{\rho_f V_{\mathrm{ch}} D_h}{\mu_f} \tag{4}$$

Channel aspect ratio and hydraulic diameter is defined as,

$$\mathrm{AR} = \frac{H_f}{W_f}, \quad D_h = \frac{4(H_{\mathrm{ch}} W_{\mathrm{ch}})}{2(H_{\mathrm{ch}} + W_{\mathrm{ch}})} \tag{5}$$

Local Nusselt number and local heat transfer coefficient are defined as

$$N_u(x) = \frac{h(x)D_h}{K_f}, h(x) = \frac{q'}{T_{w,\mathrm{av}}(x) - T_{f,\mathrm{av}}(x)} \tag{6}$$

Similarly, the average Nusselt number and average heat transfer coefficient are defined as

$$N_{u,\mathrm{av}} = \frac{h_{\mathrm{av}}D_h}{K_f}, h_{\mathrm{av}} = \frac{1}{L_{\mathrm{ch}}}\int_0^{L_{\mathrm{ch}}} h(x)\mathrm{d}x. \tag{7}$$

4 Results and Discussions

This section presents the simulation results of channel confinement and hydraulic diameter effect on heat transfer enhancement for all cases considered in the present study.

4.1 Validation of the Computed Results

The Nusselt number computed in the present study are compared with the values predicted from the correlation of Bejan [9] for developing a flow. Figure 2 shows variation of Nusselt number for two different Reynolds numbers, i.e., for 500 and 1500. From the figure, it is observed that close match exists between computed values and literature results.

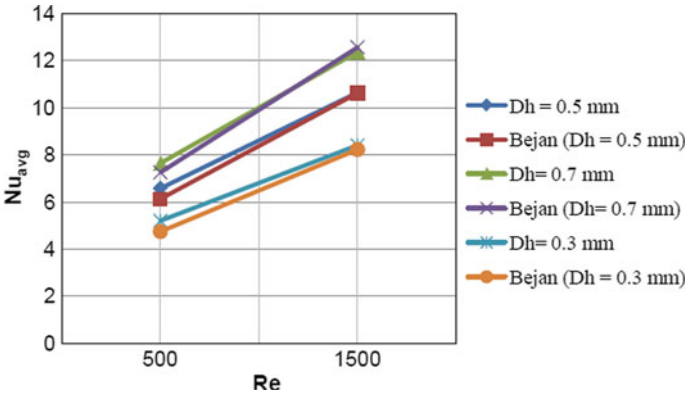

Fig. 2 Validation of the present results (Nusselt number)

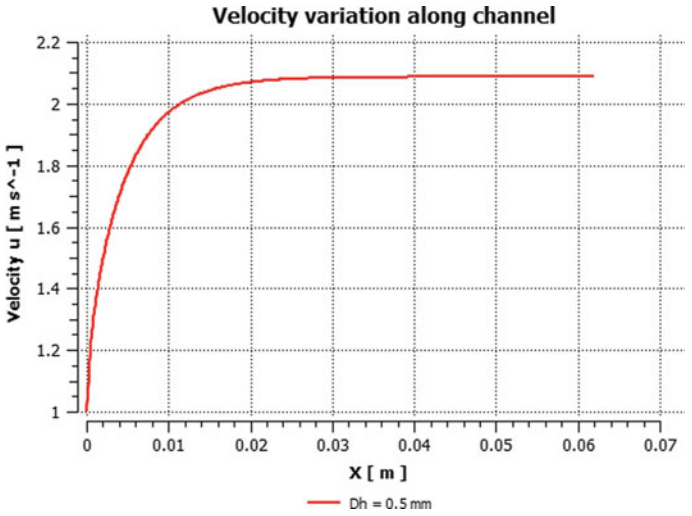

Fig. 3 Validation of the present results (hydrodynamic entry length)

4.2 Hydrodynamic Entry Length

The velocity variation along the channel length for hydraulic diameter of 0.5 mm is shown in Fig. 3. For Re = 500, the fully developed flow is observed at around 10 mm from the inlet. This hydrodynamic entry length value is compared with the value obtained from the Eq. (8) available in the literature. The computed value of entry length exactly matches with the literature.

For a fully developed laminar flow, the hydrodynamic entry length can be calculated from the following relation:

$$\delta \mathrm{hx} = 0.04\,\mathrm{Dh}\,\mathrm{Re} \tag{8}$$

4.3 Comparison of Fluid and Wall Temperature

This section explains the effect of hydraulic diameter on heat transfer in the microchannel while keeping aspect ratio value as 1. To understand the effect of geometric parameter on heat transfer enhancement, the temperature variation along wall and fluid is shown in Figs. 4 and 5 for Re = 500. Figure 4 shows the temperature contour along the constant heat flux wall. The temperature from the inlet to outlet varies from 300 to 326 K for the case Dh = 0.5 mm. The variation in temperature along the fluid is shown in Fig. 5. The same case has taken for understanding the temperature variation. But, in this case, the range of temperature from inlet to outlet is being 300–306 K. From the above two cases, the temperature variation in fluid is very small compared

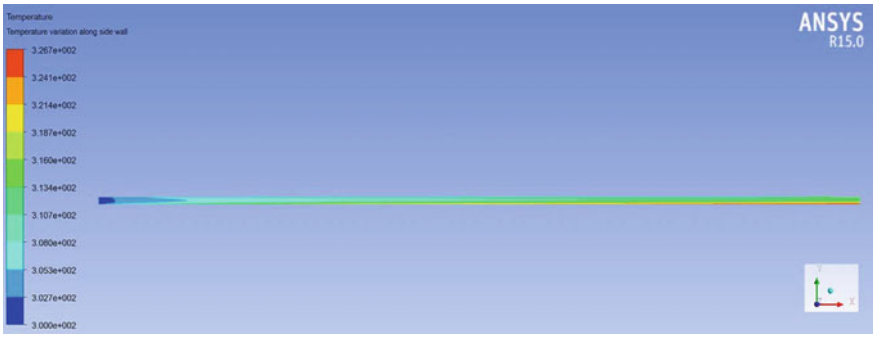

Fig. 4 Temperature distribution along wall

Fig. 5 Temperature distribution along fluid

to the temperature variation along wall. Thus, the geometry variation has significant effect on heat transfer.

4.4 Effect of Hydraulic Diameter on Heat Transfer

The average Nusselt number variation for the range of hydraulic diameter from 0.1 to 1 mm while keeping AR = 1 for $Re = 500$ and $Re = 1500$ is shown in Fig. 6. The constant heat flux value is applied at bottom and side walls while the top wall is imposed with adiabatic condition. The hydraulic diameter variation gives significant effect on Nusselt number where the average value of Nu is found to increase with increasing Dh value. For thermally developing flow, the Nu value increases gradually for both the cases, i.e., $Re = 500$ and $Re = 1500$.

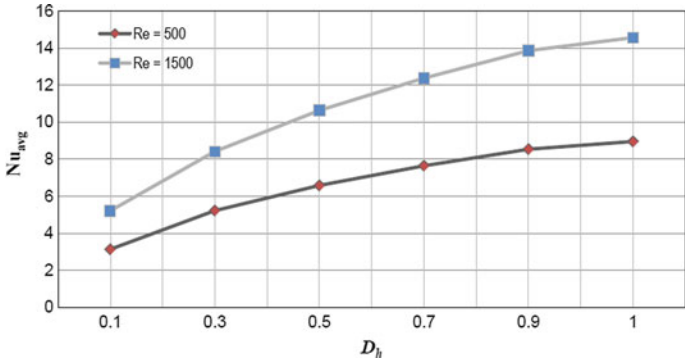

Fig. 6 Effect of hydraulic diameter on Nusselt number

5 Conclusions

In this work, a three-dimensional rectangular micro-channel is studied numerically to understand the effect of channel confinement and hydraulic diameter on heat transfer characteristics. Micro-channel of different hydraulic diameter (0.1–1 mm) with fixed AR is analyzed over a range of Reynolds number. Fluent 15 is used to simulate the simplified thin-walled model. In this study, the constant wall heat flux boundary condition is applied except for top wall, which is considered as adiabatic. The effect of hydraulic diameter variation is favorable from heat transfer point of view. Based on the simulation results, we can conclude that the effect of the hydraulic diameter and channel confinement on heat transfer is more important and average Nusselt number value increases with increasing hydraulic diameter for thermally developing flow.

References

1. Kheirabadi, A.C., Groulx, D.: Cooling of server electronics: a design review of existing technology. Appl. Therm. Eng. **105**, 622–638 (2016)
2. Tuckerman, D.B., Pease, R.F.W.: High-performance heat sinking for VLSI. IEEE Electron Dev. Lett. **2**, 126–129 (1981)
3. Peng, X.F., Peterson, G.P., Wang, B.X.: Frictional flow characteristics of water flowing through rectangular microchannels. Exp. Heat Transf. **7**(4), 249–264 (1994)
4. Mokrani, O., Bourouga, B., Castelain, C., Peerhossaini, H.: Fluid flow and convective heat transfer in flat microchannels. Int. J. Heat Mass Transf. **52**(5–6), 1337–1352 (2009)
5. Liu, D., Garimella, S.V.: Investigation of liquid flow in microchannels. AIAA J Thermophys. Heat Transf. **18**, 65–72 (2004)
6. Sahar, A., Özdemir, M., Fayyadh, E., Wissink, J., Mahmoud, M., Karayiannis, T.: Single phase flow pressure drop and heat transfer in rectangular metallic microchannels. Appl. Therm. Eng. **93**, 1324–1336 (2016)

7. Gunnasegaran, P., Mohammed, H., Shuaib, N., Saidur, R.: The effect of geometrical parameters on heat transfer characteristics of microchannels heat sink with different shapes. Int. Commun. Heat Mass Transf. **37**(8), 1078–1086 (2010)
8. Wang, H., Chen, Z., Gao, J.: Influence of geometric parameters on flow and heat transfer performance of micro-channel heat sinks. Appl. Therm. Eng. **107**, 870–879 (2016)
9. Bejan, A.: Convection Heat Transfer. Wiley, New Jersey (2004)

Numerical Study on Performance of Savonius-Type Vertical-Axis Wind Turbine, with and Without Omnidirectional Guide Vane

Mahammad Sehzad Alli and S. Jayavel

Abstract Savonius-type vertical-axis wind turbine is a suitable candidate for decentralized power generation in urban locations, due to its self-starting nature, large starting torque and ability to accept wind from any direction. In the present work, 2D, transient CFD analysis was performed on an *S*-shaped Savonius vertical-axis wind turbine (VAWT) using ANSYS Fluent 15.0, and the results thus obtained are validated by comparing with the experimental result published in the literature. Numerical study on the effect of omnidirectional guide vane (ODGV) on power- and torque coefficients of *S*-shaped Savonius VAWT is carried out. The results showed that the presence of ODGV increases power and torque, thus the performance of VAWT is increased in the presence of ODGV. Further, the computations are systematically extended to study the effect of ODGV in the range of 0.45–0.8 tip-speed ratio (λ). Optimal performance of the VAWT is noted at a tip-speed ratio of 0.6.

Keywords Savonius rotor · Omnidirectional guide vane · Numerical simulation Vertical-axis wind turbines

1 Introduction

Rapid urbanization and the subsequent increase in power consumption have taken a toll on the environment. Currently, two-thirds of the energy demand in India is met using fossil-based non-renewable resources [1]. To reduce the dependence on conventional energy resources and minimize its impacts on the environment, use of renewable energy is promoted. In the urban area, the localization of energy production can be achieved using renewable energy-based microgrids. Most of them rely on solar energy. However, the quantity of energy obtained from solar panels depends

M. S. Alli · S. Jayavel (✉)
IIITDM Kancheepuram, Chennai 600127, Tamil Nadu, India
e-mail: sjv@iiitdm.ac.in

M. S. Alli
e-mail: mds16m007@iiitdm.ac.in

D. Srinivasacharya and K. S. Reddy (eds.), *Numerical Heat Transfer and Fluid Flow*, Lecture Notes in Mechanical Engineering,
https://doi.org/10.1007/978-981-13-1903-7_52

on the solar intensity at that particular time, location and climate. Hence, harvesting additional renewable energy from the wind can augment the capacity of such microgrids and can help in generating additional revenue by supplying back the excess available power to the main grid. This research work aims to augment the renewable energy-based microgrid system by developing a suitable wind turbine.

The Savonius VAWT was proposed by S. J. Savonius in 1922 [2]. The advantages of Savonius rotor are many [3], viz., it is independent of wind direction, therefore does not require a yaw system, has relatively large start-up torque, has simple structure and low cost and produces less operating noise. However, Savonius turbines have some drawbacks such as relatively low power coefficient and low rotational velocity.

The wind turbine performance is assessed using the power coefficient, *Cp*, Eq. (1) [4].

$$C_p = \frac{P_{\text{rotor}}}{P_{\text{wind}}} = C_m \lambda \tag{1}$$

where C_m and λ are defined as $C_m = \frac{M}{\frac{1}{2}\rho V_o^2 A_s R}$, $\lambda = \frac{\omega R}{V_o}$, P is shaft power, M is moment, ρ is air density, V_o is free-stream air velocity, A_s is projected area, R is radius, C_m is coefficient of moment, ω is angular velocity and λ is the tip-speed ratio of the wind turbine.

2 Problem Description and Solution Methodology

2.1 Geometry and Computational Domain

Numerical computations are carried out to study the performance of S-bucket Savonius VAWT as shown in Fig. 1a using ANSYS Fluent 15.0. The buckets have a semicircular profile and have a full 180° arc with a diameter of 500 mm. The thickness of the bucket is taken as 1.5 mm. Further, ODGV is attached to study its impact on performance and torque characteristics. The detailed dimensions of the 2D S-bucket are shown in Fig. 1b. The gap width, *s*, separating the inside edges of the buckets, is kept such that the non-dimensional gap width, *s*/*d*, is 1.5. The radius of the rotor, *R*, is measured from the centre of rotation to the outer edge of the buckets, thus it is measured to be 464 mm. The span of the rotor is taken as 1 m. The rotor geometry corresponds to the data available in [5]. The ODGV design corresponds to the data available in [6], such that the number of the guide vanes is 4, θ is 20°, ϕ_r is 30° and $\frac{D_{\text{si}}}{D_{\text{so}}} = 0.55$, it is illustrated in Fig. 1c.

D_{si} and D_{so} are the inner and outer diameters of ODGV, respectively. Here, we have assumed D_{si} as 1.6D and span of the guide vane to be 1 m.

Computational domain was created using a CAD software. Mesh generation has been carried in such a way to suit the complexity involved such as steep gradients near the surface and turbulence. A circular computational domain is considered for

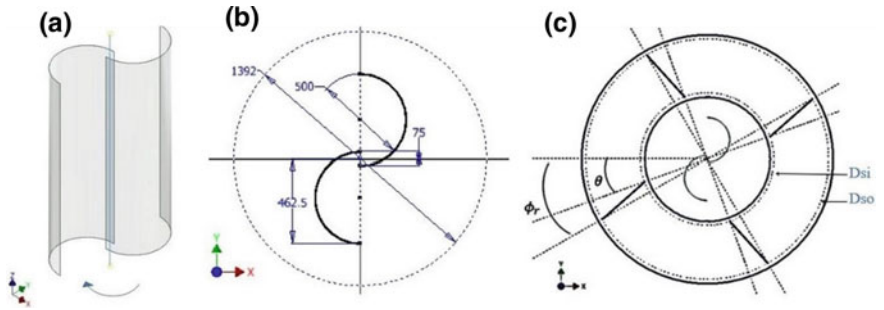

Fig. 1 Savonius VAWT **a** Pictorial view **b** *S*-bucket dimensions **c** with ODGV

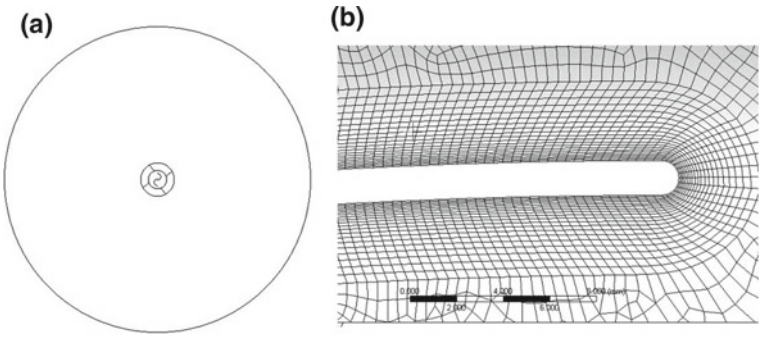

Fig. 2 **a** Computational domain. **b** Enlarged view of the mesh near the surface of bucket

numerical analysis, which has a radius 25D, for generating a structured mesh, Fig. 2a. The rotor in the rotating zone rotates in a circle of 928 mm diameter, while the rotating zone is 1.5D in diameter. The computational domain is discretized using quadrilateral elements using ANSYS Workbench. Meshing near the bucket edges are made dense as shown in Fig. 2b to capture the steep gradients.

Steady-state incompressible wind flow has been assumed uniformly distributed torque along the rotor height. The central shaft is excluded in the 2D numerical model. An appropriate thickness of the buckets is assumed, as it is not reported in the literature. The influence of end plates is neglected. For better accuracy, the y^+ value is kept low as per requirement of the turbulence model [7]. The parameter y^+ is given in Eq. (2), where U_τ is shear velocity and Δy is the grid spacing near the wall.

$$y^+ = \frac{\rho U_\tau \Delta y}{\mu} \tag{2}$$

2.2 Formulae and Solver Settings

The continuity equation for steady incompressible flow is given in Eq. (3), where v_x, v_y, v_z are the component of the velocity of the fluid in the x, y and z directions, respectively, and ρ is the density of the fluid.

$$\frac{\partial(v_x)}{\partial x} + \frac{\partial\left(v_y\right)}{\partial y} + \frac{\partial(v_z)}{\partial z} = 0 \tag{3}$$

The Reynolds-average Navier–Stokes (RANS) equation is given in Eq. (4). RANS equation can be closed using two-equation turbulence models, by applying Boussinesq's hypothesis, which states that the transfer of momentum generated by turbulent eddies can be predicted by an eddy viscosity, μ_t. According to this, the Reynolds stress tensor is proportional to the rate of strain tensor $\bar{s}_{ij}$, given in Eq. (5).

$$\frac{\partial}{\partial t}(\rho u_i) + \frac{\partial}{\partial x_j}\left(\rho u_i \rho u_j\right) = -\frac{\partial p}{\partial x_i} + \frac{\partial}{\partial x_j}\left[\mu\left(\frac{\partial u_i}{\partial x_j} + \frac{\partial u_j}{\partial x_i} - \frac{2}{3}\delta_{ij}\frac{\partial u_l}{\partial x_l}\right)\right] + \frac{\partial}{\partial x_j}\left(-\rho\overline{u_i' u_j'}\right) \tag{4}$$

$$\bar{S}_{ij} = \frac{1}{2}\left(\frac{\partial \bar{u}_i}{\partial x_j} + \frac{\partial \bar{u}_j}{\partial x_i}\right) \tag{5}$$

The most commonly used two-equation turbulence models known for better accuracy are the K–ε proposed by Jones and Launder and the K–ω model developed by Wilcox. Shear-stress transport (SST) k–ω turbulence model uses the k–ε model to obtain flow properties in the far-field (turbulent) flow region, away from the wall, but uses a modified k–ε model near the wall using the specific dissipation rate ω as a variable in lieu of the turbulent dissipation rate, ε, where, $\omega = \varepsilon/k$ [s^{-1}].

The numerical result in the present study is heavily influenced by near-wall flow, and proper modelling of this boundary layer flow can improve the accuracy of the solution. Therefore, the SST k–ω turbulence model is considered as the turbulence model for numerical analysis. The selected solver is pressure based, well suited to compute an incompressible flow field. The numerical results are validated by comparing it with the experimental results available in [5].

The solver was set to solve the RANS equations using SIMPLE (Semi-Implicit Method for Pressure-Linked Equations) method. At the inlet, the x component of the velocity is set as 7 m/s, the outlet is set with zero-gauge pressure value and the angular velocity of the rotating zone is set corresponding to the desired λ. A monitor for the moment coefficient (C_m) on the surface of the buckets is defined to obtain a mean torque value at different time steps, and it is averaged to get $C_{m\,\mathrm{avg}}$. Using Eq. (1) C_p is calculated from $C_{m\,\mathrm{avg}}$.

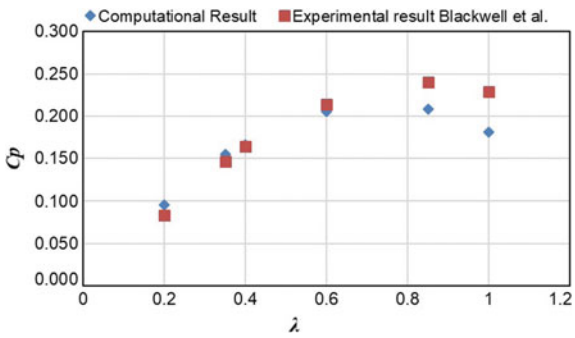

Fig. 3 Power coefficient as a function of speed ratio

3 Results and Discussion

The power coefficient, C_p values at different TSR is obtained numerically and C_p versus λ is plotted as shown in Fig. 3. This plot serves the purpose of validation. It can be noted that the results of the numerical models and the reference values have a good agreement. At higher tip-speed ratio, the deviations between experimental and numerical results are observed. At low TSR, the fluid flow at rotor bucket experiences more laminar nature [8]. The error associated with the computed results becomes considerable at higher TSRs since RANS turbulence models used in the present study assumes fully turbulent flow behaviour during the fluid flow. Other factors such as 2D simplification of the problem, discretization strategy, tolerance values, turbulence models and solution stability might have contributed to the deviation. However, at the power coefficient obtained by numerical analysis at lower TSRs ($\lambda < 0.85$) are very close to the experimental values. Hence, for further analysis of the effect of ODGV on the performance of *S*-Savonius rotor $\lambda < 0.85$ is used.

The ODGV is studied and presented in Fig. 4. It is evident that for the given configuration of ODGV, there is an 11.62% increase of power coefficient observed at $\lambda = 0.6$. If the rotor runs at optimum loading condition such that the λ hovers around 0.6, using an ODGV will positively increase the power output. Also, from Fig. 5, it is noted that the starting torque characteristic is also improved by the same percentage (11.62%).

4 Conclusion

From the result of the numerical analysis, it is evident that the SST k–ω model is the best choice for modelling the CFD problem where near-wall performance is needed to be captured, for example Savonius rotors which works primarily due to drag. Both numerical and experimental results suggest that Savonius VAWTs perform well under low (<0.8) TSR (tip-speed ratio), i.e. at low wind speed conditions. It also has a very good starting torque, hence can be used as a passive starter system for the Darrius

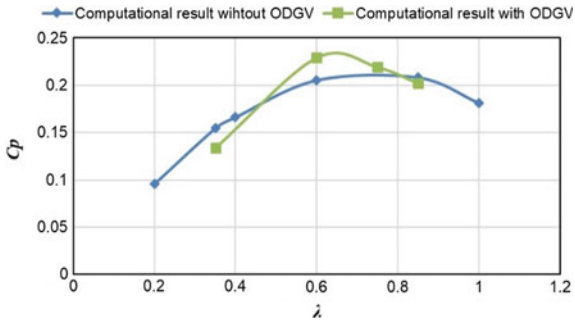

Fig. 4 Effect of ODGV on *Cp* for various TSR

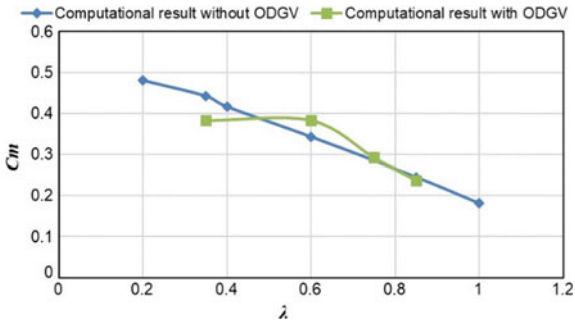

Fig. 5 Effect of ODGV on *Cm* for various TSR

rotor which lacks self-starting ability. However, with additional features like ODGV, the performance of Savonius rotor can be increased. From the numerical analysis, around 11.62% increase in the performance is obtained for the assumed configuration of ODGV. Further investigation can be performed on a different configuration of ODGV to find the best suitable geometry for Savonius rotor.

References

1. Ministry of Power, Government of India. http://www.powermin.nic.in
2. Savonius, S.J.: The S-rotor and its applications. Mech. Eng. **53**(5), 333–337 (1931)
3. Wilson, R.E., Lissaman, P.B.S.: Applied Aerodynamics of wind power machines. Research Applied to National Needs, GI-41840. Oregon State University (1974)
4. Akwa, J.V., Vielmo, H.A., Petry, A.P.: A review on the performance of Savonius wind turbines. Renew. Sustain. Energy Rev. **16**(5), 3054–3064 (2012). https://doi.org/10.1016/j.rser.2012.02.056
5. Blackwell, B.F., Sheldahl, R.E., Feltz, L.V.: Wind tunnel performance data for two- and three-bucket Savonius rotors. United States: N. p. (1977)
6. Ogawa, T., Kazuyuki, T., Suzuki, N.: Wind tunnel performance data of the savonius rotor with circular guide vanes. Bull. JSME **29**, 2109–2114 (1986). https://doi.org/10.1299/jsme1958.29.2109

7. Kacprzak, K., Liskiewicz, G., Sobczak, K.: Numerical investigation of conventional and modified Savonius wind turbines. Renew. Energy **60**, 578–585 (2013). https://doi.org/10.1016/j.renene.2013.06.009
8. Shaheen, M., El-Sayed, M., Abdallah, S.: Numerical study of two-bucket Savonius wind turbine cluster. J. Wind Eng. Ind. Aero. **37**, 78–89 (2015). https://doi.org/10.1016/j.jweia.2014.12.002

Free Convection of Nanofluid Flow Between Concentric Cylinders with Hall and Ion-Slip Effects

D. Srinivasacharya and Md. Shafeeurrahman

Abstract The natural convection of electrically conducting nanofluid flow in an annular region between two concentric circular cylinders considering Hall current and ion-slip effects. The governing equations are nondimensionalized and solved utilizing HAM. The influence of Hall, ion-slip parameter, thermophoresis parameter, the magnetic parameter, and Brownian motion on dimensionless velocity, temperature, and nanoparticle concentration are studied and represented geometrically.

Keywords MHD · Nanofluid · Concentric cylinders · Hall effect · Ion-slip effect · Free convection · HAM

1 Introduction

Nanofluid, pioneered by Choi [1], is a combination of a base fluid and small nano-sized solid particles. Choi [1] verified that the nanofluids have the highest thermal conductivity compared with the base fluids. This can be obtained even at very small volume fractions of nano-sized particles. Nanofluids have several applications of engineering in microfluidics, microelectronics, biomedical, manufacturing, solid-state lighting, transportation, scientific measurement, material synthesis, high-power X-rays, material processing and medicine etc... On the other hand, the study of free convective heat transfer in an annulus has acquired considerable attention due to its diverse application in the designs of cooling devices for electronic and microelectronic equipment, solar energy collection, etc. Number of studies were conducted on the convective heat transfer and nanofluid flow through concentric cylinders by considering distinct types of conventional base fluids with particular nanoparticles.

D. Srinivasacharya (✉)
Department of Mathematics, National Institute of Technology, Warangal 506004, India
e-mail: dsrinivasacharya@gmail.com

Md. Shafeeurrahman
e-mail: rahaman16@gmail.com

D. Srinivasacharya and K. S. Reddy (eds.), *Numerical Heat Transfer and Fluid Flow*, Lecture Notes in Mechanical Engineering,
https://doi.org/10.1007/978-981-13-1903-7_53

Dawood et al. [2] presented a review of literature on free and mixed-convection heat transfer and fluid flow in the annulus.

Interest in studying the free convective heat transfer of nanofluids in the annular is of fundamental importance due to its high range of applications in engineering. Togun et al. [3] presented a detailed review on heat transfer of free and mixed convective nanofluid flow through various annular passage configurations. The study of the flow of magnetohydrodynamics (MHD) flow of nanofluids has gained much attention due to its several engineering and industrial applications. Chamkha et al. [4] presented a review on various research work done on the MHD convection of nanofluids in various geometries and applications. The effects of Hall current on electrically conducting viscous steady fluid in channels was studied by Tani [5]. Srinivasacharya and Kaladhar [6] analyses the impact of Hall, ion-slip current effects on MHD natural convective fluid flow of couple stress fluid in an annulus. Odelu and Naresh Kumar [7] investigated the influence of the Hall and ion-slip on unsteady two-dimensional MHD natural convection heat and mass transfer of couple stress fluid in a porous medium between expanding or contracting walls with chemical reaction, Soret and Dufour effects. Motsa and Shateyi [8] numerically analyzed the impacts of Hall current and ion-slip parameter on the magnetomicropolar fluid flow through a porous medium with suction, variable thermal diffusivity, and chemical reaction.

2 Mathematical Formulation

Consider the nanofluid flow in the annular space between two infinitely long concentric cylinders of radius a and b ($a < b$) and kept at temperatures T_a and T_b, respectively. Assume that the outer cylinder is rotating with a uniform angular velocity Ω, whereas the inner cylinder is constant. The flow is induced by the rotation of the exterior cylinder. The flow is subjected to a standard uniform magnetic field B_0 in an axial direction. The assumption of very small magnetic Reynolds number leads to neglect of the induced magnetic field. Assume relatively high electron-atom collision frequency, so that the impact of Hall and ion-slip cannot be omitted. Thermophysical characteristics of the nanofluid are taken as constant. The velocity component along φ direction is u, dimensionless temperature is T, and nanoparticle volume fraction is ϕ. Under the above assumptions and along with Boussinesqs approximation, the governing equations are

$$\frac{\partial u}{\partial \varphi} = 0 \tag{1}$$

$$\frac{\partial p}{\partial r} - \frac{\rho u^2}{r} + \frac{\sigma\, B_0^2\, \beta_h\, u}{(\alpha_e^2 + \beta_h^2)} = 0 \tag{2}$$

$$\mu \frac{\partial}{\partial r}\left[\frac{1}{r}\frac{\partial}{\partial r}(r\,u)\right] + (1-\phi)\rho_f g\,\beta_T (T-T_a) - (\rho_p - \rho_f)\,g(\phi-\phi_a) - \frac{\sigma\, B_0^2\,\alpha_e\, u}{(\alpha_e^2+\beta_h^2)} = 0 \tag{3}$$

$$\alpha\left[\frac{\partial^2 T}{\partial r^2} + \frac{1}{r}\frac{\partial T}{\partial r}\right] + \frac{\mu}{(\rho c)_p}\left[\left(\frac{\partial u}{\partial r}\right)^2 - 2\,\frac{u}{r}\,\frac{\partial u}{\partial r} + \left(\frac{u}{r}\right)^2\right] + \tau\left[D_B\frac{\partial T}{\partial r}\frac{\partial \phi}{\partial r} + \frac{D_T}{T_0}\left(\frac{\partial T}{\partial r}\right)^2\right] = 0 \tag{4}$$

$$D_B\left[\frac{\partial^2 \phi}{\partial r^2} + \frac{1}{r}\frac{\partial \phi}{\partial r}\right] + \frac{D_T}{T_0}\left[\frac{\partial^2 T}{\partial r^2} + \frac{1}{r}\frac{\partial T}{\partial r}\right] = 0 \tag{5}$$

where the density is ρ, the pressure is p, the specific heat capacity is C_p, the viscosity coefficient is μ the acceleration due to gravity is g, the electrical conductivity is σ, ion-slip parameter is β_i, Hall parameter is β_h, Brownian diffusion coefficient is D_B, the coefficients of thermal expansion is β_T, thermophoretic diffusion coefficient is D_B, the effective thermal diffusivity is α, the coefficient of thermal conductivity is $K_f = \alpha\,(\rho\,C)_p$, the mass diffusivity is D, and the mean fluid temperature is T and $\alpha_e = 1 + \beta_h\,\beta_i$ is a constant.

The conditions on the boundary are

$$\begin{aligned} u = 0,\quad T = T_a,\quad \phi = \phi_a \ \text{ at } \ r = a,\\ u = b\Omega,\quad T = T_b,\quad \phi = \phi_b \ \text{ at } \ r = b, \end{aligned} \tag{6}$$

Introducing the following nondimensional variables:

$$\lambda = \frac{r^2}{b^2},\ f(\lambda) = \frac{u\sqrt{\lambda}}{\Omega}, \theta = \frac{T-T_a}{T_b - T_a},\ S = \frac{\phi-\phi_a}{\phi_b-\phi_a},\ P = \frac{bp}{\mu\,\Omega} \tag{7}$$

in Eqs. 1–5, we get the nonlinear differential equations as (8)–(10)

$$4\,f''\lambda + \sqrt{\lambda}\,(\theta - N_r S) - \frac{Ha^2\,\alpha_e\,f}{{\alpha_e}^2 + {\beta_h}^2} = 0 \tag{8}$$

$$\lambda^3\theta'' + \lambda^2\theta' + B_r\left[(f')^2 - 2\,\lambda\,f\,f' + (f)^2\right] + P_r\,N_b\,\lambda\,\theta'\,S' + P_r\,N_t\,\lambda^2\,(\theta')^2 = 0 \tag{9}$$

$$\lambda\,S'' + S' + \frac{N_t}{N_b}(\lambda\,\theta'' + \theta') = 0 \tag{10}$$

where the derivative with respect to λ is denoted by the prime, the Prandtl number is $Pr = \dfrac{\mu\,C_P}{k_f}$, Hartman number is $Ha^2 = \dfrac{\sigma\,{B_0}^2\,b^2}{\mu}$, Brinkman number is

$Br = \dfrac{\mu\,\Omega^2}{k_f\,(T_b - T_a)}$, the Brownian motion parameter is $N_b = \dfrac{\tau\,D_B(\phi_b - \phi_a)}{\nu}$, thermoporesis parameter is $N_t = \dfrac{\tau\,D_T(T_b - T_a)}{T_a\,\nu}$, and the buoyancy ratio is $N_r = \dfrac{(\rho_p - \rho_f)(\phi_b - \phi_a)}{\rho_f \beta_T (T_b - T_a)(1 - \phi)}$.

The corresponding boundary conditions (6) are

$$\begin{array}{l} S = 0,\ \theta = 0,\ f = 0 \ \text{ at } \ \lambda = \lambda_0 \\ S = 1,\ \theta = 1,\ f = b \ \text{ at } \ \lambda = 1 \end{array} \tag{11}$$

3 Results and Discussion

The system of nonlinear differential equations Eqs. (8)–(10) and along with boundary conditions (11) is solved using Homotopy analysis method [9].

The influence of magnetic parameter Ha, Brownian motion parameter N_b, thermophoresis parameter N_t, and Hall parameter β_h and ion-slip β_i on the velocity $f(\lambda)$, temperature $\theta(\lambda)$, and nanoparticle volume fraction $S(\lambda)$ are shown graphically in Figs. 1, 2, 3, 4, 5, 6, 7, 8, 9, 10, 11, and 12. To study the effect of these parameters, the remaining parameters are taken as $B_r = 0.5$, $P_r = 1.0$, and $N_r = 1.0$.

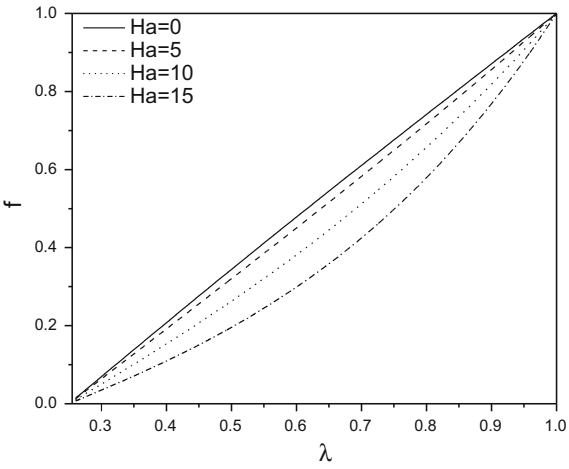

Fig. 1 Effect of magnetic parameter on velocity

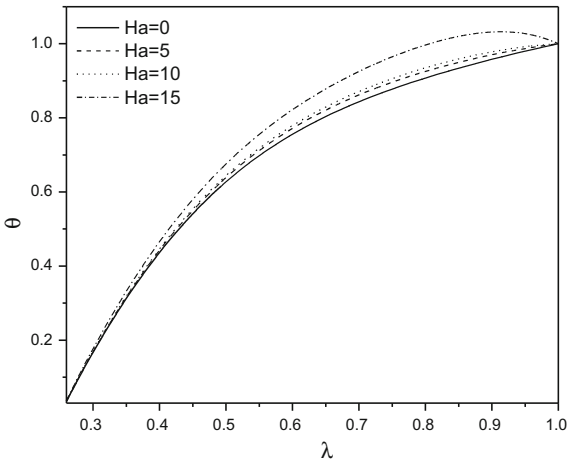

Fig. 2 Effect of magnetic parameter on temperature

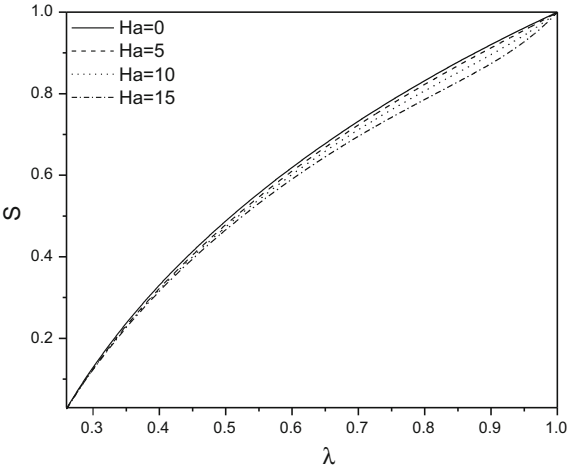

Fig. 3 Effect of magnetic parameter on nanoparticle concentration

Figures 1, 2 and 3 represents the influence of the magnetite parameter Ha on dimensionless velocity, temperature, and nanoparticle volume fraction. Figure 1 reveals that the dimensionless velocity is decaying with the rise in Ha. The magnetic field which is applied orthogonally to the flow direction gives a resistive force known as Lorentz force. This Lorentz force resists the flow of nanofluid therefore the velocity decreases. Figure 2 presents the variations in dimensionless temperature with Ha. From this figure, it observed that the temperature $\theta(\lambda)$ is increasing with the increase in Ha. Figure 3 depicts the variations of $S(\lambda)$ with Ha. A decay in a nanoparticle volume fraction $S(\lambda)$ is noticed as the magnetic parameter Ha increases.

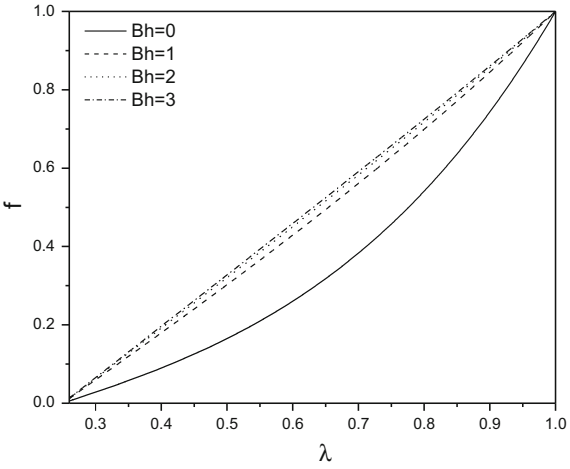

Fig. 4 Effect of Hall parameter on velocity

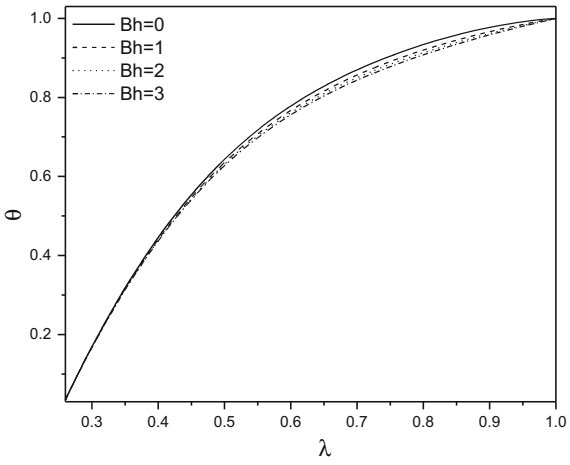

Fig. 5 Effect of Hall parameter on temperature

The variation of the velocity $f(\lambda)$, temperature $\theta(\lambda)$ and nanoparticle volume fraction $S(\lambda)$ with Hall parameter β_h is presented in Figs. 4, 5 and 6. It is noticed from Fig. 4 that the velocity is incrementing with a rise in the valued of the Hall parameter β_h . From Fig. 5, it is observed that, the dimensionless temperature $\theta(\lambda)$ is decreasing with an increase in β_h. There is an increment in a nanoparticle volume fraction $S(\lambda)$ with the increment in the value of β_h as depicted in Fig. 6. The inclusion of Hall parameter reduces the effective conductivity and hence drops the magnetic resistive force. Hence, increase in β_h raises the velocity component $f(\lambda)$, the nanoparticle volume fraction $S(\lambda)$ and decreases temperature $\theta(\lambda)$.

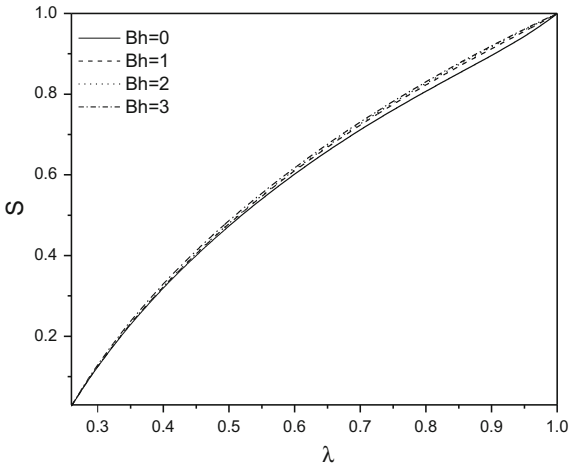

Fig. 6 Effect of Hall parameter on nanoparticle concentration

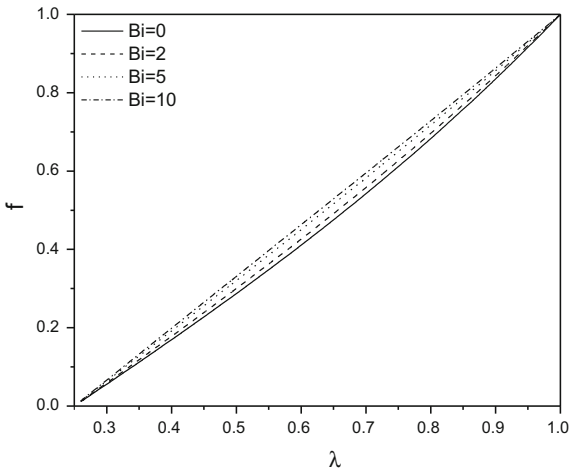

Fig. 7 Effect of ion-slip parameter on velocity

The variation of the velocity in flow direction $f(\lambda)$, temperature $\theta(\lambda)$, and nanoparticle volume fraction $S(\lambda)$ with ion-slip parameter β_i are depicted in Figs. 7, 8, and 9. Figure 7 reveals that the velocity in flow direction is enhanced with the enhancement in the parameter β_i . From Fig. 8, it is seen that the temperature $\theta(\lambda)$ decreases with the increase in β_i. The nanoparticle volume fraction $S(\lambda)$ is enhanced with an increase in β_i as shown in Fig. 9. The effective conductivity increases as increase in β_i, hence the damping force on the dimensionless velocity decreases and due to this the dimensionless velocity increases.

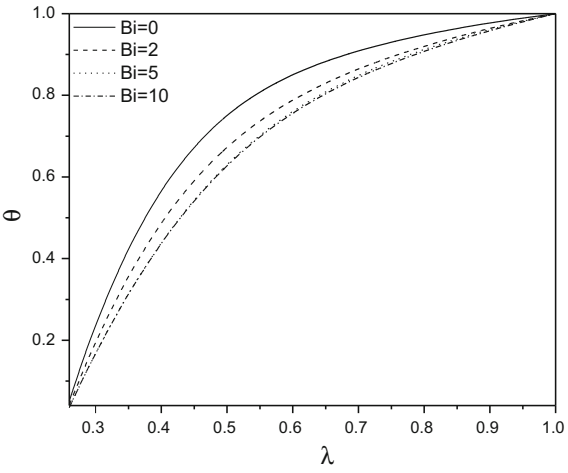

Fig. 8 Effect of ion-slip parameter on temperature

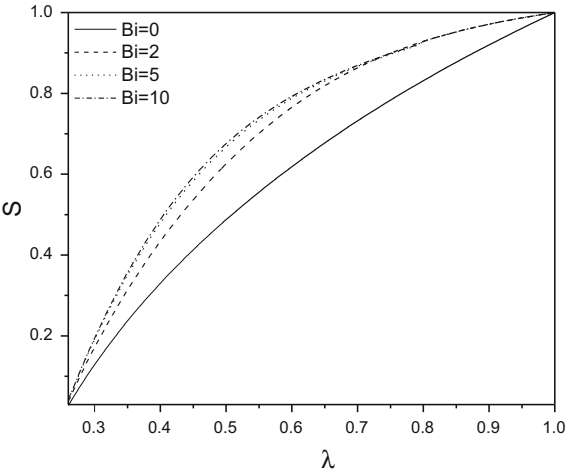

Fig. 9 Effect of ion-slip parameter on nanoparticle concentration

The impact of the thermophoresis parameter N_t on the dimensionless velocity $f(\lambda)$, the dimensionless temperature $\theta(\lambda)$, and nanoparticle volume fraction $S(\lambda)$ are depicted in Figs. 10, 11, and 12. The dimensionless velocity $f(\lambda)$ is raising with rise in N_t as shown in Fig. 10. Figure 11 reveals that the dimensionless temperature $\theta(\lambda)$ is enhanced with an enhancement in N_t. Increase of N_t leads to increases the effective conductivity, hence the nanoparticle volume fraction $S(\lambda)$ is decreasing as recognized in Fig. 12.

The influence of the Brownian motion parameter N_b on the velocity $f(\lambda)$, dimensionless temperature $\theta(\lambda)$, and nanoparticle concentration $S(\lambda)$ are depicted in

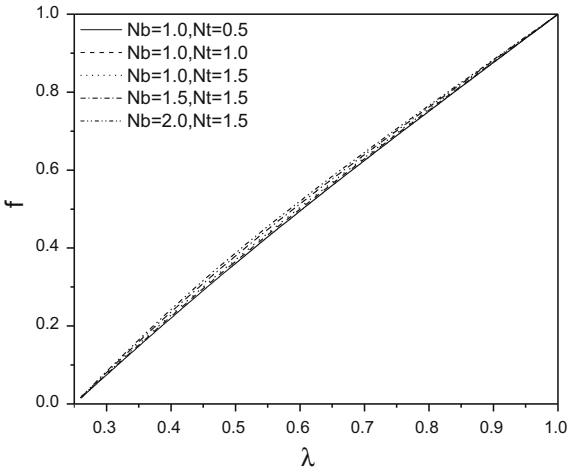

Fig. 10 Effect of thermophoresis and Brownian motion parameters on velocity

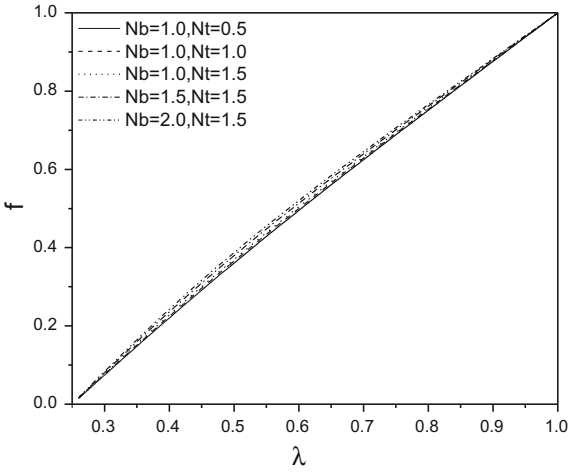

Fig. 11 Effect of thermophoresis and Brownian motion parameters on temperature profile

Figs. 10, 11, and 12. The velocity $f(\lambda)$ is increasing with the increment in the value of N_b as shown in Fig. 10. Figure 11 explains that the dimensionless temperature $\theta(\lambda)$ rises with the rise in the value of N_b. Enhancement in N_b leads to increase in the effective conductivity, therefore nanoparticle volume fraction $S(\lambda)$ is decreasing as given in Fig. 12.

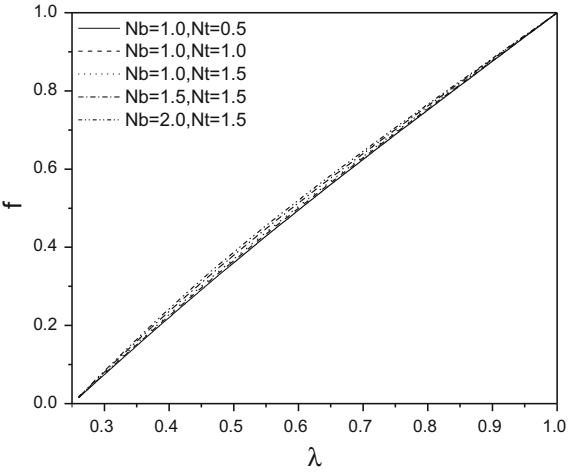

Fig. 12 Effect of thermophoresis and Brownian motion parameters on nanoparticle concentration profile

4 Conclusions

This article investigates the effects of thermophoresis, Brownian motion, magnetic, and Hall and ion-slip parameter on the natural convective flow of nanofluid through the annulus between two concentric coaxial cylinders. The nondimensional nonlinear differential equations are solved using the HAM procedure. The main findings are encapsulated below:

- The dimensionless velocity and nanoparticle concentration decreases, whereas the dimensionless temperature rises with the increment in magnetic parameter.
- As the Hall parameter increments, the dimensionless velocity and the nanoparticle concentration rise but the dimensionless temperature decreases.
- The increment in ion-slip parameter leads to enhance the dimensionless velocity and the nanoparticle concentration and decrease in the dimensionless temperature.

References

1. Choi, S.U.S.: Enhancing thermal conductivity of fluids with nanoparticles. In: Singer, D., Wang, H. (eds.) Development and Applications of Non-Newtonian Flows, pp. 99–106. American Society of Mechanical Engineers, New York (1995)
2. Dawood, H.K., Mohammed, H.A., Sidik, N.A.C., Munisamy, K.M., Wahid, M.A.: Forced, natural and mixed-convection heat transfer and fluid flow in annulus: A Rev. Int. Commun. Heat Mass Transf. **62**, 45–57 (2015)
3. Togun, H., Abdulrazzaq, T., Kazi, S.N., Badarudin, A., Kadhum, A.A.H., Sadeghinezhad, E.: A review of studies on forced, natural and mixed heat transfer to fluid and nanofluid flow in an annular passage. Renew. Sustain. Energy Rev. **39**, 835–856 (2014)

4. Chamkha, A.J., Jena, S.K., Mahapatra, S.K.: MHD convection of nanofluids: a review. J. Nanofluids **4**(3), 271–292 (2015)
5. Tani, I.: Steady flow of conducting fluids in channels under transverse magnetic fields with consideration of Hall effects. J. Aerosp. Sci. **29**, 297–305 (1962)
6. Srinivasacharya, D., Kaladhar, K.: Analytical solution of MHD free convective flow of couple stress fluid in an annulus with Hall and Ion-slip effects. Nonlinear Anal. Model. Control **16**(4), 477–487 (2011)
7. Odelu, O., Naresh Kumar, N.: Hall and Ion slip effects on free convection heat and mass transfer of chemically reacting couple stress fluid in a porous expanding or contracting walls with soret and dufour effects. Front. Heat Mass Transf. **5**, 22–34 (2014)
8. Motsa, S.S., Shateyi, S.: The effects of chemical reaction, Hall, and Ion-Slip currents on MHD micropolar fluid flow with thermal diffusivity using a novel numerical technique. J. Appl. Math. **2012** Article ID 689015, 30 pages (2012)
9. Liao, S.J.: Beyond Perturbation. Introduction to Homotopy Analysis Method. Chapman and Hall/CRC Press, Boca Raton (2003)

Chemically Reacting Radiative Casson Fluid Over an Inclined Porous Plate: A Numerical Study

MD. Shamshuddin, S. R. Mishra and Thirupathi Thumma

Abstract The present study analyzes unsteady magnetohydrodynamic free convection flow of a chemically reacting Casson fluid flow over an inclined porous plate. The thermal radiation effects have also been considered. The governing partial differential equations are transformed to nonlinear partial differential equations by using nondimensional quantities. The solutions of these simplified coupled nonlinear equations are calculated using a Galerkin finite element method with weighted residual approach. The physical significance of emerging physical parameters on flow field, temperature, and concentration profiles is presented through graphs and discussed.

Keywords Casson fluid · Inclined plate · Thermal radiation
Viscous dissipation · Mass transfer · Chemical reaction

1 Introduction

Most of the investigations have considered MHD (Magnetohydrodynamic) flow, heat and mass transfer in porous and nonporous media. MHD features in a wide spectrum of modern industrial processes including bubble levitation, alloy manufacture, nuclear heat transfer control, power generators, etc. Casson fluids (sauce, jelly, human

MD. Shamshuddin (✉)
Department of Mathematics, Vaagdevi College of Engineering,
Warangal 506005, Telangana, India
e-mail: shammaths@gmail.com

S. R. Mishra
Department of Mathematics, Siksha 'O' Anusandhan Deemed to be University,
Bhubaneswar 751030, Odisha, India
e-mail: satyaranjan_mshr@yahoo.co.in

T. Thumma
Department of Mathematics, B V Raju Institute of Technology,
Narsapur, Medak 502313, Telangana, India
e-mail: thirupathi.thumma@gmail.com

D. Srinivasacharya and K. S. Reddy (eds.), *Numerical Heat Transfer and Fluid Flow*, Lecture Notes in Mechanical Engineering,
https://doi.org/10.1007/978-981-13-1903-7_54

blood, honey, etc.) first coined by Casson [1] constitute a significant advance in the fluid dynamic technology. Hussain et al. [2] used Laplace transform to analyze the impact of heat transfer in MHD flow of Casson fluid with Newtonian heating, which was again examined by Khalid et al. [3] and Das et al. [4] to obtain closed-form solution. Owing to high-temperature thermal radiation, the heat transfer and chemical species present under a large temperature are significant. By considering radiation and chemical reaction effects various analytical procedures have been implemented for Casson fluid over oscillating channels [5–8]. These studies all demonstrated the significant influence of thermal radiation and chemical reaction on thermofluid dynamic characteristics in Casson fluids.

External convective boundary layer flows over horizontal or vertical flat plates have been studied by many researchers. Recently, some contributions dealing with oblique surfaces which include Gurram et al. [9] who used perturbation technique, and Jain and Preeti [10] who used Crank–Nicolson implicit finite difference method. This motivation leads us to develop a mathematical model for radiative chemically reacting Casson thermo-solutal transport from a tilted permeable plate. Finite element computational solutions are developed to illustrate the influence of magnetic field parameter, Casson parameter, thermal and solutal Grashof numbers, plate inclination angle, phase angle, thermal radiation parameter, and first-order chemical reaction parameter on key characteristics of flow phenomena. Extensive interpretation of computations is provided.

2 Mathematical Formulation

Free convective flow of unsteady two-dimensional magnetohydrodynamic Casson fluid from an inclined porous plane (with inclination angle α to the vertical) is considered. The plane oscillates in its own plane with velocity $V = U\ H(t')\ \mathrm{Cos}\ (\omega' t')$ fixed at $y = 0$, which is measured in the normal to the direction of the plate; thereafter, the plate is maintained at constant wall temperature T_w and concentration C_w. Assume that the plate temperature and concentration are greater than the ambient temperature T_∞ and concentration C_∞. A uniform magnetic field of strength B_0 is applied in the direction perpendicular to the plate. Induced magnetic field is neglected due to the assumption of low Reynolds number. Owing to high temperature, the thermal radiation effects are included in the energy equation. The reactive species present in magnetic Casson fluid obeys first-order chemical reaction. The constructive equations for the Casson fluid can be referred in Khalid et al. [3].

Under the above assumptions, the equation that describes the physical situation with species concentration conservation equation is given as follows, Khalid et al. [3] and Reddy et al. [8]:

$$\rho\ \frac{\partial u'}{\partial t'} = \mu_B\left(1+\frac{1}{\gamma}\right)\frac{\partial^2 u'}{\partial y'^2} - \sigma\ B_0^2\ u' - \frac{\mu}{K_1}\phi\ u' + \rho\ g\ \beta_T\left(T'-T_\infty\right)\cos\alpha\ + \rho\ g\ \beta_C\left(C'-C_\infty\right)\cos\alpha, \tag{1}$$

$$\rho C_p\frac{\partial T}{\partial t'} = \kappa\frac{\partial^2 T}{\partial y'^2} - \frac{\partial q_r}{\partial y}, \tag{2}$$

$$\frac{\partial C}{\partial t'} = D\frac{\partial^2 C}{\partial y^2} - K'r\left(C'-C_\infty\right) \tag{3}$$

The relevant and appropriate initial and boundary conditions are given as follows:

$$t<0: \left\{ u'=0,\ T'=T_\infty,\ C'=C_\infty \text{ for all } \ y>0 \right.$$

$$t\geq 0 \begin{cases} u'=U\ H\ \left(t'\right)\ \mathrm{Cos}\ \left(\omega' t'\right),\ T=T_w, C=C_w, \text{ at } \ y=0 \\ u'\to 0, \quad T'\to T_\infty, \qquad C'\to C_\infty \qquad\qquad \text{as } \ y\to\infty \end{cases} \tag{4}$$

Here, $u', t', T', C', \mu_B, \gamma, \rho, g, \beta_T, \ \beta_C, Cp, \alpha, \kappa, \sigma, \mu, \phi$ and K_1 are the velocity of fluid in x-direction, time, temperature, concentration, plastic dynamic viscosity, Casson parameter, density, acceleration due to gravity, volumetric coefficient of thermal expansion, volumetric coefficient of solutal expansion, specific heat at constant pressure, thermal conductivity, electric conductivity of the fluid, fluid dynamic viscosity, porosity of the fluid, and permeability of the fluid, respectively. Although the primitive conservation equation and boundary conditions can be solved with a variety of numerical methods, e.g., Crank–Nicolson difference scheme, the solution requires explicit data for the thermophysical properties. It is, therefore, judicious to render the system dimensionless. Following Rosseland approximation [11], the net radiative heat flux $\frac{\partial q_r}{\partial y'} = \frac{16\,\sigma^* T_\infty'^3}{3k^*}\frac{\partial^2 T'}{\partial y'^2}$ and nondimensional variables are

$$u=\frac{u'}{U}, y=\frac{U}{\nu}y', t=\frac{U^2}{\nu}t', \theta=\frac{T'-T_\infty}{T_w-T_\infty},$$
$$\varphi=\frac{C'-C_\infty}{C_w-C_\infty}, \omega'=\frac{\nu}{U^2}\omega. \tag{5}$$

Assimilating the nondimensional variables (5) into (1)–(4) yields the following system of unsteady nondimensional partial differential equations:

$$\frac{\partial u}{\partial t} = \left(1+\frac{1}{\gamma}\right)\frac{\partial^2 u}{\partial y^2} - Nu + (Gr\theta + Gm\varphi)\cos\alpha, \tag{6}$$

$$\frac{\partial\theta}{\partial t} = \frac{1}{\Gamma}\frac{\partial^2\theta}{\partial y^2}, \tag{7}$$

$$\frac{\partial\varphi}{\partial t} = \frac{1}{Sc}\frac{\partial^2\varphi}{\partial y^2} - Kr\ \varphi \tag{8}$$

Dimensionless initial and boundary conditions are

$$t < 0 : \left\{ u = 0,\ \theta = 0,\ \phi = 0 \text{ for all } \ y > 0 \right.$$

$$t \geq 0 : \begin{cases} u = H\ (t)\ \text{Cos}\ (\omega t),\ \theta = 1,\ \ \phi = 1 \ \ \text{at} \ \ y = 0 \\ u \to 0, \qquad\qquad\qquad \theta \to 0,\ \phi \to 0 \ \text{as} \ \ y \to \infty \end{cases} \tag{9}$$

where $N = \left(M^2 + (1/K)\right)$ and $\Gamma = (1 - (4/3R + 4))Pr$. Here, the nondimensional parameters are given as follows: $\gamma = \mu_B \sqrt{2\pi c}/P_y$ is the dimensionless Casson parameter, $Gr = \nu\ g\ \beta_T (T_w - T_\infty)/U^3$ is the thermal Grashof number, $Gm = \nu g \beta_C (C_w - C_\infty)/U^3$ is the species Grashof number, $M^2 = \sigma\ B_0^2\ \nu/\rho\ U^2$ is the magnetic body force parameter, $K = K_1\ U^2/\phi\ \nu^2$ is the permeability parameter, $Pr = \nu \rho Cp/\kappa$ is the Prandtl number, $R = kk^*/4\sigma^* T_\infty^3$ is the conduction–radiation parameter, $Sc = \nu/D$ is the Schmidt number, and $Kr = K' r \nu/U^2$ is the first-order chemical reaction parameter.

3 Numerical Solution with Galerkin Finite Element Method

The transformed, coupled boundary value problems (6)–(8) with (9) are solved employing finite element method (FEM), a numerical method. Variational finite element method is detailed in Reddy [12] and Bathe [13]. A brief description of fundamental steps that occur in FEM can be referred in Shamshuddin et al. [14]. For computational purpose, $y_{\max} = 4$ represents the infinity.

Skin friction, rate of heat, and mass transfer in nondimensionalized form are given as follows:

$$C_f = \left(1 + \frac{1}{\gamma}\right) u'(0),\ Nu/Re_x = -\theta'(0), \quad \text{and}\ Sh/Re_x = -\varphi'(0) \tag{10}$$

4 Results and Discussion

Khalid et al. [3] focused principally on the influence of heat transfer and that to a vertical plate. Herein, we address both heat and mass transfer effects of an inclined porous plate under the influence of thermal radiation and chemical reaction via finite element method. Pertinent parameters effecting the flow are depicted graphically in Figs. 1, 2, 3, 4, 5, 6, 7, and 8. Figure 1 shows the influence of M on the velocity profile. It is observed that with the increase in magnetic parameter, the amplitude of the velocity as well as the boundary layer thickness decreases. Physically, this results

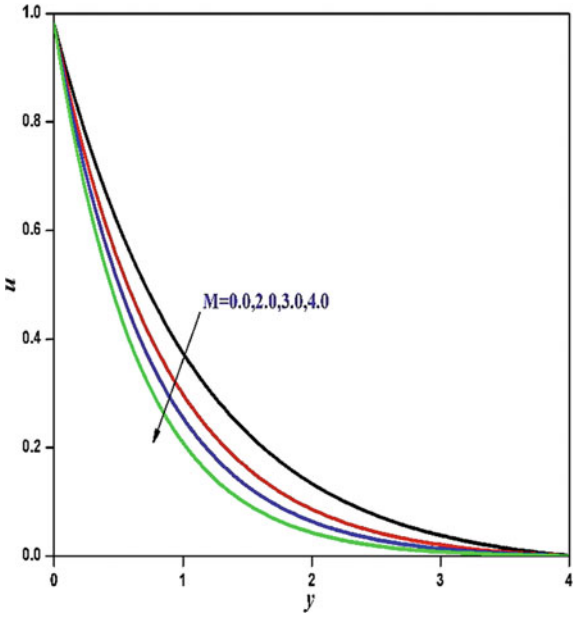

Fig. 1 Effect of M on velocity profiles

from the impeding nature of the transverse magnetic field, which exerts a retarding Lorentzian body force on the free convective flow. With the increasing values of M, the magnetohydrodynamic drag decelerates the flow, i.e., suppresses the velocities across the boundary layer. Figure 2 illustrates the impact of Casson parameter γ on velocity; an increase in the Casson parameter results in the depreciation in the velocity profiles. Figures 3 and 4 show the variations in velocity distributions for different values of Gr and Gm. The velocity profiles of inclined plate are enhanced with an increase in thermal Grashof number as well as solutal Grashof number. This is attributing to the dominance of buoyancy forces over the viscous forces, which serves to assist momentum diffusion and accelerates the flow. Figure 5 shows the effect of angle of inclination (α) of the surface on velocity profiles. It is clear to be remarked that the velocity profile decreases as angle of inclination increases. Furthermore, the buoyancy effects decrease to a component of the maximum buoyancy force for a vertical plate, since the buoyancy forces scale with the factor $\cos\alpha$. Hence, the fluid attains high-velocity profiles for the vertical plate, i.e., $\alpha = 0$ and progressively decreases with greater inclination of the plate. Figure 6 illustrates the evolution in linear velocity distributions with different values of phase angle, ωt. A weak oscillatory behavior is computed for the linear velocity and with increasing phase angle (four different values are chosen), there is a progressive deceleration in the flow. In fact, at maximum phase angle, flow reversal is induced since the linear velocities attain negative values at $\omega t = \pi$. At zero phase angle, the maximum velocity is achieved at the plate, whereas for $\omega t = \pi$, the maximum velocity is attained in the

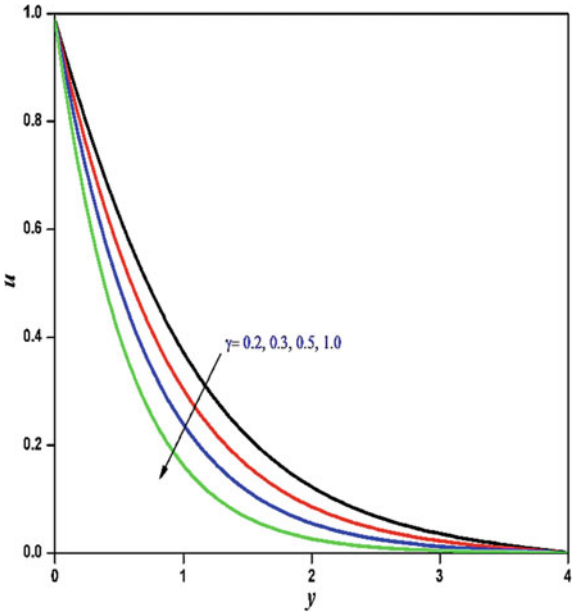

Fig. 2 Effect of γ on velocity profiles

free stream. Strong damping is, therefore, generated in the flow with increasing phase angle. From Fig. 7, it is clear to remark that the thermal boundary layer thickness decreases with an increase in radiation–conduction parameter. Therefore, the fluid temperature also reduces with greater values of R. It is noticed from Fig. 8 that with an increase in chemical reaction concentration, the distribution decreases. Physically, in case of destructive chemical reaction, the original species is destroyed significantly. Therefore, molecular diffusion of species leads to decrease in magnitude of concentration, and as a result, the concentration boundary layer thickness decreases. Finally, the numerical computation for the physical parameters is obtained and presented in Table 1. The validation of the presented results is obtained and found to be in good agreement with Khalid et al. [3]. It is also observed that Prandtl number increases both the local skin friction and Nusselt number. Thermal Grashof number and the phage angle reduce the skin friction whereas magnetic and porosity increases significantly. Both Schmidt number and chemical reaction parameter favor to increase the Sherwood number.

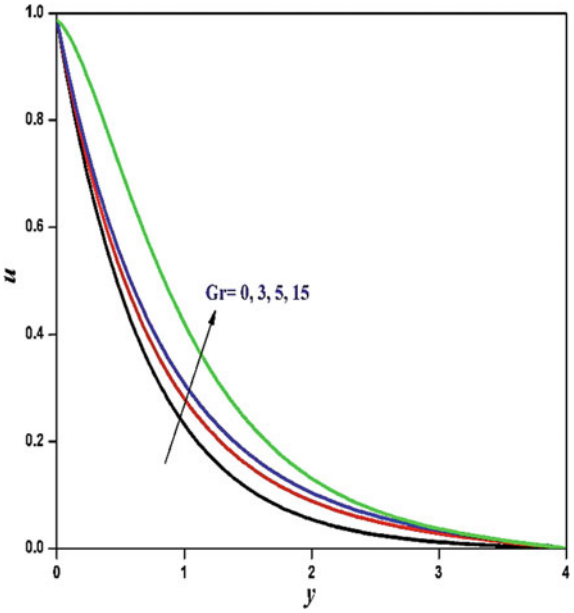

Fig. 3 Effect of *Gr* on velocity profiles

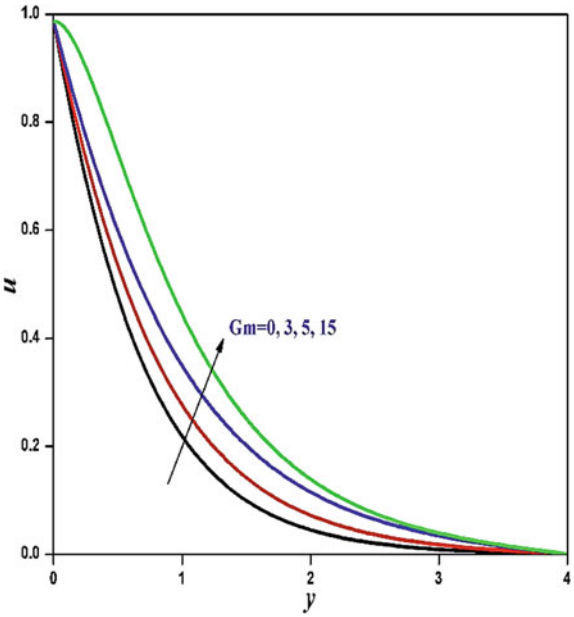

Fig. 4 Effect of *Gm* on velocity profiles

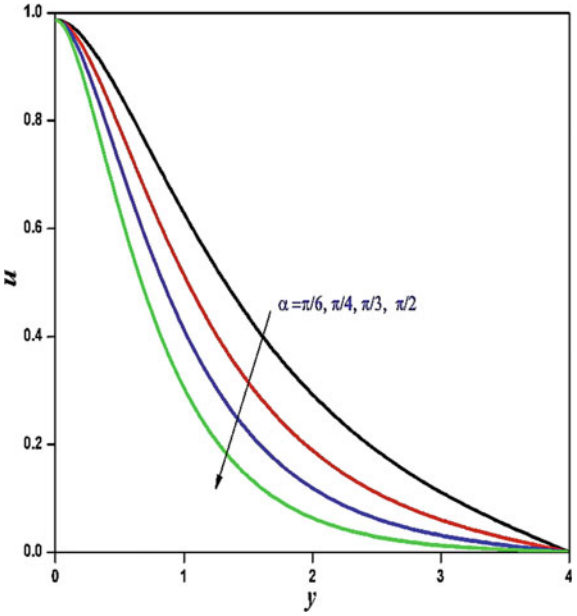

Fig. 5 Effect of α on velocity profiles

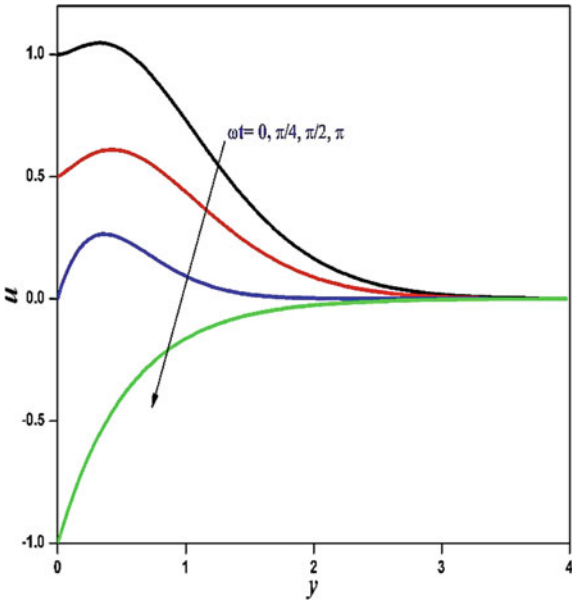

Fig. 6 Effect of ωt on velocity profiles

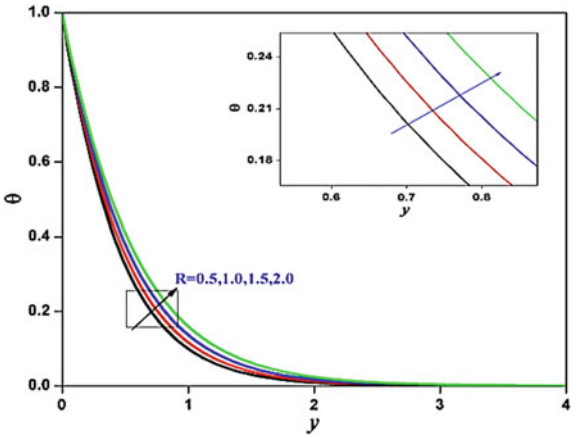

Fig. 7 Effect of R on temperature profiles

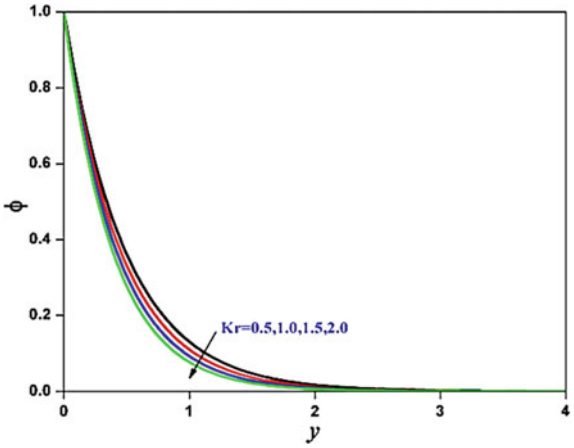

Fig. 8 Effect of Kr on concentration profiles

5 Conclusions

Casson fluid model is a particular type of non-Newtonian fluid that is widely used for modeling blood flow in narrow arteries. The main findings of the present mathematical analysis are as follows. The present analysis has shown that increasing M, γ, α, ωt decelerates the linear velocity and conversely accelerates the flow as Gr and Gm increase. Increasing radiative effect elevates the temperature magnitudes. Increasing chemical reaction parameter depresses the concentration magnitudes. Finally, FEM achieves very rapid convergence and highly accurate solution and shows excellent promise in simulating Casson fluid dynamic problems. Hence, in view of the results

Table 1 Local skin friction and Nusselt and Sherwood numbers when $Gm = \alpha = 0$, $R \to \infty$

									Analytical results		FEM results		
Pr	*Gr*	γ	ωt	*M*	*K*	*t*	*Sc*	*Kr*	C_f	Nu	C_f	*Nu*	*Sh*
0.3	3	0.5	$\pi/4$	0.5	0.2	0.3	∞	0	1.029920	0.564	1.0299371	0.5646	–
0.71							∞	0	1.291660	0.867	1.2916732	0.8678	–
	5						∞	0	0.856995	–	0.8569471	–	–
		1					∞	0	0.939520	–	0.9394304	–	–
			$\pi/2$				∞	0	1.050090	–	1.0501406	–	–
				1.0			∞	0	1.084720	–	1.0848311	–	–
					1.0		∞	0	0.670201	–	0.6702979	–	–
						0.5	∞	0	0.692367	–	0.6925091	–	–
0.3						0.6	∞	0	–	0.398	–	0.3991	–
							0.6	0	–	–	–	–	0.5935
							1.0	0.5	–	–	–	–	0.7014
							0.6	0.5	–	–	–	–	1.2028

obtained, we conclude that the present study may be considered as an improvement in the studies of the mathematical modeling of blood flow in narrow arteries.

Acknowledgements Authors are thankful to the reviewers and conference chair, NHTFF-2018 for their insightful and constructive suggestions, which enhanced the quality and novelty of the paper significantly.

References

1. Casson, M.: A flow equation for pigment-oil suspensions of the printing ink type. In: Mills, C.C. (ed.) Rheology of Disperse Systems. Oxford, Pergamon pp. 84–104 (1959)
2. Hussain, A., Salleh, M.Z., Khan, I., Tahar, R.M.: Heat transfer in magnetohydrodynamic flow of a Casson fluid with porous medium and Newtonian heating. J. Nanofluids **6**, 1–10 (2017)
3. Khalid, A., Khan, I., Khan, A., Shafie, S.: Unsteady MHD free convection flow of Casson fluid past over an oscillating vertical plate embedded in a porous medium. Eng. Sci. Tech: Int. J **18**(3), 309–317 (2015)
4. Das, M., Mahato, N., Nandkeolyar, R.: Newtonian heating effect on unsteady hydromagnetic Casson fluid flow past a flat plate with heat and mass transfer. Alexandria Eng. J. **54**(4), 871–879 (2015)
5. Hussain, A., Salleh, M.Z., Khan, I., Tahar, R.M.: Unsteady heat transfer flow of a Casson fluid with newtonian heating and thermal radiation. J. Teknologi **78**(4), 1–7 (2016)
6. Mabood, F., Khan, W., Ismail, A.I.M.: Multiple slips effects on MHD Casson fluid flow in porous media with radiation and chemical reaction. Can. J. Phys. **94**(1), 26–34 (2016)
7. Kataria, H.R., Patel, H.R.: Radiation and chemical reaction effects on MHD Casson fluid flow past an oscillating vertical plate embedded in porous medium. Alexandria Eng. J. **55**(1), 583–595 (2016)
8. Reddy, S.H., Raju, M.C., Reddy, E.K.: Radiation absorption and chemical reaction effects on MHD flow of heat generating Casson fluid past oscillating vertical porous plate. Front. Heat Mass Transf. **7**, 21 (2016). https://doi.org/10.5098/hmt.7.21

9. Gurram, D., Balamurugan, K.S., Raju, V.C.C., Vedavathi, N.: Effect of chemical reaction on MHD Casson fluid flow past an inclined surface with radiation. SKIT Reas. J. **7**(1), 53–59 (2017)
10. Jain, S., Gupta, P.: Numerical study of unsteady inclined MHD Casson fluid flow and heat transfer through porous medium along vertical sheet. In: Global and Stochastic Analysis, special issue: 25th International Conference of Forum for Interdisciplinary Mathematics; pp. 33–40, MUK Publications (2017)
11. Brewster, M.Q.: Thermal Radiative Transfer and Properties. Wiley, New York (1992)
12. Reddy, J.N.: An Introduction to the Finite Element Method. McGraw-Hill, New York (1985)
13. Bathe, K.J.: Finite Element Procedures. Prentice-Hall, New Jersey (1996)
14. Shamshuddin, M.D., Anwar Beg, O., Ram, M.S., Kadir, A.: Finite element computation of multi-physical micropolar transport phenomena from an inclined moving plate in porous media. Indian J. Phys. **92**(2), 215–230 (2017). https://doi.org/10.1007/s12648-017-1095-y

Field-Driven Motion of Ferrofluids in Biaxial Magnetic Nanowire with Inertial Effects

Sharad Dwivedi

Abstract This work deals with the field-driven motion of magnetic nanofluids in biaxial ferromagnetic nanowire in the presence of inertial effects and crystallographic defects. We obtained the analytical results under the theoretical model of extended Landau–Lifshitz–Gilbert equation comprising the nonlinear dissipation components, viz., dry friction and viscous along with the inertial effects. More specifically, using the regular perturbation expansion technique, we derive an expression for the leading order traveling wave solutions under the action of the small transverse magnetic field.

Keywords Ferrofluids · Domain wall · Inertia · Nonlinear dissipations Micromagnetism

1 Preamble

In recent years, the study of ferrofluids, a colloidal liquid made of ferromagnetic nanoparticles, has attracted a huge attention due to its tremendous application in various sectors such as in modern electronic devices, magnetic sensors, nuclear systems, biomedical, and environmental sciences (cf. [1]). In storage devices, ferromagnetic nanowires (nanostrips) are enormously used to design the new magnetic memories. One of the most recent advancements is the racetrack memory [1], a three-dimensional storage device in which an array of U-shaped ferromagnetic nanowires is used to encode the information. In these memories, the information is accumulated as a pattern of the domain along the nanowires. Domains are the uniform magnetized regions in the medium separated by the thin continuum zones referred as domain walls (DWs). For the comprehensive description of magnetic domains, we refer the reader to the excellent monograph by Hubert and Schäfer (cf. [2]).

S. Dwivedi (✉)
SRM Research Institute and Department of Mathematics, SRM Institute of Science and Technology, Chennai 603 203, India
e-mail: sharadiitm@gmail.com

D. Srinivasacharya and K. S. Reddy (eds.), *Numerical Heat Transfer and Fluid Flow*, Lecture Notes in Mechanical Engineering,
https://doi.org/10.1007/978-981-13-1903-7_55

In this report, we delineate the zero-order traveling wave solutions (TWs) for a one-dimensional theoretical model of the extended Landau–Lifshitz–Gilbert equation with an inclusion of inertial effects. In recent works, there are primarily two techniques that have been extensively used to explain the DW motion. The first approach is based on the regular perturbation expansion technique in which we establish a regular asymptotic expansion considering the transverse magnetic field (TMF) and material anisotropy as a small parameter (cf. [3–6]). Moreover, the other approach relies on approximating the dynamics near the DW center (cf. [7–9]). We adopt the former approach to examine the DW motion.

The paper is organized in the following manner. In "Micromagnetic model and governing dynamics", we describe the theoretical model under consideration and the equation of motion which elucidate the evolution of magnetization inside the medium. In "Explication of DW motion", we characterize the DW propagation under the small TMF. More precisely, we derive an expression for the static wall profile in two faraway domains which separate a transverse domain wall (TDW) and then we investigate the dynamics of TWs in the presence of an applied TMF.

2 Micromagnetic Model and Governing Dynamics

We conceive a straight infinite ferromagnetic nanowire with the circular cross section. It is considered to be uniform in shape and placed along the $\mathbf{e}_1$-direction, $(\mathbf{e}_1, \mathbf{e}_2, \mathbf{e}_3)$ denotes the standard basis of $\mathbb{R}^3$. The magnetization inside the nanowire is given by the time-dependent spontaneous unitary vector field $\mathbf{u} = (u_1, u_2, u_3)$ with $\mathbf{u}(x,t) = \mathbf{U}(x,t)/U_s$, where U_s represents the saturation value of magnetization. We consider a biaxial nanowire with uniaxial anisotropy in the along the wire axis, i.e., toward $\mathbf{e}_1$-direction and the hard-axis anisotropy along the perpendicular $\mathbf{e}_2$-direction. We assume the easy-axis also referred as energetically preferred orientation of magnetization vector toward $\mathbf{e}_1$-direction. Further, we keep this system to an applied TMF $H_{ext} = H_1\mathbf{e}_1 + H_3\mathbf{e}_3$ which is constant in both the time and space variables.

A tail-to-tail TDW (types of DW in which the magnetization at the center of the wall oriented perpendicular to the wire axis) is supposed to be nucleated along the nanowire as portrayed in Fig. 1. More precisely, we take into an account of a TDW of width λ which separates the domains with $\mathbf{u}(x,t) \sim \mathbf{u}^*$ as $x \to -\infty$ and the domain with $\mathbf{u}(x,t) \sim \mathbf{u}^\sharp$ as $x \to +\infty$ together with the static wall constraints $u_t \to 0$ and $u_x \to 0$ as $|x| \to \infty$.

The one-dimensional generalized Landau–Lifshitz–Gilbert equation comprising the nonlinear dissipations and inertial effects is described as follows (cf. [7–10]):

$$\partial_t \mathbf{u} + \left[\alpha_G\left(1 + \frac{\alpha_v}{\gamma^2}\left(\partial_t \mathbf{u}\right)^2\right) + \frac{\lambda\alpha_d}{|\partial_t \mathbf{u}|}\right](\mathbf{u} \times \partial_t \mathbf{u}) + \alpha_G \tau\,(\mathbf{u} \times \partial_{tt}\mathbf{u}) = \gamma\left(\mathbf{u} \times H_{eff}\right), \tag{1}$$

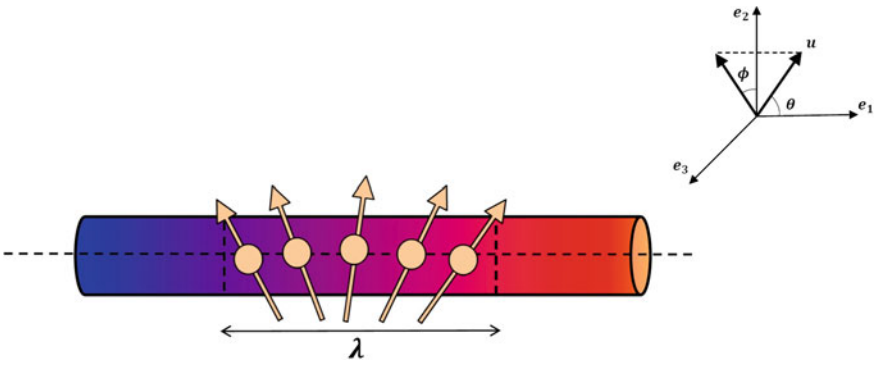

Fig. 1 Sketch of a tail-to-tail TDW in a biaxial ferromagnetic nanowire along with the reference axes exhibiting the polar and azimuthal angle as θ and φ, respectively

with

$$H_{eff} = \frac{2A_{ex}}{\mu_0 U_s^2}\partial_{xx}\mathbf{u} + \frac{2K_1}{\mu_0 U_s^2}u_1\mathbf{e}_1 - \frac{2K_2}{\mu_0 U_s^2}u_2\mathbf{e}_2 + (-u_2\mathbf{e}_2 - u_3\mathbf{e}_3) + H_1\mathbf{e}_1 + H_3\mathbf{e}_3.$$

Throughout the paper, $\partial_x = \frac{\partial}{\partial x}$ and $\partial_{xx} = \frac{\partial^2}{\partial x^2}$ stand for the first- and second-order partial derivatives, respectively. In Eq. (1), second term on the L.H.S. describes the energy dissipation in the system and consists of linear, nonlinear viscous, and dry-friction dissipation terms, respectively. More precisely, linear viscous dissipation also known as Gilbert dissipation characterizes the dissipation of energy in the ideal ferromagnets while the nonlinear viscous dissipation delineates the large angle variation in the DW motion and the dry-friction dissipation reflects the energy dissipation due to the dislocations, impurities, and other defects present in the material. The positive parameters α_G, α_v, and α_d reflect the standard phenomenological Gilbert damping, nonlinear viscous, and dry-friction dissipation factors, respectively. Also, the positive constant γ is defined in terms of Landè factor g, electron charge e, permeability of the vacuum μ_0, and the electron mass m_e as $\gamma = (\mu_0 U_s g e)/m_e$.

Furthermore, the subsequent term elucidates the inertial effects in which the parameter τ represents the relaxation time of the angular momentum describing the relaxation of magnetization acceleration from the inertial dynamic regime to precessional dynamic regime. However, the term on the R.H.S. of Eq. (1) depicts the precession of magnetization toward the total effective field H_{eff}. In the considered expression of total effective field H_{eff}, the terms denote the exchange, anisotropy (easy-axis and hard-axis), demagnetizing, and the applied TMF, respectively. Also, A_{ex}, K_1, and K_2 stand for the exchange, easy-axis anisotropy, and hard-axis anisotropy constants, respectively. We remark that in ferromagnets, except for few favorable geometries such as a straight ferromagnetic nanowire with circular cross section (cf. [11]) and uniform magnetized ellipsoid (cf. [12, 13]), the stray field calculations are highly complicated and require a numerical evaluation.

Next, we propose the dimensionless space, inertial, and time variables $\tilde{x} = x\sqrt{\frac{K_1}{A_{ex}}}$, $\tilde{\tau} = \gamma\tau$ and $\tilde{t} = \gamma t$, to reduce Eq. (1) in the dimensionless form (cf.[14]):

$$\partial_{\tilde{t}}\mathbf{u} + \left[\alpha_G\left(1 + \alpha_v\left(\partial_{\tilde{t}}\mathbf{u}\right)^2\right) + \frac{\alpha_d}{|\partial_{\tilde{t}}\mathbf{u}|}\right](\mathbf{u} \times \partial_{\tilde{t}}\mathbf{u}) + \alpha_G\tilde{\tau}\,(\mathbf{u} \times \partial_{\tilde{t}\tilde{t}}\mathbf{u}) = \left(\mathbf{u} \times \tilde{H}_{eff}\right), \tag{2}$$

with

$$\tilde{H}_{eff} = \tilde{K}_1\partial_{\tilde{x}\tilde{x}}\mathbf{u} + \tilde{K}_1 u_1\mathbf{e}_1 - (\tilde{K}_2 + 1)u_2\mathbf{e}_2 - u_3\mathbf{e}_3 + \tilde{H}_{ext}.$$

In Eq. (2), $\tilde{K}_1 = 2K_1/\left(\mu_0 U_s^2\right)$ and $\tilde{K}_2 = 2K_2/\left(\mu_0 U_s^2\right)$ denote the dimensionless constants and $\tilde{H}_{ext} = \left(\tilde{H}_1, 0, \tilde{H}_3\right)$ exhibits the dimensionless applied TMF.

3 Explication of DW Motion

To analyze the DW motion, we use the spherical coordinate system and express the unitary magnetization vector field as

$$\mathbf{u}(\tilde{x}, \tilde{t}) = (\cos\theta, \sin\theta\cos\varphi, \sin\theta\sin\varphi)\,. \tag{3}$$

In Eq. (3), $\theta(\tilde{x}, \tilde{t})$ represents the polar angle and $\varphi(\tilde{x}, \tilde{t})$ exhibits the azimuthal angle of magnetization as exhibited in Fig. 1. In the polar system, Eq. (2) gives the pair of partial differential equations of the form:

$$\begin{aligned}
&\sin\theta\,(\partial_{\tilde{t}}\varphi) + \left[\alpha_G\left(1 + \alpha_v\left((\partial_{\tilde{t}}\theta)^2 + \sin^2\theta\,(\partial_{\tilde{t}}\varphi)^2\right)\right)\right.\\
&\left.+\alpha_d\left((\partial_{\tilde{t}}\theta)^2 + \sin^2\theta\,(\partial_{\tilde{t}}\varphi)^2\right)^{-1/2}\right](\partial_{\tilde{t}}\theta) + \alpha_G\tilde{\tau}\,(\partial_{\tilde{t}\tilde{t}}\theta) - \alpha_G\tilde{\tau}\sin\theta\cos\theta\,(\partial_{\tilde{t}}\varphi)^2\\
&= -\tilde{H}_1\sin\theta - \sin\theta\cos\theta + \tilde{H}_3\cos\theta\sin\varphi + \tilde{K}_1(\partial_{\tilde{x}\tilde{x}}\theta)\tilde{K}_1\sin\theta\cos\theta(1 + (\partial_{\tilde{x}}\varphi)^2)\\
&-\frac{1}{2}\tilde{K}_2\sin 2\theta\cos^2\varphi,
\end{aligned} \tag{4}$$

$$\begin{aligned}
&-(\partial_{\tilde{t}}\theta) + \left[\alpha_G\left(1 + \alpha_v\left((\partial_{\tilde{t}}\theta)^2 + \sin^2\theta\,(\partial_{\tilde{t}}\varphi)^2\right)\right)\right.\\
&\left.+\alpha_d\left((\partial_{\tilde{t}}\theta)^2 + \sin^2\theta\,(\partial_{\tilde{t}}\varphi)^2\right)^{-1/2}\right]\sin\theta\,(\partial_{\tilde{t}}\varphi) + \alpha_G\tilde{\tau}\sin\theta\,(\partial_{\tilde{t}\tilde{t}}\varphi)\\
&+ 2\alpha_G\tilde{\tau}\cos\theta\,(\partial_{\tilde{t}}\theta)\,(\partial_{\tilde{t}}\varphi) = \tilde{H}_3\cos\varphi + \tilde{K}_1\sin\theta(\partial_{\tilde{x}\tilde{x}}\varphi)2\tilde{K}_1\cos\theta(\partial_{\tilde{x}}\theta)(\partial_{\tilde{x}}\varphi)\\
&+\frac{1}{2}\tilde{K}_2\sin\theta\sin 2\varphi.
\end{aligned} \tag{5}$$

With the help of Eqs. (4) and (5), we derive an expression for the static profile of magnetization vector in the two faraway domains separated a TDW of width λ. In the left domain, as $\tilde{x} \to -\infty$, we consider the polar and azimuthal angle of magnetization vector as θ^* and φ^*, respectively, which in turn gives the closed-form expression of $\mathbf{u}^*$. In addition, due to the symmetrical nature of TDW about the DW center, as $\tilde{x} \to +\infty$, the two angles $\pi - \theta^*$ and φ^* yield the direction of magnetization $\mathbf{u}^\sharp$ on the right domain. We use the static and DW condition to derive the expression for θ^* and φ^*:

$$\left(\partial_{\tilde{t}}\theta^*\right) = 0,\ \left(\partial_{\tilde{t}}\varphi^*\right) = 0 \text{ and } \left(\partial_{\tilde{x}}\theta^*\right) = \left(\partial_{\tilde{x}\tilde{x}}\theta^*\right) = 0;\ \left(\partial_{\tilde{x}}\varphi^*\right) = \left(\partial_{\tilde{x}\tilde{x}}\varphi^*\right) = 0. \quad (6)$$

Under the light of Eqs. (6), (4), and (5) renders

$$-\tilde{H}_1 \sin\theta^* + \tilde{H}_3 \cos\theta^* \sin\varphi^* - \tilde{K}_1 \sin\theta^* \cos\varphi^* - \tilde{K}_2 \sin\theta^* \cos\theta^* \cos^2\varphi^* - \sin\theta^* \cos\theta^* = 0, \quad (7)$$

$$\tilde{H}_3 \cos\varphi^* + \tilde{K}_2 \sin\theta^* \sin\varphi^* \cos\varphi^* = 0. \quad (8)$$

On solving Eqs. (7) and (8), we obtain

$$\theta^* = \cos^{-1}\left(\frac{-\tilde{H}_1}{1+\tilde{K}_1+\tilde{K}_2}\right);\ \ \varphi^* = \sin^{-1}\left(\frac{-\tilde{H}_3(1+\tilde{K}_1+\tilde{K}_2)}{\tilde{K}_2\left(\left(1+\tilde{K}_1+\tilde{K}_2\right)^2 - \tilde{H}_1^2\right)^{1/2}}\right). \quad (9)$$

It is worth to mention that under the prescribed conditions, the TDW structure exists as long as the longitudinal component of an applied TMF $\tilde{H}_1$ remains smaller than the entity $\left(1+\tilde{K}_1+\tilde{K}_2\right)$. We establish the closed-form explicit expression of magnetization orientation $\mathbf{u}^*$ and $\mathbf{u}^\sharp$ in the two distant domains with the help of Eq. (9). Moreover, the static wall profiles of magnetization do not depend on the inertial effect and remain unchanged.

To understand the dynamic properties of TDW under the small magnetic field, we seek the solutions of Eqs. (4) and (5) depending on the various parameters along with the prescribed boundary conditions. We use the perturbation expansion technique to capture the long-time behavior of the solutions. In this method, we write the solution in a regular asymptotic expansion form by taking the parameters $\tilde{H}_{ext}$, $\tilde{K}_2$ to be small. To carry out the analysis, we introduce an infinitesimal scaling parameter ε and set $\tilde{H}_{ext} = (\varepsilon h_1, 0, \varepsilon h_3)$, $\tilde{K}_2 = \varepsilon k_2$, and $\bar{t} = \varepsilon\tilde{t}$.

Using the regular asymptotic expansion, we attempt for a solution of Eqs. (4) and (5) in the following form which depends on $\tilde{x}$ and $\bar{t}$ only:

$$\theta(\tilde{x},\tilde{t}) = \theta_0(\tilde{x},\bar{t}) + \varepsilon\theta_1(\tilde{x},\bar{t}) + \cdots, \quad (10)$$

$$\varphi(\tilde{x},\tilde{t}) = \varphi_0(\tilde{x},\bar{t}) + \varepsilon\varphi_1(\tilde{x},\bar{t}) + \cdots. \quad (11)$$

along with the boundary condition

$$\mathbf{u}(\pm\infty, \bar{t}) = (\pm 1, 0, \varepsilon h_3) + O(\varepsilon^2). \tag{12}$$

By substituting Eqs. (10) and (11) in Eqs. (5) and (6), we have the following couple of equations, to the zero order of parameter ε:

$$\frac{\alpha_d}{\left((\partial_{\bar{t}}\theta_0)^2 + \sin^2\theta_0\,(\partial_{\bar{t}}\varphi_0)^2\right)^{1/2}}\,(\partial_{\bar{t}}\theta_0) = \tilde{K}_1\,(\partial_{\tilde{x}\tilde{x}}\theta_0) - \tfrac{1}{2}\tilde{K}_1\left(1 + (\partial_{\tilde{x}}\varphi_0)^2\right)\sin 2\theta_0 - \tfrac{1}{2}\sin 2\theta_0, \tag{13}$$

$$\frac{\alpha_d}{\tilde{K}_1\left((\partial_{\bar{t}}\theta_0)^2 + \sin^2\theta_0\,(\partial_{\bar{t}}\varphi_0)^2\right)^{1/2}}\sin\theta_0\,(\partial_{\bar{t}}\varphi_0) = 2\cos\theta_0\,(\partial_{\tilde{x}}\theta_0)\,(\partial_{\tilde{x}}\varphi_0) + \sin\theta_0\,(\partial_{\tilde{x}\tilde{x}}\varphi_0)\,. \tag{14}$$

The only meaningful solution which is consistent with the boundary condition given by Eq. (12) takes the form $\varphi_0\,(\tilde{x}, \tau) = \varphi^*$. Under this situation, Eq. (13) renders

$$(\partial_{\tilde{x}\tilde{x}}\theta_0) - \frac{\left(1 + \tilde{K}_1\right)}{2\tilde{K}_1}\sin 2\theta_0 = \frac{\alpha_d}{\tilde{K}_1}. \tag{15}$$

It is difficult to find an explicit analytical solution to Eq. (15); however, an approximate solution under the assumption of small angle deviation can be obtained and given as

$$\left(\theta_0 + \left(\frac{2\alpha_d}{1+\tilde{K}_1}\right)\right) + \left(\left(\theta_0 + \left(\frac{2\alpha_d}{1+\tilde{K}_1}\right)\right)^2 - \left(\left(\frac{2\alpha_d}{1+\tilde{K}_1}\right)^2 - \frac{C_1}{\mu}\right)\right)^{1/2} = e^{\mu\tilde{x}+C_2}, \tag{16}$$

where the constants $C_1 = -\left(2\left(\alpha_d/\tilde{K}_1\right)\theta^* + \mu\,(\theta^*)^2\right)$ and $\mu = \left(1 + \tilde{K}_1\right)/2\tilde{K}_1$. Also, we determine the integration constant C_2 at the center of the DW ($0 \le \theta \le \pi$) by applying the condition that at $\theta = (\pi/2)/2$, $\tilde{x} = \bar{x}\left(\bar{t}\right)$, $\bar{x}\left(\bar{t}\right)$ stands for the time-varying position of the center of DW and $(d\bar{x}/d\tau)$ represents the DW velocity. We remark that the obtained analytical solution exists locally and valid only in the vicinity of the center of DW. In addition, the solution of Eq. (15) imitates the classical Walker-type form in the absence of nonlinear dissipation α_d and given as (cf. [15]):

$$\theta_0\left(\tilde{x}, \bar{t}\right) = 2\arctan\left(e^{-\left(\sqrt{\mu}\tilde{x} - \tilde{x}(\bar{t})\right)}\right). \tag{17}$$

4 Conclusion

In this report, we investigated the field-induced TDW dynamics in biaxial ferromagnetic nanowire in the presence of inertial and crystallographic effects. We notice that even the zero-order traveling wave solution is difficult to obtain under the prescribed boundary conditions, i.e., to find an analytical solution which exists globally. It is worth to point out that to capture the ultrafast magnetization processes, we need to draw our attention toward the higher order traveling wave solutions. In nutshell, this work opens the door for some relevant problems in the same research lines such as to obtain the steady DW velocity, threshold, and breakdown value of the external sources for which the DW motion remains in the steady-state dynamic regime.

References

1. Yu, W., Xie, H.: A review on nanofluids: preparation, stability mechanisms, and applications. J. Nanomater. **2012**, 1 (2012)
2. Hubert, A., Schäfer, R.: Magnetic Domains: the Analysis of Magnetic Microstructures. Springer Science & Business Media (2008)
3. Goussev, A., Lund, R.G., Robbins, J.M., Slastikov, V., Sonnenberg, C.: Domain wall motion in magnetic nanowires: an asymptotic approach. Proc. R. Soc. A **469**(2160), p. 20130308 (The Royal Society) (2013)
4. Goussev, A., Lund, R.G., Robbins, J.M., Slastikov, V., Sonnenberg, C.: Fast domain-wall propagation in uniaxial nanowires with transverse fields. Phys. Rev. B **88**(2), 024425 (2013)
5. Lu, J.: Statics and field-driven dynamics of transverse domain walls in biaxial nanowires under uniform transverse magnetic fields. Phys. Rev. B **93**(22), 224406 (2016)
6. Dwivedi, S., Dubey, S.: On the evolution of transverse domain walls in biaxial magnetic nanowires. Mater. Today Proc. **4**(9), 10555–10559 (2017)
7. Consolo, G., Valenti, G.: Traveling wave solutions of the one-dimensional extended landau-lifshitz-gilbert equation with nonlinear dry and viscous dissipations. Acta applicandae Math. **122**(1), 141–152 (2012)
8. Dwivedi, S., Dubey, S.: On dynamics of current-induced static wall profiles in ferromagnetic nanowires governed by the Rashba Field. Int. J. Appl. Comput. Math. **3**(1), 27–42 (2017)
9. Dwivedi, S., Dubey, S.: Field-driven motion of ferrofluids in ferromagnetic nanowire under the influence of inertial effects. Procedia Eng. **127**, 3–9 (2015)
10. Wegrowe, J.E., Ciornei, M.C.: Magnetization dynamics, gyromagnetic relation, and inertial effects. Am. J. Phys. **80**(7), 607–611 (2012)
11. Dwivedi, S., Dubey, S.: On the stability of steady-states of a two-dimensional system of ferromagnetic nanowires. J. Appl. Anal. **23**(2), 89–100 (2017)
12. Agarwal, S., Carbou, G., Labbé, S., Prieur, C.: Control of a network of magnetic ellipsoidal samples. Math. Control Related Fields **1**(2), 129–147 (2011)
13. Dubey, S., Dwivedi, S.: On controllability of a two-dimensional network of ferromagnetic ellipsoidal samples. Differ. Equ. Dyn. Syst. 1–21 (2018)
14. Depassier, M.C.: Speed of field-driven domain walls in nanowires with large transverse magnetic anisotropy. EPL Europhys. Lett. **111**(2), 27005 (2015)
15. Schryer, N.L., Walker, L.R.: The motion of 180 domain walls in uniform dc magnetic fields. J. Appl. Phys. **45**(12), 5406–5421 (1974)

Analytical Study of Fluid Flow in a Channel Partially Filled with Porous Medium with Darcy–Brinkman Equation

J. Sharath Kumar Reddy and D. Bhargavi

Abstract Analytical study of the fluid flow in the developed region of a parallel-plate channel partially filled with a porous medium has been studied. A porous substrate is inserted in the middle of the channel. The Darcy–Brinkman equation is used to describe the fluid flow in the porous region. At the fluid–porous interface, continuity in velocity and jump in the tangential stresses are employed. Analytical solutions are obtained for velocity, flow rate, and the skin friction coefficient. The effects of the parameters such as Darcy number, Da, porous fraction, γ_p, stress jump coefficient, and β on the flow variables have been studied. The effects of these parameters are considered in order to study hydrodynamics in the channel configuration.

Keywords Darcy–Brinkman equation · Fully developed · Porous medium Partially filled with porous medium

1 Introduction

Several researchers have studied the fluid flow and heat transfer in porous medium, in recent times in view of their significant applications in situations such as enhanced recovery of oil by thermal methods, cooling of electronic components, risk assessment of disposal of nuclear waste, and proton exchange membrane (PEM) fuel cells.

The slip condition at the fluid–porous interface has been considered by several authors. Beavers and Joseph [1] were the first to consider this slip condition, whereas Saffman [2] gave theoretical justification for this condition. The conditions of the continuity in velocity and shear stresses at the interface have been used by Vafai and Kim [3]. Ochoa-Tapia and Whitaker [4, 5] considered the continuity in velocity and

J. Sharath Kumar Reddy (✉) · D. Bhargavi
Department of Mathematics, National Institute of Technology, Warangal 506004, India
e-mail: jskreddy.amma@gmail.com

D. Bhargavi
e-mail: bhargavi@nitw.ac.in

D. Srinivasacharya and K. S. Reddy (eds.), *Numerical Heat Transfer and Fluid Flow*, Lecture Notes in Mechanical Engineering,
https://doi.org/10.1007/978-981-13-1903-7_56

jump in the tangential stresses. These interface conditions have been used extensively by Kuznetsov [6] and Bhargavi et al. [7]. However, the problem of channel partially filled with porous medium using Darcy–Brinkman equation in porous media without using the boundary layer approximation has not received much attention.

In view of the above, in this paper, flow in a channel is with porous medium at the center, assuming that flow in porous medium is described by Darcy–Brinkman equation. The flow in the fluid region is described by Poiseuille description. The effects of relevant parameters on flow variables such as velocity, flow rate, and the skin friction coefficient have been studied.

2 Mathematical Formulation

The governing equations are rendered nondimensional by introducing the following nondimensional variables:

$$Y = \frac{y}{H},\ U_p = \frac{u_p \mu_f}{\left(-\frac{\mathrm{d}p}{\mathrm{d}x}\right) H^2},\ U_f = \frac{u_f \mu_f}{\left(-\frac{\mathrm{d}p}{\mathrm{d}x}\right) H^2},$$
$$U_i = \frac{u_i \mu_f}{\left(-\frac{\mathrm{d}p}{\mathrm{d}x}\right) H^2},\ u_{\mathrm{ref}} = \left(-\frac{\mathrm{d}p}{\mathrm{d}x}\right) H^2/\mu_f. \tag{1}$$

In Eq. (1), Y is the nondimensional coordinate and U is the nondimensional velocity. The subscripts f and p refer to fluid and porous regions. The nondimensional porous layer thickness γ_p, which shall be referred to as porous fraction, is defined by

$$\gamma_p = l_p/H \tag{2}$$

On introducing the nondimensional variables given by Eq. (1), the governing equation for conservation of momentum in the fluid and the porous regions and the boundary conditions in nondimensional form become

Fluid region:

$$\frac{\mathrm{d}^2 U_f}{\mathrm{d}Y^2} + 1 = 0 \quad \text{for} \quad -\frac{1}{2} \le Y \le -\frac{\gamma_p}{2} \tag{3}$$

Porous region:

$$\frac{\mathrm{d}^2 U_p}{\mathrm{d}Y^2} - \frac{\varepsilon}{Da} U_p + \varepsilon = 0 \quad \text{for} \quad -\frac{\gamma_p}{2} \le Y \le 0. \tag{4}$$

In Eq. (4), Da, the Darcy number and ε are defined by

$$Da = K/H^2 \quad \text{and}\ \varepsilon = \mu_f/\mu_{\mathrm{eff}}. \tag{5}$$

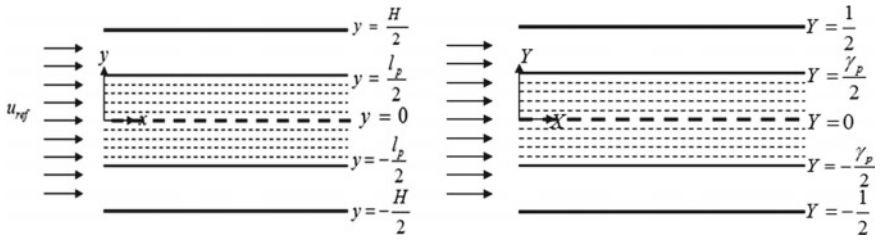

(a) Dimensional (b) Non-dimensional

Fig. 1 Physical model and the coordinate system

Nondimensional Boundary Conditions

$$\frac{dU_p}{dY} = 0 \quad \text{at} \quad Y = 0 \,(\text{Symmetry condition}) \tag{6}$$

$$U_f = 0 \quad \text{at} \quad Y = -1/2 \tag{7}$$

$$U_f = U_p = U_i, \frac{dU_f}{dY} - \frac{1}{\varepsilon}\frac{dU_p}{dY} = \frac{\beta}{\sqrt{Da}}U_i \quad \text{at} \quad Y = -\gamma_p/2. \tag{8}$$

It may be noted that the boundary conditions given by Eqs. (6)–(8) in Fig. 1 are written for the half channel, making use of the symmetry. The conditions given in Eq. (8) ensure the continuity in velocity and jump in the tangential stresses that have been given by Ochoa-Tapia and Whitaker [4, 5] at the interface.

3 Velocity Profiles

Fluid region: Upon solving Eq. (3) along with the boundary conditions given by Eqs. (7) and (8), velocity in the fluid region is obtained as

$$U_f[Y] = -\frac{(1+2Y)\left[8U_i + (\gamma_p - 1)(2Y + \gamma_p)\right]}{8(\gamma_p - 1)}, \tag{9}$$

where

$$U_i = -\left\{\frac{\sqrt{Da}\left[4\sqrt{Da}\left(e^{\gamma_p\sqrt{\frac{\varepsilon}{Da}}} - 1\right) - \left(1 + e^{\gamma_p\sqrt{\frac{\varepsilon}{Da}}}\right)\sqrt{\varepsilon}(\gamma_p - 1)\right](\gamma_p - 1)}{4\left[2\sqrt{Da\varepsilon} + e^{\gamma_p\sqrt{\frac{\varepsilon}{Da}}}\left(2\sqrt{Da\varepsilon} + (\beta\sqrt{\varepsilon} - 1)(\gamma_p - 1)\right) + (\beta\sqrt{\varepsilon} + 1)(\gamma_p - 1)\right]}\right\}. \tag{10}$$

Porous region: Similarly, solving Eq. (4) along with the boundary conditions given by Eqs. (6) and (8) velocity in the porous region is obtained as

$$U_p[Y] = \frac{e^{-Y\sqrt{\frac{\varepsilon}{Da}}}\left[U_i e^{\frac{\gamma_p}{2}\sqrt{\frac{\varepsilon}{Da}}}\left(1+e^{2Y\sqrt{\frac{\varepsilon}{Da}}}\right)+Da\left(e^{Y\sqrt{\frac{\varepsilon}{Da}}}-e^{\frac{\gamma_p}{2}\sqrt{\frac{\varepsilon}{Da}}}+e^{(Y+\gamma_p)\sqrt{\frac{\varepsilon}{Da}}}-e^{\frac{(4Y+\gamma_p)}{2}\sqrt{\frac{\varepsilon}{Da}}}\right)\right]}{1+e^{\gamma_p\sqrt{\frac{\varepsilon}{Da}}}}. \tag{11}$$

New normalized velocities are defined by

$$U_{f,N}[Y] = \frac{U_f[Y]}{u_{\text{ref}}},\ U_{p,N}[Y] = \frac{U_p[Y]}{u_{\text{ref}}},\ U_{i,N}[Y] = \frac{U_i[Y]}{u_{\text{ref}}}, \tag{12}$$

where

u_{ref} is the average velocity defined by

$$u_{\text{ref}} = 2\left[\int_{-1/2}^{-\gamma_p/2} U_f dY + \int_{-\gamma_p/2}^{0} U_p dY\right]. \tag{13}$$

$U_{f,N}$, $U_{p,N}$ expressions are not given explicitly, since U_f, U_p, and u_{ref} expressions are given in Eqs. (9), (11), and (13).

Skin friction coefficient:

$$C_{ff} = \frac{1}{Re}\left(\frac{dU_{f,N}}{dY}\right)_{|Y=-\frac{1}{2}}. \tag{14}$$

4 Result and Discussions

It has been assumed that $\varepsilon = \mu_f/\mu_{\text{eff}} = 1$. The channel is referred to as the clear fluid channel when $\gamma_p = 0$. Similarly, when $\gamma_p = 1.0$, the geometry shall be referred to as the channel fully filled with the porous material. When the porous fraction is $0 < \gamma_p < 1.0$, the channel is referred as the channel partially filled with the porous material.

4.1 Limiting Cases

Clear Fluid Channel: By setting $\gamma_p = 0$ in Eqs. (9), (10), and (13), U_f for the clear fluid reduce to

$$U_{f,N}[Y] = \frac{3}{2}\left(1-4Y^2\right). \tag{15}$$

Channel fully filled with the porous material: Similarly, putting $\gamma_p = 1.0$ in Eqs. (10), (11), and (13), U_p for the channel fully filled with porous material reduce to

$$U_{p,N}[Y] = \frac{\left[\cosh\left(\frac{\sqrt{\varepsilon}}{2\sqrt{Da}}\right) - \cosh\left(\frac{Y\sqrt{\varepsilon}}{\sqrt{Da}}\right)\right]\sqrt{\varepsilon}}{\sqrt{\varepsilon}\,\cosh\left(\frac{\sqrt{\varepsilon}}{2\sqrt{Da}}\right) - 2\sqrt{Da}\,\sinh\left(\frac{\sqrt{\varepsilon}}{2\sqrt{Da}}\right)}. \tag{16}$$

Equations (15) and (16) are available in Schlichting and Gersten [8], Haji-Sheikh and Vafai [9], and Bhargavi and Sharath Kumar Reddy [10], respectively.

4.2 Velocity Profiles

Variation of fully developed velocity profiles of $U_{f,N,}$ $U_{p,N}$ is shown in Fig. 2a for $\gamma_p = 0.2$, $Da = 0.005$ and Fig. 2b for $\gamma_p = 0.8$, $Da = 0.005$ for different values of $\beta = -0.7$, -0.5, 0, 0.5, and 0.7. Variation of fully developed velocity profiles $U_{f,N,}$ $U_{p,N}$ is shown in Fig. 3a for $\gamma_p = 0.2$, $Da = 0.05$ and Fig. 3b for $\gamma_p = 0.8$, $Da = 0.05$ for different values of $\beta = -0.7$, -0.5, 0, 0.5, and 0.7. As β increases, the velocity in the fluid region decreases, whereas velocity in the porous region increases at a lower porous fraction, say $\gamma_p = 0.2$. Whereas for $\gamma_p = 0.8$, this behavior is reversed. This may be due to β. For $\beta = 0$ (i.e., no jump in the tangential stresses), the slopes are equal at the interface, though they differ when $\beta \neq 0$. This can be seen from Figs. 2 and 3. The maximum value of velocity decreases as γ_p increases. As Da increases, the velocity in the porous region increases for a given γ_p and for all β, whereas velocity in the fluid region decreases for a given γ_p and for all β. This is due to retain mass balance in a channel partially filled with porous material. As β increases, the flow rate increases for small porous fraction, $\gamma_p = 0.2$, whereas flow rate is constant for higher $\gamma_p = 0.8$. This is due to the quantity of porous medium larger in channel partially filled with porous material. Hence, when there is a small porous fraction, effect of stress jump coefficient is more, which means tangential stresses in the fluid region are higher than tangential stresses in the porous medium.

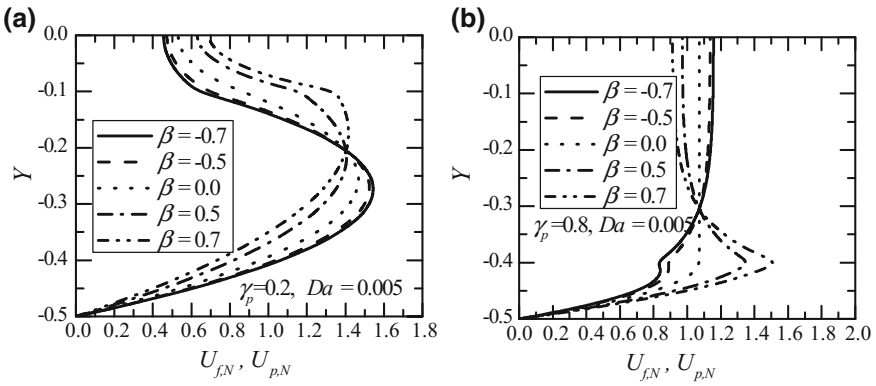

Fig. 2 Velocity profiles at different values of β, for **a** $\gamma_p = 0.2$ and **b** $\gamma_p = 0.8$ for $Da = 0.005$

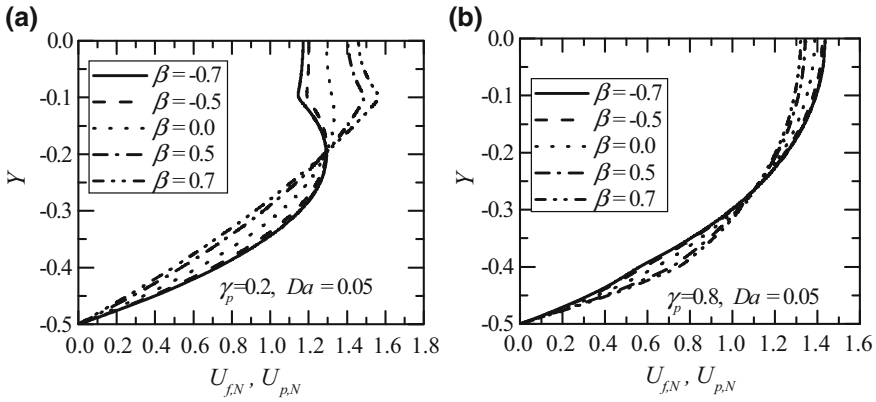

Fig. 3 Velocity profiles at different values of β, for **a** $\gamma_p = 0.2$ and **b** $\gamma_p = 0.8$ for $Da = 0.05$

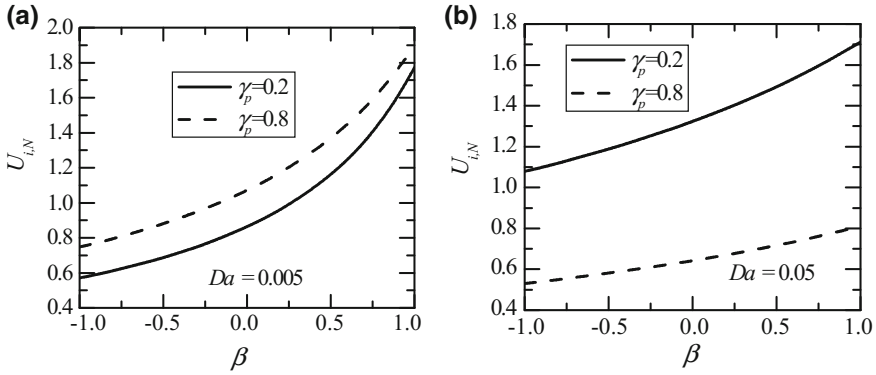

Fig. 4 Interfacial velocity with β for $\gamma_p = 0.2$ and 0.8 for **a** $Da = 0.005$, **b** $Da = 0.05$

Interfacial velocity: Variation of interfacial velocity $U_{i,N}$ with β is shown in Fig. 4a for $Da = 0.005$, Fig. 4b for $Da = 0.05$ for $\gamma_p = 0.2$ and 0.8. From Fig. 4a, b, as β increases, the interfacial velocity increases for all Da and γ_p. As Da increases, the interfacial velocity decreases. As Da is larger, the larger interfacial velocity becomes zero. If Da is larger, then porous region behaves like a fluid region so there will not be any interface in the channel.

Skin friction coefficient: Variation of ReC_{ff} with porous fraction, γ_p, is shown in 5a for $Da = 0.005$, Fig. 5b for $Da = 0.05$ for different β. From Fig. 5a, b, ReC_{ff} increases up to certain γ_p and then decreases. From Fig. 5a, as β increases, ReC_{ff} decreases up to $\gamma_p \approx 0.7$ and then increases up to $\gamma_p = 1.0$. This behavior is the same for Fig. 5b. But the value of γ_p decreases as Da increases. As Da increases, say $Da = 1.0$, $ReC_{ff} \rightarrow 6$ given in Schlichting and Gersten [8].

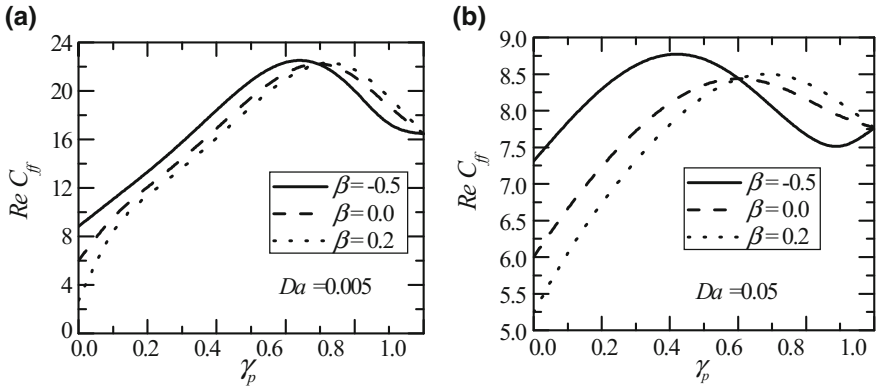

Fig. 5 Skin friction coefficient ReC_{ff} with γ_p at different values of β for **a** $Da = 0.005$, **b** $Da = 0.05$

5 Conclusions

Fluid flow in parallel-plate channels partially filled with porous medium has been studied analytically by assuming fully developed flow condition. The porous insert of thickness, l_p, placed symmetrically in the middle of the channel. The problem is characterized by Darcy number, *Da,* the porous fraction, γ_p, and stress jump coefficient, β. Analytical results are obtained for the velocity, flow rate, and the skin friction coefficient. The effects of *Da*, γ_p, and β on flow variables have been studied. So, when there is a less quantity of porous medium, then the slope in the fluid region is higher than the slope in the porous region.

1. Fully developed velocity in the fluid region decreases and velocity in the porous region increases for lower porous fraction, as stress jump coefficient increases. But this behavior is reversed for higher porous fraction for all Darcy numbers.
2. Skin friction coefficient, ReC_{ff}, attains maximum value at a certain porous fraction and then decreases for all Darcy numbers.
3. Flow rate increases for small porous fractions, but the flow rate is constant for higher porous fractions.

References

1. Beavers, G., Joseph, D.D.: Boundary conditions at a naturally permeable wall. J. Adv. Fluid Mech. **30**, 197–207 (1967)
2. Saffman, P.G.: On the boundary condition at the surface of a porous medium. Canadian J. Chem. Eng. **50**, 93–101 (1971)
3. Vafai, K., Kim, S.J.: Fluid mechanics of the interface region between a porous medium and a fluid layer - an exact solution. Int. J. Heat Fluid Flow. **11**, 254–256 (1990)

4. Ochoa-Tapia, J.A, Whitaker, S.: Momentum transfer at the boundary between a porous medium and homogeneous fluid-I theoretical development. Int. J. Heat Mass Transf. **38**, 2635–2646 (1995)
5. Ochoa-Tapia, J.A, Whitaker, S.: Momentum transfer at the boundary between a porous medium and homogeneous fluid-II comparison with experiment. Int. J. Heat Mass Transf. **38**, 2647–2655 (1995)
6. Kuznetsov, A.V.: Analytical investigation of the fluid flow in the interface region between a porous medium and a clear fluid in channels partially filled with a porous medium. Appl. Sci. Res. **56**, 53–67 (1996)
7. Bhargavi, D., Satyamurty, V.V, Raja Sekhar, G.P.: Effect of porous fraction and interfacial stress jump on skin friction and heat transfer in flow through a channel partially filled with porous material. J. Porous Media **12**, 1065–1082 (2009)
8. Schlichting, H., Gersten, K.: Boundary Layer Theory. Springer, Berlin (2007)
9. Haji-Sheikh, A., Vafai, K.: Analysis of flow and heat transfer in porous media imbedded inside various shaped ducts. Int. J. Heat Mass Transf. **47**, 1889–1905 (2004)
10. Bhargavi, D., Sharath Kumar Reddy, J.: Analytical investigation of laminar forced convection in a channel filled with porous material subjected to constant wall heat flux. Int. J. Special Topics Rev Porous Media **8**, 1–16 (2017)

Dissipative Effect on Heat and Mass Transfer by Natural Convection over a Radiating Needle in a Porous Medium

S. R. Sayyed, B. B. Singh and Nasreen Bano

Abstract The paper deals with the effects of buoyancy (N), Lewis number (Le), radiation parameter (R), and viscous dissipation (Ec) on the natural convective heat and mass transfer from a radiating needle in a porous medium. In the analysis of the problem, an integral approach of Von Karman type has been adopted, and the numerical values computed pertaining to the local Nusselt and local Sherwood numbers have been compared with the earlier published values. The results have been found in excellent agreement.

Keywords Natural convection · Viscous dissipation · Thermal radiation

1 Introduction

On account of the numerous engineering applications of natural convective heat and mass transfer flows with dissipation and radiation effects in groundwater pollution, moisture transport in thermal insulation, grain storage installation, hypersonic flights, gas turbines, space technology, etc., researchers like Lai et al. in [1], Lai and Kulacki in [2], Nakayama and Hossain in [3], Singh and Queeny in [4], Angirasa et al. in [5], Amahmid et al. in [6], Yih in [7], Chamakha in [8], Bansod et al. in [9], Bansod in [10], Singh and Chandarki in [11], Vyas and Shrivastava in [12], Vyas and Ranjan in [13], Chauhan and Kumar in [14], Baoku et al. in [15] and Babu in [16], etc. have done pioneering work in this flow field by taking various geometrical configurations.

The objective of the present paper is to do the integral analysis of the effects of viscous dissipation, radiation, buoyancy, and Lewis number on the flow in conjunction with heat and mass transfer from radiating needle embedded in a porous medium. To serve the purpose, an integral method of Von Karman type has been employed on the lines of Singh and Chandarki in [11].

S. R. Sayyed (✉) · B. B. Singh · N. Bano
Department of Mathematics, Dr. Babasaheb Ambedkar Technological University, Lonere, Raigad 402103, Maharashtra, India
e-mail: srsayyed786@gmail.com

D. Srinivasacharya and K. S. Reddy (eds.), *Numerical Heat Transfer and Fluid Flow*, Lecture Notes in Mechanical Engineering,
https://doi.org/10.1007/978-981-13-1903-7_57

2 Mathematical Formulation of the Problem

By taking the Darcys law, boundary layer and Boussinesq approximations, and the radiative fluid properties into consideration, the similarity boundary layer equations governing the flow field are given in cylindrical coordinates as (cf. Lai et al. [1])

$$f' = \frac{1}{2}(\theta + N\phi) \tag{1}$$

$$(1+R)\theta'' = \frac{1}{2\eta}[af'\theta - [2(1+R) + f]\theta'] - \eta Ecf''^2 \tag{2}$$

$$\phi'' = \frac{1}{2\eta}[bLef'\phi - (2 + Lef)\phi'] \tag{3}$$

with boundary conditions given by

$$\eta = \eta_0 : f + (a-1)\eta f' = 0, \theta = 1, \phi = 1 \tag{4}$$

$$\eta \to \infty : f' = 0, \theta = 0, \phi = 0. \tag{5}$$

The schematic diagram of the flow model is as shown in Fig. 1. Here, N represents the buoyancy ratio; f', θ, and ϕ represent the dimensionless velocity, temperature, and concentration profiles, respectively; Le represents Lewis number; Ec is the Eckert number, and R is the radiation parameter. Furthermore, the primes denote derivatives with respect to the similarity variable η, $\eta \in [0, \infty)$.

Here, a and b are the constant. In the present analysis, it has been shown that the Eqs. (1)–(3) permit solutions for the case $a = b = 1$ which represents a vertical needle with linear temperature and concentration.

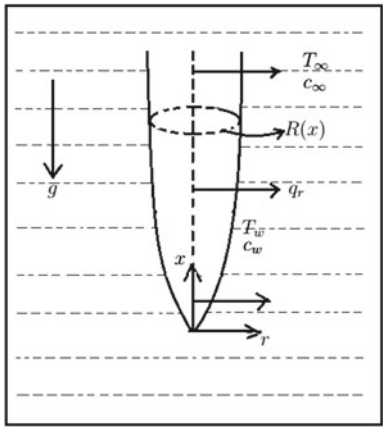

Fig. 1 Physical model and coordinate system

One can study the relative significance of the mass and thermal diffusion with the help of buoyancy ratio (N). Here, $N = 0$ represents flow driven purely by thermal buoyancy; $N = \infty$ represents flow which is purely mass driven; $N > 0$ represents aiding flow, and $N < 0$ an opposing flow.

3 Integral Treatment

The energy Eq. (2) and the mass transfer Eq. (3) can be integrated with respect to η from $\eta = \eta_0$ to $\eta = \infty$, to obtain for $a = b = 1$.

$$-2\eta_0 (1 + R)\, \theta'(\eta_0) = 2 \int_{\eta_0}^{\infty} f'\, \theta \, d\eta + \frac{Ec}{4} \int_{\eta_0}^{\infty} \eta^2 \, f''^2 \, d\eta \tag{6}$$

$$-\eta_0 \, \phi'(\eta_0) = Le \int_{\eta_0}^{\infty} f' \, \phi \, d\eta. \tag{7}$$

Now, the temperature and the concentration profiles can be expressed exponentially in the following manner so that they satisfy the buoyancy conditions (4)–(5):

$$\theta(\eta) = exp\left\{-\left(\frac{\eta - \eta_0}{\delta_T}\right)\right\} \tag{8}$$

$$\phi(\eta) = exp\left\{-\xi\left(\frac{\eta - \eta_0}{\delta_T}\right)\right\}. \tag{9}$$

In the above equations, δ_T represents an arbitrary scale for thermal boundary layer thickness, while ξ represents the ratio of thermal boundary thickness to the concentration boundary layer thickness.

Equations (6)–(7), by taking into account the relation (1) and using relations (8) and (9), get reduced to two distinct expressions for δ_T as

$$\left[\frac{1}{2} + \frac{N}{\xi + 1} - \frac{Ec}{8} - \frac{N\xi Ec}{(\xi + 1)^2}\right]\delta_T^2 + \frac{\eta_0 Ec}{4}\left(1 + \frac{4N\xi}{(\xi + 1)^2}\right)\delta_T - \eta_0^2 \frac{Ec}{4}\left(\frac{1}{2} + \frac{2N\xi}{\xi + 1} + \frac{\xi}{2}\right) - 2\eta_0(1 + R) = 0 \tag{10}$$

and

$$Le\left[\frac{1}{\xi + 1} + \frac{N}{2\xi}\right]\delta_T^2 - 2\eta_0 \xi = 0. \tag{11}$$

The thermal boundary layer thickness δ_T is governed by the above two Eqs. (10)–(11). From Eqs. (10) and (11), we, respectively, obtain

$$\delta_T^* = \frac{\delta_T}{2\eta_0^{\frac{1}{2}}}, \tag{12}$$

where

$$\delta_T = -\frac{\left[2(1+R)\eta_0 - \frac{4\eta_0\xi^2\left[\frac{1}{2}-\frac{Ec}{8}-\frac{EcN\xi}{(\xi+1)^2}+\frac{N}{\xi+1}\right]}{Le[(N+2)\xi+N]}\right] + \frac{1}{4}Ec\,\eta_0^2\left(\frac{1}{2}+\frac{\xi}{2}+\frac{2N\xi}{\xi+1}\right)}{Ec\,\eta_0\left(1+\frac{4N\xi}{(\xi+1)^2}\right)} \tag{13}$$

and

$$\delta_T = \frac{2\eta_0^{\frac{1}{2}}}{Le^{\frac{1}{2}}}\,\xi\left[\frac{\xi+1}{(N+2)\xi+N}\right]^{\frac{1}{2}}. \tag{14}$$

Equations (10) and (11) can be combined to obtain the algebraic equation

$$A_9\xi^9 + A_8\xi^8 + A_7\xi^7 + A_6\xi^6 + A_5\xi^5 + A_4\xi^4 + A_3\xi^3 + A_2\xi^2 + A_1\xi + A_0 = 0, \tag{15}$$

where the coefficients $A_0, A_1, \ldots, A_9$ have been calculated using MATHEMATICA software.

The value of ξ is determined from Eq. (15) by using computer software MATHEMATICA.

As ξ is determined from Eq. (15), the local Nusselt and local Sherwood numbers, which are of main interest in terms of heat and mass transfer, respectively, are given as

$$Nu = \frac{\eta_0^{\frac{1}{2}}(Ra)^{\frac{1}{2}}}{\delta_T^*} \quad \text{and} \quad Sh = \eta_0^{\frac{1}{2}}\,Le^{\frac{1}{2}}\left[\frac{(N+2)\xi+N}{\xi+1}\right]^{\frac{1}{2}}(Ra)^{\frac{1}{2}}$$

4 Results and Discussion

The combined effect of buoyancy (N), Lewis number (Le), radiation (R), and viscous dissipation (Ec) on the rate of heat and mass transfer from a vertical needle are investigated numerically and graphically and are presented in Table 1 and in Figs. 2, 3, 4, and 5

Table 1 shows the comparison of numerical values of heat and mass transfer coefficients obtained in the present analysis with the corresponding values of Lai

Table 1 Variation of local Nusselt and local Sherwood numbers for $R = 0$ and $Ec = 0$

Le	N	Present $(Nu(Ra)^{-\frac{1}{2}})$	Lai et al. [1] $(Nu(Ra)^{-\frac{1}{2}})$	Le	N	Present $(Sh(Ra)^{-\frac{1}{2}})$	Lai et al. [1] $(Sh(Ra)^{-\frac{1}{2}})$
0.1	0	0.0900	0.1368	0.1	0	0.01537	0.0168
	2	0.18516	0.1824		2	0.04393	0.0540
	4	0.245422	0.2384		4	0.059638	0.0594
	6	0.293533	0.2868		6	0.071965	0.0682
	8	0.334794	0.3283		8	0.082463	0.0848
	10	0.371497	0.3698		10	0.091765	0.0896

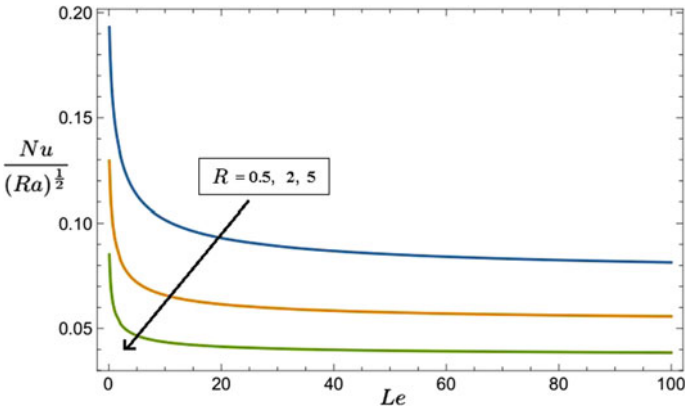

Fig. 2 Local Nusselt number versus Lewis number ($Ec = 0.1$, $N = 4$)

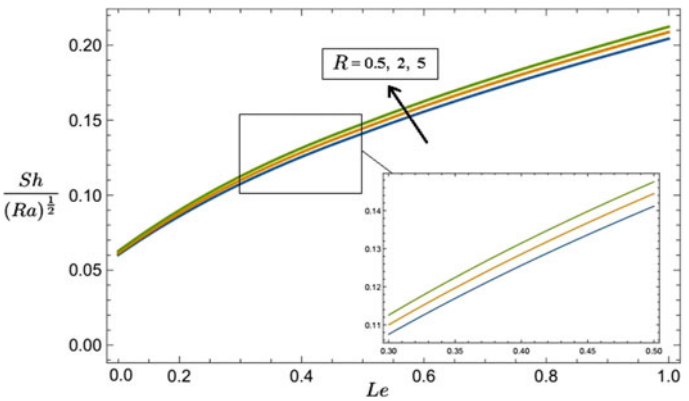

Fig. 3 Local Sherwood number versus Lewis number ($Ec = 0.1$, $N = 4$)

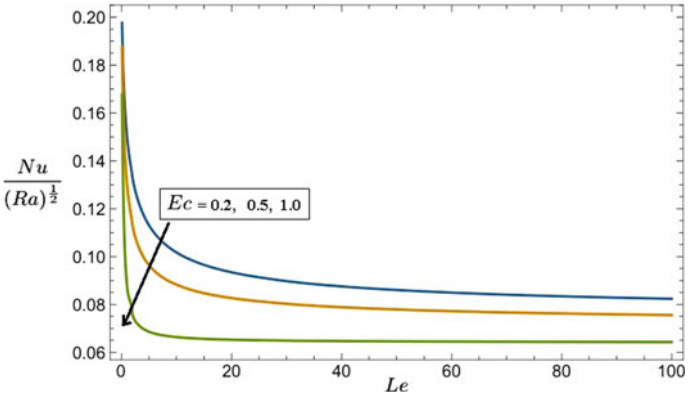

Fig. 4 Local Nusselt number versus Lewis number ($R = 0.4$, $N = 4$)

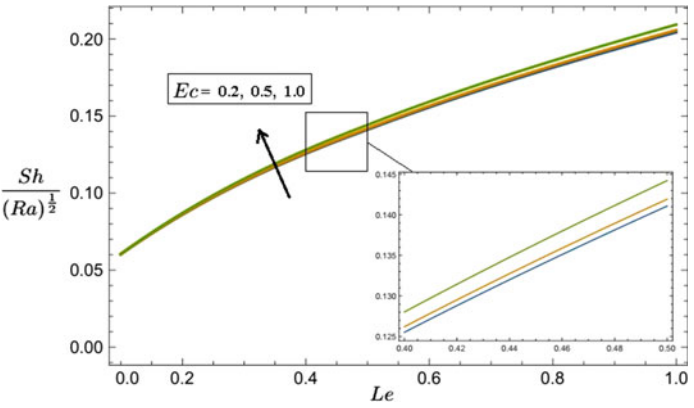

Fig. 5 Local Sherwood number versus Lewis number ($R = 0.4$, $N = 4$)

et al. [1] obtained through scale analysis in the absence of radiation and viscous dissipation. It is evident from Table 1 that the results are in good agreement.

Figures 2 and 3 explain the effect of radiation parameter (R) on the rates of heat and mass transfer for fixed values of N and Ec($N = 4$, $Ec = 0.1$). A decline in the heat transfer rate but a rise in the mass transfer rate is observed for increasing values of R.

The variations of heat and mass transfer rates along with Ec are given in Figs. 4 and 5 for fixed values of N & R ($N = 4$, $R = 0.4$). It is noted that the rate of heat transfer decreases, whereas the rate of mass transfer is boosted subject to increasing Ec.

5 Conclusion

The following significant conclusions are drawn from the analysis:

1. An increase in the values of buoyancy ratio (N) shows an increase in both the heat and mass transfer rates.
2. The heat transfer rate exhibits a decreasing trend, while the mass transfer rate shows an increasing trend for the increasing values of radiation parameter.
3. With an increase in the values of Eckert number (Ec), the heat transfer rate decreases while the mass transfer rate increases.

References

1. Lai, F.C., Choi, C.Y., Kulacki, F.A.: Coupled heat and mass transfer by natural convection from slender bodies of revolution in porous media. Int. Commun. Heat Mass Transf. **17**(15), 609–620 (1990). https://doi.org/10.1016/0735-1933(90)90009-9
2. Lai, F.C., Kulacki, F.A.: Coupled heat and mass transfer by natural convection from vertical surfaces in porous media. Int. J. Heat Mass Transf. **34**(4–5), 1189–1194 (1991). https://doi.org/10.1016/0017-9310(91)90027-C
3. Nakayama, A., Hossain, M.A.: An integral treatment for combined heat and mass transfer by natural convection in a porous medium. Int. J. Heat Mass Transf. **38**(4), 761–765 (1995). https://doi.org/10.1016/0017-9310(95)93012-7
4. Singh, P.: Queeny. Free convection heat and mass transfer along a vertical surface in a porous medium. Acta Mech. **123**(1–4), 69–73 (1997). https://doi.org/10.1007/BF01178401
5. Angirasa, D., Peterson, G.P., Pop, I.: Combined heat and mass transfer by natural convection with opposing buoyancy effect in a fluid saturated porous medium. Int. J. Heat Mass Transf. **40**(12), 2755 (1997). https://doi.org/10.1016/S0017-9310(96)00354-7
6. Amahmid, A., Hasnaoui, M., Mamou, M., Vasseur, P.: Boundary layer flows in a vertical porous enclosure induced by opposing buoyancy forces. Int. J. Heat Mass Transf. **42**(19), 3599–3608 (1999). https://doi.org/10.1016/S0017-9310(99)00019-8
7. Yih, K.A.: Coupled heat and mass transfer by free convection over a truncated cone in porous media: VWT/VWC or VHF/VMF. Acta Mech. **137**(1–2), 83–97 (1999). https://doi.org/10.1007/BF01313146
8. Chamkha, A.J.: Coupled heat and mass transfer by natural convection about a truncated cone in the presence of magnetic field and radiation effects. Numer. Heat Transf. **39**(5), 511–530 (2001). https://doi.org/10.1080/10407780120202
9. Bansod, V.J., Singh, P., Rathishkumar, B.V.: Heat and mass transfer by natural convection from a vertical surface to the stratified Darcian fluid. J. Porous Media **5**(1), 57–66 (2002). https://doi.org/10.1615/JPorMedia.v5.i1.60
10. Bansod, V.J.: The Darcy model of the boundary layer flows in a horizontal porous medium induced by combined buoyancy forces. J. Porous Media **6**(4), 273–281 (2003). https://doi.org/10.1615/JPorMedia.v6.i4.60
11. Singh, B.B., Chandarki, I.M.: Integral treatment of coupled heat and mass transfer by natural convection from a cylinder in porous media. Int. Commun. Heat Mass Transf. **36**(3), 269–273 (2009). https://doi.org/10.1016/j.icheatmasstransfer.2008.11.007
12. Vyas, P., Shrivastava, N.: Radiative MHD flow over a non-isothermal stretching sheet in a porous medium. App. Math. Sci. **4**(50), 2475–2484 (2010)
13. Vyas, P., Ranjan, A.: Dissipative MHD boundary layer flow in a porous medium over a sheet stretching non-linearly in the presence of radiation. App. Math. Sci. **4**(63), 3133–3142 (2010)

14. Chauhan, D.S., Kumar, V.: Radiation effects on mixed convection flow and viscous heating in a vertical channel partially filled with a porous medium. Tamkang J. Sci. Eng. **14**(2), 97–106 (2011). https://doi.org/10.6180/jase.2011.14.2.02
15. Baoku, I.G., Israel- Cookey, C., Olajuwan, B.I.: Influence of thermal radiation on a transient MHD Coutte flow through a porous medium. J. App. Fluid Mech. **5**(1), 81–87 (2012)
16. Babu, P.R., Rao, J.A., Sheri, S.: Radiation effect on MHD heat and mass transfer flow over a shrinking sheet with mass suction. J. App. Fluid Mech. **7**(4), 641–650 (2014)

Numerical Solution of Sixth Order Boundary Value Problems by Galerkin Method with Quartic B-splines

Sreenivasulu Ballem and K. N. S. Kasi Viswanadham

Abstract In this paper, Galerkin method with quartic B-splines has been developed to solve a sixth order boundary value problem. The approximation solution has been modified into a form, which takes care of given boundary conditions. For the illustration purpose of the present method, we have solved sixth order linear and nonlinear boundary value problems. The numerical results are compared with the exact solutions.

Keywords Sixth order boundary value problem · Galerkin method
Quartic B-splines · Absolute error

1 Introduction

Consider a general sixth order linear boundary value problem

$$a_0(x)y^{(6)}(x) + a_1(x)y^{(5)}(x) + a_2(x)y^{(4)}(x) + a_3(x)y'''(x) + a_4(x)y''(x) + a_5(x)y'(x) + a_6(x)y(x) = b(x), c < x < d \quad (1)$$

subject to boundary conditions

$$y(c) = A_0, y(d) = C_0, y'(c) = A_1, y'(d) = C_1, y''(c) = A_2, y''(c) = C_2 \quad (2)$$

where A_0, C_0, A_1, C_1, A_2, and C_2 are finite real constants and $a_0(x)$, $a_1(x)$, $a_2(x)$, $a_3(x)$, $a_4(x)$, $a_5(x)$, $a_6(x)$, and $b(x)$ are all the continuous functions defined on the interval $[c, d]$.

S. Ballem (✉)
Department of Mathematics, Central University of Karnataka, Kalaburagi 585 367, India
e-mail: sreenivasm.maths@gmail.com

K. N. S. Kasi Viswanadham
Department of Mathematics, National Institute of Technology, Warangal, India

D. Srinivasacharya and K. S. Reddy (eds.), *Numerical Heat Transfer and Fluid Flow*, Lecture Notes in Mechanical Engineering,
https://doi.org/10.1007/978-981-13-1903-7_58

There are various physical processes in which a sixth order boundary value problem arises in various areas of science and engineering, which include astrophysics, structural engineering, optimization, and economics. For the applications of sixth order boundary value problems, one can refer [1–4]. For the existence and uniqueness for the solutions of these types of problems, one can refer [5]. Analytical solutions to these problems are available in rare cases. The researchers have developed numerical methods such as finite difference method, homotopy analysis method, variation of parameters method, variational iteration method, differential transformation method, Ritz method, Sinc–Galerkin method, Adomain decomposition method, etc. Siddiqi et al. [6, 7] used the quintic and septic spline techniques to solve special case of sixth order boundary value problems. Kasi Viswanadham and Murali Krishna [8] developed a sextic B-spline Galerkin method to solve a special case of sixth order boundary value problem. Kasi Viswanadham and Shwori Raju [9] developed the solution of a general sixth order boundary value problem by using quintic B-spline collocation method.

The present paper aims to present Galerkin method with quartic B-splines to solve the boundary value problems of the type (1)–(2). The quasilinearization technique has been applied to convert the nonlinear problem into a sequence of linear problems [10]. The present method has been applied to solve each one of the generated linear problems. The limit of solutions of these linear problems is the solution of the nonlinear problem. The justification for using the Galerkin method is given in [11–13].

2 Description of the Method

The quartic B-splines and its properties are defined in Prenter [14], Carl de-Boor [15], and Schoenberg [16]. Now suppose that the approximate solution of Eqs. (1) and (2) is given by

$$y(x) = \sum_{j=-2}^{n+1} \alpha_j B_j(x) \tag{3}$$

where $\alpha_j's$ are the nodal parameters to be determined and $B_j(x)$'s are quartic basis functions. If the approximation satisfies the given boundary conditions, then it gives more accurate results. Accordingly, the basis functions are redefined into a new set of basis functions. The redefinition of the basis functions is given below.

Applying the given boundary conditions of (2) to the approximation (3), we get

$$A_0 = y(c) = y(x_0) = \sum_{j=-2}^{1} \alpha_j B_j(x_0), C_0 = y(d) = y(x_n) = \sum_{j=n-2}^{n+1} \alpha_j B_j(x_n) \tag{4}$$

$$A_1 = y'(c) = y'(x_0) = \sum_{j=-2}^{1} \alpha_j B'_j(x_0),\ C_1 = y'(d) = y'(x_n) = \sum_{j=n-2}^{n+1} \alpha_j B'_j(x_n) \tag{5}$$

$$A_2 = y''(c) = y''(x_0) = \sum_{j=-2}^{1} \alpha_j B''_j(x_0),\ C_2 = y''(d) = y''(x_n) = \sum_{j=n-2}^{n+1} \alpha_j B''_j(x_n). \tag{6}$$

Eliminating $\alpha_{-2}, \alpha_{-1}, \alpha_0, \alpha_{n-1}, \alpha_n$, and α_{n+1} from Eqs. (3) to (6), the approximation for $y(x)$ can be obtained as

$$y(x) = w(x) + \sum_{j=1}^{n-2} \alpha_j \tilde{B}_j(x) \tag{7}$$

$$w(x) = w_2(x) + \frac{A_2 - w_2''(x_0)}{Q_0''(x_0)} Q_0(x) + \frac{C_2 - w_2''(x_n)}{Q_{n-1}''(x_n)} Q_{n-1}(x)$$

$$w_2(x) = w_1(x) + \frac{A_1 - w_1'(x_0)}{P_{-1}'(x_0)} P_{-1}(x) + \frac{C_1 - w_1'(x_n)}{P_n'(x_n)} P_n(x)$$

$$w_1(x) = \frac{A_0}{B_{-2}(x_0)} B_{-2}(x) + \frac{C_0}{B_{n+1}(x_n)} B_{n+1}(x)$$

$$\tilde{B}_j(x) = \begin{cases} Q_j(x) - \frac{Q_j''(x_0)}{Q_0''(x_0)} Q_0(x), & j = 1 \\ Q_j(x), & j = 2, 3, \ldots, n-3 \\ Q_j(x) - \frac{Q_j''(x_n)}{Q_n''(x_n)} Q_n(x), & j = n-2. \end{cases}$$

$$Q_j(x) = \begin{cases} P_j(x) - \frac{P_j'(x_0)}{P_{-1}'(x_0)} P_{-1}(x), & j = 0, 1 \\ P_j(x), & j = 2, 3, \ldots, n-3 \\ P_j(x) - \frac{P_j'(x_n)}{P_n'(x_n)} P_n(x), & j = n-2, n-1. \end{cases}$$

$$P_j(x) = \begin{cases} B_j(x) - \frac{B_j(x_0)}{B_{-2}(x_0)} B_{-2}(x), & j = -1, 0, 1 \\ B_j(x), & j = 2, 3, \ldots, n-3 \\ B_j(x) - \frac{B_j(x_n)}{B_{n+1}(x_n)} B_{n+1}(x), & j = n-2, n-1, n. \end{cases}$$

Applying the Galerkin method to (1) with the new set of basis functions $\left\{\tilde{B}_j(x),\ j = 1, 2, \ldots, n-2\right\}$, we get

$$\int_{x_0}^{x_n} \left[a_0(x)y^{(6)}(x) + a_1(x)y^{(5)}(x) + a_2(x)y^{(4)}(x) + a_3(x)y'''(x) + a_4(x)y''(x)\right.$$

$$\left. + a_5(x)y'(x) + a_6(x)y(x)\right]\tilde{B}_i(x)\mathrm{d}x = \int_{x_0}^{x_n} b(x)\tilde{B}_i(x)\,\mathrm{d}x, \quad \text{for } i = 1, 2, \ldots, n-2. \tag{8}$$

The first three terms on the left side of the above equation have been integrated by parts. The resulting terms are substituted in (8). After applying the approximation (7), we get a system of equations as

$$A\alpha = B \tag{9}$$

$$A = [a_{ij}];$$

$$a_{ij} = \int_{x_0}^{x_n} \left\{\left[-\frac{\mathrm{d}^3}{\mathrm{d}x^3}(a_0(x)\tilde{B}_i(x)) + \frac{\mathrm{d}^2}{\mathrm{d}x^2}(a_1(x)\tilde{B}_i(x)) - \frac{\mathrm{d}}{\mathrm{d}x}(a_2(x)\tilde{B}_i(x))\right.\right.$$
$$\left. + a_3(x)\tilde{B}_i(x)\right]\tilde{B}_j'''(x) + a_4(x)\tilde{B}_i(x)\tilde{B}_j''(x)$$
$$\left. + a_5(x)\tilde{B}_i(x)\tilde{B}_j'(x) + a_6(x)\tilde{B}_i(x)\tilde{B}_j(x)\right\}\mathrm{d}x \tag{10}$$

for $i = 1, 2, \ldots, n-2$; $j = 1, 2, \ldots, n-2$.

$$b_i = \int_{x_0}^{x_n} \left\{b(x)\tilde{B}_i(x) + \left[\frac{\mathrm{d}^3}{\mathrm{d}x^3}(a_0(x)\tilde{B}_i(x)) - \frac{\mathrm{d}^2}{\mathrm{d}x^2}(a_1(x)\tilde{B}_i(x)) + \frac{\mathrm{d}}{\mathrm{d}x}(a_2(x)\tilde{B}_i(x))\right.\right.$$
$$\left.\left. - a_3(x)\tilde{B}_i(x)\right]w'''(x) - a_4(x)\tilde{B}_i(x)w''(x) - a_5(x)\tilde{B}_i(x)w'(x) - a_6(x)\tilde{B}_i(x)w(x)\right\}\mathrm{d}x \tag{11}$$

for $i = 1, 2, \ldots, n-2$; and $\alpha = \left[\alpha_1\, \alpha_2 \ldots \alpha_{n-2}\right]^{\mathrm{T}}$.

3 Procedure to Find a Solution for Nodal Parameters

A general element in the matrix A is evaluated by $\sum_{m=0}^{n-1} I_m$, where $I_m = \int_{x_m}^{x_{m+1}} r_i(x)r_j(x)Z(x)\mathrm{d}x$ and $r_i(x)$, $r_j(x)$ are the quartic B-spline basis functions or their derivatives. We can observe that $I_m = 0$, if $(x_{i-2}, x_{i+3}) \cap (x_{j-2}, x_{j+3}) \cap (x_m, x_{m+1}) = \varphi$. To evaluate each I_m, we used five point Gauss–Legendre quadrature formula. With this, we can observe that the coefficient matrix A is a nine diagonal band matrix. Using the band matrix method, the system $A\alpha = B$ has been solved to get the nodal parameter vector α.

4 Numerical Results

To illustrate the proposed method, we have solved one linear and one nonlinear boundary value problems. The absolute errors of approximations got by the proposed method are presented in Table 1.

Example 1 Consider the linear boundary value problem

$$y^{(6)} + y''' + xy'' - xy = (-114 + 72x - 3x^2 - 6x^3)\mathrm{e}^{-x}, 0 < x < 1$$
$$\text{subject to } y(0) = 0,\ y(1) = \mathrm{e}^{-1},\ y'(0) = 0,\ y'(1) = 2\mathrm{e}^{-1},\ y''(0) = 0,\ y''(1) = \mathrm{e}^{-1}. \tag{12}$$

The exact solution for (12) is $y(x) = x^3\mathrm{e}^{-x}$. The space variable domain [0,1] is divided into 10 equal subintervals. The maximum absolute obtained is 8.842908×10^{-07}.

Example 2 Consider the nonlinear boundary value problem

$$y^{(6)} - 20\mathrm{e}^{-36y} = -40(1+x)^{-6}, \quad 0 < x < 1 \tag{13}$$

subject to $y(0)=0$, $y(1)=ln2/6$, $y'(0)=1/6$, $y'(1)=1/12$, $y''(0)=-1/6$, $y''(1)=-1/24$. The exact solution for the above problem is $y(x)=ln(1+x)/6$. Applying quasilinearization technique [10] to (13), we get the sequence of linear boundary value problems as

$$y^{(6)}_{(n+1)} + 720\mathrm{e}^{-36y_{(n)}}y_{(n+1)} = 720\mathrm{e}^{-36y_{(n)}}y_{(n)} + 20\mathrm{e}^{-36y_{(n)}} - 40(1+x)^{-6}, \quad n = 0, 1, 2, 3, \ldots. \tag{14}$$

$$\text{subject to } y_{(n+1)}(0) = 0, \quad y_{(n+1)}(1) = ln2/6, \quad y'_{(n+1)}(0) = 1/6, \quad y'_{(n+1)}(1) = 1/12,$$

$$y''_{(n+1)}(0) = -1/6, \quad y''_{(n+1)}(1) = -1/24.$$

Table 1 Numerical results of Examples 1 and 2

x	Absolute errors for example 1	Absolute errors for example 2
0.1	7.311464E−07	1.117587E−08
0.2	8.842908E−07	1.583248E−07
0.3	6.631017E−07	3.539026E−07
0.4	1.452863E−07	5.960464E−07
0.5	2.756715E−07	6.631017E−07
0.6	5.215406E−07	5.811453E−07
0.7	4.023314E−07	3.352761E−07
0.8	3.874302E−07	2.011657E−07
0.9	3.576279E−07	1.117587E−07

The space variable domain [0,1] is divided into 10 equal subintervals. The maximum absolute obtained is 6.631017×10^{-07}.

5 Conclusions

The numerical solution of linear and nonlinear two point sixth order boundary value problems by Galerkin method with quartic B-splines is presented. To get a more approximate solution, the quartic B-splines are defined into a new set. It is found that the obtained results are giving a little error. The strength of the developed method lies in the easiness of its application, accuracy, and efficiency.

References

1. Glatmaier, G.A.: Numerical simulations of stellar convection dynamics at the base of the convection zone. Geophys. Fluid Dyn. **31**, 137–150 (1985)
2. Toomore, J., Zahn, J.P., Latour, J., Spiegel, E.A.: Stellar convection theory II: single-mode study of the second convection zone in A-type stars. Geophys. J. **207**, 545–563 (1976)
3. Chandrasekhar, S.: Hydrodynamics and Hydromagnetic Stability. Dover, New York (1981)
4. Siddiqi, S.S., Twizell, E.H.: Spline solutions of linear sixth-order boundary value problems. Int. J. Comput. Math. **60**, 295–304 (1996)
5. Agarwal, R.P.: Boundary Value Problems for Higher Order Differential Equations. World Scientific, Singapore (1986)
6. Siddiqi, S.S., Akram, G., Nazeer, S.: Quintic spline solutions of linear sixth order boundary value problems. Appl. Math. Comput. **189**, 887–892 (2007)
7. Siddiqi, S.S., Akram, G.: Septic spline solutions of sixth order boundary value problems. J. Comput. Appl. Math. **215**, 288–301 (2008)
8. Kasi Viswanadham, K.N.S., Murali Krishna, P.: Sextic B-spline Galerkin Method for sixth boundary value problems. Int. J. Math. Sci. Comput. Appl. **4**, 377–387 (2010)
9. Kasi Viswanadham, K.N.S., Showri Raju, Y.: Quintic B-spline collocation method for sixth boundary value problems. Global J. Res. Eng. **12**, 1–9 (2012)
10. Bellman, R.E., Kalabaa, R.E.: Quasilinearzation and Nonlinear Boundary Value Problems. American Elsevier, New York (1965)
11. Bers, L., John, F., Schecheter, M.: Partial Differential Equations. John wiley Inter Science, New York (1964)
12. Lions, L., Magenes, E.: Non-Homogeneous Boundary Value Problem and Applications. Springer, Berlin (1972)
13. Mitchel, A.R., Wait, R.: The Finite Element Method in Partial Differential Equations. Wiley, London (1977)
14. Prenter, P.M.: Splines and Variational Methods. Wiley, New York (1989)
15. Carl de-Boor.: A Pratical Guide to Splines. Springer, Berlin (2001)
16. Schoenberg, I.J.: On Spline Functions. MRC Report 625. University of Wisconsin (1966)

Numerical and Experimental Studies of Nanofluid as a Coolant Flowing Through a Circular Tube

N. Praveena Devi, Ch. Srinivasa Rao and K. Kiran Kumar

Abstract In this paper, a comparison is made between the numerical and experimental results of nanofluid as a coolant flowing through the circular tube. Effect of nanofluid as a heat transportation fluid is studied both experimentally and numerically. Numerical simulations are performed using commercial computational dynamics software ANSYS FLUENT. Experimental studies are carried out on an in-house test rig. Al_2O_3/water and CuO/water nanofluids are prepared and used for experimentation. Two-phase homogeneous model is considered for the simulation of nanofluid flows. Thermo-hydraulic parameters such as heat transfer coefficient and friction factor are calculated and compared for different Reynolds numbers in laminar flow regime (Re varies between 200 and 2000) and different nanofluid concentrations (varies between 1 and 3% V/V). Performance parameter index is used to compare nanofluid thermo-hydraulic behavior with that of base fluid. It is concluded that nanofluids are good substitute for conventional fluids.

Keywords Nanofluids · Heat transfer · Laminar flow

1 Introduction

Many engineering applications require either quick heat transfer or less temperature rise of working fluid across the heat source. For example, electronic components need to be maintained at 65 °C, wherein the inlet temperature of fluid may be around 45 °C (in tropical counties like India). That means allowable temperature gradient is only 20 °C. At the same time, many electronic appliances will not allow to increase

N. Praveena Devi (✉)
S R Engineering College, Warangal 506004, Telangana, India
e-mail: praveenadevi@gmail.com

Ch. Srinivasa Rao
Andhra University, Visakhapatnam, Andhra Pradesh, India

K. Kiran Kumar
National Institute of Technology, Warangal, Telangana, India

D. Srinivasacharya and K. S. Reddy (eds.), *Numerical Heat Transfer and Fluid Flow*, Lecture Notes in Mechanical Engineering,
https://doi.org/10.1007/978-981-13-1903-7_59

the effective heat transfer area. Hence, it is customary to increase the heat transfer coefficient of working fluid. Conventional working fluids such as air, water, and ethylene glycol have low thermal conductivity values which restrict its usage for high heat flux conditions. Addition of high thermal conductive solid particles to the base fluid increases heat transfer rates. However, the size of the particles is very important as it may lead to agglomeration and settling down. Hence, in the last decade, researchers are concentrating on use of nano-sized particles (size less than 100 nm) to prepare heat transportation fluid, which is termed as "nanofluid". However, addition of nanoparticles into base fluid increases the pressure drop [1]. Applications of nanofluids can be found in different engineering fields such as solar energy harvesting [2], nuclear reactor cooling [3], electronic cooling [4], etc. Al_2O_3/water nanofluid with 1.6% V/V concentration increases heat transfer coefficient up to 47% compared to the base fluid [5].

The main objective of this paper is to carry out numerical and experimental investigations to predict the thermo-hydraulic behavior of nanofluid flowing through a circular tube.

2 Experimental Setup

Figure 1 shows the flow loop schematic and components used for the present investigation. Figure 2 shows the actual experimental setup. Test rig a closed-loop setup where heat is added at along the length of channel, and flow rate is controlled by means of regulating valve in order to maintain required Reynolds number. Heated working fluid is cooled in the pin-fin heat exchanger before it is collected in the storage tank. Temperatures are measured at different locations as shown in the schematic, and all values are recorded using DAQ. Rotameter is calibrated before and after the experimentation.

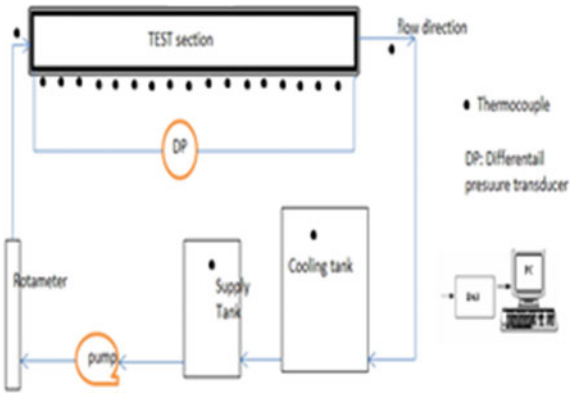

Fig. 1 Schematic of the test facility

Fig. 2 Photograph of test facility

Nanopowders are purchased from reliable supplier. Nanoparticles with mean size of 40 nm are mixed with DI water by means of ultrasound sonicator. C-TAB is used as surfactant.

Data reduction

Heat transfer transferred:

$$Q = h.A.\Delta T_{\mathrm{m}} = V.I = m.c_p.(T_{\mathrm{out}} - T_{\mathrm{in}})$$

Here, measured values are as follows:

1. T_{out} and T_{in} are temperatures of fluid at the outlet and inlet of test section, respectively.
2. m is the mass flow rate.
3. V and I are voltage and current.
4. ΔT_{m} is the mean temperature can be measured using wall and fluid temperatures. With known surface area "A" and measured c_p (from standard correlations), heat transfer coefficient "h" can be calculated. With known "h", Nusselt number (Nu) can be calculated.

   Pressure drop across test section is given by

$$\Delta P = \frac{flv^2}{2gd}$$

Performance parameter is defined as

$$K = \frac{Nu_{\mathrm{nanofluid}}/\Delta P_{\mathrm{nanofluid}}}{Nu_{\mathrm{water}}/\Delta P_{\mathrm{water}}}$$

2.1 Numerical Modeling and Simulation Procedure

Figure 3 shows the geometry and meshing of the circular pipe which is considered for the purpose of present study. Three governing equations, mass, momentum, and energy for the incompressible, laminar, and steady state with no radiation effect, are given below (Table 1):

$$\text{Continuity equation: } \nabla \cdot \left(\rho_m \vec{V}_m\right) = 0$$

$$\text{Momentum equation: } \nabla \cdot \left(\rho_m \vec{V}_m \vec{V}_m\right) = -\nabla p + \nabla \cdot \left[\mu_m \left(\nabla \vec{V}_m + \nabla \vec{V}_m^T\right)\right]$$

$$\text{Energy equation: } \nabla\left(\rho_m C_m \vec{T}_m \vec{V}_m\right) = \nabla \cdot (K_{\text{eff}} \nabla T)$$

To solve the above equations, base fluid properties are taken from NIST software. Nanofluid properties calculated from the standard correlations given by Drew [6],

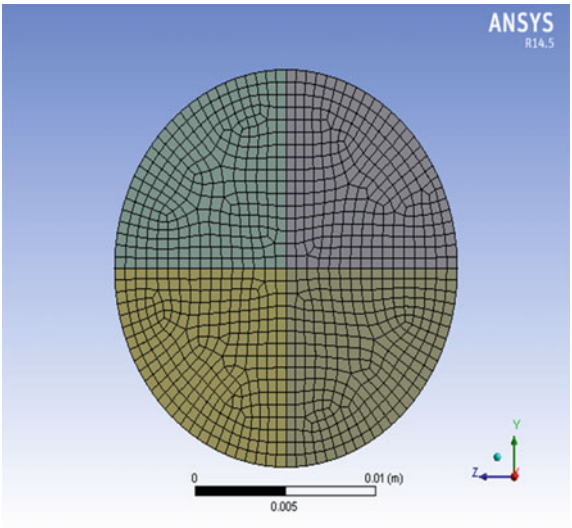

Fig. 3 Cross-sectional view of pipe modeled for simulation

Table 1 Details of numerical and experimental modeling

Parameter	Numerical	Experimental
Pipe diameter (m)	0.0134	0.0134
Pipe length (m)	2	2
Material	SS	SS
Flow	Laminar ($Re = 200$–2000)	
Pipe roughness	Smooth	NA
Boundary condition	Heat flux	Heat flux

Yang et al. [7], Brinkman [8], and Hamilton [9] for density, specific heat, viscosity, and thermal conductivity, respectively, are used. Uniform velocity at the inlet and no-slip boundary conditions is adopted. Grid independency test is performed in order to save the computational time. Appropriate residual values and under-relaxation factors are adopted in order to get the accurate results.

3 Results and Discussion

Figures 4 and 5 show the experimental and numerical results drawn as ratio of Nusselt number ratio (ratio of Nusselt number of nanofluid to the Nusselt number of water) as a function of Reynolds number and volume fraction. Comparison is made among the considered working fluids, i.e., Al_2O_3/water and CuO/water. It can be observed that numerical results are well matched with experimental results and difference between them is within the valid limits of ±15%. By increasing Reynolds number from 200 to 2000, Nusselt number ratio of Al_2O_3/water nanofluid is increased from 1.054 to 1.083 which is 3% and for CuO/water nanofluid, Nusselt number ratio is increased from 1.062 to 1.109 which is 5%. This clearly indicates the usefulness of nanofluid in place of water for the cooling purpose. Similarly, from Figs. 4 and 5, it can be depicted that, for any Reynolds number flow, heat transfer rate is more for higher concentration. However, it is to worth note that Nusselt number ratio of CuO/water nanofluids is more than Al_2O_3 nanofluid, for any Reynolds number and any concentration, within the range of study.

Numerical and experimental results are compared in Figs. 6 and 7. From Fig. 6, it can be interpreted that pressure drop of Al_2O_3/water nanofluid increases with the Reynolds number. Also, friction factor has strongly affected by the concentration. This trend may be attributed to the higher viscosities at higher concentrations. The same trend is observed for CuO/water nanofluid as well. As concentration increases, pressure drop increases substantially. So, it can be concluded that, within the laminar

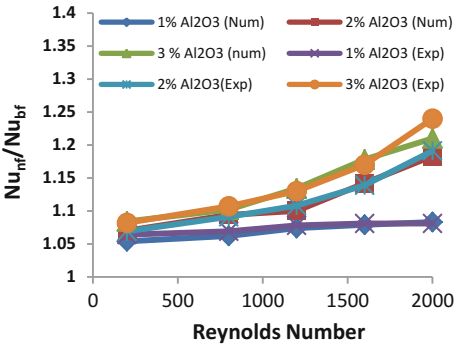

Fig. 4 Variations of Al_2O_3 nanofluid-to-water ratio of average Nusselt number (Nu_{nf}/Nu_{bf}) with particle volume concentration for different values of Reynolds number

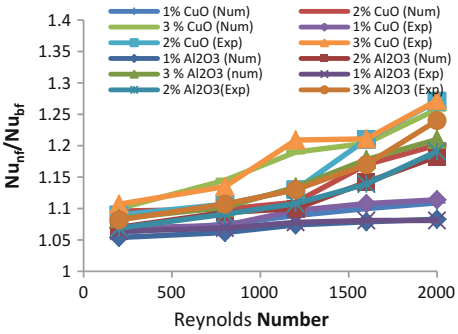

Fig. 5 Variations of CuO nanofluid-to-water ratio of average Nusselt number (Nu_{nf}/Nu_{bf}) with particle volume concentration for different values of Reynolds number

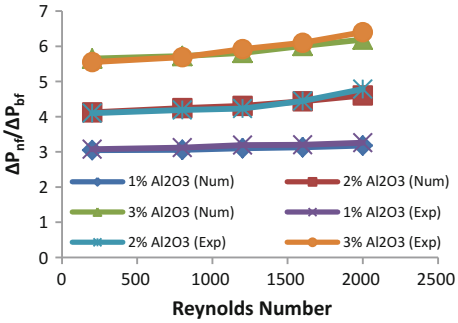

Fig. 6 Variations of Al_2O_3 nanofluid-to-water ratio of pressure drop (Δ_{nf}/Δ_{bf}) with Reynolds number (Re) for different values of particle volume concentration

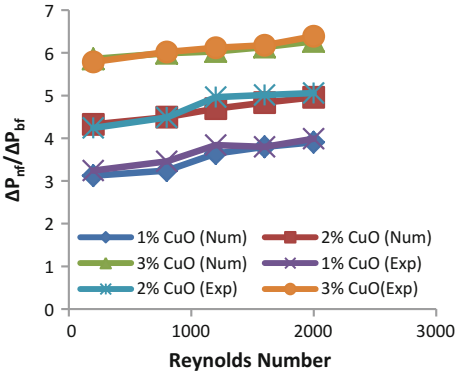

Fig. 7 Variations of CuO nanofluid-to-water ratio of pressure drop (Δ_{nf}/Δ_{bf}) with Reynolds number (Re) for different values of particle volume concentration

flow regime, pressure drop is a strong function of concentration rather than Reynolds number.

Further to accomplish the usefulness of nanofluid in place of conventional water, a term "performance parameter (k)" is used. Since heat transfer coefficient is favorable and pressure drop is unfavorable with the nanofluid flows, performance parameter is the good index for evaluation. From Figs. 8 and 9, it can be seen that, as concentration increases, performance index increases initially and reaches maximum and thereafter starts decreasing. This can be attributed to the disproportional change in

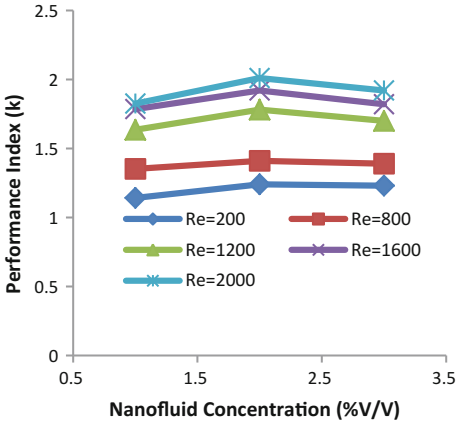

Fig. 8 Variation of performance index (k) of Al_2O_3/water with Re and concentration

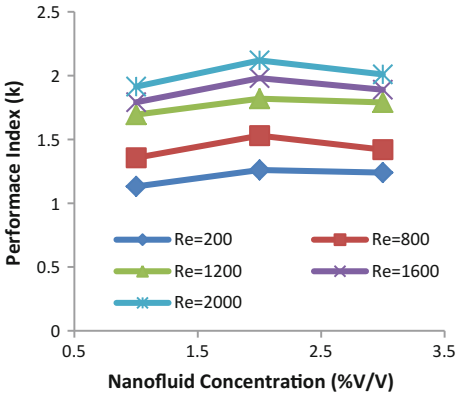

Fig. 9 Variation of performance index (k) of CuO/water with Re and concentration

the thermophysical properties of the working fluid. Increase in the pressure drop is offsetting the increase in Nusselt number. Similar trend is observed in the both working fluids considered here.

4 Conclusions

This study presents the experimental and numerical results on thermo-hydraulic behavior of nanofluid flowing through a circular channel. Laminar flow conditions are adopted (Varied from 200 to 2000) and concentration varied from 1 to 3%. Comparison is made between Al_2O_3/water nanofluid and CuO/water nanofluid. It can be concluded that Nusselt number is significantly higher for nanofluids compared to the water. Meanwhile, the efficacy of using nanofluids is evaluated against the

pressure drop. Finally, to evaluate the combined effect of thermal and hydraulic behavior, performance index is calculated and presented.

It can be concluded that

1. Nusselt number of nanofluid is substantially more than base fluid and this value increased with concentration and Reynolds number.
2. Compared to Al_2O_3/water nanofluid, CuO/water nanofluid shows good thermal behavior.
3. Since both pressure drop and Nusselt number are increasing with concentration, there needs a trade-off to choose the concentration for specific application.

Acknowledgements The present work is carried out under a project sponsored by UGC, GoI (MRP-6230/15(SERO/UGC)). The financial support offered by UGC is gratefully acknowledged.

References

1. Yang, Y.-T., Tsai, K.-T., Wang, Y.-H., Lin, S.-H.: Numerical study of microchannel heat sink performance using nanofluids. Int. Commun. Heat Mass Transf. **57**, 27–35 (2014)
2. OmidMahian, et al.: A review of the applications of nanofluids in solar energy. Int. J. Heat Mass Transf. **57**, 582–594 (2013)
3. Roubort, J.: Nanofluids Industrial Cooling. ANL Michellin, North America (2009)
4. Nguyen, C.T., Roy, G., Gauthier, C., Galanis, N.: Heat transfer enhancement using Al_2O_3-water nanofluid for an electronic liquid cooling system. Appl. Therm. Eng. **27**, 1501–1506 (2007)
5. Wen, D., Ding, Y.: Experimental investigation into convective heat transfer of nanofluids at the entrance region under laminar flow conditions. Int. J. Heat Mass Transf. **47**(24), 5181–5188 (2004)
6. Drew, D.A., Passman, S.L.: Theory of Multicomponent Fluids. Springer, Berlin (1999)
7. Yang, S.M., Tao, W.Q.: Heat Transfer, 3rd edn. Higher Education Press, Beijing (1998)
8. Brinkman, H.C.: The viscosity of concentrated suspensions and solutions. J. Chem. Phys. **20**, 571–581 (1952)
9. Hamilton, R.L., Crosser, O.K.: Thermal conductivity of heterogeneous two-component systems. Ind. Eng. Chem. Fundam. **1**, 187–191 (1962)

Influence of Slip on Peristaltic Motion of a Nanofluid Prone to the Tube

K. Maruthi Prasad and N. Subadra

Abstract Influence of slip on peristaltic motion of a nanofluid prone to the tube is studied under the assumption of long wavelength and low Reynolds number. The equations governing the flow are solved and closed-form expressions for velocity, pressure drop, time-averaged flux and frictional force have been obtained. The effects of various parameters like Brownian motion parameter, thermophoresis parameter, local temperature Grashof number, local nanoparticles Grashof number, slip parameter and inclination on these flow variables have been studied. Streamline patterns and trapping phenomena have been studied and sketched through graphs at the end.

Keywords Nanofluid · Permeable walls · Brownian motion parameter Thermophoresis parameter · Local temperature Grashof number · Local nanoparticle Grashof number

1 Introduction

'Peristalsis is a mechanism of fluid transport that occurs widely in many physiological situations such as food mixing and chyme movement in the intestines, movement of ovum in the female fallopian tube, transport of urine through ureters'. Peristaltic motion of Newtonian fluids has been investigated by many researchers under various conditions [1–3].

Nanometer dimension materials show unique physical and chemical characteristics. Therefore, nanotechnology has a vast contribution in the industry. Nanofluids

K. Maruthi Prasad
Department of Mathematics, School of Technology,
GITAM University, Hyderabad Campus, Hyderabad 502329, Telangana, India

N. Subadra (✉)
Department of Mathematics, Geethanjali College of Engg. & Tech.,
Cheeryal (V), Keesara (M), Medchal Dist 501301, Telangana, India
e-mail: nemani.subhadra@gmail.com

D. Srinivasacharya and K. S. Reddy (eds.), *Numerical Heat Transfer and Fluid Flow*, Lecture Notes in Mechanical Engineering,
https://doi.org/10.1007/978-981-13-1903-7_60

have many applications on heat transfer. Subject to wide-ranging applications of nanofluids, several researchers investigated peristaltic flow with nanofluids [4–6].

No-slip boundary condition has been used by many of the researchers at the walls of the vessels. But arteries show permeable nature in physiological systems. Therefore, there exists some amount of slip at the walls. Some of the researchers who studied in this area are [7–9]. However, the influence of slip on peristaltic motion of nanofluid in an inclined tube has not been studied.

Motivated by these studies, the influence of slip on peristaltic motion of nanofluid prone to tube under the assumption of long wavelength and low Reynolds number is investigated. The nonlinear coupled equations of the temperature profile and nanoparticle phenomenon are solved by using homotopy perturbation technique. The analytical solutions of velocity, pressure rise, frictional force and effect of heat and mass transfer coefficients are obtained. The effects of various parameters on these flow variables are investigated graphically.

2 Mathematical Formulation

Consider the peristaltic motion of an incompressible nanofluid in an inclined tube. The tube is having radius 'a' with uniform cross section and sinusoidal waves are travelling along the boundary of the tube with constant speed c, amplitude b and wavelength λ. Also, suppose that the tube is prone with the horizontal axis at an angle α. Here, heat transfer and nanoparticle phenomenon have been considered. The temperature at the walls of the tube is $\bar{T}_o$ and nanoparticle volume fraction is $\bar{C}_o$. Cylindrical polar coordinate system $\left(\bar{R}, \bar{\theta}, \bar{Z}\right)$ is considered, such that $\bar{Z}$ axis accords with the middle line of the tube and $\bar{R}$ is at right angles to it. The geometry of the wall surface is given by

$$\bar{R} = \bar{h}\left(\bar{z}, \bar{t}\right) = a + b\mathrm{Sin}\frac{2\pi}{\lambda}\left(\bar{Z} - c\bar{t}\right). \tag{1}$$

By using the transformation

$$\begin{aligned} \bar{z} &= \bar{Z} - c\bar{t}, \quad \bar{r} = \bar{R}, \\ \bar{w} &= \bar{W} - c, \quad \bar{u} = \bar{U} \quad \bar{\theta} = \bar{\theta}, \end{aligned} \tag{2}$$

from stationary to moving frame and introducing the non-dimensional quantities.

The governing equations for an incompressible nanofluid prone to the tube under lubrication theory are defined as

$$\frac{\partial u}{\partial r} + \frac{u}{r} + \frac{\partial w}{\partial z} = 0, \tag{3}$$

$$\frac{\partial P}{\partial r} = -\frac{\cos\alpha}{F} \tag{4}$$

$$\frac{\partial P}{\partial z} - \frac{\sin\alpha}{F} = \frac{1}{r}\frac{\partial}{\partial r}\left(r\frac{\partial w}{\partial r}\right) + G_r\tilde{\theta} + B_r\tilde{\sigma} \tag{5}$$

$$0 = \frac{1}{r}\frac{\partial}{\partial r}\left(r\frac{\partial\tilde{\theta}}{\partial r}\right) + N_b\frac{\partial\tilde{\sigma}}{\partial r}\frac{\partial\tilde{\theta}}{\partial r} + N_t\left(\frac{\partial\tilde{\theta}}{\partial r}\right)^2 \tag{6}$$

$$0 = \frac{1}{r}\frac{\partial}{\partial r}\left(r\frac{\partial\tilde{\sigma}}{\partial r}\right) + \frac{N_t}{N_b}\left(\frac{1}{r}\frac{\partial}{\partial r}\left(r\frac{\partial\tilde{\theta}}{\partial r}\right)\right). \tag{7}$$

The dimensionless boundary conditions are

$$\frac{\partial w}{\partial r} = 0,\ \frac{\partial\tilde{\theta}}{\partial r} = 0,\ \frac{\partial\tilde{\sigma}}{\partial r} = 0 \text{ at } r = 0 \tag{8}$$

$$w = -k\frac{\partial w}{\partial r}, \tilde{\theta} = 0,$$

$$\tilde{\sigma} = 0 \text{ at } r = h = 1 + \varepsilon\ \sin\ 2\pi z. \tag{9}$$

3 Solution of the Problem

The coupled equations of temperature profile and nanoparticle phenomenon are solved using homotopy perturbation method as done by He [10]. By solving Eqs. (6) and (7) using boundary conditions (8) and (9), the expressions for temperature profile and nanoparticle phenomenon are obtained as follows:

$$\tilde{\theta}(r,z) = \left(\frac{r^4 - h^4}{64}\right)(N_b - N_t) \tag{10}$$

$$\tilde{\sigma}(r,z) = -\left(\frac{r^2 - h^2}{4}\right)\frac{N_t}{N_b}. \tag{11}$$

Substituting the Eqs. (10) and (11) in Eq. (5) and applying boundary conditions of Eqs. 7–8, the expression for velocity is obtained as

$$\begin{aligned} w = {} & \frac{dp}{dz}\left(\frac{r^2}{4} - \frac{h^2}{4} - \frac{kh}{2}\right) - \frac{\sin\alpha}{F}\left(\frac{r^2}{4} - \frac{h^2}{4} - \frac{kh}{2}\right) \\ & - G_r(N_b - N_t)\left(\frac{r^6}{2304} - \frac{r^2h^4}{256} + \frac{h^6}{288} - \frac{kh^5}{192}\right) \\ & + B_r\left(\frac{N_t}{N_b}\right)\left(\frac{r^4}{64} - \frac{r^2h^2}{16} + \frac{3h^4}{64} + \frac{kh^3}{16}\right). \end{aligned} \tag{12}$$

Further, non-dimensional flux q, pressure gradient $\frac{dp}{dz}$ and pressure rise over the wavelength ΔP_λ are calculated.

$$\Delta P_\lambda = qL_1 + L_2, \tag{13}$$

where

$$q = -\frac{dp}{dz}\left(\frac{h^3k}{2} + \frac{h^4}{8}\right) + \frac{\sin\alpha}{F}\left(\frac{h^3k}{2} + \frac{h^4}{8}\right) - G_r(N_b - N_t)\left(\frac{5h^8}{3072} - \frac{kh^7}{192}\right) + B_r\left(\frac{N_t}{N_b}\right)\left(\frac{h^6}{48} + \frac{kh^5}{16}\right)$$

$$L_1 = \int_0^1 -\frac{1}{S}\mathrm{d}z$$

$$L_2 = -\int_0^1 \frac{\sin\alpha}{F}\mathrm{d}z - G_r(N_b - N_t)\int_0^1\left(\frac{5h^8}{3072} - \frac{kh^7}{192}\right)\frac{1}{S}\mathrm{d}z + B_r\left(\frac{N_t}{N_b}\right)\int_0^1\left(\frac{h^6}{48} + \frac{kh^5}{16}\right)\frac{1}{S}\mathrm{d}z.$$

Then, the time-averaged flux $\bar{Q}$ and dimensionless friction force $\bar{F}$ are calculated.

4 Results and Discussions

In the previous section, the expressions for velocity, pressure rise, time-averaged flux and frictional force have been calculated. Different graphs have been drawn by using Mathematica 9.0 software. It is noticed from Figs. 1, 2 and 3 that the pressure rise $(-\Delta p_\lambda)$ increases with the increase of thermophoresis parameter N_t, local nanoparticle Grashof number (B_r) and inclination (α) and decreases with the increase of Brownian motion parameter (N_b), local temperature Grashof number (G_r) and slip parameter (k). It can be seen from Figs. 4, 5 and 6 that the absolute value of the frictional force $\left(\left|\bar{F}\right|\right)$ decreases with the increase of Brownian motion parameter (N_b) and slip parameter (k) and increases with the increase of thermophoresis parameter (N_t), local temperature Grashof number (G_r), local nanoparticle Grashof number (B_r) and inclination (α). It is noticed from Figs. 7, 8 and 9 that the size of the trapped bolus enhances with the increase of thermophoresis parameter (N_t) and slip parameter (k) and the size of the trapped bolus reduces with the increase of Brownian motion parameter (N_b).

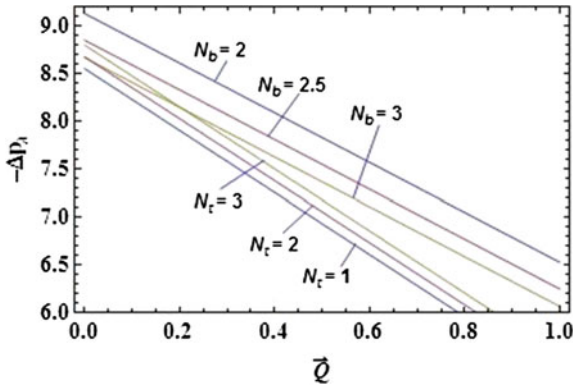

Fig. 1 Effect of $\bar{Q}$ and N_b, N_t on $(-\Delta P_\lambda)$

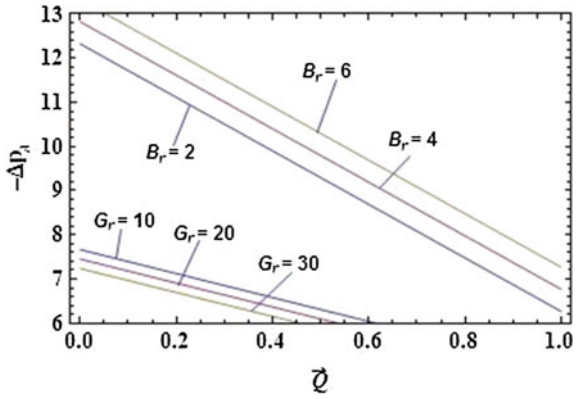

Fig. 2 Effect of $\bar{Q}$ and G_r, B_r on $(-\Delta P_\lambda)$

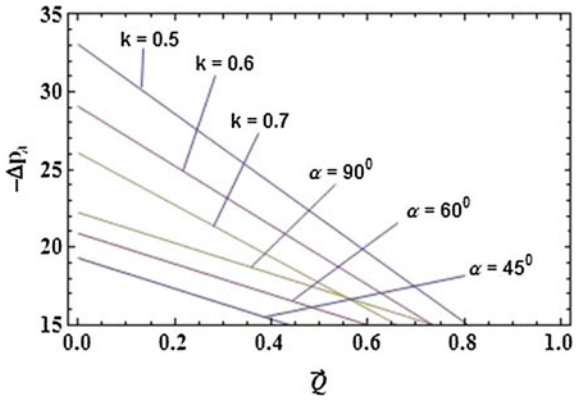

Fig. 3 Effect of $\bar{Q}$ and α, k on $(-\Delta P_\lambda)$

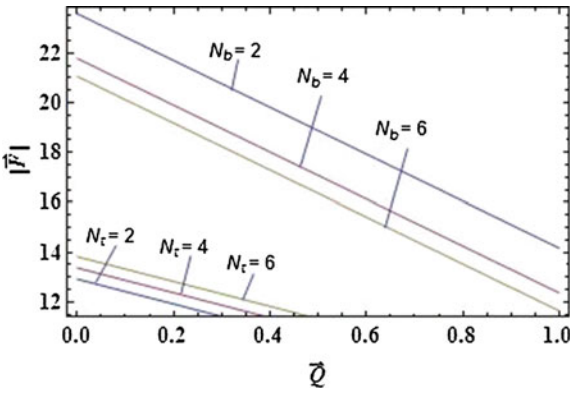

Fig. 4 Effect of $\bar{Q}$ and N_B, N_t on $|\bar{F}|$

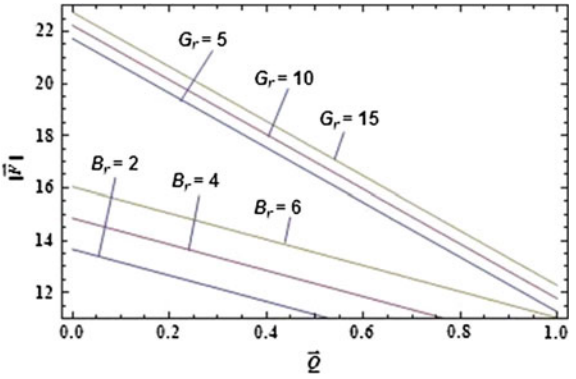

Fig. 5 Effect of $\bar{Q}$ and G_r, B_r on $|\bar{F}|$

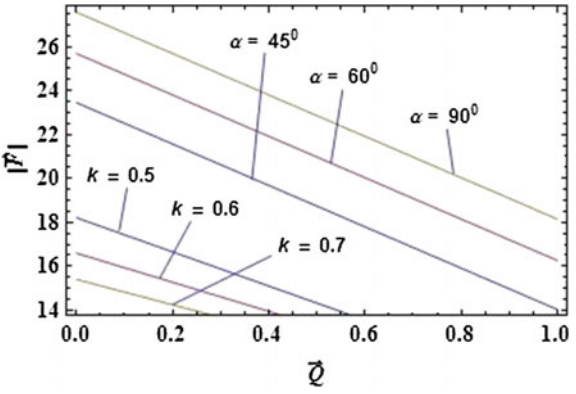

Fig. 6 Effect of $\bar{Q}\&\alpha, kon|\bar{F}|$

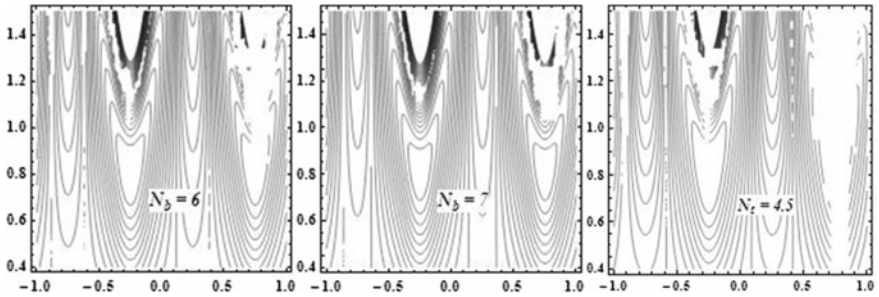

Fig. 7 Streamline patterns for different values of N_b

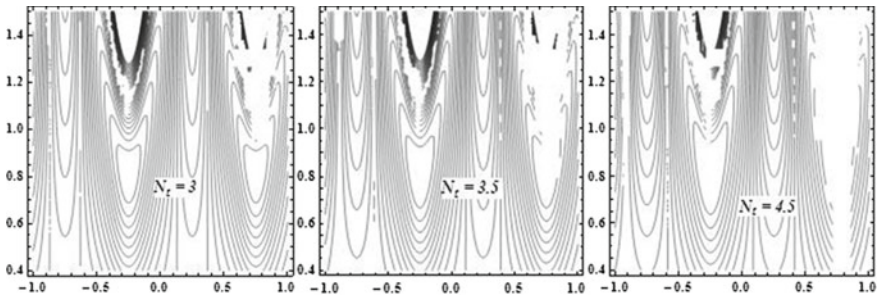

Fig. 8 Streamline patterns for different values of N_t

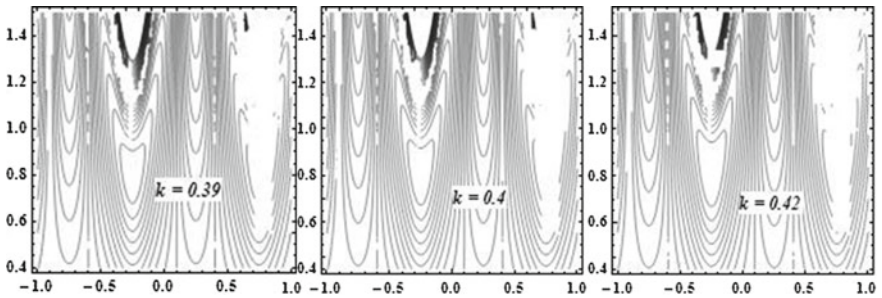

Fig. 9 Streamline patterns for different values of k

5 Conclusion

Influence of slip on peristaltic motion of nanofluid model prone to the tube has been investigated using long wavelength and low Reynolds number approximations. Pressure rise, frictional force and streamline patterns for the nanofluid in an inclined tube have been shown graphically for different variables. It is noticed that the pressure rise increases with the increase of thermophoresis parameter, local nanoparticle Grashof number and inclination and decreases with the increase of Brownian motion param-

eter, local temperature Grashof number and slip parameter. It is also observed that the size of the trapped bolus increases with the increase of thermophoresis parameter and slip parameter and decreases with the increase of Brownian motion parameter.

References

1. Fung, Y.C., Yih, C.S.: Peristaltic transport. J. Appl. Mech. **35**(4), 669–675 (1968). https://doi.org/10.1115/1.3601290
2. Shapiro, A.H., Jaffrin, M.Y., Weinberg, S.L.: Peristaltic pumping with long wavelengths at low Reynolds number. J. Fluid Mech. **37**(4), 799–825 (1969). https://doi.org/10.1017/S0022112069000899
3. Misra, J., Pandey, S.: Peristaltic transport of a non-Newtonian fluid with a peripheral layer. Int. J. Eng. Sci. **37**(14), 1841–1858 (1999)
4. S. U.S. Choi, J. A. E. (1995). Enhancing thermal conductivity of fluids with nanoparticles. ASME FED. *Proceedings of the ASME International Mechanical Engineering Congress and Exposition*, *66*
5. Noreen Sher Akbar, S.N.: Erratum to: peristaltic flow of a nanofluid in a non-uniform tube. Heat Mass Transf. **48**(3), 451–459 (2012). http://doi.org/10.1007/s00231-011-0892-7
6. Abbasi, F., Hayat, T., Alsaedi, A.: Peristaltic transport of magneto-nanoparticles submerged in water: model for drug delivery system. Phys. E **68**, 123–132 (2015)
7. Chu, W.K.-H., Fang, J.: Peristaltic transport in a slip flow. Eur. Phys. J. B-Condens. Matter Complex Syst. **16**(3), 543–547 (2000)
8. Sobh, A.M.: Peristaltic slip flow of a viscoelastic fluid with heat and mass transfer in a tube. Math. Probl. Eng. (2012)
9. Tuljappa, A.: Slip effect on the peristaltic flow of a fractional second grade fluid through a cylindrical tube (2015)
10. He, J.-H.: Approximate analytical solution for seepage flow with fractional derivatives in porous media. Comput. Methods Appl. Mech. Eng. **167**(1–2), 57–68, 1 Dec 1998 (1998). Retrieved from http://works.bepress.com/ji_huan_he/34

Exact Solutions of Couple Stress Fluid Flows

Subin P. Joseph

Abstract Exact solutions of non-Newtonian fluid flows are very rare. In this paper, the couple stress fluid flows are considered and certain exact solutions of these flows are derived. The governing equations of motion of an incompressible steady-state couple stress fluid in the absence of body forces and body couples are considered. Certain special cases are discussed where these equations can be converted to ordinary differential equations, which can be solved in terms of special functions.

Keywords Exact solution · Couple stress fluid · Special functions

1 Introduction

The exact solutions of differential equations play an important role in analyzing any physical phenomena. A large number of physical phenomena are governed by nonlinear partial differential equations. To find an exact solution of such problems is a tedious task in most of the cases. In the case of Newtonian fluid flows, the partial differential equations are nonlinear so that exact solutions are difficult to obtain. The available exact solutions in this case are very less. The solutions available in the literature are mainly in one- or two-dimensional flows or axisymmetric flows [4, 10]. Most of the solutions are derived under restricted conditions which reduce the nonlinear partial differential equations to ordinary differential equations that can be solved. There are other methods such as semi- analytical methods and similarity methods to solve certain type of flows. But it is found that most of the real fluids appearing in industrial applications are non-Newtonian fluids. The constituent equations of such flows are much more complicated. So, the exact solutions of such flows are very rare in the literature. Due to the nonlinearity and occurrence of higher partial derivative in

S. P. Joseph (✉)
Department of Mathematics, Government Engineering College,
Wayanad, Thalapuzha 670-644, Kerala, India
e-mail: subinpj@gecwyd.ac.in
URL: http://www.gecwyd.ac.in/faculty/489/

D. Srinivasacharya and K. S. Reddy (eds.), *Numerical Heat Transfer and Fluid Flow*, Lecture Notes in Mechanical Engineering,
https://doi.org/10.1007/978-981-13-1903-7_61

such equations, the availability of exact solutions even in one-dimensional flows are difficult to obtain. Obtaining solutions through numerical analysis of such flows are also difficult and time consuming. Exact solutions are needed to check the degree of exactness of such numerical techniques developed. In this paper, certain exact solutions of non-Newtonian fluid flows which are characterized as couple stress fluids are obtained. There are some papers which dealt with unidirectional couple stress fluid flows [1–3]. Also, some authors studied two-dimensional flows of such fluids [5, 6]. In the next section, the constituent equations of couple stress fluid flows are given. In the third section, some possible exact solutions of such flows are derived. Some concluding remarks on the results obtained are given in the last section.

2 Couple Stress Fluids

The governing equations of motion of an incompressible steady-state couple stress fluid in the absence of body forces and body couples are given by [8]

$$\nabla \cdot \boldsymbol{v} = 0 \tag{1}$$

and

$$(\boldsymbol{v}\boldsymbol{\nabla})\boldsymbol{v} = -\frac{\nabla p}{\rho} + \nu\nabla^2\boldsymbol{v} - \eta\nabla^4\boldsymbol{v}, \tag{2}$$

where $\boldsymbol{v}$ is the velocity vector, ρ is the constant density, p is the pressure, ν is the coefficient of kinematic viscosity, and η is the parameter due to couple stress. Taking the curl of this equation, the vorticity equation of couple stress fluids is obtained as

$$\nabla \times (\boldsymbol{v} \times \boldsymbol{\omega}) + \nu\nabla^2\boldsymbol{\omega} - \eta\nabla^4\boldsymbol{\omega} = 0 \tag{3}$$

where $\boldsymbol{\omega} = \nabla \times \boldsymbol{v}$ is the vorticity vector. Any vector $\boldsymbol{v}$ satisfying this equation gives a possible velocity field of a couple stress fluid. If $\eta = 0$, this becomes the vorticity equation of an incompressible Navier–Stokes fluid flow under conservative body forces. The generalized Beltrami flow of an incompressible Navier–Stokes equation is characterized by the equations [9]

$$\nabla \times (\boldsymbol{v} \times \boldsymbol{\omega}) = 0 \tag{4}$$

and

$$\nabla^2\boldsymbol{\omega} = 0 \tag{5}$$

There are several papers dealing with the exact solutions of these equations, which give rise to solutions of Navier–Stokes flows. In the case of steady couple stress flows

under consideration, the equations to be satisfied by a generalized Beltrami flow are the Eq. (4) and the equation

$$\nu\nabla^2\boldsymbol{\omega} - \eta\nabla^4\boldsymbol{\omega} = 0 \tag{6}$$

In the next section, certain exact solutions of generalized Beltrami flows in couple stress fluids satisfying Eqs. (1), (4), and (6) are derived. For real flows, boundary conditions are needed. But considering the difficulty of such real problems, the theme of this paper is limited to obtain theoretically possible solutions. So, no specific boundary conditions or initial conditions are prescribed while obtaining such theoretical solutions.

3 Exact Solutions

Since the flow is incompressible, it is assumed that the velocity vector field $\boldsymbol{v}$ is the curl of some vector field $\boldsymbol{A}$. Then, Eq. (1) is trivially satisfied. To obtain some particular solutions, it is also assumed that this velocity potential takes some special forms. Then substitute these special forms in the above Eqs. (4) and (6). This will result in certain differential equations, which may be solved to obtain the solutions of generalized Beltrami flows in couple stress fluids. Different forms of the velocity potential and corresponding solutions are given below.

3.1 Velocity Potential $\boldsymbol{A = \left(0, 0, f(x^2 + y^2)\right)}$

Consider the case where there exists a stream function in the following form:

$$\psi(x, y) = f(x^2 + y^2) \tag{7}$$

Then, the velocity vector and the vorticity vector become

$$\boldsymbol{v} = (2yf'(x^2 + y^2), -2xf'(x^2 + y^2), 0) \tag{8}$$

and

$$\boldsymbol{\omega} = (0, 0, -4(f'(x^2 + y^2) + (x^2 + y^2)f''(x^2 + y^2))) \tag{9}$$

Then we can easily verify that the Eq. (4) is satisfied. So this is a solution to an incompressible steady-state couple stress fluid flow if it satisfies Eq. (6). Substituting in this equation, on simplification, it is obtained that $(0, 0, D(u)) = 0$, where $D(u) = 16(-2\nu f''(u) - 4(-6\eta + u\nu)f^{(3)}(u) + (72\eta u - u^2\nu)f^{(4)}(u) + 36\eta u^2 f^{(5)}(u) + 4\eta u^3 f^{(6)}(u))$ and $u = x^2 + y^2$. So any solution to the differential equation $D(u) = 0$ will give an exact solution of an incompressible steady-state couple stress fluid flow.

One of the exact solutions of this equation is given by

$$c_1 I_0\left(\sqrt{\frac{\nu u}{\eta}}\right) \tag{10}$$

where $I_0(t)$ denotes the modified Bessel function of first kind of order zero and c_1 is any constant. Hence, an exact solution of the incompressible steady-state couple stress fluid flow is given by the velocity field

$$\left(c_1 \nu y\ {}_0F_1\left(2; \frac{(x^2+y^2)\nu}{4\eta}\right)/4\eta, -c_1 \nu x\ {}_0F_1\left(2; \frac{\nu(x^2+y^2)}{4\eta}\right)/4\eta, 0\right) \tag{11}$$

and the vorticity field is given by

$$\left(0, 0, -c_1 \nu\ {}_0F_1\left(1; \frac{\nu}{4\eta}(x^2+y^2)\right)/\eta\right) \tag{12}$$

where ${}_0F_1(a, t)$ is the confluent hypergeometric function in the variable t [7]. Another important exact solution of this equation is given by

$$c_2 K_0\left(\sqrt{\nu(x^2+y^2)/\eta}\right) \tag{13}$$

where $K_0(t)$ denotes the modified Bessel function of second kind of order zero and c_2 is any constant. Hence, another exact solution of the incompressible steady-state couple stress fluid flow is given by the velocity field

$$\left(-c_2\sqrt{\nu} y\ K_1\left(\sqrt{\nu(x^2+y^2)/\eta}\right), c_2\sqrt{\nu} x\ K_1\left(\sqrt{\nu(x^2+y^2)/\eta}\right), 0\right)/\sqrt{\eta(x^2+y^2)} \tag{14}$$

and the vorticity field is given by

$$\left(0, 0, -c_2 \nu\ K_0\left(\frac{\nu(x^2+y^2)}{\eta}\right)/\eta\right) \tag{15}$$

The third important solution for this differential equation can be expressed in terms of Meijer G-function [7]

$$G_{p,q}^{m,n}\left(t \,\middle|\, \begin{matrix} a_1, \ldots, a_p \\ b_1, \ldots, b_q \end{matrix}\right) \tag{16}$$

in the variable t and is given by

$$c_3 (x^2+y^2)^{\frac{3}{2}} G_{2,4}^{2,2}\left(\frac{\nu(x^2+y^2)}{4\eta} \,\middle|\, \begin{matrix} -\frac{1}{2}, -\frac{1}{2} \\ -\frac{1}{2}, -\frac{1}{2}, -\frac{3}{2}, -\frac{3}{2} \end{matrix}\right) \tag{17}$$

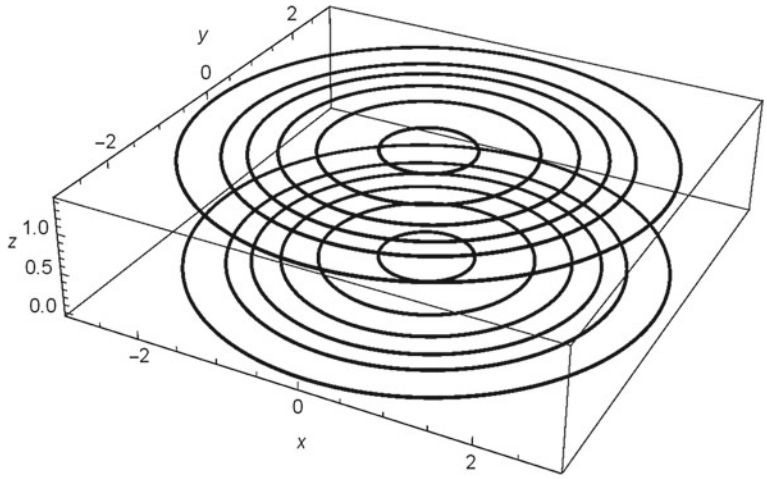

Fig. 1 Certain stream lines of the flow given by Eq. (11)

Hence, the third exact solution of the incompressible steady- state couple stress fluid flow is given by the velocity field

$$2c_3(x^2+y^2)^{\frac{1}{2}}\left(y\,G^{2,1}_{1,3}\left(\frac{\nu(x^2+y^2)}{4\eta}\,\middle|\,\begin{matrix}-\frac{1}{2}\\ -\frac{1}{2},-\frac{1}{2},-\frac{3}{2}\end{matrix}\right),\right.$$
$$\left.-x\,G^{2,1}_{1,3}\left(\frac{\nu(x^2+y^2)}{4\eta}\,\middle|\,\begin{matrix}-\frac{1}{2}\\ -\frac{1}{2},-\frac{1}{2},-\frac{3}{2}\end{matrix}\right),0\right) \tag{18}$$

and the vorticity field is given by

$$\left(0,0,-16c_3\eta\,K_0\left(\sqrt{\frac{\nu(x^2+y^2)}{\eta}}\right)/\sqrt{\nu}\right) \tag{19}$$

Some stream lines of the first solution are given in Fig. 1. The other two solutions also have similar stream lines.

3.2 *Velocity Potential* $A = \left(0, \frac{z+f(r)}{r}, 0\right)$

Now, consider the case where there exist an axisymmetric stream function in cylindrical coordinates in the following form:

$$\psi(r,z) = z + f(r) \tag{20}$$

Then, the velocity vector and the vorticity vector become

$$\boldsymbol{v} = \left(-\frac{1}{r}, 0, \frac{f^{'}(r)}{r}\right) \tag{21}$$

and

$$\boldsymbol{\omega} = \left(0, \frac{f^{'}(r) - rf^{''}(r)}{r^2}, 0\right) \tag{22}$$

This is a solution to an incompressible steady-state couple stress fluid flow if it satisfies Eq. (3). Substituting in this equation and on simplification, it can be seen that $\psi(r, z)$ is steam function of such a flow if $f(r)$ satisfies the ordinary differential equation

$$3\left((\nu-1)r^2 - 15\eta\right)f^{'}(r) + r\left(45\eta - 3(\nu-1)r^2\right)f^{''}(r) + r^2\left((2\nu-1)r^2 - 24\eta\right)f^{(3)}(r) + r^3(9\eta - \nu r^2)f^{(4)}(r) + \eta r^5 f^{(6)}(r) - 3\eta r^4 f^{(5)}(r) = 0 \tag{23}$$

So any solution to this differential equation will give an exact solution of an incompressible steady-state couple- stress fluid flow. One of the important exact solution for this equation is given by

$$c_1 r^4\ {}_1F_2\left(1 + \frac{1}{2\nu}; 2, 3; \frac{\nu r^2}{4\eta}\right) \tag{24}$$

where ${}_1F_2(a; b, c; t)$ is the generalized hypergeometric function in the variable t [7]. Hence, an exact solution of the incompressible steady-state couple stress fluid flow is given by the velocity field

$$\left(-\frac{1}{r}, 0, 4c_1 r^2\ {}_1F_2\left(1 + \frac{1}{2\nu}; 2, 3; \frac{\nu r^2}{4\eta}\right) + \frac{c_1(2\nu+1)r^4\ {}_1F_2\left(2 + \frac{1}{2\nu}; 3, 4; \frac{\nu r^2}{4\eta}\right)}{24\eta}\right) \tag{25}$$

and the vorticity field is given by

$$\left(0, -\frac{c_1}{1152\eta^2}\left(9216\eta^2 r\ {}_1F_2\left(1 + \frac{1}{2\nu}; 2, 3; \frac{\nu r^2}{4\eta}\right) + (2\nu+1)(4\nu+1)r^5\ {}_1F_2\left(3 + \frac{1}{2\nu}; 4, 5; \frac{\nu r^2}{4\eta}\right) + 384\eta r^3\ {}_1F_2\left(2 + \frac{1}{2\nu}; 3, 4; \frac{\nu r^2}{4\eta}\right)\right), 0\right) \tag{26}$$

3.3 Velocity Potential $A = (0, r^2 f(r), 0)$

Consider the axisymmetric stream function given by $\psi(r, z) = r^3 f(r)$. Here, $f(r)$ is multiplied by r^3 to reduce the difficulty of solving the resulting differential equation. Then, the velocity vector and the vorticity vector become

$$\boldsymbol{v} = (0, 0, r^2 f'(r) + 3rf(r)) \tag{27}$$

and

$$\boldsymbol{\omega} = \left(0, -r^2 f''(r) - 5rf'(r) - 3f(r), 0\right) \tag{28}$$

Also, we can easily verify that Eq. (4) is satisfied. Substituting these in Eq. (6), it is easy to see that $f(r)$ should satisfy the ordinary differential equation

$$\begin{aligned} &rf'(r)(9\eta - 3\nu r^2) + 2r^3 f^{(3)}(r)(12\eta - 5\nu r^2) + r^4 f^{(4)}(r)(54\eta - \nu r^2) \\ &\quad + \eta r^6 f^{(6)}(r) + 15r^5 f^{(5)}(r) - 3r^2 f''(r)(9\eta + 7\nu r^2) + f(r)(3\nu r^2 - 9\eta) = 0 \end{aligned} \tag{29}$$

So any solution to this differential equation will give an exact solution of an incompressible steady-state couple stress fluid flow. One of the important exact solution that can be obtained for this equation is given by

$$c_1 \frac{1}{r}\, {}_0F_1\left(2; \frac{\nu r^2}{4\eta}\right) \tag{30}$$

Hence, an exact solution of the incompressible steady-state couple stress fluid flow is given by the velocity field

$$\left(0, 0, 2c_1\, {}_0F_1\left(1; \frac{\nu r^2}{4\eta}\right)\right) \tag{31}$$

and the vorticity field is given by

$$\left(0, -c_1 \nu r\, {}_0F_1\left(2; \frac{\nu r^2}{4\eta}\right)/\eta, 0\right) \tag{32}$$

Another important exact solution of this equation is given by

$$\frac{1}{r^2} K_1\left(-r\sqrt{\frac{\nu}{\eta}}\right) \tag{33}$$

Hence, the second exact solution of the incompressible steady-state couple stress fluid flow is given by the velocity field

$$\left(0, 0, \sqrt{\frac{\nu}{\eta}} K_0 \left(-r\sqrt{\frac{\nu}{\eta}}\right)\right) \tag{34}$$

and the vorticity field is given by

$$\left(0, -\nu K_1 \left(-r\sqrt{\frac{\nu}{\eta}}\right)/\eta, 0\right) \tag{35}$$

3.4 Conclusion

In this paper, certain exact solutions of incompressible steady-state couple stress fluid flows are derived. The correctness of our solutions has been verified by directly substituting the solutions to the corresponding ordinary differential equations. Here, no boundary conditions or initial conditions are considered. Since the availability of exact solutions of couple stress fluid flow is very rare, the solutions that are obtained in this paper can be utilized to explore the properties of such flows. Also, availability of such exact solutions can be used for checking any numerical code developed for studying real flows occurring in nature or in laboratory. Three types of flows which admit exact solutions in terms of special functions are discussed. Even in the simplified versions of velocity potentials, the solutions obtained are in terms of special functions such as generalized hypergeometric functions or Meijer G-functions.

Acknowledgements The author acknowledges the financial support from Technical Education Quality Improvement Programme (TEQIP) Phase-II project (MHRD, Government of India) for doing this research and presenting this paper.

References

1. Devakar, M., Iyengar, T.K.V.: Nonlinear analysis. Model. Control **1**(2) (2008)
2. Devakar, M., Iyengar, T.K.V.: Generalized stokes' problems for an incompressible couple stress fluid. Int. J. Math. Comput. Nat. Phys. Eng. **8**(1) (2014)
3. Devakar, M., Sreenivasu, D., Shankar, B.: Analytical solutions of couple stress fluid flows with slip boundary conditions. Alexandria Eng. J. (2014)
4. Drazin, P.G., Riley, N.: The Navier-Stokes Equation: A Classification of Flows and Exact Solutions. Cambridge University Press, New York (2006)
5. Islam, S., Zhou, C.Y.: Exact solutions for two dimensional flows of couple stress fluids. Z. Angew. Math. Phys. **58** (2007)
6. Khan, W., Yousafzai, F.: Advanced Trends in Mathematics, vol. 1 (2014)
7. Olver, F.W.J. (Ed.).: NIST Handbook of Mathematical Functions. Springer (2010)

8. Stokes, V.K.: Couple stresses in fluids. Phys. Fluids **9** (1966)
9. Wang, C.Y.: Exact solutions of the Navier-Stokes equations-the generalized Beltrami flows, review and extension. Acta Mech. **81** (1990)
10. Wang, C.Y.: Exact solutions of the steady-state Navier-Stokes equations. Ann. Rev. Fluid. Mech. **23** (1991)

Finite Element Study of Convective Heat and Mass Transfer of Two Fluids in a Vertical Channel of Variable Width with Soret and Dufour Effects

B. Suresh Babu, G. Srinivas and G. V. P. N. Srikanth

Abstract A mathematical model for convective heat and mass transfer of two immiscible fluids in a vertical channel of variable width with thermo-diffusion, diffusion-thermal effects is presented. The governing boundary layer equations generated for momentum, angular momentum, energy and species concentration are solved with appropriate boundary conditions using Galeriken finite element method. The effects of the pertinent parameters are studied in detail. Furthermore, the rate of heat transfer, mass transfer, and shear stress near both the walls is analyzed.

Keywords Micropolar fluid · Viscous fluid · Finite element method · Magnetic field · Soret and Dufour effects

1 Introduction

The subject of micropolar fluids attained a higher degree by many researchers because when the fluid is with the suspended particles we cannot analyze the properties of fluid flow by regular Newtonian fluid characteristics. Eringen [1] had taken initiation in describing the subject of micropolar fluids. Chamkha et al. [2] analyzed the free convection of micropolar fluid in a vertical channel.

The diffusion effects namely thermal-diffusion (Soret) and diffusion-thermo (Dufour) are highly important in fluid mechanics. The problems concerned to heat and mass transference and density variations with temperature and concentration lead to integrated buoyancy force under convection. The diffusion impacts influence the flow field in boundary layer over a vertical channel. Anwar Beg et al. [3] described the

B. Suresh Babu (✉)
Sreyas Institute of Engineering and Technology, Hyderabad 500068, Telangana, India
e-mail: bsureshmaths@gmail.com

G. Srinivas
Guru Nanak Institute of Technology, Hyderabad 500009, Telangana, India

G. V. P. N. Srikanth
VNR VJIET, Hyderabad 500090, Telangana, India

D. Srinivasacharya and K. S. Reddy (eds.), *Numerical Heat Transfer and Fluid Flow*, Lecture Notes in Mechanical Engineering,
https://doi.org/10.1007/978-981-13-1903-7_62

thermal-diffusion and diffusion-thermo impacts by numerically studying the free convection MHD heat and mass transfer over a stretching layer with saturated permeable structure. The MHD flow of two immiscible fluids between moving plates has been investigated by Stamenkovic et al. [4]. For many years, scientists and engineers have been showing interest in two phase flows, which arise in many industrial applications. The two-phase fluid flow phenomena are important in pipe flows, fluidized beds, sedimentation, gas purification, transport processes, and shock waves. Malashetty and Leela [5, 6] studied two-fluid flow in a vertical channel. Such investigations are beneficial to understand the slag layer effects over heat transfer features of a coal-fired magnetohydrodynamic generator. Vajravelu et al. [7] dealt with the heat tranfer through hydromagnetic unstable motion of two immiscible between two plates. Umavathi et al. [8] determined the stable and unstable motion of immiscible fluid in a horizontal system. Prathap Kumar [9] investigated the systematic solution for a solute dispersal in a conducting immiscible fluid moving within two horizontal sheets under transverse magnetic effect. Ramana murthy et al. [10] resolved the issue of stable Poiseuille flow of two immiscible incompressible micropolar fluids within two horizontal sheets of uniform wall temperatures in accordance with entropy mechanisms. Suresh Babu et al. [11] studied the heat and mass transfer along a vertical channel filled with micropolar and viscous fluids. Gupta et al. [12] described the state of stable completely progressed flow and heat transference of two immiscible MHD and viscous fluid, partly occupied with permeable medium and pure fluid. The motion of 2-immiscible stress fluids within two homogeneous permeable beds was dealt by Srinivas et al. [13]. Motivated by the above studies, in the present study emphasis is given to diffusion effects on heat and mass transfer of immiscible flows in a vertical channel of variable viscous layer width. Highly nonlinear and coupled governing differential equations are solved numerically using finite element method.

2 Mathematical Formulation

The two infinite plates are kept at $Y = -h_1$ and $Y = h_2$ initially as shown in Fig. 1. The first region occupies micropolar fluid and the other with viscous fluid. Here, the buoyancy force determines the fluid flow. The governing equations for the problem are developed with the assumptions that the flow is assumed to be 1D, steady, laminar, immiscible, and incompressible, the transport characteristics of the two fluids are kept at constant, the flow of the fluid is fully developed and $T_1 > T_2$, $C_1 > C_2$.

2.1 Governing Equations

Region-1:

$$\frac{d\nu_1}{dY} = 0, \rho_1 = \rho_0[1 - \beta_{1T}(\tau_1 - \tau_0) - \beta_{1C}(\phi_1 - \phi_0)] \tag{1}$$

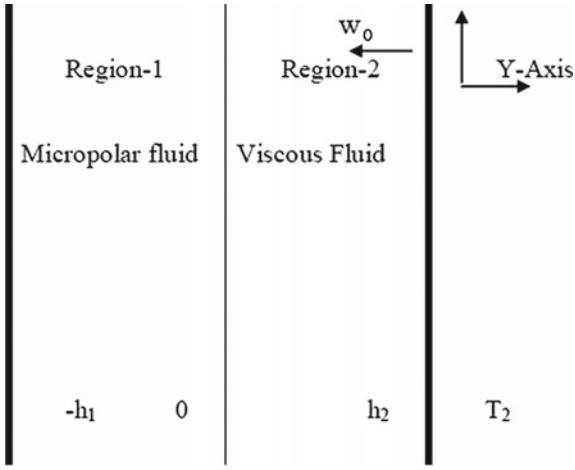

Fig. 1 Schematic diagram

$$\frac{\mu_1 + K}{\rho_1}\frac{d^2\nu_1}{dY^2} + \frac{K}{\rho_1}\frac{d\eta}{dY} + g\beta_{1T}(\tau_1 - \tau_0) + g\beta_{1C}(\phi_1 - \phi_0) - \frac{\sigma B_0^2 \nu_1}{\rho_1} = 0 \tag{2}$$

$$\gamma\frac{d^2\eta}{dY^2} - K\left[2\eta + \frac{d\nu_1}{dY}\right] = 0 \tag{3}$$

$$\frac{k_1}{\rho_1 C_p}\frac{d^2\tau_1}{dY^2} + \frac{1}{\rho_1 C_p}\left[\mu_1\left(\frac{d\nu}{dY}\right)^2 + \frac{\rho_1 D_1 K_{T1}}{C_{S1}}\frac{d^2\phi_1}{dY^2}\right] = 0 \tag{4}$$

$$D_1\frac{d^2\phi}{dY^2} + \frac{D_1 K_{T1}}{T_M}\frac{d^2\tau_1}{dY^2} = 0 \tag{5}$$

Region-2:

$$\frac{d\nu_2}{dY} = 0, \rho_2 = \rho_0[1 - \beta_{2T}(\tau_2 - \tau_0) - \beta_{2C}(\phi_2 - \phi_0)] \tag{6}$$

$$\frac{\mu_2}{\rho_2}\frac{d^2\nu_2}{dY^2} + g\beta_{2T}(\tau_2 - \tau_0) + g\beta_{2C}(\phi_2 - \phi_0) - \frac{\sigma B_0^2 \nu_2}{\rho_2} = 0 \tag{7}$$

$$\frac{k_2}{\rho_2 C_p}\frac{d^2\tau_2}{dY^2} + \frac{1}{\rho_2 C_p}\left[\mu_2\left(\frac{d\nu_2}{dY}\right)^2 + \frac{\rho_2 D_2 K_{T2}}{CS_2}\frac{d^2\phi_2}{dY^2}\right] = 0 \tag{8}$$

$$D_2\frac{d^2\phi}{dY^2}+\frac{D_2K_{T2}}{T_M}\frac{d^2\tau_2}{dY^2}=0 \tag{9}$$

The following boundary and interface conditions proposed by Arimen [14] are considered to solve the following system of equations (1)–(9): $\nu_1=0$ at $Y=-h_1$, $\nu_2=-w_0$ at $Y=h_2$, $U_2=-w_0$ at $Y=h_2$,
$\nu_1(0)=\nu_2(0)$, $\tau=\tau_1 at Y=-h_1$, $\tau=\tau_2 at Y=h_2$, $\tau_1(0)=\tau_2(0)$,
$\phi=\phi_1$ at $Y=-h_1$, $\phi=\phi_2$ at $Y=-h_1$, $\phi_1(0)=\phi_2(0)$, $\eta=0$ at $Y=-h_1$,
$\mu_1+K\frac{d\nu_1}{dY}+K\eta=\mu_2\frac{d\nu_2}{dY}$ at Y = 0, $\frac{d\eta}{dY}=0$, $k_1\frac{d\tau_1}{dY}=k_2\frac{d\tau_2}{dY}$ at Y = 0,
$D_1\frac{d\phi_1}{dY}=D_2\frac{d\phi_2}{dY}$ at Y = 0.
The following variables are used to convert the system of equations (1)–(7) to dimensionless form:
y = $\frac{Y}{h_1}$(region-1), y = $\frac{Y}{h_2L}$(region-2), $u_1=\frac{\nu_1}{\nu_0}$(region-1), $u_2=\frac{\nu_2}{w_0}$(region-2),
$\theta_1=\frac{\tau_1-\tau_0}{\Delta T}$, $\theta_2=\frac{\tau_2-\tau_0}{\Delta T}$, N = $\frac{h_1}{\nu_0}\eta$, $j=h^2$, $\kappa=\frac{K}{\mu_1}$, $\varphi_1=\frac{\phi_1-\phi_0}{\Delta\phi}$, $\varphi_2=\frac{\phi_2-\phi_0}{\Delta\phi}$,
$R_e=\frac{\nu_0h_1}{\upsilon_1}$, $Gr=\frac{g\beta_{1T}\Delta\tau h_1^3}{\upsilon_1^2}$, $Gc=\frac{g\beta_{1C}\Delta\tau h_1^3}{\upsilon_1^2}$, $Sr=\frac{D_1K_{T1}\Delta\tau}{T_M\Delta}$.
The dimensionless forms of governing equations thus obtained are as follows:
Region-1:

$$\frac{d^2N}{dy^2}-\frac{2\kappa}{2+\kappa}(2N+\frac{du_1}{dy})=0 \tag{10}$$

$$(1+\kappa)\frac{d^2u_1}{dy^2}+\kappa\frac{dN}{dy}+\frac{Gr}{R}\theta_1+\frac{Gc}{R}\varphi_1-Mu_1=0, \tag{11}$$

$$\frac{1}{PrR_e}\frac{d^2\theta_1}{dy^2}+\frac{Ec}{R}(\frac{du_1}{dy})^2+\frac{Du}{R}\frac{d^2\varphi_1}{dy^2}=0,\ \frac{1}{ScR_e}\frac{d^2\varphi_1}{dy^2}+Sr\frac{d^2\theta_1}{dy^2}=0 \tag{12}$$

Region-2:

$$L^2\frac{d^2u_2}{dy^2}+\frac{m}{b_1\rho h^2}\frac{Gr}{R}\theta_2+\frac{m}{b_2\rho h^2}\frac{Gc}{R}\varphi_2-\frac{mM}{h^2}u_2=0 \tag{13}$$

$$\frac{\rho h}{\alpha}\frac{1}{PrR_e}\frac{d^2\theta_2}{dy^2}+\frac{\rho h}{m}\frac{Ec}{R}(\frac{du_2}{dy})^2+\frac{c_sh}{DK_T}\frac{D_u}{R_e}\frac{d^2\varphi_2}{dy^2}=0 \tag{14}$$

$$\frac{h}{D}(\frac{1}{ScR_e})\frac{d^2\varphi_2}{dy^2}+\frac{h}{K_tD}Sr\frac{d^2\theta_2}{dy^2}=0 \tag{15}$$

The dimensionless boundary and interface conditions thus formed are as follows:
$u_1=0$ at y = −1, $u_2=-1$ at y = L, $u_1(0)=u_2(0)$, $\theta_1=1$ at y = −1, $\theta_2=0$ at y = 1, $\theta_1(0)=\theta_2(0)$, φ_1 at y = −1, $\varphi_2=0$ at y = 1, $\varphi_1(0)=\varphi_2(0)$, N = 0 at y = −1, $\frac{du_1}{dy}+\frac{K}{1+\kappa}$, $N=\frac{1}{mh(1+\kappa)}\frac{du_2}{dy}$ at y = 0.

3 Solution of the Problem

The finite element method as described by Reddy [15] has been implemented to solve the dimensionless coupled differential equations generated by the fluid flows. The widths of the viscous region is considered as L. For the problem discussed here, it is considered that each region is divided into 100 linear elements and each element is 3 nodded.

4 Results and Discussion

The numerical solution of the system of equations is analyzed for different values of the governing parameters. The profiles are studied with fixed values Gr = 5, Gc = 5, Re = 3, M = 3, = 0.1, Du = 0.08, Sr = 0.1, Sc = 0.66, Sr = 0.001 excepting the varying parameter. Figures 2, 3, 4, and 5 illustrate the effect of Gr and Gc on velocity, angular velocity. As Gr and Gc increase the velocity and angular velocity increase substantially. The buoyancy enhances the flow in both regions, i.e., thermal buoyancy force dominates the viscous force in both regions of the channel and it is found to be more in micropolar region. The lowest velocity corresponds to Gr = 2. Higher Gr values boost up the flow in both regions. Figures 6 and 7 illustrate the effect of Re. The reduction of velocity is found with the increase of Re due to domination of inertial force on viscous force in both regions of the channel and found more drastic in viscous region. Also reduces the microrotation with increase of Re. Figures 8 and 9 explain the effect of Dufour number (Du) on temperature and diffusion. As Du increases, i.e., molecular diffusivity increases and it is noticed that the temperature decreases and the diffusion profiles increases with increase of Du.

Figures 10 and 11 depict the effect of Sr on temperature and diffusion, as Sr increases increases an increase in the temperature and the decay in the fluid concentration is observed. Figures 12 and 13 depict the effect of Sc on temperature and diffusion, as Sc increases it is noticed that the temperature decreases concentration of the fluid increases with increase of Sc.

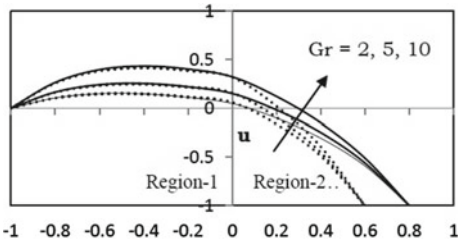

Fig. 2 Velocity profiles with Gr

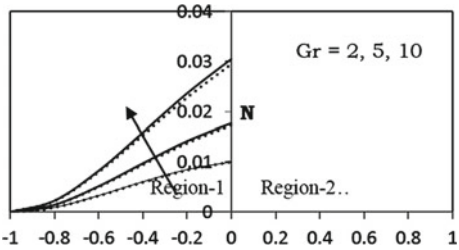

Fig. 3 Microrotation profiles with Gr

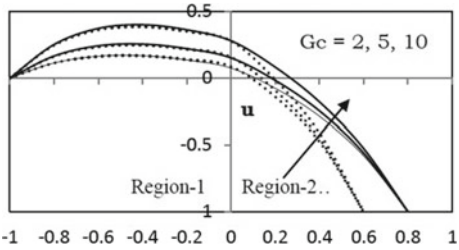

Fig. 4 Velocity profiles with Gc

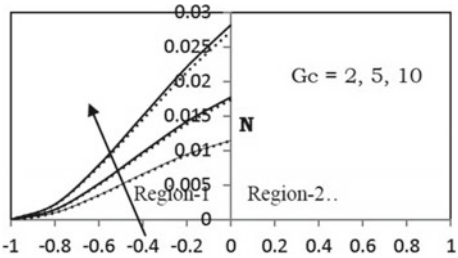

Fig. 5 Microrotation profiles with Gc

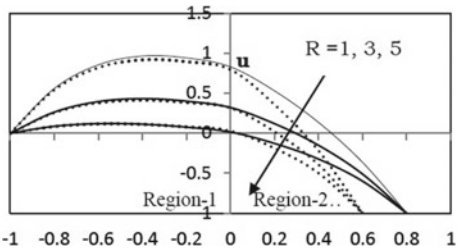

Fig. 6 Velocity profiles with R

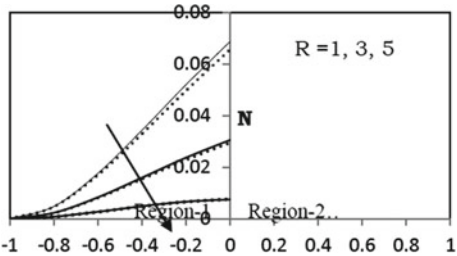

Fig. 7 Microrotation profiles with Gc

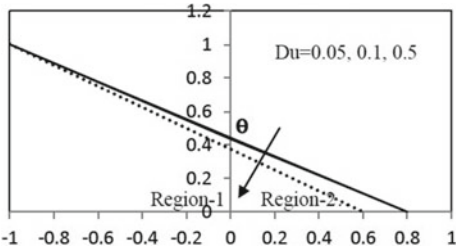

Fig. 8 Temperature profiles with Du

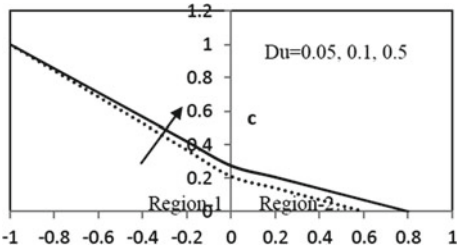

Fig. 9 Concentration profiles with Du

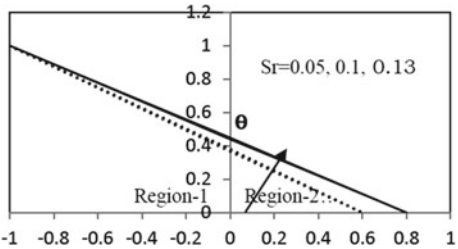

Fig. 10 Temperature profiles with Sr

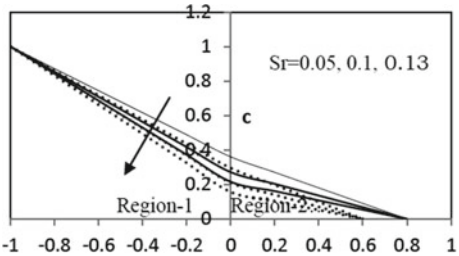

Fig. 11 Concentration profiles with Sr

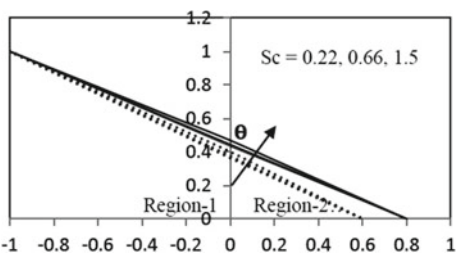

Fig. 12 Temperature profiles with Sc

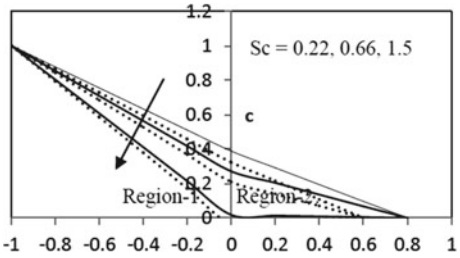

Fig. 13 Temperature profiles with Sc

Table 1 illustrates that the absolute shear stress enhances with increase of Gr Gc on both the boundaries. For the increase of Re, the stress reduces on both the boundaries. Table 2 illustrates that heat transfer rate decreases on the left boundary and enhances on the right boundary Sr, Sc. For Du, the effect is reversal Table 3 explains rate of mass transfer increase on the boundary at and decrease at the boundary for the parameters Sr, Sc because the rise in convection and inertial forces leading to enhance the concentration.

Table 1 Shear stress values

L	Gr	St-I	St-II	Gc	St-I	St-II	R	St-I	St-II
0.8	2	−0.7128	2.43951	2	−0.74944	2.48635	1	−3.56296	3.57305
0.8	5	−1.08569	2.58882	5	−1.08569	2.58882	2	−1.70547	2.83547
0.8	10	−1.70725	2.83778	10	−1.64609	2.75955	5	−0.58843	2.38967
0.6	2	−0.70319	3.23412	2	−0.73823	3.29385	1	−3.46199	4.5879
0.6	5	−1.06424	3.41276	5	−1.06424	3.41276	2	−1.66419	3.70742
0.6	10	−1.66605	3.71064	10	−1.60756	3.61087	5	−0.58268	3.17433

Table 2 Nusselt number values

L	Du	Nu-I	Nu-II	Sr	Nu-I	Nu-II	Ec	Nu-I	Nu-II
0.8	0.05	0.555931	0.555942	0.05	0.565096	0.544494	0.001	0.556363	0.555451
0.8	0.1	0.556661	0.555113	0.1	0.556363	0.555451	0.002	0.556047	0.55675
0.8	0.5	0.565483	0.546527	0.13	0.55086	0.562354	0.1	0.524944	0.684568
0.6	0.05	0.624778	0.626497	0.05	0.633626	0.611761	0.001	0.624841	0.626456
0.6	0.1	0.624885	0.626429	0.1	0.624841	0.626456	0.002	0.624504	0.628208
0.6	0.5	0.480479	0.868736	0.13	0.619266	0.635781	0.1	0.591306	0.800688

Table 3 Sherwood number values

L	Du	Sh-I	Sh-II	Sr	Sh-I	Sh-II	Sc	Sh-I	Sh-II
0.8	0.05	0.728628	0.338354	0.05	0.639395	0.450318	0.22	0.6109	0.486086
0.8	0.1	0.728198	0.338815	0.1	0.728374	0.338628	0.66	0.728374	0.338628
0.8	0.5	0.723008	0.343099	0.13	0.784427	0.268265	1.5	0.981557	0.0208
0.6	0.05	0.78963	0.349488	0.05	0.704496	0.491933	0.22	0.677403	0.537283
0.6	0.1	0.789561	0.349503	0.1	0.789589	0.349498	0.66	0.789589	0.349498
0.6	0.5	1.90769	−1.52595	0.13	0.843583	0.259119	1.5	1.03589	−0.06278

5 Conclusions

The reduction of width of viscous region leads to decrease of magnitude of shearing stress on the left wall and increase on the right wall, heat transfer rate rises on both boundaries and the same effect is obtained for mass transfer rate. The effect of the change of thickness of one layer does not shown significance on the other layer because of the immiscibility. The temperature is found to be linear across the channel for all the effects and the temperature is reduced with reduction of viscous region.The diffusion falls rapidly in the micropolar region than viscous region due to density variations. It is very clear near the interface.The diffusion is enhanced with reduction of viscous region.The shearing effect is observed more in viscous region than micropolar region.

References

1. Eringen, A.C.: Simple microfluids. Int. J. Eng. Sci. **2**(2), 205–207 (1964). https://doi.org/10.1016/0020-7225(64),90005-9
2. Chamkha, A.J., Groan, T., Pop, I.: Fully developed free convection of a micropolar fluid in a vertical channel. Int. Commun. Heat Mass Transf. **29**(8), 1119–1127 (2002). https://doi.org/10.1016/s0735-1933(02),00440-2
3. Anwar Beg, O.A., Bakier, Y., Prasad, V.R.: Numerical study of free convection mhd heat and mass transfer from a stretching surface to a saturated porous medium with Soret and Dufour effects. Comput. Mater. Sci. **46**(1), 57–65 (2009). https://doi.org/10.1016/j.commatsci.2009.02.004
4. Stamenkovic, Z., Nikodijevic, D., Kocic, M., Nikodijevic, J.: Mhd flow and heat transfer of two immiscible fluids with induced magnetic field effects. Thermal Sci. **16**(3), 323–336 (2012). https://doi.org/10.2298/tsci120430172s
5. Malashetty, M.S., Leela, V.: Magnetohydrodynamic heat transfer in two phase flow. Int. J. Eng. Sci. **30**(3), 371–377 (1992). https://doi.org/10.1016/0020-7225(92)90082-r
6. Malashetty, M.S., Leela, V.: Magnetohydrodynamic heat transfer in two fluid flow. In: Proceedings of National Heat Transfer conferences, Phase Change Heat Transfer (1991)
7. Vajravelu, K., Arunachalam, P.V., Sreenadh, S.: Unsteady flow of two immiscible conducting fluids between two permeable beds. J. Math. Anal. Appl. **196**(3), 1105–1116 (1995)

8. Malashetty, M.S., Umavathi, J.C., Kumar, J.P.: Flow and heat transfer in an inclined channel containing fluid layer sandwiched between two porous layers. J. Porous Media. **8**(5), 443–453 (2005). https://doi.org/10.1615/jpormedia.v8.i5.30
9. Prathap Kuma, J., Umavathi, J.C., Pop, I., Biradar, B.M.: Fully developed mixed convection flow in a vertical channel containing porous and fluid layer with isothermal or isoflux boundaries. Transp. Porous Media. **80**(1), 117–135 (2009). https://doi.org/10.1007/s11242-009-9347-8
10. Ramana Murthy, J.V., Srinivas, J.: Second law analysis for Poiseuille flow of immiscible micropolar fluids in a channel. Int. J. Heat Mass Transf. **65**, 254–264 (2013). https://doi.org/10.1016/j.ijheatmasstransfer.2013.05.048
11. Suresh Babu, B., Srinivas, G., Srikanth, G.V.P.N.: Finite element analysis of diffusion effects on convective heat and the mass transfer of two fluids in a vertical channel. Int. J. Auto. & Mech. Eng. **14** (1), 3998–4012 (2016). https://doi.org/10.15282/ijame.14.1.2017.14.0324
12. Gupta, V.G., Jain, A., Jha, A.K.: Convective effects on MHD flow and heat transfer between vertical plates moving in opposite direction and partially filled with a porous medium. J. Appl. Math. Phys. **4**(2), 341–358 (2016). https://doi.org/10.4236/jamp.2016.42041
13. Jangili, D.S., Josyula, R.M.: Flow of two immiscible couple stress fluids between two permeable beds. J. Appl. Fluid Mech. **9** (1), 501–507 (2016). https://doi.org/10.18869/acadpub.jafm.68.224.24013
14. Ariman, T., Turk, M.A., Sylvester, N.D.: Micro continuum fluid Mechanics-a review. Int. J. Eng. Sci. **11**(8), 905–930 (1973). https://doi.org/10.1016/0020-7225(73)90038-4
15. Reddy, J.N.: An Introduction to the Finite Element Method, 3rd edn. McGraw-Hill, New York (2006)

Thermal Modeling of a High-Pressure Autoclave Reactor for Hydrothermal Carbonization

D. Sushmitha and S. Srinath

Abstract In the present study of hydrothermal carbonization, the waste biomass sample collected from near local wood mills is processed in a high-pressure autoclave reactor by varying the temperature, i.e., at 180, 200, and 220 °C and residence time (1, 3.5 and 6 h) to investigate the thermal behavior of the autoclave reactor. A simplified dynamic analytical model is built based on the lumped capacitance method. The overall heat capacity and thermal resistance of the reactor is subjected to external heat flux supplied by the external heater. In this model, the reactor inside temperature is simulated by discretizing the reactor into its components and solving the equations using finite difference method in MATLAB. The main temperatures required for modeling is heater temperature, temperatures of top and bottom surface of the reactor were measured during the process through which heat loss takes place to the surroundings. Simulation results are in good agreement with the experimental results. For the hydrothermal carbonization of waste biomass, the experiment shows that the maximum yield of hydrochar was obtained at a temperature of 180 °C at a residence time of 1 h.

Keywords Hydrothermal carbonization (HTC) · Hydrochar · High-pressure autoclave reactor · Lumped heat capacitance

1 Introduction

Hydrothermal carbonization (HTC) is a thermochemical conversion process by which organic material is converted into carbonized material, known as hydrochar. HTC is performed at the temperature range of 180–260 °C during which biomass

D. Sushmitha (✉) · S. Srinath
Department of Chemical Engineering, National Institute of Technology, Warangal 506002, Telangana, India
e-mail: sushmitha.devadasu@gmail.com

S. Srinath
e-mail: srinathnitw@gmail.com

D. Srinivasacharya and K. S. Reddy (eds.), *Numerical Heat Transfer and Fluid Flow*, Lecture Notes in Mechanical Engineering,
https://doi.org/10.1007/978-981-13-1903-7_63

is submerged into water and is heated under pressure (10–60 bar) for 5 min–12 h. During the HTC process three main products forms: solid (hydrochar), liquid (bio-oil mixed with water) and small fractions of gases (mainly CO_2) [1, 2].

As the HTC process is carried out in the presence of water, therefore, is not affected by the high moisture content of the feedstock. This unique advantage of the HTC process eliminates the pre-drying requirement of wet biomass, which is a huge energy-intensive process and a financial load in biomass pre-processing especially when performed under conventional thermal pre-treatments like slow-pyrolysis and dry torrefaction

These process can yield nano-size and micro-size carbon particles, which has properties like high heating value, better thermal and chemical stability and have good adsorption capacity. The liquid product also has some important chemicals, which can be used for further applications [1–3]. In view of the importance of hydrothermal carbonization, the waste biomass sample is processed in a high-pressure autoclave reactor to study the effect on hydrochar by varying the process parameter.

For the analyzing the thermal behavior of high-pressure autoclave reactor, a thermal model was made based on the lumped capacitance method. This thermal model was compared with the actual temperature profile which was experimentally generated.

2 Thermal Modeling of Autoclave Reactor

This model is based on the lumped capacitance method, which reduces the thermal system to a number of discrete components, assuming that the temperature difference inside each object is negligible. In the present case, it is considered just one component, i.e., the HTC reactor, with its overall heat capacity and thermal resistance, subjected to the external heat flux by the electrical heater.

The assumption taking for developing this model

1. The temperature at each point inside the reactor is identical.
2. The temperature at the wall surface and bottom surface is uniform.
3. Heat loss is taking place from the top and a bottom surface of the reactor.
4. The thermal conductivity of water is not changing with time and temperature.

The overall energy balance equation is given by [4]

Rate of accumulation of energy = energy input − energy output − energy loss to the surrounding.

$$C_0 \frac{\mathrm{d}T}{\mathrm{d}t} = \frac{(T_h - T)}{R_0} - Q \tag{1}$$

The overall thermal resistance of the reactor shell is defined as

$$R_0 = R_{\text{cond}} + R_{\text{conv}} \tag{2}$$

where

$$R_{\text{cond}} = \frac{1}{2\pi K_{\text{st}} L}\left(\ln \frac{r_o}{r_i}\right) \tag{3}$$

$$R_{\text{conv}} = \frac{1}{(2\pi r_i L)h_c} \tag{4}$$

Heat capacity of the system is defined as the sum of heat capacity of water and heat capacity of stainless steel

$$C_0 = C_w + C_s \tag{5}$$

where

$$C_w = m_w * C_{\text{pw}} \tag{6}$$

$$C_{\text{st}} = m_{\text{st}} * C_{\text{pst}} \tag{7}$$

Heat loss to the surrounding is given by

$$Q = h_a A_t (T_t - T_0) + h_a A_b (T_h - T_0) \tag{8}$$

As the physical properties of water vary with the temperature so that some of the correlation has been used to define the physical properties of water as a function of time. The physical properties of stainless steel were assumed to be constant.

Change in specific heat of water as a function of temperature is given by [5]

$$C_{\text{pw}} = 2.7637 \times 10^5 - 2.0907 \times 10^3 \times T + 8.1250 \times T^2 - 1.4116 \times 10^{-2} \times T^3 + 9.3701 \times 10^{-6} \times T^4 \tag{9}$$

Change in viscosity of water as a function of temperature is given by [6]

$$\mu_w = 2.414 * 10^{-5} * 10^{\left(\frac{247.8}{T-140}\right)} \tag{10}$$

The change in the density of water as a function of temperature is given by [7]

$$\rho_w = 1000 * \left(1 - \frac{(T + 288.9414)(T - 3.9863)^2}{508{,}929.2 * (T + 68.12963)}\right) \tag{11}$$

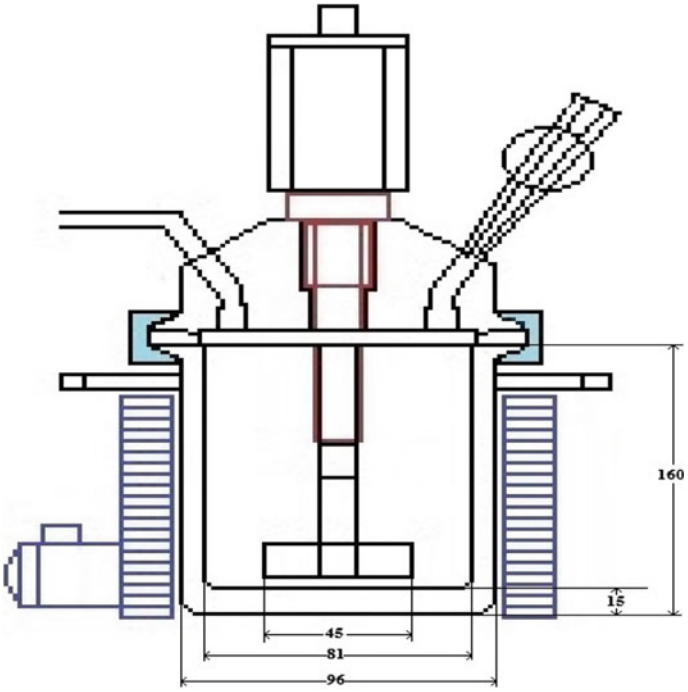

The heat transfer coefficient of the water inside the reactor is the function of temperature, and also varies during the HTC process. The heat transfer coefficient of water inside a reactor is defined by using Chilton, Drew, and Jebens' correlation [8]

$$\frac{h_c d}{k} = A * (\mathrm{Re})^{0.667} (\mathrm{Pr})^{0.33} \left(\frac{\mu_w}{\mu_{w\mathrm{wall}}} \right)^{.14} \tag{12}$$

where $A = 0.56$ for turbine-type stirrer.

The Reynolds number for water inside the reactor is defined as [9]

$$\mathrm{Re} = \left(\frac{L^2 * N * \rho_w}{\mu_w} \right) \tag{13}$$

And the Prandtl number is defined as [9]

$$\mathrm{Pr} = \left(\frac{C_{\mathrm{pw}} * \mu}{k} \right) \tag{14}$$

The overall energy balance equation will be solved by Eq. (1).

Assuming that

$$T' = T_h - T \tag{15}$$

Equation (1) will be

$$-\frac{\mathrm{d}T'}{\mathrm{d}t} = \left(\frac{T' - R_0 Q}{\tau_0}\right) \tag{16}$$

where

$$\tau_0 = R_0 C_0 \tag{17}$$

Integrating the Eq. (16) gives

$$\int_{T_h - T_o}^{T_h - T} \frac{\mathrm{d}T'}{T' - R_0 Q} = -\int_0^t \frac{\mathrm{d}t}{\tau_0} \tag{18}$$

Final expression for the thermal balance of reactor balance is

$$T = (T_h - Q R_0) + (T_0 - T_h + Q R_0)\exp\left(-\frac{t}{\tau_0}\right) \tag{19}$$

The value of thermal, physical, and geometrical parameters are shown in Table 1. To test the model, experimental tests were performed by recording the temperature data in different sections of the reactor. The experimentally measured temperature profile was measured by a thermocouple which was placed inside the reactor. As the reactor shell was surrounded by the heating pad, the heater imposes the heat to the outer surface of it. So the temperature profile T_h imposed by the heater was measured using a thermocouple which was placed in such a way that it touches the outside surface of the reactor shell. The heat loss was taking place from the top and bottom surface of the reactor. The assumption has been taken that the bottom surface temperature was equal to the reactor shell surface temperature. So the bottom surface temperature was T_{exp}. To measure the heat loss from the top surface of the reactor, a thermocouple was placed which recorded the temperature of the top surface at each time interval. The temperature of the reactor at various places was recorded by various thermocouples at 60 s time interval.

The HTC reaction was carried out for the 200 °C reaction temperature. Once the heater was switched on, the heating pad started to heat the reactor. The heater was controlled by the PID controller. When the inside temperature of the reactor reaches 200 °C, the heater stopped automatically and the reactor temperature was maintained by the controller in the same condition. The temperature was recorded until the temperature inside the reactor reaches the steady state condition.

The simulating temperature was calculated by using the temperature profile imposed by the heater at each time interval. By substituting thermal, physical, and geometrical parameters into Eq. (19) based on that interval temperature data the simulation temperature was calculated. The initial temperature was 27 °C which increases up to 200 °C for 52 min. The temperature was recorded for more 10 min to

Table 1 Thermal, physical and geometrical parameters of the thermal model

Parameter	Value (unit)
T_0	25 (°C)
M_w	0.15 (kg)
M_{st}	5 (kg)
r_o	0.049 (m)
r_i	0.0405 (m)
L	0.16 (m)
D_a	0.045 (m)
b	0.015 (m)
N	150 (rpm)
A_t	0.39 (m^2)
A_b	0.0075 (m^2)
C_{pst}	500 (J/kg K)
K_{st}	16.3 (W/mK)
k	0.643 (W/mK)
h_a	30 (W/mK)

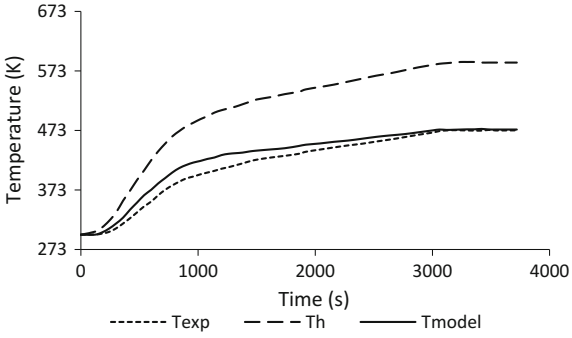

Fig. 1 Thermal model: experiment versus model temperature profile inside the reactor

reach the steady-state condition. The simulation temperature profile was generated after the calculating the temperature at each time interval.

The simulating profile (T_{model}) based on the actual temperature profile (T_h) imposed by the reactor external heater is shown in the Fig. 1. The dashed line represents the temperature profile imposed by the reactor. The solid line represents the simulating profile while the dotted line represents the experimentally measured temperature profile. It is clearly observed from Fig. 1 that simulating temperature profile following the same trend as an experimentally measured temperature profile. The simulating profile shows the relative error of less than the 7% of the experimental temperature profile.

2.1 Algorithm for Thermal Modeling

The modeling of the thermal behavior of an autoclave reactor was performed on the MATLAB script file. The algorithm for the simulation are follows:

1. Define all the thermal, physical, and geometrical parameters in the script file.
2. Define the shell outer surface temperature (measured by using thermocouples, act as input for the reactor) at each time interval in form of vector.
3. Define the top surface temperature of the reactor (heat loss taking place) at the same time interval in form of vector.
4. Define each variable which is a function of the temperature (specific heat of water, viscosity of water, density of water, and heat capacity) inside the for loop,
5. Define the Reynolds number and Prandtl number for the stirrer batch reactor to calculate the heat transfer coefficient between the reactor wall and water inside the for loop.
6. Define the function for heat loss and the inside reactor temperature (T) inside the for loop.
7. Run the simulation for the T (temperature inside the reactor).

3 Conclusion

The simulating profile based on the actual temperature profile imposed by the reactor external heater was carried out successfully. The simulation temperature profile shows the same trend as experimentally observed temperature profile with a relative error of less than 7%.

References

1. Mumme, J., Eckervogt, L., Pielert, J., Diakité, M., Rupp, F., Kern, J.: Bioresour. Technol. **102**, 9255–9260 (2011)
2. Benavente, V., Calabuig, E., Fullana, A.: J. Anal. Appl. Pyrol. **113**, 89–98 (2015)
3. Libra, J.A., Ro, K.S., Kammann, C., Funke, A., Berge, N.D., Neubauer, Y., Titirici, M.-M., Fühner, C., Bens, O., Kern, J., Emmerich, K.-H.: Biofuels **2**, 71–106 (2011)
4. Baratieri, M., Basso, D., Patuzzi, F., Castello, D., Fiori, L.: Chem. Eng. Trans. **43**, 505–510 (2015)
5. Liley, P.E., Thomson, G.H., Friend, D.G., Daubert, T.E., Buck, E.: Perry's Chemical Engineers' Handbook. Physical and Chemical Data, Section 2, 7th edn. McGraw-Hill, New York (1997)
6. Al-Shemmeri, T.: Engineering Fluid Mechanics, pp. 17–18. Ventus Publishing ApS (2012)
7. McCutcheon, S.C., Martin, J.L., Barnwell Jr., T.O.: Water quality. In: Maidment, D.R. (ed.) Handbook of Hydrology. McGraw-Hill, New York (1993)
8. Chilton, T.H., Drew, T.B., Jebens, R.H.: Ind. Eng. Chem. **36**, 510–516 (1944)
9. McCabe, W.L., Smith, J.C.: Unit Operations of Chemical Engineering. McGraw-Hill, New York (1967)

Effects of MHD and Radiation on Chemically Reacting Newtonian Fluid Flow over an Inclined Porous Stretching Surface Embedded in Porous Medium

Ch. RamReddy and T. Pradeepa

Abstract An attempt has been made to investigate the influence of magnetic field and radiation on the Newtonian fluid flow over an inclined porous stretching sheet embedded in a porous medium in the presence of chemical reaction effect. In addition, heat and mass flux conditions are taken into consideration. The system of nonlinear differential equations is obtained using similarity transformations and hence solved using spectral quasilinearization method. The effects of physical parameters on velocity, temperature, and concentration are displayed graphically and salient features are discussed.

Keywords MHD · Thermal radiation · Chemical reaction
Darcy porous medium

1 Introduction

The study of magnetic properties of an electrically conducting fluid is known as Magnetohydrodynamics(MHD). Magnetohydrodynamic boundary layer with heat and mass transfer over a stretching sheet is found in various geophysical and engineering applications such as geothermal reservoirs, nuclear reactors cooling, thermal insulation, catalytic reactors of packed-bed, and enhanced oil recovery. Ishak et al. [1] considered the MHD stagnation point flow toward the stretching sheet. Ibrahim and Shankar [2] investigated the boundary layer flow and heat transfer of an electrically conducting nanofluid past a porous stretching sheet by considering the velocity, thermal, and solutal slip boundary conditions. The effect of radiation on heat and mass transfer plays an immense role in manufacturing industries for the fins design, nuclear power plants, turbines of gas, steel rolling, etc. The influence of radiation on magneto-hydrodynamics flow, heat, and mass transfer has become more

Ch. RamReddy (✉) · T. Pradeepa
Department of Mathematics, National Institute of Technology, Warangal 506004, India
e-mail: chittetiram@gmail.com

T. Pradeepa
e-mail: pradeepa.23@gmail.com

D. Srinivasacharya and K. S. Reddy (eds.), *Numerical Heat Transfer and Fluid Flow*, Lecture Notes in Mechanical Engineering,
https://doi.org/10.1007/978-981-13-1903-7_64

prominent industrially. Raptis and Perdikis [3] analyzed the influence of magnetic field on laminar flow of an incompressible and electrically conducting viscous fluid over a nonlinear stretching sheet with chemical reaction effect. Rashidi et al. [4] examined the free convective flow over a permeable stretching sheet with buoyancy, radiation, and magnetic field effects.

The study of heat and mass transfer problems embedded in a porous medium has predominantly elevated during the past decades ascribed to immense applications in engineering and industrial process such as food processing, pollutant dispersion in aquifers, storage of nuclear waste material, etc. A review of convective heat and mass transfer in the porous medium is presented in the books by Ingham and Pop [5] and Nield and Bejan [6]. The analysis of boundary layer flow over an inclined stretching sheet has gained much attention in recent years owing to its significant applications in engineering and industrial applications. For instance, paper production, hot rolling, plastic films drawing, glass–fiber, cooling of metallic sheets in a cooling bath, wire drawing, etc. A few literature is noticed on the fluid flow through inclined stretching sheet with various effects [7–9].

The aim of the present article is to study the effect of radiation on laminar boundary layer flow of an electrically conducting and chemical reacting fluid over an inclined stretching sheet embedded in a porous medium subject to heat and mass flux conditions. Further, the resulting nonlinear equations are solved numerically using Spectral Quasilinearization Method.

2 Mathematical Formulation

Consider the steady, 2-*D* and laminar flow of viscous, incompressible and electrically conducting fluid past an inclined stretching porous sheet with an acute angle *A*, embedded in a porous medium. The surface is assumed to be porous and moving with velocity $U = ax$, (where a is the constant called stretching rate). Let x-axis be taken along the leading edge of the inclined stretching sheet and y-axis be taken perpendicular to it and extends parallel to x-axis. The fluid is considered to be gray, emitting and absorbing radiation but non-scattering medium, and approximation of Rosseland is used to describe the radiative heat flux in the energy equation. A nonuniform magnetic field is applied normal to the flow direction. The induced magnetic field is ignored based on the assumption of low magnetic Reynolds number.

Under the above assumptions along with Boussinesq's approximation, the governing equations are

$$\frac{\partial u}{\partial x} + \frac{\partial v}{\partial y} = 0 \tag{1}$$

$$\frac{1}{\varepsilon^2}\left(u\frac{\partial u}{\partial x} + v\frac{\partial u}{\partial y}\right) = \frac{\nu}{\varepsilon}\frac{\partial^2 u}{\partial y^2} + g\left[\beta_T(T - T_\infty) + \beta_C(C - C_\infty)\right]\cos A - \frac{\nu u}{K_p} - \frac{\sigma B_0^2 u}{\varepsilon \rho} \tag{2}$$

$$u\frac{\partial T}{\partial x}+v\frac{\partial T}{\partial y}=\frac{k}{\rho C_p}\frac{\partial^2 T}{\partial y^2}+\frac{4\sigma_1}{3\rho C_p k^*}\frac{\partial^2}{\partial y^2}\left(4T_\infty^3 T-3T_\infty^4\right) \tag{3}$$

$$u\frac{\partial C}{\partial x}+v\frac{\partial C}{\partial y}=D\frac{\partial^2 C}{\partial y^2}-K_1\left(C-C_\infty\right) \tag{4}$$

where u and v are components of Darcy velocity along the direction of x and y, respectively, ε is the porosity, T is the temperature, C is concentration, g is the acceleration due to gravity, μ is the coefficient of viscosity, σ is the electrical conductivity, C_p is the specific heat, K_p is the permeability, k is the thermal conductivity of the fluid, σ_1 is the Stefan–Boltzmann constant, k^* is the mean absorption coefficient, ρ is the density, B_0 is the magnetic field intensity, β_T is the thermal expansion coefficient, β_C is the solutal expansion coefficient, α is the thermal diffusivity, D is the mass diffusivity, K_1 is the chemical reaction. In Eq. (3), the last term is obtained by assuming that the differences in temperature within the flow are very small and power function may be expressed as temperature linear function by neglecting the terms of higher order.

The associated boundary conditions are

$$u=U=ax,\ v=v_w,\ -k\frac{\partial T}{\partial y}=q_w=E_0x^r, \tag{5a}$$

$$-D\frac{\partial C}{\partial y}=m_w=E_1x^r \text{ at } y=0$$

$$u=0,\ T=T_\infty,\ C=C_\infty \text{ as } y\to\infty \tag{5b}$$

where v_w is the suction-injection velocity, E_0 and E_1 are positive constants. Here, r is the exponent parameter of heat or mass flux. The accelerating sheet is subject to uniform heat or mass flux when $r=0$.

In view of the continuity equation (1), we introduce the stream function ψ by

$$u=\frac{\partial\psi}{\partial y},\quad v=-\frac{\partial\psi}{\partial x} \tag{6}$$

Introduce the following similarity transformations

$$\eta=\left(\frac{a}{\nu}\right)^{1/2}y,\ f(\eta)=\frac{\psi}{(a\nu)^{1/2}x},\ T-T_\infty=\frac{E_0x^r}{k}\sqrt{\frac{\nu}{a}}\theta(\eta), \tag{7}$$

$$C-C_\infty=\frac{E_1x^r}{D}\sqrt{\frac{\nu}{a}}\phi(\eta)$$

Substitute Eqs. (6) and (7) in Eqs. (1)–(4) and boundary conditions (5), we get the following system of nonlinear ordinary differential equations

$$\frac{1}{\varepsilon}f''' + \frac{1}{\varepsilon^2}ff'' - \frac{1}{\varepsilon^2}f'^2 - \frac{1}{\varepsilon}M^2 f' - \frac{1}{Da}f' + (Gr\theta + Gc\phi)\cos A = 0 \tag{8}$$

$$\frac{1}{Pr}\left(1 + \frac{4}{3}R\right)\theta'' + f\,\theta' - rf'\theta = 0 \tag{9}$$

$$\frac{1}{Sc}\phi'' + f\,\phi' - rf'\phi - \gamma\phi = 0 \tag{10}$$

where the prime shows differentiation with respect to η, $R = \dfrac{4\sigma_1 T_\infty^3}{kk^*}$ is the Radiation parameter, $Pr = \dfrac{\mu C_p}{k}$ is the Prandtl number, $\gamma = \dfrac{K_1}{D}$ is the Chemical reaction parameter, $Da = \dfrac{K_p a}{\nu}$ is the Darcy number, $Sc = \dfrac{\nu}{D}$ is the Schmidt number, $M = \dfrac{\sigma B_0^2}{\rho a}$ is the Magnetic parameter, $Gr = \dfrac{g^*\beta_T E_0}{a^2 k}\sqrt{\dfrac{\nu}{a}}$ is thermal Grashof number, $Gc = \dfrac{g^*\beta_c E_1}{a^2 D}\sqrt{\dfrac{\nu}{a}}$ is solutal Grashof number, and ε is the porosity.

The associated boundary conditions (5) in terms of f, θ, and ϕ are

$$f(\eta) = \lambda, \quad f'(\eta) = 1, \quad \theta'(\eta) = -1, \quad \phi'(\eta) = -1 \quad \text{at} \quad \eta = 0 \tag{11a}$$

$$f'(\eta) = 0, \quad \theta(\eta) = 0, \quad \phi(\eta) = 0 \quad \text{as} \quad \eta \to \infty \tag{11b}$$

In the boundary conditions, $\lambda = -v_w(a\nu)^{1/2}$ is the suction/injection parameter. If $\lambda > 0$ represents the suction velocity and $\lambda < 0$ denotes injection velocity.

3 Results and Discussion

The system of nonlinear homogeneous differential equations Eqs. (8)–(10) and along with boundary conditions (11) is solved numerically using spectral quasilinearization method [10, 11]. The solutions for velocity, temperature, and concentration have been computed for both suction and injection velocities are shown graphically in Figs. 1, 2, 3, 4, 5, 6, 7, 8, 9, 10, 11, 12, 13, 14, and 15. In order to study the effects of M, R, A, Da and γ, computations have been carried out for $Pr = 0.72$, $Sc = 0.22$, $\varepsilon = 0.9$, $r = 1$, $Gr = 5.0$ and $Gc = 5.0$.

Figures 1, 2, and 3 display the effect of the magnetic parameter on velocity, temperature, and concentration for both suction and injection. Figure 1 reveals that the velocity reduces with the magnetic parameter enhancement for both suction and

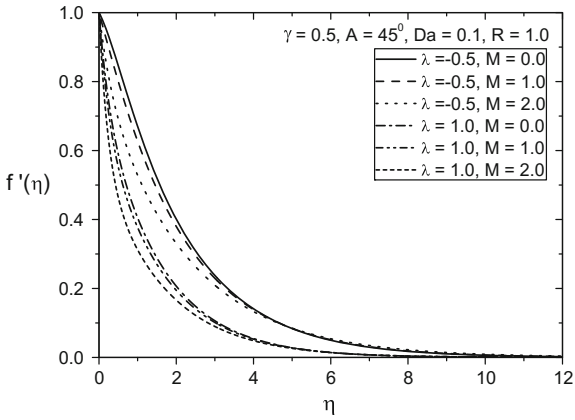

Fig. 1 Effect of M on velocity profile

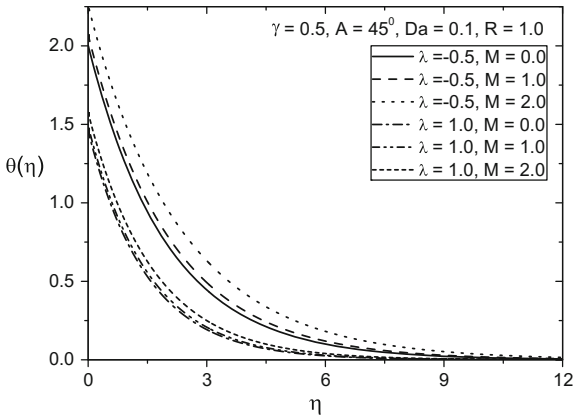

Fig. 2 Effect of M on temperature profile

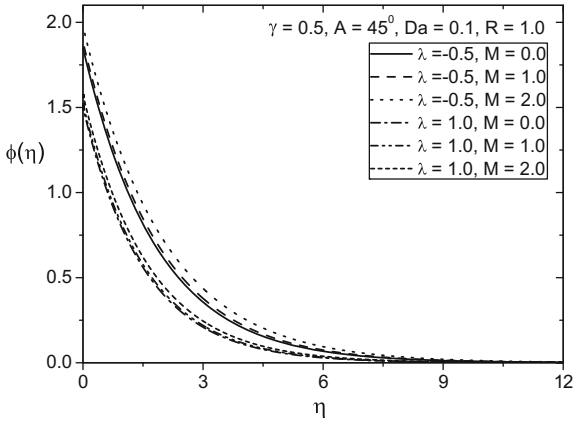

Fig. 3 Effect of M on concentration profile

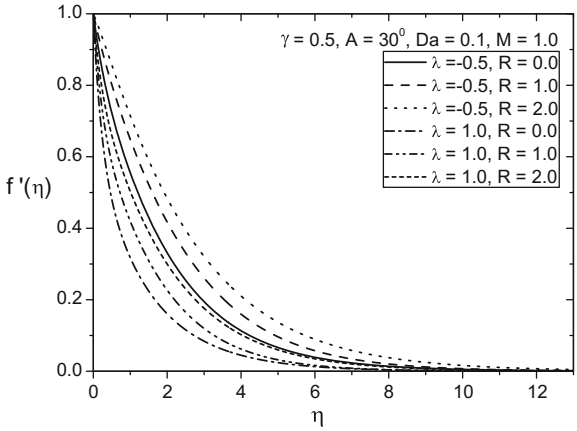

Fig. 4 Effect of *R* on velocity profile

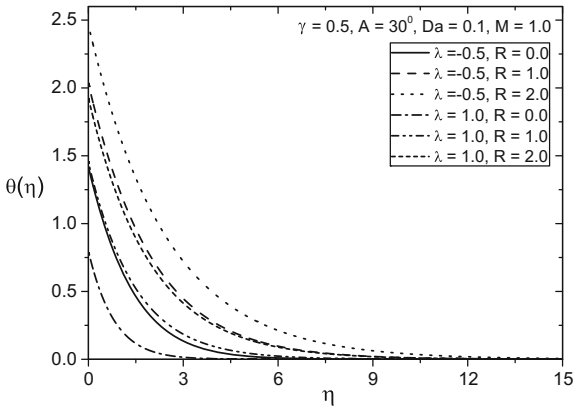

Fig. 5 Effect of *R* on temperature profile

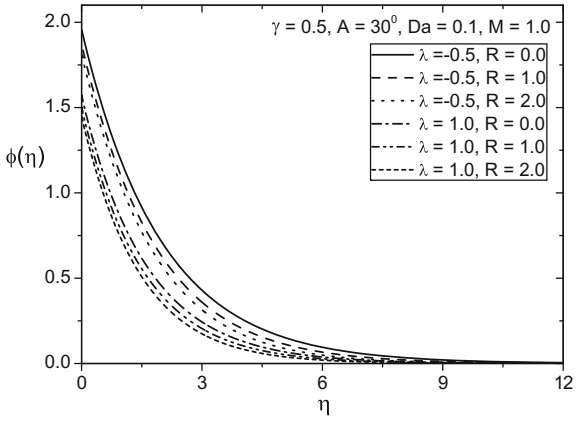

Fig. 6 Effect of *R* on concentration profile

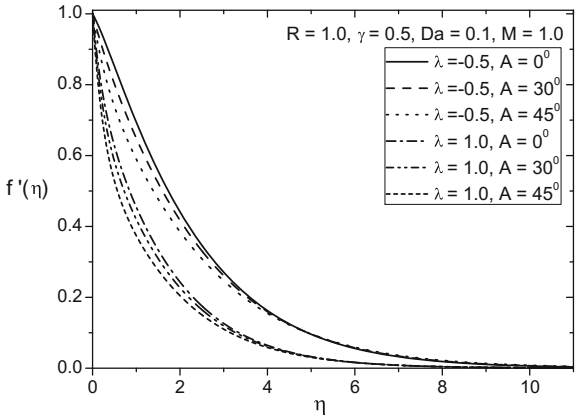

Fig. 7 Effect of *A* on velocity profile

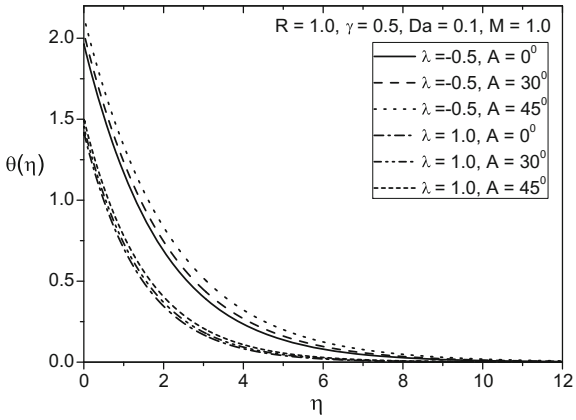

Fig. 8 Effect of *A* on temperature profile

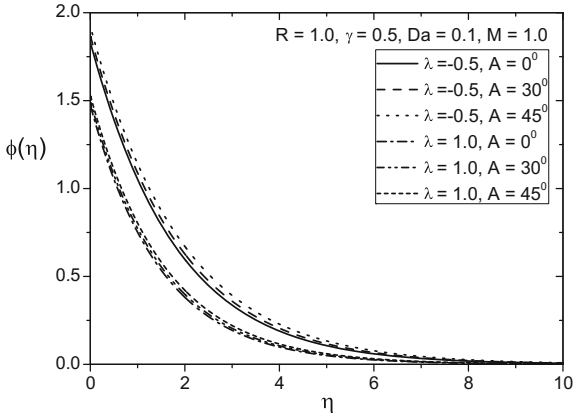

Fig. 9 Effect of *A* on concentration profile

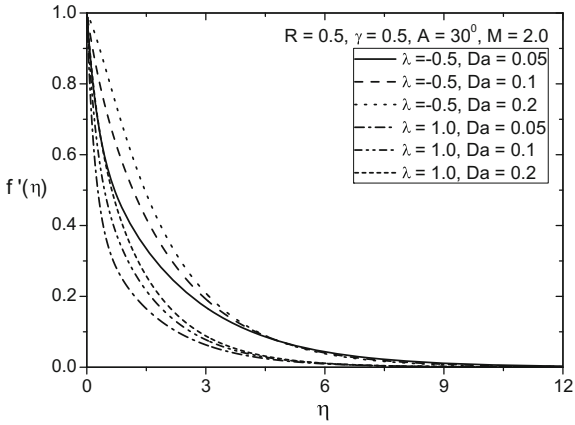

Fig. 10 Effect of *Da* on velocity profile

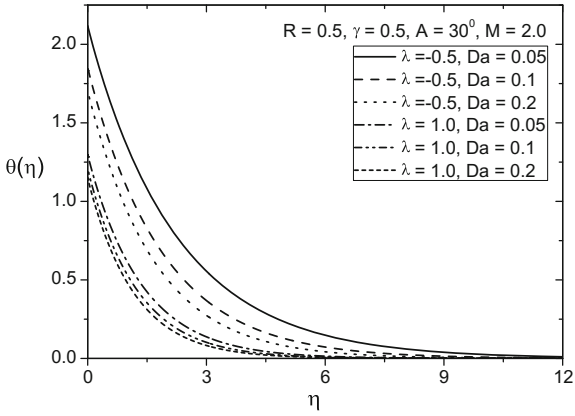

Fig. 11 Effect of *Da* on temperature profile

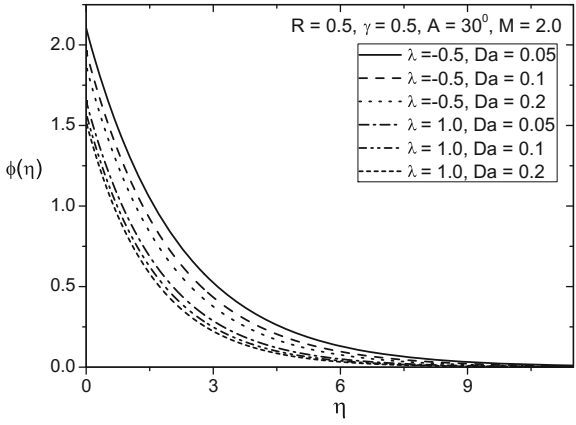

Fig. 12 Effect of *Da* on concentration profile

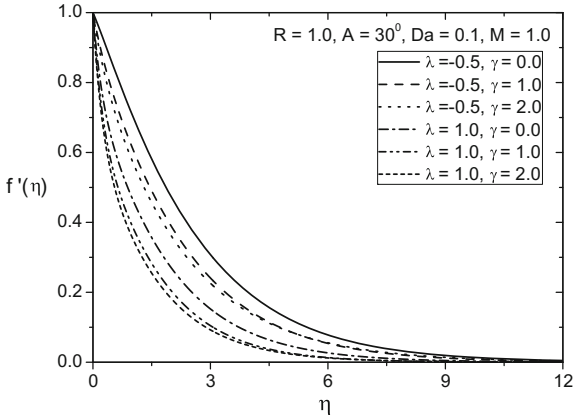

Fig. 13 Effect of γ on velocity profile

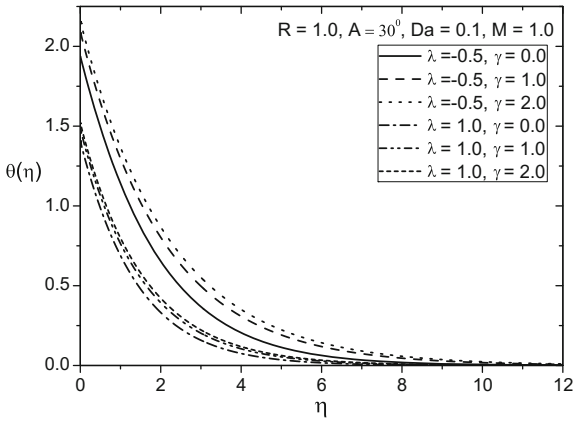

Fig. 14 Effect of γ on temperature profile

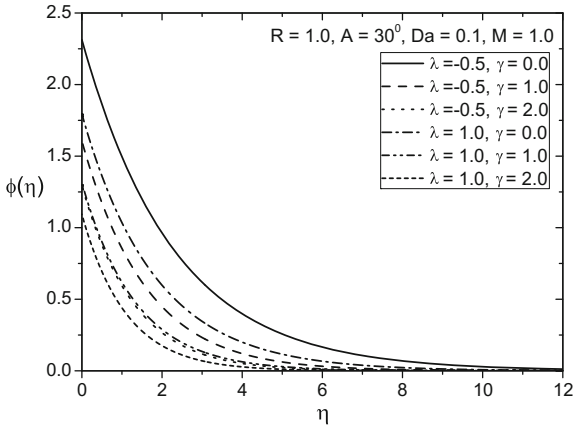

Fig. 15 Effect of γ on concentration profile

injection. This is due to the fact that, the introduction of a transverse magnetic field normal to the direction of flow has a tendency to form the drag called as Lorentz force which tends to resist the flow. Hence, the velocity reduces as the magnetic parameter enhances. Figure 2 depicts that the temperature enhances with an increase in the magnetic parameter. As explained above, the transverse magnetic field creates a resistive force which is called as the Lorentz force of an electrically conducting fluid. By increasing the friction between its layers the Lorentz force makes the fluid experience a resistance and hence increases the temperature. As the magnetic parameter increases, the concentration increases as shown in Fig. 3.

Figures 4, 5, and 6 represent the effect of radiation on velocity, temperature, and concentration for both suction and injection cases. As the radiation parameter increases the velocity raises for both suction and injection as shown in Fig. 4. For both suction and injection cases, the temperature increases with an increase of radiation parameter. The concentration decreases with the rise of the radiation parameter for both injection and suction. From Figs. 4, 5, and 6 observed that the velocity and temperature are more, whereas concentration is less in the presence of radiation as compared with those values in the absence of radiation.

Figures 7, 8, and 9 display the effect of angle of inclination on nondimensional velocity, temperature, and concentration for both $\lambda = -0.5$ and $\lambda = 1.0$. Figure 7 illustrates that for both the cases of suction and injection, the velocity reduces with the rise of angle of inclination parameter. With the increment of angle of inclination parameter, the temperature and concentration are enhanced for both $\lambda = -0.5$ and $\lambda = 1.0$ as depicted in Figs. 8 and 9.

The variation of velocity, temperature, and concentration with the Darcy parameter are portrayed in Figs. 10, 11 and 12 for both suction and injection. Figure 10 depicts that the dimensionless velocity increases with the increase of Darcy parameter for both suction and injection. For both $\lambda = -0.5$ and $\lambda = 1.0$, the temperature reduces with an increase of Darcy parameter which is shown in Fig. 11. Figure 12 displays that the concentration diminishes with an increase of Darcy parameter for both $\lambda = -0.5$ and $\lambda = 1.0$.

The effect of chemical reaction parameter on the velocity, temperature, and concentration are shown in Figs. 13, 14, and 15 for both suction and injection. Figure 13 depicts that the dimensionless velocity reduces with the increase of chemical reaction parameter for both suction and injection. For both $\lambda = -0.5$ and $\lambda = 1.0$, the temperature increases with the increase of chemical reaction parameter which is shown in Fig. 14. Figure 15 reveals that concentration decreases with the increase of chemical reaction parameter for both suction and injection. This is due to the fact that the chemical reaction in this system results in the consumption of the chemical and hence results in the decrease of concentration.

4 Conclusions

In this paper, thermal radiation and chemical reaction effects on the boundary layer flow of an electrically conducting Newtonian fluid over an inclined stretching sheet embedded in a porous medium, have been investigated. The governing equations are solved by using spectral quasilinearization method. The main conclusions are summarized as follows:

- Velocity increases with an increase of radiation and Darcy parameters whereas it reduces with magnetic, chemical reaction, and angle of inclination parameters.
- The temperature reduces with increase of Darcy parameter, but it enhances with an increase of magnetic, radiation, chemical reaction, and angle of inclination parameters.
- The concentration increases with magnetic and angle of inclination parameters, but decreases with an increase of radiation, chemical reaction, and Darcy parameters.

References

1. Ishak, A., Jafar, K., Nazar, R., Pop, I.: MHD stagnation point flow towards a stretching sheet. Stat. Mech. Appl. **388**, 3377–3383 (2009)
2. Ibrahim, W., Shankar, B.: MHD boundary layer flow and heat transfer of a nanofluid past a permeable stretching sheet with velocity, thermal and solutal slip boundary conditions. Comput. Fluids **75**, 1–10 (2013)
3. Raptis, A., Perdikis, C.: Viscous flow over a non-linearly stretching sheet in the presence of a chemical reaction and magnetic field. Int. J. Non-Linear Mech. **41**, 527–529 (2006)
4. Rashidi, M.M., Rostami, B., Freidoonimehr, N., Abbasbandy, S.: Free convective heat and mass transfer for MHD fluid flow over a permeable vertical stretching sheet in the presence of the radiation and buoyancy effects. Ain Shams Eng. J. **5**(3), 901–912 (2014)
5. Ingham, D.B., Pop, I.: Transport Phenomena in Porous Media II. Pergamon, Oxford (2002)
6. Nield, D.A., Bejan, A.: Convection in Porous Media, 4th edn. Springer, New York (2013)
7. Abo-Eldahab, E.M., El-Aziz, M.A.: Blowing/suction effect on hydromagnetic heat transfer by mixed convection from an inclined continuously stretching surface with internal heat generation/absorption. Int. J. Therm. Sci. **43**(7), 709–719 (2004)
8. Ali, M., Alim, M.A., Alam, M.S.: Similarity solution of heat and mass transfer flow over an inclined stretching sheet with viscous dissipation and constant heat flux in presence of magnetic field. Procedia Eng. **105**, 557–569 (2015)
9. Afridi, M.I., Qasim, M., Khan, I., Shafie, S., Alshomrani, A.S.: Entropy generation in magnetohydrodynamic mixed convection flow over an inclined stretching sheet. Entropy **19**(1), 10 (2017)
10. Motsa, S.S., Dlamini, P.G., Khumalo, M.: Spectral relaxation method and spectral quasilinearization method for solving unsteady boundary layer flow problems. Adv. Math. Phys. **2014**, 1–12 (2014)
11. RamReddy, Ch., Pradeepa, T., Srinivasacharya, D.: Similarity Solution for free convection flow of a micropolar fluid under convective boundary condition via Lie scaling group transformations. Adv. High Energy Phys. **2015**, 1–16 (2015)

Couple-Stress Fluid Flow Due to Rectilinear Oscillations of a Circular Cylinder: Case of Resonance

T. Govinda Rao, J. V. Ramana Murthy and G. S. Bhaskara Rao

Abstract The flow due to a circular cylinder oscillating rectilinearly, about its axis of symmetry in a couple-stress fluid is considered. There occurs a rare but an important special case referred to as resonance flow. The material constants satisfy a specific relation called resonance condition. In this case, the flow is analyzed under Stokesian approximation. The velocity component of the flow is derived. The effect of physical parameters like Reynolds number and couple-stress parameter on the drag is analyzed through graphs.

Keywords Couple-stress fluids · Rectilinear oscillations · Resonance flow Drag

1 Introduction

The fluids, used in many technological applications do not satisfy the regular Newtonian stress and strain rate relations. These fluids are referred to as non-Newtonian fluids. We consider couple-stress fluid, which is one of such non-Newtonian fluids. Several flow problems concerning with couple-stress fluids have been studied by many authors over the past five decades, ever since Stokes [1] introduced the couple-stress fluid theory. Lakshmana Rao et al. [2–5] examined the oscillatory flows generated due to circular cylinder, sphere, spheroid, and elliptic cylinder in micropolar fluids to determine the drag or couple on the oscillating body. However, in all these problems, as far as the authors know, a special case, which is branded as "Resonance" type that arises when the material parameters of the fluids are related in a particular form (to be stated later) have not been investigated till now.

T. Govinda Rao (✉) · G. S. Bhaskara Rao
Department of Basic Sciences and Humanities, Gudlavalleru Engineering College, Gudlavalleru 521356, Andhra Pradesh, India
e-mail: govind.tangudu@gmail.com

J. V. Ramana Murthy
Department of Mathematics, NITW, Warangal 506004, Telangana, India

D. Srinivasacharya and K. S. Reddy (eds.), *Numerical Heat Transfer and Fluid Flow*, Lecture Notes in Mechanical Engineering,
https://doi.org/10.1007/978-981-13-1903-7_65

The flow problems in couple-stress fluids have been attracting many researchers due to their mathematical interest and importance in many applications. Ramkissoon et al. [6, 7] and Rajagopal [8] considered a flow generated due to longitudinal and torsional oscillations of a rod in polar fluids and non-Newtonian fluids. In these papers, the authors analyzed drag on the object. The flows due to longitudinal and torsional oscillations of a cylinder in various fluids were investigated by different authors [9–12]. Ramana Murthy et al. [13–15] studied a flow of micropolar fluid under transverse magnetic field with suction. Aparna et al. [16] studied the oscillatory flow of micropolar fluid due to a rotating a permeable sphere. Nagaraju et al. [17] examined the longitudinal and torsional oscillations of a cylinder in a micropolar fluid. Recently, the resonance-type flows due to a circular cylinder in micropolar fluids [18] are investigated.

In this paper, we propose to investigate this case of resonance-type flow, in couple-stress fluids, due to rectilinear oscillations of a circular cylinder about its axis of symmetry.

2 Basic Equations

The basic equations of an incompressible couple-stress fluid introduced by Stokes [1] are given by

$$\operatorname{div} \bar{Q} = 0 \tag{1}$$

$$\rho\left(\frac{\partial \bar{Q}}{\partial \tau} + \bar{Q}.\nabla\bar{Q}\right) = -\nabla P - \mu\nabla\times\nabla\times\bar{Q} - \eta\nabla\times\nabla\times\nabla\times\nabla\times\bar{Q} \tag{2}$$

where $\bar{\mathrm{Q}}$ is fluid velocity vector, ρ is density, τ is time, μ is viscosity coefficient. The stress tensor T and couple-stress tensor M satisfy the constitutive equations as follows:

$$T = -PI + \lambda(\nabla_1.Q)I + \mu\left(\nabla_1 Q + (\nabla_1 Q)^T\right) + \frac{1}{2}I\times(\nabla_1.M) \tag{3}$$

$$M = mI + 2\eta\nabla_1(\nabla_1\times Q) + 2\eta'[\nabla_1(\nabla_1\times Q)]^T \tag{4}$$

3 Statement and Formulation of the Problem

A circular cylinder of radius a and of infinite length is performing rectilinear oscillations with velocity $U_0 e^{i\sigma\tau}$ about its diameter in an incompressible couple-stress fluid. A cylindrical coordinate system (R, θ, Z) with origin on the axis of the cylinder is considered. Hence, the fluid velocity will be in cross-sectional plane with the base vectors $(\mathbf{e}_r, \mathbf{e}_\theta)$. The geometry of the present problem as shown in (Fig. 1):

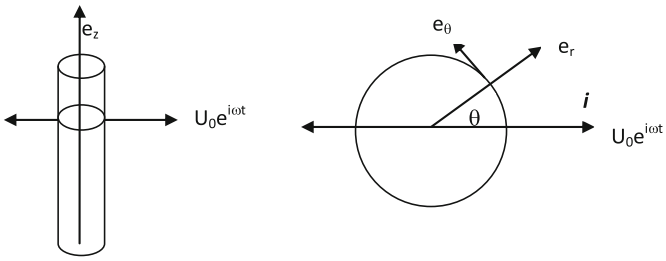

Fig. 1 Geometry of the oscillating cylinder

The velocity is assumed as:

$$\boldsymbol{Q} = \mathrm{e}^{i\sigma\tau}(U(R,\theta)\boldsymbol{e_r} + V(R,\theta)\boldsymbol{e_\theta}) \tag{5}$$

The following nondimensional scheme is introduced.

$$R = ar,\ U = U_0 u,\ V = U_0 v,\ \mathbf{Q} = \mathbf{q}U_0,\ P = p\rho U_0^2,\ \tau = \frac{\mathrm{at}}{U_0} \tag{6}$$

The following are nondimensional parameters, viz., ω is frequency parameter, S is couple-stress parameter, and Re is oscillations Reynolds number for couple-stress fluids.

$$\varpi = \frac{\sigma a}{U_0}, s = \frac{\mu a^2}{\eta}, \mathrm{Re} = \frac{\rho U_0 a}{\mu},\ \mathrm{Re}.\varpi = \frac{\rho\sigma a^2}{\mu} \tag{7}$$

Substituting (5) in (1) we notice that stream function ψ can be introduced as

$$u = \frac{1}{r}\frac{\partial\psi}{\partial\theta} \text{ and } v = -\frac{\partial\psi}{\partial r},\quad \text{i.e.,}\quad \boldsymbol{q} = \nabla\times(\psi\boldsymbol{e}_z) \tag{8}$$

Using (5), (6), (7) in (2) we get

$$\mathrm{Re}.S\frac{\partial\boldsymbol{q}}{\partial\boldsymbol{t}} = -\mathrm{Re}.S.\nabla p - S\nabla\times\nabla\times\boldsymbol{q} - \nabla\times\nabla\times\nabla\times\nabla\times\boldsymbol{q} \tag{9}$$

Substituting Eq. (8) in Eq. (9) and after eliminating pressure we get

$$\nabla^2\left(\nabla^2-\lambda_1^2\right)\left(\nabla^2-\lambda_2^2\right)\psi = 0 \tag{10}$$

where $\nabla^2 = \frac{\partial^2}{\partial r^2} + \frac{1}{r}\frac{\partial}{\partial r} + \frac{1}{r^2}\frac{\partial^2}{\partial\theta^2}$

$$\lambda_1^2 + \lambda_2^2 = S \quad \text{and} \quad \lambda_1^2\lambda_2^2 = \mathrm{Re}.S.i\varpi \tag{11}$$

The solution for ψ if $\lambda_1 \neq \lambda_2$ in (10) is given in [2]. The solution for ψ for the case, $\lambda_1 = \lambda_2$ cannot be obtained as a limiting case of $\lambda_1 \to \lambda_2$. This case is referred to as '*Resonance*'. This resonance occurs if the material coefficients follow the following relation in dimensional form.

$$S = 4\mathrm{Re}.i\varpi \tag{12}$$

In this paper, we are interested in the solution for ψ for the case of resonance $\lambda_1 = \lambda_2 = \lambda$. In this case, the equations for ψ is given by

$$\nabla^2\left(\nabla^2 - \lambda^2\right)^2 \psi = 0 \tag{13}$$

4 Boundary Conditions

The cylinder is oscillating in the direction of X-axis. Using the no-slip and hyper-stick conditions on the cylinder, we get

$$u = \cos\,\theta \text{ and } v = -\sin\,\theta \text{ on } r = 1 \quad \text{and} \quad \upsilon_\Gamma = \frac{1}{2}(\mathrm{curl}\,\boldsymbol{q})_\Gamma = 0 \text{ on } r = 1 \tag{14}$$

5 Solution of the Problem

To match with the boundary conditions, stream function ψ is assumed in the form

$$\psi = f(r)\sin\,\theta \tag{15}$$

Substituting (15) in (13), we get f for Resonance case as

$$D^2\left(D^2 - \lambda^2\right)^2 f = 0 \quad \text{with } D^2 = \frac{\mathrm{d}^2}{\mathrm{d}r^2} + \frac{1}{r}\frac{\mathrm{d}}{\mathrm{d}r} - \frac{1}{r^2} \tag{16}$$

From the conditions in (14) and (15), the conditions on f are obtained as

$$f(1) = f'(1) = 1 \text{ and } \quad D^2 f = 0 \quad \text{on } r = 1 \tag{17}$$

Since the equation for f is linear, f is considered as

$$f = A_0 f_0 + A_1 f_1 + A_2 f_2,$$

with

$$D^2 f_0 = 0, \left(D^2 - \lambda^2\right) f_1 = 0 \quad \text{and} \quad \left(D^2 - \lambda^2\right)^2 f_2 = 0 \tag{18}$$

On solving (18), the solution for f is obtained as

$$f(r) = \frac{A_0}{r} + A_1 K_1(\lambda r) + A_2 \lambda r K_1'(\lambda r) \tag{19}$$

We notice that

$$D^2 f_1 = \lambda^2 f_1 \quad \text{and} \quad D^2 f_2 = \lambda^2 (2 f_1 + f_2) \tag{20}$$

The constants A_0, A_1, A_2 are obtained from the boundary conditions (17) in matrix form as

$$\begin{bmatrix} 1 & K_1(\lambda) & \lambda K_1'(\lambda) \\ -1 & \lambda K_1'(\lambda) & \left(\lambda^2 + 1\right) K_1(\lambda) \\ 0 & K_1(\lambda) & \lambda K_1'(\lambda) + 2K_1(\lambda) \end{bmatrix} \begin{bmatrix} A_0 \\ A_1 \\ A_2 \end{bmatrix} = \begin{bmatrix} 1 \\ 1 \\ 0 \end{bmatrix} \tag{21}$$

On solving the Eq. (21) for A_0, A_1, A_2, we get completely f and hence ψ.

6 Pressure

By comparing components in Eq. (9), the pressure is obtained as follows.

$$\mathrm{Re}.S \frac{\partial p}{\partial r} = -\mathrm{Re}.Si\varpi \frac{1}{r} \frac{\partial \psi}{\partial \theta} + \frac{S}{r} \frac{\partial}{\partial \theta} \left(\nabla^2 \psi\right) - \frac{1}{r} \frac{\partial}{\partial \theta} \left(\nabla^4 \psi\right) \tag{22}$$

$$\mathrm{Re}.S \frac{\partial p}{\partial \theta} = \mathrm{Re}.Si\varpi r \frac{\partial \psi}{\partial r} - Sr \frac{\partial}{\partial r} \left(\nabla^2 \psi\right) + r \frac{\partial}{\partial r} \left(\nabla^4 \psi\right) \tag{23}$$

By using (19) and integrating, we get in nondimensional form

$$p = \frac{i\omega A_0}{r} \cos\theta \tag{24}$$

7 Drag Acting on the Cylinder Per Length L

$$\text{Drag} = D^* = aL \int_0^{2\pi} \left(T_{rr}^* \cos\theta - T_{\theta r}^* \sin\theta\right)|_{R=a} \mathrm{d}\theta \tag{25}$$

On simplifying (25), the drag D^* on the cylinder (without the factor $e^{i\varpi t}$) is given as

$$D^* = -\pi L \mu U_0 \mathrm{Re}.i\varpi (1 + 2A_0)$$

nondimensional form

$$D = \mathrm{Real}\left\{i\varpi \mathrm{Re}(1 + 2A_0)e^{i\varpi t}\right\} \tag{26}$$

8 Results and Discussions

The roots $x^2 - Sx + i\omega \mathrm{Re}S = 0$ are taken as the values of λ^2. Hence,

$$\lambda = \sqrt{x} = \begin{cases} \sqrt{\frac{S \pm \sqrt{S^2 - 4S.\mathrm{Re}.i\omega}}{2}} & \text{for nonresonance} \\ \sqrt{\frac{S}{2}} & \text{for resonance} \end{cases}, \tag{27}$$

Here ω, Re, and c are chosen independently, with $0 \leq c \leq 1$, $\mathrm{Re} \ll 1$ and $\omega \gg 1$ such that ω.Re is not negligibly small (say>1) then λ is obtained from (27). Then A_0, A_1, and A_2 and hence ψ and drag are obtained. To get the physical quantity, the corresponding real part of the quantities are taken.

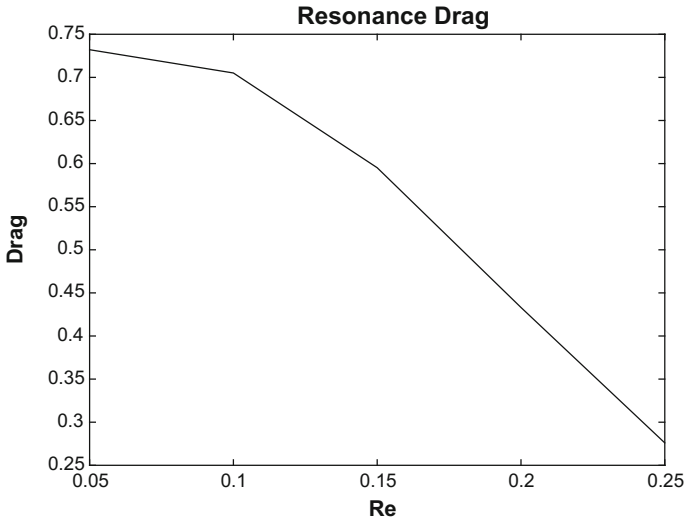

Fig. 2 Drag versus Reynolds number

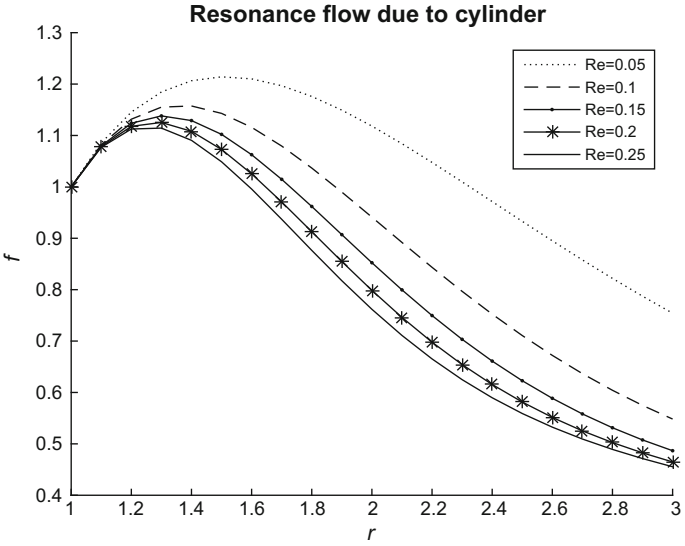

Fig. 3 Stream function f versus distance r

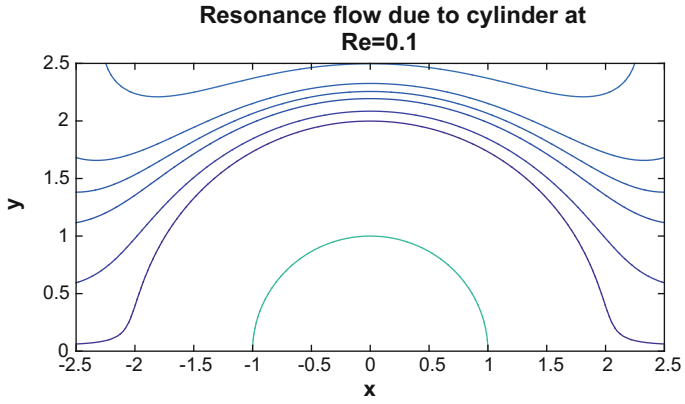

Fig. 4 Stream lines at Re = 0.1

We observe that (from Fig. 2) Drag decreases as Reynolds number increases which is an opposite behavior for nonresonance case (from Fig. 3). As Reynolds number increases stream values decrease. From Fig. 4, the flow of the fluid is similar to a flow past a fluid cylinder which is enclosing the original solid cylinder.

Acknowledgements The authors express their gratitude to the referees for their constructive and helpful review of the paper and for valuable remarks. And also hope you to consider this paper for publication.

References

1. Stokes, V.K.: Couple stress in fluids. Phys. Fluids **9**, 1709–1715 (1966)
2. Lakshmana Rao, S.K., Bhujanga Rao, P.: The oscillations of a sphere in a micro-polar fluid. Int. J. Eng. Sci. **9**, 651–672 (1971)
3. Lakshmana Rao, S.K., Bhuganga Rao, P.: Circular cylinder oscillating about a mean position in an incompressible micro-polar fluid. Int. J. Eng. Sci. **10**, 185–191 (1972)
4. Lakshmana Rao, S.K., Iyengar, T.K.V., Venkatapathi Raju, K.: The rectilinear oscillations of an elliptic cylinder in an incompressible micro-polar fluid. Int. J. Eng. Sci. **25**, 531–548 (1987)
5. Lakshmana Rao, S.K., Iyengar, T.K.V.: Analytical and computational studies in couple stress fluid flows (a UGC research project no. C8-4/82 SR III) (1980)
6. Ramkissoon, H., Majumdar, S.R.: Flow due to the longitudinal and torsional oscillations of a cylinder. Z. Angew. Math. Phys. **41**, 598–603 (1990)
7. Ramkissoon, H., Easwaran, C.V., Majumdar, S.R.: Longitudinal and torsional oscillations of a rod in a polar fluid. Int. J. Eng. Sci. **29**(2), 215–221 (1991)
8. Rajagopal, K.R.: Longitudinal and torsional oscillation of a rod in a non-Newtonian fluid. Acta Mech. **49**, 281–285 (1983)
9. Stokes, V.K.: Theories of Fluids with Microstructure. Springer, New York (1984)
10. Bandelli, R., Lapczyk, I., Li, H.: Longitudinal and torsional oscillations of a rod in a third grade fluid. Int. J. Non-Linear Mech. **29**, 397–408 (1994)
11. Pontrelli, G.: Longitudinal and torsional oscillations of a rod in an Oldroyd-B fluid with suction or injection. Acta Mech. **123**, 57–68 (1997)
12. Calmelet-Eluhu, C., Majumdar, D.R.: Flow of a micropolar fluid through a circular cylinder subject to longitudinal and torsional oscillations. Math. Comput. Model. **27**(8), 69–78 (1998)
13. Ramana Murthy, J.V., Bahali, N.K.: Steady flow of micropolar fluid through a circular pipe under a transverse magnetic field with constant suction/injection. Int. J. Appl. Math. Mech. **5**(3), 1–10 (2009)
14. Ramana Murthy, J.V., Bahali, N.K., Srinivasacharya, D.: Unsteady flow of micropolar fluid through a circular pipe under a transverse magnetic field with suction/injection. Selçuk J. Appl. Math. **11**(2), 13–25 (2010)
15. Ramana Murthy, J.V., Nagaraju, G., Muthu, P.: Numerical solution of longitudinal and torsional oscillations of a circular cylinder with suction in a couple stress fluid. ARPN J. Eng. Appl. Sci. **5**, 51–63 (2010)
16. Aparna, P., Ramana Murthy, J.V.: Rotary oscillations of a permeable sphere in an incompressible micropolar fluid. Int. J. Appl. Math. Mech. **8**(16), 79–91 (2012)
17. Nagaraju, G., Ramana Murthy, J.V.: Unsteady flow of a micropolar fluid generated by a circular cylinder subject to longitudinal and torsional oscillations. Theoret. Appl. Mech. **41**(1), 71–91 (2014) (TEOPM7, Belgrade)
18. Ramana Murthy, J.V., Bhaskara Rao, G.S., Govinda Rao, T.: Resonance type flow due to rectilinear oscillations of a circular cylinder in a micropolar fluid. In: Proceedings of 59th Congress of ISTAM, Bangalore, India, pp. 1–7, 17–20 Dec 2014

Effect of Heat Generation and Viscous Dissipation on MHD 3D Casson Nanofluid Flow Past an Impermeable Stretching Sheet

Thirupathi Thumma, S. R. Mishra and MD. Shamshuddin

Abstract The impact of heat generation viscous dissipation and thermal radiation on an unsteady three dimensional magnetohydrodynamic Casson nanofluid flow over an impermeable stretching sheet under time dependent velocity, convective wall temperature and zero mass flux boundary conditions is elaborated numerically. Thermophoresis and Brownian motion and low magnetic Reynolds number are accounted in this model. The governing boundary layer non-linear partial differential equations are transformed into the coupled ordinary differential equations with similarity transformations and then solved numerically for convergent solutions. The numerical results so obtained are depicted with the aid of the graphs and elaborated in tabular form also these results indicate that the fluid velocity, temperature and concentration profiles are greatly influenced by the pertinent physical parameters which governs the flow problem. The numerical computations which exists in the literature are used for validating the numerical results so obtained and are found to be in good correlation.

Keywords Cason nanofluid · Magnetohydrodynamics · Viscous dissipation · Heat generation · Zero mass flux

T. Thumma (✉)
Department of Mathematics, B V Raju Institute of Technology,
Narsapur, Medak 502313, Telangana, India
e-mail: thirupathi.thumma@gmail.com

S. R. Mishra
Department of Mathematics, Siksha 'O' Anusandhan Deemed to be University,
Bhubaneswar 751030, Odisha, India
e-mail: satyaranjan_mshr@yahoo.co.in

MD. Shamshuddin
Department of Mathematics, Vaagdevi College of Engineering,
Warangal 506005, Telangana, India
e-mail: shammaths@gmail.com

D. Srinivasacharya and K. S. Reddy (eds.), *Numerical Heat Transfer and Fluid Flow*, Lecture Notes in Mechanical Engineering,
https://doi.org/10.1007/978-981-13-1903-7_66

1 Introduction

Nanofluid was first introduced by Choi [1]. From a stretching sheet the transport phenomena have attracted many researchers and in this area Sakiadis [2, 3] was presented the pioneering work. Further, Sakiadis model was extended by Crane [4]. To study the rheological properties of non-Newtonian fluids researchers proposed various type of non-Newtonian fluid models such as, the rate type and the integral type. The non-Newtonian fluids are pertinent due to their potential applications in biomedical applications, production process, industry and food processing. The Casson fluid is categorized as differential type non-Newtonian fluid model and is defined as shear thinning fluid at zero shear rate, zero viscosity at infinite shear rate and below yield stress at which no flow occurs. Examples for Casson fluid are blood, molten chocolate, honey, soup, concentrate fruit juice and yoghurt. At high and low shear rates the Casson fluid model is very accurate. Therefore, recently researchers investigated Casson fluid flows past a various geometries under several boundary conditions in 2D and 3D spaces which includes Nadeem [5], Haq [6], Mukhopadhyay [7], Bhattacharyya [8] and Pramanik [9]. Very recently, Ibrahim and Makinde [10] examined the 2D MHD stagnation point flow of Casson nanofluid over a stretching sheet with $f'(0) = 1 + \delta(1 + \gamma^{-1})f''(0)$ and $\theta'(0) = -\mathrm{Bi}(1 - \theta(0))$ boundary conditions by adopting RKF45 method with shooting technique. Gnaneswara Reddy et al. [11] adopted KBM to investigate numerically the influence of double stratification on MHD 3D Casson nanofluid flow over a stretching sheet with linear velocities $f'(0) = 1$ and $g'(0) = \lambda$ and stratified temperature and concentration $\theta(0) = (1 + S_t)$, $\phi(0) = (1 + S_m)$ and the same problem is extended by Gnaneswara Reddy et al. [12] with the effect of second order slip $f'(0) = 1 + \beta_1 f''(0) + \beta_2 f'''(0)$. Sulochana et al. [13] presented slip boundary condition, $\theta'(0) = -\mathrm{Bi}_1(1 - \theta(0))$ and $\phi'(0) = -\mathrm{Bi}_2(1 - \phi(0))$ solved by using classical RK method shooting technique. The SRM (Spectral Relaxation Method) is adopted by Oyelakin et al. [14] to investigate the effects of on Casson nanofluid flow over a stretching sheet under $f'(0) = 1 + \delta f''(0)$, $\theta'(0) = -\mathrm{Bi}(1 - \theta(0))$ and $\mathrm{Nb}\phi'(0) + \mathrm{Nt}\theta'(0) = 0$ boundary conditions.

Motivated by the literature survey cited above and in view of the widespread of engineering and industrial applications, the prime aim of this paper is to explore the 3D MHD Casson nanofluid flow over an impermeable stretching sheet under zero mass flux and convective wall temperature boundary conditions. To predict the characteristics of heat transfer the thermal radiation, heat generation and viscous dissipation are considered. To explore the impact of diverse parameters on flow characteristics RK method integrated with shooting technique is implemented and the results are plotted and elaborated numerically by using tables. Validation of the present results is obtained with that of earlier in a particular case.

2 Analysis and Solution of the Problem

Three-dimensional, transient, incompressible, MHD flow of an electrically conducting Casson nanofluid over a linearly stretching sheet with velocities $u_w(x) = cx/(1-\lambda t)$ and $v_w(x) = by/(1-\lambda t)$ along x and y directions respectively has been considered, where b, c are constants and $\lambda \geq 0$. The fluid is placed along z -axis and the physical model is illustrated in Nadeem et al. [15]. A uniform magnetic field of strength B_o is applied in the transverse direction z axis which is normal to the sheet and induced magnetic field is assumed to be negligible, therefore it justifies small magnetic Reynolds number. It is assumed that the temperature $T_w = T_\infty + (b_1 x^2)/(1-\lambda t)^2$ and concentration $C_w = C_\infty + (b_2 x^2)/(1-\lambda t)^2$ at the stretching sheet surface are vary with space and while the ambient temperature and concentration are T_∞ and C_∞ as $y \to \infty$ respectively. The nanofluid is assumed to be thermal equilibrium, single phase, no external force (such as gravity) is taken into account and there is no slip occurs between the base fluid and nanoparticles. It is also assumed that u_w, v_w, T_w and C_w are valid only for $t < (1/\lambda)$ but not when $\lambda = 0$. Subject to the aforementioned assumptions along with rheological equation [7] of state for an isotropic flow, the boundary layer approximations for the continuity, momentum, energy and species concentration equations following Nadeem et al. [15], the governing boundary layer equations for Casson nanofluid are as follows:

$$\frac{\partial u}{\partial x} + \frac{\partial v}{\partial y} + \frac{\partial w}{\partial z} = 0 \tag{1}$$

$$\frac{\partial u}{\partial t} + u\frac{\partial u}{\partial x} + v\frac{\partial u}{\partial y} + w\frac{\partial u}{\partial z} = \upsilon\left(1 + \frac{1}{\beta}\right)\frac{\partial^2 u}{\partial z^2} - \frac{\sigma B_o^2}{\rho_f}u \tag{2}$$

$$\frac{\partial v}{\partial t} + u\frac{\partial v}{\partial x} + v\frac{\partial v}{\partial y} + w\frac{\partial v}{\partial z} = \upsilon\left(1 + \frac{1}{\beta}\right)\frac{\partial^2 v}{\partial z^2} - \frac{\sigma B_o^2}{\rho_f}v \tag{3}$$

$$\begin{aligned}\frac{\partial T}{\partial t} + u\frac{\partial T}{\partial x} + v\frac{\partial T}{\partial y} + w\frac{\partial T}{\partial z} &= \frac{K_T}{\rho c_p}\frac{\partial^2 T}{\partial z^2} + \frac{1}{\rho c_p}\frac{16\sigma^* T_\infty^3}{3k^*}\frac{\partial^2 T}{\partial z^2} + \frac{Q_0}{\rho c_p}(T - T_\infty) \\ &+ \frac{\mu}{\rho c_p}\left(1 + \frac{1}{\beta}\right)\left(\frac{\partial u}{\partial z}\right)^2 + \frac{(\rho c)_p}{(\rho c)_f}\left[D_B\frac{\partial C}{\partial z}\frac{\partial T}{\partial z} + \frac{D_T}{T_\infty}\left(\frac{\partial T}{\partial z}\right)^2\right]\end{aligned} \tag{4}$$

$$\frac{\partial C}{\partial t} + u\frac{\partial C}{\partial x} + v\frac{\partial C}{\partial y} + w\frac{\partial C}{\partial z} = D_B\frac{\partial^2 C}{\partial z^2} + \frac{D_T}{T_\infty}\frac{\partial^2 T}{\partial z^2} \tag{5}$$

The phenomena of zero mass flux and convective temperature effects near the boundary layer surface has many applications in nuclear plants, transpiration process, prevention of energy etc. which motivates to consider the present flow problem with the following boundary conditions:

$$at\ z = 0;\quad \left\{ \begin{array}{r} u = u_w,\ v = v_w,\ w = 0,\ -k_f \dfrac{\partial T}{\partial z} = h_f(T_w - T), \\ D_B \dfrac{\partial C}{\partial z} + \dfrac{D_T}{T_\infty} \dfrac{\partial T}{\partial z} = 0 \end{array} \right\} \qquad (6)$$
$$as\ z \to \infty\ \{u \to 0,\ v \to 0,\ T \to T_\infty,\ C \to C_\infty$$

Here u, v and w are the velocity components along the x-axis, y-axis and z-axis directions respectively, υ is the kinematic viscosity, $\beta = \mu_B\sqrt{2\pi c}/p_y$ is the Casson nanofluid parameter, σ be the electrical conductivity, K_T is thermal diffusivity, $\tau = (\rho c)_p/(\rho c)_f$ be the ratio of heat capacities of both nanoparticle and base fluid, D_B is the Brownian and D_T is the thermophoretic diffusion coefficient, Q_0 is the heat generation constant, k_f is the thermal conductivity, h_f is the convective heat transfer coefficient. Using the following similarity transformations [13]

$$u = cxf'(\eta)/1 - \lambda t,\ v = cyg'(\eta)/1 - \lambda t,\ w = -\sqrt{(c\upsilon/1 - \lambda t)}\,(f(\eta) + g(\eta)),$$
$$\eta = z\sqrt{c/\upsilon(1 - \lambda t)}, a = b/c,\ T_w = T_\infty + ((b_1x^2)/(1 - \lambda t)^2)\theta(\eta),$$
$$C_w = C_\infty + ((b_2x^2)/(1 - \lambda t)^2)\phi(\eta) \qquad (7)$$

Using Eq. (7) in Eqs. (1)–(6), the boundary layer equations and boundary conditions in dimensionless form are:

$$\left(\frac{1}{\beta} + 1\right)f''' - A\left(f' + \frac{\eta}{2}f''\right) - f'^2 + (f + g)f'' - Mf' = 0 \qquad (8)$$

$$\left(\frac{1}{\beta} + 1\right)g''' - A\left(g' + \frac{\eta}{2}g''\right) - g'^2 + (f + g)g'' - Mg' = 0 \qquad (9)$$

$$(1 + \frac{4}{3}R)\frac{\theta''}{\mathrm{Pr}} - A\left(2\theta + \frac{\eta}{2}\theta'\right) - 2f'\theta + (f + g)\theta' + \left(1 + \frac{1}{\beta}\right)\mathrm{Ec}f''^2$$
$$+ \mathrm{Nb}\phi'\theta' + \mathrm{Nt}\theta'^2 + Q\theta = 0 \qquad (10)$$

$$\phi'' - A\ \mathrm{Pr}\ Le\left(2\phi + \frac{\eta}{2}\phi\right) - 2\,\mathrm{Pr}\,Lef'\phi + \mathrm{Pr}\,Le(f + g)\phi' + (\mathrm{Nt}/\mathrm{Nb})\theta'' = 0 \qquad (11)$$

$$f(0) = 0,\ f'(0) = 1,\ g(0) = 0,\ g'(0) = a,\ \theta'(0) = -\mathrm{Bi}(1 - \theta(0)),$$
$$\mathrm{Nb}\phi'(0) + \mathrm{Nt}\theta'(0) = 0\,\mathrm{and}\,f'(\eta) = g'(\eta) = \theta(\eta) = \phi(\eta) = 0\,as\,\eta \to \infty \qquad (12)$$

where f, g, θ and ϕ are functions of η represents velocities along x, y directions, temperature and concentration distributions respectively. The non-dimensional parameters are: $A = \lambda/c$ is the unsteadiness parameter, $M = \sigma B_o^2/\rho c$ is the magnetic field parameter (Hartmann number), $\mathrm{Pr} = \upsilon\rho c_p/K_T$ is the Prandtl number, $Q = Q_0/c\rho c_p$ is the heat generation parameter, $\mathrm{Nb} = \tau(D_B(C_w - C_\infty))/\upsilon$ is the Brownian motion parameter, $R = 4\sigma^* T_\infty^3/(kk^*)$ is the radiation parameter, $\mathrm{Ec} = c^2/b_1c_p$ is the Eckert number, $\mathrm{Nt} = ((\rho c)_p/(\rho c)_f)(D_T(T_w - T_\infty))/\upsilon T_\infty$ is the thermophoresis parameter, $Le = K_T/D_B\rho c_p$ is the Lewis number, $\mathrm{Bi} = (h_f/k_0)\sqrt{\upsilon/c}$ is the Biot number. Here prime denotes derivatives with respect to η and $a = b/c$ is the velocity ratio.

Furthermore, the physical quantities of interest are the skin friction coefficient C_f, the local Nusselt number Nu_x and local Sherwood number Sh_x in its non-dimensional form can be expressed as $\mathrm{Re}_x^{1/2} C_{f_x} = (1 + (1/\beta))(f''(0))$, $(x/y)\mathrm{Re}_x^{1/2} C_{f_y} = (c(1 + (1/\beta))(g''(0))$, $\mathrm{Re}_x^{-1/2} Nu_x = -\theta'(0)$ and $\mathrm{Re}_x^{-1/2} Sh_x = -\phi'(0)$, here $\mathrm{Re}_x = xu_w/\upsilon$ is the local Reynolds number.

Numerical solution of the transformed nonlinear coupled and non-homogeneous ordinary differential Eqs. (8)–(11) subject to the boundary conditions Eq. (12) are obtained by using Runge-Kutta iterative scheme integrated with shooting technique. The domain of the problem is discretized and free stream boundary condition $\eta \to \infty$ are replaced by $f'(\eta_{\max}) = g'(\eta_{\max}) = \theta(\eta_{\max}) = \phi(\eta_{\max}) = 8$ where $\eta_{\max}$ is sufficient large value of η at which boundary conditions are satisfied. For convergence criterion the difference between two successive approximations used sufficiently small ($\leq 10^{-6}$).

Comparison analysis of skin friction coefficient, local Nusselt number and local Sherwood number is made with [15] the results, in the absence of radiation, viscous dissipation and heat generation which are documented in Tables 1 and 2. It is evident from Tables 1 and 2 that present numerical values correlate closely and found to be in good agreement. Therefore, confidence in the present numerical solutions is highly justified. From Table 3 it is observed that increase in M enhances the $-(1 + (1/\beta))f''(0)$, $-c(1+(1/\beta))g''(0)$ and $-\phi'(0)$ while the opposite behaviour is observed for Nusselt number. With an increasing values of Q, R and Ec the values of $-\phi'(0)$ whereas reverse trend is observed for $-\theta'(0)$.

Table 1 Comparative analysis for $\mathrm{Re}_x^{1/2} C_{f_x}$ and $c\mathrm{Re}_x^{1/2} C_{f_y}$ when $\beta \to \infty$, $c = 0.5$

M	β	$-(1 + (1/\beta))f''(0)$	$-c(1 + (1/\beta))g''(0)$	$-(1 + (1/\beta))f''(0)$	$-c(1 + (1/\beta))g''(0)$
		Nadeem et al. [15]		Present results	
0	1	1.5459	0.6579	1.545721	0.657654
10	1	4.7263	2.3276	4.726932	2.327452
10	5	3.6610	1.8030	3.661216	1.803365

Table 2 Comparative analysis for $-\theta'(0)$ and $-\phi'(0)$ when $\beta \to \infty$, $c = 0.5$

Nt	Nb	$-\theta'(0)$	$-\phi'(0)$	$-\theta'(0)$	$-\phi'(0)$
		Nadeem et al. [15]		Present results	
0.3	0.3	0.293872	1.585361	0.2938735	1.5853624
0.5	0.3	0.277199	1.584743	0.2771968	1.5847478
0.7	0.5	0.177710	1.774545	0.1777114	1.7745436
0.7	0.7	0.109759	1.810687	0.1097523	1.8106845

Table 3 Numerical values for the distinct values of the variables M, Q, R and Ec

M	Q	R	Ec	$-(1+(1/\beta))f''(0)$	$-c(1+(1/\beta))g''(0)$	$-\theta'(0)$	$-\phi'(0)$
1				3.2952	0.7869	0.3263	−0.1087
3				4.0579	0.9844	0.3147	−0.1049
	0.3			3.0779	0.73005	0.3295	−0.1098
	0.7			3.0779	0.73005	0.3051	−0.1077
		0.2		3.0779	0.73005	0.3391	−0.1130
		0.6		3.0779	0.73005	0.3266	−0.1088
			0.01	3.0779	0.73005	0.3472	−0.1157
			0.1	3.0779	0.73005	0.3295	−0.1098

3 Results and Discussion

The behaviour of diverse parameters A, β, M, Nb, Nt, Q, R and Ec on $f'(\eta)$, $g'(\eta)$, $\theta(\eta)$ and $\phi(\eta)$ in Casson nanofluid boundary layer regime are interpreted in Figs. 1, 2, 3, 4, 5, 6, 7 and 8. From the figures it is seen that increase in A, the values of thermal and concentration boundary layer thickness is decreased which are shown in Figs. 1 and 2. This is due to heat loss at the surface and the Brownian motion intensify the particle displacements away from the stretching sheet surface. Thus the rate of cooling is much faster for transient flows. The variations of velocity distributions with respect to Casson parameter β are shown in Fig. 3. It is evident from Fig. 3 that momentum boundary layer thickness is decreased due to an increase in Casson parameter causes plastic dynamic viscosity which intern induces the resistance of the fluid motion.

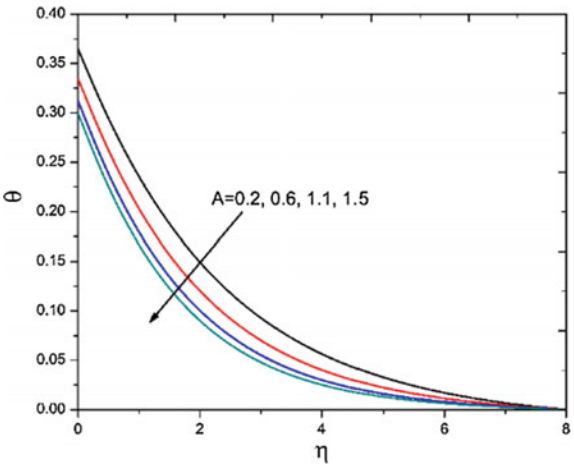

Fig. 1 Effect of A on θ

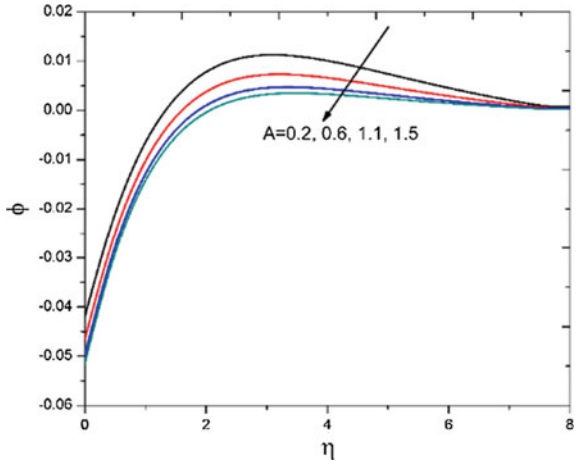

Fig. 2 Effect of A on ϕ

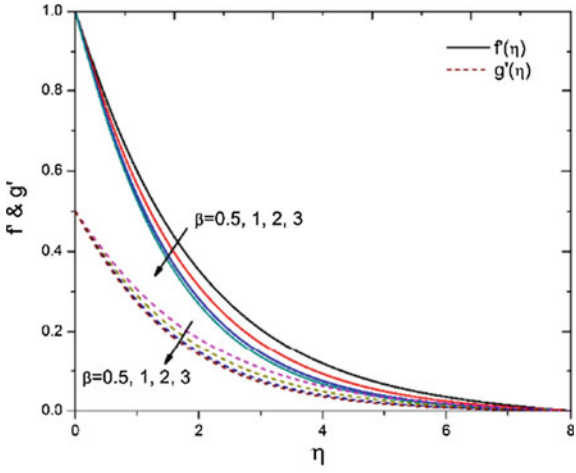

Fig. 3 Effect of β on f' and g'

Hence with increasing Casson parameter velocities in both the directions are decreased. Whenever we apply magnetic field to the electrically conducting fluid, the dual interaction between the two forces causes an opposing force called as Lorentzian force, due to this an increase in M decrease the thickness of the momentum boundary layer and hence the velocities of the fluid flow as shown in Fig. 4. The effect of Nb and Nt on $\phi(\eta)$ are shown in Fig. 5. It is evident from the graph that increasing values of Nt first causes decrease in $\phi(\eta)$ while the reverse trend is noticed for increasing Nb near the surface of the sheet up to certain value of η but afterwards reverse trend is remarked for both the parameters. The influence of Q, R and Ec on $\theta(\eta)$ are shown in Figs. 6, 7 and 8. The increase in parameter values enhances the thermal boundary layer thickness due to releasing of heat energy to the fluid flow and hence increases in the temperature profiles.

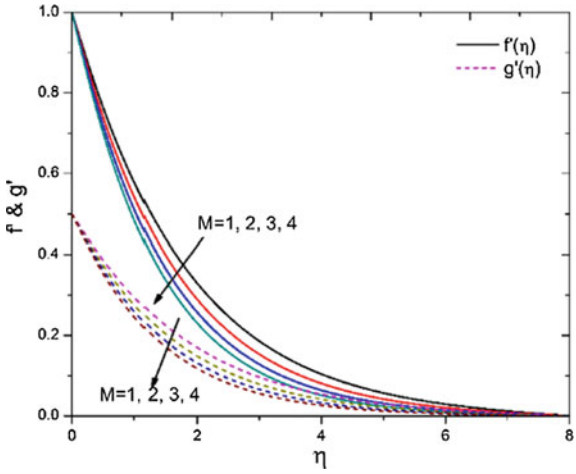

Fig. 4 Effect of M on f' and g'

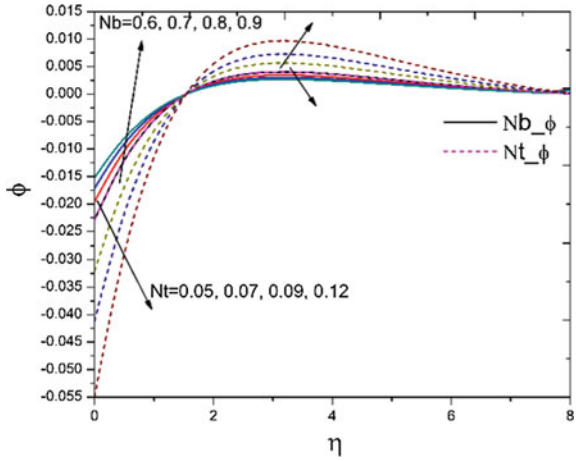

Fig. 5 Effect of Nb and Nt on ϕ

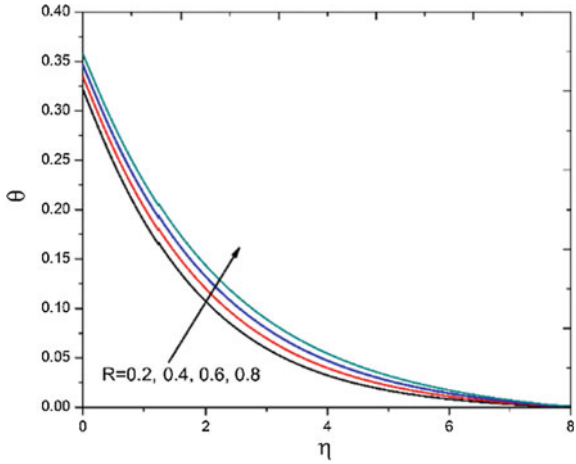

Fig. 6 Effect of R on θ

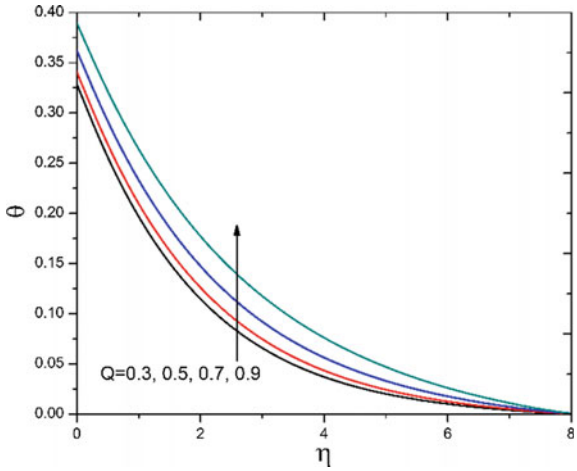

Fig. 7 Effect of Q on θ

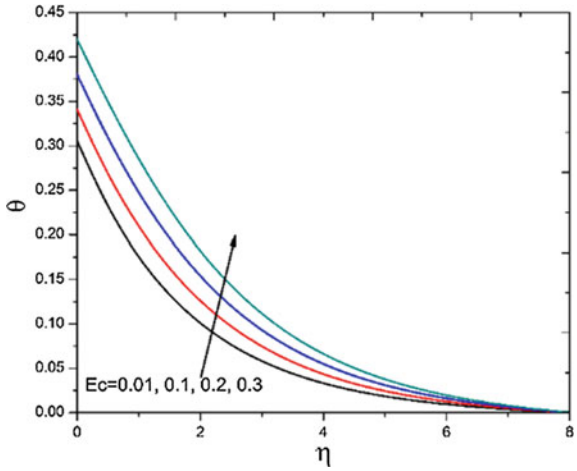

Fig. 8 Effect of Ec on θ

4 Conclusions

The effect of heat generation and viscous dissipation on MHD 3D Casson nanofluid flow past an impermeable stretching sheet are studied in the present paper. Similarity transformations is used to transform the governing boundary layer equations into ordinary differential equations. Finally, numerical computations are obtained and compared with earlier literature which found to be in good agreement. The important findings are summarized as below.

Velocity profile decreases for increasing values of Magnetic field and Casson parameter, Temperature of the Casson nanofluid increases for heat source, radiation, Eckert number and Brownian motion parameter whereas it is decreased for unsteady parameter and thermophoretic parameter, Concentration is decreased for unsteadiness parameter. For M, Q, R and Ec Nusselt number is decreased while opposite trend is observed in Sherwood number. With increase in M, skin friction is increased.

Acknowledgements The authors are grateful to the reviewers and conference chair, NHTFF-2018 for their valuable suggestions which helped to improve the quality of the paper.

References

1. Choi, S.U.S.: Enhancing thermal conductivity of fluids with nanoparticles. Developments and Applications of Non-Newtonian Flows, ASME Fluids Division, vol. 66, pp. 99–105 (1995)
2. Sakiadis, B.C.: Boundary layer behavior on continuous solid surfaces: I. Boundary layer equations for two–dimensional and axisymmetric flow. AIChemE J. **7**, 26–28 (1961)
3. Sakiadis, B.C.: Boundary layer behavior on continuous solid surfaces: II. The boundary layer on a continuous flat surface. AIChemE J. **7**, 221–225 (1961)
4. Crane, L.J.: Flow past a stretching plate. Z. Angew. Math. Phys. **21**, 645–647 (1970)
5. Nadeem, S., Haq, R.U., Lee, C.: MHD flow of a Casson fluid over an exponentially shrinking sheet. Sci. Iranica B **19**(6), 1550–1553 (2012)
6. Haq, R.U., Nadeem, S., Khan, Z.H., Okedayo, T.G.: Convective heat transfer and MHD effects on Casson nanofluid flow over a shrinking sheet. Cent. Eur. J. Phys. **12**(12), 862–871 (2014)
7. Mukhopadhyay, S., Chandra Mondal, I., Chamkha, A.J.: Casson fluid flow and heat transfer past a symmetric wedge. Heat Transf. Asian Res. **42**(8), 665–675 (2013)
8. Bhattacharyyaa, K., Hayat, T., Alsaedic, A.: Analytic solution for magnetohydrodynamic boundary layer flow of Casson fluid over a stretching/shrinking sheet with wall mass transfer. Chin. Phys. B **22**(2), article id 024702 (1–6) (2013). https://doi.org/10.1088/1674-1056/22/2/024702
9. Pramanik, S.: Casson fluid flow and heat transfer past an exponentially porous stretching surface in the presence of thermal radiation. Ain Shams Eng. J. **5**, 205–217 (2014)
10. Ibrahim, W., Makinde, O.D.: Magnetohydrodynamic stagnation point flow and heat transfer of Casson Nanofluid past a stretching sheet with slip and convective boundary condition. J. Aerosp. Eng. **29**(2), article id 04015037 (1–11) (2016). https://doi.org/10.1061/(ASCE)AS.1943-5525.0000529
11. Gnaneswara Reddy, M., Padma, P., Gorla, R.S.R.: Influence of double stratification on MHD three dimensional Casson nanofluid flow over a stretching sheet: a numerical study. J. Nanofluids **6**(1), 71–79 (2017). https://doi.org/10.1166/jon.2017.1296

12. Gnaneswara Reddy, M., Manjula, J., Padma, P.: Influence of second order velocity slip and double stratification on MHD 3D Casson nanofluid flow over a stretching sheet. J. Nanofluids **2**(3), 436–446 (2017). https://doi.org/10.1166/jon.2017.1342
13. Sulochana, C., AshwinKumar, G.P., Sandeep, N.: Similarity solution of 3D Casson nanofluid flow over a stretching sheet with convective boundary conditions. J. Niger. Math. Soc. http://dx.doi.org/10.1016/j.jnnms.2016.01.001 (2016)
14. Oyelakin, I.S., Mondal, S., Sibanda, P.: Unsteady Casson nanofluid flow over a stretching sheet with thermal radiation, convective and slip boundary conditions. Alexandria Eng. J. **55**(2), 1025–1035 (2016). https://doi.org/10.1016/j.aej.2016.03.003
15. Nadeem, S., Ul Haq, R., Sher Akbar, N.: MHD three-dimensional boundary layer flow of Casson nanofluid past a linearly stretching sheet with convective boundary condition. IEEE Trans. Nanotechnol. **13**(1), 109–115 (2014)

Radiation, Dissipation, and Dufour Effects on MHD Free Convection Flow Through a Vertical Oscillatory Porous Plate with Ion Slip Current

K. V. B. Rajakumar, K. S. Balamurugan, Ch. V. Ramana Murthy and N. Ranganath

Abstract In this paper, the Dufour, radiation absorption, chemical reaction, and viscous dissipation effects on unsteady magneto hydrodynamic free convective flow through a semi-infinite vertical oscillatory porous plate of time-dependent permeability with Hall and ion slip current in a rotating system were investigated. The governing equations of the problem are solved by using Multiple Regular Perturbation law. The possessions of various parameters on velocity, temperature, and concentration are shown graphically.

Keywords Dufour · Hall effect · Ion Slip current · MHD
Multiple Regular Perturbation law · Viscous dissipation

Nomenclature

B Magnetic field
B_0 Magnetic component
B^* Concentration expansion coefficient
C^* Dimensionless fluid concentration

K. V. B. Rajakumar (✉)
Kallam Haranadhareddy Institute of Technology, Rayalaseema University, Guntur, AP, India
e-mail: kvbrajakumar@gmail.com

K. S. Balamurugan
Department of Mathematics, RVR & JC College of Engineering, Guntur, AP, India

Ch. V. Ramana Murthy
Department of Mathematics, Sri Vasavi Institute of Engineering & Technology, Krishna, AP, India

N. Ranganath
Rayalaseema University, Guntur, AP, India

D. Srinivasacharya and K. S. Reddy (eds.), *Numerical Heat Transfer and Fluid Flow*, Lecture Notes in Mechanical Engineering,
https://doi.org/10.1007/978-981-13-1903-7_67

C_W Concentration at the plate
C_∞ Concentration outside of the plate
Dr Dufour number
Gr Grashof number
Gr Modified Grashof number
g Acceleration due to gravity
K_r Chemical reaction parameter
k Magnetic permeability of the porous medium
N_u Nusselt number
Pr Prandtl number
Q_0 Heat absorption quantity
Sc Schmidt number
T_W Temperature at the plate
T_∞ Temperature outside of the boundary lyre
T^* Dimensionless fluid temperature
U_0 Uniform velocity
U Dimensionless primary velocity
W Dimensionless secondary velocity
ξ Heat generation/absorption coefficient
Ω Rotational velocity component
η Radiation parameter
τ_w Skin friction coefficient
β Thermal expansion coefficient
β_e Hall parameter
β_i Ion slip parameter
α Heat source parameter
ϑ Kinematic velocity
ρ Density of the fluid
σ_ρ Electrical conductivity
σ Thermal conductivity

1 Introduction

As ion slip and Hall currents are likely to be essential in flows of laboratory plasma when a strong magnetic field of a uniform strength is applied, the attention of the researchers is drawn due to their varied significance in liquid metals, electrolytes land ionized gases. The Hall effect is the having of a voltage effect over an electrical conductor, transverse to an electric current in the transmitter and an electromagnetic field and opposite to the current. It is found by Hall et al. [1]. The present improvement of magneto-hydrodynamic application is towards a solid magnetic field and towards a low thickness of the gas. Under this condition, the Hall current becomes important. That significance is considered by numerous analysts. Anika et al. [2] the effect of Hall, ion slip over an infinite vertical plate for micropolar fluid within the magnetic

field was investigated. Srinivasacharya et al. [3] analyzed the significance of Hall and ion slip parameters on the steady mixed convective flow of a nanofluid in a vertical channel. From this paper, I observed that the increase of Hall parameter leads to the increase in velocity and temperature, but the induced flow velocity and nanoparticle concentration is decreased. Srinivasacharya et al. [4] analyzed Hall and ion slip effect on mixed convective flow through a vertical channel with couple stress fluid. Bilal et al. [5] magneto-micropolar nanofluid flow in a porous medium over a stretching sheet with suction or injection was analyzed. In this investigation hall and ion slip effects were considered. The energy flux caused due to composition gradient is known as diffusion thermo effect or Dufour effect. Ojjela et al. [6] investigated the Hall and ion slip current on free convection flow, heat and mass transform of an electrically conducting couple stretch fluid through permeable channels with chemical reaction, Dufour, and Soret effects. Alivene et al. [7] combined the influence of radiation, viscous dissipation and Hall effects on MHD free convective heat, and mass transfer flow of a viscous fluid past a stretching sheet was investigated.

Motivated by the above studies, the main objective of this paper is to study the effect of the Dufour, radiation absorption, chemical reaction, and viscous dissipation on unsteady MHD free convective flow through a semi-infinite vertical oscillatory porous plate of time-dependent permeability with Hall and ion slip current in a rotating system.

2 Mathematical Formulation

Consider the two-dimensional unsteady laminar flow of a viscous incompressible, electrically conducting fluid past a semi-infinite vertical moving porous plate $y = 0$ with the x-axis is considered as along the plate. The plate velocity is assumed as

$U(t) = U_0\,(1 + \cos nt)$ oscillates in t with a frequency n. Let the x*and y* are the dimensional distance along the perpendicular to the plate and t* is the time. The physical model of the flow problem is shown in Fig. 1. u* and v* are the components of dimensional velocities along x*and y* directions. The flow is considered to be in x-direction which is taken along the plate in upward direction and y-axis is normal to it. At first, the fluids as well as the plate are at rest but for time $t > 0$ the whole system is allowed to rotate with a constant angular velocity Ω about the y-axis. Assuming transverse magnetic field of the uniform strength B_0 to be utilizable normal to the plate. Viscous dissipation, radiation absorption, the heat source, and Dufour effects are considered.

Hence dimensional governing equations are

$$\left[\frac{\partial u^*}{\partial \tau^*}\right] = \vartheta\left[\frac{\partial^2 u^*}{\partial y^{*2}}\right] + g\beta\left(T^* - T_\infty^*\right) + g\beta^*\left(C^* - C_\infty^*\right) + 2\Omega w^* - \frac{\nu}{k^*}\left[u^*\right] - \frac{B_0^2\sigma_e[\alpha_e u^* + \beta_e w^*]}{\rho\left[\alpha_e^2 + \beta_e^2\right]} \tag{1}$$

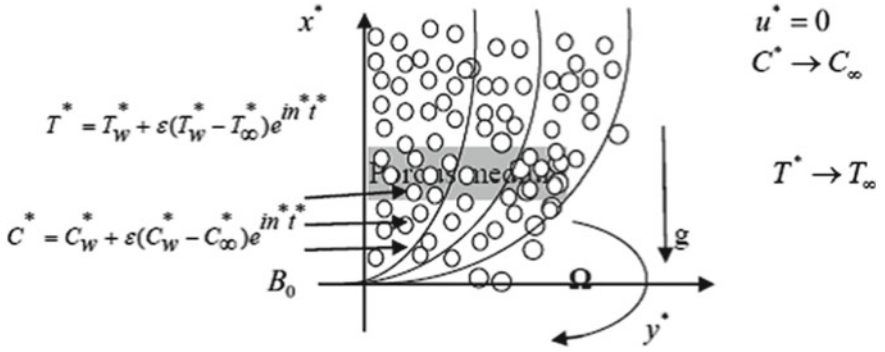

Fig. 1 The physical model in the problem

$$\left[\frac{\partial w^*}{\partial \tau^*}\right] = \vartheta\left[\frac{\partial^2 w^*}{\partial y^{*2}}\right] - 2\Omega\left[u^*\right] - \frac{\vartheta}{k^*}\left[w^*\right] + \frac{B_0^2\sigma_e[\beta_e u^* - \alpha_e w^*]}{\rho\left[\alpha_e^2 + \beta_e^2\right]} \tag{2}$$

$$\left[\frac{\partial T^*}{\partial \tau^*}\right] = \frac{K}{\rho C_p}\left[\frac{\partial^2 T^*}{\partial y^{*2}}\right] + \frac{D_m K_T}{C_S C_P}\left[\frac{\partial^2 C^*}{\partial y^{*2}}\right] + \frac{Q_0}{\rho C_p}\left[T^* - T_\infty^*\right] - \frac{1}{k\rho C_p}\frac{\partial q_r^*}{\partial y^*} + \frac{\vartheta}{C_p}\left[\left(\frac{\partial u^*}{\partial y^*}\right)^2 + \left(\frac{\partial w^*}{\partial y^*}\right)^2\right] + R^*\left[C^* - C_\infty^*\right] \tag{3}$$

$$\left[\frac{\partial C^*}{\partial \tau^*}\right] = D_m\left[\frac{\partial^2 C^*}{\partial y^{*2}}\right] - K_r\left[C^* - C_\infty^*\right] \tag{4}$$

The initial and boundary conditions are as follows:

$$\left.\begin{array}{l} \text{at } y^* = 0 \left\{\begin{array}{l} u^* = U_0\left[1 + \frac{\varepsilon}{2}\left(e^{in^*t^*} + e^{-in^*t^*}\right)\right],\ w^* = 0, \\ T^* - T_w^* = \varepsilon(T_w^* - T_\infty^*)e^{in^*t^*},\ C^* - C_w^* = \varepsilon(C_w^* - C_\infty^*)e^{in^*t^*} \end{array}\right. \\ \text{as } y^* \to \infty\ u^* = 0,\ w^* = 0,\ T^* = T_\infty^*,\ C^* = C_\infty^* \end{array}\right\} \tag{5}$$

Using the relation in the radiative heat flux (q_r) for the optically thin non-gray gas near equilibrium is given by $\frac{\partial q_r}{\partial y} = 4I^1 T[T - T_1]$, $I^1 = \int_0^\infty K_{\lambda_1 w}\frac{\partial e_{b\lambda_1}}{\partial T}d\lambda_1$, the porous medium is taken to be $k^* = k_0\left[1 + \varepsilon e^{-nt}\right]$. Introducing the following nondimensional quantities in the (1)–(4):

$$\left.\begin{array}{l} U_0 u = u^*,\ U_0 w = w^*,\ \vartheta y = y^* U_0,\ t\vartheta = U_0^2\tau^*,\ nU_0^2 = \vartheta n^* \\ T^* - T_\infty^* = \left(T_w^* - T_\infty^*\right)\theta,\ C^* - C_\infty^* = \left(C_w^* - C_\infty^*\right)\phi, \end{array}\right\} \tag{6}$$

$$\left[\frac{\partial u}{\partial t}\right] = \left[\frac{\partial^2 u}{\partial y^2}\right] + G_r[\theta] + G_m[\phi] + 2R[w] - \gamma[u] - \frac{M[\alpha_e u + \beta_e w]}{\left[\alpha_e^2 + \beta_e^2\right]} \tag{7}$$

$$\left[\frac{\partial w}{\partial t}\right] = \left[\frac{\partial^2 w}{\partial y^2}\right] - 2R[u] - \gamma[w] + \frac{M[\beta_e u - \alpha_e w]}{\left[\alpha_e^2 + \beta_e^2\right]} \tag{8}$$

$$\left[\frac{\partial \theta}{\partial t}\right] = \frac{1}{Pr}\left[\frac{\partial^2 \theta}{\partial y^2}\right] - N[\theta] + Dr\left[\frac{\partial^2 \phi}{\partial y^2}\right] + \mathrm{Ec}\left[\frac{\partial F}{\partial y}\frac{\partial \overline{F}}{\partial y}\right]^2 + R_a[\phi] \tag{9}$$

$$\left[\frac{\partial \phi}{\partial t}\right] = (\mathrm{Sc})^{-1}\left[\frac{\partial^2 \phi}{\partial y^2}\right] - K_r[\phi] \tag{10}$$

Here

$\xi = \frac{\vartheta Q_0}{\rho U_0^2 C_P}$, $M = \frac{\sigma_e B_0^2 \vartheta}{\rho U_0^2}$, $G_m = \frac{\vartheta \beta^* g\left[C_w^* - C_\infty^*\right]}{U_0^2}$, $R = \frac{\Omega \vartheta}{U_0^2}$, $Sc = \frac{\vartheta}{D_m}$, $Pr = \frac{\rho \vartheta C_p}{\sigma}$, $\gamma = \frac{\vartheta^2}{k^* U_0^2}$, $K_r = \frac{k_1 \vartheta}{V_0^2}$, $N = [\xi + \eta]$, $\alpha_e = 1 + \beta_e \beta_i$, $F = u + iw$, $Ec = U_0^2 (C_p)^{-1}\left[T_w^* - T_\infty^*\right]^{-1}$, $K_r = \left(V_0^2\right)^{-1} k_1 \vartheta$, $G_r = \vartheta \beta g\left[T_w^* - T_\infty^*\right]\left(U_0^2\right)^{-1}$ $\lambda = \left[\left[2Ri + \gamma\right] + M[-\alpha_e + i\beta_e]\left[\alpha_e^2 + \beta_e^2\right]^{-1}\right]$, $\eta = 4\vartheta I'\left(K_p C_p U_0^2\right)^{-1}$, $R_a = R^* \vartheta\left[C_w^* - C_\infty^*\right]\left(U_0^2\left[T_w^* - T_\infty^*\right]\right)^{-1}$, $Dr = D_m K_T\left[C_w^* - C_\infty^*\right]\left(\vartheta C_S C_P\left[T_w^* - T_\infty^*\right]\right)^{-1}$

Equations (7) and (8) are displayed, in a reduced form, as

$$\frac{\partial F}{\partial t} = \frac{\partial^2 F}{\partial y^2} + G_r \theta + G_m \phi - \lambda F \tag{11}$$

$$\left.\begin{array}{l} \text{At } y = 0 \; F = \left[1 + \frac{\varepsilon}{2}\left(\mathrm{e}^{int} + \mathrm{e}^{-int}\right)\right] = 1, \; \theta = 1 + \varepsilon \mathrm{e}^{int}, \; \phi = 1 + \varepsilon \mathrm{e}^{int} \\ \text{As } y \to \infty \; F \to 0, \; \theta \to 0, \; \phi \to 0 \end{array}\right\} \tag{12}$$

3 Method of Solution

The resulting system of nonlinear ODEs Eqs. (9), (10) and (11) subject to the boundary conditions presented in Eq. (12) has been explored numerically through Multiple Regular Perturbation law.

$$\left.\begin{array}{l} F = F_0(y) + \varepsilon \mathrm{e}^{int} F_1(y) + o\left(\varepsilon^2\right), \; \theta = \theta_0(y) + \varepsilon \mathrm{e}^{int} \theta_1(y) + o\left(\varepsilon^2\right) \\ \phi = \phi_0(y) + \varepsilon \mathrm{e}^{int} \phi_1(y) + o\left(\varepsilon^2\right) \end{array}\right\} \tag{13}$$

Substitute (13) in Eqs. (9), (10), and (12) then we get

$$F_0'' - \lambda F_0 = -G_r \theta_0 - G_m \phi_0 \tag{14}$$

$$F_1'' - (\lambda + ni)F_1 = -G_r\theta_1 - G_m\phi_1 \tag{15}$$

$$\theta_0'' - PrN\theta_0 = -Pr\ Dr\phi_0'' - Pr\,\mathrm{Ec}\left(F_0'\right)^2 - PrR_a\phi_0 \tag{16}$$

$$\theta_1'' - Pr(N + in)\theta_1 = -PrDr\phi_1'' - 2Pr\,\mathrm{Ec}F_0'F_1' - PrR_a\ \phi_1 \tag{17}$$

$$\phi_0'' - S_cK_r\phi_0 = 0 \tag{18}$$

$$\phi_1'' - S_c(K_r + n)\phi_1 = 0 \tag{19}$$

Corresponding boundary conditions are

$$\left.\begin{array}{l} F_0 = 1,\ F_1 = 0\ , \theta_0 = 1\ \theta_1 = 1,\ \phi_0 = 1\ , \phi_1 = 1,\ \text{at } y\ = 0 \\ F_0 = 0,\ F_1 = 0,\ \theta_0 \to 0,\ \theta_1 \to 0,\ \phi_0 \to 0, \phi_1 \to 0,\ \text{as } y \to \infty \end{array}\right\} \tag{20}$$

First, we solve Eqs. (17) and (19) by using Eq. (20). Then

$$\phi_0 = \mathrm{e}^{-\left(\sqrt{ScKr}\right)y} \tag{21}$$

$$\phi_1 = \mathrm{e}^{-\left(\sqrt{Sc(Kr+n)}\right)y} \tag{22}$$

Now using multi-parameter perturbation technique and assuming $\mathrm{Ec} \ll 1$.

$$\left.\begin{array}{l} F_0 = F_{00} + \mathrm{Ec}F_{01} + 0(\varepsilon)^2,\ \theta_0 = \theta_{00} + \mathrm{Ec}\theta_{01} + 0(\varepsilon)^2, \\ F_1 = F_{10} + \mathrm{Ec}F_{11} + 0(\varepsilon)^2,\ \theta_1 = \theta_{10} + \mathrm{Ec}\theta_{11} + 0(\varepsilon)^2 \end{array}\right\} \tag{23}$$

$$F_{00}'' - \lambda F_{00} = -G_r\ \theta_{00} - G_m\ \phi_0 \tag{24}$$

$$F_{01}'' - \lambda F_{01} = -G_r\ \theta_{01} \tag{25}$$

$$F_{10}'' - [\lambda + ni]F_{10} = -G_r\theta_{10} - G_m\phi_1 \tag{26}$$

$$F_{11}'' - [\lambda + ni]F_{11} = -G_r\theta_{11} \tag{27}$$

$$\theta_{10}'' - Pr[N + in]\theta_{10} = -R_a\phi_1 Pr - PrDr\ \phi_1'' \tag{28}$$

$$\theta_{01}'' - PrN\theta_{01} = -PrF_{00}'F_{00}' \tag{29}$$

$$\theta_{11}'' - Pr[N + in]\theta_{11} = -2PrF_{00}'F_{10}' \tag{30}$$

$$\theta_{01}'' - PrN\theta_{01} = -PrF_{00}'F_{00}' \tag{31}$$

$$\theta_{00}'' - PrN\ \theta_{00} = -PrR_a\ \phi_0 - Pr\ Dr\ \phi_0'' \tag{32}$$

$$\left.\begin{array}{l}\text{at } y = 0; \quad F_{00} = 1,\ F_{01} = 0,\ F_{10} = 0,\ F_{11} = 0,\ \theta_{00} = 1,\ \ \theta_{01} = 0, \theta_{10} = 1,\ \ \theta_{11} = 0 \\ \text{As } y \to \infty\ F_{00} = 0, \quad F_{01} = 0, \quad F_{10} = 0,\ F_{11} = 0, \theta_{00} = 0, \theta_{01} = 0, \theta_{10} = 0,\ \theta_{11} = 0\end{array}\right\} \tag{33}$$

Solve Eqs. (23)–(32) subject to boundary conditions by using (33).

3.1 *Velocity (F), Temperature (θ) and Concentration (ϕ)*

By virtue of Eqs. (9), (10), (11) we obtain for the velocity, temperature, and concentration as follows:

$$\left.\begin{array}{l}F = \left[(F_{00} + \mathrm{Ec}F_{01}) + \varepsilon \mathrm{e}^{\mathrm{int}}(F_{10} + \mathrm{Ec}F_{11})\right],\ \theta = \left[(\theta_{00} + \mathrm{Ec}\theta_{01}) + \varepsilon \mathrm{e}^{\mathrm{int}}(\theta_{10} + \mathrm{Ec}\theta_{11})\right] \\ \phi = \phi_0 + \varepsilon \mathrm{e}^{\mathrm{int}}\phi_1\end{array}\right\} \tag{34}$$

4 Results and Discussion

In the present study, we have taken $t = 1.0$, $n = 0.5$, $\epsilon = 0.03$, $\eta = 0.003$ $\xi = 0.03$ while Dr, β_i and β_e are varied over a range, which listed in the figures. The variations in velocity and temperature profiles with y for various values in Dr and β_i are shown in Figs. 2, 3, 6 and 7. These figures reflect that with increase in Dr and β_i, there is an increase in fluid velocity and temperature. In Figs. 4 and 5, it is noticed that the velocity and temperature decrease with the increase of β_i.

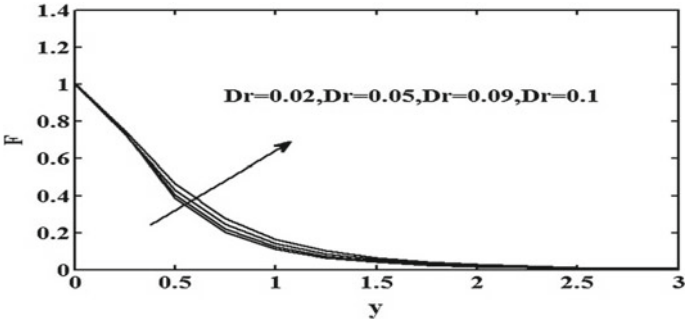

Fig. 2 Velocity profile for different values of *Dr*

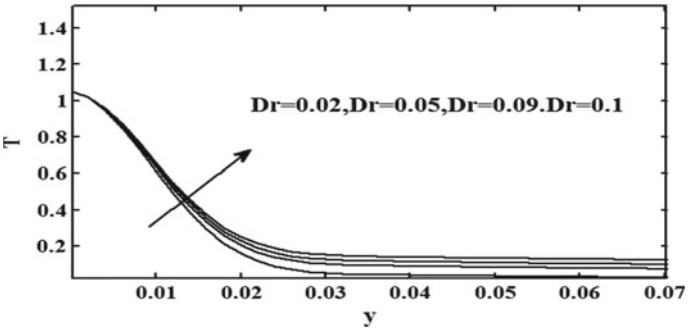

Fig. 3 Temperature for different values on *Dr*

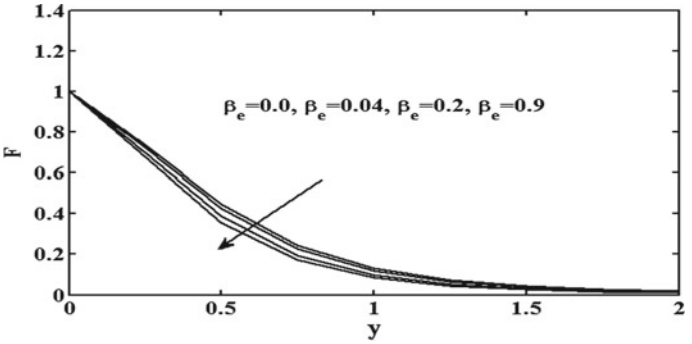

Fig. 4 Effect of β_e on velocity

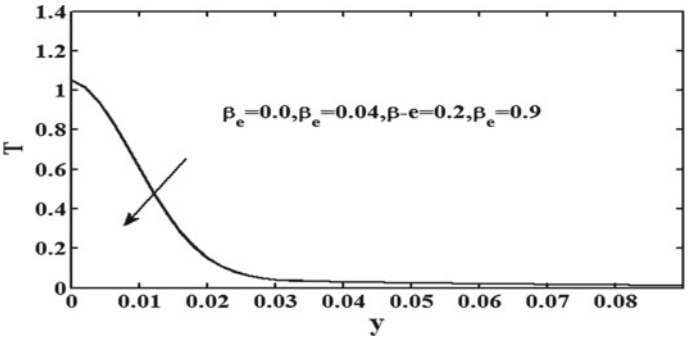

Fig. 5 Temperature profile for effect of β_e

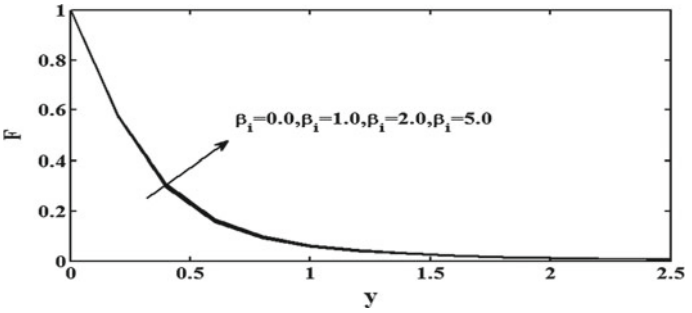

Fig. 6 Velocity profile for different values of β_i

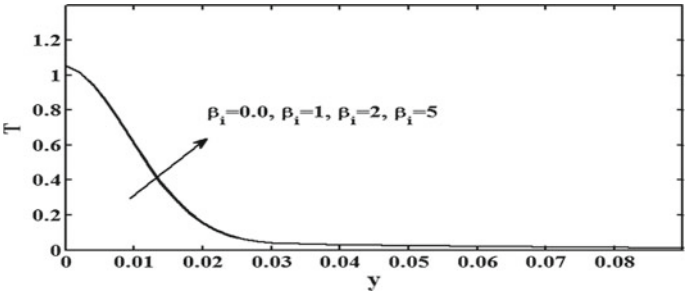

Fig. 7 Effect of β_i for different values on temperature

5 Conclusions

- As the Ion slip parameter β_i increases, the velocity and temperature profiles decrease but the velocity and temperature decrease with increases of Hall current parameter β_e.
- As the Dufour effect parameter Dr increases, the velocity and temperature increase.

References

1. Hall, E.: On a new action of the magnet on electric currents. Am. J. Math. **2**, 287–292 (1879)
2. Anika, N., Hoque, M., Hossain, S.: Thermal diffusion effect on unsteady viscous MHD microplar fluid flow through an infinite vertical plate with hall and ion-slip current. Procedia Eng. **105**, 160–166 (2015)
3. Srinivasacharya, D., Shafeeurrahaman, M.: Mixed convection flow of nanofluid in a vertical channel with hall and ion-slip effects. Front. Heat Mass Trans. **8**(11) (2017)
4. Srinivasacharya, D., Kaladhar, K.: Analytical solution for hall and ion-slip effects on mixed convection flow of couple stress fluid between parallel disks. Math. Comput. Model. **57**, 2494–2509 (2013)
5. Bilal, M., Hussain, S., Sagheer, M.: Boundary layer flow of magneto-microplar nanofluid flow with Hall and ion-slip effects using variable thermal diffusivity. Bull. Pol. Acad. Sci. Tech. Sci. **65**(3), 383–390 (2017)
6. Ojjela, O., Naresh Kumar, N.: Hall and ion slip effects on free convection heat and mass transfer of chemically reacting couple stress fluid in a porous expanding or contracting walls with Soret and Dufour effects. Front. Heat Mass Transf. **5**(22) (2014)
7. Alivene, S.: Effect of Hall current, thermal radiation, dissipation and chemical reaction on hydro magnetic non-Darcy mixed convective heat and mass transfer flow past a stretching sheet in the presence of heat sources. Adv. Phys. Theor. Appl. **61** (2017)

Bottom Heated Mixed Convective Flow in Lid-Driven Cubical Cavities

H. P. Rani, V. Narayana and Y. Rameshwar

Abstract The mixed convective flow of air in three-dimensional cubical lid-driven cavity flows are carried out numerically. The top lid assumed to be slide in its own plane at a constant speed. The horizontal walls are kept at an isothermal temperature in which the bottom wall has high temperature than the top. Numerical results are acquired for the control parameters arising in the system, namely, the Reynolds number (*Re*) in the range of 100–400 and the Richardson number (*Ri*) varying from 10^{-3} to 10. The fluid flow and heat transfer characteristics are visualized using the contours of streamlines, isotherms, vortex corelines with respect to different *Ri* and *Re*. The results are compared with the experimental/numerical results available in the literature and are found to be in good agreement.

Keywords Mixed convection · Vortex coreline · Richardson number

1 Introduction

The problem of the laminar incompressible three-dimensional (3D) mixed convection lid-driven cubical cavity has a large number of applications in engineering and science such as crystal growth, electronic device cooling, food processing, metal casting and phase change as the freezing of water for latent thermal storage systems, solar power collector, glass production, etc. A number of numerical experiments for a free convection dominated heat transfer has been conducted for the past few decades, few of such numerical experiments are called as the benchmark solutions, which are used in investigating the performance of numerical methodologies and solving the incompressible laminar Navier–Stokes equations for complicated problems. From the literature, it is found that majority of numerical work has been confined to 2D

H. P. Rani (✉) · V. Narayana
Department of Mathematics, National Institute of Technology, Warangal, India
e-mail: hprani@nitw.ac.in

Y. Rameshwar
Department of Mathematics, College of Engineering, Osmania University, Hyderabad, India

D. Srinivasacharya and K. S. Reddy (eds.), *Numerical Heat Transfer and Fluid Flow*, Lecture Notes in Mechanical Engineering,
https://doi.org/10.1007/978-981-13-1903-7_68

flow. Kosef and Street [1, 2] stressed the necessity to study the 3D nature of the flows arising in the lid-driven cavity due to the presence of no-slip boundary conditions along with the sparse characteristics of incompressible flows. A similar problem was numerically analyzed by Iwatsu and Hyun [3] with the moving top wall kept at higher temperature than at the bottom wall for the possibility of air temperature distribution for a wide range of control parameters such as $10^2 \leq Re \leq 2000$, and $0 \leq Ri \leq 10$. Both 2D and 3D lid-driven cavity problems are analyzed by Mohammad and Viskanta [4]. They established that this movement of the lid in a cavity can get rid of all convective cells due to bottom heating. For a 2D lid-driven cavity, the effect of buoyancy on the flow and heat transfer for higher values of Pr was analyzed by Moallemi and Jang [5] with $10^2 \leq Re \leq 2000$ for different levels of the Ri. They showed that free convection contribution always assists the forced convection magnitude. The mixed convection in a top wall moving lid-driven 2D cavity was examined by Prasad et al. [6]. They showed that when the negative Grashof number (Gr) is more and aspect ratio (AR) is equal to 0.5 and 1.0, a strong convection is exhibited, and when AR is 2, a Hopf bifurcation is observed. Sharif [7] analyzed a supplementary flow visualization of a laminar incompressible combined free and forced convective heat transfer in 2D rectangular driven cavities with AR of 10. They observed that the local Nusselt number (Nu) at the heated moving wall initiates with a higher value and decreases rapidly to a lower value towards the right side. However, the Nu at the cold wall shows the fluctuations close to the right wall. This is due to the presence of a vortex at the cold wall. In an inclined cavity with $Ri = 0.1$, Benkacem et al. [8] remarked that the average Nu augments slowly with the inclination while for $Ri = 10$, it increases rapidly in the case of natural convection. Aydin et al. [9] analyzed the mixed convection in a shear and buoyancy-driven cavity with lower wall heated and moving cold sidewalls. With the motivation of the above work, in the present article, the mixed convective flow of air in 3D cubical lid-driven cavity flows are carried out numerically. Numerical results are obtained for $100 < Re < 400$ and $0.001 < Ri < 10$. The fluid flow and heat transfer characteristics are visualized using the contours of streamlines, isotherms, vortex corelines with respect to different Ri and Re.

2 Physical System

The lid-driven 3D cavity filled with air is considered as shown in Fig. 1.

The top wall, $Y = L(m)$, is moving in its own plane with a constant velocity U_0 (m/s), and the other boundary walls are at rest. The top and bottom walls are kept at the isothermal temperature in which the bottom wall has the higher temperature (T_H) than the top wall (T_C) with $\Delta T = T_H - T_C > 0$. Also, the remaining four walls are assumed as adiabatic.

Steady laminar 3D nondimensional form for the conservation of mass, momentum, and energy equations with an inclusion of the buoyant Boussinesq approximations for the density variation is written as

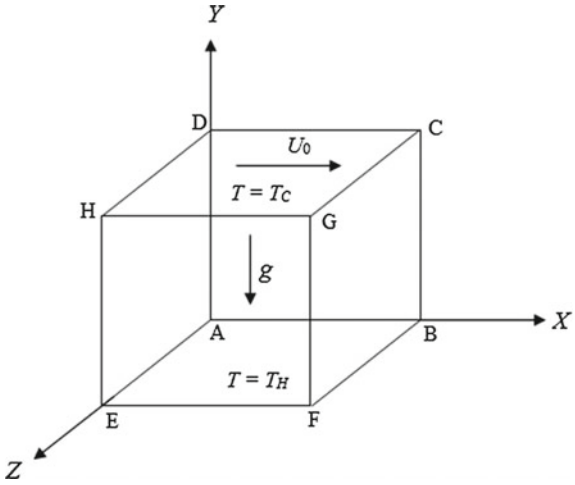

Fig. 1 3D cubical-driven cavity of length L

$$\text{div}\, \boldsymbol{V} = 0 \tag{1}$$

$$(\boldsymbol{V} \,.\, \text{grad})\boldsymbol{V} = -\text{grad}\, p + \frac{1}{Re} \,.\, \nabla^2 \boldsymbol{V} + Ri \,.\, T^* \boldsymbol{e} \tag{2}$$

$$(\boldsymbol{V} \,.\, \text{grad}) T^* = \frac{1}{Re \,.\, \text{Pr}} . \nabla^2 T^* \tag{3}$$

where $\boldsymbol{V} = (U, V, W)$, $\mathbf{e} = (0, 1, 0)$, p, t, and $T^* = \frac{T - T_C}{\Delta T}$ represents dimensionless velocity vector along (X, Y, Z) directions, the unit vector in the vertical direction, pressure, time, and temperature, respectively. The reference scales for nondimensionalization are U_0, ρU_0^2, and L/U_0 for velocity, pressure, and time, respectively, $Re = U_0 L/\nu$, Rayleigh number $Ra = \frac{g\beta(\Delta T)L^3}{\nu\alpha}$, where β is the thermal expansion coefficient, ν is the kinematic viscosity; Grashof number $Gr = \frac{g\beta(\Delta T)L^3}{\nu^2}$, and g is the gravity; Prandtl number $Pr = \nu/\alpha$; and the mixed convection parameter, $Ri = \frac{\text{Gr}}{Re^2}$.

For the above mathematical problems (1)–(3), the boundary conditions are

$\boldsymbol{V} = (1, 0, 0)$ at $Y = 1$ and $\boldsymbol{V} = 0$ at $Y = 0$, $X = 0, 1$, and $Z = 0, 1$

$T^* = 1$ at $Y = 0$, and $T^* = 0$ at $Y = 1$ and $\frac{\partial T^*}{\partial X} = 0$, at $X = 0, 1$ and $\frac{\partial T^*}{\partial Z} = 0$, $Z = 0, 1$.

The nondimensional heat transfer rate at the hot wall is calculated by the Nusselt number, whose local value along the hot wall is given by $Nu = \left(\frac{\partial T^*}{\partial Y}\right)_{Y=0}$. The average Nusselt number is obtained by integrating the local Nusselt number along the hot wall and is calculated as $\overline{\text{Nu}} = -\int_{X=0}^{X=1} \int_{Z=0}^{Z=1} \left(\frac{\partial T^*}{\partial Y}\right)_{Y=0} \text{d}X\, \text{d}Z$.

Table 1 Validation of present simulations with respect to $\overline{Nu}$ at the hot wall for $Re = 400$ and $Ri = 1$

Present work	1.518
Iwatsu et al. [3]	1.50
Ouertatani et al. [10]	1.528

3 Numerical Method

The flow model, geometry, the initial and boundary conditions for this problem were set in the buoyant Boussinesq SimpleFoam of the computational fluid dynamics solver, namely, OpenFOAM. It is a steady-state solver for the buoyant flow of incompressible fluids including Boussinesq approximation. To calculate the spatial derivatives, the second-order upwind finite volume numerical method was used. For acceleration means, conjugate gradient squared method was used. Divergent and Laplacian terms are discretized by the QUICK and Gauss linear schemes respectively.

Table 1 shows the comparison between the present laminar solution and numerical results found in the literature [3, 10] in terms of $\overline{\mathrm{Nu}}$ along the hot wall. There is an excellent agreement between the present results and the results available in the literature.

4 Results and Discussion

The simulated results are presented in terms of isotherms and streamlines in terms of the control parameters arising in the system.

Figure 2 depicts the isotherms for different *Re* and *Ri*. The patterns of isotherms show that for the small *Ri* (=0.001), the mechanically driven forced convection controls the buoyancy-driven convection. Figure 2a, d, show the forced convection induced by the movement of lid. While as *Ri* augmented to the value 1, the buoyant convection deforms the isotherms and these 3D structures become stronger further when *Re* moved to the value of 400 (Fig. 2c, f). The deformation of the isotherm field increases with *Ri*. Especially, the flow is dominated by the buoyancy and the heat transfer is controlled due to the natural convection, assigning that the forced convection due to the movement of the lid is almost absent. For $Ri = 1$, an agreement between the these free and forced convections, is clearly seen in Fig. 2b.

Figure 3 illustrates the streamlines and the vorticity in the cubical cavity for different *Re* and *Ri*. There are two similar vortices in the cavity and interact with each other at the middle of the cavity. The swirling nature of the streamlines around the vortex line in each case is clearly seen. The vortex corelines have their origin/end at the bounding walls and surrounded by the streamlines. The strength of the vorticity increases as *Re* or *Ri* increases. The energy exchange between the two closed vortices occurs at the middle of the cavity.

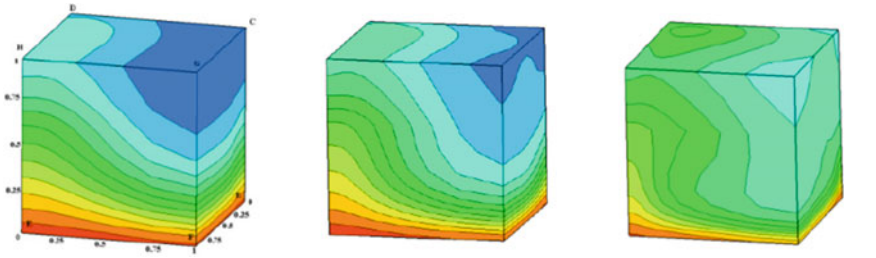

(a) Re =100, Ri = 0.001 (b) Re =100, Ri = 1 (c) Re =100, Ri = 10

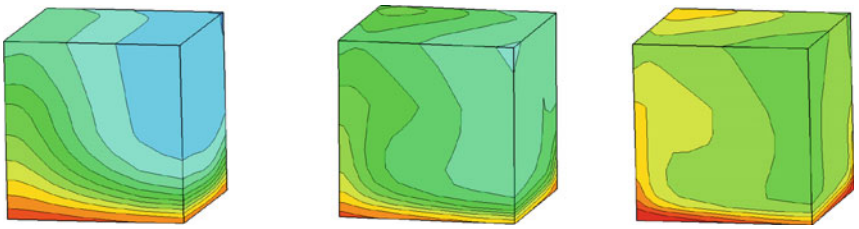

(d) Re =400, Ri = 0.001 (e) Re =400, Ri = 1 (f) Re =400, Ri = 10

Fig. 2 Isotherms for different Ri and Re

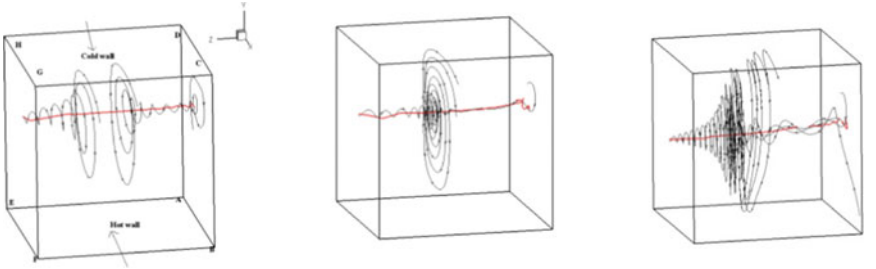

(a) Re =100, Ri = 0.001 (b) Re =100, Ri = 1 (c) Re =100, Ri = 10

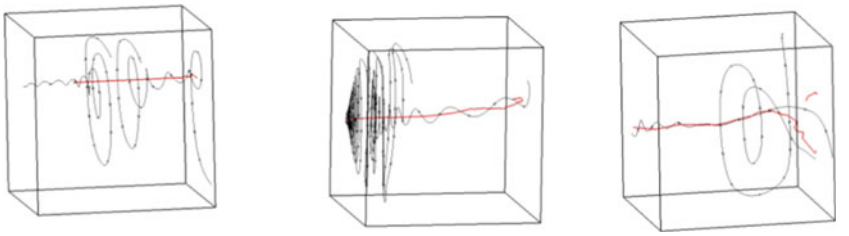

(d) Re =400, Ri = 0.001 (e) Re =400, Ri = 1 (f) Re =400, Ri = 10

Fig. 3 Visualizing vortex corelines and streamtraces for different Re and Ri

5 Conclusion

The present investigation directed the 3D mixed convection in a cubical lid-driven cavity for suitable collaboration of three different *Re* and *Ri* values and their effects are explored with respect to behaviors of the fluid flow and thermal fields. With lower *Re* values, the isotherm maintains a two dimensionality but when *Re* is large, the thermal field shows vigorous three dimensionalities for small *Ri* values. On the other hand, the stabilizing buoyancy effects become dominant at large *Ri*. In the considered problem the heat transfer rate is mostly convective and the three dimensionality of the thermal field is weak.

The implications of *Ri* play a key role in $\overline{\mathrm{Nu}}$ at the vicinity of the walls. When *Ri* is large, overall heat transfer is vanquished, and the conductive heat transfer model prevails. For very small values of *Ri* with the combination of large *Re*, complex 3D structures are noticeable. It can be concluded that the present results show that the overall heat is enhanced by vigorous forced convection.

References

1. Koseff, J.R., Street, R.L.: Visualization studies of a shear driven three dimensional recirculating flow. J. Fluids Eng. **106**, 21–29 (1984)
2. Koseff, J.R., Street, R.L.: On end wall effects in a lid driven cavity flow. J. Fluids Eng. **106**, 385–389 (1984)
3. Iwatsu, R., Hyun, J.M.: Three dimensional driven-cavity flows with a vertical temperature gradient. Int. J. Heat Mass Transf. **38**, 3319–3328 (1995)
4. Mohammad, A.A., Viskanta, R.: Laminar flow and heat transfer in Rayleigh-Benard convection with shear. Phys. Fluids **4**, 2131–2140 (1992)
5. Moallemi, M.K., Jang, K.S.: Prandtl number effects on laminar mixed convection heat transfer in a lid-driven cavity. Int. J. Heat Mass Transf. **35**, 1881–1892 (1992)
6. Prasad, Y.S., Das, M.K.: Hopf bifurcation in mixed flow inside a rectangular cavity. Int. J. Heat Mass Transf. **50**, 3583–3598 (2007)
7. Sharif, M.A.R.: Laminar mixed convection in shallow inclined driven cavities with hot moving lid on top and cooled from bottom. Appl. Therm. Eng. **27**, 1036–1042 (2007)
8. Benkacem, N., Ben Cheikh, N., Ben Beya, B.: Three-dimensional analysis of mixed convection in a differentially heated lid-driven cubic enclosure. J. Appl. Mech. Eng. **4**, 3 (2015)
9. Aydin, O., Yang, W.J.: Mixed convection in cavities with a locally heated lower wall and moving sidewalls. Numer. Heat Trans Part A Appl. **37**, 695–710 (2000)
10. Ouertatani, N., Ben Cheikh, N., Ben Beya, B., Lili, T., Campo, A.: Mixed convection in a double lid-driven cubic cavity. Int. J. Thermal Sciences **48**, 1265–1272 (2009)

Effect of Magnetic Field on the Squeeze Film Between Anisotropic Porous Rough Plates

P. Muthu and V. Pujitha

Abstract In this paper, the effect of externally applied magnetic field on squeeze film lubrication between anisotropic porous and rough rectangular plate is studied. A general probability density function with nonzero mean, skewness, and variance is used to model the roughness. Analytical expressions for pressure and load carrying capacity are derived. Runge–Kutta method is used to calculate thickness of the squeeze film. Externally applied magnetic field and surface roughness improve the squeeze film lubrication mechanism. The anisotropic nature of porous surface increases the squeeze film characteristics as compared with isotropic porous case.

Keywords Squeeze film · Anisotropic porous medium · Magnetic field

1 Introduction

The study of squeeze film mechanism has significant applications in gears, bearing, and engines. This study is also useful in understanding the mechanism of human joints. From the literature, it is understood that all bearing surfaces are rough and the order of the height of the roughness asperities is same as that of mean separation of plates. Christensen [1] developed a stochastic model to study the effect of roughness on lubrication mechanism and assumed a symmetric probability density function with zero mean. Prakash and Tiwari [2], Bujurke and Naduvinamani [3] used Christensen's model for the analysis of effect of surface roughness on squeeze film lubrication between porous plates. In general, the surface roughness is not symmetric. Andharia et al. [4] used an asymmetric probability density function with nonzero mean, variance, and skewness to model the roughness. Lin [5] analyzed the influence of magnetic field between smooth rectangular plates with electrically conducting fluid as lubricant. Bujurke et al. [6] studied the effect of surface roughness

P. Muthu (✉) · V. Pujitha
Department of Mathematics, NIT Warangal, Warangal 506004, Telangana, India
e-mail: muthuatbits@gmail.com

D. Srinivasacharya and K. S. Reddy (eds.), *Numerical Heat Transfer and Fluid Flow*, Lecture Notes in Mechanical Engineering,
https://doi.org/10.1007/978-981-13-1903-7_69

on squeeze film between rectangular plates in the presence of transverse magnetic field by assuming an asymmetric probability density function with nonzero mean and variance.

In this paper, an attempt has been made to study the combined effect of surface roughness, external magnetic field, and anisotropic nature of porous material on squeeze film between finite rectangular plates. An asymmetric probability density function which has nonzero mean, skewness, and variance is considered.

2 Analysis

Figure 1 represents the squeeze film geometry. Consider the squeeze film mechanism between rectangular plates where one plate is moving with velocity dH/dT towards bottom fixed plate. Let L_1 and L_2 be the length and width of the plates, respectively. The modified Darcy's law for the fluid flow in the porous region is given as [7]

$$\mathbf{V}' = -\frac{K}{\mu}\nabla p' \tag{1}$$

where $\mathbf{V}' = (u', v', w')$ is the velocity vector in porous region, K is the anisotropic permeability tensor, and p' is pressure in porous region. It is assumed that principle directions of K are constant and parallel to the coordinate axis. Hence the $K = \begin{bmatrix} k_x & 0 & 0 \\ 0 & k_y & 0 \\ 0 & 0 & k_z \end{bmatrix}$ where (k_x, k_y, k_z) are the constant permeability coefficients in (x, y, z) directions, respectively.

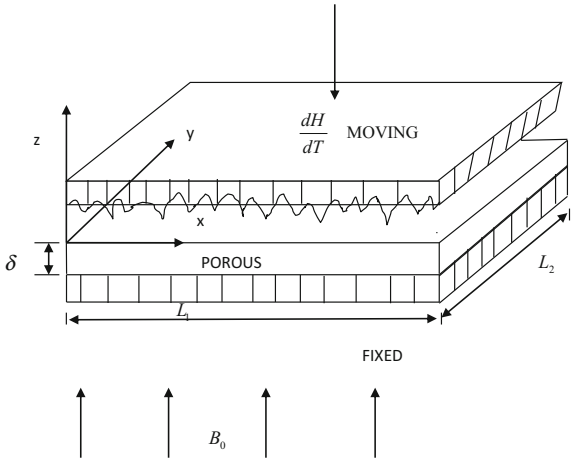

Fig. 1 Geometry of the problem

Due to the surface roughness, the fluid film height has two parts $h(T)$ and h_r. Hence the film height is: $H = h(T) + h_r$, where $h(T)$ represents the height of the smooth part and h_r is a random variable measured from the nominal level. The h_r has the probability density function $g(h_r)$ where $-c < h_r < c$, and c indicates the maximum deviation from nominal level. α, ϵ and σ are mean, skewness and standard deviation of the randomly varying quantity, given as, $\alpha = E(h_r)$, $\sigma^2 = E((h_r - \alpha)^2)$, $\epsilon = E((h_r - \alpha)^3)$ where E is the mathematical expectation given by

$$E(R) = \int_{-\infty}^{\infty} R\, g(h_r)\, dh_r \tag{2}$$

Assume that α and ϵ can take both negative and positive values whereas σ takes always positive values [6]. In the system, isothermal, incompressible electrically conducting fluid is taken as lubricant. In the z-direction, a constant magnetic field B_0 is considered. The fluid film is assumed to be thin and inertia free. Except Lorentz force, remaining body forces are negligible. Further, the induced magnetic field is small in comparison with the applied magnetic field. Therefore, under the above assumptions, the governing equations of fluid flow in two different regions are given as

$$\text{For film region:} \quad \frac{\partial p}{\partial x} = \mu \frac{\partial^2 u}{\partial z^2} - \bar{\sigma} {B_0}^2 u \tag{3}$$

$$\frac{\partial p}{\partial y} = \mu \frac{\partial^2 v}{\partial z^2} - \bar{\sigma} B_0^2 v \tag{4}$$

$$\frac{\partial p}{\partial z} = 0 \tag{5}$$

$$\frac{\partial u}{\partial x} + \frac{\partial v}{\partial y} + \frac{\partial w}{\partial z} = 0 \tag{6}$$

$$\text{For porous region:} \quad u' = -\frac{k_x}{\mu} \frac{\partial p'}{\partial x} \left(1 + \frac{k_x \bar{\sigma} B_0^2}{\mu m'}\right)^{-1} \tag{7}$$

$$v' = -\frac{k_y}{\mu} \frac{\partial p'}{\partial y} \left(1 + \frac{k_y \bar{\sigma} B_0^2}{\mu m'}\right)^{-1} \tag{8}$$

$$w' = -\frac{k_z}{\mu} \frac{\partial p'}{\partial z} \tag{9}$$

$$\frac{\partial u'}{\partial x} + \frac{\partial v'}{\partial y} + \frac{\partial w'}{\partial z} = 0 \tag{10}$$

where (u, v, w) are the velocity components along the (x, y, z) directions in film region, ρ is density, p is pressure, μ is dynamic viscosity of the fluid, $\bar{\sigma}$ is electrical conductivity, B_0 is applied magnetic field, and m' is porosity.

Boundary Conditions are

$$\text{At} \quad z = 0: \quad u = v = 0 \quad \text{and} \quad w = w' \tag{11}$$

$$\text{At} \quad z = H: \quad u = v = 0 \quad \text{and} \quad w = \frac{dH}{dT}. \tag{12}$$

From Eqs. (3) and (4) by using (11) and (12), we get u and v,

$$u = \frac{h_0^2}{\mu M^2}\frac{\partial p}{\partial x}\left\{\cosh\left(\frac{Mz}{h_0}\right) - 1 - \frac{\left[\cosh\left(\frac{MH}{h_0}\right) - 1\right]}{\sinh\left(\frac{MH}{h_0}\right)}\sinh\left(\frac{Mz}{h_0}\right)\right\} \tag{13}$$

$$v = \frac{h_0^2}{\mu M^2}\frac{\partial p}{\partial y}\left\{\cosh\left(\frac{Mz}{h_0}\right) - 1 - \frac{\left[\cosh\left(\frac{MH}{h_0}\right) - 1\right]}{\sinh\left(\frac{MH}{h_0}\right)}\sinh\left(\frac{Mz}{h_0}\right)\right\} \tag{14}$$

where M denotes the Hartmann number defined by $M = B_0 h_0\left(\frac{\bar{\sigma}}{\mu}\right)^{\frac{1}{2}}$.

Substituting Eqs. (13) and (14) in Eq. (6) and integrating with respect to z and using the boundary conditions on w, we get the modified Reynolds equation as

$$\frac{\partial}{\partial x}\left\{\frac{h_0^3}{\mu M^3} f(H, M)\frac{\partial p}{\partial x}\right\} + \frac{\partial}{\partial y}\left\{\frac{h_0^3}{\mu M^3} f(H, M)\frac{\partial p}{\partial y}\right\} = \frac{dH}{dT} + \frac{k_z}{\mu}\left[\frac{\partial p'}{\partial z}\right]_{z=0} \tag{15}$$

where $f(H, M) = \dfrac{MH}{h_0} - 2\tanh\left(\dfrac{MH}{2h_0}\right)$. By taking the mathematical expectation on both sides of Eq. (15), we get

$$\frac{\partial^2 E(p)}{\partial x^2} + \frac{\partial^2 E(p)}{\partial y^2} = \frac{\mu M^3}{h_0^3}\frac{1}{E\left(f(H, M)\right)}\left\{E\left(\frac{dH}{dT}\right) + \frac{k_z}{\mu}\left[\frac{\partial p'}{\partial z}\right]_{z=0}\right\} \tag{16}$$

where

$$E(f(H, M)) = \frac{M}{h_0}(h + \alpha) - 2\tanh\left(\frac{Mh}{2h_0}\right) - \frac{\left(1 - \tanh^2\left(\frac{Mh}{2h_0}\right)\right)}{12}$$
$$\left[\frac{12M\alpha}{h_0} - \frac{M^3}{h_0^3}\left(\epsilon + \alpha^3 + 3\alpha\sigma^2\right)\right]$$

From Eqs. (7) to (9), the governing equation for the pressure in the porous region is obtained as

$$\frac{k_x}{d_1}\frac{\partial^2 p'}{\partial x^2} + \frac{k_y}{d_2}\frac{\partial^2 p'}{\partial y^2} + k_z\frac{\partial^2 p'}{\partial z^2} = 0 \tag{17}$$

where $d_1 = 1 + \dfrac{k_x}{m'}\dfrac{M^2}{h_0^2}$ and $d_2 = 1 + \dfrac{k_y}{m'}\dfrac{M^2}{h_0^2}$. The boundary conditions for solving Eq. (16) are:

$$E(p) = 0 \quad \text{at} \quad x = 0, L_1 \quad \text{and} \quad y = 0, L_2 \tag{18}$$

The boundary conditions for solving Eq. (17) are:

$$p' = 0 \quad \text{at} \quad x = 0, L_1 \quad \text{and} \quad y = 0, L_2 \tag{19}$$

$$\frac{\partial p'}{\partial z} = 0 \quad \text{at} \quad z = -\delta \tag{20}$$

$$\text{and} \quad E(p) = p' \quad \text{at} \quad z = 0. \tag{21}$$

3 Squeeze Film Characteristics

The solution of Eq. (17) is written as

$$p'(x, y, z) = \sum_{m=1}^{\infty} \sum_{n=1}^{\infty} A_{mn} \sin(\alpha_m x) \sin(\beta_n y) \cosh[\gamma_{mn}(z + \delta)] \tag{22}$$

where $\alpha_m = \frac{m\pi}{L_1}$, $\beta_n = \frac{n\pi}{L_2}$, $\gamma_{mn} = \left(\frac{\alpha_m^2 k_x}{d_1 k_z} + \frac{\beta_n^2 k_y}{d_2 k_z}\right)^{1/2}$. From the Eq. (21), we get

$$E(p) = \sum_{m=1}^{\infty} \sum_{n=1}^{\infty} B_{mn} \sin(\alpha_m x) \sin(\beta_n y) \tag{23}$$

From the orthogonal condition of the eigen functions, A_{mn} is written as

$$A_{mn} = \frac{-16\mu \frac{dh}{dt}}{\alpha_m \beta_n L_1 L_2} M^3 \left(h_0^3 E(f(H, M)) \cosh(\gamma_{mn}\delta)(\alpha_m^2 + \beta_n^2) + k_z M^3 \gamma_{mn} \sinh(\gamma_{mn}\delta)\right)^{-1} \tag{24}$$

if m and n are odd and $A_{mn} = 0$, otherwise.

The nondimensional form of film pressure is

$$\frac{-E(p)h_0^3}{\mu L_1^2 \frac{dh}{dT}} = \bar{p} = \frac{16 M^3 \bar{\delta}\sqrt{\beta}}{\pi^2} \sum_{m=odd}^{\infty} \sum_{n=odd}^{\infty} \frac{\sin(m\pi\bar{x}) \sin(\frac{n\pi\bar{y}}{\beta})}{\bar{C}_{mn}} \tag{25}$$

where $\bar{C}_{mn} = mn \left[E(f(\bar{H}, M))(m^2 + \frac{n^2}{\beta^2})\pi^2 \bar{\delta}\sqrt{\beta} + \Psi_0 \bar{\gamma}_{mn} M^3 \tanh(\bar{\gamma}_{mn}\bar{\delta}\sqrt{\beta})\right]$

The load carrying capacity can be determined from

$$E(W) = \int_{x=0}^{L_1} \int_{y=0}^{L_2} E(p)\, dx\, dy \tag{26}$$

The nondimensional load carrying capacity is

$$\frac{-E(W)h_0^3}{\mu L_1^3 L_2 \frac{dh}{dT}} = \bar{W} = \frac{64\bar{\delta}\sqrt{\beta}}{\pi^4} \sum_{m=odd}^{\infty} \sum_{n=odd}^{\infty} \frac{M^3}{mn\bar{C}_{mn}} \tag{27}$$

We define the dimensionless response time as [5], $\bar{T} = \frac{E(W)h_0^2}{\mu L_1^3 L_2} T$.

$$\frac{d\bar{h}}{d\bar{T}} = \frac{-\pi^4}{64\bar{\delta}\sqrt{\beta}M^3 \sum_{m=odd}^{\infty} \sum_{n=odd}^{\infty} (mn\bar{C}_{mn})^{-1}} \tag{28}$$

Equation (28) is a nonlinear, first-order ordinary differential equation, which can be solved using Runge–Kutta method of order four with the initial condition $\bar{h} = 1$ at $\bar{T} = 0$ and with step size $\Delta\bar{T} = 0.01$.

4 Results and Discussion

The combined effect of external magnetic field, anisotropic nature of porous material, and surface roughness on squeeze film lubrication is studied. α, σ, and ε are parameters of the surface roughness and M signifies the magnetic field. Permeability of the porous material is characterized by ψ_0.

Variation of $\bar{p}$ with $\bar{x}$ is shown in Fig. 2 for different values of M as well as for different values of $k_y/k_x = 0.1$ and 1 (isotropic case). The external magnetic field reduces the velocity of the lubricant flowing out of the plate. The asperities of the

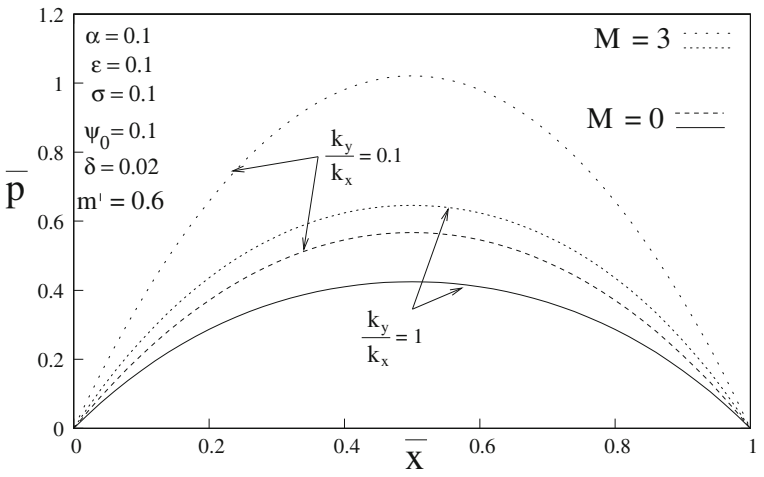

Fig. 2 Effect of M on $\bar{p}$

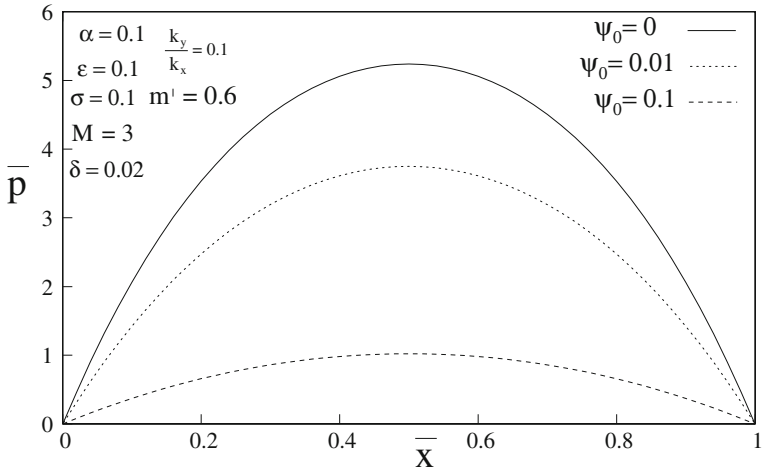

Fig. 3 Effect of ψ_0 on $\bar{p}$

surface roughness decrease the leakage of lubricant. Due to this, the lubricant is retained in the system. This increases the pressure distribution between the plates. Figure 3 shows the variation of $\bar{p}$ with $\bar{x}$ for different values of the permeability parameter ψ_0. As ψ_0 increases the pressure decreases. Figure 4 indicates the variation of $\bar{p}$ with $\bar{x}$ for different values of α. Variation of squeeze film pressure for different values of ϵ is shown in the Fig. 5 and it can be observed that positively

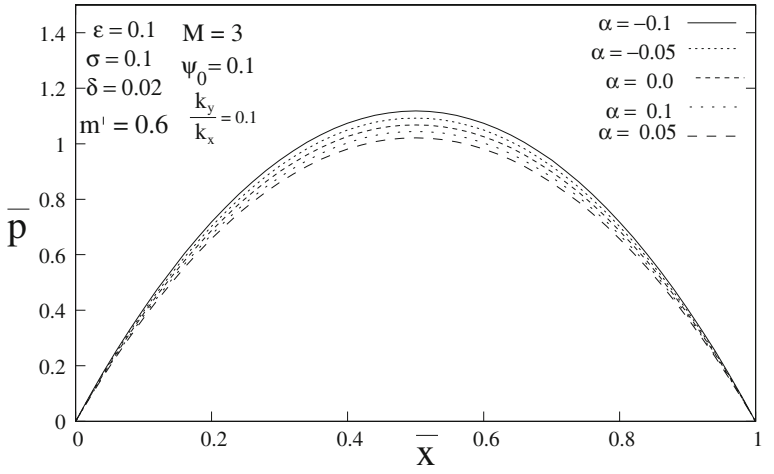

Fig. 4 Effect of α on $\bar{p}$

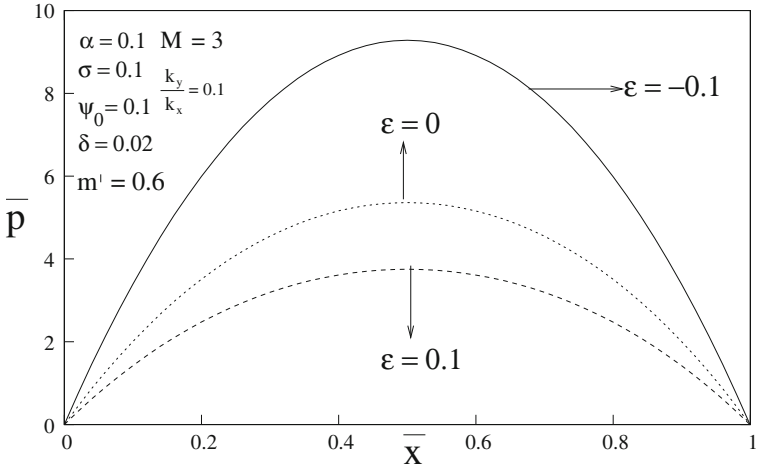

Fig. 5 Effect of ϵ on $\bar{p}$

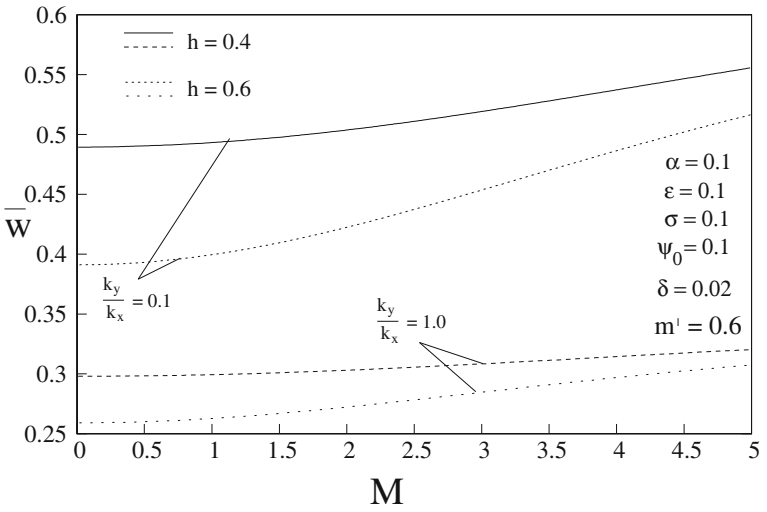

Fig. 6 Effect of k_y/k_x on $\bar{W}$

skewed roughness decreases the squeeze film pressure $\bar{p}$ whereas negatively skewed roughness increases the pressure.

Figure 6 indicates the variation of load carrying capacity with Hartmann number M. As Hartmann number M increases the load carrying capacity also increases for both isotropic and anisotropic porous materials. Figures 7 and 8 indicate the variation of $\bar{h}$ as a function of $\bar{T}$ for different values of M for both isotropic and anisotropic cases. The time height relationship for nonporous case is shown in Fig. 9.

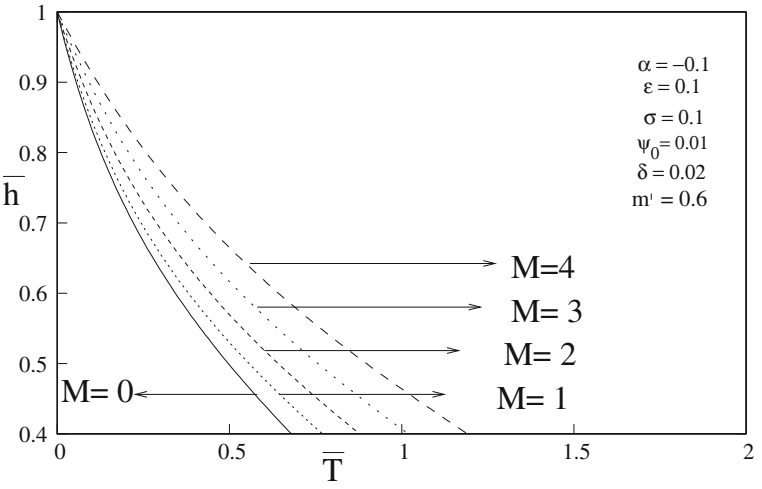

Fig. 7 Effect of M on $\bar{h}$, $k_y/k_x = 0.1$

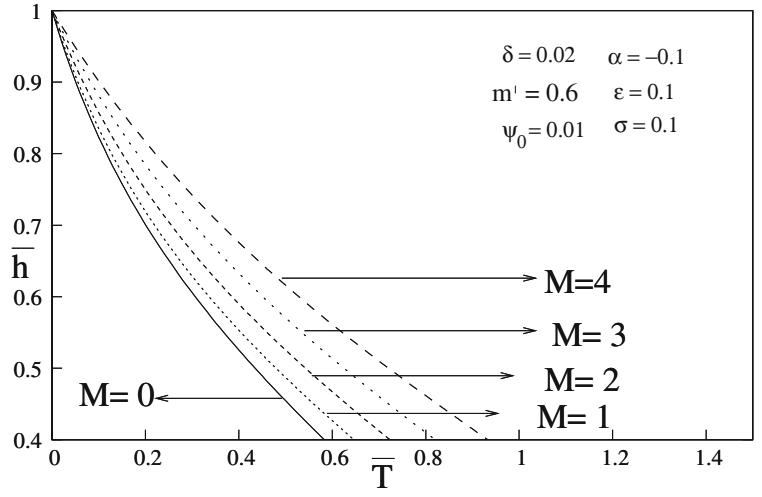

Fig. 8 Effect of M on $\bar{h}$, $k_y/k_x = 1$

5 Conclusions

In this paper, we have studied squeeze film lubrication between an anisotropic porous plate and a plate with surface roughness. Further, the effect of applied magnetic field on the performance of lubrication mechanism is seen. Variation of squeeze film

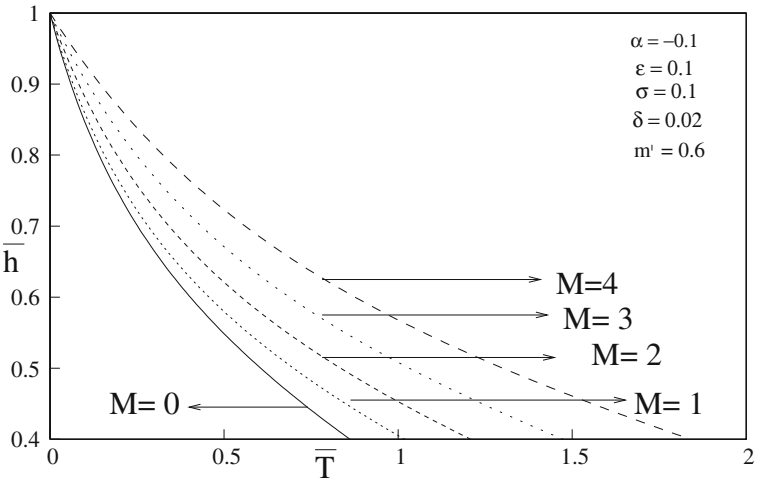

Fig. 9 Effect of M on $\bar{h}$, $\psi_0 = 0$

pressure, load carrying capacity, and response time under the influence of different parameters are noted. It is observed that positively skewed roughness decreases the squeeze film pressure. This study may be useful in understanding the mechanism of synovial joints.

References

1. Christensen, H.: Stochastic models for hydrodynamic lubrication of rough surfaces. Proc. Inst. Mech. Eng. J. J. Eng. Tribol. **184**(55), 1013–1022 (1969–1970)
2. Prakash, J., Tiwari, K.: An analysis of the squeeze film between porous rectangular plates including the s urface roughness effects. J. Mech. Eng. Sci. **24**(1), 45–49 (1982)
3. Bujurke, N.M., Naduvinamani, N.B.: A note on squeeze film between rough anisotropic porous rectangular plates. Wear **217**, 225–230 (1998)
4. Andharia, P.I., Gupta, J.L., Deheri, G.M.: Effect of surface roughness on hydrodynamic lubrication of slider bearings. Tribol. Trans. **44**(2), 291 (2001)
5. Lin, J.-R.: Magnetohydrodynamic squeeze film characteristics for finite rectangular plates. Ind. Lubr. Tribol. **55**(2), 84–89 (2003)
6. Bujurke, N.M., Naduvinamani, N.B., Basti, D.P.: Effect of surfaceroughness on magnetohydrodynamic squeezefilm characteristics between finite rectangular plates. Tribol. Int. **44**, 916–921 (2011)
7. Fathima, S.T., Naduvinamani, N.B., Shivakumar, H.M., Hanumagowda, B.: A study on the performance of hydromagnetic squeeze film between anisotropic porous rectangular plates with couplestress fluid. Tribol. Int. **9**(1), 1–9 (2014)

A Numerical Study on Heat Transfer Characteristics of Two-Dimensional Film Cooling

Vashista G. Ademane, Vijaykumar Hindasageri and Ravikiran Kadoli

Abstract Determination of reference temperature and heat transfer coefficient in case of three temperature problems such as film cooling is one of the fundamental tasks in the design of gas turbines. In the present work, a two-dimensional numerical simulation is carried out for flat surface with 35° angle of injection from slot in case of film cooling problem. The reference temperature, which is represented as film cooling effectiveness, and heat transfer coefficient on the flat surface for different blowing ratio are studied. Heat transfer coefficient obtained from the present simulation is compared with the experimental results from the literature and found to be matching at lower blowing ratios. Turbulence intensity is found to a major contributor in enhancing the heat transfer coefficient. There is an increase in heat transfer with the blowing ratio due to increased turbulence intensity is observed.

Keywords Film cooling · Effectiveness · Heat transfer coefficient
Turbulence intensity

1 Introduction

The efficiency of gas turbine engines mainly depends upon the temperature of the inlet hot gas. But there is a limitation on the inlet temperature due to the thermal stresses developed in turbine blades. So blades are cooled by taking a part of compressed air and passing them from inside of the blade surface and ejecting out through small holes into the mainstream. The coolant air coming out from the blade surface will

V. G. Ademane · R. Kadoli
Department of Mechanical Engineering, National Institute of Technology, Surathkal 575025, Karnataka, India

V. Hindasageri (✉)
Department of Mechanical Engineering, K.L.S's Vishwanathrao Deshpande Rural Institute of Technology, Haliyal 581329, Karnataka, India
e-mail: vkhnitk@gmail.com

D. Srinivasacharya and K. S. Reddy (eds.), *Numerical Heat Transfer and Fluid Flow*, Lecture Notes in Mechanical Engineering,
https://doi.org/10.1007/978-981-13-1903-7_70

create a layer of low-temperature fluid which is a well-established technique known as film cooling.

Major parameters which affect the performance of film cooling are blowing ratio, density ratio, injection angle, hole geometry, turbulence intensity, and mainstream Reynolds number. These parameters are studied on flat surfaces with jet injecting at certain angles to the surface. The experimental work on flat surface film cooling was done by many researchers. Experiments on film cooling have been conducted by [1] from circular holes and later [2] reported heat transfer study. Effect of boundary layer thickness, Reynolds number and free stream turbulence intensity on film cooling is reported by [3, 4] conducted experiment and numerical study.

With the development of different computational techniques and turbulence models, the effort involved in the analysis of the film cooling has reduced. A three-dimensional numerical studies on film cooling was conducted by [5].

Studies are reported on slot jet film cooling by [6, 7], where the secondary air was injected at different angles through a rectangular slot on a flat surface. A 2D numerical simulation of film cooling was carried out by [8, 9]. Numerical and experimental work with various slot angles was performed by [10] and they found that for jet angle larger than 40°, the formation of a recirculation bubble in the downstream of jet. They concluded that the optimum value for the injection angle lies between 30° and 40° to the mainstream. Recently the study of [8] was extended by [11] and conducted numerical investigation for two different Reynolds number with density ratio varying from 1.1 to 5 and blowing ratios of 1–3. They suggested a relation that yields an optimum film cooling effectiveness based on velocity ratio which is nearly equal to sine of the angle of injection.

Even though there are numerous work in the area of film cooling still there is a lack of fundamental understanding on the physics of the fluid behaviour. Many researchers reported on film cooling effectiveness but a few study have been conducted on the heat transfer between the fluid and the surface.

In the present work, a two-dimensional numerical study on a flat surface film cooling is conducted using a commercial simulation software, ANSYS FLUENT. The film cooling effectiveness and the heat transfer coefficient is computed for different blowing ratios. Heat transfer coefficient is compared with the experimental results available in the literature. Effect of turbulence level on the variation of heat transfer coefficient is discussed.

2 Problem Formulation and Boundary Conditions

The domain for computational study in the present work is shown in Fig. 1. The geometrical dimensions for the domain are considered based on the work of [5]. The secondary fluid is made to enter through the slot of width D, into the mainstream with an angle of 35° to the surface. The value of D is considered as 5 mm in the present study. The grid required for the computational domain is generated using ANSYS ICEM with non-uniform structured grid, as shown in Fig. 2. Capturing the turbulent

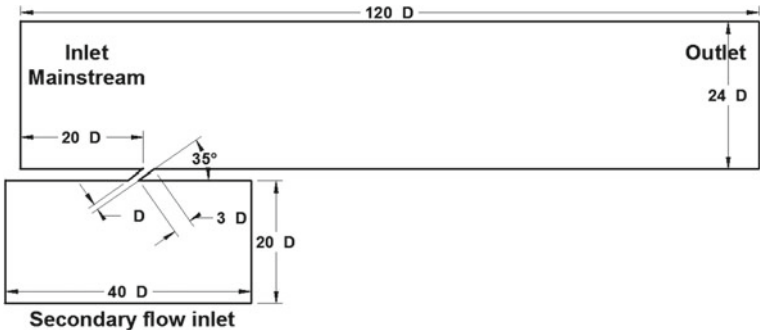

Fig. 1 Geometry of the flow domain considered for the present study

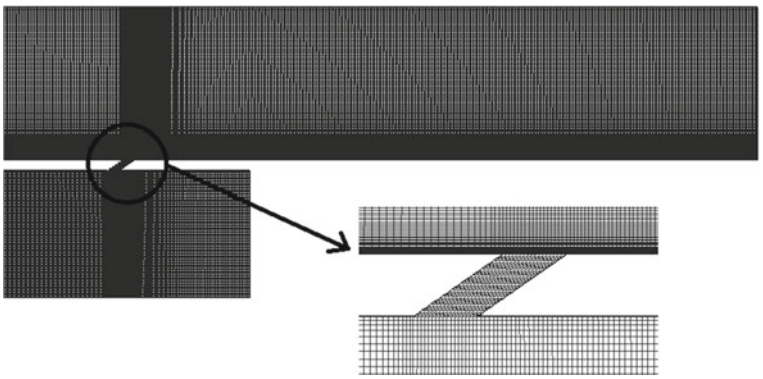

Fig. 2 A structured mesh generated with zoomed view near the mixing region of fluids

boundary layer needs very fine grid size near the wall with a $y+$ value close to unity. The zoomed view in Fig. 2 shows the formation of very fine grid near the wall.

Air is used as working fluid in the present simulation and the solution domain is considered as a 2D, steady, incompressible and turbulent flow. The governing equations solved for continuity, momentum and energy conservation and the Reynolds stress for turbulence are modeled by using Realizable k-ε turbulence model. Second-order upwind interpolation scheme is used for the discretization and equations are solved by using SIMPLE algorithm procedure.

In this study, the velocity and temperature are specified at the inlet of mainstream and outlet is considered as constant zero gauge pressure. The secondary flow is introduced as mass flow inlet into the plenum. A uniform velocity of 20 m/s with a temperature of 300 K is mentioned at the inlet of both primary and the secondary. Turbulence intensity is given 2% with length scale as 1/10th of the inlet extent as mentioned in [5]. Other boundaries are considered as wall and the turbulence scalars are solved by using enhanced wall treatment near wall boundaries.

3 Result and Discussions

3.1 Heat Transfer Coefficient

The heat transfer coefficient is calculated as

$$h = \frac{q''}{(T_w - T_\infty)} \tag{1}$$

where q'' is the heat flux applied on the wall surface and T_w is the computed wall temperature. While calculating the heat transfer coefficient, the temperature of the mainstream and the secondary fluid is maintained equal and is denoted as T_∞. In the case where temperature of primary and secondary flows are different, the fluid temperature has to be replaced by the corresponding reference temperature.

Heat transfer coefficient is represented in terms of ratio of heat transfer coefficient with film cooling to the without film cooling. Figure 3a, b shows the distribution of heat transfer coefficient for flat surface in the downstream direction of injection for blowing ratios of 0.5 and 1.0, respectively. Also, the results are compared with the experimental results of [2] for the case of film cooling through circular holes. When the blowing ratio is very low, the heat transfer is not greatly affected due to the secondary injection. As shown in Fig. 3a, the heat transfer coefficient is nearly equal to with that of without film cooling. The comparison of the present simulation with the experimental result of three-dimensional film cooling shows similar behaviour. In the region immediately downstream of injection, there is a slight decrease in the heat transfer can be observed in both experimental as well as numerical results. The addition of mass flux into the boundary layer results in decreasing the heat transfer near to the injection region, but in the far downstream this effect will disappear making the ratio equal to 1.

In Fig. 3b, a slight decrease in the heat transfer can be observed near the jet exit in the experimental result of [2], but in the present simulation, there is an increase in heat transfer to 1.3 times that of without injection. The reason may be attributed to the spreading of the jet in lateral direction will reduce the velocity of the jet and hence heat transfer would be less.

A comparison of heat transfer coefficient obtained from the present simulation for blowing ratio from 0.5 to 2.0 is shown in Fig. 4. When the blowing ratio is below 1.0, there is a small increase in heat transfer coefficient in the immediate downstream of injection is observed. But at higher blowing ratio, there is significant increase in the heat transfer coefficient is noted compared to the case without injection. Not only near the jet exit but in the far downstream but also heat transfer has increased to almost 1.6–1.8 times higher than that of without injection.

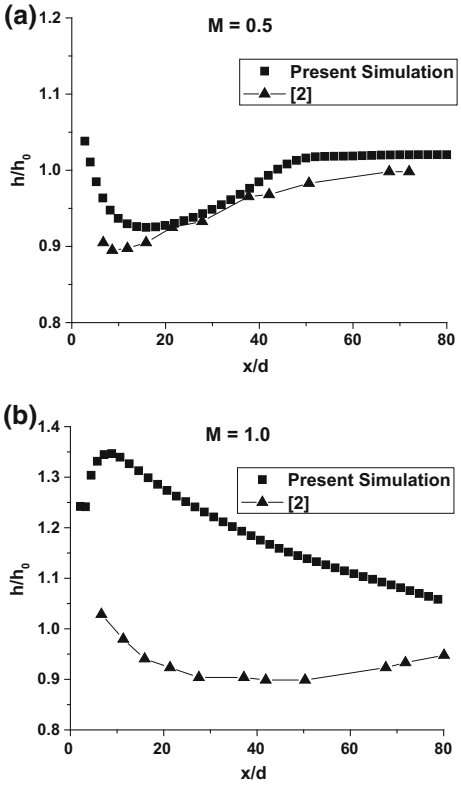

Fig. 3 Heat transfer coefficient distribution along the flat surface form the injection point

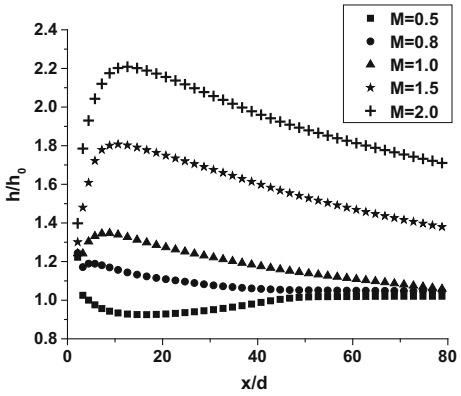

Fig. 4 Comparison of heat transfer coefficient for different blowing ratios

3.2 Turbulence Intensity

One of the major reasons behind the increase in heat transfer coefficient is due to turbulence created at the mixing region. Increase in the blowing ratio will increase

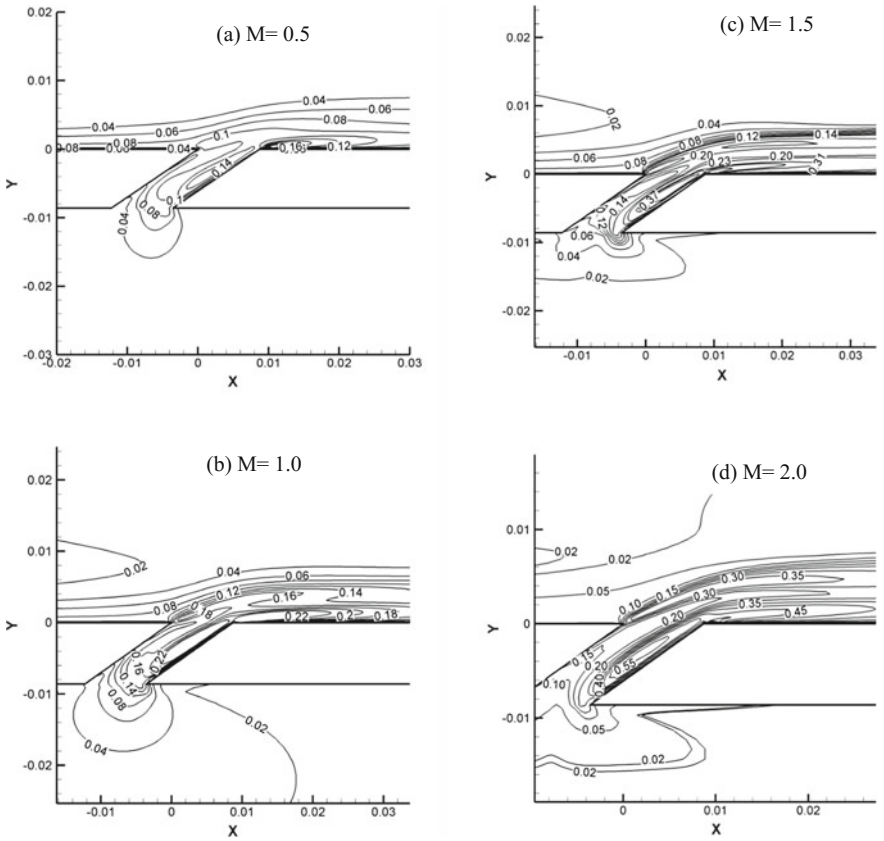

Fig. 5 Turbulence level in the region of interaction of two streams for different blowing ratios

the turbulence due to increased velocity of secondary fluid. And hence heat transfer increases. Figure 5a–d shows the distribution of turbulence intensity in the region of interaction of the two fluid streams for blowing ratios of 0.5, 1.0, 1.5 and 2.0. The turbulence intensity at the free stream is given as 2%. Increased turbulence level is observed at the jet exit and in the immediate downstream region of the flow near the surface.

When the blowing ratio is at 0.5, a slight increase in the turbulence level of 12–14% is observed and it has covered a very small region as shown in Fig. 5a. Since the addition of coolant fluid will reduce the temperature of the boundary layer, at lower blowing ratio, there is a decrease in heat transfer coefficient is identified as shown in Fig. 3a. As the blowing ratio is increased to 1.0, turbulence intensity is also increased to 20–22%. When the blowing ratio is increased to 1.5 and 2.0, there is a drastic increase in the turbulence level is identified and is greater than 30 and 40%, respectively. When Figs. 4 and 5 are compared, it can be clearly observed that as

the turbulence intensity is increased, there is an increase in heat transfer coefficient. This increased turbulence level can be attributed to the increase in the blowing ratio.

4 Conclusion

A two-dimensional numerical simulation is carried out for film cooling on flat surface with inclined slot of 35° angle of injection. The film cooling effectiveness and the heat transfer coefficient are investigated for different blowing ratios and results for heat transfer coefficient are compared with the experimental results from the literature. Following conclusions were made from the present study,

- The heat transfer coefficient computed form two-dimensional analysis matches with the experimental results only at lower blowing ratios.
- At higher blowing ratios there is a significant increase in heat transfer coefficient than the experimental results.
- Primary reason behind the increase of heat transfer coefficient is due to increased turbulence intensity at the mixing region of two fluids.
- Increase in the secondary flow velocity induces turbulence in the flow.

References

1. Goldstein, R.J., Eckert, E.R.G., Ramsey, J.W.: Film cooling with injection through holes: adiabatic wall temperatures downstream of a circular hole. J. Eng. Power **90**(4), 384–393 (1968)
2. Eriksen, V.L., Goldstein, R.J.: Heat transfer and film cooling following injection through inclined circular tubes. J. Heat Transf. **96**(2), 239–245 (1974)
3. Kadotani, K., Goldstein, R.J.: Effect of mainstream variables on jets issuing from a row of inclined round holes. J. Eng. Power **101**(2), 298–304 (1979)
4. Bergeles, G., Gosman, A.D., Launder, B.E.: Double-row discrete-hole cooling: an experimental and numerical study. J. Eng. Power **102**(2), 498–503 (1980)
5. Walters, D.K., Leylek, J.H.: A systematic computational methodology applied to a three-dimensional film-cooling flow field. ASME J. Turbomach. **119**(4), 777–785 (1997)
6. Papell, S.S.: Effect on gaseous film cooling of coolant injection through angled slots and normal holes. Technical Note D-299, NASA Lewis Research Center (1960)
7. Fitt, A.D., Ockendon, J.R., Jones, T.V.: Aerodynamics of slot-film cooling: theory and experiment. J. Fluid Mech. **160**, 15–27 (1985)
8. Sarkar, S., Bose, T.K.: Numerical simulation of a 2-D jet-cross flow interaction related to film cooling applications: effects of blowing rate, injection angle and free-stream turbulence. Sadhana **20**(6), 915–935 (1995)
9. Kassimatis, P.G., Bergeles, G.C., Jones, T.V., Chew, J.W.: Numerical investigation of the aerodynamics of the near-slot film cooling. Int. J. Numer. Meth. Fluids **32**(1), 85–104 (2000)
10. Jia, R., Sundén, B., Miron, P., Léger, B.: A numerical and experimental investigation of the slot film-cooling jet with various angles. J. Turbomach. **127**(3), 635–645 (2005)
11. Singh, K., Premachandran, B., Ravi, M.R.: A numerical study on the 2d film cooling of a flat surface. Numer. Heat Transf. Part A Appl. **67**(6), 673–695 (2015)

Instability Conditions in a Porous Medium Due to Horizontal Magnetic Field

A. Benerji Babu, N. Venkata Koteswararao and G. Shivakumar Reddy

Abstract Oscillatory convective instability in a porous medium due to horizontal magnetic field was studied using the Darcy–Lapwood–Brinkman model with Boussinesq approximation is used to study linear stability analysis. Finite amplitude solutions are obtained for force-free boundary conditions. An explicit expression at the onset of convection in terms of leading parameters of the system is obtained.

Keywords Darcy–Lapwood–Brinkman model · Linear stability · Bifurcation point · Horizontal magnetic field

1 Introduction

Convection in a plane horizontal fluid heated from below and cooled from above is a typical problem in hydrodynamic stability theory. Thompson [1] and Chandrashekar [2] were studied the effect of vertical magnetic field on the onset of convection. The margin of monotones instability is pretentious only by the vertical component of the magnetic field. However, the property of isotropy is kept in the case of a purely vertical magnetic field. Magnetoconvection in an electrically conducting fluid in a nonporous medium has been studied widely by Chandrasekhar, S., Proctor and Weiss [3], Tagare [4–6], Jones and Roberts [7], Kloosterziel and Carnevale [8], and Brand et al. [9, 10]. Palm et al. [11] investigated Rayleigh–Benard convection problem in a porous medium. Brand and Steinberg [12] investigated convecting instabilities in binary liquid in a porous medium. Palm et al. [11] and Brand et al. [12] have made use of Darcy's law. However, horizontal magnetoconvection in a porous medium has not received any attention in spite of its applications in geophysical and planetary fluid dynamics. In this paper, we showed that convection arises in the form of rolls with the axes parallel to horizontal magnetic field.

A. Benerji Babu (✉) · N. Venkata Koteswararao · G. Shivakumar Reddy
Department of Mathematics, National Institute of Technology Warangal, Warangal, Telangana, India
e-mail: benerji77@gmail.com

D. Srinivasacharya and K. S. Reddy (eds.), *Numerical Heat Transfer and Fluid Flow*, Lecture Notes in Mechanical Engineering,
https://doi.org/10.1007/978-981-13-1903-7_71

2 Basic Equations

The thermally and electrically conducting fluid in an unbounded horizontal layer of a thinly packed porous medium with a magnetic field "H_o" of depth "d" is in the horizontal x-direction. This layer is heated from below, and the top and bottom bounding surfaces of the layer are assumed to be force-free. The temperature variation across the force-free boundaries is "$\Delta T'$". The flow in the thinly packed porous medium is governed by the Darcy–Lapwood–Brinkman model. The dimensionless equations are

$$\nabla.\overline{V} = 0,\ \nabla.\overline{H} = 0, \tag{1}$$

$$\frac{1}{M^2\phi Pr_1}\left[\frac{\partial \overline{V}}{\partial t} + \frac{1}{\phi}(\overline{V}.\nabla)\overline{V}\right] - Q\frac{Pr_2}{Pr_1}(\overline{H}.\nabla)\overline{H} - Q\frac{\partial \overline{H}}{\partial y}$$
$$= -\nabla\left(\frac{P}{MPr_1} + \frac{Q}{2}\frac{Pr_2}{Pr_1}|\overline{H}|^2 + QH_y\right) - \frac{1}{MD_a}\overline{V} + \frac{\Lambda}{M}\nabla^2\overline{V} + R\theta\hat{e}_z, \tag{2}$$

$$\frac{\partial \theta}{\partial t} + \frac{1}{M}(\overline{V}.\nabla)\theta = \frac{w}{M} + \nabla^2\theta, \tag{3}$$

$$\phi\frac{Pr_2}{Pr_1}\frac{\partial \overline{H}}{\partial t} - M\nabla^2\overline{H} = \nabla\times(\overline{V}\times\hat{e}_y) + \frac{Pr_2}{Pr_1}\nabla\times(\overline{V}\times\overline{H}). \tag{4}$$

Using Eqs. (2), (3), and (4) can be reduced in a form

$$Lw = N, \tag{5}$$

$$L = (D_\phi D_{Pr_1} - Q\partial_y^2)D\nabla^2 - \frac{R}{M}\nabla_h^2 D_\phi, \tag{6}$$

$$N = QD\nabla^2\frac{Pr_2}{Pr_1}\partial_y[(\overline{H}.\nabla)w - (\overline{V}.\nabla)H_z]$$
$$+ DD_\phi\hat{e}_z.\left\{[\frac{1}{M^2\phi^2 Pr_1}\nabla\times[(\overline{V}.\nabla)\overline{\omega} - (\overline{\omega}.\nabla)\overline{V}]]\right.$$
$$\left. - [Q\frac{Pr_2}{Pr_1}\nabla\times[(\overline{H}.\nabla)\overline{J} - (\overline{J}.\nabla)\overline{H}]]\right\} - \frac{R}{M}\nabla_h^2 D_\phi(\overline{V}.\nabla)\theta, \tag{7}$$

$$\nabla_h^2 = (\frac{\partial^2}{\partial x^2} + \frac{\partial^2}{\partial y^2}),\ D = \left(\frac{\partial}{\partial t} - \nabla^2\right),\ D_\phi = \left(\phi\frac{Pr_2}{Pr_1}\frac{\partial}{\partial t} - M\nabla^2\right),$$

$$D_{Pr_1} = \left(\frac{1}{M^2\phi Pr_1}\frac{\partial}{\partial t} + \frac{1}{MD_a} - \frac{\Lambda}{M}\nabla^2\right).$$

3 Boundary Condition

For absolutely conducting upper and lower borders, $z = 0$ and $z = 1$ with $\theta = 0$, $H_z = 0$ and $w = 0$.

4 Linear Stability Analysis

The stability of the problem is by considering

$$w = W(z)e^{i(lx+my)+pt}. \tag{8}$$

In $Lw = 0$, we get an equation

$$\begin{aligned}&\left\{(D^2-q^2-p)\left(M(D^2-q^2)-p\phi\frac{Pr_2}{Pr_1}\right)(D^2-q^2)\left[\frac{\Lambda}{M}(D^2-q^2)\right.\right.\\&\left.\left.-\frac{1}{MD_a}-\frac{p}{M^2\phi Pr_1}\right]+\frac{Rq^2}{M}\left(M(D^2-q^2)-p\phi\frac{Pr_2}{Pr_1}\right)\right\}W\\&=\{-Qm^2(D^2-q^2)(D^2-q^2-p)\}W.\end{aligned} \tag{9}$$

We assume force-free boundary conditions, and then $W = D^2W = 0$ on $z = 0$, $z = 1$. Thus, we can assume $W = \sin \pi z$.

4.1 *Marginal Stability When Rayleigh Number* R *Is a Dependent Variable*

Putting $W(z) = \sin \pi z$ and $p = i\omega$ into Eq. (9), we get

$$R = \frac{M}{q^2}\left[A_1 + i\omega(A_2\omega^2 + A_3)\right], \tag{10}$$

$$\begin{aligned}A_1 = K\left[\left(m^2MQ\delta^4+\frac{M\delta^6}{Da}+M\delta^8\Lambda\right)+\left(\frac{\delta^4\Lambda\phi^2Pr_2^2}{MPr_1^2}+\frac{\delta^2\phi^2Pr_2^2}{DaMPr_1^2}\right.\right.\\\left.\left.+\frac{m^2Q\phi^2Pr_2}{Pr_1}-\frac{\delta^4}{\phi Pr_1}\right)\omega^2-\frac{\phi Pr_2^2}{M^2Pr_1^3}\omega^4\right],\end{aligned} \tag{11}$$

$$A_2 = K\left[\frac{\delta^2\phi Pr_2^2}{M^2Pr_1^3}+\frac{\phi^2Pr_2^2}{DaMPr_1^2}+\frac{\delta^2\Lambda\phi^2Pr_2^2}{MPr_1^2}\right], \tag{12}$$

$$A_3 = K\left[m^2MQ\delta^2+\frac{M\delta^4}{Da}+M\delta^6\Lambda+\frac{\delta^6}{\phi Pr_1}-\frac{m^2Q\phi\delta^2Pr_2}{Pr_1}\right]. \tag{13}$$

where $K = \frac{\delta^2}{\left(M^4\delta^4+\omega^2\phi^2\frac{Pr_2^2}{Pr_1^2}\right)}$, $\delta^2 = (\pi^2 + q^2)$, and $q^2 = l^2 + m^2$.

4.1.1 Stationary Convection ($\omega = 0$)

Substituting $\omega = 0$ in Eq. (12), we get

$$R_s = \frac{\delta_s^2}{q_s^2}\left[\delta_s^2\left(\frac{1}{Da} + \delta_s^2\Lambda\right) + Qm^2\right], \tag{14}$$

where R_s is the value of Rayleigh number for stationary convection. The critical Rayleigh number R_s gives the onset of stationary convection at Pitchfork bifurcation. Take $l^2 = x$, $m^2 = y$ then $\delta^2 = x + y + \pi^2$ and $q^2 = x + y$. Take $x = 0$,

$$Ry = (y + \pi^2)Q + (y + \pi^2)^2\left[\frac{1}{Da} + (y + \pi^2)\Lambda\right] \tag{15}$$

differentiate w.r.t y and substitute R in the above equation. We get

$$2\Lambda\left(\frac{m}{\pi}\right)^6 + \left(3\Lambda + \frac{Q}{\pi^2} + \frac{1}{Da\pi^2}\right)\left(\frac{m}{\pi}\right)^4 - \frac{Q}{\pi^4}\left(\frac{m}{\pi}\right)^2 = \frac{Q}{\pi^4} + \frac{1}{Da}\pi^2 + \Lambda \tag{16}$$

$m_{sc} = \left(\frac{Q\pi^2}{2\Lambda}\right)^{\frac{1}{6}}$ and the critical Rayleigh number $R_{sc} \approx \left(\frac{Q\pi^2}{2\Lambda}\right)^{\frac{2}{3}}$.

4.1.2 Oscillatory Convection ($\omega^2 > 0$)

For oscillatory convection,

$$A_2\omega^2 + A_3 = 0 \tag{17}$$

$$\omega^2 = \frac{-M^2\phi^2 Pr_1^2\left[M\phi Pr_1(Dam^2Q + \delta^2 + Da\delta^4\Lambda) + Da(\delta^4 - m^2QPr_2)\right]}{\phi^2 Pr_2^2\left(Da\delta^2 + M(1 + Da\delta^2\Lambda)\phi Pr_1\right)}, \tag{18}$$

A necessary condition for $\omega^2 > 0$ is $\frac{Pr_2}{Pr_1} > \frac{1}{\phi}$. Substituting ω^2 into real part of Eq. (10) by taking $Da \to 0$, we get

$$R_o = \frac{\delta^2}{B_2 q_0^2}\left[\delta_0^4 + Qm^2B_1\right] \tag{19}$$

where $B_1 = \frac{M^2Pr_1^2}{(MPr_1+\phi Pr_2)(1+M\Lambda\phi Pr_1)}$,

$$B_2 = \frac{\phi^3 Pr_2^2}{(MPr_1 + \phi Pr_2)(1 + M\Lambda\phi^2 Pr_2)}.$$

However, it is not sufficient condition and we must have another condition

$$Q > \frac{\frac{M\delta_o^2}{Da} + \delta_o^2\left(M\Lambda + \frac{1}{\phi Pr_1}\right)}{m^2\left(\phi\frac{Pr_2}{Pr_1} - M\right)} \tag{20}$$

$$m_c = \left[\frac{(QPr_2 - MPr_1)Q\phi}{(1 + M\Lambda\phi Pr_1)}\right]^{\frac{1}{2}} \text{ and } m_{sc} = \left(\frac{Q\pi^2}{2\Lambda}\right)^{\frac{1}{6}}$$

From the monotonic dependence of m_c and m_{sc} on Q, we may conclude that for $Pr_2 > Pr_1$, there exist a $Q(M, \Lambda, \phi, Pr_1, Pr_2)$ such that for $Q < Q(M, \Lambda, \phi, Pr_1, Pr_2)$, the onset of first instability will be stationary convection at Hopf bifurcation. $Q(M, \Lambda, \phi, Pr_1, Pr_2)$ is a function of Prandtl numbers Pr_1 and Pr_2 and for $Q = Q(M, \Lambda, \phi, Pr_1, Pr_2)$ and $R_{ct} = R_{oc}(q_{oc}) = R_{sc}(q_{sc})$ but $q_{oc} \neq q_{sc}$. The critical wave number obtained for $q = q_{oc}$ forms the following equation:

$$2\left(\frac{m}{\pi}\right)^6 + 3\left(\frac{m}{\pi}\right)^4 = 1 + \frac{Q}{\pi^2}\frac{M^2Pr_1^2}{(MPr_1 + \phi Pr_2)(1 + M\Lambda\phi Pr_1)}. \tag{21}$$

From the above equation, we will not give positive roots for $Pr_2 \gg Pr_1$. For large Chandrasekhar number $Q \to \infty$, we have

$$m_{oc} = \left(\frac{Q\pi^4M^2Pr_1^2}{2(MPr_1 + \phi Pr_2)(1 + M\Lambda\phi Pr_1)}\right)^{\frac{1}{6}} \text{ and } R_{oc} = \frac{1}{B_2}\left(\frac{QB_1\pi^4}{2}\right)^{\frac{1}{6}}. \tag{22}$$

4.2 Marginal Stability When Rayleigh Number R Is an Independent Variable

Putting $W = \sin\pi z$ into (11), we get a third-order polynomial in p of the following form:

$$p^3 + Bp^2 + Cp^2 + D = 0, \tag{23}$$

where

$$B = \delta^2 + Pr_1\left(M\left(\frac{1}{Da} + \delta^2\Lambda\right)\phi + \frac{M\delta^2}{\phi Pr_2}\right), \tag{24}$$

$$C = \frac{1}{DaM\phi Pr_1}(Da\delta^6 + M\delta^2(Dam^2Q + \delta^2 + Da\delta^4\Lambda)\phi Pr_1 + (-Daq^2R + \delta^4 + Da\delta^6\Lambda)\phi^2Pr_2), \tag{25}$$

$$D = \frac{1}{\delta^2 Pr_2} M^2(-q^2 R\delta^2 + m^2 Q\delta^4 + \delta^6 Da + \delta^8 \Lambda) Pr_1^2. \tag{26}$$

In cubic polynomial (23), B is always positive. The classification of stability modes of the system is the roots of Eq. (23). Unstable means there exists at least one root of Eq. (23) with $Re(p) > 0$; stable means all roots of Eq. (23) with $Re(p) < 0$. We get pitchfork difurcation when $D = 0$ and $BC - D > 0$. We get the Hopf bifurcation when $D > 0$ and $BC - D = 0$.

4.2.1 Stationary Convection ($w = 0$)

When $p = 0$, the cubic equation becomes $D = 0$

$$\frac{1}{\delta^2 Pr_2} M^2(-q^2 R\delta^2 + m^2 Q\delta^4 + \delta^6 Da + \delta^8 \Lambda) Pr_1^2 = 0$$

$$R_s = \frac{\delta^2}{q^2}\left[Qy + \frac{1}{Da}(y + \pi^2) + \Lambda(y + \pi^2)^2\right], \tag{27}$$

Take $x = 0$ then $R_s = \frac{y+\pi^2}{y}\left(\delta^2\left(\frac{1}{Da} + \delta_\Lambda^2\right) + Qm^2\right)$ minimizing R_s by differentiating w.r.t y

$$R = 3\Lambda(y + \pi^2)^2 + 2\left(\frac{1}{Da}\right)(y + \pi^2) - Q\pi^2,\ m_{sc} = \left[\left(\frac{R}{3\Lambda}\right)^{\frac{1}{2}} - \pi^2\right]^{\frac{1}{2}}.$$

where $Da \to \infty$. We consider only positive values of m. We get critical Chandraseker number

$$Q = Q_{sc}(R) = \frac{9\pi^2 \Lambda R - 4\sqrt{3\Lambda} R}{3(\sqrt{R} - \sqrt{3}\pi^2\sqrt{\Lambda})}. \tag{28}$$

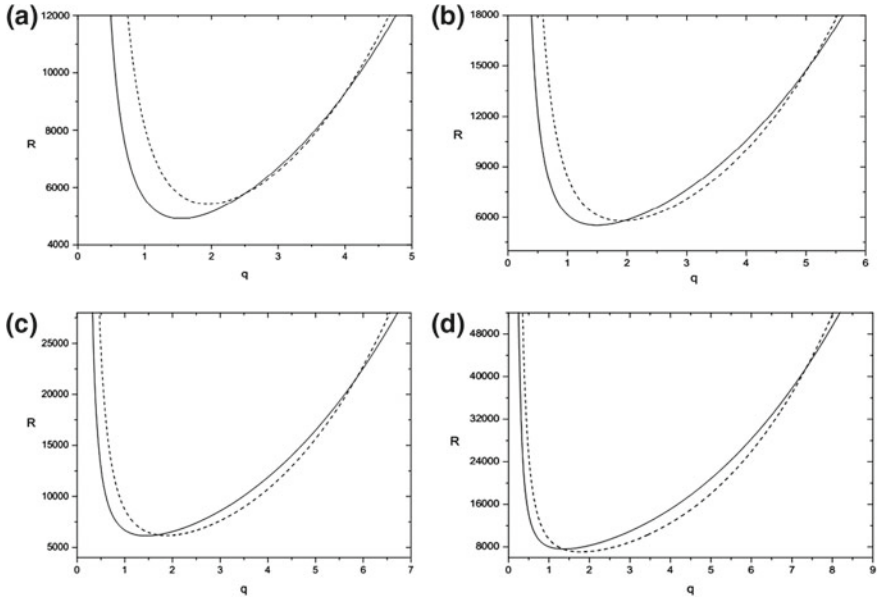

Fig. 1 Solid lines represent stationary convection R_s and dotted lines represent oscillatory R_0. Numerically calculated marginal stability curves are plotted in $(R-q)$-plane for $Da = 1500$; $\Lambda = 2$; $M = 0.9$; $Pr_1 = 1$; $Pr_2 = 1.65$; $\varphi = 0.85$ **a** $Q = 550$, **b** $Q = 650$, **c** $Q = 750$, **d** $Q = 100$

4.2.2 Oscillatory Convection ($w^2 > 0$)

The classification of the modes of the system is given in [12]. The positive D is not enough to discuss the system stability. The sign of $BC - D$ is along with the sign of D for the stability of the system. Thus, $BC - D = 0$ given $\Lambda(y + \pi^2)^3 + QB_1 y(y + \pi^2)^2 - RB_2 y = 0$. Comparing Eq. (27) with (15), we get $Q = QB_1$ and $R = RB_2$. We get

$$m_{oc} = \left[\left(\frac{RB_1}{3\Lambda}\right)^{\frac{1}{2}} - \pi^2\right]^{\frac{1}{2}} \text{ and } Q_{oc} = \frac{9\pi^2 \Lambda RB_1 - 4\sqrt{3\Lambda}RB_1}{B_2 3\left(\sqrt{RB_1} - \sqrt{3}\pi^2\sqrt{\Lambda}\right)} \tag{29}$$

5 Conclusion

We investigated linear stability analysis of convection in a porous medium due to horizontal magnetic field at the onset of convection identified. We determine the stability regions for stationary convection for force-free boundary conditions. Evolved the parameter values that were emerge rolls at the onset of convection. We get Takens–Bogdanov bifurcation point and co-dimensional two bifurcation points. Figures 1

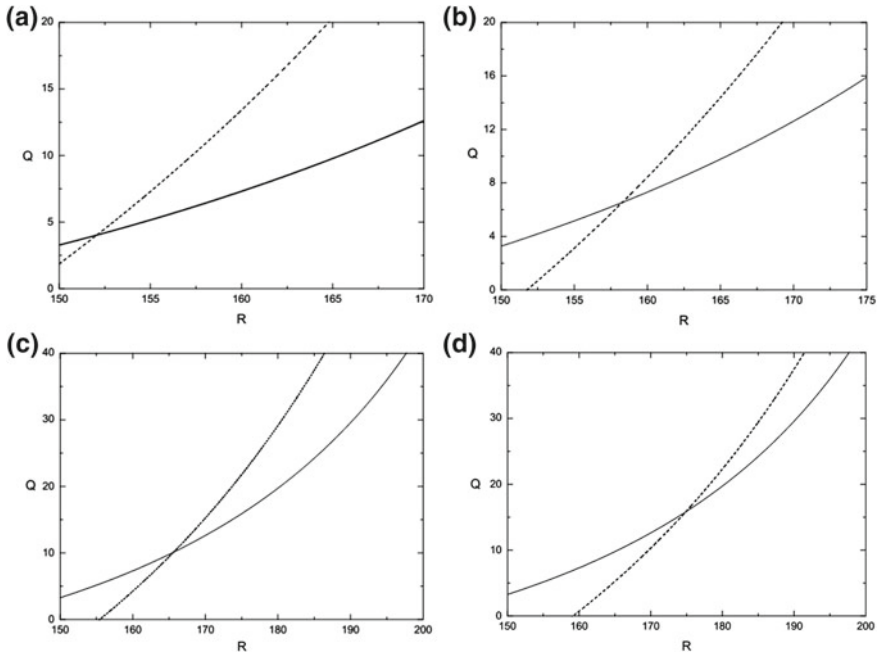

Fig. 2 Stationary convection Q_s curves are solid lines and Oscillatory convection Q_o are dotted lines at $M = 1$, $Pr_2 = 4$, $\phi = 0.9$, $\Lambda = 0.85$ **a** $Pr_1 = 1.85$, **b** $Pr_1 = 1.9$, **c** $Pr_1 = 1.95$, **d** $Pr_1 = 2$.

and 2 show that the effects of Q and porous parameters made the system more stable. The presence of horizontal magnetic field changes the flow structure from monocellularity to multicellularity convective patterns.

References

1. Thompson, W.B.: The London, Edinburgh, and Dublin Philosophical and Science, 7, 42 (1951)
2. Chandrasekhar, S.: Hydrodynamic and Hydromagnetic Stability. Dover, Oxford University (1961)
3. Proctor, M.R.E., Weiss, N.O.: Magnetoconvection. Rep. Prog. Phys. 1317 (1982)
4. Tagare, S.G., Benerji Babu, A.: J. Porous Medium 823 (2007)
5. Tagare, S.G., Benerji Babu A., Rameshwar, Y.: Int. J. Heat Mass Transf. **51**, 1168 (2008)
6. Tagare, S.G.: J. Plasma Phys. **58**, 395 (1997)
7. Jones, C.A., Roberts, P.H.: Geophys. Astrophys. Fluid Dyn. **93**, 289 (2000)
8. Kloosterziel, R.C., Carnevale, G.F.: J. Fluid Mech. **490**, 333 (2003)
9. Brand, H.R., Steinberg, V.: Phys. Lett. **93A**, 333 (1983b)
10. Brand, H.R., Steinberg, V.: Physica **119A**, 327 (1983a)
11. Palm, E., Weber, J.E., Kvernvold, O.: Journal of Fluid Mech. **64**, 153 (1972)
12. Brand, H.R., Lomdahl, P.S., Newell, A.C.: Physica **D23**, 345 (1986)

Mathematical Analysis of Steady MHD Flow Between Two Infinite Parallel Plates in an Inclined Magnetic Field

V. Manjula and K. V. Chandra Sekhar

Abstract The present paper deals with the study of incompressible fluid flow of electrically conducting fluid between two parallel porous plates under the influence of the inclined magnetic field. In the present study, a special focus has been emphasised to identify MHD flow of a compressible fluid between parallel plates. However, a fluid moves through a magnetic field, an electric field will be generated, and as a result current may be induced. The interaction of magnetic field with the combination of conducting fluid modifies the flow. The nature of the fluid is strongly dependent on the orientation of magnetic field. The flow between parallel plates is the fundamental theme and basis for understanding the dynamics of fluid flow. Hence, the mathematical analysis of effects of magnetic parameter with fluid velocity at various angles of previous work was analysed, and the velocity profile in the absence of magnetic field and perpendicular to direction of fluid flow were depicted graphically. As such, a modest attempt is made to analyse the effects of Hartmann number at various angles of inclination, regarding the solution in the absence of magnetic field, which are presented.

Keywords Introduction · General solution

1 Introduction

In fluid dynamics, MHD flow between parallel plates is classical. The solution has tremendous applications in power generations, polymer technology, petroleum industry, purification of crude oil, sprays, etc. Hartmann and Lazarus studied the flow of a conducting fluid between two infinite parallel plates under the influence of a transverse uniform magnetic field. Then, the problem was extended by Serclif [1], Drake [2], Singh and Ram [3]. Attia et al. [4]. Again, Abdeen [5] throw some light on the concept of velocity and temperature distributions between parallel porous plates with Hall effect and variable properties. Chand et al. [6] stressed the effect of Hall current and rotation on heat transfer in MHD flow with focus on dusty fluid in porous channel.

V. Manjula (✉) · K. V. Chandra Sekhar
K L University, Vaddeswaram, A.P., India
e-mail: manjulavinnakota11@gmail.com

D. Srinivasacharya and K. S. Reddy (eds.), *Numerical Heat Transfer and Fluid Flow*, Lecture Notes in Mechanical Engineering,
https://doi.org/10.1007/978-981-13-1903-7_72

Srikala and Kesavareddy [7] gave commendable contributions towards steady MHD Couette flow of an incompressible viscous fluid through porous medium between two infinite parallel plates under the effect of inclined magnetic field Kirubhashankar et al. [8] revealed the importance of topic.

Kieima and Manyonge [9] explored the topic of the steady MHD Poisulle fluid flow between infinite parallel porous plates. Parvin et al. [10] brought valuable data on unsteady MHD flow through parallel porous Plates. Joseph and Daniel [13] revealed the importance of unsteady MHD flow with heat transfer. Further C.B. Singh's contributions [14] about the concept is recognizable. Finally Kiema and Manyonge [15] had shown vivid picture on the steady MHD poiselle flow fluid flow between infinite parallel plates. This motivates me to consider mathematical analysis of steady MHD flow between parallel plates with inclined magnetic field. I could cherish basic structure from text books Chorlton et al. [16, 17] and the above references.

2 Mathematical Formulation

Consider MHD fluid flow as incompressible fluid between parallel porous plates separated by a distance h. X-axis is taken as the flow parallel to the direction of the flow The MHD phenomena can be described by an electrically conducting fluid with velocity V. Let B be the magnetic field and assume that the flow is steady. The interaction of two fields, velocity and magnetic fields, and an electric field E can be induced perpendicular to both V and M. It is denoted by

$$E = V \times B \tag{1}$$

According to Ohm's law

$$J = \sigma \tag{2}$$

J = Density of induced current in the conducting fluid
σ = Electrical conductivity = scalar

From (1) and (2),

$$J = \sigma(V \times B) \tag{3}$$

$$\text{Lorentz force } F = J \times B \tag{4}$$

Maxwell's equations together with ohms law and law of magnetic conservation are

$$\nabla \times E = -\frac{\partial B}{\partial t} \tag{5}$$

$$\nabla \times H = J + \frac{\partial D}{\partial t} \tag{6}$$

where H = Magnetic field intensity and D = Electric displacement vector

$$J = \sigma(E + V \times B)$$

$$\nabla.B = 0 \tag{7}$$

$$\nabla.D = 0 \tag{8}$$

The continuity and momentum equations for incompressible fluid are

$$\nabla.V = 0 \tag{9}$$

$$\rho\left\{\frac{\partial V}{\partial t} + (\nabla.V)V\right\} = -\nabla P + \mu\nabla^2 u + J \times B \tag{10}$$

Basic assumptions are

The fluid flow is steady and incompressible,
The fluid flow is laminar and unidirectional in x-axis, and
The fluid is electrically neutral.

Hence, the governing equations reduce to

$$\frac{\partial \mathrm{v}}{\partial \mathrm{y}} = 0 \tag{11}$$

$$-\frac{1}{\rho} + \frac{\partial p}{\partial x} + v\frac{\partial^2 u}{\partial y^2} + \frac{F_X}{\rho} = 0 \tag{12}$$

$$-\frac{1}{\rho}\frac{\partial p}{\partial y} = 0 \tag{13}$$

F_x component of magnetic force in x-direction

$$\frac{F_x}{\rho} = -\frac{\sigma}{\rho}B_0^2 u^1 \tag{14}$$

$$\frac{\partial^2 u^1}{\partial y^{1^2}} - \frac{\sigma}{\mu}B_0^2 u^1 = \frac{1}{u}\frac{\partial p^1}{\partial x^1} \tag{15}$$

$$\rightarrow \frac{\partial^2 u^1}{\partial y^{1^2}} - \frac{\sigma}{\mu}B_0^2 \sin(\alpha)u^1 = \frac{1}{u}\frac{\partial p^1}{\partial x^1} \tag{16}$$

Here, α is the angle between v and B, α ϵ (0, π)

Differentiating (16)

$$\frac{\mathrm{d}^2 p^2}{\mathrm{d}x^{1^2}} = 0 \rightarrow \frac{\mathrm{d}p^1}{\mathrm{d}x^1} = -C$$

$$\frac{\mathrm{d}^2u}{\mathrm{d}y^2} - \frac{\sigma}{\mu}\mathrm{B}_0^2\mathrm{L}^2\sin^2\alpha\, u = \frac{1}{\mu}\frac{\mathrm{d}p}{\mathrm{d}x} \tag{17}$$

$$\frac{\mathrm{d}^2u}{\mathrm{d}y^2} - M^2u - \frac{1}{\mu}\frac{\mathrm{d}p}{\mathrm{d}x} = 0$$

where $M^2 = \left(\frac{\sigma}{\rho}\right)B_0^2L^2\sin\alpha$

$$M = H_a \sin\alpha$$

where H_a is the Hartmann number given by

$$H_a^2 = \frac{\sigma B_0^2 L^2}{\mu}$$

It can be expressed as

$$\frac{d^2u}{dy^2} - M^2u + \mathrm{c} = 0 \tag{18}$$

The boundary conditions are $u = 0$, $y = \pm 1$.
v does not change with $y, \frac{\partial \mathrm{u}}{\partial \mathrm{y}} = 0$
The x and y momentum equations are

$$v_0\frac{\partial u}{\partial y} = v\frac{\partial^2 u}{\partial y^2} - \frac{1}{\rho}\frac{\partial p}{\partial x} \tag{19}$$

$$-\frac{1}{\rho}\frac{\partial p}{\partial y} = 0 \tag{20}$$

(20) becomes $\frac{\partial p}{\partial x} = \frac{p}{v}\frac{\partial^2 \mathrm{u}}{\partial \mathrm{y}^2} - \mathrm{v}_0\frac{\partial \mathrm{u}}{\partial \mathrm{y}}$

$$\frac{\mathrm{d}p}{\mathrm{d}x} = \frac{\rho}{v}\frac{\mathrm{d}^2u}{\mathrm{d}y^2} - v_0\frac{\mathrm{d}u}{\mathrm{d}y} + \frac{p}{\mu} - M^2u = 0 \tag{21}$$

$$\frac{\mathrm{d}^2u}{\mathrm{d}y^2} - \frac{v_0}{v}\frac{\mathrm{d}u}{\mathrm{d}y} = -\frac{p}{\rho v} \tag{22}$$

By adding M^2u,

$$\frac{\mathrm{d}^2u}{\mathrm{d}y^2} - \frac{v_0}{v}\frac{\mathrm{d}u}{\mathrm{d}y} + \frac{p}{\mu} - M^2u = 0 \tag{23}$$

$$\frac{\mathrm{d}^2u}{\mathrm{d}y^2} - r\frac{\mathrm{d}u}{\mathrm{d}y} - M^2u + s = 0 \tag{24}$$

where $r = \frac{v_0}{v}$ and $s = \frac{p}{\mu}$ are constants.

3 General Solution

The ratio of electromagnetic force to viscous force is known as the Hartmann number.

Ha = 0.5, 1.5, 2.5 Angle $\alpha = 15$

$$U = 119.47431302270012 + \mathrm{e}^{-0.016468779308101065y}C[1] + \mathrm{e}^{1.016468779308101y}C[2]$$

$$U = 13.272280841462607 + \mathrm{e}^{-0.13300078988892264y}C[1] + \mathrm{e}^{1.1330007898889227y}C[2]$$

$$U = 4.777728142490964 + \mathrm{e}^{-0.3176851472296657y}C[1] + \mathrm{e}^{1.3176851472296658y}C[2]$$

Ha = 0.5, 1.5, 2.5 Angle $\alpha = 30$

$$U = 3.197953309881676 + \mathrm{e}^{-0.43562813125728533x}C[1] + \mathrm{e}^{1.4356281312572854x}C[2]$$

$$\mathbf{U} = 5.327650506126797 + \mathrm{e}^{-0.2908223567907018x}C[1] + \mathrm{e}^{1.2908223567907018x}C[2]$$

$$\mathbf{U} = 1.2800819252432156 + \mathrm{e}^{-0.8462540622037135x}C[1] + \mathrm{e}^{1.8462540622037136x}C[2]$$

Ha = 0.5, 1.5, 2.5, Angle $\alpha = 45$

$$U = 16.005121638924457 + \mathrm{e}^{-0.11233977496158129x}C[1] + \mathrm{e}^{1.112339774961581x}C[2]$$

$$U = 1.778030653248462 + \mathrm{e}^{-0.6725357137418033x}C[1] + \mathrm{e}^{1.6725357137418033x}C[2]$$

$$U = 1.1314137014199241 + \mathrm{e}^{-0.9204576727238303x}C[1] + \mathrm{e}^{1.9204576727238303x}C[2]$$

Ha = 0.5, 1.5, 2.5, Angle $\alpha = 90$

$$U = 0.8888888888888888 + \mathrm{e}^{-1.0811388300841895x}C[1] + \mathrm{e}^{2.08113883008419x}C[2]$$

$$U = 8 + C(1)\mathrm{e}^{-0.20710678118654754x} + C(2)\mathrm{e}^{1.2071067811865475x}$$

$$U = 0.32 + \mathrm{e}^{-2.0495097567963927x}C[1] + \mathrm{e}^{3.0495097567963922x}C[2]$$

Angle $\alpha = 0$

$$U = 2x + \mathrm{e}^{x} C[1] + C[2]$$

According to boundary conditions $u = 0$, $y = 1$ and $u = 0$, $y = -1$, the solutions are as follows:

Angle-0, $U = \left[\{x\}, -\frac{1}{2}\mathrm{e}^{-x}\left(3 - 4\mathrm{e}^{x} + \mathrm{e}^{2x}\right)\right]$

Angle $\alpha = 15$, Ha $= 0.5$

$$U = \left[\{y\}, -1.6040824826650273\mathrm{e}^{-0.016468779308101065y}(72.90887017079228 - 74.48140249259822\mathrm{e}^{0.016468779308101065y} + 1.\mathrm{e}^{1.0329375586162022y})\right]$$

Angle $\alpha = 15$, Ha $= 1.5$,

$$U = \{y\}, -1.0845958426118651y(10.431166915160706 - 12.237075157416257\mathrm{e}^{0.13300078988892264y} + 1.\mathrm{e}^{1.2660015797778454y})$$

Angle $\alpha = 90$, Ha $= 0.5$

$$U = \left[\{y\}, -0.8623600458475917\mathrm{e}^{-0.20710678118654754y}(7.2983536139105825 - 9.276867636112483\mathrm{e}^{0.20710678118654754y} + 1.\mathrm{e}^{1.414213562373095y})\right]$$

4 Results and Discussions

The solution of the velocity equations for various values of α is presented. The solution along with graphical plots of the equation is presented for boundary conditions $u = 0$, $y = 1$ and $u = 0$, $y = -1$. According to previous work, the increase of Hartmann number leads to decrease of velocity. By the application of constant inclined magnetic field, velocity decreases due to the Lorentz force generated. By increasing the angle of inclination, there is no change in the direction of flow but by the removal of the magnetic parameter the flow becomes parabolic. All calculations are carried out for $r = 1$, $s = 2$. The solutions for angle of 15°, 30°, and 45° of Hartmann numbers Ha $= 0.5$, 1.5, 2.5 are presented. The solution plots through Mathematica are

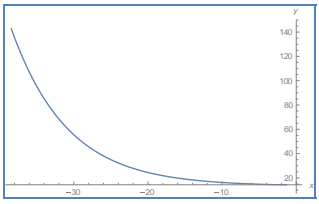

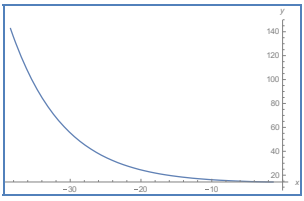

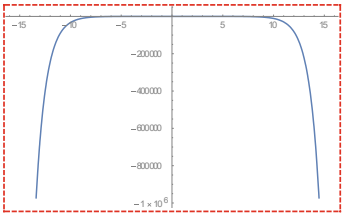

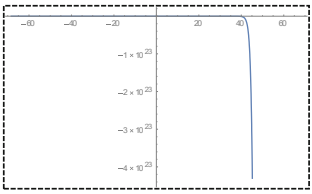

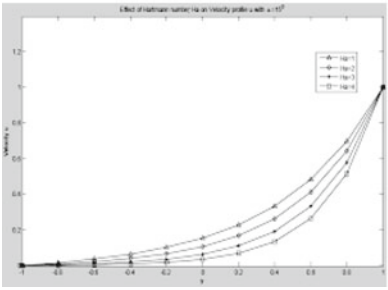

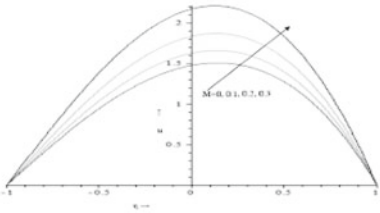

5 Conclusion

The above analysis is a class of solution of MHD flow between two infinite parallel plates in an inclined magnetic field as presented. The solutions with boundary conditions are represented graphically. Figures are drawn for Ha = 0.5, 1.5, and 2.5 at angles of 0, 15, 30, 45, and 90°. Velocity profiles give us steady laminar flow under the influence of transverse magnetic field and parabolic nature for $\alpha = 0$

References

1. Sercliff, J.A.: Proc. Camb. Phil. Soc. **52**, 573–583 (1956)
2. Drake, D.G.: Quart. J. Mech. Appl. Math. **18**, 1–10 (1965)
3. Singh, C.B., Ram, P.C.: J. Sci. Res. (B.H.U.) **lXXVIII**(2) (1978)
4. Attia, H.A., Sayed-Ahmed, M.E.: Ital. J. Pure Appl. Math. (2010). ISSN 2239–0227
5. Abdeen, A.A.: Eng. Trans. **2** (2012)
6. Chand, K., Singh, K.D., Sharma, S.: Indian J. Pure Appl. Phys. **51** (2013). ISSN 0975-1041
7. Srikala, L., Kesavareddy, E.: IJES **3**(9) (2014). ISSN 2319-1813
8. Kirubhashankar, C.K., Ganesh, S., Mohamed Ismail, A.: Int. J. Adv. Mech. Automobile Eng. (IJAMAE) **1** (2014). ISSN 2349-1485
9. Kieima, D.W., Manyonge, W.A.: J. IJSRIT **2** (2015). ISSN 2313-3759
10. Parvin, A., Dola, T.A., Alam, M.M.: In: AIP Conference Proceedings, 1754 (2016)
11. Ganesh, S., Krishnambal, S.: J. Appl. Sci. **6** (2006). ISSN 1812–5654
12. Singh, C.B.: Kenya J. Sci. **15**(2) (2014). ISSN 1992-1950
13. Joseph, K.M., Daniel, S.: IJMSI **2**(3) (2014). ISSN 2321-4767
14. Singh, C.B.: J. Sci. Ser. **15**(2) (2014)

15. Kiema, D.W., Manyonge, W.A., Bitok, J.K.: J. Appl. Math. Bioinform. **5**(19) (2015). ISSN 1792-6602
16. Chorlton, F. (ed.): Textbook of Fluid Dynamics. CBS Publishers, New Delhi (2004)
17. Bansal, J.L.: Viscous Fluid Dynamics, 2nd edn. Oxford and IBH Publishing Co., Ltd., New Delhi (2004)

Laminar Mixed Convection Flow of Cu–Water Nanofluid in a Vertical Channel with Viscous Dissipation

Surender Ontela, Lalrinpuia Tlau and D. Srinivasacharya

Abstract The influence of viscous dissipation on mixed convection laminar flow of a nanofluid in a vertical channel is investigated. A case of Cu–water-based nanofluid is considered employing the Das–Tiwari model. The resultant coupled momentum energy equations are solved using the homotopy analysis method after non-dimensionalization. The influence of pertinent parameters on the flow characteristics is analyzed in both the cases where the channel walls are symmetrically and asymmetrically heated.

Keywords Mixed convection · Nanofluid · Vertical channel · Viscous dissipation · Homotopy analysis method

1 Introduction

Ever since Choi [1] coined the term nanofluid, theoretical and experimental studies on the topic have seen a rapid rise. The study of nanofluids has been a topic of great interest for more than a decade, in view of its industrial applications. Nanofluids are used in cooling technology, medical applications like cancer therapy, drug delivery, etc.

The influence of viscous heating on mixed convection flow in a vertical channel was studied in great detail by Barletta [2–4] for symmetric and asymmetric heating of the channel walls and channel walls with prescribed heat fluxes. Barletta, Lazzari, and Magyari [5] investigated buoyant Poiseuille Couette flow with viscous dissipation in a vertical channel. Magyari, Pop, and Storesletten [6] and Sheikholeslami et al. [7] explored the influence of transverse magnetic field on nanofluid flow in a semi-porous channel. Studies on mixed convection flow of nanofluid in a vertical channel under various physical conditions were reported by several authors (Xu and Pop [8];

S. Ontela (✉) · L. Tlau
Department of Mathematics, National Institute of Technology Mizoram, Aizawl 796012, India
e-mail: reddysurender3@gmail.com

D. Srinivasacharya
Department of Mathematics, National Institute of Technology Warangal, Warangal 506004, Telangana, India

D. Srinivasacharya and K. S. Reddy (eds.), *Numerical Heat Transfer and Fluid Flow*, Lecture Notes in Mechanical Engineering,
https://doi.org/10.1007/978-981-13-1903-7_73

Akgul and Pakdemirli [9]). Motivated by these works, in this paper, we have made an attempt to explore the influence of viscous dissipation on mixed convection flow of nanofluid in a vertical channel.

2 Formulation of the Problem

A steady laminar flow of a Cu–water nanofluid in a channel is considered. The x-axis is taken parallel to walls of the channel and y-axis normal to the wall. The velocity component u is taken along the x-axis as shown in Fig. 1. The momentum and energy balance equations are

$$\mu_{nf}\frac{d^2u}{dy^2} + g(\rho\beta)_{nf}(T - T_0) - \frac{dp}{dx} = 0 \tag{1}$$

$$\alpha_{nf}\frac{d^2T}{dy^2} + \frac{\mu_{nf}}{(\rho C_p)_{nf}}\left(\frac{du}{dy}\right)^2 = 0 \tag{2}$$

and the associated boundary conditions are

$$u\left(-\frac{L}{2}\right) = u\left(\frac{L}{2}\right) = 0;\ T\left(-\frac{L}{2}\right) = T_1;\ T\left(\frac{L}{2}\right) = T_2 \text{ with } T_2 \geq T_1 \tag{3}$$

where p is the pressure, g is the acceleration due to gravity, and T is the temperature. And, ρ_{nf} is the density, β_{nf} is the thermal expansion coefficient, $(C_p)_{nf}$ is the specific heat capacity, and μ_{nf} is the coefficient of viscosity of nanofluid. The thermophysical properties of base fluid and nanofluid are given in Table 1.

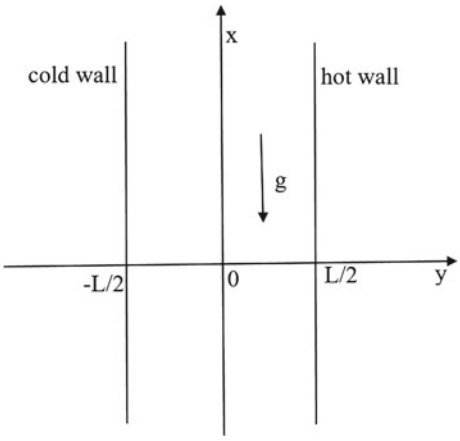

Fig. 1 Schematic diagram with coordinate axes

Table 1 Thermophysical properties of base fluid and nanoparticles

Physical property	Base fluid (Water)	Copper
C_p (J/kg K)	4179	385
ρ (kg/m^3)	997.1	8933
K (W/m K)	0.613	401
$\beta \times 10^{-5}$ (K^{-1})	21	1.67

Invoking the following nondimensional variables

$$U = \frac{u}{U_0}, \theta = \frac{T - T_0}{\Delta T}, X = \frac{x}{D}, Y = \frac{y}{D}, T_0 = \frac{T_1 + T_2}{2}, R_T = \frac{T_1 + T_2}{\Delta T}$$

into Eqs. (1)–(3), we have the following dimensionless form:

$$(1-\phi)^{-2.5}U'' + \left[1 - \phi + \phi\frac{(\rho\beta)_s}{(\rho\beta)_f}\right]Ri\theta + A = 0 \tag{4}$$

$$\frac{\alpha_{nf}}{\alpha_f}\theta'' + Br\frac{\mu_{nf}}{\mu_f}\frac{1}{\left[1 - \phi + \phi\frac{(\rho\beta)_s}{(\rho\beta)_f}\right]}U'^2 = 0 \tag{5}$$

The associated boundary conditions in dimensionless form are

$$U\left(-\frac{1}{4}\right) = U\left(\frac{1}{4}\right) = 0; \theta\left(-\frac{1}{4}\right) = \frac{-R_T}{2}; \theta\left(\frac{1}{4}\right) = \frac{R_T}{2} \tag{6}$$

where $Gr = \frac{g\beta_f \Delta T D^3}{\nu_f}$ is the Grashof number, $Re = \frac{U_0 D}{\nu_f}$ is the Reynolds number, $A = \frac{-D^2}{U_0}\frac{dP}{dx}$ is the dimensionless pressure gradient, $\alpha_{nf} = \frac{\mu_{nf}}{(\rho C_p)_{nf}}$ is the thermal diffusivity of the nanofluid, $\alpha_f = \frac{\mu_f}{(\rho C_p)_f}$ is the thermal diffusivity of the base fluid, $Br = \frac{\mu_f U_0^2}{\Delta T K_f}$ is the Brinkman number, and $Ri = \frac{Gr}{Re}$ is the mixed convection parameter. The dimensionless Nusselt numbers are calculated as

$$Nu_1 = \left.\frac{d\theta}{dY}\right|_{Y=-\frac{1}{4}} = \theta'\left(-\frac{1}{4}\right); Nu_2 = \left.\frac{d\theta}{dY}\right|_{Y=\frac{1}{4}} = \theta'\left(\frac{1}{4}\right) \tag{7}$$

3 Results and Discussion

The coupled ordinary differential equations (4)–(5) along with the boundary conditions (6) are solved using Homotopy Analysis Method (HAM) [10]. The h-curves (shown in Figs. 2 and 3) are plotted, and the optimum values of the h are fixed

Fig. 2 h_1 curve

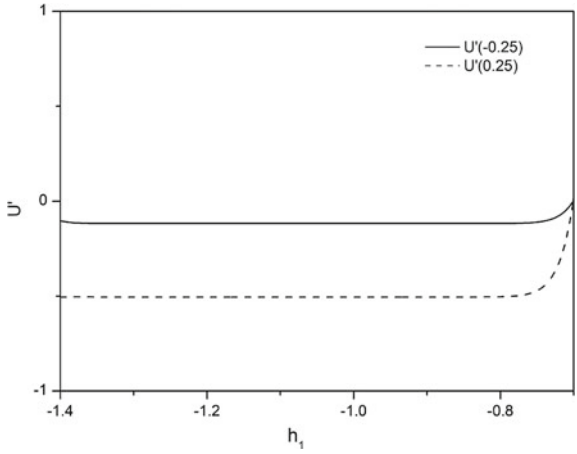

Fig. 3 h_2 curve

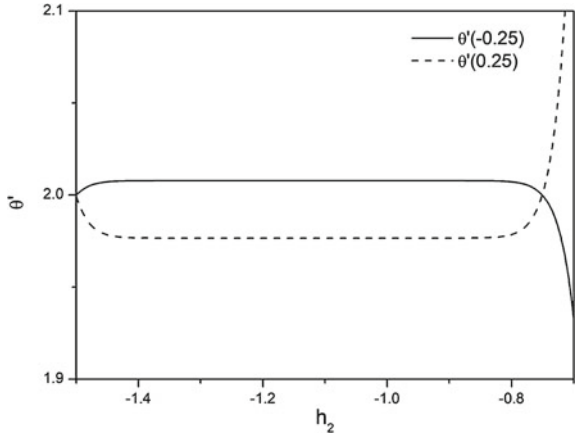

as $h_1 = -0.68$ and $h_2 = -0.95$ obtained from the average residual error analysis with different orders of approximation of the solutions. When $\phi = 0.0$, the values of Nusselt numbers calculated using HAM are compared with that of Barletta [2], and results are found to be in good agreement, as presented in Table 2.

3.1 Asymmetric Heating

In this case, the boundary temperatures are different, i.e., $T_2 > T_1$, $R_T = 1$.

Figure 4 shows that the velocity decreases with an increase in the nanoparticle volume fraction. This is due to the increase in density of the fluid with increase in nanoparticle concentration. An increase in the Brinkman number causes a slight increase in the velocity profile as shown in Fig. 5. An increase in Brinkman number

Table 2 Comparison of values of Nu_1 and Nu_2 for asymmetric heating with $Ri = 100$, $\phi = 0.0$ with that of Barletta [2]

Br	Nu_1		Nu_2	
	Barletta [2]	Present	Barletta [2]	Present
0	2	2	2	2
0.05	2.048	2.05302	1.918	1.91197
0.01	2.099	2.10798	1.834	1.82141
0.02	2.205	2.22425	1.657	1.63203
0.03	2.319	2.35002	1.471	1.43038
0.04	2.443	2.48672	1.271	1.21471
0.05	2.578	2.63616	1.058	0.982796

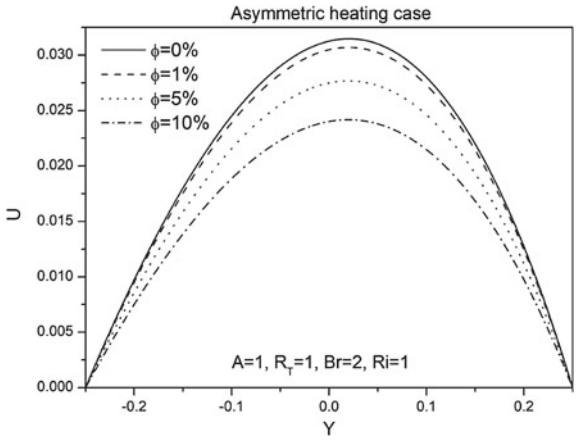

Fig. 4 Effect of ϕ on velocity

and nanoparticle volume fraction have minimal effect on temperature as shown in Figs. 6 and 7.

An increase in the Brinkman number increases the Nusselt number on the left wall as shown in Fig. 8. An increase in the nanoparticle volume fraction diminishes the Nusselt number on the left wall as shown in Fig. 9. An increase in the Brinkman number causes the Nusselt number to decrease on the right wall of the channel as shown in Fig. 10, while the increase in nanoparticle volume fraction causes the Nusselt number to increase on the right wall of the channel as shown in Fig. 11.

3.2 Symmetric Heating

In this case, the temperatures of the walls of the channel are same, i.e., $T_2 = T_1$, $R_T = 0$.

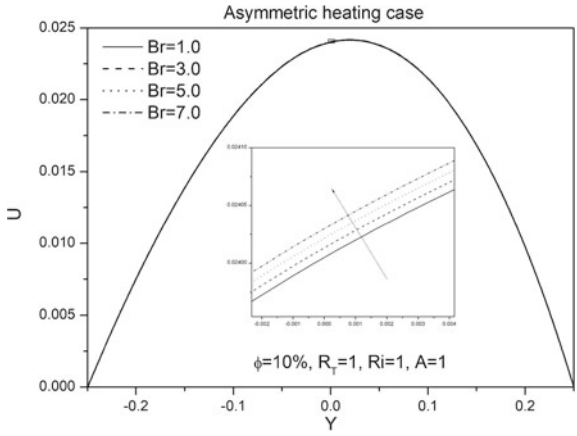

Fig. 5 Effect of Brinkman number on velocity

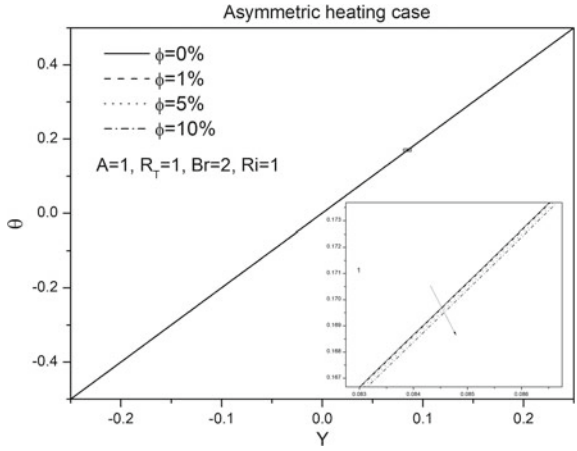

Fig. 6 Effect of ϕ on temperature

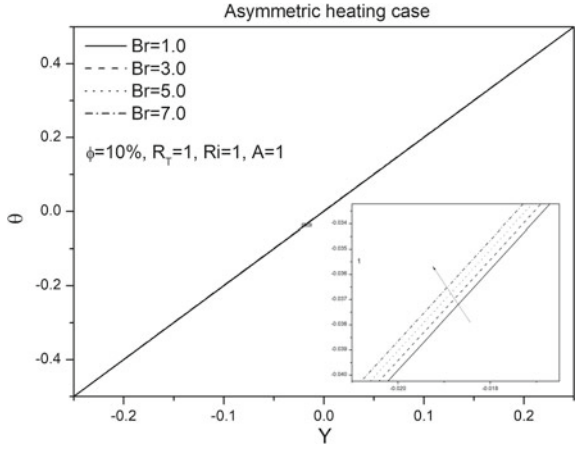

Fig. 7 Effect of Brinkman number on temperature

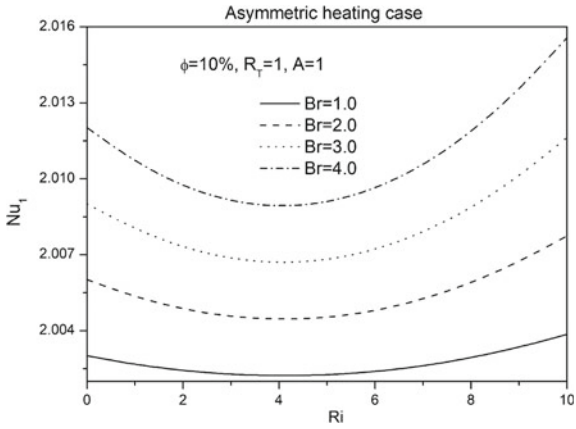

Fig. 8 Effect of Brinkman number on Nusselt number

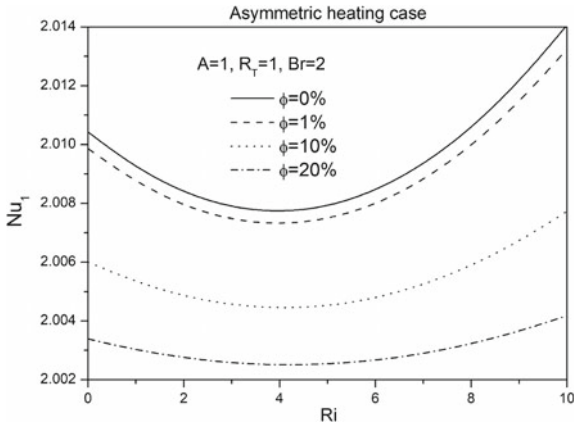

Fig. 9 Effect of ϕ on Nusselt number

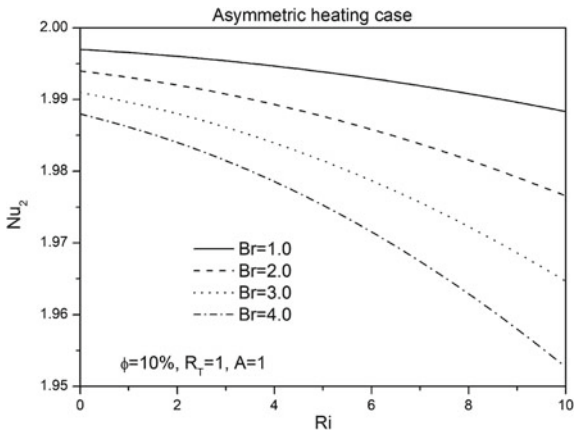

Fig. 10 Effect of Brinkman number on Nusselt number

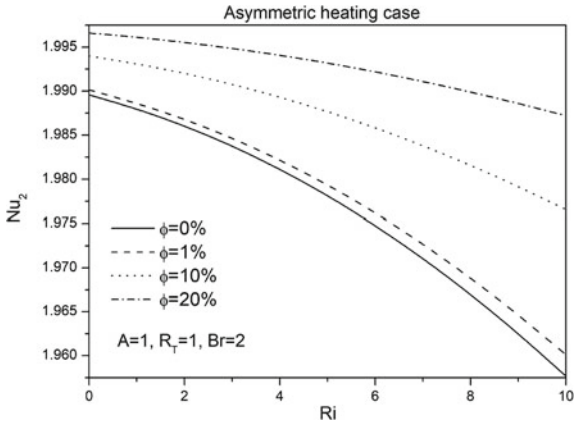

Fig. 11 Effect of ϕ on Nusselt number

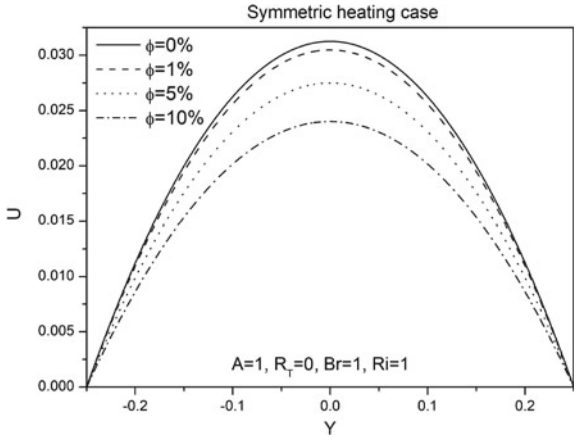

Fig. 12 Effect of ϕ on velocity

An increase in the nanoparticle volume fraction decreases the velocity as shown in Fig. 12. Figure 13 shows that there is a slight increase in the velocity profile with an increase in the Brinkman number. The temperature decreases with an increase in the nanoparticle volume fraction as shown in Fig. 14, while it increases with increase in the Brinkman number as depicted in Fig. 15.

An increase in Br increases the Nusselt number on left wall as shown in Fig. 16, while it decreases on right wall as shown in Fig. 18. The Nusselt number decreases with an increase in nanoparticle volume fraction on left wall as shown in Fig. 17, and it increases on right wall as shown in Fig. 19.

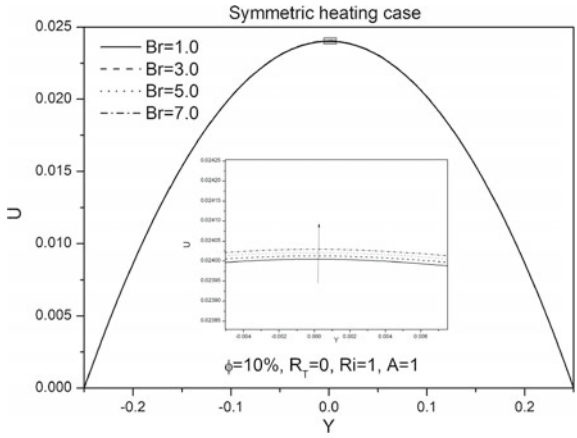

Fig. 13 Effect of Brinkman number on velocity

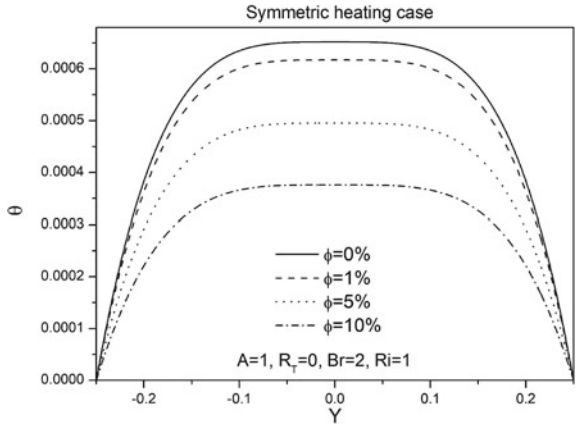

Fig. 14 Effect of ϕ on temperature

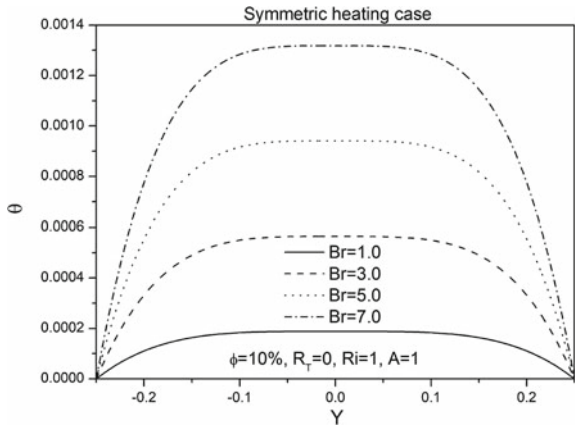

Fig. 15 Effect of Brinkman number on temperature

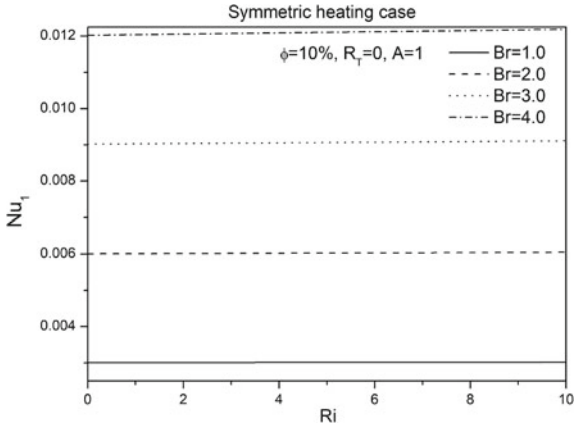

Fig. 16 Effect of Brinkman number on Nusselt number

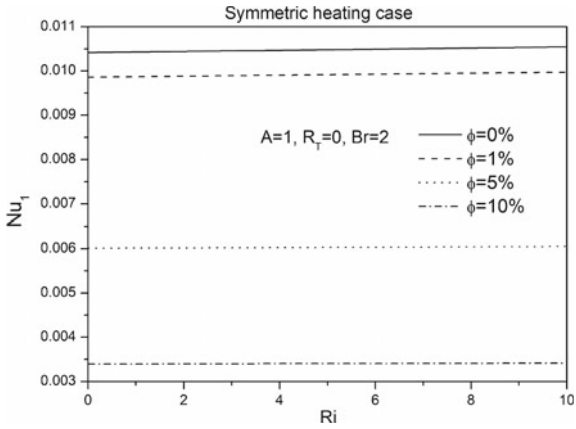

Fig. 17 Effect of ϕ on Nusselt number

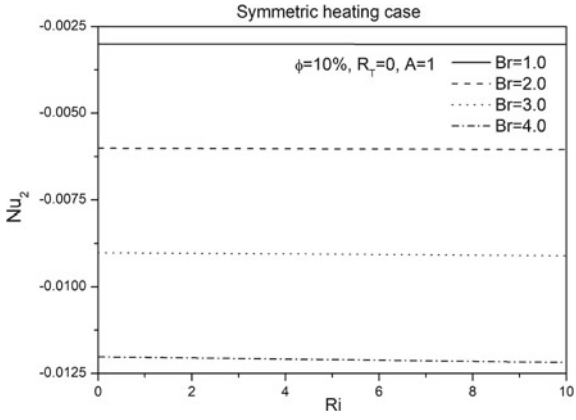

Fig. 18 Effect of Brinkman number on Nusselt number

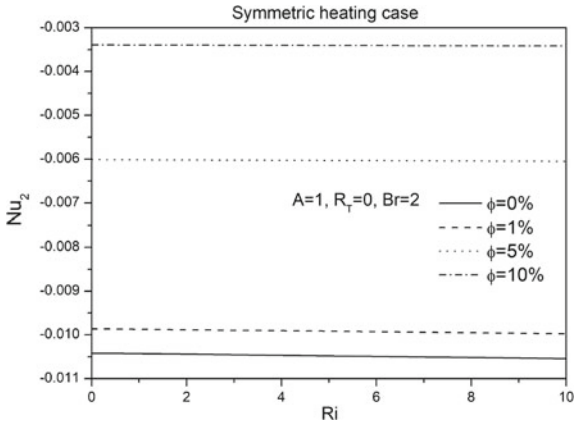

Fig. 19 Effect of ϕ on Nusselt number

4 Conclusion

The laminar mixed convection flow of Cu–water nanofluid in a vertical channel in the presence of viscous dissipation has been investigated. The HAM has been successfully applied to solve the governing equations. An increase in nanoparticle volume fraction decreases the velocity, temperature, and heat transfer coefficient on the left wall but increases heat transfer coefficient on the right wall of the channel in both symmetric and asymmetric heating cases. But the opposite orientation is observed in the case of an increase in Brinkman number.

References

1. Choi, S.U.S.: Enhancing thermal conductivity of fluids with nanoparticles. Developments and Applications of Non-Newtonian Flows, FED-Vol. 231/MD-Vol. 66, pp. 99–105 (1995)
2. Barletta, A.: Laminar mixed convection with viscous dissipation in a vertical channel. Int. J. Heat Mass Transf. **41**, 3501–3513 (1998). https://doi.org/10.1016/S0017-9310(98)00074-X
3. Barletta, A.: Combined forced and free convection with viscous dissipation in a vertical circular duct. Int. J. Heat Mass Transf. **42**, 2243–2253 (1999). https://doi.org/10.1016/S0017-9310(98)00343-3
4. Barletta, A.: Laminar convection in a vertical channel with viscous dissipation and buoyancy effects. Int. Commun. Heat Mass Transf. **26**(2), 153–164 (1999). https://doi.org/10.1016/S0735-1933(99)00002-0
5. Barletta, A., Lazzari, S., Magyari, E.: Buoyant PoiseuilleCouette flow with viscous dissipation in a vertical channel. Z. Angew. Math. Phys. **59**, 1039–1056 (2008). https://doi.org/10.1007/s00033-008-7080-8
6. Barletta, A., Magyari, E., Pop, I., Storesletten, L.: Unified analytical approach to the Darcy mixed convection with viscous dissipation in a vertical channel. Int. J. Therm. Sci. **47**, 408–416 (2008). https://doi.org/10.1016/j.ijthermalsci.2007.03.014
7. Sheikholeslami, M., Hatami, M., Ganji, D.D.: Analytical investigation of MHD nanofluid flow in a semi-porous channel. Powder Technol. **246**, 327–336 (2013). https://doi.org/10.1016/j.powtec.2013.05.030

8. Xu, H., Pop, I.: Fully developed mixed convection flow in a vertical channel filled with nanofluids. Int. Commun. Heat Mass Transf. **39**, 1086–1092 (2012). https://doi.org/10.1016/j.icheatmasstransfer.2012.06.003
9. Akgul, M.B., Pakdemirli, M.: Numerical analysis of mixed convection of nanofluids inside a vertical channel. Int. J. Comput. Methods **13**(3), 1650012 (16 p.) (2016). https://doi.org/10.1142/S0219876216500122
10. Liao, S.: Beyond Perturbation. Introduction to Homotopy Analysis Method. Chapman and Hall/CRC Press, Boca Raton (2003)

A New Initial Value Technique for Singular Perturbation Problems Using Exponentially Finite Difference Scheme

Narahari Raji Reddy

Abstract In the present analysis, an ε-uniform initial value technique is presented for solving singularly perturbed problems for linear and semi-linear second-order ordinary differential equations arising in a chemical reactor theory having a boundary layer at one end point. In this computational technique, the original problem is reduced to an asymptotically equivalent first-order singular initial value problem and a terminal boundary value problem. The required approximate solution is obtained using Box and Trapezoidal schemes after introducing an exponential factor to the singular perturbed initial value problem. Accuracy and efficiency of this technique are validated by considering error estimates and with well-established numerical examples.

Keywords Singular perturbation problems · Boundary value problems · Boundary layer · Exponential fitted difference scheme · Box and trapezoidal schemes

1 Introduction

In the fields of fluid mechanics, elasticity, and chemical reactor theory, there is a huge scope to have a problem of singular perturbation with a small parameter (disturbance) ε to analyze flow phenomena of convection–diffusion problems. This type of problems was solved numerically by Ascher and Weis [1], Lin and Su [2], Vulanovic [3, 4], and asymptotically by O'Malley [5, 6], Nayfeh [7], Kevorkian and Cole [8], Bender and Orszag [9], Eckhaus [10], Van Dyke [11], and Bellman [12].

Exceptional studies are available in the literature to provide the approximate solutions for convection–diffusion problems with different finite difference methods. A comprehensive evaluation of convection–diffusion initial and boundary value problems with uniform numerical methods can be seen in the textbook by Doolan

N. Raji Reddy (✉)
Department of Mathematics, Jyothishmathi Institute of Technology & Science, Karimnagar 505481, Telangana, India
e-mail: narahari.rajireddy@gmail.com

D. Srinivasacharya and K. S. Reddy (eds.), *Numerical Heat Transfer and Fluid Flow*, Lecture Notes in Mechanical Engineering,
https://doi.org/10.1007/978-981-13-1903-7_74

and Miller [13]. Bawa and Clavero [14] discussed the problems of singularly perturbed reaction–diffusion with higher order global solution and normalized flux. In work of Ervin and Layton [15], the approximation of the un-weighted derivative is considered only at the outside of the layer, whereas Kopteva and Stynes [16] are utilized special kinds of nonuniform meshes (namely, piecewise-uniform Shishkin mesh and Bakhvalov mesh) to derive the derivative approximation on the entire domain. Recently, Raji Reddy and Mohapatra [17] discussed the stability of an exponentially fitted finite difference scheme for evaluating singularly perturbed two-point boundary value problems using fitting factor.

Analysis of singular perturbations problems is a field of great interest to applied mathematicians. In view of this interest, we consider the following singular perturbation problem:

$$\varepsilon y''(x) + a(x)y'(x) - b(x)y(x) = f(x), \tag{1}$$

for $x \in \Delta = (0, 1)$ with the boundary conditions

$$y(0) = \alpha \text{ and } y(1) = \beta, \tag{2}$$

where ε is a small positive parameter such that $0 < \varepsilon \ll 1$ and α, β are given nonnegative constants. We assume that $a(x), b(x)$ and $f(x)$ are sufficiently continuously differentiable functions in the interval $\bar{\Delta} = [0, 1]$. Moreover, we assume that $a(x) \geq M > 0$ though out the interval $\bar{\Delta}$, where M is a positive constant and $b(x) \leq 0$. Under these assumptions, the problem (1)–(2) has a unique solution $y(x)$ which exhibits a boundary layer of width $O(\varepsilon)$ at $x = 0$ for small values of ε [6, 8]. Note that if $a(x) \leq M < 0$ then the boundary layer occurs at the right end $x = 1$. Here, we discuss the problem of having the left end boundary layer and the results for the right end boundary layer are analogous.

Let Y^N be the numerical approximation, N be the number of mesh elements used, y be the solution of the continuous problem and $\|y\|_\Delta = \max_{x\in\Delta}|y(x)|$ be the maximum point-wise norm, and the error constant C be independent of any perturbation parameters and the mesh parameter N. A numerical method is said to be parameter uniform of order p if

$$\left\|y - Y^N\right\|_{\Delta^N} \leq C_p N^{-p}, \ p > 0,$$

where Δ^N is the discretization of Δ (domain of the problem), and the constant C_p is independent of any perturbation parameters and the mesh parameter N. In other words, the numerical approximations Y^N converge to y for all values of ε in the range $0 < \varepsilon \ll 1$.

2 Description of the Method

First, the given interval $\bar{\Delta} = [0, 1]$ is divided into N equal subintervals, each of length h. Let $0 = x_0 < x_1 < x_2 < \cdots < x_N = 1$ be the mesh points such that $x_i - x_{i-1} = h =$ constant for $i = 1, 2, \ldots, N$. Let $\Delta^N = \{x_i\}_{i=0}^N$. Thus, we have $x_i = ih$ for $\forall 0 \leq i \leq N$. The outer region solution as an asymptotic expansion is of the form

$$y(x) = \sum_{i=0}^{\infty} y_n(x)\varepsilon^n \tag{3}$$

where $y_n(x)$ are unknown functions to be determined and for any 'n', there exist a constant B_n such that

$$\left|y(x, \varepsilon) - y^n(x, \varepsilon)\right| \leq B_n \varepsilon^{N+1} \tag{4}$$

On substituting $y(x)$ from (3) into (1), we get

$$\begin{aligned} &\varepsilon\left(y_0'' + \varepsilon y_1''(x) + \varepsilon^2 y_2''(x) + \cdots\right) + a(x)\left(y_0' + \varepsilon y_1'(x) + \varepsilon^2 y_2' + \cdots\right) \\ &\quad - b(x)\left(y_0 + \varepsilon y_1 + \varepsilon^2 y_2(x) \cdots\right) = f(x) \end{aligned} \tag{5}$$

with

$$y_0(1) + \varepsilon y_1(1) + \varepsilon^2 y_2(1) + \cdots = \beta \tag{6}$$

Equating the coefficients of like powers of ε on both sides of (5) and (6), we obtain the problems for the terms $y_0(x)$, $y_1(x)$, $y_2(x)$, … of the series (3) as follows:

$$a(x)y_0(x) - b(x)y_0(x) = f(x), \text{ with } y_0(1) = \beta \tag{7}$$

$$y_{k-1}''(x) + a(x)y_k'(x) - b(x)y_k(x) = 0, \text{ with } y_k(1) = 0, k = 1, 2, 3, \ldots \tag{8}$$

Solving (7) and (8), we get $y_0(x)$, $y_1(x)$, $y_2(x)$ … and hence $y(x)$ given in (3) is obtained next. We shall call this solution throughout as an outer solution and write it as $y_{\text{out}}(x)$. Now integrating (1) from x to 1 and neglecting $\varepsilon y'(1)$, we get

$$\varepsilon y'(x) + a(x)y(x) = z(x), \tag{9}$$

with

$$y(0) = \alpha, \tag{10}$$

where $z(x)$ is given by $z(x) = a(1)y(1) - \theta(x)$

Here, $\theta(x)$ is the solution of the following initial value problem:

$$\theta' = -\big(a'(x)y_{\text{out}}(x) + b(x)y_{\text{out}}(x) + f(x)\big) \tag{11}$$

with

$$\theta(1) = 0, \tag{12}$$

where $y(x)$ is replaced with the outer solution $y_{\text{out}}(x)$ in Eq. (11).

Therefore, the new initial value problem is

$$Ly(x) \equiv \varepsilon y'(x) + a(x)y(x) = z^*(x), \tag{13}$$

with

$$y(0) = \alpha \tag{14}$$

From (11) to (12) and $z(x)$, one can easily get $\{z_i\}_{i=0}^{N}$. We next solve the singular initial value problem (13)–(14) by an exponentially fitted finite difference scheme given in the next section.

Now describe the initial value problem (13)–(14) by the exponentially fitted finite difference scheme (EFFD) [15]

$$L^N u_i \equiv \varepsilon\sigma(\rho)D^+u_i + a_i u_i = z_i^*, \quad i = 0(1)N-1 \tag{15}$$

with

$$u_0 = \alpha, \tag{16}$$

where $\sigma(\rho) = \frac{\rho a(0)}{1-\exp(-\rho a(0))}$. But by Box and Trapezoidal scheme for Eqs. (17)–(18), it is given by

$$\varepsilon\sigma(\rho)\left[\frac{u_{i+1}-u_i}{h}\right] + \frac{a_i u_i + a_{i+1}u_{i+1}}{2} = \frac{z_i^* + z_{i+1}^*}{2} \tag{17}$$

with

$$u_0 = \alpha. \tag{18}$$

We can approximate the solution of boundary value problem (1)–(2) by approximating the initial value problem (15)–(16). One can easily solve (17)–(18) by forward substitution.

3 Error Estimates

In this section, we derive error estimates using the maximum principle. Now, we will show that the exponentially fitted finite difference scheme given in Sect. 3 is of $O(h)$ uniformly in ε.

Lemma 4.1 *(Continuous Maximum Principle) Consider the problem (13)–(14). If*

$$y(x) \geq 0,\ Ly(x) \geq 0,\ \forall x \in \Delta,\ \text{then } y(x) \geq 0 \text{ for } \forall x \in \bar{\Delta}$$

Proof It can be easily proven by contradiction, let $x^* \in \bar{\Delta}$ be such that $y(x^*) = \min_{x \in \Delta} y(x)$ and assume that $y(x^*) < 0$.

Then, it is clear that $y'(x^*) = 0$, so therefore $Ly(x^*) \equiv \varepsilon y'(x^*) + a(x^*)y(x^*) < 0$, which is contradiction to the statement.

Lemma 4.2 *(Stability) Consider the problem (13)–(14). Then, the solution of the problem satisfies*

$|y(x)| \leq C\, max\{|y_0|, max|Ly(x)|\}$, *for* $x \in \bar{\Delta}$ *where C is a positive constant.*

Proof Define $\phi^{\pm} = C \max\{|y_0|, \max|Ly(x)|\} \pm y(x)$

It is clear that $\phi^{\pm}(x) \geq 0$, and $L\phi^{\pm}(x) \equiv a(x)C\{|y_0|,\ \max|Ly(x)|\} \pm y(x) \geq 0$

Therefore, by Lemma 4.1, we get $\phi^{\pm}(x) \geq 0$, $x \in \bar{\Delta}$.

Thus, we get $|y(x)| \leq \mathrm{C} \max\{|y_0|, \max|Ly(x)|\}$.

Lemma 4.3 *(Discrete Maximum Principle) Consider the scheme (15)–(16). If* u_i *be a mesh function such that* $u_0 \geq 0$ *and* $L^N u_i \geq 0$ *for all* $x_i \in \Delta^N$, *then* $u_i \geq 0$ *for all* $x_i \in \Delta^N$.

Proof Suppose that there exists a positive integer k such that $u_{k+1} < 0$ and $u_{k+1} = \min_{0 \leq j \leq N} u_j$

Then, we have

$$L^N u_i \equiv \varepsilon\sigma_i(\rho)D_+u_i + a_i u_i = \varepsilon\sigma_i(\rho)\tfrac{u_{i+1}-u_i}{h} + a_i u_i$$
$$< 0, \text{ which is a contradiction.}$$

Hence the result.

Lemma 4.4 *(Discrete Stable Principle) If* u_i *is any mesh function in the scheme (15)–(16), then* $|u_i| \leq C\, max\left\{|u_0|,\ \max_{x_i \in \Delta^N}\left|L^N u_i\right|\right\}$, *where C is a positive constant.*

Proof Define $\Phi_i^{\pm} = C \max\left\{|u_0|,\ \max_{x_i \in \Delta^N}\left|L^N u_i\right|\right\} \pm u_i$.

It is clear that $\Phi_0^{\pm} \geq 0$, and $L^N \Phi_i^{\pm} \equiv a_i C \left\{ |u_0|, \max_{x_i \in \Delta^N} \left| L^N u_i \right| \right\} \pm L^N u_i \geq 0$, for a proper choice of C. Then, by maximum principle, we get $\Phi_i^{\pm} \geq 0, \forall x_i \in \Delta^N$; thus, we get $|u_i| \leq C \max \left\{ |u_0|, \max_{x_i \in \Delta^N} \left| L^N u_i \right| \right\}$. Hence the result.

Lemma 4.5 *If $u(x)$ and u_i be the solutions of the problems (13)–(14) and (15)–(16), respectively, then we have $|u(x) - u_i| \leq Ch$, where C is independent of i, h and ε.*

Proof Reference [15].

Theorem 4.1 *If $y(x)$ is the solution of Eqs. (1)–(2) and u^N is the solution of Eqs. (17)–(18), then $\left| y(x) - u^N \right| \leq C(h + \varepsilon)$ for some positive constant C.*

Proof It is easy to see that the problems (1)–(2) and (13)–(14) are equivalent. Equation (13) is obtained from Eq. (9) after replacing $z(x)$ by $z^*(x)$.

By Lipchitz condition, with $|y(x) - y_{out}(x)| < \varepsilon$, for $x \in \bar{\Delta}$ we get $|z(x) - z^*(x)| \leq C\varepsilon$.

Let $p(x) = y(x) - u(x)$, where $u(x)$ is the solution of Eq. (13).

Now by Lemma 4.2 for $p(x)$, we get $|p(x)| \leq C|z(x) - z^*(x)|$, that is, $|y(x) - u(x)| \leq C\varepsilon$ for $x \in \bar{\Delta}$.

Now, we have

$$\begin{aligned} L^N\left(u - u^N\right)(x_i) &= \left(L^N - L\right)u(x_i) \\ &= \varepsilon(\sigma - 1)D^+ u_i + \varepsilon\left(D^+ u_i - u_i'\right) + \left(\frac{a_i u_i + a_{i+1} u_{i+1}}{2} - a_i u_i\right) \\ &\quad + \left(\frac{g_i + g_{i+1}}{2} - g_i\right). \end{aligned}$$

Taking the absolute value, we get

$$\begin{aligned} \left|L^N\left(u - u^N\right)(x_i)\right| &\leq \varepsilon|\sigma - 1|\left|D^+ u_i\right| + \varepsilon\left|D^+ u_i - u_i'\right| + \left|\frac{a_{i+1}u_{i+1} - a_i u_i}{2}\right| + \left|\frac{g_{i+1} - g_i}{2}\right| \\ &= \left|\frac{\sigma - 1}{\rho}\right||u_{i+1} - u_i| + \varepsilon\left|D^+ u_i - u_i'\right| + \left|\frac{a_{i+1}u_{i+1} - a_i u_i}{2}\right| \\ &\quad + \left|\frac{g_{i+1} - g_i}{2}\right| \end{aligned}$$

But we have $a_{i+1} = a(x_i + h) = a(x_i) + o(h) \approx a_i$. Similarly, $g_{i+1} \approx g_i$.

$$\left|L^N\left(u - u^N\right)(x_i)\right| \leq \left|\frac{\sigma - 1}{\rho}\right||u_{i+1} - u_i| + \varepsilon\left|D^+ u_i - u_i'\right| + \frac{a_i}{2}|u_{i+1} - u_i| \leq Ch.$$

By Lemma 4.4, we get

$$\left|u_i - u^N(x)\right| \leq Ch.$$

But by triangular inequality and by Lemma 4.5, we get

$$\left|y(x) - u^N\right| \leq |y(x) - u(x)| + |u(x) - u_i| + \left|u_i - u^N(x)\right| \leq C(h + \varepsilon).$$

Hence the theorem.

4 Numerical Examples and Results

The applicability and advantages of the present method have demonstrated the consideration of linear and nonlinear singular perturbation problems with left end boundary layers which are broadly examined in the literature. The maximum absolute errors for the problems are presented in the tables for different values of ε and N. For any value of ε and N, the exact maximum absolute point-wise errors E_ε^N and the corresponding rates of convergence are calculated by

$$E_\varepsilon^N = \max_{0\leq i\leq N} |y(x_i) - y_i| \quad \text{and} \quad r_\varepsilon^N = \log_2\left(\frac{E_\varepsilon^N}{E_\varepsilon^{2N}}\right),$$

where y_i is the exact solution and $y(x_i)$ is the numerical solution obtained by using N number of mesh subintervals. The ε-uniform nodal errors and the numerical rates of ε-uniform convergence are computed using $E^N = \max_{0\leq\varepsilon\leq 1} E_\varepsilon^N$ and $r^N = \log_2\left(\frac{E^N}{E^{2N}}\right)$.

The maximum absolute errors E_ε^N, the rates of convergence r_ε^N, ε-uniform nodal errors E^N, and the numerical rates of ε-uniform convergence r^N have been presented in the tables.

Example 5.1 Now consider the nonhomogeneous linear problem ([17], Example 2):

$$\varepsilon y''(x) + y'(x) = 1 + 2x,\ y(0) = 0,\ y(1) = 1.$$

The exact solution is

$$y(x) = x(x + 1 - 2\varepsilon) + (2\varepsilon - 1)\left(1 - \exp\left(-\frac{x}{\varepsilon}\right)\right) \Big/ \left(1 - \exp\left(-\frac{1}{\varepsilon}\right)\right).$$

The outer solution is $y_{\text{out}}(x) = x^2 + x - 1 + 2\varepsilon(1 - x)$ (Table 1).

Example 5.2 In this example, we consider the nonlinear problem ([10], p. 56):

$$\varepsilon y''(x) + y(x)y'(x) - y(x) = 0,\ y(0) = -1,\ y(1) = 3.9995.$$

The concerned linear problem is $\varepsilon y''(x) + (x + 2.9995)y'(x) = x + 2.9995$ (Table 2).

The uniformly valid approximation [5] is $y(x) = x + C_1 \tan \mathrm{h}\left(\left(\frac{C_1}{2}\right)\left(\frac{x}{\epsilon} + C_2\right)\right)$,

where

$$C_1 = 2.9995,\ C_2 = \left(\frac{1}{C_1}\right)\log_e\left(\frac{(C_1-1)}{(C_1+1)}\right).$$

5 Conclusions

A numerical asymptotic scheme is presented for solving two-point singularly perturbed boundary value problems with boundary layer at left end point. Initially, the given problem is converted into two initial value problems for the computation of approximate solution of the given problem. The outer solution of the problem is calculated first and then using this, we calculated the solution of the first initial value problem. With the help of this solution, the second initial value problem is solved with box and trapezoidal schemes. Numerical results are considered for various values of ε and the respective results given in tables. Also, the rate of convergence and maximum absolute errors is tabulated separately. It is noticed that the numerical results of present method are closely approximated to the exact solutions.

Table 1 Maximum point-wise errors E_ε^N and the rate of convergence r_ε^N for Example 5.1

ε	Number of intervals (N)					
	16	32	64	128	256	512
1e−4	9.179e−2 0.9847	4.634e−2 0.9924	2.314e−2 0.9963	1.168e−2 0.9981	5.851e−3 0.9988	2.928e−3
1e−8	9.179e−2 0.9847	4.638e−2 0.9925	2.331e−2 0.9962	1.168e−2 0.9980	5.852e−3 0.9991	2.928e−3
$E^N\ r^N$	9.179e−2 0.9847	4.638e−2 0.9945	2.331e−2 0.9962	1.168e−2 0.9980	5.852e−3 0.9991	

Table 2 Maximum point-wise errors E_ε^N and the rate of convergence r_ε^N for Example 5.1

ε	Number of intervals (N)					
	16	32	64	128	256	512
1e−4	3.092e−2 0.9926	1.554e−2 0.9963	7.792e−3 0.9981	3.901e−3 0.9989	1.952e−3 0.9986	9.770e−4
1e−8	3.092e−2 0.9926	1.554e−2 0.9963	7.792e−3 0.9981	3.901e−3 0.9989	1.952e−3 0.9986	9.770e−4
$E^N\ r^N$	3.092e−2 0.9926	1.554e−2 0.9963	7.792e−3 0.9981	3.901e−3 0.9989	1.952e−3 0.9986	

References

1. Ascher, U., Weis, R.: SIAM J. Sci. Stat. Comput. **5**, 811 (1984)
2. Lin, P., Su, Y.: Appl. Math. Mech. **10**, 1005 (1989)
3. Vulanovic, R.: Computing **41**, 97 (1989)
4. Vulanovic, R., Vychisl, Zh.: Mat. Mat. Fiz. **31**, 522 (1991)
5. O'Malley, R.E.: Introduction to Singular Perturbations. Academic Press, New York (1974)
6. O'Malley, R.E.: Singular Perturbation Methods for Ordinary Differential Equations. Springer, New York (1991)
7. Nayfeh, A.H.: Introduction to Perturbation Techniques. Wiley, New York (1981)
8. Cole, J.D., Kevorkian, J.: Perturbation Methods in Applied Mathematics. Springer, New York (1979)
9. Bender, C.M., Orszag, S.A.: Advanced Mathematical Methods for Scientist and Engineers. McGraw-Hill, New York (1978)
10. Eckhaus, W.: Matched Asymptotic Expansions and Singular Perturbations. North-Holland, Amsterdam (1973)
11. Van Dyke, M.: Perturbation Methods in Fluid Mechanics. Parabolic Press, Stanford (1975)
12. Bellman, R.: Perturbation Techniques in Mathematics, Physics and Engineering, Holt. Rinehart & Winston, New York (1964)
13. Doolan, E.P., Miller, J.J.H., Schilders, W.H.A.: Uniform Numerical Methods for Problems with Initial and Boundary Layers. Boole Press, Dublin (1980)
14. Bawa, R.K., Clavero, C.: Appl. Math. Comput. **216**, 2058 (2010)
15. Ervin, V., Layton, W.: SIAM J. Sci. Comput. **8**, 265 (1987)
16. Kopteva, N., Stynes, M.: Appl. Numer. Math. **39**, 47 (2001)
17. Raji Reddy, N., Mohapatra, J.: Natl. Acad. Sci. Lett. **38**, 355 (2015)